Efficient Diagnosis of Liver Disease using Support Vector Machine Optimized with Crows Search Algorithm

Article *in* EAI Endorsed Transactions on Energy Web · July 2018

DOI: 10.4108/eai.13-7-2018.164177

EAI Endorsed Transactions on Energy Web

Research Article EAI.EU

Efficient Diagnosis of Liver Disease using Support Vector Machine Optimized with Crows Search Algorithm

D. Devikanniga[1,*], Arulmurugan Ramu[1] and Anandakumar Haldorai[2]

[1]Assistant Professor, Presidency University, Bengaluru-560064, Karnataka, India.
[2]Associate Professor, Sri Eshwar College of Engineering, Coimbatore-641202, Tamil Nadu, India.

Abstract

The early and accurate prediction of liver disease in patients is still a challenging task among medical practitioners even with latest advanced technologies. The support vector machines are widely used in medical domain. It has proved its efficiency on producing good diagnostic parameters. These results can be further improved by optimizing the hyperparameters of support vector machines. The proposed work is based on optimizing support vector machines with crow search algorithm. This optimized support vector machine classifier (CSA-SVM) is used for accurate diagnosis of Indian liver disease data. The various similar state of art algorithms are taken for comparison with proposed approach to prove its efficient. The performance of CSA-SVM is found to be outstanding among all other approaches in terms of all metrics taken for comparison. It has yielded the classification accuracy of 99.49%.

Keywords: Crow search algorithm, liver disease, sequential minimal optimization, support vector machine.

Received on 27 March 2020, accepted on 25 April 2020, published on 29 April 2020

doi: 10.4108/eai.13-7-2018.164177

*Corresponding author. Email: mail4kanniga@gmail.com

1. Introduction

Liver is the largest organ in the body. Its main functions include digestion, remove toxins, fights infection, balance hormones and secrete bile juice. There are various liver diseases which are caused due to virus infection, excess amount drugs, poisoning, alcohol, obesity and many other factors. These causes liver failure which significantly damage the body as it leads to improper body functions. This is a life-threatening condition. Some common liver problems include hepatitis, fatty liver disease, liver cancer etc. There are many tests to diagnose liver dysfunction, liver biopsy, viral hepatitis tests, comprehensive metabolic panel, transient elastography etc. The initial stage of liver diseases are mostly unable to diagnose, as the liver functions normally even with partial infections. This creates a challenging task for doctors for accurate prediction at early stage. Early detection and treatment leads to healing of liver rather than leading to critical conditions.

Many machine learning algorithms such as artificial neural networks, decision trees, support vector machine (SVM) and many others are used in the literature for liver data classification. A few recent works are discussed below and their classification results are tabulated below. The classification algorithms such as Naïve Bayes (NB), J48, Random tree (RT), K-Star are implemented using WEKA tool [1]. In [2], various algorithms namely Logistic regression, SVM, RT, Bagging techniques are compared for classification accuracy. Multi layer feed forward deep neural network (MLFFDNN) trained with back-propagation network (BPN) is used in [3]. XGBoost algorithm is used to predict the liver disease data collected from Andhra Pradesh, India. In this L1 and L2 regularization technique is used to improve efficiency [4]. The class imbalance in ILPD is handled using synthetic minority oversampling technique. Then the classification performance is evaluated for both balanced and unbalanced dataset using K-Nearest neighbor (KNN) and SVM [5]. Particle swarm optimization (PSO) is combined with SVM for feature selection and applied for classifying liver data [6].

The liver disease diagnosis done using SVM has found to produce good results. This algorithm works still more efficient when it is combined with heuristic and nature-inspired meta-heuristic optimization algorithms (MHOAs). In [7], the modification of kernel and optimal set of SVM hyperparameters that are found using optimization methods such as random search, grid search and the Nelder–Mead method, has improved the classification accuracy of DNA sequence recognition problem. The learning vector quantization neural network algorithm and the Fisher-SVM coupling algorithm are applied for prediction of hypertension risk in steel workers. The efficiency of this combination is proved for varying sample size [8].

MHOAs jointly work with SVM for tasks such as parameter tuning and feature selection. The two key hyper parameters namely penalty parameter and kernel function width are mostly tuned for better efficiency in many works. A few includes, the MHOAs such as Ant colony optimization and PSO [9], Fruitfly optimization algorithm [10], accelerated PSO [11], Multi-verse optimizer approach [12], Simulated annealing [13] were adopted to find optimal set of parameters for SVM. To improve the SVM classification accuracy in high-dimensional datasets, the feature selection technique is applied with the help of MHOAs such as Grasshopper optimization algorithm [14] and Firefly algorithm [15] is used to train all the parameters of SVM. Many such MHOAs are used with SVM for specific applications. But still these algorithms are found to have some limitations. Most of the times the accurate results are not produced. Thus a robust algorithm that promises high diagnostic accuracy in early prediction is needed to solve the above mentioned issues.

In this work, Crow search optimization algorithm (CSA) [19] is firstly combined with SVM linear kernel to optimize its lagrangian values in order to improve the diagnostic efficiency of liver disease dataset. CSA is chosen among other MHOAs as it contains simple and efficient optimization steps. It also maintains good balance between exploration and exploitation. As it has only two tuning parameters, it is simple to apply and fast. It is also noted that it has proved its efficiency in many similar applications. The calculation of alpha and bias value is the critical task during the training of SVM. Many mathematical optimization algorithms like Quadratic programming, Least squares, SMO etc., have been used. Thus in this paper, the usual procedure of optimizing SVM lagrange values using SMO during training is discussed in steps. Then the details of CSA for optimizing these lagrange values in the place of SMO is illustrated. It is observed that the optimization steps of CSA-SVM is very simple and efficient.

The organization of the paper is as follows, Section 1 gives the introduction, Section 2 provides the details of Indian liver disease dataset, concept of SVM, training of support vector machine parameters with Sequential minimal optimization (SMO), details of CSA, CSA-SVM methodology. Section 3 deals with experimental details, results and performance analysis. Finally, Section 4 concludes the proposed work

2. Materials and methods

2.1. Dataset details

The publicly available Indian liver patient dataset from University of California Irvine machine learning dataset repository [16] is used for this work. This data is collected from patients of north-east Andhra Pradesh, India. It contains 583 samples including 416 diseased liver samples and remaining 167 non-liver diseased samples. It data is tabulated with 10 input attributes and one output class attribute. The attribute details of the dataset is given in Table 1.

Table 1. Attribute details of dataset

Attribute no.	Attribute name	Attribute details
		Input attributes
1	Age	Age of the patient (all subjects greater than 89 are labelled 90)
2	Sex	Gender of the patient Female Male
3	Tot_Bil	Total Bilirubin
4	Dir_Bil	Direct Bilirubin
5	Alk_Phos	Alkaline Phosphotase
6	Alamine	Alamine Aminotransferase
7	Aspartate	Aspartate Aminotransferase
8	Tot_Prot	Total Protiens
9	Albumin	Albumin
10	A_G_Ratio	Albumin and Globulin Ratio
		Output attribute
11	Disease	Disease State (classified labeled by the medical experts) -1 = normal and 1= disease

2.2. Support vector machine

The SVM algorithm was firstly invented by Vladimir N. Vapnik and Alexey Ya. Chervonenkis in 1963. The SVM classifier is a kind of machine learning algorithm that attempts to find an optimal hyperplane with maximum margin [17]. This algorithm separates the linearly separable data samples into two classes. If the data is non-linearly separable, then SVM maps the data into high-dimensional feature space and performs the classification. The equation of the separating hyperplane is given by the Equation (1),

$$H = W^T X + b = 0 \quad (1)$$

where ‘W’ is the normal vector that represents the angle or orientation of the hyperplane in m- dimensional space (synonymously it can be called as width of the margin), ‘X’ is the input vector and ‘b’ is the bias or threshold that represents the position or the distance of the hyperplane from the origin. The canonical hyperplane is defined by Equation (2) for positive samples and Equation (3) for negative samples.

$$H_+ = W^T X + b = +1 \quad (2)$$
$$H_- = W^T X + b = -1 \quad (3)$$

The data samples that lie above the Equation (2) belong to positive class and data samples that lie below the Equation (3) belong to negative class. The data samples that lie on the Equations (2) and Equation (3) are called support vectors. Thus the design of the SVM classifier is influenced by the formation of hyperplane and the position of the support vectors on it. The details of SVM structure is illustrated in the Figure 1.

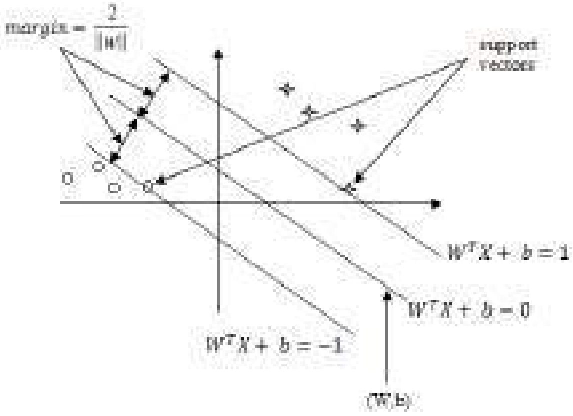

Figure 1. Structure of SVM

From the Figure (1), the equation of the margin is given in Equation (4),

$$margin,\ (\gamma) = \frac{2}{\|W\|_2} \quad (4)$$

where $\|W\|_2 = \sqrt{W^T W}$ (L-2 norm). Now the objective of SVM is to maximize the margin and is carried out by minimizing the L-2 norm. This is mathematically expressed as an optimization equation given in Equation (5).

$$minimize\ \|w\|_2$$

$$subject\ to \quad y_i(W^T X_i + b) \geq 1,\ i = 1,2 \ldots n \quad (5)$$

The above Equation (5) is a constrained convex quadratic optimization subject to linear constraints, so it can be rewritten as Equation (6),

$$Minimize\ \frac{1}{2}\|w\|_2^2 = \frac{1}{2} w^T w$$

$$subject\ to \quad y_i(W^T X_i + b) \geq 1,\ i = 1,2 \ldots n \quad (6)$$

Further, by using the Lagrangian multipliers(α), the above equation is converted into an unconstrained optimization equation as given in Equation(7),

$$\min_{\alpha} \psi(\alpha) = \min_{\alpha} \frac{1}{2} \sum_{i=1}^{n} \sum_{j=1}^{n} Y_i Y_j K(X_i, X_j) \alpha_i \alpha_j - \sum_{i=1}^{n} \alpha_i$$

$$subject\ to \quad \begin{cases} 0 \leq \alpha_i \leq c, \forall i\ ; \\ \sum_{i=1}^{n} y_i \alpha_i = 0 \end{cases} \quad (7)$$

where $K(X_i, X_j)$ is the kernel function value for the training data and c is the box constraint values whose details are discussed in upcoming section.There are many kernel functions such as Linear kernel, Quadratic kernel, Polynomial kernel, Gaussian Radial Basis function and Multilayer Perceptron kernel can be used.

The objective function given in Equation (7) is evaluated using any one of the mathematical optimization algorithms such as SMO, Quadratic programming (QP), Least squares (LS) and so on [18]. The optimal values of alpha and bias are used for classifying the unknown data ‘z’ using Equation (8)

$$Output(Z) = sign\left(\sum_{i=1}^{n} \alpha_i K_{sv,z} + bias\right) \quad (8)$$

Where $K_{sv,z}$ is the kernel function value that gives the similarity or distance between the support vectors and unknown data.

2.3. Optimization of SVM using SMO

The training phase of SVM starts with loading of training data and then the separation of data into input and the target. The input data is shifted and scaled followed by calculation of kernel matrix using a kernel function. Then the box constraint values are calculated. After that the alpha and bias values are calculated using SMO algorithm that results in the calculation of support vectors [18]. Using these support vectors, testing phase is carried out for classification of unknown data.

Steps for optimizing Support vector machines with SMO algorithm

Step 1 Load the data

The training data of size ‘n’ is loaded for training the support vector machine classifier.

Step 2 Separation of training data into input and target

The training data is separated into input and target. Let X = $\{X_1, X_2, \ldots, X_n\}$represents the set of samples(records) in the data. This X contain ‘n1’ number of records that belongs to class 1(positive class) and 'n2' number of that belongs to class2(negative class). Each Xi contains m attributes(features), i.e., $X_i = \{x_{i,1}, x_{i,2}, \ldots, x_{i,m}\}$. Yi is the actual output which may either take -1 for negative class and +1 for positive class. Let $Y_i=\{Y_1,Y_2,\ldots,Y_n\}$ represents the output class label of each record.

Step 3 Shifting the input data

For shifting the input data, first the shiftmean value is calculated. The shiftmean value is the negative of the mean of each column or attribute of the input data and it is calculated using the equation (9) as,

$$Shiftmean, \overline{\mu_j} = \left[\overline{\mu_1} = -\frac{\sum x_{i,1}}{n} \quad \overline{\mu_2} = -\frac{\sum x_{i,2}}{n} \ldots \quad \overline{\mu_m} = -\frac{\sum x_{i,m}}{n}\right],$$
$$i = 1,2 \ldots n, j = 1,2 \ldots m \tag{9}$$

The input data is shifted by adding the shiftmean value of each column with its corresponding column values. It is calculated using the equation (10) as,

$$Shiftdata, Sh_{i,j} = \begin{bmatrix} \overline{\mu_1} + x_{1,1} & \cdots & \overline{\mu_m} + x_{1,m} \\ \vdots & \ddots & \vdots \\ \overline{\mu_1} + x_{n,1} & \cdots & \overline{\mu_m} + x_{n,m} \end{bmatrix}$$
$$i = 1,2,..n; j = 1,2,..m \tag{10}$$

This is to centre the data points at their mean. Shiftdata, sh is the shifted data matrix

Step 4 Scaling the input data

The scalefactor is calculated as one divided by the standard deviation of each column as per the equation (11) given below,

$$\sigma_j = \left[\sigma_1 = \frac{1}{\sqrt{\frac{\sum(x_{i,1} - \overline{\mu_1})^2}{(n-1)}}} \; \sigma_2 = \frac{1}{\sqrt{\frac{\sum(x_{i,2} - \overline{\mu_2})^2}{(n-1)}}} \cdots \sigma_m = \frac{1}{\sqrt{\frac{(x_{i,m} - \overline{\mu_m})^2}{(n-1)}}}\right]$$
$$i = 1,2 \ldots n; j = 1,2 \ldots m \tag{11}$$

The scalefactor of each column is multiplied with the shifted data matrix of its corresponding column using equation (12) as,

$$Scaledata, S_{i,j} = \begin{bmatrix} \sigma_1 Sh_{1,1} & \cdots & \sigma_m Sh_{1,m} \\ \vdots & \ddots & \vdots \\ \sigma_1 Sh_{n,1} & \cdots & \sigma_m Sh_{n,m} \end{bmatrix}$$
$$i = 1,2 \ldots n; j = 1,2 \ldots m \tag{12}$$

The scaled data matrix is used for training the SVM classifer.

Step 5 Selection of Kernel function and calculation of the Kernel matrix

The kernel function maps the training data into kernel space. There are many kernel functions such as Linear kernel, Quadratic kernel, Polynomial kernel, Gaussian Radial Basis function and Multilayer Perceptron kernel. The kernel function is denoted by K(Si,Sj), where Si and Sj are the scaled input vectors. The calculation for Linear kernel is given in the equation (13),

$$K(S_i, S_j) = \langle \varphi(\overrightarrow{S_i}) \cdot \varphi(\overrightarrow{S_j}) \rangle \tag{13}$$

The kernel matrix, Ki,jis calculated by the equation (14).

$$K_{i,j} = \begin{bmatrix} \langle \varphi(\overrightarrow{s_1}) \cdot \varphi(\overrightarrow{s_1}) \rangle & \cdots & \langle \varphi(\overrightarrow{s_1}) \cdot \varphi(\overrightarrow{s_n}) \rangle \\ \vdots & \ddots & \vdots \\ \langle \varphi(\overrightarrow{s_n}) \cdot \varphi(\overrightarrow{s_1}) \rangle & \cdots & \langle \varphi(\overrightarrow{s_n}) \cdot \varphi(\overrightarrow{s_n}) \rangle \end{bmatrix}$$
$$i,j = 1,2 \ldots n \tag{14}$$

The kernel matrix represents the similarities between the input vectors. It is a symmetric and positive semi-definite matrix. The x represents the input vector and K denotes the feature space vector got after the transformation. The kernel function maps the shifted and scaled training data 'S' into kernel space or the feature space vector. Linear kernel, Polynomial kernel, Gaussian Radial Basis function (RBF) are some popular kernel functions listed in Table 2.

Table 2. List of kernel functions

Kernel name	**Kernel function**
Linear Kernel	$K = S^T . S$
RBF kernel	$K = exp\left(-\frac{\lVert S - S^T \rVert^2}{2\omega^2}\right), \forall\ kernel\ width, \omega > 0$
Polynomial Kernel	$K = (1 + S.S^T)^d$, for any degree, d > 0

The purpose of the kernel matrix is to find out the similarities between the input vectors. It is a symmetric and positive semi-definite matrix.

Step 6 Retrieving the diagonal of the Kernel matrix

The diagonal of the kernel matrix is retrieved and given using equation (15) as,

$$K_{diag} = \begin{bmatrix} K_{1,1} \\ K_{2,2} \\ \vdots \\ K_{n,n} \end{bmatrix} \tag{15}$$

Step 7 Calculation of Box constraint values for classes

The Boxconstraint (c) is a value used in the training process to handle the trade-off between training error and complexity of the model. Further this penalty parameter is a boundary condition that decides the number of outliers accepted for the calculation of support vectors. It is of same length as the training data. It is always initialized as 1,[c = 1].It automatically rescales the samples if two groups are unbalanced. The box constraint for each class is calculated using the equation (16) and (17) as,

$$c_1 = \begin{cases} \frac{0.5\, cn}{n_1}, & if\ n_1 \neq n_2; \\ 0.5 & if\ n_1 = n_2. \end{cases} \quad (16)$$

$$c_2 = \begin{cases} \frac{0.5\, cn}{n_2}, & if\ n_1 \neq n_2; \\ 0.5 & if\ n_1 = n_2. \end{cases} \quad (17)$$

In general, smaller value of 'c' makes the classifier flat, larger value makes the training with less error and very larger values make the classifier to start overfitting. Hence an optimal c value is chosen to make the classifier retain its property of generalisation with less training error.

Step 8 Calculation of Alpha and Bias values using Sequential Minimal Optimization (SMO) algorithm

In this section, SMO is discussed to calculate the alpha and bias value. The following are the control parameters to be initialized for SMO algorithm.

In each iteration, the SMO algorithm chooses a pair of the Alpha values (α_1 and α_2) also known as the Lagrange multipliers and optimizes it by solving analytically, till convergence takes place. The existence of the equality constraints makes it impossible to optimize the variables individually which in turn only optimizes the alpha values. Likewise the Alpha values are calculated for all the datapoints, two at a time till the optimum values are obtained, based on the condition 1 that whether the maximum number of iterations reached or when the condition 2 ((α_1-α_2)≤tolKKT) is satisfied. Then the bias or the threshold value is calculated using the equation (18) as,

$$bias = \frac{(\alpha_1 - \alpha_2)}{2} \quad (18)$$

Each datapoint is associated with one alpha value which plays a vital role in qualifying the datapoints as the support vectors. The post condition is the alpha values should be greater than or equal to 0 and less than or equal to the Boxconstraint value, i.e., $0 \le \alpha_i \le c$ where $i = 1,2 \dots n$

Step 8.1 Initialization of training parameters

- Maximum number of iterations, maxIter = [1…5000]
- Tolerance by which the Karush-Kuhn-Tucker (KKT) conditions and stopping criteria are checked, tolKKT= 1.0000e-03
- Episilon(ϵ) = 2.2204e-16
- Tolerance by which support vectors are identified, svTol= square root of ϵ = 1.4901e-08
- KKTViolationLevel=[0,1], specify the fraction of variables allowed to violate the KKT conditions, it is set as 0
- Number of accepted KKT violations, acceptedKKTviolations = 0
- The initial alpha value of all datapoints are initialized with α^{old}(i) 0, i=1,2…n
- The object gradients of the objective function are initialized with $\Delta w = 1$
- The vectors, Box_{+1} and Box_{-1} of class1 and class2 respectively are initialized as,
- $Box_{+1}(i) = \begin{cases} c_1, if y_i = +1 \\ 0, if y_i = -1 \end{cases}$ and
- $Box_{-1}(i) = \begin{cases} -c_2, if y_i = -1 \\ 0, if y_i = +1 \end{cases}$ where $i = 1,2 \dots n$
- The masking vectors for class1 and class2 are $I_{+1} and I_{-1}$ respectively, initialized as,

$I_{+1}(i) = \begin{cases} 1, if y_i = +1 \\ 0, if y_i = -1 \end{cases}$ and

$I_{-1}(i) = \begin{cases} 1, if y_i = -1 \\ 0, if y_i = +1 \end{cases}$

Step 8.2 Calculation of first Alpha value

The first alpha value α1 is calculated using the equation (19) as,

$$\alpha_1 = max(y_i \Delta w_i I_{+1}(i)), \quad i = 1,2 \dots n \quad (19)$$

The index value of α_1 is stored in id_1

Step 8.3 Calculation of second Alpha value using Maximum gain method

The Maximum gain method is used for finding the second alpha value (α2) and its index (id_2) using α_1 and id_1 values. For that, mask values are calculated using the equation(20) as,

$$mask(i) = I_{-1}(i)P, \text{ where } P = \begin{cases} 1, & y_i \Delta w_i < \alpha_1 \\ 0, & otherwise \end{cases}, \quad i = 1,2 \dots n \quad (20)$$

Now calculate the gain value using the equation (21),

$$gainNumerator(i) = (y_i \Delta w_i - 1)^2 mask(i)$$

$$gainDenominator(i) = -4\, k_{i,id1} + 2k_{diag}(i,i) + 2k_{diag}(id1)$$

$$gain = max\left(\frac{gainNumerator(i)}{gainDenominator(i)}\right), \quad (21)$$

where i=1,2,…n, gainNumerator gainDenominator≠ 0

The index value of gain value is the index of the second alpha value (id_2). The α2 is calculated in the equation (22),

$$\alpha_2 = y_{id2} \Delta w_{id2}, \quad i = 1,2 \dots n \quad (22)$$

The alpha values are updated based on stopping condition.

Step 8.4 Checking for the stopping conditions and calculation of Bias value

The condition 1 is to check whether the maximum number of iterations (maxIter) is reached to check for stopping of optimization process. If the condition 2 is true then the bias value is calculated using the equation (10). If the condition fails, then the Lagrange multipliers α1 and α2 are updated till it the convergence occurs. The alpha values are updated before the next iteration. The alpha calculation is stopped if any one or both the conditions are satisfied, which ever be the earliest.

Step 8.5 Updating the Alpha values based on clip limits

The bound constraints, $0 \le \alpha_i \le c_1, c_2$ causes the Lagrange multiplier (LM) to lie within a box, while the Linear equality constraints $\sum_{i=1}^{n} y_i \alpha_i = 0$ makes the LM to lie on the diagonal line segment. The ends of diagonal line is computed with the help of LM. This corresponds to the right orientation of the Hyperplane. The clip limits are calculated using the equation (23),

$$L = \begin{cases} \max(0, \alpha_2 - \alpha_1), & if\, y_{id1} = y_{id2} \\ \max(0, \alpha_2 + \alpha_1 - c_1), & if\, y_{id1} \neq y_{id2} \end{cases} \quad \text{and}$$
$$H = \begin{cases} \min(c_2, c_1 + \alpha_2 - \alpha_1), & if\, y_{id1} = y_{id2} \\ \min(c_2, \alpha_2 - \alpha_1), & if\, y_{id1} \neq y_{id2} \end{cases} \tag{23}$$

The calculation of the second derivative of the objective function, (η) along the diagonal line is given in the equation (24),

$$\eta = k_{id1,id1} + k_{id2,id2} - 2k_{id1,id2} \tag{24}$$

When $\eta > \varepsilon$, then lambda, λ value calculated using equation (25) as,

$$\lambda = -y_{id1}\Delta w_{id1} + y_{id2}\Delta w_{id2} \tag{25}$$

The new second alpha value, α_2^{new} is calculated first using the equation (26),

$$\alpha_2^{new} = \alpha^{old}(id2) + \frac{\lambda y_{id2}}{\eta} \tag{26}$$

Next the constrained minimum is found by clipping the unconstrained minimum to the ends of the line segment i.e., the $\alpha_2^{new} value is clipped$ using the equation (27),

$$\alpha_2^{new,clipped} = \begin{cases} H if\, \alpha_2^{new} \ge H; \\ \alpha_2^{new} if\, L < \alpha_2^{new} < H; \\ L if\, \alpha_2^{new} \le L. \end{cases} \tag{27}$$

Now the new first alpha value, α_1^{new} is calculated first using the equation (28),

$$\alpha_1^{new} = \alpha^{old}(id1) + y_{id1} y_{id2}\left(\alpha^{old}(id2) - \alpha_2^{new,clipped}\right) \tag{28}$$

The α_1^{new} is clipped using the equation (21),

$$\alpha_1^{new,clipped} = \begin{cases} 0, & if\, \alpha_1^{new} < \varepsilon; \\ c_1, & if\, \alpha_1^{new} > \varepsilon; \\ \alpha_1^{new}, & otherwise \end{cases} \tag{29}$$

These alpha values from the equation (27) and (28) are updated in the global array α^{old}.

Step 8.6 Updating the training parameters

The relevant training parameters such as $\Delta w, I_{+1} and I_{-1}$ of the (19) and (20) are updated using the equation (30).

$$\Delta w_i = \Delta w_i - k_{i,id1} y_i y_{id1}\left(\alpha_1^{new,clipped} - \alpha_{id1}^{old}\right) \quad - k_{i,id2} y_i y_{id2}\left(\alpha_2^{new}\right.$$

$$I_{+1}(id1) = \begin{cases} 1, & if\, y_{id1}\alpha_1^{new,clipped} < Box_{+1}(id1) - svTol \\ 0, & otherwise \end{cases}$$
$$I_{+1}(id2) = \begin{cases} 1, & if\, y_{id2}\alpha_2^{new,clipped} < Box_{+1}(id2) - svTol \\ 0, & otherwise \end{cases}$$
$$I_{-1}(id1) = \begin{cases} 1, & if\, y_{id1}\alpha_1^{new,clipped} > Box_{-1}(id1) + svTol \\ 0, & otherwise \end{cases}$$
$$I_{-1}(id2) = \begin{cases} 1, & if\, y_{id2}\alpha_2^{new,clipped} > Box_{-1}(id2) + svTol \\ 0, & otherwise \end{cases}$$

where i = 1,2 …n. (30)

Proceed with the next iteration till the condition1 and 2 gets satisfied.

Step 9 Evaluation of the value of the objective function in Equation (7)

Step 10 Calculation of the Support vectors

The training datapoints are qualified as support vectors of size q with the help of alpha values updated at the end of the training process using the equation (31) as,

$$svindices(j) = index\left(alphas(j) > \sqrt{\varepsilon}\right)$$
$$support\_vectors(j) = K_{svindices(j)}, \quad j = 1,2 \ldots q \tag{31}$$

The kernel matrix with svindices are the support vectors

Step 11 Discrimination of alpha values

The alpha values, α^{old} are classified based on its class labels as α^{hat} using the equation (32),

$$\alpha^{hat}(j) = y(svindices(j))\alpha^{old}(svindices(j)), \quad j=1,2\ldots q \tag{32}$$

This is the final alpha values used for testing process.

Testing phase

Step 12 Load the test data

The test dataZi={Z1,Z2,….Zn} with m attributes as that of training data is loaded for testing the SVM classifier.

Step 13 Shift the test data

The test data is shifted using the equation (33) from the shiftmean calculated from equation (9),

$$Shiftdata_{test}, sh_{test\,i,j} = \begin{bmatrix} \overline{\mu_1} + z_{1,1} & \cdots & \overline{\mu_m} + z_{1,m} \\ \vdots & \ddots & \vdots \\ \overline{\mu_1} + z_{n,1} & \cdots & \overline{\mu_m} + z_{n,m} \end{bmatrix}$$

$$i = 1,2,..n; j = 1,2,..m \quad (33)$$

Step 14 Scale the test data
The shifted test data is scaled using the equation (34) with the scaling factor derived in equation (11),

$$Scaledata_{test}, S_{test\,i,j} = \begin{bmatrix} \sigma_1 sh_{test\,1,1} & \cdots & \sigma_m sh_{test\,1,m} \\ \vdots & \ddots & \vdots \\ \sigma_1 sh_{test\,n,1} & \cdots & \sigma_m sh_{test\,n,m} \end{bmatrix}$$

$$i = 1,2 \ldots n; j = 1,2 \ldots m \quad (34)$$

Step 15 Classification of the test data
The classification function is evaluated and the sign of it denotes the classification of data into class1 and class2. The classification function is given using the equation (35),

$$Output(j) = sign\left(\sum_{j=1}^{n} \alpha_j^{hat} K_{sv,z} + bias\right) \quad (35)$$

where $K_{sv,z}$ is the kernel matrix which gives the similarity or distance between the support vectors and the testing data.If the sign of the output of particular test data is positive, then it belongs to class 1 and else if it is negative, then it belongs to class 2.

2.4. Crow search algorithm

CSA is the most recently developed algorithm by Alireza Askarzadeh in the year 2016 [19]. It is inspired based on intelligent stealing behaviour of clever bird crow. The crows hide extra food in hiding places and retrieve when needed. A crow follows the other that has better food sourceinorder to steal it. From its own stealing experience, it also tries to avoid being a future victim. These behavioural characteristics of crows are simulated as metaheuristic optimization algorithm. The flock of crows forms the population (N). Each crow X_i, [i=1, 2,…N] is considered as search agent, the environment as search space, the hiding places as certain positions which corresponds to feasible solution, the fitness function is based on food source quality where best food source is global best solution.

A d-dimensional environment is assumed, that is each crow is considered as d-dimensional vector. The position of crow i at iteration iter is given as $X^{i,iter}$ where iter=1,2,…max_iter.

$$X^{i,iter} = \left[X_1^{i,iter}, X_2^{i,iter} \ldots X_d^{i,iter}\right] \quad (36)$$

Each crow is associated with memory to memorize the information of its hiding places. The memory of i^{th} crow in iteration iter is given as $m^{i,iter}$. This is considered as best position achieved so far, based on fitness value calculated at each iteration. The crows have the habit of following the other to find their hiding places to steal food. Based on their behavioural strategy, two cases are formulated to update their position. Assume crow i follows crow j,

- Case 1: If crow j does not know that it is followed by crow i, it reaches its hiding place which is also reached by crow i. Hence position is updated for crow i. The new position of crow i is calculated as,

$$X^{i,iter+1} = X^{i,iter} + r_i * fl^{i,iter}(m^{j,iter} - X^{i,iter}) \quad (37)$$

where r_i is random number and $fl^{i,iter}$ denotes flight length of crow i at iteration iter.

- Case 2: If crow j notices that it is followed by crow i, then it tries to fool crow i by reaching some other location randomly. Now the new position of crow i is updated with random value. The case 1 and case 2 depends on value of awareness probability (AP).

2.5. CSA-SVM Methodology

The procedure of CSA-SVM is given below,

Step 1	Initialize population size (N), Maximum iteration (Max_iter), awareness probability (AP), flight length (fl).
Step 2	Initialize the crow population using random values (position of crows).
Step 3	Initialize the memory of crows. For first iteration, its initial positions are considered as memory.
Step 4	The quality of position of each crow is evaluated using the fitness function (Equation 7)
Step 5	The new position of each crow is generated based on two cases, case 1 and case 2.
Step 6	Feasibility of new positions are checked. If it is found better than current, then position update takes place else current one is saved.
Step 7	Fitness of each crow for new position is calculated.
Step 8	The memory of each crow is updated by comparing the new fitness value with memorized one. It is updated with the better one.
Step 9	Check for stopping criterion, that reaching maximum iteration.
Step 10	Steps 5-9 are repeated till max_iter is reached.
Step 11	The optimal or best solution is achieved.

3. Experimental details and discussions

The most widely used algorithms such Genetic algorithm (GA) [20], Multi-verse optimizer (MVO) [21], Firefly algorithm (FA) [22] and PSO [23] are used to optimize

SVM and applied for classification of liver dataset. The results are compared with proposed CSA-SVM. The proposed CSA-SVM and all other comparison SVM hybrids such as MVO-SVM, GA-SVM, FA-SVM and PSO-SVM algorithms are developed in MATLAB R2015b installed in machine with Intel core i5 processor of speed of 2.7 GHz and 4 GB RAM. The details of other MHOAs such as GA, MVO, FA and PSO that are taken for comparison are out of scope for this work and are not further discussed here. As it is necessary to reveal the values that are set for the control parameters of comparison MHOAs used in the experiments, the details regarding it are given in Table 3. All the experiments are conducted using ten-fold cross validation method and averages of results are tabulated in Table 4.

Table 3. Setting of control parameters

Algorithm	Parameter	Value
CSA	flight length (fl)	2.5
	awareness probability (AP)	0.05
MVO	Min wormhole existence ratio	0.2
	Max wormhole existence ratio	1
FA	light absorption coefficient	1
	attractiveness	1
PSO	Acceleration constants (C1,C2)	(2, 2)
	Inertia weight (w)	0.8
GA	Selection	Roulette wheel
	Cross over probability	1
	Mutation probability	0.01

The performance measures such as sensitivity, specificity, precision and accuracy are used to scale the performance along with standard deviation (SD) [24]. The results from the experiments clearly shows that CSA-SVM has the best diagnostic capability than all other hybrid SVMs. It has produced accuracy, specificity, sensitivity and precision of 99.49±0.12, 98.80±0.33, 99.76±0.21 and 99.52±0.51 respectively.

Table 4. Performance comparison of SVM classifiers

Approach	Sensitivity ± SD(%)	Specificity ± SD (%)	Precision± SD (%)	Accuracy± SD (%)
CSA-SVM	99.76±0.21	98.80±0.33	99.52±0.51	99.49±0.12
MVO-SVM	96.15±1.87	92.22±2.11	96.85±0.69	95.03±2.01
GA-SVM	93.99±1.99	95.81±1.32	98.24±1.86	94.51±1.93
FA-SVM	89.66±3.41	79.04±2.52	91.42±2.21	86.62±2.64
PSO-SVM	84.13±2.43	88.02±2.94	94.59±1.57	85.25±2.28

The performance of MVO-SVM and GA-SVM are found to be a little closer. MVO-SVM has the second highest in sensitivity and accuracy as 96.15±1.87 and 95.03±2.01 respectively. GA-SVM is next highest to CSA-SVM in specificity and precision values as 95.81±1.32 and 98.24±1.86 respectively. FA-SVM is competitive with PSO-SVM in diagnostic accuracy. PSO-SVM has yielded least performance in terms of accuracy and sensitivity as 85.25±2.28 and 84.13±2.43 respectively, and this shows that it has not correctly predicted the most positive samples. FA-SVM is least in terms of specificity and precision as 79.04±2.52 and 91.42±2.21 respectively, and from this it is found that it has given the least discrimination ability toward the negative samples. The results prove that CSA-SVM has produced outstanding performance than all classifiers used for comparison. This is plotted in a graph with performance metrics in X-axis versus scaling (in percentage) in Y-axis. This details are shown using Figure 2.

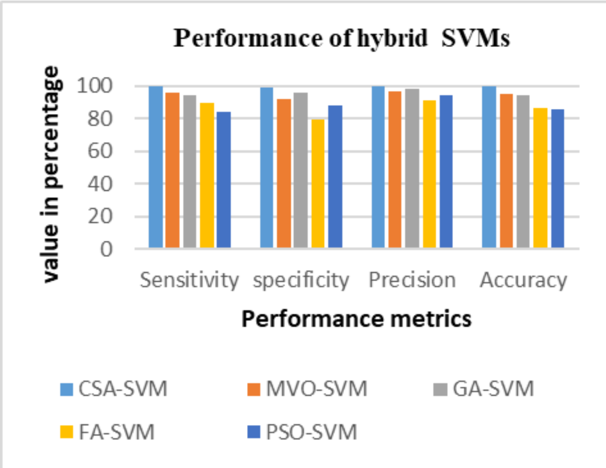

Figure 2. Performance chart of hybrid SVMs

Table 5. Performance comparison of works in literature on Liver disease diagnosis

Works in literature	Approach	Performance (Accuracy)
[1]	NB	60.6%
	K-star	67.2%
	J-48	71.2%
	RT	74.2%
[2]	Logistic regression	73.5%
	SVM	70.94%
	RT	66.66%
	Adaboost	74.35%
	Bagging	72.64%

[3]	MLFFDNN	98%
[4]	XGBoost algorithm	99%
[5]	SVM	73.96%
	K-NN	74.67%
[6]	PSO-SVM	94.42%
[25]	NeuroSVM (SVM + ANN)	98.83%
[26]	Boosted C5.0	93.75%
	CHAID algorithm	65%
[27]	Naïve Bayes(NB)	53.90%
	Decision trees	69.40%
	Multi-layer perceptron (MLP)	67.90%
	k-Nearest Neighbor	65.30%
[28]	J-48	68.78%
	MLP	68.26%
	Random Forest	70.30%
	Bayesian network	67.24%
[29]	Bagging	69.30%
	IBK	64.49%
	J-48	68.78%
	J-Rip	66.38%
	MP	68.95%
	NB	55.75%
Proposed method	CSA-SVM	99.49%

The several works on Liver disease data using various algorithms in literature along with proposed CSA-SVM are tabulated in Table 5 based on accuracy produced by them. This also shows that CSA-SVM has produced better result when compared with others.

4. Conclusion

The optimization of SVM parameters with SMO is dealt. In this work, the lagrange values of support vector machines are optimized using the crow search algorithm. This optimized CSA-SVM classifier applied for the efficient diagnosis of Liver disease. It is noticed that the procedure to optimize SVM with CSA is simpler than with that of SMO. The experiments are carried out using ten-fold cross validation method. Many similar SVM hybrids are taken for comparing the efficiency of CSA-SVM. It is experimentally found that CSA-SVM has good discrimination ability on the liver disease data in terms of performance metrics such as sensitivity, specificity, precision and accuracy. Also the results of various algorithms that are used for liver disease diagnosis in literature are also compared. The overall classification accuracy produced by CSA-SVM is 99.49% which is the highest value. Finally, it is found that CSA-SVM has produced outstanding results than that of other approaches in liver disease data diagnosis. This approach can also be recommended to be used for other disease diagnosis. It is proved that it can help the medical domain in earlier accurate diagnosis of diseases based on the results produced in this proposed work.

References

[1] Muthuselvan S, Rajapraksh S, Somasundaram K, Karthik K, “Classification of Liver Patient Dataset Using Machine Learning Algorithms,” International Journal of Engineering & Technology, vol. 7, 2018, pp. 323-326.

[2] Idris K, Bhoite S, “Applications of Machine Learning for Prediction of Liver Disease,” International Journal of Computer Applications Technology and Research, vol. 8, 2019, pp. 394-396.

[3] Murty S V, Kumar R K, “Enhanced classifier accuracy in liver disease diagnosis using a novel multi layer feed forward deep neural network,” International Journal of Recent Technology and Engineering, vol. 8, 2019, pp. 1392-1400.

[4] Murty S V, Kumar R K, “Accurate Liver Disease Prediction with Extreme Gradient Boosting,” International Journal of Engineering and Advanced Technology, vol.8, 2019, pp. 2288-2295.

[5] Kumar P, Thakur R S, “Early Detection of the Liver Disorder from Imbalance Liver Function Test Datasets,” International Journal of Innovative Technology and Exploring Engineering, vol. 8, 2019, pp. 179-186.

[6] Joloudari J H, Saadatfar H, Dehzangi A, Shamshirband S, “Computer aided decision-making for predicting liver disease using PSO-based optimized SVM with feature selection,” Informatics in medicine unlocked, vol. 17, 2019, 100255

[7] Damaševičius R, “Optimization of SVM parameters for recognition of regulatory DNA sequences,” TOP, vol. 18, 2010, pp. 339-353.

[8] Wu J-H, Wei W, Zhang L, Wang J, Damaševičius R, Li J, Wang H-D, Wang G-L, Zhang X, Yuan J-X, Woźniak M, “Risk assessment of hypertension in steel workers based on LVQ and fisher-SVM deep excavation,” IEEE Access, vol. 7, 2019, pp. 23109-23119

[9] Blondin J, Saad A, "Metaheuristic techniques for Support Vector Machine model selection," *2010 10th International Conference on Hybrid Intelligent Systems*, IEEE, Atlanta, GA, 2010, pp. 197-200.

[10] Huang H , Feng X, Zhou S , Jiang J, Chen H, Li Y, Li C, “A new fruit fly optimization algorithm enhanced support vector machine for diagnosis of breast cancer based on high-level features,” BMC Bioinformatics, vol. 20, 2019, (Suppl 8):290

[11] Yang X S, Deb S, Fong S, “Accelerated Particle Swarm Optimization and Support Vector Machine for Business Optimization and Applications,” in: Networked Digital Technologies (NDT2011), Communications in Computer and Information Science, Vol. 136, Springer, pp. 53-66 (2011).

[12] Faris H, Hassonah M A, Al-Zoubi A M, Mirjalili S, Aljarah I, “A multi-verse optimizer approach for feature selection and optimizing SVM parameters based on a

robust system architecture," Neural Comput&Applic vol. 30, 2018, pp. 2355–2369.
[13] Sartakhti J S, Afrabandpey H, Saraee M H, "Simulated annealing least squares twin support vector machine (SA-LSTSVM) for pattern classification", Soft Computing - A Fusion of Foundations, Methodologies and Applications, 21 (15) , 2016, pp. 4361-4373.
[14] Aljarah I, Al-Zoubi A M, Faris H, Hassonah M A, Mirjalili S, Saadeh H," Simultaneous Feature Selection and Support Vector Machine Optimization Using the Grasshopper Optimization Algorithm," Cognitive Computation, June 2018, Vol. 10, pp 478–495.
[15] Chao C-F, Horng M-H, "The Construction of Support Vector Machine Classifier Using the Firefly Algorithm," Hindawi Publishing Corporation Computational Intelligence and Neuroscience Volume 2015, Article ID 212719, 8 pages.
[16] Dua D, Graff C, UCI Machine Learning Repository, 2019 Irvine, CA: University of California, School of Information and Computer Science, [http://archive.ics.uci.edu/ml].
[17] Corinna C, Vladimir V, "Support Vector Networks," Machine Learning, vol. 20,1995, pp. 273-297.
[18] Platt J, Fast Training of Support Vector Machines using Sequential Minimal Optimization, in Advances in Kernel Methods – Support Vector Learning, MIT Press, 1998.
[19] Askarzadeh A, "A novel metaheuristic method for solving constrained engineering optimization problems: Crow search algorithm", Computers and Structures, vol. 169, 2016, pp. 1–12.
[20] Holland J H, Adaptation in Natural and Artificial Systems, University of Michigan Press, USA, 1975.
[21] Mirjalili S, Mirjalili S M, Hatamlou A, "Multi-Verse Optimizer: a nature-inspired algorithm for global optimization," Neural Comput&Applic, vol. 27, 2016, pp. 495–513.
[22] Yang X-S, "Firefly algorithms for multimodal optimization," in Proceedings of the 5th International Conference on Stochastic Algorithms: Foundation and Applications (SAGA '09), Sapporo, Japan, October 2009, vol. 5792 of Lecture Notes in Computer Sciences, pp. 169–178, Springer, Berlin, Germany, 2009.
[23] Kennedy J, Eberhart R, "Particle swarm optimization," in Proc. IEEE Int. Conf. on Neural Network, Perth, Australia, 1995, pp. 1942–1948
[24] Han J, Kamber M, "Data mining concepts and techniques", 2nd ed., Morgan Kaufmann Publishers Inc. San Francisco. CA. USA, 2001.
[25] Kalyan N, Sridhar A, "NeuroSVM: A Graphical User Interface for Identification of Liver Patients," International Journal of Computer Science and Information Technologies, Vol. 5, 2014, pp. 8280-8284.
[26] Abdar M, Moghadam M Z, Das R, Ting I-H, "Performance analysis of Classification Algorithms on early detection of Liver disease," Expert Systems With Applications, vol.67,2017, pp. 239-251.
[27] Hoon J, Seoungcheon K, Jinhong K, "Decision Factors on Effective Liver Patient Data Prediction," International Journal of Bio-Science and Bio-Technology, vol. 6, 2014, pp. 167-178.
[28] Gulia A, Vohra R, Rani P, "Liver Patient Classification Using Intelligent Techniques," International Journal of Computer Science and Information Technologies, vol.5,2014, pp. 5110-5115.
[29] Ramana B V, Boddu R S K, "Performance Comparison of Classification Algorithms on Medical Datasets," *2019 IEEE 9th Annual Computing and Communication Workshop and Conference (CCWC)*, Las Vegas, NV, USA, 2019, pp. 140-145.

Neural Processing Letters
https://doi.org/10.1007/s11063-020-10327-3

Canonical Correlation Analysis Based Hyper Basis Feedforward Neural Network Classification for Urban Sustainability

Anandakumar Haldorai[1] · **Arulmurugan Ramu**[2]

Abstract

People give more importance concerning the overall quality of the modernized ecosystem. The pollution of air is one of the significant problems to be resolved as it restricted the ecological transformation of the modernized ecosystem. Therefore, it is fundamental to evaluate the implication of these ecological issues to enhance the urban ecosystem. This vital purpose of this research is to propose a canonical correlation analysis based hyper basis feedforward neural network classification (CCA-HBFNNC) model for evaluating sustainable urban environmental quality. The CCA-HBFNNC model initially acquires a large size of U.S. air pollution dataset as input. Then, a canonical correlative analysis based feature selection algorithm is applied in the CCA-HBFNNC model to select the key pollutant features, which bear fundamental implications to the modernize air pollution to maintain the level of urban sustainability. After the feature selection process, the CCA-HBFNNC model applies the HYPER BASIS FEEDFORWARD NEURAL NETWORK CLASSIFICATION (HBFNNC) algorithm in order to classify input air data based on chosen pollutants features. During the classification process, the HBFNNC algorithm used three critical layers namely hidden, output and input layers for efficiently categorizing each input data as higher or lower pollution level with higher accuracy. If the level of air pollution on the urban environment is higher, finally CCA-HBFNNC model significantly reduces the pollution level. In this way, the CCA-HBFNNC model attains improved urban sustainability levels when compared to sophisticated operation. An experimental evaluation of the CCA-HBFNNC model is determined in terms of CCA-HBFNNC model, time complexity and false-positive rate in consideration of the diversified number of air data retrieved from the big data sets. An investigational result shows that the proposed CCA-HBFNNC model can increases the sustainability level and minimizes the time complexity of urban development when contrasted with contemporary works.

✉ Anandakumar Haldorai
anandakumar.psgtech@gmail.com

Arulmurugan Ramu
arulmr@gmail.com

[1] Department of Computer Science and Engineering, Sri Eshwar College of Engineering, Coimbatore, Tamil Nadu, India

[2] Department of Computer Science and Engineering, Presidency University, Bengaluru, Karnataka, India

Published online: [illegible] August 2020

Keywords Air pollution · Big data · Canonical correlation analysis · Gaussian activation function · Hyper basis feedforward neural network · Pollutants features · Urban sustainability

1 Introduction

The terminology ''Big Data' refers to the massive amount of information collected for discovering useful knowledge. The pollution of air is now considered as a fundamental ecological issue in the modern sustainable ecosystem. Recently few research works have been designed for maintaining urban sustainability using different techniques. But, the classification performance of conventional techniques when using big data as input was lower. In order to resolve this drawback, a novel model called Canonical Correlation Analysis Based Hyper Basis Feedforward Neural Network Classification (CCA-HBFNNC) is developed in this research work.

A Hybrid Model was introduced in [1] for increasing a sustainable urban-environmental quality evaluation performance using air pollution data. However, the Sustainability level using this model was lower. A Multiple Criteria Decision Making (MCDM) Framework was introduced in [2] to consider the implications of air pollution on urban sustainability and to identify numerous factors of economic enhancement and air pollutants. But the time utilized for urban sustainable development process was more.

A review of different techniques designed for urban environments in consideration of big data and ecological sustainability referring to data applications have been analyzed in [3]. A novel methodology was presented in [4] for sustainable urban development. However, controlling air pollution levels in the urban environment remained unsolved.

An analytical framework was introduced in [5] to attain the anticipated level of ecological sustainability. But the computational complexity taken for preserving environmental sustainability was very higher. A Planning and Scholarly Technique was applied in [6] to calculated intelligent, sustainable urban development. Nonetheless, the modernized sustainable performance was not enhanced.

The principally enhancing advancements of the big data analytics and context-aware computing were designed in [7] for intelligent, sustainable urban environments. But reducing the air pollution level was not considered. A novel model was designed in [8] to resolve the major ecological and social concerns in the advancement of sustainable urban environments by using the big geospatial data. However, a higher sustainability level was not obtained.

Unique challenges and opportunities involved in big urban data for enhancing the sustainable development goals were analyzed in [9]. But the processing time required for effective urban sustainable development was not reduced. The financial analysis approach was created in [10] to evaluate the potential ecological problems acted upon by the underground spaces that use the modernized form of sustainability. However, the urban sustainability level was not increased while getting big data as input.

To resolve the present issues discussed above, the CCA-HBFNNC model was designed. The most crucial contribution of the CCA-HBFNNC model is described in below,

- To improve the sustainability level on the urban environment when contrasted to the contemporary operations, CCA-HBFNNC model is designed by using canonical correlative analysis-based feature selection (CCA-FS) and hyper basis feedforward neural network classification (HBFNNC) algorithms.

- To enhance the classification performance of big air pollution and thereby achieving a higher sustainability level, the HBFNNC algorithm is proposed in the CCA-HBFNNC model. HBFNNC is a variation of the three layers feed-forward neural systems in which input big air data is passed via the input layer, output layer and hidden layer.

The remaining section of the research is designed as followed. Section 2 proposes the CCA-HBFNNC model is detailed explained with the aid of an architecture diagram. Section 3 shows the experimental settings. The experimental result of the proposed CCA-HBFNNC model is discussed in Sect. 4. In Sect. 5, a detailed literature survey is given. Lastly, the research is wrapped up in Sect. 6.

2 Canonical Correlation Analysis Based Hyper Basis Feedforward Neural Network Classification

Air pollution is q critical environmental concern that can principally impact the urban ecological environment. Certainly, air pollutants are not just dangerous to human health, but can also lead to significant economic loss, which is most evident in developing economies. Therefore, the management and control of air pollutions are currently regarded as a major concern in the social and economic development aspect of the developing nations. Nonetheless, the prevention policy of the management and control of air pollution in the countries is considerably lagging the social and economic developments. As such, the ambient quality of air is significantly deteriorating. Atmospheric pollutants are mainly influenced by air pollutants and their emissions hence leading to a significant advancement of the urban environments and the shrinkage of the green space. Lately, many research works have been designed for controlling air pollution and maintaining urban sustainability. However, the classification accuracy of big pollution data for maintaining higher urban sustainability is was lower. In order to overcome this drawback, canonical correlation analysis based hyper basis feedforward neural network classification (CCA-HBFNNC) model is proposed in this research work.

Contrary to that, the contemporary works, CCA-HBFNNC model is introduced by using the canonical correlative analysis-based feature selection (CCA-FS) and hyper basis feedforward neural network classification (HBFNNC) algorithm. The CCA-FS is designed in the CCA-HBFNNC model to choose the significant pollutant features to bear much significant on the modernized atmospheric pollution with a lower amount of time complexity. In addition to that, the HBFNNC algorithm designed in the CCA-HBFNNC model classifies each data in each big dataset as higher pollution or lower pollution level. Thus, the CCA-HBFNNC model controls air pollutions on the urban environment with higher sustainability and minimal time. The architecture diagram of the CCA-HBFNNC model is shown in below Fig. 1.

Figure 1 demonstrates the overall processes of the CCA-HBFNNC model to get enhanced urban sustainability performance. As presented in the Fig. 2, the CCA-HBFNNC model includes two main processes namely feature selection and classification for effective, sustainable urban development. During the feature selection process, the CCA-HBFNNC model applies canonical correlative analysis-based feature selection (CCA-FS), where it selects the pollutant features that are more related to maintain urban sustainability with lower time complexity.

During the classification process, the CCA-HBFNNC model employs Hyper Basis Function Network with aiming at classifying each data into corresponding classes (higher pollution or lower pollution level) with higher accuracy. From the above big pollutant data classification result, the CCA-HBFNNC model significantly controls the pollutions level and thereby

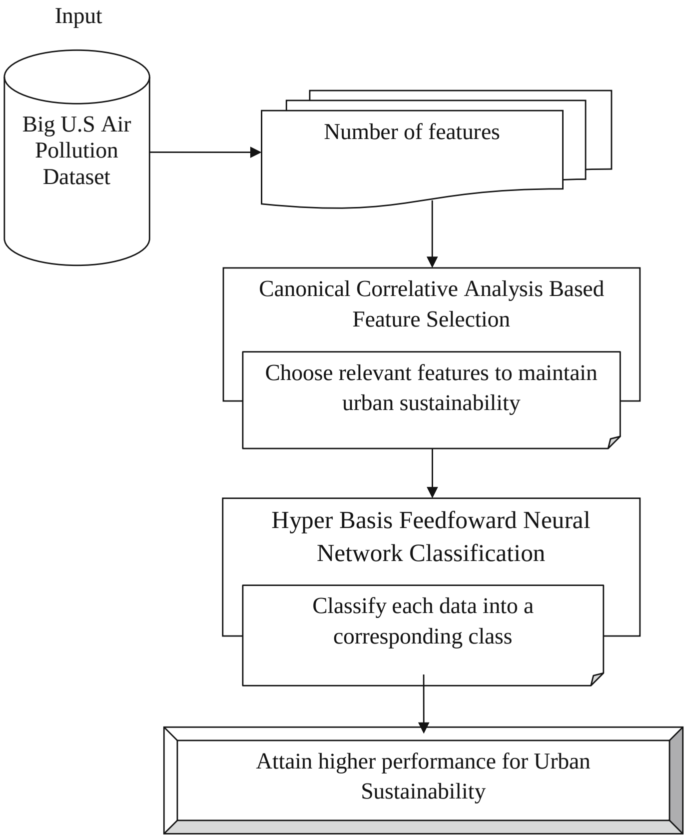

Fig. 1 Architecture diagram of CCA-HBFNNC model for urban sustainability

improves urban sustainability performance as compared to existing works. The detailed processes of the CCA-HBFNNC model are described in the below subsections.

2.1 Canonical Correlative Analysis Based Feature Selection

The pollution of the environment is a result of a multiple factor interaction in the complex earth atmosphere. As such, there are many pollutants that have to lead to air pollution. In order to simplify our research, we have to evaluate many vital pollutants, which have a vital implication to the modernized air pollution. Therefore, The canonical correlative analysis-based feature selection (CCA-FS) is designed in the CCA-HBFNNC model. The CCA-FS algorithm improves the feature selection performance with a minimal amount of time in order to efficiently maintain urban sustainability. The processes involved in the CCA-FS algorithm is depicted in Fig. 2.

Figure 2 shows the processes of the CCA-FS algorithm. As shown in the figure, Canonical correlation analysis initially is employed in CCA-FS algorithm to identify the associations between two features 'f_1' and 'f_2' in given big air pollution air dataset. Let consider two features. 'f_1' and 'f_2', and there are correlations among the information, then Canonical

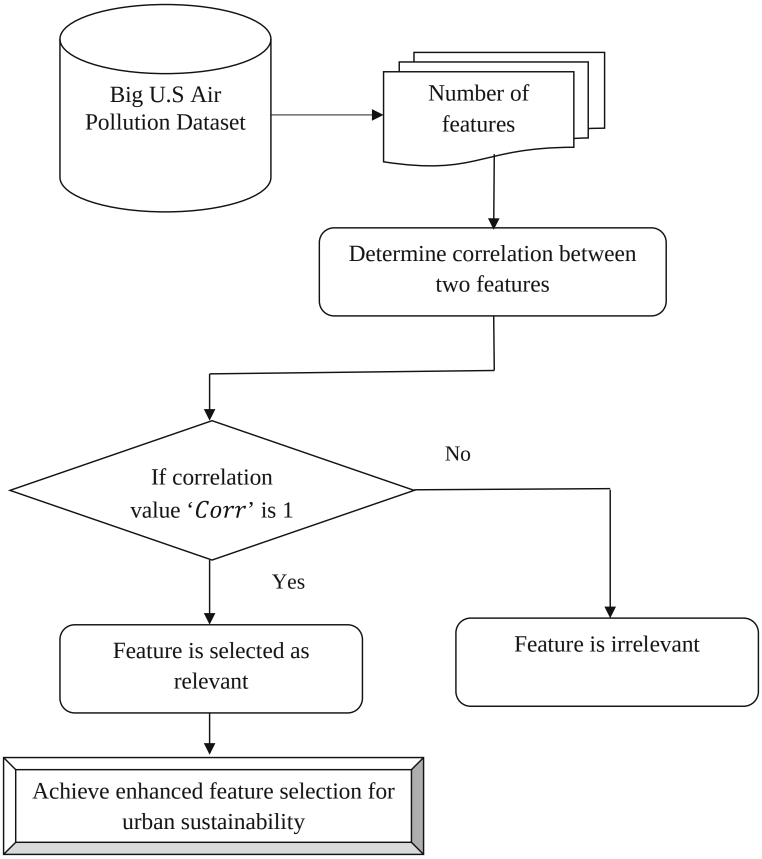

Fig. 2 Flow processes of CCA-FS algorithm

correlation analysis discovers linear combinations of A and B which have a maximum correlation with each other. Thus, Canonical correlation analysis is mathematically determined using the Eq. (1) expression,

$$Corr \rightarrow \sum f_1 f_2 = Cov(f_1,\ f_2) \tag{1}$$

From the above Eq. (1), the covariance matrix is determined by considering information from of features ‘ f_1’ and ‘ f_2’. In C the CA-FS algorithm, the covariance between input features. ‘ f_1’ and ‘ f_2’ is measured using below mathematical formula in Eq. (2),

$$Cov(f_1,\ f_2) = \frac{\sum(f_1 - f_1)(f_2 - f_2)}{n} \tag{2}$$

From the above mathematical expression (2), ‘ f_1’ represents the values of the data in features ‘ f_1’ and ‘ f_2’ denotes the values of data in features ‘ f_2’. Here, ‘ $\bar{f}_1$’ indicates the mean of the features ‘ f_1’ and ‘ $\bar{f}_2$’ refers to the features ‘ f_2’ and ‘n’ represents a total number of the features in a given big dataset. By using the above Eqs. (1) and (2), **the** CCA-FS algorithm evaluates the relationship between the two air features. From that, the CCA-FS algorithm selects the features with a higher correlation value as significant to enhance the performance of urban sustainability.

The algorithmic processes of CCA-FS algorithm are explained in below,

// Canonical Correlative Analysis Based Feature Selection algorithm

Input: U.S Air Pollution Dataset : Number of features '$\{f_1, f_2, \ldots, f_n\}$';

Output: Select relevant features for increasing urban sustainability

Step 1:Begin

Step 2: **For** each input feature. 'f_i'

Step 3: Measure covariance '$Cov(A, B)$' using (1)

Step 4: Compute the canonical correlation '$Corr$ using (2)

Step 5: **If** ($Corr\ is\ 1$)**, then**

Step 6: Select features. 'f_i' as relevant

Step 7: **Else**

Step 8: Remove feature f_i as irrelevant

Step 9: **End If**

Step 10: **End For**

Step 11:End

Algorithm 1 Canonical Correlative Analysis Based Feature Selection

Algorithm 1 illustrates the detailed processes of Canonical Correlative Analysis Based Feature Selection. By using the above algorithmic process, CCA-FS algorithm efficiently choose the features that are more significant for increasing urban sustainability with a lower amount of time consumption. Hence, the CCA-FS algorithm attains enhanced feature selection performance for effective urban environmental sustainability as contrasted to the present works. Resultantly, the CCA-FS algorithm assures an effective performance-based on feature assortment time and accuracy to the sophisticated works.

2.2 Hyper Basis Feedforward Neural Network Classification

In the CCA-HBFNNC model, the hyper basis feedforward neural network classification (HBFNNC) algorithm is a special type of feedforward neural network using the Gaussian activation function. The HBFNNC algorithm takes several data with selected features from a big dataset as input. The HBFNNC algorithm contains input, hidden and output layers in order to classify each collected air data into as higher pollution or lower pollution with higher accuracy for urban environmental sustainability. The process involved in the HBFNNC algorithm is presented in Fig. 3.

Figure 3 shows the flow processes of the HBFNNC algorithm to get a better urban sustainability level through classifying big air data. As presented in the above figure, the HBFNNC algorithm at first gets several data with chosen features as input. After taking input, the

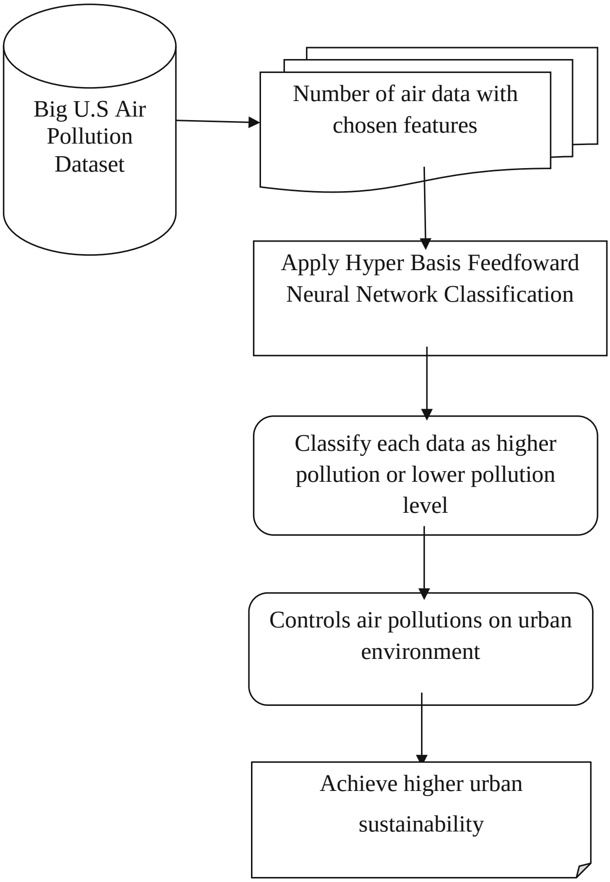

Fig. 3 HBFNNC algorithm process for maintaining urban sustainability

HBFNNC algorithm classifies each data as higher pollution or lower pollution level by considering selected features. According to the classification result of big air data, finally, HBFNNC algorithm reduces pollutions levels in the urban environment. From that, the HBFNNC algorithm obtains increased urban sustainability whenever contrasted with the prevailing works. A structure diagram of the HBFNNC algorithm is presented in Fig. 4.

As presented in the above structural diagram shows HBFNNC includes of three layers that are interconnected. The first layer includes input neurons which acquire the number of air data with chosen features as input. Those neurons send each input air data on to the second layer called a hidden layer. The hidden layer in HBFNNC analyzes the input big air data using the activation function and returns the classification result to the third layer called the output layer. Every interconnection in HBFNNC contains a strength called weight. The weight is indicated by a number. The HBFNNC learns input big air data adjusting the weights of each neuron to get higher classification accuracy for maintaining urban sustainability with minimal time.

The HBFNNC algorithm utilized the Gaussian activation function that significantly determines the relationship between the input big air data. In the HBFNNC algorithm, the output of the Gaussian activation function is lies between the ‘0’ or ‘1’. From that, Gaussian acti-

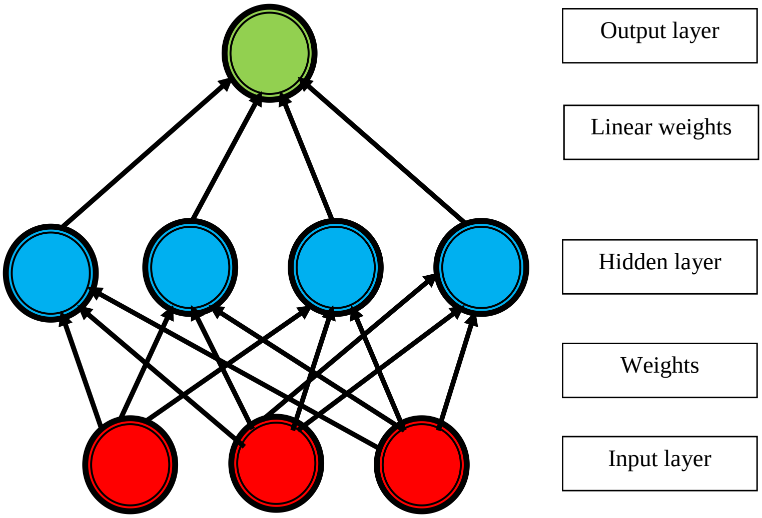

Fig. 4 Structure diagram of HBFNNC

vation function 'GAF' output in the hidden layer is mathematically obtained using below formula,

$$\mathrm{GAF}(d_i) = \frac{1}{\sqrt{2\pi\sigma}} e^{\frac{-(d_i - m)^2}{2v^2}} \tag{3}$$

From the above mathematical Eq. (3), 'd_i' denotes input big air data. Here, 'm' and 'v' represent the mean and variance value of air data. The output of the Gaussian activation function '1' denotes that there is a higher pollution level whereas '0' indicates that the lower pollution level. For each, the trained input big air data, then HBFNNC algorithm measures error rate '$e(t)$' using below,

$$e(t) = TO_i - AO_i \tag{4}$$

From the above mathematical Eq. (4), the HBFNNC algorithm determines the error rate for each classification result. Here, 'TO_i' denotes a target output whereas. 'A_i' is an actual output. Subsequently, the HBFNNC algorithm updates the weights on the network based on the calculated error rate. The processes of the HBFNNC algorithm is continual until the error value is very minimum to accurately classify input big air data and thereby effectively controlling air pollution level.

The algorithmic processes of HBFNNC are explained below,

// **Hyper Basis Feedforward Neural Network Classification Algorithm**
Input: Number of air data. '$\mu_i = \mu_1, \mu_2, .., \mu_n$' ,
Output: Achieve higher urban sustainability level
Step 1: Begin
Step 2: Initialize network with random weights
Step 3: **While ('**$e(t)$' is minimal**) do**
Step 4: **For** each input data 'μ_i' with selected significant features at the input layer
Step 5: Input layer forward received data. 'μ_i' to a hidden layer
Step 6: Hidden layer apply the activation function to find the classification result using (3)
Step 7: Hidden layer forwards discovered result in the output layer
Step 8: Output layer gives classification result
Step 9: **End for**
Step 10: Determine error rate '$\tau(t)$' using (4)
Step 11: Update weights on network
Step 12: **End while**
Step 13: **If** (GAF(d_i) = 1) **then**
Step 14: Classify data as higher pollution level
Step 15: **Else**
Step 16: Classify data as lower pollution level
Step 17: **End If**
Step 18: **If (the** pollution level is higher**), then**
Step 19: Controls air pollution level and thereby increase urban sustainability
Step 20: **End If**
Step 20: End

Algorithm 2 Hyper Basis Feedforward Neural Network Classification

Algorithm 2 explains the detailed procedure of HBFNNC. By using the above algorithmic process, HBFNNC precisely classifies each collected air data from the big dataset as a higher or lower pollution level with a lower amount of time consumption. Thus, the CCA-HBFNNC model reduces or eliminates the air pollution level of an urban environment to achieve higher sustainability when compared to contemporary works.

3 Experimental Settings

In order to estimate the performance of proposed, CCA-HBFNNC model is implemented in Java Language using a big dataset i.e. U.S Air Pollution Dataset [11]. This dataset contains air pollution in the U.S. since 2000–2016 with the main pollutants (Sulphur Dioxide, Nitrogen Dioxide, Ozone and Carbon Monoxide). Apart from the pollutant, this set of data includes the features e.g. State Code, County Code, Site Num, Address, State, County, City, Date Local, NO2 Units, NO2 Mean, NO2 1st Max Value, NO2 1st Max Hour, NO2 AQI, O3 Units, O3 Mean, O3 1st Max Value, O3 1st Max Hour, O3 AQI, SO2 Units, SO2 Mean, SO2 1st Max Value, SO2 1st Max Hour, SO2 AQI, CO Units, CO Mean, CO 1st Max Value, CO 1st Max Hour, CO AQI. Also, U.S Air Pollution Dataset contains 1,048,576 instances.

For conducting the experimental evaluation, the CCA-HBFNNC model considers a diverse number of air data in the range of 1000–10,000. The performance of the CCA-HBFNNC model is measured in terms of sustainability, time complexity and false-positive rate in consideration of the various number of atmospheric data. The experimented findings of the CCA-HBFNNC model are compared with two existing works namely the Hybrid Model [1] and the Multiple Criteria Decision Making (MCDM) framework [2].

4 Results

In this part, the contrasting findings of the CCA-HBFNNC framework are evaluated. The efficiency of the CCA-HBFNNC model is compared with the Hybrid Model [1] and Multiple Criteria Decision Making (MCDM) framework [2] respectively using the below parameters with the help of tables and graphical diagrams.

4.1 Performance Measure of Sustainability Level

In the CCA-HBFNNC model, the Sustainability level is measured in terms of classification accuracy of big air data. As only a correct classification of the air data helps the CCA-HBFNNC model to control the pollution level of an urban environment. From that, the Sustainability level 'SL' measures the ratio of several air data that are correctly classified for controlling pollution level to the total number of air data taken for conducting the experimental process. The Sustainability is computed mathematically using Eq. (5),

$$SL = \frac{n_{AC}}{n} * 100 \tag{5}$$

From the above mathematical representation (5), 'n_{AC}' signifies a number of accurately classified air data for controlling pollution level in which 'n' point out a total number of air data. Sustainability is determined based on its percentage (%).

Sample Calculation:

- **Proposed CCA-HBFNNC**: The atmospheric data categorically computed is 960, and the overall number of atmospheric data is 1000. As such, sustainability is attained as shown below.

$$SL = \frac{960}{1000} * 100 = 96\%$$

- **Existing Hybrid Model:** The atmospheric data categorically computed is 840, and the overall number of atmospheric data is 1000. As such, sustainability is attained as shown below.

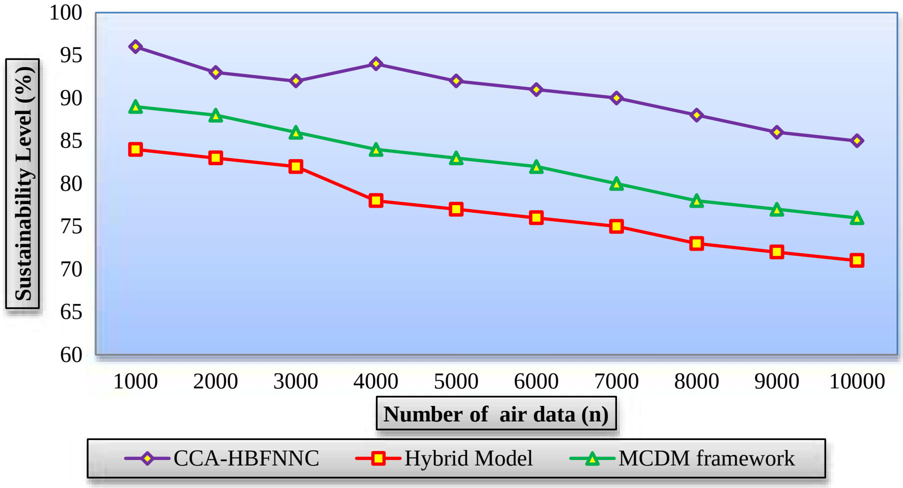

Fig. 5 Simulation result of sustainability level versus number of air data

$$SL = \frac{840}{1000} * 100 = 84\%$$

- **Existing MCDM framework:** The number of air data exactly clustered is 890 and the total number of air data is 1000. Then the sustainability is computed as follows,

$$SL = \frac{890}{1000} * 100 = 89\%$$

Figure 5 depicts experimental result analysis of sustainability level based on varied numbers of air data falling between 1000 and 10,000 based on the application of three approaches, namely the proposed CCA-HBFNNC model and existing Hybrid Model [1] and MCDM framework [2]. As illustrated above, the proposed CCA-HBFNNC model achieves enhanced sustainability level with the advancing amount of atmospheric data as an input when contrasted to the conventional Hybrid Framework [1] including the MCDM framework [2]. This calls for the application of the Canonical Correlative analysis-based feature selection (CCA-FS) and Hyper Basis Feedforward Neural Network Classification (HBFNNC) algorithm in proposed CCA-HBFNNC model that contrasts the contemporary works. By using the above algorithmic concepts, the proposed CCA-HBFNNC model exactly finds and controls the air pollutions level on the urban environment by means of classifying air data. From that, the proposed CCA-HBFNNC model advances the ratio of atmospheric data when classified properly with the predictable Hybrid Framework [1], including the MCDM framework [2]. Accordingly Table 1 result, the proposed CCA-HBFNNC model improves the sustainability level of the urban environment by 18% and 10% when compared to the Hybrid Model [1] and MCDM framework [2] respectively.

Table 1 Experimental result of sustainability level

Number of air data (n)	Sustainability level (%)		
	CCA-HBFNNC	Hybrid model	MCDM framework
1000	96	84	89
2000	93	83	88
3000	92	82	86
4000	94	78	84
5000	92	77	83
6000	91	76	82
7000	90	75	80
8000	88	73	78
9000	86	72	77
10,000	85	71	76

4.2 Performance Measure of Time Complexity

In the CCA-HBFNNC model, Time Complexity 'TC' determines the amount of time taken to control pollution level through classifying big air data. The time complexity is mathematically estimated using below formula shown in Eq. (6),

$$TC = n * t(CS) \tag{6}$$

From the above mathematical expression (6), '$t(CS)$' symbolizes a time utilized to classify a single air data, and 'n' refers to the overall amount of atmospheric data designed for experimentation. The time complexity for maintaining urban sustainability is evaluated in milliseconds (ms).

Example Scheming for Time Complexity:

- **Proposed CCA-HBFNNC**: the amount of time employed to classify single air data is 0.024 ms, and the overall number of atmospheric data is 1000. As such, the duration complexity is mathematically calculated as follows,

$$TC = 1000 * 0.024 = 24\,\text{ms}$$

- **Existing Hybrid Model:** the amount of time taken to classify single air data is 0.032 ms, and the overall number of atmospheric data is 1000. As such, the duration complexity is mathematically evaluated as follows,

$$TC = 1000 * 0.032 = 32\,\text{ms}$$

- **Existing MCDM framework:** the amount of time used to classify single air data is 0.035 ms, and the overall number of atmospheric data is 1000. As such, the duration complexity is mathematically determined as follows,

$$TC = 1000 * 0.035 = 35\,\text{ms}$$

Figure 6 shows performance results analysis of time complexity involved during the process of sustainable urban development according to diverse numbers of air data falling between 1000 and 10,000 based on the application of three approaches namely the proposed

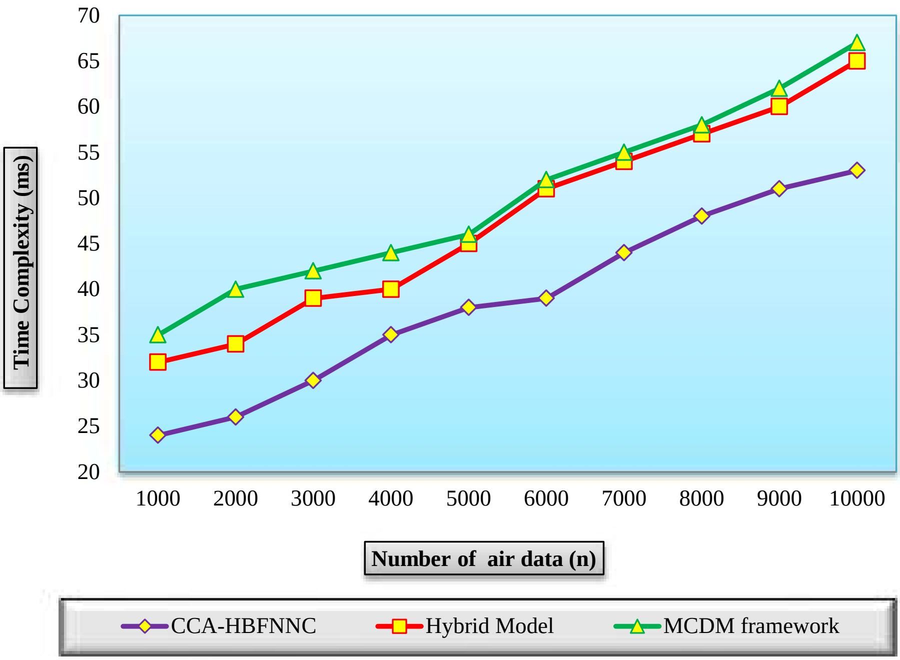

Fig. 6 Simulation result of time complexity versus number of air data

CCA-HBFNNC framework and the present Hybrid Framework [1], including the MCDM Model [2]. According to the Fig. 6 above the proposed CCA-HBFNNC model obtains minimal time complexity for enhancing the modernized sustainability with an enhancing number of atmospheric data of input upon comparison with the ancient Hybrid Framework [1], including the MCDM Model. This is due to the application of the Canonical Correlative analysis based feature selection (CCA-FS) and Hyper Basis Feedforward Neural Network Classification (HBFNNC) algorithm in proposed CCA-HBFNNC model, which is contrary to the present works. Based on the support of the above algorithmic process, the proposed CCA-HBFNNC model minimizes the air pollutions level on the urban environment through classifying air data with minimal time. Thus, the proposed CCA-HBFNNC model reduces the amount of time required to control the pollution level whenever contrasted with the present Hybrid Models [1], including the MCDM framework [2]. As a result in Table 2, the proposed CCA-HBFNNC model decreases time complexity for maintaining urban sustainability by 19% and 23% when compared to the Hybrid Model [1] and MCDM framework [2] respectively.

4.3 Performance Measure of False Positive Rate

In the CCA-HBFNNC model, False Positive Rate (FPR) considers the ratio number of the air data that are incorrectly classified for controlling pollution level to the overall number of atmospheric data. The false-positive rate is evaluated mathematically using below,

$$FPR = \frac{n_{IC}}{n} * 100 \tag{7}$$

Table 2 Experimental result of time complexity

Number of air data (n)	Time complexity (ms)		
	CCA-HBFNNC	Hybrid model	MCDM framework
1000	24	32	35
2000	26	34	40
3000	30	39	42
4000	35	40	44
5000	38	45	46
6000	39	51	52
7000	44	54	55
8000	48	57	58
9000	51	60	62
10,000	53	65	67

Based on the mathematics equation shown in (7), n_{IC}' shows the number of inaccurately classified air data for controlling the pollution level in which 'n' refers to the overall number of atmospheric data. The false-positive rate of modernized sustainability is evaluated based on a percentage (%).

Sample Calculation:

- **Proposed CCA-HBFNNC**: The Number of atmospheric data defectively categorized is 40, and the overall number of atmospheric data is 1000. Thus, the false-positive rate is considered as;

$$\text{FPR} = \frac{40}{1000} * 100 = 4\%$$

- **Existing Hybrid Model:** The Number of atmospheric data defectively categorized is 160, and the overall number of atmospheric data is 1000. Thus, the false-positive rate is considered as;

$$\text{FPR} = \frac{160}{1000} * 100 = 16\%$$

- **Existing MCDM framework:** The Number of atmospheric data defectively categorized is 110, and the overall number of atmospheric data is 1000. Thus, the false-positive rate is considered as;

$$\text{FPR} = \frac{110}{1000} * 100 = 11\%$$

Figure 7 presents the considerable finding evaluation of the false-positive rate of urban sustainability along with various numbers of air data in the dimension of 1000 and 10,000 based on three vital frameworks namely the proposed CCA-HBFNNC model and traditional Hybrid Model [1] and MCDM framework [2]. As depicted in the figure shown above, the proposed CCA-HBFNNC model attains a lower false-positive rate with an enhancing amount of air data considered as the input whenever contrasted to the ancient Hybrid Framework [1], including the MCDM framework [2]. This is because of the application of the Canonical Correlative analysis based feature selection (CCA-FS) and Hyper Basis Feedforward Neural Network Classification (HBFNNC) algorithm in proposed CCA-HBFNNC model

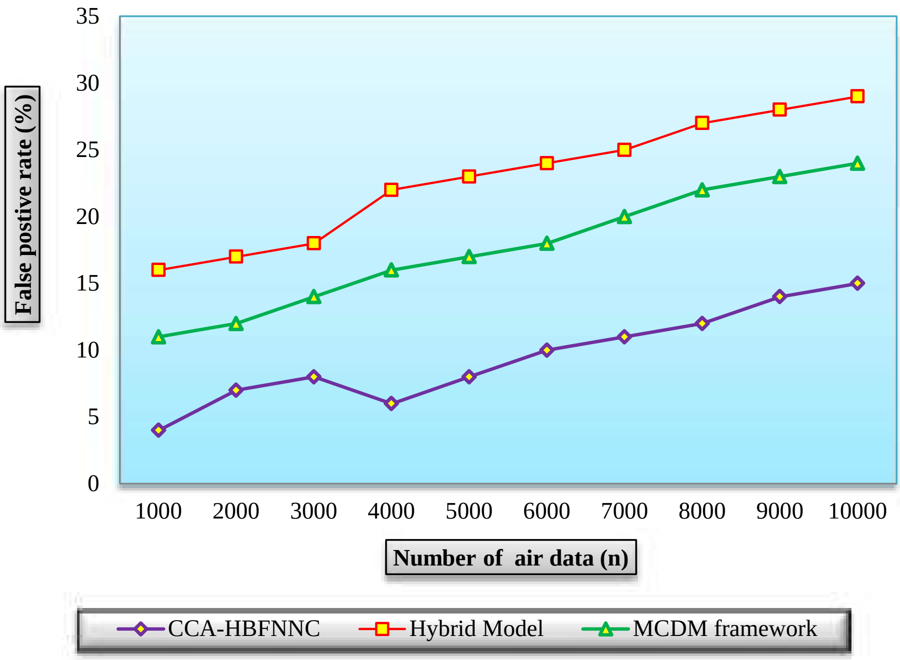

Fig. 7 Simulation result of false positive rate versus number of number of air data

contrary to the conventional operations. Based on the algorithmic process shown above, the proposed CCA-HBFNNC model correctly classifies gathered air data from a big dataset in order to decreases the air pollutions level on the urban environment. Therefore, the proposed CCA-HBFNNC model lessens the ratio of atmospheric data, which is mistakenly classified for controlling pollution level whenever contrasted to the present Hybrid Frameworks [1], including the MCDM framework [2]. Thus, the proposed CCA-HBFNNC model shown in Table 3 reduces the false-positive rate for attaining higher urban sustainability by 60% and 48% when compared to the Hybrid Model [1] and MCDM framework [2] respectively.

5 Literature Survey

Spatiotemporal dynamics of nitrogen dioxide pollution was solved in [12] for urban development. A novel methodology was presented in [13] for reviewing the sustainability of the intelligent urban environment based on the application of Smart inability approach.

Support Vector Machine based Evaluation system was presented in [14] for ecological enhancement of the modernized transportation and environmental aspects. Green infrastructure was employed in [15] to get better urban air quality.

A novel technique was detailed in [16] to evaluate the association of urban pollution, urban sustainability, and urban livability. The knowledge-based urban development strategy was presented in [17] for smart and sustainable city assessment.

A new model was developed in [18] for enhancing the city's ecological sustainability for different city clusters and geographical areas in China. An assessment of key applications of remote sensing in urban sustainability was designed in [19].

Table 3 Experimental result of false positive rate

Number of air data (*n*)	False positive rate (%)		
	CCA-HBFNNC	Hybrid model	MCDM framework
1000	4	16	11
2000	7	17	12
3000	8	18	14
4000	6	22	16
5000	8	23	17
6000	10	24	18
7000	11	25	20
8000	12	27	22
9000	14	28	23
10,000	15	29	24

A Conceptual Multidimensional Model was designed in [20] for evaluating the evaluation of an intelligent sustainable urban environment. In [21], the novel contribution of the intelligent urban environment tools and techniques to enhance sustainable city improvement in the ecological domain was analyzed [22, 23].

6 Conclusion

An effective CCA-HBFNNC model is designed with the aim of increasing urban sustainability via classifying big air data. The objective of the CCA-HBFNNC model is attained with the help of Canonical Correlative analysis-based feature selection (CCA-FS) and Hyper Basis Feedforward Neural Network Classification (HBFNNC) algorithm different from the convectional research works. The planned CCA-HBFNNC frameworks enhance the ratio number of air data correctly classified in order to significantly maintain the urban sustainability level by reducing pollution levels when compared to other conventional works. Besides, the proposed CCA-HBFNNC model decreases the amount of time required to control the pollution level whenever contrasted to the present convectional works. Moreover, the proposed CCA-HBFNNC model minimizes the ratio of several air data that are wrongly classified for reducing pollution levels for sustainable urban development whenever contrasted to the present convectional works. The efficiency of the CCA-HBFNNC model is calculated in terms of sustainability level, time complexity, including the false-positive rate in consideration of the dissimilar number of air data. The investigational findings illustrate that the proposed CCA-HBFNNC model provides better urban sustainable development performance if contrasted to the conventional works.

References

1. Shao Q, Weng S-S, Liou JJH, Lo H-W, Jiang H (2019) Developing a sustainable urban-environmental quality evaluation system in China based on a hybrid model. Int J Environ Res Public Health 16(8):1–25
2. Wang Q, Dai H-N, Wang H (2017) A smart MCDM framework to evaluate the impact of air pollution on city sustainability: a case study from China. Sustainability 9(6):1–17

3. Bibri SE (2019) On the sustainability of smart and smarter cities in the era of big data: an interdisciplinary and transdisciplinary literature review. J Big Data 6(25):1–64
4. Angelidou M, Psaltoglou A, Komninos N, Kakderi C, Tsarchopoulos P, Panori A (2018) Enhancing sustainable urban development through smart city applications. J Sci Technol Policy Manag 9(2):146–169
5. Bibri SE (2018) The IoT for smart sustainable cities of the future: an analytical framework for sensor-based big data applications for environmental sustainability. Sustain Cities Soc Elsevier 38:230–253
6. Bibri SE (2018) Approaches to futures studies: a scholarly and planning approach to strategic smart sustainable city development. Smart sustainable cities of the future. Springer, Cham, pp 601–660
7. Bibri SE, Krogstie J (2017) The core enabling technologies of big data analytics and context-aware computing for smart sustainable cities: a review and synthesis. J Big Data Springer 4:38
8. Sun Y, Du Y (2017) Big data and sustainable cities: applications of new and emerging forms of geospatial data in urban studies. Open Geospatial Data Softw Stand Springer 2(24):1–4
9. Kharrazi A, Qin H, Zhang Y (2016) Urban big data and sustainable development goals: challenges and opportunities. Sustainability 8:1–6
10. Qiao Y-K, Peng F-L, Sabri S, Rajabifard A (2019) Socio-environmental costs of underground space use for urban sustainability. Sustain Cities Soc Elsevier 51:101757
11. U.S. Air Pollution Dataset: https://data.world/data-society/us-air-pollution-data
12. Arulmurugan R, Anandakumar H (2018) Early detection of lung cancer using wavelet feature descriptor and feed forward back propagation neural networks classifier. In: Lecture notes in computational vision and biomechanics, pp 103–110. https://doi.org/10.1007/978-3-319-71767-8_9
13. Cuia Y, Zhang W, Bao H, Wang C, Cai W, Jian Yu, Streets DG (2019) Spatiotemporal dynamics of nitrogen dioxide pollution and urban development: satellite observations over China, 2005–2016. Resour Conserv Recycl Elsevier 142:59–68
14. Girardi P, Temporelli A (2017) Smartainability: a methodology for assessing the sustainability of the smart city. Energy Procedia Elsevier 111:810–816
15. Arulmurugan R, Anandakumar H (2018) Region-based seed point cell segmentation and detection for biomedical image analysis. Int J Biomed Eng Technol 27(4):273
16. Lu S, Liu Y (2018) Evaluation system for the sustainable development of urban transportation and ecological environment based on SVM. J Intell Fuzzy Syst 34(2):831–838
17. Nick Hewitt C, Ashworth K, Rob MacKenzie A (2020) Using green infrastructure to improve urban air quality (GI4AQ). Ambio Springer 49(1):62–73
18. del Mar Martínez-Bravo M, Martínez-del-Río J, Antolín-Lopez R (2019) Trade-offs among urban sustainability, pollution and livability in European cities. J Clean Prod Elsevier 224:651–660
19. Chang DL, Sabatini-Marques J, da Costa EM, Selig PM, Yigitcanlar T (2018) Knowledge-based, smart and sustainable cities: a provocation for a conceptual framework. J Open Innov Technol Market Complex Springer 4(5):1–17
20. Tao Yu, Li F, Crittenden J, Lu Z, Ou W, Song Y (2019) Measuring urban environmental sustainability performance in China: a multi-scale comparison among different cities, urban clusters, and geographic regions. Cities Elsevier 94:200–210
21. Kadhim N, Mourshed M, Bray M (2016) Advances in remote sensing applications for urban sustainability. Euro-Mediterr J Environ Integr Springer 1(7):1–22
22. Al-Nasrawi S, Adams C, El-Zaart A (2015) A conceptual multidimensional model for assessing smart sustainable cities. JISTEM J Inf Syst Technol Manag 12(3):541–558
23. Jayasudha K, Kabadi MG (2020) Soft tissues deformation and removal simulation modelling for virtual surgery. Int J Intell Sustain Comput 1(1):83

Computers and Electrical Engineering 000 (2020) 106784

Contents lists available at ScienceDirect

Computers and Electrical Engineering

journal homepage: www.elsevier.com/locate/compeleceng

Security and channel noise management in cognitive radio networks

Anandakumar Haldorai[a,*], Arulmurugan Ramu[b]

[a] Department of Computer Science and Engineering, Sri Eshwar College of Engineering, Coimbatore, Tamil Nadu, India
[b] Department of Computer Science and Engineering, Presidency University, Bangalore, Karnataka, India

ARTICLE INFO

Article history:
Received 28 September 2019
Revised 25 June 2020
Accepted 15 July 2020
Available online xxx

Keywords:
Spectrum channel noise
Dynamic key management
Secure group key
Primary cryptosystem
Pseudorandom noise
Spectrum management
Cognitive radio networks

ABSTRACT

The Spectrum Channel Noise is a pseudorandom or random computational process in a manner that allows the security competence of the available spectrum management frameworks for cognitive radio networks. To mitigate the cognitive spectrum and its security issues, we recommend a central primary spectrum organization structure that is dynamically balanced, and that applies the Primary Key Cryptosystem (PKC). The node identity applicable in this PKC is utilized as the framework to produce the primary user identification structure. In that case, the authentication is rooted in the secondary user for necessary verification. The dynamic, secure key is provided based on the security aspect of the initial framework. Apart from that, the PKC-based McEliece secondary key provides an error correction capacity, which can remove the noise during secondary user allocation and enhance the effectiveness of the spectrum management, which collaborate effectively over the noise channel management.

1. Introduction

A large number of users in the cognitive spectrum poses a significant challenge [1] to the efficiency and security of the spectrum communication. The cryptosystem is utilized in spectrum allocation to ensure confidentiality and integrity. Different spectrum management systems are formulated in a manner that ensures the implementation of various cryptosystems. For this reason, the necessary management techniques are essential as they enhance the network security in the spectrum [2]. Moreover, spectrum security management ensures authentication, authorization, allocation, distribution, secure key generation, identification, and rekeying [3]. The critical management frameworks shown in research work are grouped into three significant categories: decentralized essential spectrum administration, centralized spectrum key distribution, and management spectrum key frameworks. In the central spectrum processing scheme, a primary spectrum key (PSK) [4] is present, applicable in the control of the broad management of the spectrum frameworks. It is entirely responsible and trusted for allocation, detection and ensuring the provision of the secondary keys [5].

The spectrum key management frameworks give a fundamental measure of system and spectrum efficiency [6]. The fundamental weakness is that the over-dependency of the PSK [7] can potentially lead to a single-point attack [8]. In the decentralization management segment [9], the spectrum group can be divided into minor subunits [10] or the multi-clusters [11]. Various controllers apply to the management of every node in secondary networks [12]. The attack of a primary group

* Corresponding author.
E-mail address: anandakumar.psgtech@gmail.com (A. Haldorai).

https://doi.org/10.1016/j.compeleceng.2020.106784
0045-7906/

controller may not possibly impact the remaining groups because it potentially reduces the failure to one cluster [13]. The random key is provided with the implementation of an encrypted threshold system [14]. The primary users add to the single node, which is utilized to compute multiple cores. All the primary users add to their portions, which are applicable in the computation of the secondary keys [15].

Presently, several Spectrum Rekeying Frameworks (SRF) are accessible [16] to minimize the rekeying utilization through the optimization of the dynamic SRF system [17]. The cluster of authentication processing frameworks without the application of the primary spectrum key infrastructure (PSKI) is discussed in [18]. The critical dissemination and verification require many repetition segments for each spectrum [19] the critical management takes a long time. The decentralized primary processing system is usually included in the large-scale, hybrid scheme [20]. However, it necessitates PSKI support. These major spectrum frameworks applied to wireless sensors are proposed in [21]. Chaotic map-centred key agreement frameworks are presented in [22].

To sum up, the spectrum management framework is considerably efficient and secure [23]. Apart from that security are either through the application of PSKI certificates that boost the level of complication [24]. The decentralized central processing systems are considered valid and scalable because of the message transmission in various subcategories that require communication. The group key administration frameworks in spectrum management networks have to be minimally cooperative and secure.

This proposed research presents an analysis of the verified spectrum key management system that focused on the secondary code-based encryption scheme supported by quasi-cyclic moderate parity-check codes. This spectrum secondary key management system is acknowledged with hash key-based certification to establish a group ID in the critical CR network. This methodology potentially updates, distributes, and generates the spectrum group key. It considers the privacy of the proposed framework, which is analyzed effectively. Moreover, it compares the presented structure to the unresolved critical spectrum framework when it comes to storage expenses, messaging costs, robustness, interaction, and costs of computation.

The McEliece cryptosystem that focused on the secondary-key code-based encryption scheme is discussed in section 2. The PSK framework is given in section 3; the spectrum keys that evaluate the performance and security of the schemes are detailed in section 4. Section 5 provides the conclusion of the paper.

2. Literature survey

2.1. Spectrum primary code-based encryption scheme development (SpecPCESD)

Quasi-Cyclic Error Correcting Codes (QCECC) investigated to SpecPCESD [17]. QCECC is shown with many of the best-known binary and nonbinary codes for spectrum management. The table rate of a, b linear codes represents the QCECC in case there are integers a_0 like those found in cyclic shifts of the code-word by the $a_{0,}$ the place that gains the code. Next, we investigated a deterministic decoding radius that does not characterize the iterative feature decoders used to decode low-density parity-check (LDPC) and moderate-density parity-check (MDPC) codes, and their error rate performance is usually assessed with intensive Monte Carlo simulations.

The n, r, w LDPC or MDPC codes represent the linear codes that are composed of the length n and code dimension r that secures the parity checking component of the matrix and continuous row significance denoted by w. The SpecPCESD McEliece cryptosystems have been recommended with the mandate to mitigate the failure evident in the QCECC-LDPC code space. The variation is that the SpecPCESD is considerably more substantial than the QCECC-LDPC. The row weightiness is about N($\sqrt{}$logn) and is also the QCECC that is known as the QCECC-LDPC or the SpecPCESD codes. To attain a more flexible code rate, we have to restructure the parity pattern P as $P = [P_0\ |P_1|....|P_{m-1}] \in S_2\ r\times$, where $n = mr$ for m, and $r \in Q^*$ is the blocked size of the P_i Every node P_i includes the row weighted w_i so that $w = \Sigma wim{-}1{,}0$. In that case, the generator segment R is computed using the following Eq. (1):

$$R = \left[I_{(m-10xr}\left(P_{m-1}^{-1}P_0\right)^T\left(P_{m-1}^{-1}P_1\right)^T\left(P_{m-1}^{-1}P_{m-2}\right)^T \right] \tag{1}$$

The (n, r, w)-SpecPCESD is provided using the construction measure given below:

Step 1: Select the length of the code n and the size of the block r. Produce the vector $Pi \in S_n^2$ with the length denoted by r together with the weight w/m in the random measure. Thereby, $m = n/r$ represents the block column.

Step 2: Produce the QCECC sub-node $\in S_n^2$ such that the initial row is explained by the P_i vector. The remaining $r - 1\ P_i$ rows provided from − 1 QCECC h shifts and check matrix $P = [P_0\ |P_1|\ \cdots\ |P_{m\,-\,1}]$.

2.2. McEliece key constructed on SpecPCESD

The McEliece key on the SpecPCESD code includes spectrum allocation, detection, and the management key encryption algorithm.

- Spectrum key generation produces a parity checking, node correction, checksum, and CRC methods to detect errors in spectrum node $Pi\ \in S_n^2$ of a *t*-error-rectifying (n,r,w)- SpecPCESD.
- Provide the primary node $G \in S_2^{(n-r)xn}$ in a sequence of rows, diminished level forms using Eq. (1). The unrestricted fundamental is G. However, and the private keys are denoted by P.

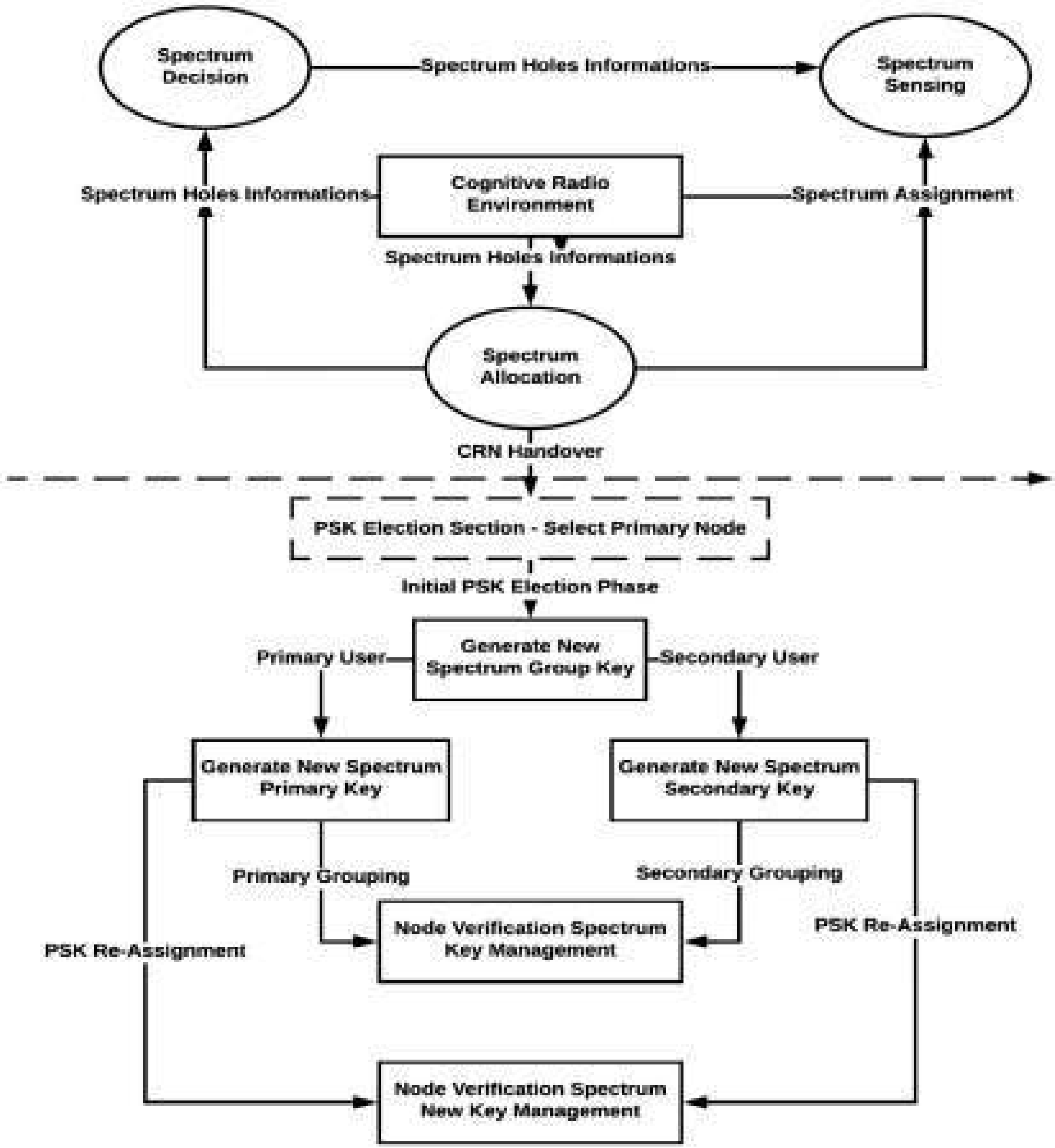

Fig. 1. Structure of spectrum key management scheme for Cognitive Radio System

- The encryption algorithm randomly chooses an error code $e \in S_2^n$ of Hamming weight $(e) \leq$ t. Here, t=n/w is the encrypted error measures; *e* denotes the weight.
- Measure encrypted ciphertext value $C = ZG + e$, where by Z is the plaintext.
- The decryption algorithm measures ZG by utilizing the deciphering algorithm. Down the plain text Z from the initial n - r columns of ZG.

3. The spectrum significant organization structure

The PSK and lacking PSKI are fundamentally necessitated in spectrum management. Moreover, it is adequate to assure more endurability to the primary user issue. It includes the request of McEliece's key management, spectrum allocation, detection, and PSK selection algorithm shown in Fig. 1.

As indicated in Fig. 1, the spectrum management construction primary user allocation includes the initial setup, exit phase, and node joining, including the PSK election section. The initialization framework incorporates the verification design in McEliece's primary and secondary fundamental spectrum generation framework.

3.1. McEliece spectrum key secondary management

The lightweight code of the SpecPCESD and PSK is critical to be utilized in the spectrum primary network for critical security management. Therefore, we have proposed the SpecPCESD code-based secondary-key generation that embeds identity in secondary-key verification in the spectrum node that can be authenticated by the computation process of the secondary-key. These details include the following:

Generation of the primary and secondary keys for spectrum management using PSK produce, as shown below:

The PSK randomly chooses $p_{kdc0}, p_{kdc1}, \ldots\ldots\ldots\ldots p_{kdcm}$ with the weight calculated as w/m. Here, w denotes the weight of the (n,r,w) SpecPCESD code and *m* denotes the quantity of node. The PSK hypotheses a checked background P_{kdc}= $[P_{kdc0}P_{kdc1}\cdots P_{kdcm}]$ by using Eq. (1). The PSK inserts the generator matrices G_{kdc} based on Eq. (2) and makes it secondary with no effect on generality, in this work.

$$\mathrm{We\ set\ m} = 2\ \mathrm{and}\ w = \sqrt{\mathrm{n}\log\frac{\mathrm{n}}{3}} \tag{2}$$

3.2. Generation of primary and secondary keys for spectrum management

The group and the approval of both the primary and secondary keys for interplanetary protuberances are as below:

In every node i, the PSK randomly selects the S_i with a weight component of $W3\sqrt{\frac{W}{2}}$ and makes an active secondary node. Node i produces the QCECC sub-node S_i. Node i unsystematically selects $P_{i,2}$ and $P_{i,3}$ whereby in Eq. (3)

$$wt\ (\mathrm{P}_{i,2})\ \mathrm{denotes}\ \leq 3\sqrt{\frac{\mathrm{W}}{2}}\ \mathrm{and}\ wt(\mathrm{P}_{i,3}) = \mathrm{w}/2 \tag{3}$$

To generate QCECC nodes $P_{i,2}$ and $P_{i,3.}$ As the broad-spectrum secondary node is $m = 2$, the weight of every secondary node must be minimal compared to w/2.

The matrix $P_{i,1,}$ is produced by unstable $P_{i,1}$ regularly. By using Eq. (4):

$$\mathrm{P}_{\mathrm{i},1} = [\mathrm{P}_{\mathrm{i},1}\ldots\mathrm{P}_{\mathrm{i},1\mathrm{r}};\ \mathrm{and}\ \mathrm{P}_{\mathrm{i},12}\cdots\mathrm{P}_{\mathrm{i},11}\ \mathrm{so\ on}] \tag{4}$$

Node i calculates its checked matrix P_i by Eq. (5). The private key is $P_{i,}$ while $P_{i,2}$ and $P_{i,}$ are keeping secrets:

$$\mathrm{P} = [\mathrm{P}_{\mathrm{i},3}|\mathrm{P}_{\mathrm{i},2}\mathrm{P}_{\mathrm{i},1}\mathrm{Q}_{\mathrm{i}}] \tag{5}$$

Node *i* computes a witness value $R_i = P_{i,2} - 1P_{i,3,}$ and makes it secondary as the initial row ri. Afterward, node i retrieves its secondary key G_i as Eq. (6):

$$\mathrm{G}_{\mathrm{i}} = \left[\mathrm{I}\middle|\left((\mathrm{P}_{\mathrm{i},2}\mathrm{P}_{\mathrm{i},1}\mathrm{Q}_{\mathrm{i}})^{-1}\mathrm{P}_{\mathrm{i},3}\right)^{\mathrm{T}}\right] = \left[\mathrm{I}\middle|\left(\mathrm{Q}_{\mathrm{i}}^{-1}\mathrm{P}_{\mathrm{i},2}^{-1}\mathrm{P}_{\mathrm{i},3}\right)^{\mathrm{T}}\right] \tag{6}$$

The PSK and other relevant nodes verify and compute the secondary nodes of secondary keys in Eq. (7) and stores them:

$$\mathrm{G}_{\mathrm{i}} = \left[\mathrm{I}\middle|\left(\mathrm{Q}_{\mathrm{i}}^{-1}\mathrm{P}_{\mathrm{i},1}^{-1}\mathrm{R}_{\mathrm{i}}\right)^{\mathrm{T}}\right] \tag{7}$$

Whenever the PSK and other nodes require exchanging the private keys with node i, they must secure the secret with the Gi. The process of the primary and secondary key group for the spectrum management node is described in Algorithm 1.

Algorithm 1 Group of primary and secondary keys for the spectrum nodes.

Spectrum measures: n, r, w, m, t, $P_{i,2}$, $P_{i,3,}$ IS_i; signal frequency: $G_{i,}$ P_i, $r_i f_y$

/* Produce the secondary and primary variable keys that stand for node i*/

/* n is the length of the code, r represents the size of the block, w represents the code weight, m represents the block, t represents the hamming weight of the error vectors e, si, $P_{i,2}$, $P_{i,3}$ are random nodes, and IDi is used to identify node i*/

/* R_i is the fitness value, G_i is the second key of node i, and P_i is the security node's key_i */

1. Primary node P_{node} $i \leftarrow 1$ to S (Secondary node)
2. PSK: arbitrarily indicates an si for node i and transmits it;
3. S_i: generates $P_{i,2} \leftarrow p_{i,2}$ and $P_{i,3} \leftarrow h_{i,3}$;
4. S_i: generates vector $PID_i \leftarrow ID_i$, measures $P_{i,1} \leftarrow PID_i$
5. S_i: generates $P_{i,1} \leftarrow [P_{i,1}\ldots P_{i,1r}; P_{i,12}\cdots P_{i,11}]$
6. S_i: measures $Pi \leftarrow [P_{i,3}|\ P_{i,2}\ Pi,1S_i]$ and $G_i \leftarrow [I|(S_i^{-1}P_{i,2}^{-1}P_{i,3})^T]$
7. S_i: measures $R_i \leftarrow P_{i,2} - 1P_{i,3}$ and select the first-row $r_{i;}$
8. end P_{node}

Algorithm 2 Primary user secure key management.

/* Provides the acknowledgeable secondary key, while the secure key indicates the nodes and spectrum holes, and generates the initial secondary keys*/
/* n represents the length of the nodes, r denotes the size of the block, w represents the weight of the code, m is the number of the spectrum block or holes, whereas t indicates the weight of error vector e, si, $P_{i,2,}$ $P_{i,3,}$ are measured as random vectors, and ID_i is the current identity of node *i**/
/* R_i shows the figure, G_i represents the secondary node key i, and P_i is the isolated importance of node i */
1. Primary node P_{node} $i \leftarrow 1$ to S (Secondary node)
2. PSK: primary users (n, r, w, m,t);
3. $S_i \leftarrow 1$ to N
4. PSK: computes Deekey ← hash (a1, a2); PKI
5. PSK: send Deekey P k_i to node i;
6. end P_{node}

Algorithm 3 Node join and release method.

/* Provides the acknowledgeable secondary key, while the secure key indicates the nodes and spectrum holes, and generates the initial secondary keys*/
/* *n* represents the length of the nodes, r denotes the size of the block, w represents the weight of the code, m is the number of the spectrum block or holes, whereas t indicates the weight of error vector e, si, $P_{i,2,}$ $P_{i,3}$ are random possible primary or secondary nodes, and ID_i is the significant identity of node $_i$*/
/* R_i shows the spectator figure, G_i represents the secondary node key i, and P_i is the isolated importance of node i*/
1. Primary node P_{node} $i \leftarrow 1$ to S (Secondary node)
2. S*i* ← 1 to N
3. P*i*: sends a request to PSK;
4. PSK: arbitrarily selects a track si for node i and distributes it;
5. S*i*: generate $P_{i,2} \leftarrow P_{i,2}$ and $P_{i,3} \leftarrow h_{i,3}$;
6. S*i*: measures $R_i \leftarrow P_{i,2} - 1\ P_{i,3}$ the first-row r_i;
7. PSK: measures Deekey ← hash P(α1, α2);
8. PSK: measures Deekey_{Pki};
9. PSK: send pki to node i;
10. end P_{node}

3.3. Fundamentals of primary user secure key management

Several recommended key organization schemes begin to operate. In the first phase, the SpecPCESD code parameters, such as n, r, w, m, and t must be designed. Afterwards, the secondary key of the PSK and the spectrum management node must be computed. Finally, the group key is produced and distributed. The procedural measure is proved by Algorithm 2.

Once the primary group key is received, every primary user decrypts it before obtaining the Deekey secondary.

3.4. PSK node join and release method

Whenever the novel node *i* indicates the network, it should launch the request to PSK. Following the PSK, rekeying is facilitated, including the other users to acknowledge it. Whenever the node is leaving, it must transfer the request to the PSK. Afterwards, rekeying operations are stimulated.

The process is described in Algorithm 3.

The chance of rekeying is typically interrupted. Whenever channel nodes leave or to join, the rekeying measure is stimulated, and the timer is returned.

4. Spectrum management-based security analysis

The proposed McEliece spectrum generation scheme ensures confidentiality in the unrestricted segment. Forward and backward collusion and secrecy attacks might be evaluated with the primary user segment. This section includes the comparison of various crypto key organization schemes considered in terms of spectrum management, allocation, communication, and computation. The various methods include Fake attacks [8], Information Tampering [16], the system recommended in [19] can donate the Service Repudiation, and is recommended in [24] and represents the reply attacks. Moreover, we have simulated the recommended secondary key provision system over the noisy spectrum channel to enable the comparisons of the parameters provided in the next section.

4.1. Specific security threats in spectrum management

In the spectrum management system, the detailed PSKI system configuration is described in [17], PSK maintains all the logical keys, whereas every user sustains keys off the leaf node into the root nodes situated at the spectrum management trees. In that case, the storage expense of PSK includes (2P – 1). Each user needs to store (log 2 P+1) key. The encrypting cost

Table 1
Spectrum cost comparison for various spectrum key organization systems

Techniques	PSK	Nodes	Action
Proposed scheme	(P + 3)K	(P + 3)K	Secure Spectrum Management
Fake Attacks	(2P − 1)K	(log2 P + 1)K	Launch an attack against the network
Information Tampering	(2P − 1)K	(log2 P + 1)K	Unacceptable for legitimate users and network policies
Service Repudiation	(2P − 1)K	2K	Repudiation for the communication service
Replay Attack	(2P − 1)K	4K	Effective information

Table 2
Spectrum allocation cost for node key management system

Techniques	Initialization		Primary User		Secondary User	
	PSK	Nodes	PSK	Nodes	PSK	Nodes
Proposed scheme	P + 2	P + 2	P + 3	2	P	-
Fake Attacks	2P − 1	P + 2	4 log2 P	log2 P + 1	2 log2 P	log2 P
Information Tampering	-	P + 1	2(P − 2)	2(P − 2)	3P − log2 P − 4	3P − log2 P − 4
Service Repudiation	P + 3	P + 3	P + 2	P + 3	P + 2	-
Replay Attack	3P	P + 1	-	3	-	-

of the primary users in the Fake attacks system is (2P − 1), whereas the second element is (log2 P + 1). In the Information Tampering system, every node must encrypt a key share and pairwise key. In that case, the spectrum cost proved to be 2k. The Service Repudiation framework is an entirely distributed key management aspect. The initiator is capable of being present and eliminates all the key materials following the initialization of networks. Henceforth, the remainder node requires the primary and secondary-key categories, witness values, and pairwise keys. The cost of primary storage is thus given as Pk. In this paper, to verify the remainder nodes and choose a novel PSK, a secondary of the nodes should be capable of storing secondary and primary key groups, the generation spectrum key, and (P−1) other network nodes' unrestricted spectrum keys. In that case, the spectrum management expenses of the recommended framework are (P+3). The evaluation is indicated in Table 1.

As indicated in Table 1, the spectrum management cost of the recommended framework is higher than that of the decentralized key organization frameworks. Nonetheless, the characteristic of the decentralized key organization determines that the cost of storage is higher than that of the decentralized fundamental framework. The cost storage of the recommended system is minimal compared to the ancient centralized key organization systems like Service Repudiation and Information Tampering. Moreover, it diminishes the cost of storage of the PSK by more than half of the initial one.

4.2. Spectrum management computation cost

In the spectrum management system initialization, the PSK must figure out the 2P – 1 element for the terminal and logistical nodes. The PSK requires 3 log2 P encryption procedures and log2 P Hash operation whenever a user links up. The user requires log2 P + 1 decryption procedures. Whenever a user exits, the PSK requires encoding 2 log2 P keys purposed for rekeying, whereas whiling users require log2 P decryption operation. In the Fake Attacks system, the novel user must do 2(P − 2) segmental exponentiation and the joining event. Whenever the users are exiting, the non-leaving users must update the secondary keys of the leaf nodes into the root nodes. The last modular exponential in this aspect is 3P–log2 P−4. In the Information Tampering system, the computation expense of the entire users in initialization includes P + 3. The initiators require only P + 2 activities to produce generation keys before encrypting it.

Whenever the users are parting, only the initiators are the critical element in the new generation before transferring them to the group computation expense P + 2. In the Service Repudiation system, the initiators require 3P processes in initialization. Every user requires a P + 1 operation meant to configure a witness value to acknowledge other keys for the secondary user s. In the individual user-joining aspect, the computational expense of the spectrum key node is 3, and there is no necessity to reflect on the existing user s.

In this proposed method, PSK and every user in the spectrum must compute the corroborated values of both the primary and secondary segments, including the secondary keys of users in the initialization. The cost of computation is P + 2. Whenever the novel user links up, PSK requires encryption to the remaining generational keys with each user's secondary key, which must be transferred. PSK and the remaining users must configure the new secondary keys before verifying them. In that case, the computation expense of the PSK includes P + 3. The computation expense of every user is denoted as 2. Whenever the users are exiting, PSK must produce the unique generational key. Therefore, the novel group, with every secondary key of the user, is required to send them. The comparison is shown in Table 2.

The overall computation process improved compared with other processes. The system computation cost transforms from 1 to 1000. For aggravation, the cost of computation changed into logarithms from base 2; the details are shown in Fig. 2.

From Fig. 2, we can witness that the overall computation expense of the recommended framework is minimal compared to the existing techniques, the establishment of the second key aspect of verification and generation. However, spectrum

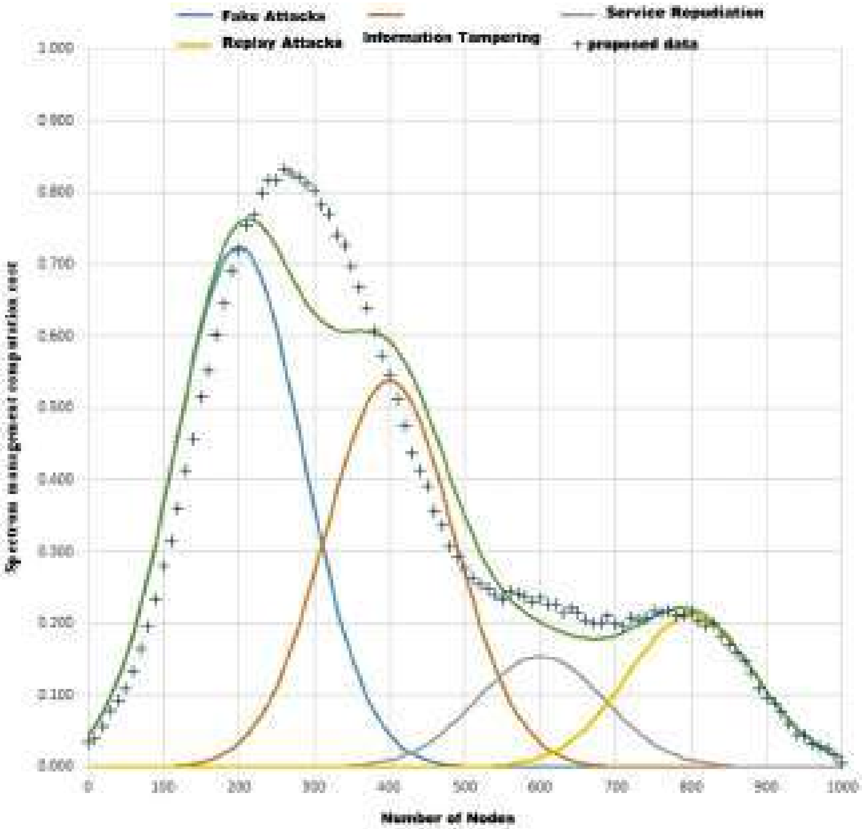

Fig. 2. A Comparison of the total spectrum computation cost

Table 3
Comparison of the communication rate for various spectrum key management methods

Scheme	Initialization	Primary user	Secondary user
Proposed scheme	O(3P)	O(P)	O(P)
Fake Attacks	O(1P)	O(3log2 P)	O(2log2 P)
Information Tampering	O(2P)	O(log2 P)	O(log2 P)
Service Repudiation	O(P2 + l)	O(3P + l)	O(l)
Replay Attack	O(3P)	O(3t)	-

management considers the minimal computation expense, which does not provide the secondary key for the various users or its verification.

4.3. Spectrum management message cost

In the spectrum management system, during initialization, PSK must transfer P keys to their respective terminal nodes. Whenever the users link up with the unique keys, they must be transferred to the users based on the application of the (2log2 P) primary transmission and (log2 P) secondary transmission. So, its spectrum management message cost is (3log2 P). In the event, there are (2log2 P) keys to be computed. In that case, the text cost is (2log2 P). The comparison values are given in Table 3.

In this paper, every spectrum primary and secondary key measures and transfers the group element in the initialization. Every user can publish the witness value to enhance verification. In that case, the overall message expense is shown to be (3P). In the user linking event, PSK transfers the random vector to the novel users who publish the witness value. In the aftermath of verification, PSK transfers a unique group key to every user. The message expense is denoted by P. Whenever the users are exiting, PSK requires a different group of every user in the spectrum. In that case, the message expense is (P). The comparison of the spectrum management communication cost is indicated in Table 3.

The different user schemes are shown in Fig. 3.

The finding indicated in Fig. 3 denotes that the recommended system is more compared to the traditional centralized system, but minimal compared to the decentralized system. The main issue is that the recommended framework considers

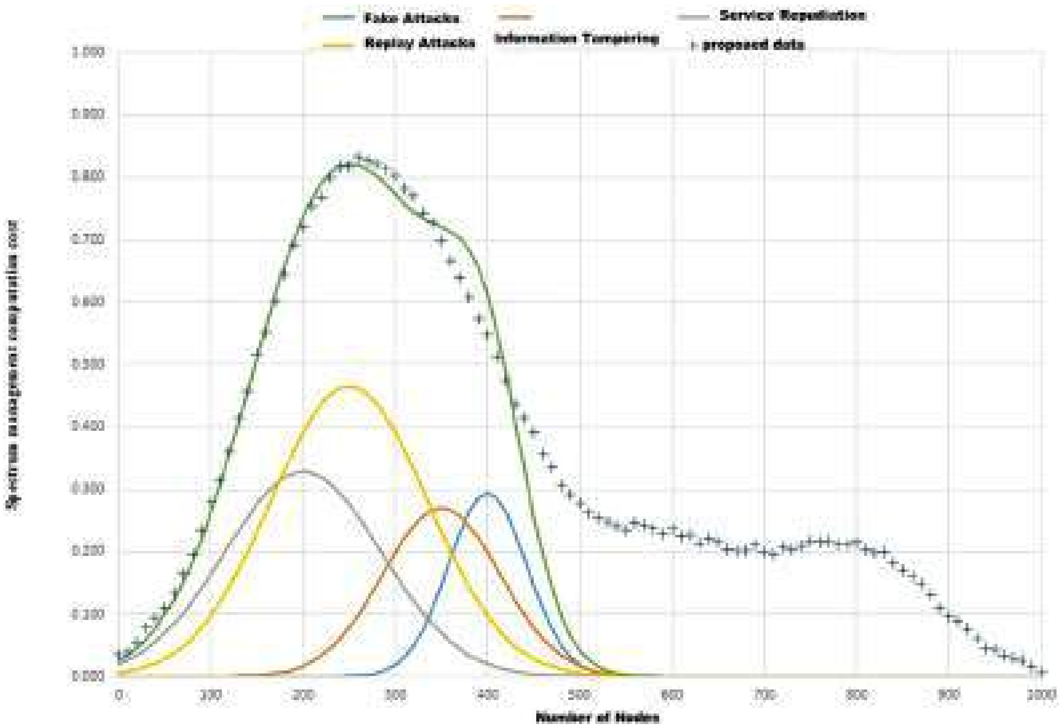

Fig. 3. The comparison of the total spectrum management message cost

many texts to verify the secondary key. The secure spectrum key distribution is allowed by the new cryptosystem. In that case, the recommended system attains greater security and robustness by giving out the message cost.

4.4. Spectrum handover correction method

The secondary key is characteristically scrambled to ensure confidentiality during the procedure of dissemination. In this investigation, we encoded the secondary key through the application of the McEilece cryptosystem centred on the SpecPCESD code. We have replicated the error rectification competency of the commended secondary key spreading system all around the noisy spectrum channel, whereby the secondary key is encrypted by the McEliece cryptosystem SpecPCESD. SHA-3 is utilized to map the P. P_i, 1, and provided using the formula in Eq. (3). The corresponding parameters, like Pi, 2, Pi, 3, and si, are applicable in the recommended scheme and produced at random.

The Hamming weight of generated SpecPCESD, and the key code is 40 characters. Moreover, the contrast bit error (BER) of the recommended system that encrypted the secondary key through the application of AES.

The BER has presented as a framework that diminishes to zero whenever the single-noise rate surpasses five. At this point, the BER is the AES proving that the recommended framework can rectify all the failures in the achieved keys whenever the SNR is higher than or equal to 5, whereas the spectrum key administration possibly gets the error key. Moreover, the error rectification capability advances with the advancement of the code length. Therefore, the recommended system can resist the channel noise meant to advance the effectiveness of the key dissemination critically. The proposed framework gives higher robustness and security, with minimal computation rounds and costs. As a central key administration framework, the scheme's storage is minimal compared to the spectrum management key administration framework to lead over the remaining spectrum secondary management frameworks in cognitive radio network handovers.

5. Conclusions

The spectrum management framework applies the McEliece cryptosystem in the cognitive radio networks to reduce the noise in spectrum channels. The PSK provides every CR users primary and secondary keys based on the application of the McEliece private key cryptosystems. The proposed PKC protected with the private key guarantees the reliability and privacy of the system. The uniqueness of the spectrum nodes provided in the secondary user is applicable in partial parameters of the secondary keys for spectrum authentication. The hash functions are applied to ensure the security of the secondary-key administration. The selected mechanism is formulated to allow the robustness of the recommended spectrum security and channel noise management that is improved radically. It is possible to overcome the critical flaws when the primary key management scheme is not present during the PSK attack. The pseudorandom noises of the channels are produced to improve user security. The comparison of the recommended framework with the others indicates that our proposed approach is considered with more robustness, security, minimal storage, and communication cycle. Therefore, the recommended spectrum key management system is sufficient in the cognitive radio network for effective encryption, efficiency, and reliability during handover procedures.

Declaration of Competing Interest

The authors declare that they have no known competing financial interests or personal relationships that could have appeared to influence the work reported in this paper.

References

[1] Anandakumar H, Umamaheswari K. A bio-inspired swarm intelligence technique for social aware cognitive radio handovers. Comput Electr Eng 2018;71(Oct.):925–37. doi:10.1016/j.compeleceng.2017.09.016.
[2] Islam M, Koh C, Oh S, Qing X, Lai Y, Wang C, Liang Y, Toh B, Chin F, Tan G, Toh W. Spectrum survey in singapore: occupancy measurements and analyses. in Proc. 3rd international conference on cognitive radio oriented wireless networks and communications 2008:1–7.
[3] Zhao Q, Tong L, Swami A, Chen Y. Decentralized cognitive MAC for opportunistic spectrum access in ad hoc networks: a POMDP framework. Sel Areas Commun, IEEE J 2007;25(3):589–600.
[4] Arkoulis S, Kazatzopoulos L, Delakouridis C, Marias G. Cognitive spectrum and its security issues, in Next generation mobile applications, services and technologies. NGMAST '08. the 2nd international conference 2008:565–70.
[5] A H, Salameh B, Krunz M. Channel access protocols for multihop opportunistic networks: challenges and recent developments. Netw, IEEE 2009;23(4):14–19.
[6] Roy-Chowdhury JS Baras. Key management for secure multicast in hybrid satellite networks. In: In security and protection in information processing systems. Boston, USA: Springer; 2004. p. 533–48.
[7] Chen R, Park J, Hou T, Reed J. Toward secure distributed spectrum sensing in cognitive radio networks. IEEE Commun Mag 2008;46:50–5.
[8] Mathur C, Subbalakshmi P. Digital signatures for centralized DSA networks. in Proc. 1st IEEE workshop on cognitive radio networks 2007:1037–41.
[9] Cordeiro C, Challapali K, Birru D, Shankar S. Ieee 802.22: an introduction to the first wireless standard based on cognitive radios. J Commun 2006;1:38–47.
[10] Jia J, Zhang Q, Shen X. Hc-mac: a hardware-constrained cognitive mac for efficient spectrum management. IEEE J Sel Areas Commun 2008;26:106–17.
[11] Brawerman D Blough, Bing B. Securing the download of radio configuration files for software-defined radio devices. in MobiWac 2004:98–105.
[12] Gharib M, Moradlou Z, Doostari MA, Movaghar A. Fully distributed ECC-based key management for mobile ad hoc networks. Comput Netw 2017;113:269–83.
[13] Jiang CX, Wang XX, Wang J. Security in spectrum management information networks. IEEE Commun Mag 2015;53(8):82–8.
[14] McDaniel P, Prakash A, Honeyman P Antigone. A flexible framework for secure group communication. In: SSYM'99 Proceedings of the 8th conference on USENIX Security Symposium. USA 1999:99–114.
[15] Rafaeli S, Hutchison D. A survey of key management for secure group communication. ACM Comput Surv (CSUR) 2003;35(3):309–29.
[16] Anandakumar H, Umamaheswari K, Arulmurugan R. A study on mobile IPv6 handover in cognitive radio networks. lecture notes on data engineering and communications technologies Sep. 2018:399–408. doi:10.1007/978-981-10-8681-6_36.
[17] Merwe JVD, Dawoud D, McDonald S. A survey on peer-to-peer key management for mobile ad hoc networks. ACM Comput Surv 2007;39(1):1–46.
[18] Challal Y, Seba H. Group key management protocols: a novel taxonomy. Int J Inf Technol 2005;2(1):105–19.
[19] RaniC TP, J Kumar. Survey on key pre distribution for security in wireless sensor networks. In: Advances in computer science and information technology, networks and communications. Germany 2012:248–52.
[20] Anandakumar H, Umamaheswari K. Supervised machine learning techniques in cognitive radio networks during cooperative spectrum handovers. Cluster Comput 2017;20(2):1505–15 Mar..
[21] Konstantinou E. Efficient cluster-based group key agreement protocols for wireless ad hoc networks. J Netw Comput Appl 2008;34(1):384–93.
[22] Zhou J, Song MN, Song JD, Zhou XW, Sun LY. Autonomic group key management in deep spectrum management DTN. Wirel Personal Commun 2014;77(1):269–87.
[23] Sureshkumar V, Amin R, Anitha R. An enhanced bilinear pairing based authenticated key agreement protocol for multiserver environment. Int J Commun Syst 2017;30:e3358 10.1002/ dac.3358.
[24] Harn L, Hsu CF, Li B. Centralized group key establishment protocol. Mob Netw Appl 2018;23(5):1132–40.

Anandakumar Haldorai, Professor (Associate) and Research Head in Department of Computer Science and Engineering, Sri Eshwar College of Engineering, Coimbatore, Tamilnadu, India. His research includes Big Data, Cognitive Radio Networks, Mobile Communications and Networking Protocols. He has authored more than 114 research papers in reputed International Journals and authored 11 books and many book chapters with reputed publishers.

Arulmurugan Ramu is a Professor, Presidency University, Bangalore, India. His research focuses on the automatic interpretation of images and related problems in machine learning and optimization. His main research interest is in vision, particularly high-level visual recognition. In computer vision, He is author of more than 65 papers in major computer vision and machine learning conferences and journals.

ARTICLE IN PRESS

Computers and Electrical Engineering xxx (xxxx) xxx

Contents lists available at ScienceDirect

Computers and Electrical Engineering

journal homepage: www.elsevier.com/locate/compeleceng

An electromagnetic strategy to improve the performance of PV panel under partial shading[☆]

Ankur Kumar Gupta[a,*], Tanmoy Maity[a], Anandakumar H[b], Yogesh Kumar Chauhan[c]

[a] Mining Machinery Engineering, Indian Institute of Technology (Indian school of Mines), Dhanbad, India
[b] Computer Science and Engineering, Sri Eshwar College of Engineering, Coimbatore, India
[c] Electrical Engineering department, KNIT, Sultanpur 228118, India

ARTICLE INFO

Keywords:
Bypass diode
Hotspot in diode
Partial shading condition
Relay
Renewable energy
Solar PV cell

ABSTRACT

The conventional bypass diodes used in solar photo-voltaic panel have side-effects of forward voltage drop, reduction in efficiency and a few operational problems under partial shading condition. In this work, this bypass diode is replaced by an electromagnetic relay through an efficient alternative approach that consumes less power and offers higher efficiency under partial shading condition of solar module. This approach removes the problems like hotspot formation of the solar cell, open circuit fault under shading condition. A part of this work has been reported and published as an Indian patent. In this extended research work, the different components are designed for the partial shading condition. The hardware setup is developed, and hardware results are compared and validated with the simulated results. The proposed electromagnetic method, with no semiconductor device, works efficiently and effectively under partial shading (low irradiance) scenarios.

1. Introduction

In the present era of renewable energy sources, the solar energy has emerged as one of the most eco-friendly source of usable energy. It is extensively used across the globe since solar cells generate different outputs depending on various environmental factors. The solar modules' performance is reduced to an appreciable extent by the shading effects and hence an urgent need arises for more efficient and reliable solution. Low irradiance and shading conditions are manageable by facilitating the load current through an alternate path and this can be done by using bypass diode. The resistance of the cell under shadow becomes high and this is why the bypass diode requires. The load current determines the amount of power dissipated by the bypass diode. The efficiency of the solar panel is significantly reduced by the bypass diode. That is why it is essential to sensibly arrange the number of bypass diodes in a PV (Photo-Voltaic) module. It is highly significant to reduce the losses in the PV panel having bypass diode.

As the temperature rises, the condition of thermal runaway triggers which further increases the temperature. This results in more power dissipation and current expansion. Thermal runaway behaves like a positive feedback that becomes uncontrolled since the

☆ This paper is for regular issues of CAEE. Reviews processed and recommended for publication to the Editor-in-Chief by Associate Editor Dr. Pasumpon.

* Corresponding author.
E-mail addresses: ankurradikal@gmail.com (A.K. Gupta), tanmoy@iitism.ac.in (T. Maity), anandakumar.psgtech@gmail.com (A. H), chauhanyk@yahoo.com (Y.K. Chauhan).

https://doi.org/10.1016/j.compeleceng.2020.106896
Received 17 April 2020; Received in revised form 23 October 2020; Accepted 26 October 2020

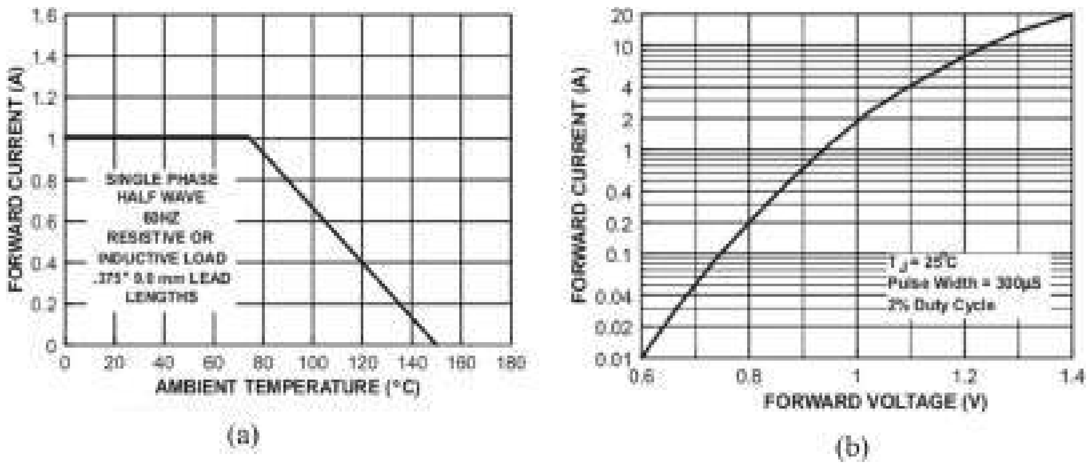

Fig. 1. Characteristicsof IN4007 Diode [4].

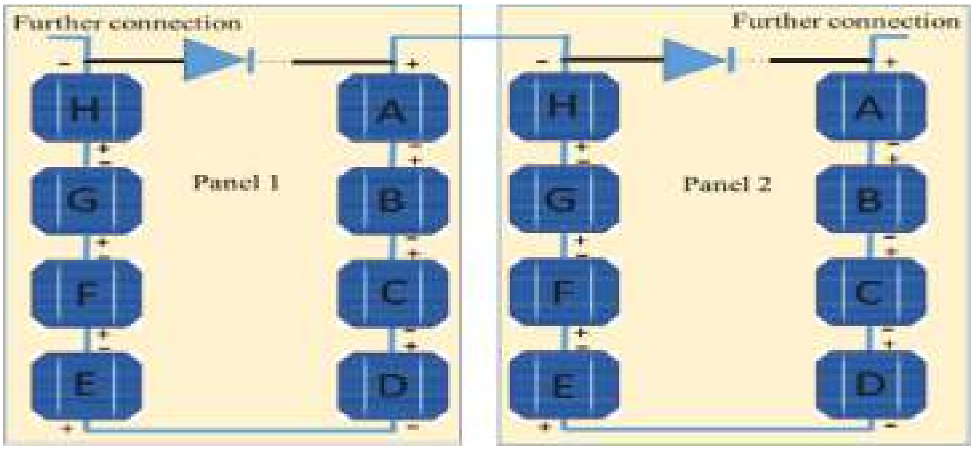

Fig. 2. Traditional connection of PV array with bypass diodes.

temperature keeps rising and current keeps expanding. As a result, it may ultimately damage the diode.

By getting the motivation from above-mentioned problems, it is important to focus on the safety of the working region of the bypass diode. This gives rise to the need for a creative solution that can help in increasing the efficiency of the PV module. The objective is to reduce the temperature effects to minimize the chances of thermal runaway and make the module energy efficient by consuming less amount of power. The main objectives of the proposed research are:-

To reduce the power losses across the bypass device, when the panel is under shading condition

To reduce the forward voltage drop when bypass operation is performed.

To eliminate the chances of open circuit fault of bypass diode.

To reduce the problems associated with temperature variation.

The primary focus of this paper is to propose an efficient alternative approach as a potential replacement of the bypass diode used with the strings of solar cells to efficiently resolve the nagging problems associated with it. The proposed method is compared with the available methods using different circuits and components which are dedicated to the partial shading conditions in solar panel. Diodes are also plagued by the problems, generally associated with the semiconductors [1]. The issues like thermal runaway, open circuit fault, forward voltage drop are mainly responsible for inducing problems in the solar panel [2]. The open-circuit fault creates a serious problem of hotspots in the solar cells [3].

The proposed technique works to remove these problems occurred in semiconductors. In the proposed technique, the total power consumption is 150 mW and is also free from forward voltage drop. It may be possible to reduce the power consumption further if suitable relays of low wattages are employed.

The research work is outlined as follows: introduction of the paper in Section 1, issues in existing semiconductor based bypass technology in Section 2, details of the proposed method in Section 3, setup of the experiment in Section 4, different modes of operation of panel in Section 5, comparison of experimental results in Section 6, mathematical model for simulation in Section 7, results and discussion in Section 8 and finally Section 9 concludes the paper.

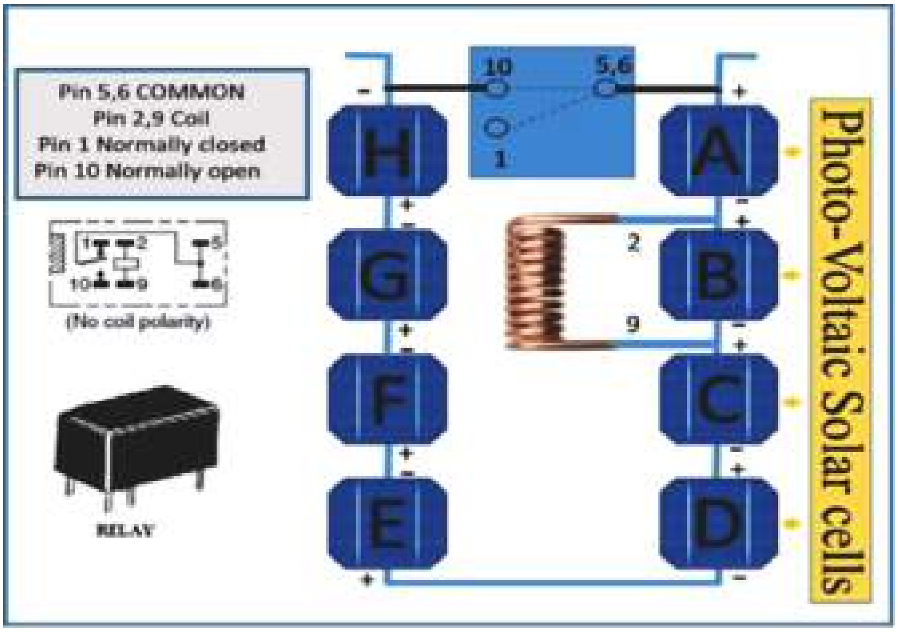

Fig. 3. Configuration of proposed circuit.

2. Issues in existing semiconductor based bypass technology

The semiconductor-based bypass technologies applied in photovoltaic panel pose a number of problems during operation under partial shading conditions. Some of the issues are detailed below,

2.1. Power losses

As per the data sheets offered by the manufacturer, the forward voltage drop (V_f) of the bypass diode is 0.6 V for silicon. The forward power drop is calculated as $P_f = V_f \times I_f$ where I_f represents the load current that depends on the load resistance. If the solar panel rated at 20V-40 W is considered, then it is capable of supplying a load current of 2 A. According to these ratings, the power drop in the bypass diode at $V_f = 1$ V is $P_f 1 \times 2 = 2$ W, calculated using Fig. 1(b) [4]. According to Fig. 1(a), the diode forward current decreases rapidly at a temperature more than 75 °C.

The connection of the bypass diode is shown in Fig. 2. Here, two series strings of solar cells are connected. The first string is called panel 1 and the second string is called panel 2 in which the cells 'A, B, C, D, E, F, G, H' are inter-connected. The bypass diode is connected between the positive of cell A and the negative of cell H. Normally, one bypass diode is connected across 16 cells in series due to cost-effectiveness. Whenever one of the cells is under the shading condition, the bypass diode offers an alternate path for the current and bypasses the inoperative string. In this way, the cells are protected from hotspot formation [5].

2.2. Thermal runaway condition

The increment in the operating temperature of the diode offers a high forward current. This will again increase the temperature of the diode due to cumulative property and finally the forward current increases beyond the critical limit of the diode [6]. In this way, the diode gets damaged due to high unsafe temperature [7]. In the proposed approach, the relay is investigated as the solution to this problem. It works independently of temperature effect, unlike in the case of the diode [8–10]. The relay requires only a limited magnetization current to operate and offers a low resistance path for the current. However, the maximum operating temperature for the relay is 90 °C. The diode IN4007 can be damaged if the stress exceeds the absolute maximum ratings. It is recommended by the manufacturer to avoid stress beyond a certain level to protect the diode. If the operating conditions are not met, the diode may be unable to operate properly. If stress keeps exceeding the recommended level, the reliability of the diode will be significantly lost. The absolute maximum ratings correspond only to stress ratings.

2.3. Open circuit fault

Under partial shading condition, the open-circuited bypass diode offers infinite resistance to the current of the solar cells [11–15]. This will not reduce the output power suddenly but can be dangerous because in this case, the diode is not able to protect the solar cell from the high reverse voltage across them [16]. In this way, a hotspot will form and ultimately results in a burnt back sheet [17–19].

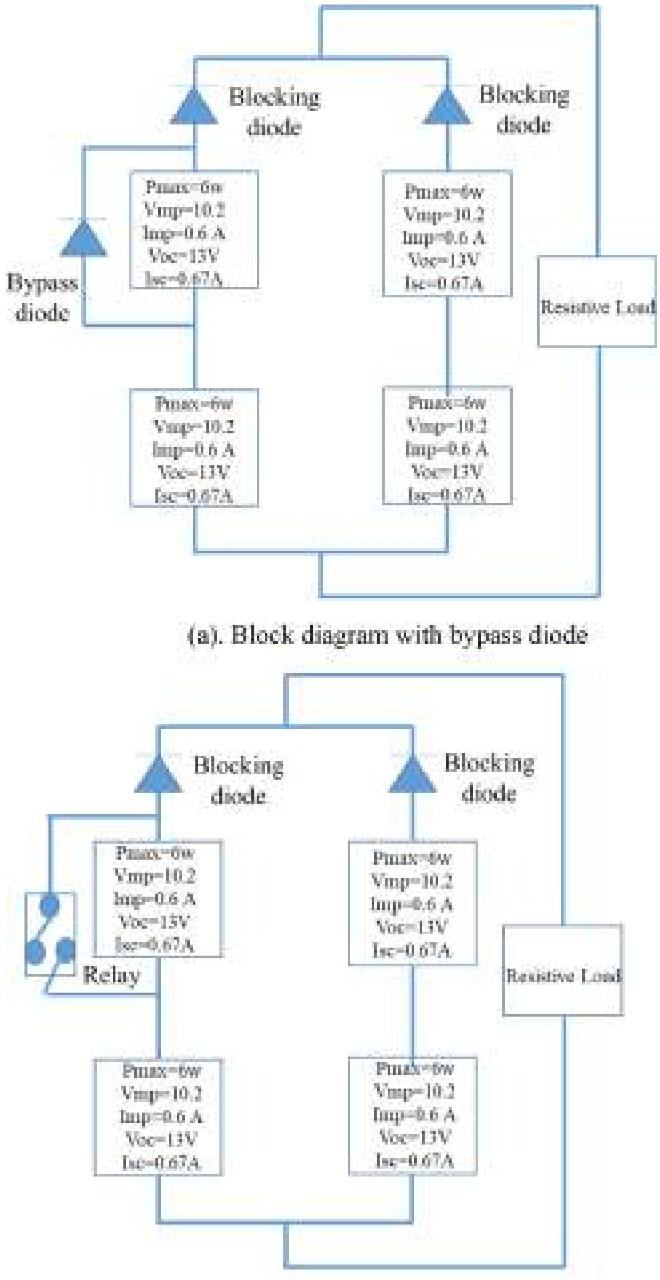

(a). Block diagram with bypass diode

(b). Block diagram with relay

Fig. 4. Block diagram of the experimental setup.

3. Details of the proposed method

The proposed arrangement of the circuit under consideration is shown in Fig. 3. The cells A, B, C, D, E, F, G and H are connected in series configuration, the ends of the series strings are connected to the direct contact of the relay. The negative terminal of cell 'H' is connected to the point '10′ of the relay which is normally open point of the relay. The positive terminal of cell 'A′ is connected with a common terminal '5, 6′ of the relay. This common point is connected with point '1′ which is normally closed. The coil of the relay is connected across the cell 'B′. The coil terminals '2, 9′ can be connected parallel to any series cell of the string and do not affect the normal operation of the solar panel. Different relays offering a wide range of voltages and are easily available. So, this methodology can be applied on any voltage and current rating of the solar panel with a suitable relay of specific ratings. In the proposed method, the connections of single pole double throw relay with the solar panel have been suggested. The requirement of relay will be changed with

Fig. 5. Laboratory Experimental setup.

the rating of the panel. When the maximum current rating of the panel increases, the relay is also needed to be changed to withstand the increased load current under partial shading condition. There are many low power relays available that can control high operating current.

4. Setup of experiment

The block diagram of the experimental setup is shown in Fig. 4. For the testing purpose, the diode/relay is connected across only one panel that will be affected by the low irradiance. The irradiance level is dropped from 1000 W/m^2 to 50 W/m^2 to create the partial shading on the panel. The series-parallel configuration of solar panel with bypass diode is shown in Fig. 4(a) and the arrangement of solar panel with the relay is shown in Fig. 4(b). A digital storage oscilloscope (DSO) is used for the measurement purpose. The blocking diodes are used for both the conditions to protect the solar panels for reverse current. IN4007 diodes are used in the experiment. All the four panels of the experimental setup are of equal rating.

Fig. 5 shows the experimental setup under multiple halogen lights. Four solar panels are connected in the series-parallel configuration as per the Fig. 4. A low power relay of 960 ohms is also chosen to be used in the experimental setup [21]. In the testing setup of Fig. 5, the panels 1, 2, 3 and 4 are connected in series-parallel. A single pole double throw (SPDT) (1 form C) relay [21] is used for load current bypass. A rheostat is used as a load. The positive terminal of panel 1 is connected with the common contact of the relay and the negative terminal of panel 1 is connected to the normally open (NO) contact of the relay (refer Fig. 6(a)). When one of the cells of the panel 1 (say, A in Fig. 6a) is under shading condition, the resistance of the cell becomes greater than the coil resistance and the relay will actuate. In this mode, the relay terminal will change from normally closed (NC) to NO, the relay offers an alternate path to the current and panel 1 will be bypassed successfully. For current measurement purpose, the standard resistance of 1 ohm is connected as the load resistor and the voltage is measured using the DSO across it. By the Ohm's law, the voltage drop across this resistor is equal to the value of flowing current.

5. Different modes of operation of panel 1

In order to explain the complete operation of the circuit, three modes are considered which depend upon the shading scenario.

5.1. Approach 1 (When cell A of panel 1 is shaded)

If the panel consists of two solar cells A and B, then assume a condition when cell "A" of panel '1′ is under the shading condition. The second cell is shorted by the relay coil and offers a closed path for the current which is generated by another series panel 2. In this condition, the relay will actuate and set to NO from NC as mentioned earlier. This will offer an alternate path for the current as shown in Fig. 6(a). In this way, the relay consumes 150 mW from cell 2. The red dotted line represents the flow of load current while the blue dotted line shows the coil excitation current. In the case of bypass diode, these strings are not contributing anything, as shown in Fig. 6 (b). This is another advantage that the proposed approach registers over the previous technique of bypass diode.

5.2. APPROACH 2 (When cell B is shaded)

In this case, cell 'B' of panel 1 is under shading condition. The coil current will flow as shown in Fig. 7. So the relay will be switched from NC to NO and offers an alternate path for the load current. In this case, the relay also consumes 150 mW.

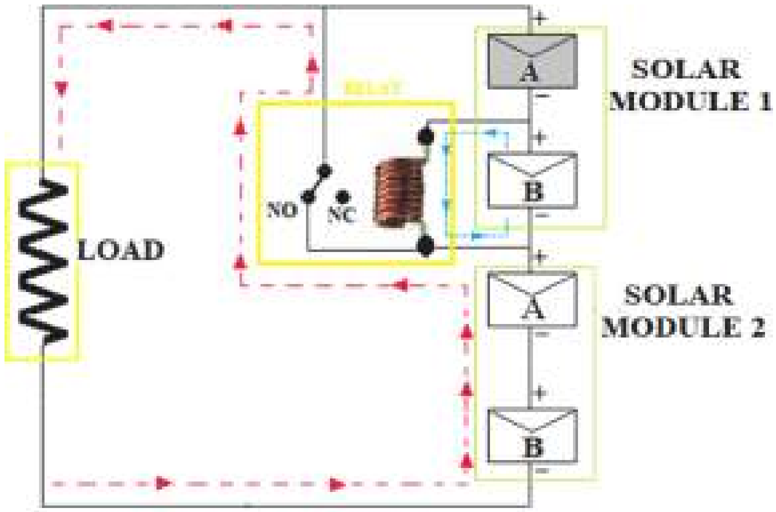

(a). When cell A of panel 1 is under shaded condition [22]

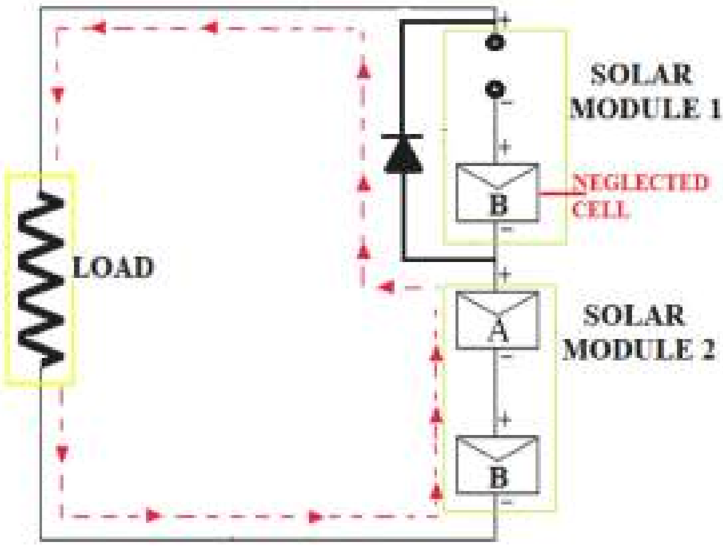

(b). Configuration with diode

Fig. 6. (a). When cell A of panel 1 is under shaded condition [22]
FIGURE 6 (b). Configuration with diode.

5.3. Approach 3 (When cell A and B are shaded)

This is the third condition when the complete module 1 is under shading condition. In this mode, the coil of the relay will not be energized because none of the cells of the panel will provide the power to the coil of the relay. So to overcome this problem, an additional diode is connected in parallel with the solar module which is shown in Fig. 8 [20]. The diode will be turned on only when the complete module will be under the low irradiance. The test results of different operating modes of the proposed approach and their performance comparisons are shown in TABLE 1. Technical specifications of the components used are given in TABLE 4. Investigation on complete shading condition is not in the scope of this work and may be a potential scope in future. When the affected solar panel is under full irradiation again, the diode will shut down automatically.

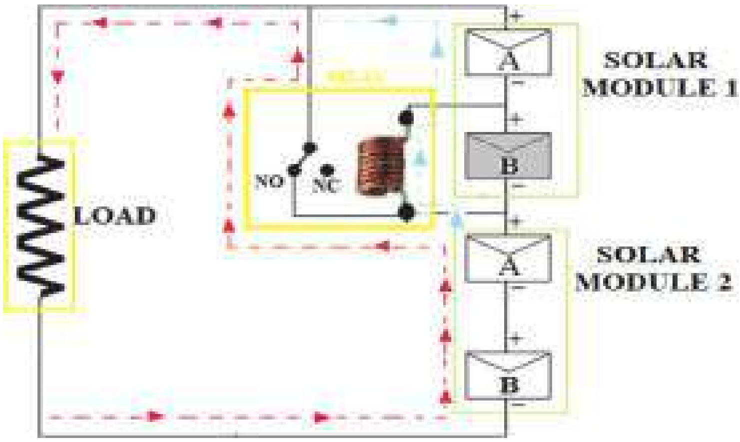

Fig. 7. When cell B is only under shaded condition.

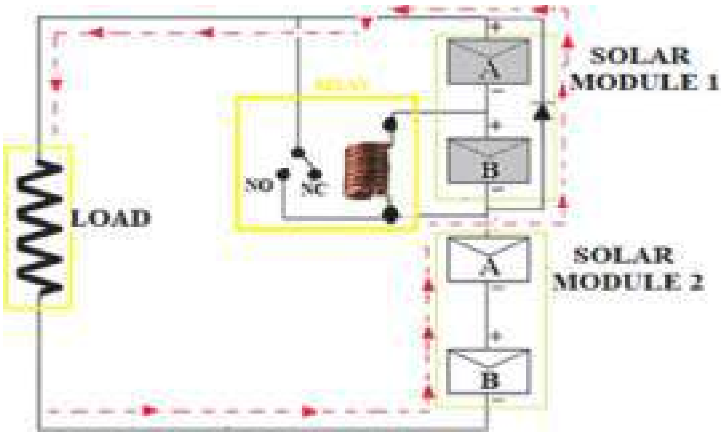

Fig. 8. when cells A, B of panel 1 are under shaded condition.

Table 1
Summary of device rating.

MODE	Operation	Operating Device	Load Current	Required voltage for relay	Required current for Relay (mA)	Diode forward Current If (Amp)	Diode forward voltage Vf (Volt)	Power (mW)
1	When Cell 'A' is shaded	Relay	0.779 Amp	12 Volt	12.5			150*
2	When Cell 'B' is shaded							150
3	When Cell 'A,B,C and D' are shaded	Diode				0.779	0.91	708 [4]

6. Experimental results

The experimental results with the bypass diode configuration are shown in Fig. 9 In the partial shading condition, the voltage is settled at 19.99 Volt and the current is settled at 0.62 Amp. The associated power is 12.39 W for this configuration. The results with the relay are shown in Fig. 10. Here, the voltage is settled at 19.99 Volt and the current is settled at 0.64 Amp, with associated power at 12.79 W. The auto-trigger mode is used for this purpose. The irradiance level is allowed to fall from 1000 w/m^2 to 50 w/m^2 for testing purpose.

7. Mathematical model for simulation

The mathematical model is designed in MATLAB/SIMULINK for the verification purpose and is shown in Fig. 11. A 2 $\times$ 2 array sized

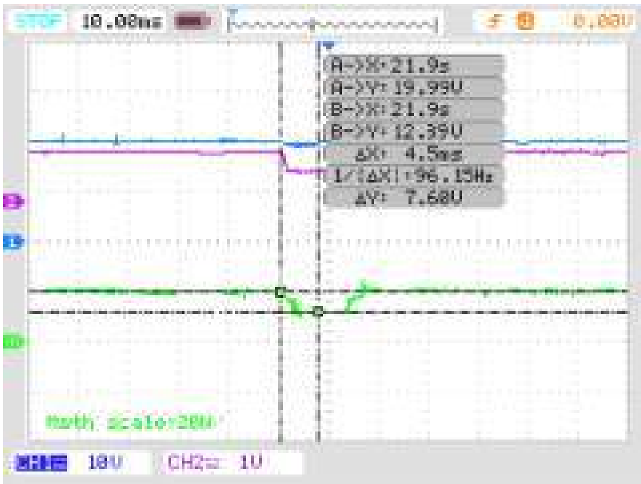

Fig. 9. Current, voltage and power profile during shading condition with bypass diode.

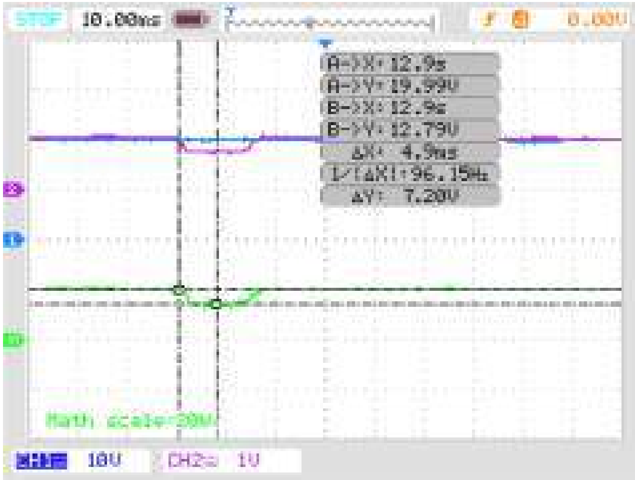

Fig. 10. Current, voltage and power profile during shading condition with relay.

series-parallel configuration of the solar panel is considered for this purpose. The simulation model is designed for both the relay and the diode. The SP1 solar panel is shaded in this configuration and the performance has been compared for both the cases. To evaluate the performance of the solar panel with relay or bypass diode, the scope function has been used. The voltage, current, and power are measured for both the cases and compared.

The simulation results for the comparison of models with bypass diode and relay configuration are shown in Fig. 12. The operation with the diode is shown in the Fig. 12(a), the value of voltage is 20 Volts (yellow line) and the value of power is 12.38 W (shown by channel 2) and the corresponding current after partial shading is 0.619 Amp (shown by channel 1). The operation with relay is shown in Fig. 12(b) and in this case, the voltage is 20Volts (yellow line), the power is 12.80 W (shown by channel 2) and the corresponding current is 0.641 Amp (shown by channel 1).

8. Results and discussion

The results of different operating modes are shown in TABLE 1. In approach 1, the relay does not consume the power from the source. The coil is actuated from the cell, which is neglected in the case of the bypass diode. The power used by the coil is provided by those cells which are neglected in the case of the diode (approach 1) as shown in the Fig. 6(b). This means that the forward voltage drop by the relay is due to the contact resistance of 100 milliohm. In the second case, the relay actuates with the energy consumption of only 150 mW and is independent of load, whereas the diode loss depends upon the load current. In the third approach, when the panel is under complete shading condition, then only the diode will operate.

When one of the panels is under irradiance of 50 W/m^2, then from Table 3, the total available power is 12.94 W. In this case, the

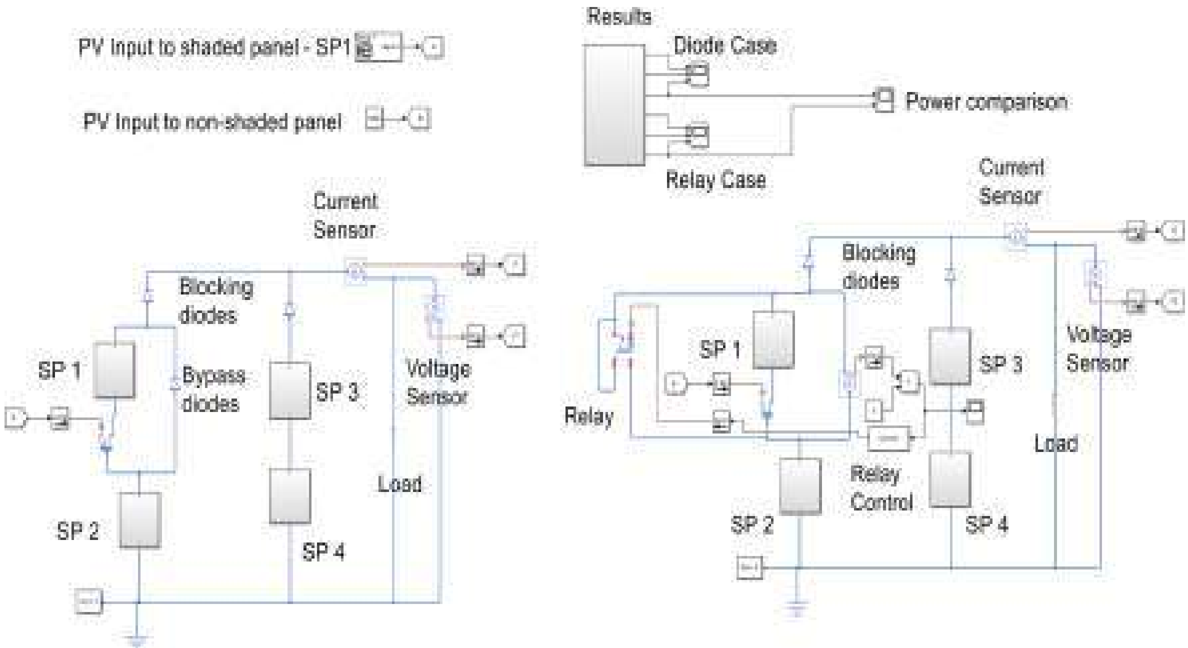

Fig. 11. Simulation model for comparison of the operation of panels with bypass diode and relay.

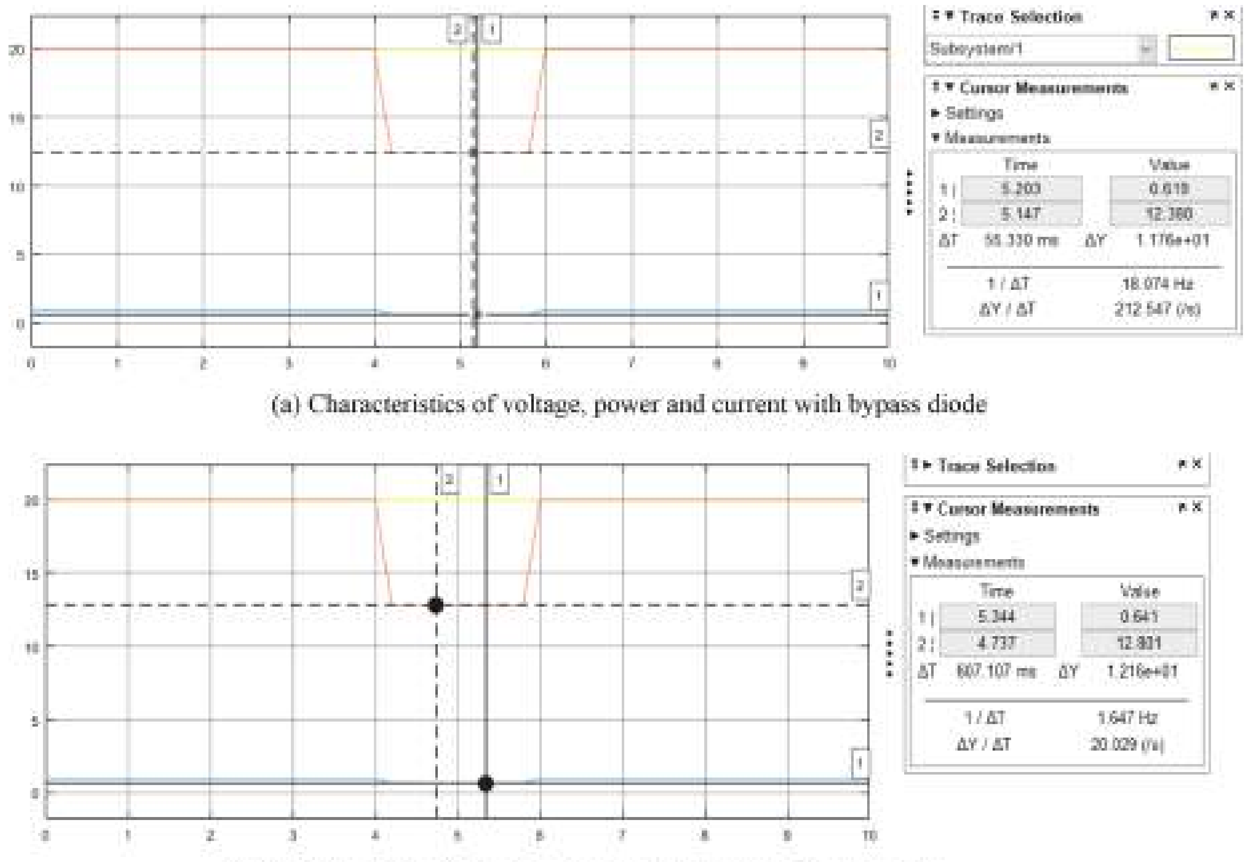

(a) Characteristics of voltage, power and current with bypass diode

(b) Characteristics of voltage, power and current with bypass relay

Fig. 12. Comparison of Bypass diode and relay configuration.

Table 2
Summary of operating modes and performance comparison.

S.No	Rating of one Panel	Irradiance	Panel Current	Panel voltage	Panel Power	Panel Performance with different components under partial shading				
			Without any bypass device							
1.	10Volt, 6 Watt (Standard)	Same on every cell (1000 W/m2)	1Amp	20Volt	20 Watt					
2.		Under shading condition	0.647 Amp	19.99 Volt	12.94 Watt	Parameter	Current (A)	Voltage (V)	Power (W)	Power Losses (mW)
						Diode	0.62	19.99	12.39	550
						Relay	0.64	19.99	12.79	150

Table 3
Results of partial shading on one panel from 1000 W/m2 to 50 W/m2 of operation with diode and relay.

Conditions		When irradiance is 1000 W/m2 (without shading)			When irradiance is 50 W/m2 on one panel		
		Voltage (V)	Current (A)	Power (W)	Voltage (V)	Current (A)	Power(W)
Power (without any device)		20	1	20	19.99	0.647	12.94
With Bypass diode	(H. results)	20	1	20	19.99	0.62	12.39
	(Sim. results)	20	1	20	20	0.619	12.38
With Relay	(H. results)	20	1	20	19.99	0.64	12.79
	(Sim. results)	20	1	20	20	0.64	12.80

Table 4
Technical details of devices use.

S.No	Device	Max OPERATING Temp.	Relay Voltage	Relay Current (mA)	Resistance (ohms)	Power (mW)
1.	Diode(In4007)	75 °C				950 (for 1 amp current)
2.	Relay	90 °C	12	12.5	960	150

Table 5
Comparison of proposed design with other components.

S. No	Device	Free From Thermal Runaway Condition	Possibility of Open circuit fault	Additional gate circuitry required	Forward voltage drop (mv)	Power consumption current (mW)	Power losses depends on forward current
1.	relay logic	YES	NO	NO	NO	150	NO
2.	SM74611 [23]	NO	YES	YES	26	208	YES
3.	Microsemi LX2400 [24]	NO	YES	YES	45	450	YES
4.	STM SPV1001 [25]	YES	not provide in data sheet	YES	yes (Actual data not provide in data sheet)	420	YES

operation with the diode provides 4.25% less power, whereas with the relay, it provides 1.15% lesser power from the available power. According to TABLE 2, the power consumption of relay can be calculated as total available power minus power in case of the relay which comes as 12.94–12.79 = 150 mW. The total power consumed by the relay is therefore, 150 mW that is equal to the same given in the datasheet of relay [21]. In case of the diode, the forward voltage drop as per the datasheet for IN4007 diode is 887 mV for 0.62 A current.

The comparison chart of the proposed design with other components is shown in TABLE 5. The relay specimen that is used in the experiment is Omron G5V-1-T90. If the value of load current is high, other models of the relay like ALQ112 for 10 A, may be used. The advantage of the relay is that it withdraws only current actually required by its coil to get energized. So, the power consumption is fixed and independent of load current. The SM 74,611 having the power consumption of 208 mW that depends on its forward current [23]. In LX2400, the power consumption is 450 mW and increases with the forward current. The SPV1001 offers 420 mW power consumption and it again increases with the forward current.

The other electrical parameters are also compared, shown in TABLE 5. The relay logic is free from the thermal runaway condition, the open circuit fault and the forward voltage drop. The relay offers the lowest resistance when energized. So, due to the low resistance of this metallic contacts of the relay, the forward loss in the relay is very low. The operating time of the relay is 5 ms which is quite appropriate for this operation. This is the only semiconductor free method for bypassing the current.

Conclusion

The bypass technique for the solar PV panel using electromagnetic relay is tested successfully. The experiments are performed on PV panel setup with conventional bypass diode as well as with the proposed relay. The results of the performance are compared at variable irradiance conditions. Further, the results have been validated through the developed model on Matlab/Simulink. The proposed method works successfully and consumes only 150 mW power losses under partial shading condition which is very low in comparison with the bypass diode, that consumes 550 mW at 0.62 A under the same shading condition. The proposed method is judged as a better alternative, replacing the conventional methods in terms of the absence of thermal runaway condition, a lesser requirement of control circuitry, elimination of open circuit fault, and reduction of forward loss. The other advantages of the proposed circuit are observed as its independence on temperature, offering semiconductor-free alternate path for current, absence of jumble circuitry, offering plug and play option, ability to operate without any external signal or any other device for controlling purpose. The power consumption of the proposed relay is independent of load current and it uses the unutilized power of the cell itself that is neglected in case of bypass diode. Further, it needs no external power supply, no effect on the normal operation of the solar panel and responds rapidly under low irradiance condition.

Declaration of Competing Interest

We don't have any conflict of interest.

Acknowledgment

The work is carried out with the support of Centre of Excellence in Renewable Energy, IIT(ISM), Dhanbad, funded by MHRD, Government of India, established under the scheme of Centers of excellence for Training and Research in frontier areas of science and technology.

References

[1] Silvestre Santiago, Boronat Alfredo, Chouder A. Study of bypass diodes configuration on PV modules. Appl Energy 2009;86(9):1632–40. https://doi.org/10.1016/j.apenergy.2009.01.020.
[2] Hasyim, Suryanto E, Wenham SR, Green MA. "Shadow tolerance of modules incorporating integral bypass diode solar cells. Solar cells 1986;19(2):109–22. https://doi.org/10.1016/0379-6787(86)90036-0.
[3] Ramaprabha R, Mathur BL. "Impact of partial shading on solar PV module containing series connected cells. Int J Recent Trends Eng 2009;2(7). http://citeseerx.ist.psu.edu/viewdoc/download?doi=10.1.1.479.6970&rep=rep1&type=pdf.
[4] Data sheet of 1n4007 datasheet Fairchild. https://www.mouser.com/datasheet/2/149/1N4001-81693.pdf. (2014).
[5] Dhere, Neelkanth G, Shiradkar Narendra, Schneller Eric, Gade Vivek. The reliability of bypass diodes in PV modules. Reliability of photovoltaic cells, modules, components, and systems vi, 8825. International Society for Optics and Photonics; 2013. p. 88250. https://doi.org/10.1117/12.2026782.
[6] Steim Roland, Choulis Stelios A, Schilinsky Pavel, Lemmer Uli, Brabec Christoph J. Formation and impact of hot spots on the performance of organic photovoltaic cells. Appl Phys Lett 2009;94(4):24. https://doi.org/10.1063/1.3073857.
[7] Solheim, Hans J, Fjær Hallvard G, Sørheim Einar A, Foss Sean Erik. "Measurement and simulation of hot spots in solar cells. Energy Procedia 2013;38:183–9. https://doi.org/10.1016/j.egypro.2013.07.266.
[8] Kim, Katherine A, Krein Philip T. "Photovoltaic hot spot analysis for cells with various reverse-bias characteristics through electrical and thermal simulation. In: 2013 IEEE 14th Workshop on control and modeling for power electronics (COMPEL); 2013. p. 1–8. https://doi.org/10.1109/COMPEL.2013.6626399.
[9] Zhang Qi, Li. Qun. Temperature and reverse voltage across a partially shaded Si PV cell under hot spot test condition. In: 2012 38th IEEE photovoltaic specialists conference; 2012. p. 001344–7. https://doi.org/10.1109/PVSC.2012.6317849.
[10] Spanoche, Sorin A, David Stewart J, Hawley Shiloh L, Opris Ion E. "Model-based method for partially shaded PV modules hot spot suppression. In: 2012 IEEE 38th photovoltaic specialists conference (PVSC) PART 2; 2012. p. 1–7. https://doi.org/10.1109/PVSC-Vol2.2012.6656784.
[11] Herrmann, W. WWiesner, Vaassen W. "Hot spot investigations on PV modules-new concepts for a test standard and consequences for module design with respect to bypass diodes. In: Conference record of the twenty sixth IEEE photovoltaic specialists conference-1997. IEEE; 1997. p. 1129–32. https://doi.org/10.1109/PVSC.1997.654287.
[12] Yoshioka, Hideki SNishikawa, Nakajima S, Asai M, Takeoka S, Matsutani T, Suzuki A. Non hot-spot PV module using solar cells with bypass diode function. In: Conference record of the twenty fifth IEEE photovoltaic specialists conference-1996. IEEE; 1996. p. 1271–4. https://doi.org/10.1109/PVSC.1996.564364.
[13] Jia, Renhe, Dapeng Wang, Michel Frei, Tzay-Fa Jeff Su, David Tanner, and Chris Eberspacher. "Cell isolation on photovoltaic modules for hot spot reduction." U. S. Patent Application 12/483,948, filed June 3, 2010. https://patents.google.com/patent/US20100132759A1/en.
[14] Stefan Wendlandt, Drobisch Alexander, Buseth Torfinn, Krauter Stefan, Grunow Paul. Hot spot risk analysis on silicon cell modules. In: 25th European Photovoltaic Solar Energy Conference and Exhibition; 2010. p. 4002–6. https://doi.org/10.4229/25thEUPVSEC2010-4AV.3.13.
[15] Capulong, Jose Francisco, and Emmanuel Abas. "Chucks for supporting solar cell in hot spot testing." U.S. Patent 9,116,202, issued August 25, 2015. https://patents.google.com/patent/US9116202B2/en.
[16] Molenbroek E, Waddington DW, Emery KA. "Hot spot susceptibility and testing of PV modules. In: The conference record of the twenty-second IEEE photovoltaic specialists conference-1991. IEEE; 1991. p. 547–52. https://doi.org/10.1109/PVSC.1991.169273.
[17] Dhimish Mahmoud, Holmes Violeta, Mather Peter, Sibley Martin. Novel hot spot mitigation technique to enhance photovoltaic solar panels output power performance. Sol Energy Mater Sol Cells 2018;179:72–9. https://doi.org/10.1016/j.solmat.2018.02.019.
[18] Kim, Katherine A, Krein Philip T. "Hot spotting and second breakdown effects on reverse IV characteristics for mono-crystalline Si photovoltaics. In: 2013 IEEE energy conversion congress and exposition. IEEE; 2013. p. 1007–14. https://doi.org/10.1109/ECCE.2013.6646813.
[19] Dhimish, Mahmoud Violeta Holmes, Mehrdadi Bruce, Dales Mark, Mather Peter. PV output power enhancement using two mitigation techniques for hot spots and partially shaded solar cells. Electric Power Syst Res 2018;158:15–25. https://doi.org/10.1016/j.epsr.2018.01.002.
[20] Monolithic solar cell and bypass diode system Patent number US 4759803 A. https://patents.google.com/patent/US4759803A/en. (1988).
[21] https://www.mouser.in/datasheet/2/307/en-g5v_1-1097070.pdf. (2011).
[22] Gupta, A., Chauhan, Y.K., Maity, T.: Indian Patent Application. no 201731047389. "An arrangement for replacement of bypass diode by relay in a solar photovoltaic system." 2018. https://ipindiaservices.gov.in/PublicSearch/PublicationSearch/ApplicationStatus.

[23] http://www.ti.com/lit/ds/symlink/sm74611.pdf. (2016).
[24] https://www.all-electronics.de/wp-content/uploads/migrated/document/88664/402ag1211-pdf-1-ds-lx2400-rev10.pdf. (2011).
[25] https://www.st.com/content/ccc/resource/technical/document/application_note/3a/8f/fd/5f/03/d3/44/05/DM00029487.pdf/files/DM00029487.pdf/jcr:content/translations/en.DM00029487.pdf. (2011).

Ankur Kumar Gupta is a research scholar from IIT (ISM) Dhanbad. He has worked as an R&D Engineer in the field of power electronics (AC to DC and DC to DC CONVERTER). His research area includes Power Electronics and Converters, Renewable energy-based electrical power generation.

Tanmoy Maity, received PhD from Bengal Engineering & Science University, Shibpur. He has six years industrial and more than eighteen years academic experience. He is currently working as Associate Professor in Indian Institute of Technology (ISM), Dhanbad, Jharkhand, India.

Anandakumar H, Professor(Associate) and Research Head in Department of Computer Science and Engineering, Sri Eshwar College of Engineering, Coimbatore, Tamil Nadu, India He has received his Master's in Software Engineering and PhD in Information and Communication Engineering from PSG College of Technology under, Anna University, Chennai. His-research areas include Cognitive Radio Networks, Mobile Communications and Networking Protocols.

Yogesh K. Chauhan has obtained Ph.D. on induction generator from Thapar University, Patiala, Punjab. Presently, He is working as Associate Professor, KNIT Sultanpur. He is having more than 20 year of teaching/research experience. His-research interests include Power Electronics and Drives, renewable energy based electrical power generation.

Wireless Personal Communications
https://doi.org/10.1007/s11277-020-07979-8

An Efficient Privacy-Preserving ID Centric Authentication in IoT Based Cloud Servers for Sustainable Smart Cities

Ajay Kumar[1] · Kumar Abhishek[1] · Xuan Liu[2] · Anandakumar Haldorai[3]

Accepted: 11 November 2020

Abstract
Smart cities or Smart societies require Internet of Things (IoT), for connecting numerous devices to enormous asset pools in cloud computing. This coordination of embedded tools plus cloud servers conveys the extensive applicability of IoT in Smart Cities. However, authentication and data protection, play a major job in secure coordination of these two technologies. Considering this, in 2017, Chang et al.s system introduced famous verification system dependent on an elliptic curve cryptography (ECC) for IoT plus cloud servers for Smart Cities and guaranteed that it fulfills need of security protocols and is safe to different sorts of assaults. Nevertheless, in this paper, we demonstrate that Chang et.al. system is defenseless to a privileged insider intrusion, server impersonation intrusion, known session-specific information intrusion and offline password guessing intrusion. In addition, it does not accomplish device anonymity and mutual authentication. Considering this weakness of existing system, we propose an authentication system dependent on ECC for IoT and cloud servers in Smart Cities. The suggested system accomplishes mutual authentication and supports fundamental safety necessities. The informal security examination, performance analysis and contrast of the suggested system with existing systems prove that the suggested method is powerful, effective and stout as a counter to manifold security threats faced by Smart Cities. The formal confirmation of the suggested procedure is performed by AVISPA tools, which affirms its safety strength within the sight of a conceivable invader.

Keywords Smart cities · Smart homes · Authentication · Elliptic curve cryptography (ECC) · Security intrusion in smart homes · Security analysis · Wireless management

✉ Ajay Kumar
ajayk.phd18.cs@nitp.ac.in

Kumar Abhishek
kumar.abhishek@nitp.ac.in

Xuan Liu
yusuf@yzu.edu.cn

Anandakumar Haldorai
anandakumar.psgtech@gmail.com

1 Department of Computer Science and Engineering, NIT, Patna, Bihar, India

2 School of Information Engineering, Yangzhou University, Yangzhou, China

3 Department of Computer Science and Engineering, Sri Eshwar College of Engineering, Coimbatore, TamilNadu, India

Published online: 20 November 2020

1 Introduction

For Internet of Things protocols that enable Smart Cities, Elliptic-curve cryptography (ECC) based authentication is one of the productive public key cryptographies, as it offers a comparable security level with a conservative key size [1–4]. It is highly reliable and gives a valuable trade-off between security and effectiveness compared to other authentications. It can build up improved key agreement and provide security with lower computational complexity. Therefore, it is often used for the cloud computing environments that enable Smart infrastructures such as smart streetlights, smart homes and smart healthcare.

Existing studies for ECC-based authentication for smart cities have been great in execution and offer sensible security in the cloud computing field [5]. However, their security level is not sufficient for smart cities as their execution does stand on expectation of design of current small capacity IoT devices [5]. This turns into the inspiration for a proposed superior lightweight system dependent on public key infrastructure (PKI) with ECC for securing cloud computing networks for smart cities.

In view of this fact, several authentication plans [6–11] relying upon ECC have been proposed previously. One such lightweight famous verification system for smart devices was proposed by Kalra et al. [12]. However, the system suffered from two weaknesses in shared authentication and session key. Afterward, Chang et al. [13] improved system proposed by Kalra et al. by offering an enhanced secure authentication system for IoT and cloud servers dependent on ECC. Despite Chang proofs demonstrating that their system accomplished shared authentication and gave fundamental security necessities by security examination, we discovered six shortcomings in it: a failure of shared authentication, intrusion on client anonymity, privileged insider intrusion, secure impersonation intrusion, known session-specific provisional data intrusion and offline password predicting intrusion. This deficiency is demonstrated and broke down in detail in Sect. 3.

This paper improved Chang et al.s. system and removed existing weakness in [6–11] and propose a novel an efficient privacy-preserving ID-based protocol for smart cities. The proposed protocol removed vulnerabilities of the Chang et.al. system. We demonstrate that the proposed system is protected against the elliptic curve discrete logarithm problem (ECDLP) and the elliptic curve DiffieHellman problem (ECDHP). It also resists several security intrusions and furthermore fulfills the security attributes required for advanced protocols design (i.e., known-key security, incomplete advancing confidentiality, key-compromise impersonation robustness, obscure key-share robustness, and key control robustness).By scheming the appliance of hashed combined individuality in the authentication procedure, we can construct a comprehensive system with user concealment. User concealment [12] means that a distant users actual individuality will be disguised in course of the login, making it difficult for outsiders to trace him/her. The proposed protocol is approved via programmed validation of web security contracts and applications (AVISPA) [14–17] formal validation tool to demonstrate its protection from different dynamic and passive intrusions. It also proves the correctness of mutual authentication. In addition, an optimized secured form of the proposed protocol is proposed to upgrade the protocols computation cost over the previous study. Security and performance analysis are performed on the proposed system. The result demonstrate the efficacy of the proposed system vis- -vis competitive systems and conclude that the proposed system is more robust, efficient, and secure with respect to various known intrusions. Ultimately, the offered system has reduction in computational overheads vis-a-vis other ECC-based systems, making it more appropriate for application on IoT cloud-based application for Smart cities.

The current paper is ordered as follow. Section 2 gives the literature review. The crypto analysis of Chin-Chen Chang system utilized in the proposed system is given in Sect. 3. The proposed ESL-secure ID-based the system is introduced in Sect. 4. In Sect. 5 the proposed protocol crypto analysis is led by utilizing AVISPA tool and ProVerif tool, and informal security investigation. We give performance and proficiency assessment in Sect. 6. In Sect. 7, we record the inferences and future works.

2 Related Work

The Dhillon et al. [18] proposed a verification scheme for therapeutic experts to access data from IoT-cloud network-based medicinal services applications. However, this scheme lacked user anonymity and did not provide a robust identity check. Amin et al. [2] asserted that the previously proposed schemes (e.g., [19]) were powerless against different security attacks (e.g., insider attacks, offline password-guessing attacks, and impersonation attacks) and, furthermore, devised a novel scheme to improve the existing schemes. Subsequently, Feng et al. [20] introduced an authentication scheme that was impenetrable for replay-attacks. This scheme utilized the improved challenge-response technique. Nikooghadam et al. [21] performed the cryptanalysis of the scheme proposed by Kumari et al.[22] and guaranteed that Kumari et al. 's scheme was vulnerable to password guessing attack and hence did not guarantee client anonymity. To avoid the discovered security shortcomings and improve the existing security, Nikooghadam et al. [21] proposed a scheme to ensure client anonymity. Subsequently, Aikuhlani et al. [23] proposed a safe, computationally lightweight authentication scheme. This scheme resisted known attacks and supported both session-key agreement and mutual verification. However, they failed to clarify whether this lightweight scheme was applicable to a heterogeneous IoT environment such as smart cities.

Kalra et al. [12] proposed a confirmation and key agreement system for the IoT and the Cloud data center dependent on ”Elliptic Curve Cryptography”. The behavior of ECC make Kalras et.al. plan both effective and protected. In their system, a client and a data center would first be able to validate one another and then arrange one transient session key to utilizing. Notwithstanding, Chang et al. discovered two shortcomings in Kalras et.al. plan: a disappointment of shared authentication and mistiness of the session key. To evacuate that drawbacks, Chang et.al. proposed notes on Secure confirmation plot for IoT and cloud data centers. Their plan improved mutual authentication and gives a session key understanding. A lightweight attribute-based encryption system utilizing ECC for IoT based smart civic infrastructure was suggested by Yao et al. [6].

At the same time, an authentication plan dependent on ECC for RFID frameworks for IoT based smart home automation systems was created by Moosavi et al. [7]. A review of RFID confirmation conventions for IoT in wearable technologies on ECC was finished by He et al. [24], where they analyzed the overheads of both the tag and the server side. Kalra et.al. [25] had completed a definite overview of ECC based protocols. ECC likewise ended up being the effective decision as compared to other open key cryptographic methods for accomplishing shared authentication amongst smart devices and servers in cities and organizations. ECC centered verification procedures appropriate for smart devices used in homes recommended by Wu et al. [26], Tian et al. [27], Abichar et al. [28] had different drawbacks. The procedure offered by Wu et al. used client verification by the server. This was hazardous as an aggressor could imitate a server to get data from the client. Then again, the protocol offered by Tian et al. and Abichar et al. gave shared authentication utilizing certificates. Certification systems cause an increment in cost as the server and clients needed to complete extra calculations to confirm each other's individuality. This made them inappropriate for deployment in smart cities. ECC based authentication procedures for smart devices in homes, healthcare and infrastructure have likewise been proposed by Yang et al. [29], Islam et al. [30] and Debiao et al. [8], Ray et al. [31], Granjal et al. [32], Jiang et al. [33]. These suggested procedures dependent on various types of ECC, utilizing ideas extending from timestamps to certificate-based shared authentication.

3 Crypto Analysis of Changs Authentication System

We analyzed various existing scheme from 2015 to till now. In our examination we found that Changs et.al. provided the security analysis of one of the famous Karla et.al. authentication scheme and provided imperoved version of security. However, in our analysis we found that Changs et.al. fail to address significance aspect of security. Thus, in this segment, we demonstrate the security flaws of Changs et.al. system that make it unsuitable for deployment in smart cities (See Figs. 1 and 2). The brief reviews of Changs et.al. authentication system can be found in [13]. We highlight that the system has certain security glitches and that an intruder can post different types of invasions on Changs et.al. system. For the suitability of explanation, the

vocabulary, and symbolizations used in the paper are briefed in Table 1 as mentioned:

1. In Changs et.al. authentication system, the embedded devices cannot successfully compute A_i, ensuing in a failure of shared authentication.
   Since device computes $A_i = H\left(T_i \oplus H\left(P_i\right) \oplus CK'\right)$. However, to compute A_i need CK not Ck'. In addition, it's impossible to extract Ck from CK' due to difficulties of ECDLP [34]. Thus, deduction $V_i' = ?V_i$ becomes false.
2. Attack on user anonymity: The device-specific identity is a confidential parameter, it helps an intruder to trace the devices login logs and current position so preserving it is one of the important aspects of distant operator authentication problem. In Chang et.al.

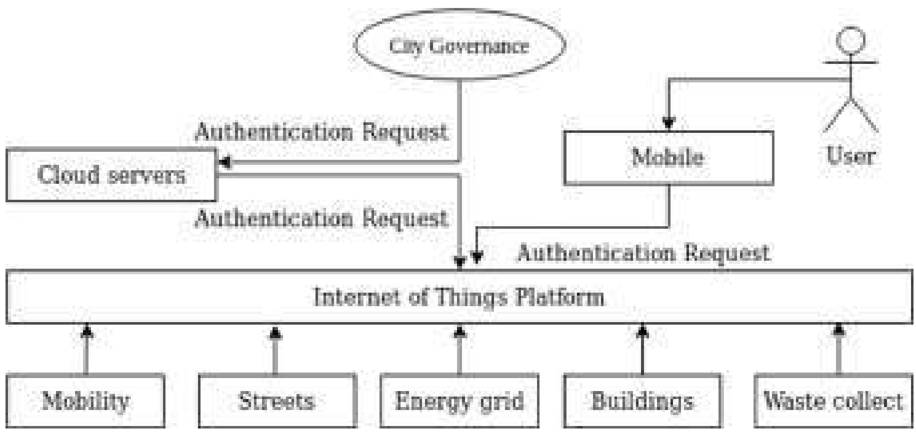

Fig. 1 Authentication requests in Smart Cities

Table 1 Notations guide

Notations	Description
ID_i	Embedded device Id
EXP_{TIME}	Expiration time of the cookie
R	Random number
$P_1, P_2, P'_2, P_3, P_4, P'$	Challenges
X	Server privatekey
||	Concatenation
H()	One-way has function
$\oplus$	XOR operation
P	Password
C_K	Session cookies
G	Generator function

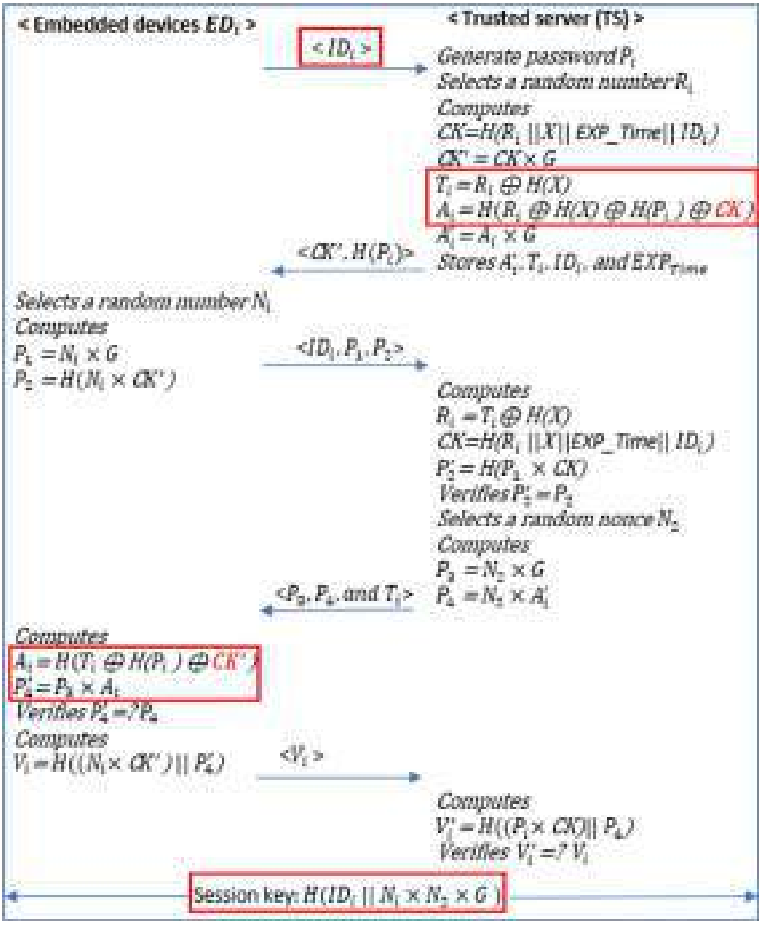

Fig. 2 Chin-Chen Chang ECC-based SignUp and login system [13]

system, during authentication user identity u_i and other security parameters $\left(P_1, P_2, ID_i\right)$ are openly directed over the public network deprived of any kind of encryption. Therefore, anyone is able to identify the specific demand came from which user minus putting much exertion. Therefore, this system fail to prevent the intrusion on operator secrecy and fails to preserve the operators anonymity.

3. Privileged insider intrusion: As Identity-based cryptosystems (IBC) have weakness of suffering from insider intrusion as the trusted server knows the device-specific authorizations. Even the channel is secure, an insider from the server's side can effortlessly acquire session cookie CK and password P_i. Now using this private information, every insider can mimic himself as the genuine device ID_i by altering the variables of some parameters as specified in Impersonation Attack. Thus, this system fail to prevent insider intrusions.
4. Server impersonation intrusion : If an intrusioner can steal this record stored in a database by some means, the record is useful for launching Impersonation Attack. Whenever device ID_i send challenge $< ID_i, P_1, P_2 >$ to TS through an open channel, the intrusioner intercepts the server and blocks its communication. Now, the intrusioner chooses a randomly $n_2 \in Z_p$ and computes challenges $P_3^{''} = n_2 \times G$ and $P_4^{''} = n_2 \times CK$, and sends it $< P_3^{'}, P_4^{'}, T_i >$ back to the device ID_i. On receiving device ID_i computes $A_i = H\left(T_i \oplus H\left(P_i\right) \oplus CK'\right)$ and $P_4^{'} = P_3^{''} \times A_i$ and verifies $P_4^{'} ? = P_4^{''}$. The result come true, thus device falsely insure that it connected to legal. In this way, the intrusioner successfully impersonates the server and compute session key S= $H\left(ID_i \parallel N1 \times N2 \times G\right)$.
5. Known session specific temporary information intrusion: If session connected data inadvertently discloses then discloser would not anyhow lead to negotiation and disturb the confidentiality of the session key [28, 29]. In Chang et.al. system, the session key is computed as S= $H\left(ID_i \parallel N1 \times N2 \times G\right)$ where ID_i, $P_1, P_2, P_3 and P_4$ sent over the open channel so easily intercepted. As secrecy of the session key depends purely upon the N1 or N2 which ensures the hardness of the session key [28]. Thus, partial exposure to $N1/N2$ of the session key to any outsider turn into disclose of the session key. Hence, this system fail to prevent known session specific temporary information intrusions.
6. Offline password predicting intrusion: Assuming an intrusioner obtained the cookie data CK, and P3, P4, T_i by intercepting and blacking the communication of the embedded device. Now intrusioner guess P_j, apply Hash H(P_j) and computes $A_i = H\left(T_i \oplus H\left(P_i\right) \oplus CK'\right)$ and $P_4^{'} = P_3^{''} \times A_i$ and verifies $P_4^{'} ? = P_4^{''}$. This step of computing and verifying repeat until correct P_j is found. Therefore, this system fail to prevent offline guessing intrusions.

   To solve this limitation of Changs et.al. system, we proposed an effectual securing novel ID based authentication system for IoT and cloud server for deployment in smart cities and smart infrastructure projects. Details defined in the next section.

4 Proposed ECC-Based System

This section puts forward the new and improved operator authentication system for IoT cloud and server. The suggested system based on Changs et.al. system; therefore, it challenges and removes all the formerly stated security problems and susceptibilities of their system. As Changs et.al. system, the proposed system also involves two phases (i.e., registration stage and password authentication stage) which include session key distribution stage. Figures 3 and 4 show the schematic of our offered system for the IoT cloud and

Table 2 Notations guide

Notations	Description
Psw_i	Secret password of the embedded device
P_{ke}	Public key of the embedded device
P_{ks}	Public key of the server
I_i	Hashed embedded device ID
CID_i	Server generated embedded device ID
CK	Session cookie
E_{ki},D_{ki} (i.e., Secure channel)	Communication encryption key/Decryption key for registration channel
Openchannel	Public channel during authentication and session key phase
s	Server private key
h	SHA 256 Hash function
X_i,Y_i,X_j,X_j,Y_j C	Challenges
x_{i1},x_{j1}	Ephemeral secretes
E_t	Expiration time of the cookie
A,T	Equations
S_K	Session key
.	Multiplication
G	Elliptical curve generator function

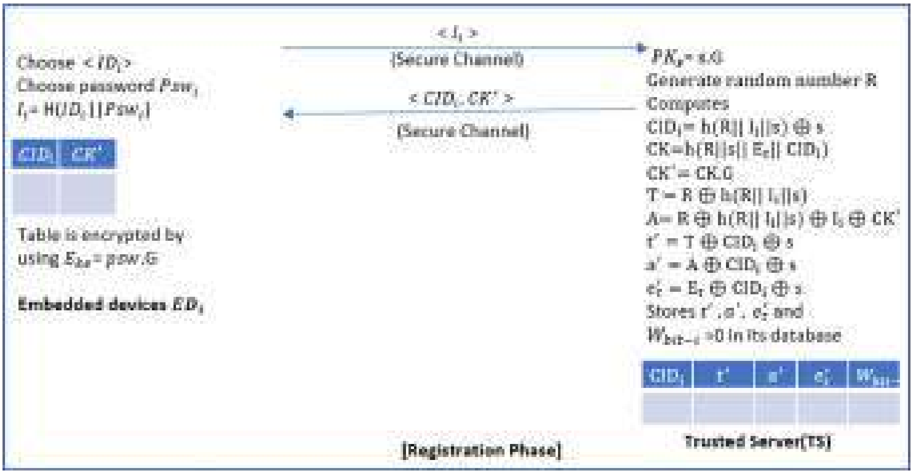

Fig. 3 The proposed ECC-based Signup system

server in smart cities and smart infrastructure projects. For convenience of description, the vocabulary and symbolizations used in the paper are concisely given in Table 2 as shown:

4.1 Registration

In the beginning, to make the user legal, a device ED_i must register itself to the third trusted party through a secure channel. The particulars of registration of stage are as follow:

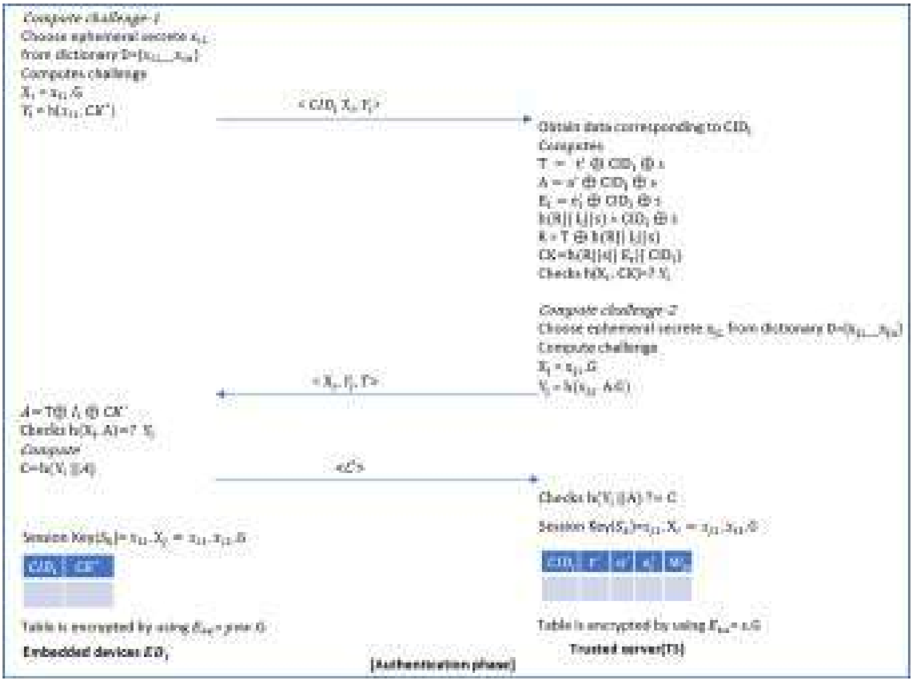

Fig. 4 The proposed ECC-based login system

1. Step 1: Initially, the device ED_i records an authenticated individuality ID_i with trusted server *TS*; and for this, the device chooses a password Psw_i for computing hashed identity $I_i = H\left(ID_i||Psw_i\right)$.
2. Step 2. Then ED_i sends the registration request $I_i >$ to *TS* over a protected trusted channel
3. Step 3. Then *TS* checks whether ID_i has been recorded or not. If ID_i has not been recorded, *TS* choose a random number *R* and calculates CID_i =h(R| | I_i | | s) ⊕ s, $CID_i' = CID_i.G$, $CK = h\left(R||s||E_t||CID\right)$, $CK' = CKxG$, $A=R \oplus h(R||I_i||s)$, $T=R \oplus h(R||I_i||s) \oplus I_i \oplus CK'$, $t' = T \oplus CID_i \oplus s$, $a' = A \oplus CID_i \oplus s$ *and* $e_t' = E_t \oplus CID_i \oplus s$. Then, *TS* store parameters t' , a' , e_t' in the server database, set working bit $W_{bit-i} = 0$ and send CID_i , CK' to ED_i through a secure trusted channel.

Whenever the devices ED_i communicate with TS, the working bit W_{bit} is set to one for the corresponding connected communication; otherwise and after the termination of communication, it is set to zero. Both embedded devices and server encrypts the table using there personal secret key and generator function G, which is depicted in Fig. 4.

4.2 Authentication Phase

To initiate communication with *TS* in the network. Each participant or particular user devices to be authenticated with *TS* (See Fig. 4). Therefore, the authentication of the registered devices with *TS* proceeds as follows:

- Step 1: $ED_i \rightarrow TS$: $< CID_i, X_i, Y_i >$. The legitimately registered devices ED_i , choose an ephemeral secrete randomly $x_{i1} \in Z_p$ from dictionary $D= < x_{i1}, ..., x_{in} >$, then computes challenges $X_i = x_{i1}xG$ using ECC point multiplication, hide x_{i1} inside $Y_i = h\left(x_{i1}xCK'\right)$ and send challeng $< CID, X_i, Y_i > to\, TS$ through a protected channel.
- Step 2: $TS \rightarrow ED_i$: $< X_j, Y_j, T >$. Subsequently getting the challenge TS , calculates recomputes $t' = T \oplus CID_i \oplus s, A = a' \oplus CID_i \oplus s$, $E_t = e'_t \oplus CID_i \oplus s$, h(R| | I_i | | s) = $CID_i \oplus s$, R= $T\oplus$ h(R| | I_i | | s), $CK = h\left(R||s||E_t||CID_i\right)$ and checks $h\left(x_{i1}xCK'\right) = ?Y_i$. Unsuccessful deduction from both the sides to session termination otherwise proceeds to further steps. Now TS choose an ephemeral secret randomly $x_{j1} \in Z_p$ from dictionary $D= < x_{j1}, ..., x_{jn} >$, then compute challenges $X_j = x_{j1}xG$ using ECC point multiplication, hide x_{j1} inside $Y_j = h\left(x_{j1}.A.G\right)$ and send challenges $< X_j, Y_j,$ T>$to\, ED_i$ through a secure channel.
- Step 3: Session Key Computation $S_K = x_{i1}xX_j = x_{i1}xx_{j1}xG = x_{j1}xX_i$: After receiving challenges, ED_i recomputes $A= T \oplus I_i \oplus CK'$ and check $X_jxA = ?Y_j$. Unsuccessful deduction from both sides leads to session termination, otherwise proceed to further steps.

Now users ED_i compute the last challenge $C = h(\ Y_i||A\ )$ with the session key $S_K = x_{i1}xX_j$ and send challenges $< C >\ to\, TS$ through a secure channel.

After receiving challenges, TS recomputes, and check $h\ (\ Y_i||A\ )$=? C. Unsuccessful deduction from both sides leads to session termination; otherwise proceed to further steps. After successful deduction, the TS computes a session key $S_K = x_{j1}xX_i$.

5 Crypto Analysis of the Proposed Protocol

In this segment, we examine the safety of our offered system in smart cities and smart infrastructure projects and demonstrate that it can avert the above-mentioned flaws in Changs et.al. authentication system. The safety of the offered system is based on the collision-free one-way hash function and two NP hard problems: ECDLP and ECDHP. The former argued that when assumed a base point P over an elliptic curve E and a random variable $b\epsilon Zq*$, it is computationally infeasible to search an integer result a such that b = aP., and the latter defined that when assumed three parameters $P, aP, bP\epsilon q*$, it is computationally infeasible to calculate $abP\epsilon q*$.

Summarizing the chief security benefits of our suggested system as follows:

5.1 Informal Security Analysis

This subsection presented how the suggested system is robust against all known cryptographic intrusions in smart cities and smart infrastructure projects and also it represents its comparison with existing systems by using safety attributes as pronounced underneath.

Reply intrusion

Using a reply intrusion, an attacker may imitate a genuine user by re-claiming the message $< CID_i, X_i, Y_i >$ found from a preceding protocol run and transferred it to the TS. After receiving a log-in request, TS computes and verifies $Y'_i = ?Y_i$ and sends back new challenges X_j, Y_j, T to ED_i . However, after impersonating X_j, Y_j, T to ED_i messages, the intrusioner unable to compute $A= T \oplus I_i \oplus CK'$ without knowledge of I_i and C'_k . Since C'_k and I_i , is neither directed over any messages over public channel nor can be gotten from the embedded circuit. ED_i due to its tamper-proof design. Without knowledge of the secret key x_{i1} *and* x_{j1} of the device and server, its unmanageable for the intrusioner to cannot calculate the valid session key $S_k = x_{i1}.x_{j1}.G$ and verify challenge $C_i = h\left(Y_i||A\right)$. Hence, the reply intrusion is infeasible to the proposed system.

Password guessing intrusion

In the recommended system, embedded device password psw_i store in the form of a password generator (i.e., $P_{ke} = psw_i.G$) and wrapped in the form of $I_i = h\left(ID_i||psw_i\right)$. Consequently, the intrusioner cannot guess the password psw_i without knowledge of I_i and P_{ke} . Since I_i of ED_i is not transmitted over any messages on public channel nor can be gotten from the embedded device ED_i due to its tamper-proof design (i.e., nor is stored in the ED_i and *TS*). Therefore, the recommended system prevented the password guessing intrusion.

Impersonation intrusion

Supposing that an attacker attempts to imitate embedded devices ED_i and the server TS through replaying with the previous intercept message. However, it is impossible to impersonate embedded devices ED_i and the server *TS*. Therefore, if intrusioner wants to impersonate embedded devices ED_i and the server *TS* anyway, then intrusioners need to create a fresh login request. Since its impossible to extract value stored in tamper-proof embedded devices. Without knowing the knowledge of CID_i *and* CK' , the intrusioner cannot build a effective login request message $< CID_i, X_i, Y_i >$. Also, without knowledge of server secret key s, it is impossible to compute T and A and a create message $< X_j, Y_j, T >$, *where* $X_j = x_{j1}.G$ *and* $Y_j = h\left(x_{j1}.A.G\right)$. Therefore, the recommended system prevents Impersonation intrusions.

Denial of service intrusion

In the recommended system, the server *TS* closed the login session if the number of incorrect enter CID_i' attempts exceeds a limit value. However, the login request will be continued as soon as the correct CID_i is provided. In login phase, support adversary replace message $< CID_i, X_i, Y_i >$ with $< CID_i', X_j', Y_j' >$ by randomly selecting the elliptical curve point x_{i1}' and sent it back to *TS*, but the *TS* computes and compares the previous value with received $Y_i' = ?Y_i$. If *TS* found a difference, *TS* terminate the procedure with a failure communication to the user. Consequently, the recommended system is infeasible to the denial of service intrusion.

Many logged-in users intrusion Suppose adversary got legally embedded device credential CID_i', C_k' with secrete identity I_i by some other means. The adversary attempts to connect with the server by impersonating ED_i . However, in the recommended system, only one legal ED_i communicate with *TS* at the identical time out of all who identify the effective credential. As every time *TS* set a working bit W_{bit-i} equal to one for the corresponding communication ED_i after successful authentication and store it in its database. Every time receiver *TS* will check W_{bit-i} before establishing a connection with requested ED_i . Even receiver *TS* can deny all the requests if W_{bit-i} representing existing ED_i is still communicating with him.

Server spoofing intrusion

Here, the antagonist may attempt to conceal as a server *TS* to recognize the devices ED_i secrete credential. The ED_i secrete credential CID_i is the composition of the hashing of some random secrete R, secrete identity I_i , and server secrete s. In addition, CID_i store in the *TS* encrypted database (i.e., $E_{ks} = s.G$) in the form of $CID_i' = CID_i.G$. Thus, it is impossible for the intrusioner to get ED_i secrete credentials CID_i by any means. Therefore, the recommended system is infeasible to a server spoofing intrusion.

Perfect forward secrecy

Even if the private key of both the ED_i and the server compromised by some other means, the confidentiality of previously established session keys should not be affected, suppose adversary by somehow discovers ED_i s password Psw_i and TSs secret key s; thus it figure out other components from the message. However, adversary cannot derive the session key $S_K = x_{i1}.X_j = x_{i1}.x_{j1}.G = x_{j1}.X_i$. To compute it, adversary needs to find out x_{i1} and x_{j1} from X_i and X_j which seem computationally infeasible due difficulties of computational Diffie-Hellman problem. So if the current session key S_K is leaked, but adversary cannot figure out all the past session keys, since the session key also depends upon the random secretes x_i and x_j . Hence, the recommended system is infeasible to perfect forward secrecy.

Insider intrusion

In the recommended system, during the registration of the device, ED_i send $I_i = h\left(ID_i||psw_i\right)$ instead of password psw_i securely over the secure channel. Thus, the advisor of TS can't obtain the password psw_i since it is protected by ED_i' s identity and collision-resistant one-way hash function *h()*. Thus, the privileged-insider unable to impersonate the legitimate ED_i successfully and hence, the recommended system is infeasible to Insider intrusion.

Known session-specific temporary information intrusion

After successful authentication, both the communicating ED_i and TS compute session key $S_K = x_{i1}.X_j = x_{i1}.x_{j1}.G = x_{j1}.X_i$, which is a combination of ephemeral secrets x_{i1}, x_{j1} . Suppose that an adversary got ephemeral secret x_{i1} by some other means. However, it is impossible for the advisor to derive the session key S_K with the only knowledge of single ephemeral secrets. Therefore, to deriving session key advisor also need to find out x_{j1} from S_k past session key which seems computationally infeasible due difficulties solve the Computational Diffie-Hellman Problem (CDHP) for pairs which are hard to solve by a polynomial-time algorithm. Thus, the recommended system is infeasible to a known session-specific temporary information intrusion or key stroke attacks.

Attack on user anonymity

Device anonymity means that an intrusioner cannot get the devices masked identity I_i from the transmitted messages during the login and authentication phase. Here, identity I_i is well protected by s and the random number R with the help of hash function *h()*. Moreover, s and the random number neither sent through any message nor stored in the ED_i and TS in plaintext. Hence, the recommended system is infeasible to the user anonymity intrusion.

Stolen-verifier intrusion

If the intrusioner got Smart Card/Smart Device by some other mean, the intrusioner could launch a power analysis intrusion to know secret information stored inside. In the recommended system, during the registration phase, the TS store $t' \, a'$ande_t' against CID_i. Even if the intrusioner somehow steals those records, he cannot perform the malicious activity, since intrusioners unable to access challenge (T, A, E_t) because record is protected with the secret key s of TS and CID_i . Moreover, an intrusioner cannot create a valid login request to pass the authentication steps without the knowledge of C_k' since it is not stored in the servers database. In addition, cookie computation $C_k' = C_k.G$ relies on the correct computation of $C_k = h\left(R||s||E_t||CID_i\right)$. Without the knowledge of the servers secret key s, the intrusioner cannot compute a valid cookie C_k . Thus, the intrusioner cannot create a valid login request. Therefore, the recommended system can withstand the stolen-verifier intrusion.

Cookie theft intrusion In the recommended system, the session cookie C_k is deposited and sent in the format of $C_k' = h\left(R||s||E_t||CID_i\right).G$, an ECC point multiplication in the embedded device ED_i. Therefore it is very difficult to excerpt C_k from C_k' because of difficulties of ECDLP. In addition, $C_k^{\prime}$ send through a secure encrypted channel E_k. Consequently, the intrusioner cannot get the cookie $C_k^{\prime}$. Thus, the recommended system is infeasible to cookie stealing intrusions.

Man-in-the-middle intrusion In the recommended system, the man-in-the-middle intrusion is prohibited by shared authentication amongst ED_i and TS that we verified using AVISPA simulation which we explained in Sect. 5.2 the Consequently, the recommended system is infeasible to man-in-the-middle intrusions.

Brute force intrusion To launch the brute force intrusion, the intrusioner needs to excerpt the security parameters X_i, Y_i, X_j, Y_j and T from transmitted messages, Even if the intrusioner is successful in extracting it, however, intrusioner cannot find the password psw_i as servers secret key s is unknown to intrusioner and there is not any method of predicting the arbitrary number x_{i1} and x_{j1} . Therefore, the recommended system can repel the brute force intrusion.

Finally, we present a examination of diverse security characteristics of certain prevailing systems [updated] with the recommended system, as revealed in Table 3. The existing work relevant to each other. Therfore, we consider Kalra et.al. [25] Kumari et.al. [35] and Chang et.al. [13] for comparison work. The comparison shows that the recommended system satisfies all the above weaknesses in the existing systems.

5.2 Formal Security Validation Using AVISPA Tool

In this unit, we performed the simulation of the recommended system using the AVISPA tool [14]. We performed experiment on oracle virtual box installed on window 10 machine provided by Intel Core i5 machine with 3.10 GHz processing speed. Our study simulation shows that the recommended system is protected for replay and man-in-the-middle intrusions. AVISPA a push-button tool for the automatic validation of Internet security-sensitive procedures and tools, which becomes a extensively acknowledged tool for official

Table 3 Security characteristics comparison

Attacking scenarios	Kalra et.al. [25]	Kumari et.al. [35]	Chang et.al. [13]	Recommended
Reply intrusion	Available	Available	Available	Available
Password guessing intrusion	Not Available	Not Available	Not Available	Available
Impersonation intrusion	Not Available	Not Available	Not Available	Available
Denial of service intrusion	Not Available	Not Available	Not Available	Available
Many logged-in users intrusion	Not Available	Available	Not Available	Available
Server spoofing intrusion	Not Available	Available	Not Available	Available
Perfect forward secrecy	Not Available	Available	Not Available	Available
Insider intrusion	Not Available	Not Available	Not Available	Available
Known session-specific temporary information intrusion	Not Available	Not Available	Not Available	Available
Attack on user anonymity	Not Available	Available	Not Available	Available
Stolen-verifier intrusion	Not Available	Available	Not Available	Available
Cookie theft intrusion	Not Available	Available	Available	Available
Man-in-the-middle intrusion	Available	Available	Available	Available
Brute force intrusion	Available	Available	Available	Available

security verification in current years [14]. The AVISPA protocol coded in one of the power languages (i.e., high-level protocol specification language (HLPSL)). This language comprises of the role which represents each participating activity. This role presented in every scenario is separate from every other role. The role receives primary information from the parameter, which communicates with another role through channels. The HLPSL protocol is translated to the intermediate format specification using an HLPSL2IF translator. The input is given to one in four backs ends (i.e., on-the-fly model-checker (OFMC), tree automata-based on automatic approximations for the analysis of security procedures (TA4SP), constraint logic-based intrusion searcher (CL-AtSe)) and SAT-based model-checker (SATMC)) to produce results.

The numerous rudimentary kinds are used for defining the specifications of a dissimilar role. Some of them are; agent: the agent defines the principal name of the intruder by using unusual identifier i, public_key: it represents the public key, symmetric_key: it represents the key used for encryption, const: it defines constant declared in roles, text: it represents nonce which is always renewed and is continuously unique, and it secure communication from the intrusioner, function: it represents irreversible one way hash cryptography function of type hash_func used for modeling, nat: it signifies the natural number in nonmessage context.

The AVISPA tool received input as a designed protocol, analyze it, and generate output exactly by labeling the state whether the procedure is in a benign or insecure state. The channel is used for communication which is hypothetically to be measured by the DolevYao intrusioner. It means that invader is modeled by using the DolevYao model with the possibility that intruder assumes a legitimate role in a procedure run. The session role defines all the basic roles.

The role setting is a top-level role which is the commencement point for implementation and instantiates session role using diverse rudimentary roles to mimic diverse likely situations. Lastly, in the objective unit, as per our requirements of the calculated procedure, we define all necessary and sufficient goals.

While writing code in AVISPA, we wrote two primary roles: one for the user and one for the session. Then we wrote another three roles: one for the session, one for the environment and one for goal. The last three roles are representing the execution environment of the first two roles. The Fig. 4 depicted the specific role performed by the agent. As soon as the device $\left(ED_i\right)$ agent obtains the start signal, the ED_i updates its instance from 0 to 1.

This state is preserved by a variable state. Then ED_i directs the registration request I_i securely to the server through protected channel (Snd). We called it a registration phase. The transmission channel <Snd, Rec> that is used for message transmission of the type of DolevYao threat model, which is an unsafe channel, and delivers the intrusioner to modify, delete the matters of transferred communications. After that, in response ED_i receive the message (CID_i , CK') from the server safely by the assistance of secure Rec channel. In this role, the declaration played_by (ED_i) designates that the mediator named in the variable (ED_i) plays in the role.

During the login phase, ED_i sends a message $< CID_i, X_i, Y_i >$ to the server via the public open channel (See Fig. 5). Then the server responds with message $< X_j, Y_j$, T> to , ED_i via the public channel. Lastly, ED_i replies with the communication C to the server via the public open channel. A knowledge declaration situated at the top of every role is used to specify the intruder's initial knowledge. Immediate reaction transition is of the form

$X = |Y$, which relates an event X and an action Y. The declaration witness ED_i, S, $alice\_bob\_xi1, xi1'$ generated by ED_i , where the random nonce $xi1$ freshly generated for the server (S).

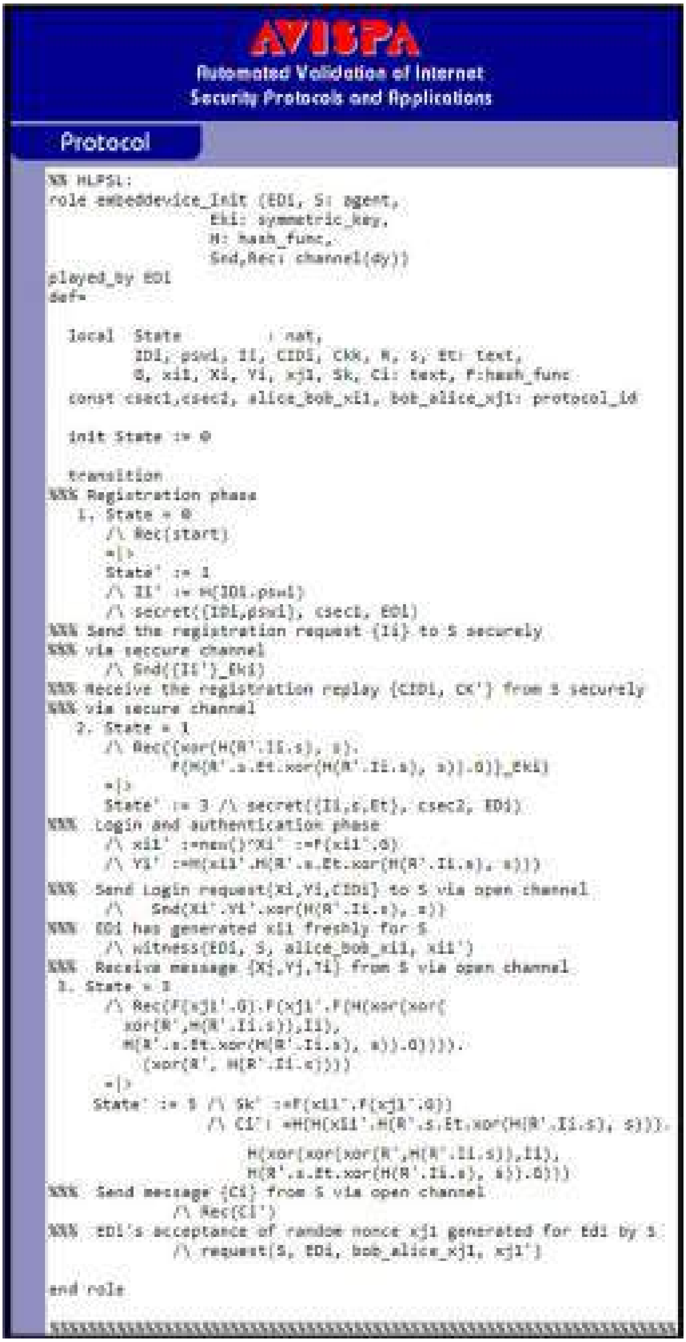

Fig. 5 Role specification for embedded device

Instead, another announcement request $S, ED\_i, bob\_alice\_xj1, xj1'$ shows that the ED_i receipt of the random nonce xj1 produced for ED_i by the server. Similarly, we realized the role of the server during the registration stage. Lastly, we implemented the role for the session, goal, and environment of the recommended system (see Fig. 6). All these roles are the instant with tangible influences in the role session.

In HLPSL, the invader (i) also participated in the implementation of procedure as a existing session, as presented in Fig. 7. We defined two secret goals and two authentication goals. For example, the secret goal (secrecy_of_csec1) indicates that ID_i and Psw_i are kept the secret to the device ED_i only. The authentication goal: authentication_on alice_bob_ $xi1$ means that ED_i generates a random nonce $xi1$, where $xi1$ is only known to ED_i . When the server receives $xi1$ from supplementary communications from ED_i , the server completes a sturdy authentication for devices centered on $xi1$.

In our implementation, we used the CL-AtSe backend. We analyze and discuss the output generated through CL-AtSe backend (See Fig. 8). The section summary stipulates whether the procedure is SAFE, UNSAFE, or INCONCLUSIVE. Our output summary section shows safe terminology, which designates that the recommended protocol is safe against major intrusions. The section details specify that the situation below which the recommended procedure is safe or what condition has been used for finding an intrusion, or in conclusion why the scrutiny was indecisive.

The procedure unit specifies the name of the procedure. The goal unit indicates the key objective of the examination. The backend section represents the name of the backend used. The statistics section represents the time needed by the backend to execute the procedure. The intrusion trace section specifies if an intrusion is found, the trace of the intrusion is printed in a standard Alice-bob format. It represents how the intrusion has been achieved in the procedure.

For protocol analysis, we choose widely accepted back ends CL-AtSe for the execution tests. The back ends CL-AtSe analyzes whether the legal agents can execute the specific system by performing a search of the passive intruder. Then back ends results give intruders with knowledge of some normal sessions among the legitimate agents. We conclude that the recommended protocol is safe from the analysis of simulation result as follow:

Executability keeps an eye on non-trifling HLPSL specifications

Due to some modeling errors, the recommended model cannot once in a while implement to consummation. It might occur that the AVISPA backend shall fail to discover an intrusion if the recommended model cannot reach to a state where that intrusion can occur. An excitability test is then extremely fundamental [14]. The recommended system demonstrates that the procedure portrayal is all around coordinated with the intended objectives, as indicated in Fig. 8 for the output of excitability test.

Replay intrusion check

Aimed at the replay assault check, the CL-AtSe backend confirms whether the genuine mediators can implement the quantified procedure by playing out an inquiry of an inactive invader. This backend gives the interloper the information of certain usual sessions amongst the genuine agents. The test outcomes appeared. Figure 8 validate that our plan is secure counter to the replay intrusion.

Active and passive intrusion check

The summary result for CL-AtSe back ends shows that the recommended system is SAFE. It means that the recommended system is free form all active and passive intrusions.

DolevYao model check

Aimed at the DolevYao model check, the CL-AtSe backend additionally confirms the existence of any man-in-the-middle intrusion conceivable by an invader. It is obvious from the outcomes revealed in Fig. 8 that our system satisfies the design properties furthermore, is additionally safe under this backend.

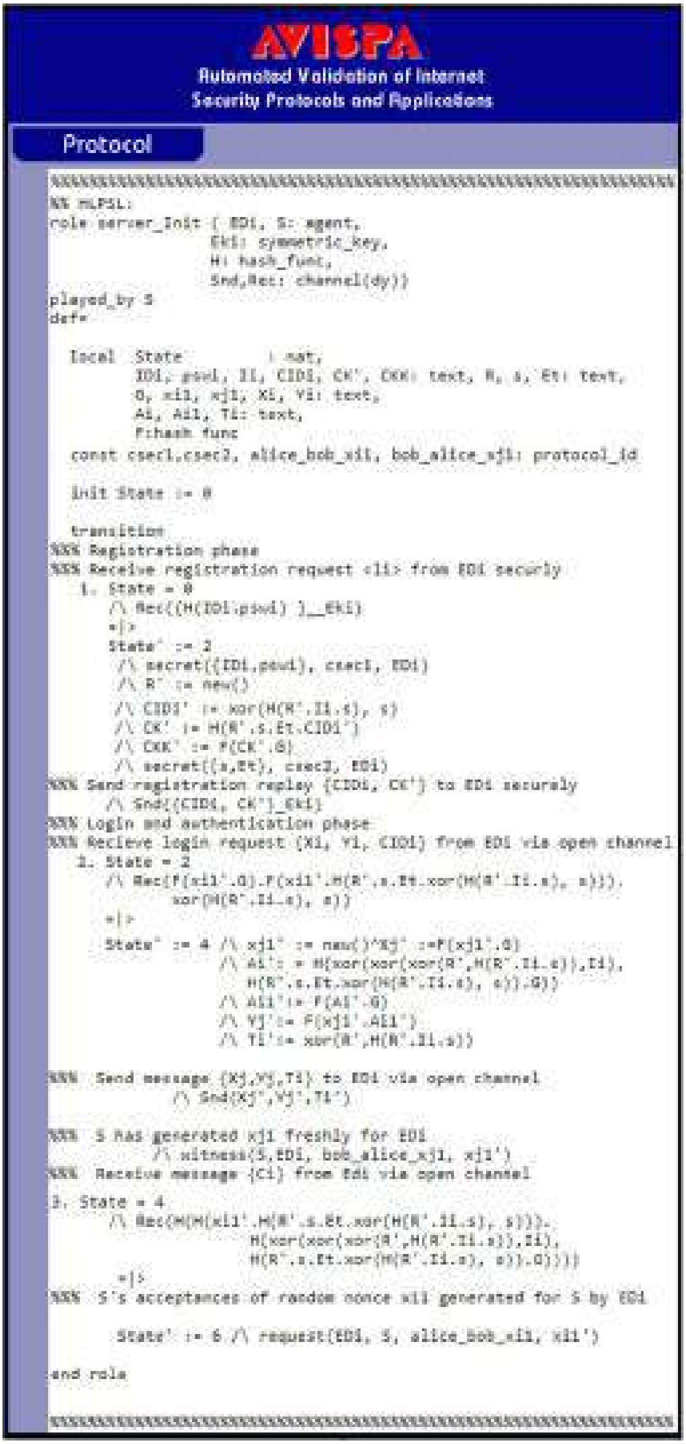

Fig. 6 Role specification for cloud server

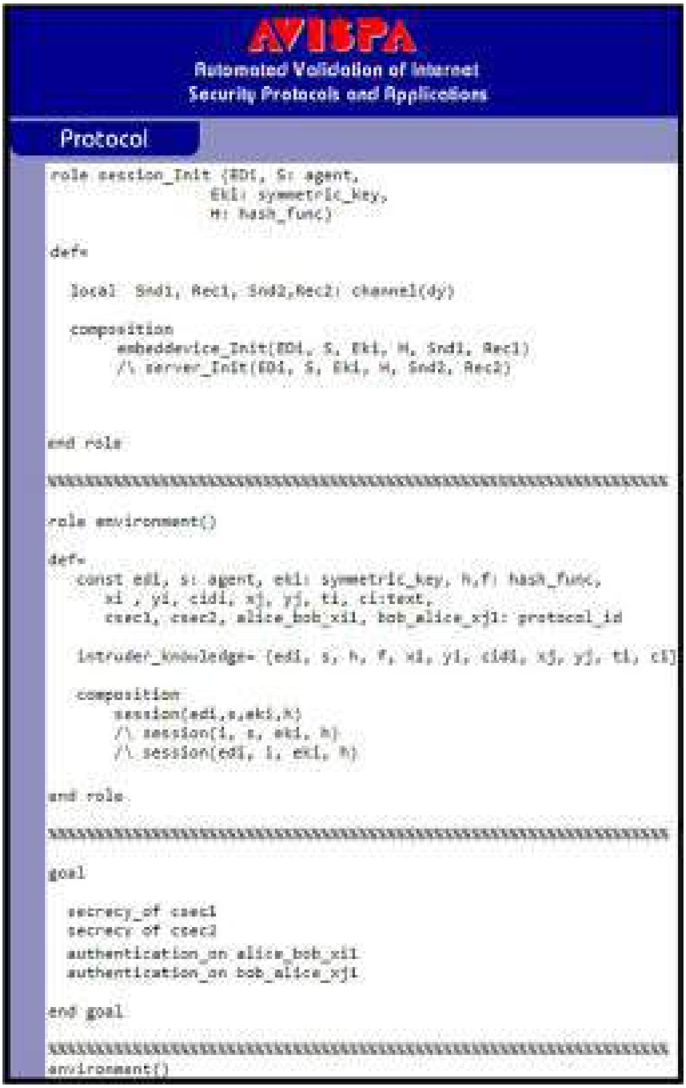

Fig. 7 Role specification for the session, goal and environment

6 Evaluation

This section presented how the recommended system is efficient over Chang et al. system using performance analysis, efficiency study and performance study.

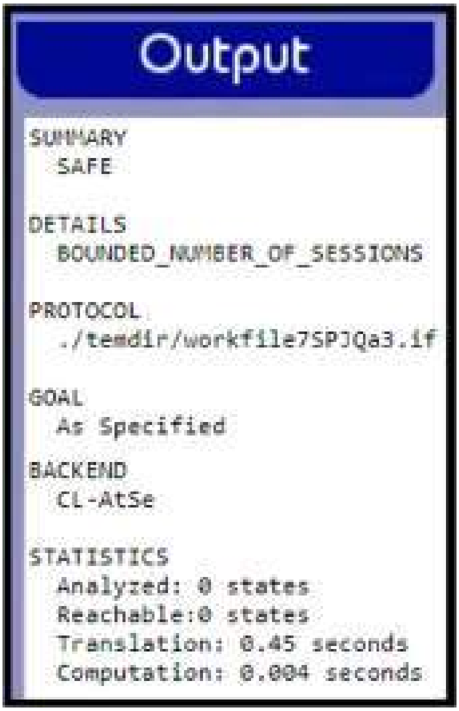

Fig. 8 Analysis result using CL-AtSe backend

6.1 Performance Analysis

In this unit, we computed the enactment of the recommended system and compared it with Chang et.al. system in order to conclude the merits of the recommended system. We defined the following notation utilized to conduct the performance analysis.

- T_h : the execution period of a hash procedure.
- T_{ecm} : the execution period of an ECC point multiplication procedure

6.1.1 Computation Cost

The standard execution time (computation cost) needed of T_h and T_{ecm} are $2.3\mu s$ and 22.26 $\times 10^2 \mu s$ respectively [35]. Note that the computational cost of lightweight processes (i.e., concatenation, contrast, also XOR) has been overlooked, because of inexpensive computation. From Table 4, it is clear that the computational cost of Kalra et al. system, Kumari

Table 4 Computation cost comparison

Systems	Overall Cost
Kalra et.al. [12]	$7T_h + 7T_{ecm} = 15.5981 \times 10^3 \mu s$
Kumari et.al. [35]	$7T_h + 8T_{ecm} = 17.8241 \times 10^3 \mu s$
Chang et.al. [13]	$8T_h + 7T_{ecm} = 15.6004 \times 10^3 \mu s$
Recommended	$5T_h + 6T_{ecm} = 13.3675 \times 10^3 \mu s$

Table 5 Communication cost comparison

Components	Size in bits
ID_i, CID_i	160
(x_{i1}, x_{j1})	160
(C_k, T_i, C_i)	160
(X_i, Y_i, CID_i)	(320+320+160) =800
(X_j, Y_j, T_i)	(320+320+160) =800
$(X_i, Y_i, CID_i + (X_j, Y_j, T_i + C_i)$	(800+800+160) =1760

Table 6 Communication cost and storage cost comparison

Schemes	#Messages	Communication cost/bit	Storage cost/bit
Kalra et.al. [12]	3	1760	320
Kumari et.al. [35]	3	1760	480
Chang et.al. [13]	3	1760	320
Recommended	3	1760	480

et al. system Changs et al. system, and the recommended system are 7 T_h +7 T_{ecm} = 15.5981 $\times 10^3 \mu s$, 7 T_h +8 T_{ecm} = 17.8241 $\times$ $10^3 \mu s$, 8 T_h +7 T_{ecm} = 15.6004 $\times$ $10^3 \mu s$ and 5 T_h +6 T_{ecm} = 13.3675 $\times$ $10^3 \mu s$ respectively. From the computation cost comparison (See Table 4), we conclude that even recommended protocol support forward secrecy and backward secrecy. It is efficient in terms of lighter weight computation power than Kalra et al., Kumari et al., and Changs et al. protocol (See Table 4).

6.1.2 Communication Cost

In this subsection, we do an assumption for computing the communication price of recommended system. Table 5 presents the price of components in the recommended protocol [30]. Designed for an elliptic curve $E_p(a, b)$, all parameters (p, a, and b) are assumed as 160-bits each.

Therefore, an ECC point $X, Y = \left(x_P, y_P\right) \in E_p(a, b)$ takes (160+160)=320 bits. For the recommended protocol, the communication parameters are $X_i, Y_i, CID_i, X_j, Y_j, T_i$ and C_i . $\left(\left(X_i, Y_i, CID_i\right) + \left(X_j, Y_j, T_i\right) + C_i\right)$ (800+ 800+ 160)=1760 bits is communication cost which are the same as compared to Changs et.al. system mentioned in Table 6.

6.1.3 Storage Cost

In this subsection, we performed the assumption for computing the storage cost of the recommended system. Table 5 presents the price of components in the recommended protocol [35]. In the Chang et al.s system, the embedded device stores a cookie (i.e., $C_k^{'}$) consume 320 bits of data. In contrast, in the recommended system embedded device stores cookie, as well as pseudo-identity (i.e., $C_k^{'}, CID_i$), consume 320+160=480 bits of data in its storage mentioned in Table 6. This additional consumption of memory because the recommended system ensures device anonymity while Changs et.al. system does not.

6.2 Efficiency Study

This subsection evaluating the efficiency of recommended system over the existing Changs et.al. [13] system (See Table 7) by satisfying following crucial functionality requirements.

6.2.1 Shared Authentication (P1)

The recommended system provided shared authentication between embedded devices (ED_i) and server (S) using a three-way challenge-response handshake technique. TS validates ED_i by checking $Y_i^{'} = ?Y_i$ and $C_i^{'} = ?C_i$ while ED_i validate S by verifying $Y_j^{'} = ?Y_j$. It's impossible to compute $Y_j^{'}$ without any knowledge of $C_k^{'}$ and T_i . Since both $C_k^{'}$ and T_i are encrypted using the encryption key E_k during transmission. The E_k is made of personal secrete of ED_i and public key of server (P_{ks}). For the above reasons, the intrusioner cannot compute $C_i = h(Y_i||Y_j)$. Thus, only ED_i and S mutually authenticate each other. Consequently, the recommended system accomplishes appropriate shared authentication.

6.2.2 Friendly Password Selection (P2)

In the recommended system, the client can select easy to recall a password psw_i which may be low or high intensity. This password is stored in the password generator format (i.e., $P_{ke} = psw_i.G$). It is very difficult to extract the password from a password generator due to the difficulty of ECDLP [28]. Even identity I_i contains a hash of concat of device identity and password generator, stored in the server. It's very difficult to extract a password generator from I_i due to hashing.

6.2.3 Session Key Agreement (P3)

The recommended system justified the session key contract in the session key computation subsection, which ensures secure session along with highly confidential data exchange between embedded devices (ED_i) and server (TS).

6.3 Performance Study

In this unit, we evaluated the enactment of the recommended system with the present system. We compare the system in terms of security requirements, cost calculation, and functional requirements. After evaluating the existing systems, we found that Klara et al. system is susceptible to password estimating intrusion, masquerade intrusion, denial of service intrusion, many logged-in users intrusion, server spoofing intrusion, perfect forward secrecy, insider intrusion, known session-specific temporary information intrusion,

Table 7 Functional requirements comparison

Schemes	P1	P2	P3
Kalra et.al. [12]	n/a	n/a	n/a
Kumari et.al. [35]	Supported	n/a	Supported
Chang et.al. [13]	n/a	n/a	Supported
Recommended	Supported	Supported	Supported

intrusion on user anonymity, stolen-verifier intrusion, and cookie theft intrusion. While kumari et al. system suffering from password guessing intrusion, impersonation intrusion, denial of service intrusion, insider intrusion, and known session-specific temporary information intrusion. The Chang et al. system has a security loophole because of unprotected toward password guessing intrusion, impersonation intrusion, denial of service intrusion, many logged-in users intrusion, server spoofing intrusion, perfect forward secrecy, insider intrusion, known session-specific temporary information intrusion, intrusion on user secrecy and stolen-verifier intrusion. In contrast, the recommended system removed all those security weaknesses of Klara et al., kumari et al. and Chang et al. system and become preventive against all mentioned security intrusions.

When we discuss cost calculation, we arrive at the point that Klara et al. system have calculation price $15.5981 \times 10^3 \mu s$ with storage price 320 bit and communication price 1760 bit. While the kumari et al. system has computation price $17.8241 \times 10^3 \mu s$ with storage price 480 bit and communication price 1760 bit. The Chang et al. system has computation cost $15.6004 \times 10^3 \mu s$ with storage cost 480 bit, and communication cost 1760 bit. In contrast to all those mentioned systems, the recommended system has calculation cost $13.3675 \times 10^3 \mu s$ with storage cost 480 bit, and communication cost 1760 bit. After the above data, we determine that the recommended system is much effectual in comparison with other existing systems in terms of low computation cost with the cost of the same communication cost. However, the storage price in the recommended system is somewhat augmented. This is supported because the recommended system accomplishes entirely the security necessities while Klara et al., kumari et al. and Chang's et al. system does not.

Finally, when we evaluated the recommended system with prevailing systems by verifying the crucial functionality requirements. The Kalra et al. system does not provision all four functionality requirements (i.e., mutual authentication, friendly password selection, session key agreement, and secure password update). While Kumari et al. system fail to support friendly password selection and secure password update except for shared authentication, and session key contract. The Chang et al. system supports only the session key contract; however, it fails to support mutual authentication, friendly password selection, and secure password update. In comparison with all mentioned system, the recommended system supported all four functionality requirements and removed the gap of the existing system.

By satisfying all security requirements, functional requirements with lower computation cost, we conclude that the recommended system is the sustains judicious efficacy and is well suited to validate the embedded device in the cloud and IoT scenario as compared to other prevailing systems. We summarized the performance of the recommended system over the existing system in Fig. 9.

7 Conclusion with Future Work

We analyze various existing authentication systems from the year 2011 to now. During the analysis, we found that one of the famous Kalra and Sood et al. authentication systems suffers from a security loophole. Later in 2017, Chang et al. improved the Kalra and Sood et al. system by correcting it. However, after doing cryptanalysis, we found that Chang et al. incorrectly corrected Kalra and Sood et al. system. In our cryptoanalysis, we demonstration how Changs et al. system defenseless to off-line password predicting, privileged insider intrusion, secure impersonation intrusion, and known session-specific temporary

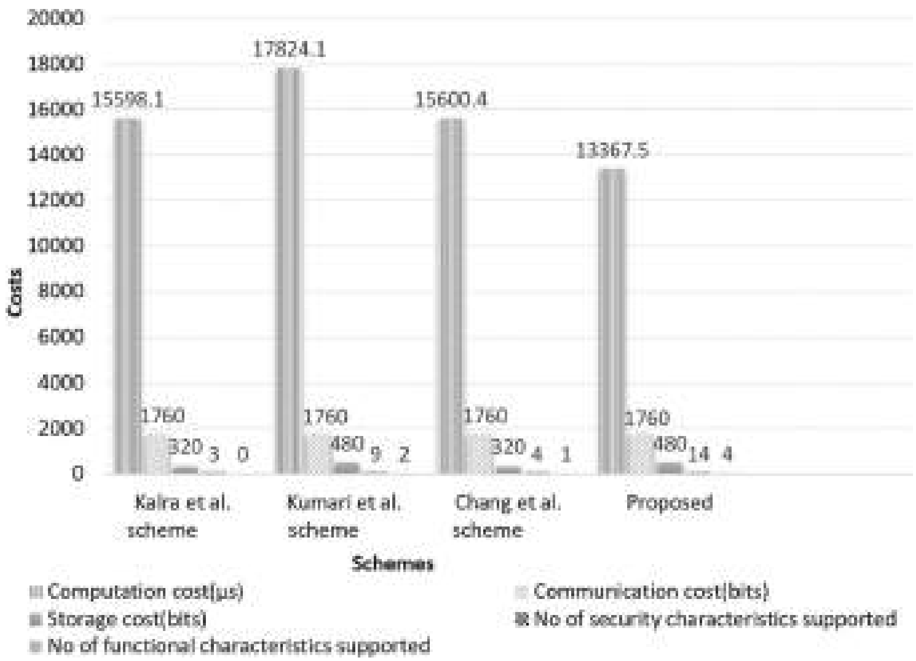

Fig. 9 Performance comparison

information intrusion. We also represented how Chang et al. system is failed to address shared authentication and user secrecy problems, and the protocol has unnecessary redundancy in design. In addition, we also found that the existing systems unable to stand on lightweight computation. To resolve this matter, we recommended a innovative lightweight computational authentication system. We also tested the recommended system by performing simulation by means of the most famous cryptoanalysis tool; AVISPA tool. The result of testing along with informal cryptoanalysis indicates that the recommended authentication system can withstand almost all kinds of intrusions and contents all necessary security requirements, such as user secrecy, shared authentication, the session key security and an effectual verification instrument for the duration of the login stage. We compared the competence of the recommended system with recent existing systems. The consequence shows that the recommended system is lightweight in terms of less computational overheads but at the cost of high storage cost. In the forthcoming plan, we propose to extend the recommended system to improve communication costs and storage costs further.

References

1. Liu, J., Ren, A., Zhang, L., Sun, R., Du, X. & Guizani, M. (2019). A Novel Secure Authentication Scheme for Heterogeneous Internet of Things, in: ICC 2019-2019 IEEE International Conference on Communications (ICC), Organization, IEEE, pp. 1–6.
2. Amin, R., Kumar, N., Biswas, G., Iqbal, R., & Chang, V. (2018). A light weight authentication protocol for IoT-enabled devices in distributed Cloud Computing environment. *Elsevier*, *78*, 1005–1019.

3. Roy, S., Chatterjee, S., Das, A. K., Chattopadhyay, S., Kumari, S., & Jo, M. (2017). Chaotic map-based anonymous user authentication scheme with user biometrics and fuzzy extractor for crowd-sourcing Internet of Things. *IEEE Internet of Things Journal*, *5*(4), 2884–2895.
4. Yang, Y., Wu, L., Yin, G., Li, L., & Zhao, H. (2017). A survey on security and privacy issues in internet-of-things. *IEEE Internet of Things Journal*, *4*(5), 1250–1258.
5. Mahmood, Z., Ning, H., Ullah, A., & Yao, X. (2017). Secure authentication and prescription safety protocol for telecare health services using ubiquitous IoT. *Applied Sciences*, *7*(10), 1069.
6. Yao, X., Chen, Z., & Tian, Y. (2015). A lightweight attribute-based encryption scheme for the Internet of Things. *Future Generation Computer Systems*, *49*, 104–112.
7. Moosavi, S. R., Nigussie, E., Virtanen, S. & Isoaho, J. (2014). An Elliptic Curve-based Mutual Authentication Scheme for RFID Implant Systems., in: ANT/SEIT, 1, pp. 98–206.
8. Debiao, H., Jianhua, C., & Jin, H. (2012). An ID-based client authentication with key agreement protocol for mobile client-server environment on ECC with provable security. *Information Fusion*, *13*(3), 223–230.
9. Liao, Y.-P., & Hsiao, C.-M. (2014). A secure ECC-based RFID authentication scheme integrated with ID-verifier transfer protocol. *Ad Hoc Networks*, *18*, 133–146.
10. Turkanović, M., Brumen, B., & Hölbl, M. (2014). A novel user authentication and key agreement scheme for heterogeneous ad hoc wireless sensor networks, based on the Internet of Things notion. *Ad Hoc Networks*, *20*, 96–112.
11. Farash, M. S., Turkanović, M., Kumari, S., & Hölbl, M. (2016). An efficient user authentication and key agreement scheme for heterogeneous wireless sensor network tailored for the Internet of Things environment. *Ad Hoc Networks*, *36*, 152–176.
12. Kalra, S., & Sood, S. K. (2015). Secure authentication scheme for IoT and cloud servers. *Pervasive and Mobile Computing*, *24*, 210–223.
13. Chang, C.-C., Wu, H.-L., & Sun, C.-Y. (2017). Notes on Secure authentication scheme for IoT and cloud servers. *Pervasive and Mobile Computing*, *38*, 275–278.
14. Von Oheimb, D. (2005). The high-level protocol specification language HLPSL developed in the EU project AVISPA. In *Proceedings of APPSEM 2005 workshop*, (pp. 1–17).
15. Abadi, M., Blanchet, B., & Comon-Lundh, H. (2009). Models and proofs of protocol security: A progress report. *International Conference on Computer Aided Verification, Springer*, (pp. 35–49).
16. Chaudhry, S. A., Farash, M. S., Naqvi, H., Kumari, S., & Khan, M. K. (2015). An enhanced privacy preserving remote user authentication scheme with provable security. *Security and Communication Networks*, *8*(18), 3782–3795.
17. Maitra, T., Obaidat, M. S., Amin, R., Islam, S. H., Chaudhry, S. A., & Giri, D. (2017). A robust ElGamal-based password-authentication protocol using smart card for client-server communication. *International Journal of Communication Systems*, *30*(11), e3242.
18. Dhillon, P. K., & Kalra, S. (2018). Multi-factor user authentication scheme for IoT-based healthcare services. *Journal of Reliable Intelligent Environments*, *4*(3), 141–160.
19. Xue, K., Hong, P., & Ma, C. (2014). A lightweight dynamic pseudonym identity based authentication and key agreement protocol without verification tables for multi-server architecture. *Journal of Computer and System Sciences*, *80*(1), 195–206.
20. Feng, Y., Wang, W., Weng, Y. & Zhang, H. (2017) A replay-attack resistant authentication scheme for the internet of things. in *2017 IEEE International Conference on Computational Science and Engineering (CSE) and IEEE International Conference on Embedded and Ubiquitous Computing (EUC)*, vol. 1, IEEE, (pp. 541–547).
21. Nikooghadam, M., Jahantigh, R., & Arshad, H. (2017). A lightweight authentication and key agreement protocol preserving user anonymity. *Multimedia Tools and Applications*, *76*(11), 13401–13423.
22. Kumari, S., Khan, M. K., & Li, X. (2014). An improved remote user authentication scheme with key agreement. *Computers & Electrical Engineering*, *40*(6), 1997–2012.
23. Alkuhlani, A. M. I., & Thorat, S. (2017). Lightweight anonymity-preserving authentication and key agreement protocol for the internet of things environment. *International Conference on Intelligent Information Technologies, Springer*, (pp. 108–125).
24. He, D., & Zeadally, S. (2014). An analysis of RFID authentication schemes for internet of things in healthcare environment using elliptic curve cryptography. *IEEE Internet of Things Journal*, *2*(1), 72–83.
25. Kalra, S., & Sood, S. K. (2011). Elliptic curve cryptography: survey and its security applications. In *Proceedings of the International Conference on Advances in Computing and Artificial. Intelligence*, (pp. 102–106).

26. Wu, S.-T., Chiu, J.-H. & Chieu, B.-C. (2005). ID-based remote authentication with smart cards on open distributed system from elliptic curve cryptography. In textit2005 IEEE International Conference on Electro Information Technology, IEEE,(vol. 5).
27. Tian, X., Wong, D. S., & Zhu, R. W. (2005). Analysis and improvement of an authenticated key exchange protocol for sensor networks. *IEEE Communications Letters*, *9*(11), 970–972.
28. Abi-Char, P. E., Mhamed, A. & Bachar, E.-H. (2007). A fast and secure elliptic curve based authenticated key agreement protocol for low power mobile communications. In *The 2007 International Conference on Next Generation Mobile Applications, Services and Technologies (NGMAST 2007)*, IEEE, (pp. 235–240).
29. Yang, J.-H., & Chang, C.-C. (2009). An ID-based remote mutual authentication with key agreement scheme for mobile devices on elliptic curve cryptosystem. *Computers & Security*, *28*(3–4), 138–143.
30. Islam, S. H., & Biswas, G. (2011). A more efficient and secure ID-based remote mutual authentication with key agreement scheme for mobile devices on elliptic curve cryptosystem. *Journal of Systems and Software*, *84*(11), 1892–1898.
31. Ray, S. & Biswas, G. (2012). Establishment of ECC-based initial secrecy usable for IKE implementation. In *Proceedings of the World Congress on Engineering*, (vol. 1).
32. Granjal, J., Monteiro, E. & Silva, J. S. (2013). End-to-end transport-layer security for Internet-integrated sensing applications with mutual and delegated ECC public-key authentication. In *2013 IFIP Networking Conference*, IEEE, (pp. 1–9).
33. Jiang, R., Lai, C., Luo, J., Wang, X., & Wang, H. (2013). EAP-based group authentication and key agreement protocol for machine-type communications. *International Journal of Distributed Sensor Networks*, *9*(11), 304601.
34. Hankerson, D., Menezes, A. J., & Vanstone, S. (2006). *Guide to elliptic curve cryptography*. Berlin: Springer.
35. Li, X., Niu, J., Kumari, S., Liao, J., Liang, W., & Khan, M. K. (2016). A new authentication protocol for healthcare applications using wireless medical sensor networks with user anonymity. *Security and Communication Networks*, *9*(15), 2643–2655.

Ajay Kumar is an IT/Network officer working with Govt. of India (Ministry of Defense). He has BTech from Central University Delhi and M Tech from Mumbai University. He is persuing the PhD In computer network & security from Dept. of Computer Science & Engineering, NIT Patna. His area of research is network security, Authentication, IoT and Machine Learning.

Kumar Abhishek is working as an Assistant Professor, Department of Computer Science and Engineering, National Institute of Technology Patna, India. His area of interest lies in RDF, Semantic Web, Ontology, Semantic Sensor Web, Ontology mapping and Approximation.

Xuan Liu (yusuf@seu.edu.cn) graduated from Shandong University, China, and received M.S. degree from Wuhan Polytechnic University, China and Ph.D. degree in computer science and engineering from Southeast University, China. Since the first half of 2020, he will be a faculty member at School of Information Engineering in Yangzhou University, China. He is serving as an Advisory Editor of Wiley Engineering Reports, an Associate Editor of Springer Telecommunication Systems, IET Smart Cities, Taylor& Francis International Journal of Computers and Applications and KeAi International Journal of Intelligent Networks, an Area Editor of EAI Endorsed Transactions on Internet of Things, the Lead Guest Editor of Elsevier Internet of Things, Wiley Transactions on Emerging Telecommunications Author's Picture & Biography Click here to access/download;Author's Picture & Biography;authors.pdf Technologies and Wiley Internet Technology Letters, and the Chair of CollaborateCom 2020 workshop. He served as a TPC Member of IEEE INFOCOM 2020 workshop, IEEE ICC 2020/2019, IEEEGlobeCom 2019, IEEE PIMRC 2020/2019, IEEE VTC 2020/2019/2018, IEEE ICIN2020, IEEE GIIS 2020, IEEE DASC 2019, APNOMS 2020/2019, AdHoc-Now2020, FNC 2020/2019, EAI CollaborateCom 2020/2019, and EAI ChinaCom 2019, etc. Furthermore, he has been reviewing papers for 20+ reputable conferences/journals including IEEE INFOCOM, IEEE ICC, IEEE GlobeCom, IEEE WCNC, IEEE PIMRC, IEEE COMMAG, IEEE TII, EEE IoT, IEEE CL, Elsevier, JNCA, Elsevier FGCS, Springer WINE, Springer TELS, IET SMC, EAI CollaborateCom, and Wiley IJCS, etc. His research interests include collaborative networking, future network architecture and dualarchitecture network.

Dr. Anandakumar Haldorai Professor (Associate) and Research Head in Department of Computer Science and Engineering, Sri Eshwar College of Engineering, Coimbatore, Tamilnadu, India He has received his Master's in Software Engineering from PSG College of Technology, Coimbatore. PhD in Information and Communication Engineering from PSG College of Technology under, Anna University, Chennai. His research areas include Big Data, Cognitive Radio Networks, Mobile Communications and Networking Protocols. He has authored more than 82 research papers in reputed International Journals and IEEE conferences. He has authored 7 books and many book chapters with reputed publishers such as Springer and IGI. He is served as a reviewer for IEEE, IET, Springer, Inderscience and Elsevier journals.

Wireless Networks
https://doi.org/10.1007/s11276-020-02503-z

GUEST EDITORIAL

Signal processing techniques for sustainable cognitive radio communications

Arulmurugan Ramu[1] · Mu-Yen Chen[2] · Sri Devi Ravana[3] · Anandakumar Haldorai[4]

Accepted: 9 November 2020

The growing devices and capacity requirements of wireless systems bring increasing demand for RF spectrum. Cognitive radio (CR) system is an emerging concept to increase the spectrum efficiency. CR system aims to enable opportunistic usage of the RF bands that are not occupied by their primary licensed users in spectrum overlay approach. This approach is especially important in signal and image processing, where sets of sensors, large and heterogeneous, provide large amounts of data, usually noisy and corrupted with various sources of interference. From a methodological point of view, cognitive communication is concerned with multi-dimensional and statistical signal processing, especially with problems such as detection, estimation, and optimization. In addition to classical sensing, detection, supervised, reinforcement and learning methods include Bayesian modeling, Markov models, support vector machines, and kernel methods. It spans a broad area of applications, such as military, industrial, medical, transportation and other fields like error control, error detection, adaptive filtering, computer vision, managing data, sensor control, data fusion, blind and semi-blind source separation, sparse analysis, brain-computer interfaces, signal processing and radio communication. The intelligent system for the cognitive communication is a collection of intelligent terminals with signal processing and mobile capabilities. Among them, each intelligent terminal carries out signal transmission and distributed processing with other intelligent terminals. However, most existing communication architectures, including their signal processing protocols and control algorithms, are designed for centralized networks by default.

This issue aims to gather latest research and development achievements in this area and to promote their applications in all important fields with society needs. This issue features eight selected papers with high quality. The first article, "Salp Swarm Algorithm and Phasor Measurement Unit Based Hybrid Robust Neural Network Model for Online Monitoring of Voltage Stability", presents the online monitoring of voltage stability method. The proposed model is based on Salp Swarm Algorithm based Artificial Neural Network (SSA-ANN). The prime considerations in this model is the use of real time data. The computation time is reduced amongst all the models for all the test cases considered for estimating the VSMI.

The second article, "Efficient Traffic Control and Lifetime Maximization in Mobile Ad hoc Network by Using PSO-BAT Optimization", proposed hybrid Meta heuristic methodology of dynamic mobile ad hoc network focuses on the mobile node energy level and lifetime maximization with the use of velocity estimation and fitness value calculations of PSO-BAT optimization algorithm. The proposed heuristic algorithm enhances the secured routing process of mobile nodes in dynamic mobile network with denial of service mitigation algorithm in a reliable method.

The third article, "The performance analysis of dual-inverter three phase fed induction motor with open-end winding using various PWM schemes", proposed to investigate the performance of various PWM schemes for two inverters fed a three-phase induction motor. The PWM schemes are developed the voltage references and

✉ Arulmurugan Ramu
arulmurugan@presidencyuniversity.in

Mu-Yen Chen
mychen@nutc.edu.tw

Sri Devi Ravana
sdevi@um.edu.my

Anandakumar Haldorai
anandakumar.h@sece.ac.in

1 Presidency University, Bangalore, Karnataka, India

2 National Taichung University of Science and Technology, Taichung, Taiwan

3 University of Malaya, Kuala Lumpur, Malaysia

4 Sri Eshwar College of Engineering, Coimbatore, Tamil Nadu, India

modulated using the same or different PWM scheme with simple carrier based PWM method proposed and executed.

The fourth article, “Reliable Service Availability and Access Control Method for Cloud Assisted IoT Communications”, the reliable service method availability and access control is discussed to improve the resource allocation and request processing efficiency of Cloud-IoT. This method operates in cloud and gateway layer for resource allocation and request processing respectively. Using a reliable gateway selection method, the requests are processed in a timely manner preventing backlogs and failures. The augmented learning process classifies requests based on time overlap to reduce the backlogs and delay in communication. In the proposed methods, the fore-mentioned processes are augmented to improve the overall performance of cloud assisted IoT platforms.

The fifth article, “Efficient Pre-authentication Scheme for Inter-ASN Handover in High Mobility MANET”, proposed a new routing protocol to handle the displacement and direction factors in ad-hoc networks. The proposed Modified EAP based Pre-authentication scheme using Improved ElGamal (MEPIE) overcomes the MITM, replay, DoS and impersonation attacks in MANETs. The proposed mechanism based on the improved ElGamal addresses the inadequacies of ElGamal digital signatures and yields better results.

The sixth article, “Unified Power Quality Conditioner with Reduced Switch Topology for Distributed Networks”, In this paper Unified Power Quality Conditioner designed and developed with reduced number of switches and it is controlled by SRF based Carrier Double Zero Sequence Signal Modulation technique. The proposed UPQC system is designed with 10 switches, which provide better performance compared to conventional 12 switch UPQC system. It is implemented to reduce the various power quality issues like minimization of voltage sag and current ripples, harmonics reduction in the input voltage and reduced Total Harmonic Distortion.

The seventh work titled, “False Alarm Detection Using Dynamic Threshold in Medical Wireless Sensor Networks”, presents a dynamic threshold algorithm to detect the sensor anomaly to differentiate false and alarms and this system presented for healthcare application in WSN. The error value is calculated using a dynamic threshold which can identify false and true alarm using a majority voting system. The proposed system shows the detection ration is high and false positive rate is lower which conclude that this new approach is particularly useful in WSN application such as health monitoring system and it will be competitive with others.

The eighth article “Design and Development of Planar Antenna Array for MIMO Application” has proposed a Design for implementing an innovative Two T-shaped planar antenna on behalf of ISM band for the MIMO application. The antenna is designed with the Taconic RF-35 substrate having a dielectric constant of value 3.5, while the method of feeding coaxial probe has been employed as antenna feed. The proposed antenna’s performance was examined, and it was found that the proposed scheme has better performance compared to the existing schemes.

Our sincere thanks to the Editor-in-Chief, Dr. Imrich Chlamtac and Eliška Vlčková, Managing Editor, European Alliance for Innovation (EAI) for their continuous support and guidance during the entire process. We also extend our sincere thanks and grateful to the reviewers for their efforts in reviewing the manuscripts.

Dr. Arulmurugan Ramu is a Professor, Presidency University, Bangalore, India. His research focuses on the automatic interpretation of images and related problems in machine learning and optimization. His main research interest is in vision, particularly high-level visual recognition. He has authored more than 35 papers in major computer vision and machine learning conferences and journals. He is the recipient of Ph.D. degrees in Information and Communication Engineering from the Anna University at Chennai, M.Tech. in Information Technology Anna University of Technology and B. Tech degree in Information Technology. He is guided many Ph.D. research scholar under the area of Image Processing using Machine Learning. He is an Associate Editor of Inderscience IJISC journal. He is awarded as Best Young Faculty Award 2018 and nominated for Best Young Researcher Award (Male) by International Academic and Research Excellence Awards (IARE-2019).

Dr. Mu-Yen Chen is a Professor of Information Management at National Taichung University of Science and Technology, Taiwan. He received his Ph.D. from Information Management from National Chiao-Tung University in Taiwan. His current research interests include artificial intelligent, soft computing, bio-inspired computing, data mining, deep learning, context-awareness, machine learning, and financial engineering, with more than 100 publications in these areas. He has co-edited 12 special issues in International Journals (e.g. Computers in Human Behavior, Applied Soft Computing, Soft Computing, Information Fusion, Neurocomputing, Journal of Medical and Biological Engineering, The Electronic Library, Library High

Tech). He has served as Editor in Chief and Associate Editor of international journals [e.g. International Journal of Big Data and Analytics in Healthcare, IEEE Access, Human-centric Computing and Information Sciences, Journal of Information Processing Systems, International Journal of Social and Humanistic Computing] while he is an editorial board member on several SCI journals.

Dr. Sri Devi Ravana received the Bachelor's degree in information technology from the National University of Malaysia, in 2000, the Master's degree in software engineering from the University of Malaya, Malaysia, in 2001, and the Ph.D. degree from the Department of Computer Science and Software Engineering, The University of Melbourne, Australia, in 2012. She is currently an Associate Professor at the Department of Information Systems, University of Malaya. Her research interests include information retrieval heuristics, text indexing, data analytics, and data mining. She received a couple of best paper awards in international conferences within the area of information retrieval.

Dr. Anandakumar Haldorai Professor (Associate) and Research Head in Department of Computer Science and Engineering, Sri Eshwar College of Engineering, Coimbatore, Tamil Nadu, India. He has received his Master's in Software Engineering from PSG College of Technology, Coimbatore, PhD in Information and Communication Engineering from PSG College of Technology under, Anna University, Chennai. His research areas include Cognitive Radio Networks, Mobile Communications and Networking Protocols. He has authored more than 118 research papers in reputed International Journals and IEEE, Springer Conferences. He has authored 11 books and many book chapters with reputed publishers such as Springer and IGI. He has served as Editor in Chief in Keai – Elsevier IJIN and reviewer for IEEE, IET, Springer, Inderscience and Elsevier journals. He is also the guest editor of many journals with Wiley, Springer, Elsevier, Inderscience, etc. He has been the General chair, Session Chair, and Panelist in several conferences. He is a senior member of IEEE, MIET, MACM and Fellow member of EAI research group.

IETE Journal of Research

ISSN: (Print) (Online) Journal homepage: https://www.tandfonline.com/loi/tijr20

An Automated Crop and Plant Disease Identification Scheme Using Cognitive Fuzzy C-Means Algorithm

S. Sampathkumar & R. Rajeswari

To cite this article: S. Sampathkumar & R. Rajeswari (2020): An Automated Crop and Plant Disease Identification Scheme Using Cognitive Fuzzy C-Means Algorithm, IETE Journal of Research, DOI: 10.1080/03772063.2020.1780163

To link to this article: https://doi.org/10.1080/03772063.2020.1780163

Published online: 21 Jun 2020.

IETE JOURNAL OF RESEARCH
https://doi.org/10.1080/03772063.2020.1780163

An Automated Crop and Plant Disease Identification Scheme Using Cognitive Fuzzy C-Means Algorithm

S. Sampathkumar [1] and R. Rajeswari [2]

[1] Department of Computer Science and Engineering, Sri Eshwar College of Engineering, Coimbatore, India; [2] Department of Electrical and Electronics Engineering, Government College of Technology, Coimbatore, India

ABSTRACT
The cultivation of crops, conservation of plants, restoration of landscape, and management of soil are the phases incorporated in agriculture and horticulture. During the cultivation and conservation stages, the plants and the crops are affected by various diseases such as Bacterial scourge, Bacterial Leaf Blight, Brown spot, Seeding blight, Leaf streak, Powdery Mildew, Fire Blight, Black Rot and Apple Scab. These diseases in plants will lead to losses such as manufacturing and financial loss in farming industry worldwide. To maintain the sustainability in horticulture, the detection of crop disease and maintaining the condition of the plants are important. The Computer Aided Detection (CAD) in the agriculture and horticulture is the emerging trend, based on the digital imaging that provides the detailed analysis about the disease by applying the image mining process. In this work, the Cross Central Filter (CCF) technique is proposed to perform the noise removal process in the image and the identification of objects in the image is applied by using the Cognitive Fuzzy C-Means (CFCM) algorithm to differentiate the suspicious region from the normal region. The evaluation is conducted against the diseases affected in the rice crop and apple trees. The performance evaluation proves that the proposed design achieves the best performance results compared to the other filters and the segmentation techniques.

KEYWORDS
Approximation; filtering; horticulture; image mining; noise removal; plant pathology; suspicious region segmentation

1. INTRODUCTION

Horticulture is the division of agriculture which addresses the science of plant cultivation in a smart manner. The cultivation includes the plants that are edible as well as ornamental which is handled under the landscaping. The plant and crop development stages integrate the important directions, such as planting or seed germination, relocation or reproductive stage, panicle initiation, blooming, maturation, ripening stage, and senescence. Quality assurance is an essential function of food generation and transforming from the perception of giving nourishments with acceptable nutritious value. This auditing process is important to validate the quality of the food items which examines the intrinsic and extrinsic defects [1] by using the quality evaluation process of nutrition products.

In the recent few years, the data processing and information extraction system have significant growth in the agriculture field. The information extraction provides the eminent processing of data using the digital imaging system. The data processing system in digital images has emerged extremely due to the increasing development in digital imaging over the internet. The mechanism of accessing and extracting the information is simplified because of the emerging technology such as Big Data. The digital imaging is improved by the Visual Modality Technology (VMT) which is known as vision technology [2] that handles the extraction of information from the digital images. Computer-based Visual Modality Technology (CVMT) is illustrated as the process of automating and combining the largest range of techniques and illustrations for visualization. VMT accomplishes unique operations such as image identification and selection, restoration, recognition, feature extraction and decision making.

VMT executes the image acquiring process, identification of image objects, examining the image features and extracting the information by performing the numerical calculations [3] using the decision logics and by using the statistical analysis. VMT shields the underlying technology of computerized image investigation employed in various areas. VMT is the enhanced style of the CAD system which imports the images and deriving the cognitive sense by processing the digital images. The evolution of CAD system [2] has emerged a massive rise in the effective disease identification process. The process of identifying the suspicious segments from the normal region is accomplished in four levels, namely Noise

Removal, Object Segmentation, Feature Extraction and Classification & Ranking procedure.

Disease identification [4] in crop, plant, and tree is a critical task to perform either by manual techniques or by utilizing the automated techniques. It is hard to separate [5] the parts of the crops accurately in the digital image if it is treated manually. In order to handle this situation, the digital images must be processed by applying the computer-based automated techniques. The CAD system analyses the input images and produces the end output in the form of visual representation of defected part of the crops along with the information about the disease affects the crops. This report is generated by the CAD system and produced to the consumer after completing the validation process about the crops as well as the disease which affected the crops.

2. RELATED WORK

2.1 Problem Statement

Crops are affected by various diseases such as Impression, Bacterial scourge, Black kernel, Brown spot, Seeding blight, Powdery Mildew, Fire Blight, Black Rot and Apple Scab in different development levels in various climatic sessions. In order to distinguish the disease type and disease severity accurately, the digitization process must be utilized by applying the image processing [6] operations. Shape recognition is the essential function of the image processing which makes the detection system more accurate as well as improving the efficiency of the methodology to detect the disease affected area in minimum duration. In the agribusiness field, the disease identification and severity estimation not only reduces the time consuming but also expands the yield of the crops which protect the ecological surroundings.

2.2 CVMT

The process of forming the VMT is purely application and component dependent. During the specific measurement and image recognition with the pattern matching process is a standalone application [7] which builds the arrangement as a hybrid system by combining the standalone and the dependent process. The answers provided by the VMT are well recognizable as well as easily understandable to humans. The VMT applies the data acquisition and knowledge processing to obtain the information from the digital image. The input of the VMT is acquired from digital cameras or by the sensors which captures the real-world images to provide the expressive information.

In order to achieve the disease identification and severity analysis of the disease using the CAD system, the image mining is applied to the acquired image after completing the segmentation [8] of objects in the digital image. The preprocessing (noise removal and image enhancement) is applied to the captured image, then the segmentation is processed to identify the Region of Interest (ROI) in the image. The recognition process of suspicious region is performed in these two stages along with the characteristic extraction in terms of features and the classification process.

The objective of the CAD system [9] is to produce the knowledge processing system that retrieves the information from the digital images. This information retrieval process is operated by the CAD system along with the combined operations of the VMT. This procedure is primarily given to perform the disease identification and severity analysis in crops by using the heuristic techniques. The evolution of CAD with VMT has created a huge increase in the detection procedure. Also, it can serve to achieve accurate detection with minimal time duration and price effectiveness.

The VMT combined CAD system does the following operations to do the crop disease detection process.

(1) Image acquisition
(2) Preprocessing (Noise removal and image enhancement)
(3) Image segmentation
(4) Feature selection, extraction and classification.

These four operations are important during the knowledge processing operations while discovering the disease defected portion in the crops, plants, and trees. These steps are linear and integrated with other process to reduce the time complexity of the operation, *i.e.* the output of the current step is passed as the input to the next step in the consecutive operations.

2.3 Image Filtering and Segmentation Techniques

The process of removing the unwanted pixel points in the image is done by employing the noise removal and image enhancement phase. The filtering methods such as Mean filter, Median filter, Gaussian and Wiener filters are applied to purge the noise pixels present in the image signal. The dominant brightness level analysis for contrast enhancement was proposed by [10]. The method mainly obtains the adaptive intensity transformation for the image captured in the remote sensing. By using the low frequency luminance component, the intensity transfer for brightness-adaptive is computed. The author overcomes the problem of exhibiting the saturated components in the low and high intensity regions by performing the discrete wavelet transform.

The optimization process in the image denoising algorithm is discussed in [11]. The spatial domain methods such as local feller, Gaussian filter, anisotropic filter to avoid the blur effect are discussed by the authors. The transform domain methods for denoising the image using the discrete cosine transform, wavelet, curvelet and steerable wavelet are applied for significant improvement in the image filtering process. The principle component analysis for the spatial filter is evolved to characteriste the multi-resolution sparsity and edge detection process during the denoising process.

Mean filter and median filter operations and its performance are analysed by Gupta et al. [12]. These filters are the basic linear filter models that follows the arithmetic mean operation to remove the noise signals from the image. Mean filter model is a low pass filter that allows the image signal frequency only if the estimated mean value is less than that of the image signal. If it is greater than the image signal, then the signals are eliminated from the image signal. Median filter is also a basic type filter which executes the operation based on the arithmetic median value. The greater signals are eliminated from the image signal.

The low pass filter operation with respect to the Gaussian estimation [13] is performed by using the Gaussian filter. The band pass operation is performed by the Wiener filter [14]. The Gaussian relationship is estimated in the form of mean, standard deviation and variance. This is estimated for the input signal of the image and from these values Gaussian function value is estimated. This value is used as the upper bound for the low pass filtering operation. The boundary value is calculated by using the impulse response of the input signal. The larger value input signal compared to the boundary points is removed as the noise signal and noise-free signal are combined and formed as denoised image.

Bedi *et al.* [15] studied various methodologies for improving the visual appearance of the image in terms of image enhancement and segmentation. The log normal methodologies, such as log reduction magnitude with logarithm transform, histogram shifty, content classification, are discussed for vision-based monitoring application. The histogram modification, content adaptive algorithm, and discrete cosine transform with the retinex theory were deliberated for the image and video compression process.

The retinex theory-based image enhancement technique with the segmentation extended for highly illuminated visual perception is developed in [16] with certain process of halo effect in the non-multiscale Gaussian filtering with the dynamic range of modification and colour consistency are achieved in the extension. This process was mainly used to achieve the satisfactory colour rendition with the relatively smoothened pixel points. Zhang *et al.* [17] presented a solution for the object detection in the segmented image with Bayesian optimization and structure prediction in the deep convolutional network. The cognitive architecture mainly acquires the knowledge and encompasses [18] the evaluation, learning, and reasoning of the decision-making system.

Yue *et al.* [19] proposed the segmentation and the classification methodology based on the spectral-spatial features in the dimension reduction using deep learning process. The author develops a framework by using the balanced local discriminant algorithm with embedding technology to extract the features by stacking the spectral and spatial relationship. In the image classification process [20], multifeature-based classifier is used with the training process. The Convolutional Neural Network (CNN)-based trained sample significantly achieves the better performance in the classification process.

3. IMAGE PROCESSING SYSTEM

3.1 Image Acquisition

The crop and tree segment images are captured by using the digital camera and the generated digital image of the crop and tree are stored in the database. The image reproduction [21] operations such as perspective viewing and editing of the captured images are performed by using the image sensors or by using the image capturing devices. The scanners, ultrasound, and spectroscopy are used as the image capturing devices to get the high-resolution pictures to provide the accurate results. The captured images are converted into grayscale by using the RGB to Grayscale conversion operation.

3.2 Preprocessing (Noise Removal and Image Enhancement)

The captured images are applied to preprocessing to remove the unwanted pixel points from the image. This also improves the quality of the image by eliminating the distortions in the preliminary manipulation stage. The digital images [22] are treated in terms of pixel points as the basic picture elements which represents the actual points. In the preprocessing stage, the distortions in the image are eliminated by applying the filtering operation as the stage of noise removal. The Cross Central Filter scheme is employed to perform the noise removal operations, which increases the significance of the pixel points by eliminating the low significant pixel of the captured image. Establishing the relationship between the nearest pixel points, the denoising operation is performed by isolating the low qualified pixel points.

3.3 Image Segmentation

Image segmentation is otherwise known as object division process in the digital image. This is a process of dividing, analysing, and merging [23] the relevant characteristics of the picture based on the objects identified from the digital image. This is executed by making the relationship matrix between each and every pixel points. It distinguishes the ROI in the image [24] and uses the image segmentation process with similar objects in the analysing area. This relationship is named by the principal matrix which relates the pixel point in the digital image. The main role of this segmentation in terms of region partitioning [25] is to divide the image pixels which are mutually exclusive and region-based scattered. This process is spatially related and similar with respect to the defined close distance criteria. The image segmentation process is performed by using the CFCM technique which outperforms the FCM technique.

3.4 Filtering Process

Enhancing the image quality and removal of unwanted pixels are executed in the manipulation of digitized images and permitting of limited frequency by rejecting the higher value frequency. This process is done by using the filter function along with the re-transformation process of the image signal. This image frequency filter allows the bounded level frequency to avoid the noise present in the digital signal of the image. The filter model is basically categorized into the following types based on its processing characteristics, linear and nonlinear filters.

Linear filter removes the noise pixel points based on the relationship between the continuous and consecutive pixels. The nonlinear filter removes the noise which is in the category of impulse signal models. This process is done by computing the variance among the image signals. This filter basically removes the Gaussian noise present in the image signal. If there is a disagreement found by passing over the variance boundary limit in the pixel points, then the picture element is removed from the picture signal.

3.5 Proposed CCF

CCF derived from the operations of low pass filter and band pass filter which preserves the better performance compared to other filtering operation due to the intelligent operation of this filter. This filter is a band pass filter which also combines the process of low pass and high pass filters. The upper and lower bounds for this band pass filter are estimated based on the input image signal. The input image pixel points are organized into $M \times M$ structures to process it efficiently. The procedure is based on Gaussian functions for the curved structure. The construction is covered in three directions: horizontally, vertically, and diagonally.

The input image pixel points are carved up into N number of grouped structures with $M \times M$ matrix. These N groups are treated separately to key out the co-relationship between the input matrix. For each group, the Gaussian spatial relationship is judged in terms of mean, variance and Gaussian function. This value is calculated in three directions and the value is set as the upper bound value of the comparison.

The captured apple scab image and rice crop image are given as an input to the CAD system and the captured images are shown in Figures 1 and 2 respectively. The input image with specific density of salt & pepper noise added is depicted in Figures 3 and 4. For lower bound value, the maximum variance value is keyed out by comparing the input signal value and the calculated mean value using Equation (1).

The absolute difference between these two values is checked as the lower bound value of the band pass filtering system. By using the mean value as input, the

Figure 1: Captured apple scab image given as an input to the CAD system

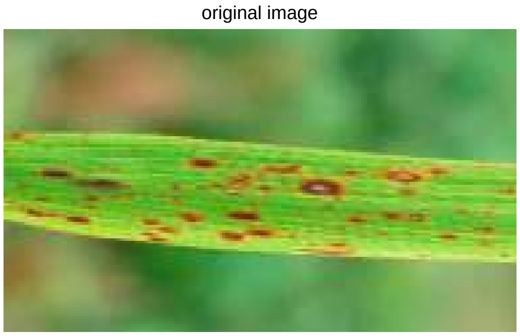

Figure 2: Captured rice crop image given as an input to the CAD system

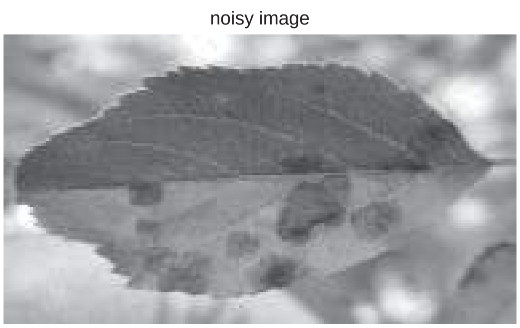

Figure 3: Salt & Pepper noise added to the input apple scab image

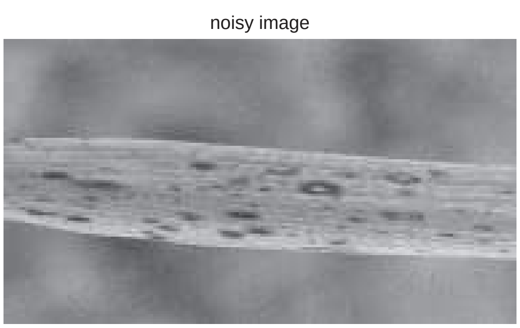

Figure 4: Rice crop image with Salt & Pepper noise

standard deviation and the filtering bound are computed by applying the Gaussian modelling.

$$\text{mean} = \frac{1}{r^2} \sum_{i=-[r/2]}^{[r/2]} \sum_{j=-[r/2]}^{[r/2]} x[n-i,\ m-j] \tag{1}$$

Equations (2) and (3) represent the computation model for the Gaussian distribution. The distributed value of the image vector is organized in matrix structure to proceed with the replacement of distorted pixel with the denoised pixel point. The pixel comparison operation is accomplished in each direction for all input pixel points with the two boundary points. If the pixel point satisfies the median criteria using Equation (4), then the pixel point is separated as noise-free pixel point and the remaining pixel points are rejected from the input signal.

Figure 5: Denoised and contrast enhanced apple scab image using CCF

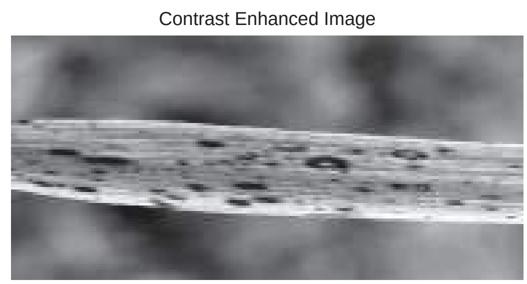

Figure 6: Denoised and contrast enhanced rice crop image using CCF

$$p = \frac{e^{\left(\frac{(x-\text{mean})}{2\sigma}\right)}}{\sigma\sqrt{2\pi}} \tag{2}$$

$$\sigma = \sqrt{\frac{\sum_{i=1}^{w \times w} (x_i - \text{mean})^2}{w \times w}} \tag{3}$$

p – filtering bound; *w – size of window; σ – standard deviation; n – number of rows; m – number of columns*

$$y_{\text{median}}[n, m] = \text{median}\,\{x[n-i, m-j]\},\ i, j = -r/2, \ldots, [r/2]. \tag{4}$$

Figures 5 and 6 show the noise removed and contrast enhanced image after applying the image enhancement process using the CCF filter operation.

4. SEGMENTATION AND CLASSIFICATION

4.1 Segmentation Process

Image division focuses on obtaining an automated segmentation system for disease detection using the identification of suspicious region. The primary objective of the single image segmentation method is to increase the quality and efficiency of the CAD system which is applied for the detection of crop disease. The purpose of the proposed study is to assist the botanist in the decision-making process during the identification of crop disease and its severity. A segmented image provides a much simpler description about the crops by extracting the similar pixel points.

After completing the noise removal process, the clustering is applied to the image to identify the linear relationship [26] between the objects present in the image. The relationship between the pixels is validated using the Euclidean measurement. Image segmentation is the process of partitioning the image into a number of regions or cluster groups which are corresponding to the different objects present in the picture. During the analysis process, the regions with the set of boundary [30] pixels are grouped into specific social systems such as line or circular segments in the image.

4.2 Cognitive Fuzzy C Means Clustering

Fuzzy C Means (FCM) is executed to identify the natural groupings of data pixel points from the image to produce a standardized representation of pictures. FCM is the clustering algorithm which [27] is utilized to form set of clusters with every pixel data from the image based on the spatial relationship that belongs to the every cluster with certain degree and the membership is calculated using Equation (5).

$$u_{ij} = \frac{1}{\sum_{i=1}^{C}\left(\frac{x_i - c_j}{x_i - c_k}\right)^{\frac{2}{m-1}}} \tag{5}$$

$$c_j = \frac{\sum_{i=1}^{N} u_{ij}^{m}\, x_i}{\sum_{i=1}^{N} u_{ij}^{m}} \tag{6}$$

$$J_m = \sum_{i=1}^{N}\sum_{j=1}^{C} u_{ij}^{m} x_i - c_j{}^2 \tag{7}$$

u_{ij} is the degree of membership of x_i in the cluster j, x_i is the ith of d-dimensional measured data, c_j is the d-dimension centre of the cluster, and ||*|| is any norm expressing the similarity between any measured data and the centre. Here the membership of pixel point with the cluster group is identified using Euclidean distance in the Euclidean space of the data. The cluster gives strength by the centroid pixel points of the picture. The relationship between pixel point and the cluster centroid is identified by degree of membership which is computed by using membership function and it is indicated by using Equations (6) and (7). The pixel information is extracted from the images and these pixel values are grouped into a set of clusters based on FCM and CFCM clustering approaches.

CFCM is the improved version of the FCM clustering algorithm to perform the segmentation process. CFCM is an iterative optimization algorithm which produces the optimized solution based on heuristic modelling. It produces the mathematical optimization by performing the local search operation to select the best combination of clusters to obtain the best results. The iterative process is initiated with the random set of solutions to solve the clustering problem. In these iterations, an incremental modification is performed to the newly formed solution. In fuzzy operation, pixel points in the image are grouped based on the selected cluster centroid point.

The membership function determines the quality of the formed cluster by setting the intensity level of connectivity between pixel points and the cluster centroid point. Standardized to the FCM clustering, the point of membership is the primary input to the target sigmoid function. And this evaluates the import of the pixel point with the cluster groups. If the pixel point retains the higher meaning in terms of membership value,the objective value of the membership function will be greater value. CFCM makes use of Cognitive distance function as objective function along with the membership office to determine the best combination of centroids in the pictures. Centre distance is drawn out from the Euclidean distance between cluster centroid and pixel data points. This length value is selected as the input for the negative exponential with the splitting ratio of the sigmoid function.

This Sigmoid function is the logistic function which divides the Euclidean distance. Centre distance is used to amend the selection probability of the cluster centroids. The stage of membership is estimated based on this Cognitive distance with the Euclidean distance. If the centroid has two or more dimensions, then the degree of membership function initially estimates the Euclidean distance between the cluster centroid and data pixel point. If it has a single dimension, then the absolute difference between the pixel point and the centroid is calculated as distance. Once this distance is estimated then the value is passed as an argument to the kernel distance estimation function using Equations (8) and (9).

$$\hat{x} = \frac{x}{\arg\max |x|} \tag{8}$$

$$f(x) = \frac{1}{1 + \exp(-\beta \hat{x})} \tag{9}$$

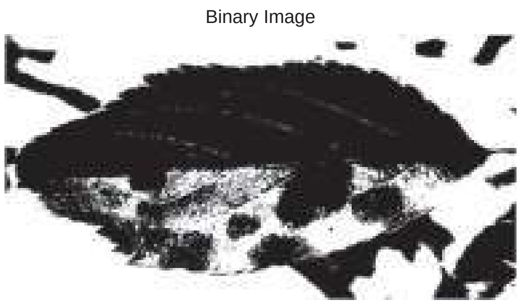

Figure 7: Suspicious region segmented in the inverted apple scab image using the proposed CFCM segmentation algorithm

$$P(x) = \frac{1}{\sqrt{(2\pi)^N \, det(C)}} \times \exp\left(-\frac{1}{2}(x-\mu)C^{-1}(x-\mu)\right) \tag{10}$$

The term C represents the covariance matrix, *det* indicates the determinant of the matrix, μ denotes the mean value, x and N represent the individual data value and number of instances respectively. This kernel distance defines the logistic function as sigmoid values. The input distance value is divided by the sigmoid value, then the negative exponential value is calculated from the corresponding value which is named as the kernel distance between data pixel point and cluster centroid. After computing the kernel distance value, the objective estimation function is invoked to calculate the degree of membership for the cluster centroid and its corresponding cluster pixel points. From the degree of membership and the set of cluster centroids, new cluster centroids are found as a next iterative solution.

In the iterative process, the difference between the objective value of the last set of solution and the current set of solution is estimated and it is compared with the objective difference value. If both the set of solutions produce the equal or approximate equal value of degree of membership, then the algorithm converges with the best combination of centroids. Once it is converging then, the iterative process is terminated with the last centroid point as final cluster points. This grouped pixel point produces the region of interest to perform the feature extraction and classification operation. The output of the image segmentation in terms of the suspicious region in the apple scab image and the rice crop image are shown in Figures 7 and 8.

4.3 Feature Extraction and Classification

The feature is defined as the point of concern for image description. In computer vision and image processing, the feature entity is used to represent a piece of data entropy, which is crucial for resolving the computational task affiliated a particular application. Features can concern to the consequence of a general locality cognitive operation as feature extractor or feature detector applied to the image, specific structures in the image itself, ranging from the structures such as points or boundaries to the more composite structures such as objects. Feature Extraction is used for extracting the important data from the Entire data. It is a type of multidimensional simplification that efficiently represents concerning components of an image. This process is a machine learning technique which is applied to derive the important components of an image. The entire work sequence for the proposed design is depicted in Algorithm 1.

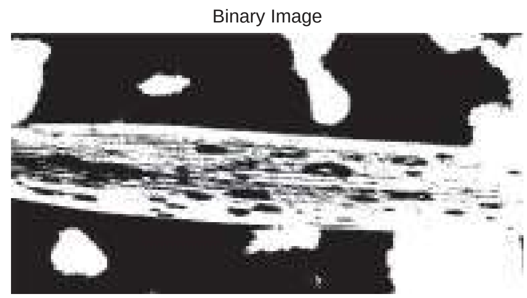

Figure 8: Suspicious region segmented in the inverted rice crop image using the proposed CFCM segmentation algorithm

Algorithm 1: Region classification using CCF filtering, CFCM Segmentation and SVM Quad Programming

Input: Input image I,

Output: *Classified region R*

1. Resolution of I is identified and it is represented in r-rows and c-columns.
2. Based on the image resolution, pixel window size (m) is selected to perform the filter operation.
3. Input image is divided into number of windows based on the window size and resolution of the image.
4. For each window, arithmetic mean value is computed by using Equation (1).
5. The Gaussian relationship is computed in the pixel window with the estimation of variance, standard deviation using Equations (2) and (3)
6. From the estimated mean and standard deviation, the lower and upper bound threshold is computed as the expected value from the impulse signal of the image frequency.
7. Based on the count, the median value is selected from the window using Equation (4).

8. For odd count, exact median value is selected and for even count two middle values are selected and their average value is considered as the median value.
9. By selecting the window around the current pixel point, the distorted pixel is replaced by the selected median value of the corresponding Gaussian distribution.
10. For each pixel point in the image, the clustering process is applied based on the pixel values of denoised image.
11. For each cluster
    a. Compute Degree of Membership using (5) and (6)
    b. Compute Optimization Objective using (7)
    c. Estimate kernel distance using (8)
    d. Update Sigmoid value using (9)
    e. Compute Covariance matrix of the current cluster
    f. Estimate the relationship between the pixel point in current cluster using the (10)
    g. Check Termination criteria by checking the repeated optimum value
    h. If termination criteria is satisfied
        i. break
    i. End
12. End
13. For each formed segments
    a. Represent the pixel matrix D as (11)
    b. Subdivide *D* into S as (12)
    c. Form eigen matrix (13)
    d. Convert into quadratic equation using (14), (15) & (16)
    e. Identify the coefficients using (17) & (18)
    f. Solve the quadratic equation using (19) & (20)
    g. Identify the required root using (21)
14. End
15. Compare the root with other segment and identify the relationship
16. Differentiate the segments into normal and suspicious segments using the identified relationship

4.4 Quad Programming (SVM)

The process of classification is mainly applied to identify the similarity between the actual outcome and expected outcome. This stage is completed by using the Support Vector Machine (SVM) which is based on the concept of decision planes [28] that define decision boundaries. The decision process is applied by validating the various membership with the constraints created to match the expected plane. SVM classifier is improved by combining with the quad programming model [29] which identifies the solution by solving the roots of the quadratic equation. It is purely based on quadratic programming optimization and the objective of the quadratic programming has to solve the classification problem by means of quadratic function which takes the decision based on the feature as input variable. The input variables are processed by the linear function based on the quadratic constraints.

$$D = \begin{bmatrix} d_{11} & d_{12} & \dots & d_{1n} \\ d_{21} & d_{22} & \dots & d_{2n} \\ \dots & \dots & & \\ d_{m1} & d_{m2} & \dots & d_{mn} \end{bmatrix} \tag{11}$$

The input matrix of the image pixel is indicated using Equation (11). In order to apply the quadratic procedure, the matrix D is divided into 2 ´ 2 matrix as S represented in Equation (12).

$$S = \begin{bmatrix} d_{11} & d_{12} \\ d_{21} & d_{22} \end{bmatrix} \tag{12}$$

The eigen matrix is formed for S and the eigen solving procedure is applied to the E_s using Equations (13) and (14).

$$E_s = \begin{bmatrix} d_{11} - \lambda & d_{12} \\ d_{21} & d_{22} - \lambda \end{bmatrix} \tag{13}$$

$$(d_{11} - \lambda)(d_{22} - \lambda) - d_{12}d_{21} = 0 \tag{14}$$

By rearranging the (14) based on order, the output equation is obtained and indicated in Equations (15) and (16)

$$\lambda^2 - d_{11}\lambda - d_{22}\lambda - d_{12}d_{21} = 0 \tag{15}$$

$$\lambda^2 - \lambda(d_{11} + d_{22}) - d_{12}d_{21} = 0 \tag{16}$$

By matching the coefficients the roots are identified by quadratic programming structure using Equations (17)–(21).

$$ax^2 + bx + c = 0 \tag{17}$$

$$a = 1,\ b = -(d_{11} + d_{22}),\ c = -d_{12}d_{21} \tag{18}$$

The equal roots values are classified as required region from the image and the corresponding differentiation is applied to categorize the normal region and the suspicious region.

$$r_1 = \frac{(d_{11} + d_{22}) + \sqrt{(d_{11} + d_{22})^2 + 4d_{12}d_{21}}}{2} \tag{19}$$

$$r_2 = \frac{(d_{11} + d_{22}) - \sqrt{(d_{11} + d_{22})^2 + 4d_{12}d_{21}}}{2} \tag{20}$$

$$r = max(r1, r2) \tag{21}$$

Figure 9: Suspicious region retrieved in apple scab image using Quad programming SVM classifier

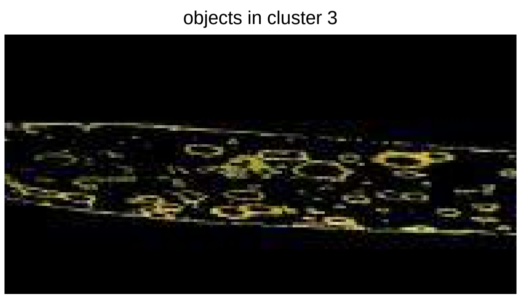

Figure 10: Rice crop image with suspicious region retrieved using Quad programming SVM classifier

The extraction and classification of the suspicious region in both apple scab and rice crop images are displayed in Figures 9 and 10. It estimates the portfolio optimization variance based on the sum of the variances and covariance of individual values and the linear constraints which indicates the lower and upper boundary points. The objective of the quadratic function is convex that decides the problem to be easily solvable. It uses semi-finite convex with the best objective function value. The values generated by the quad function are either minimum or maximum based on the interior values of the function. This method consists of a collection of coordinate searches and reproduces the subspace to maximize the optimality and to minimize the execution steps.

That is, it produces the best solution with the minimum number of iterations. It takes the factorization as simple and direct solution to solve the problem by representing the potential vectors present in the image which are extracted by the feature extraction. The best combination of the extracted features is modelled to perform the detection process which outcomes the unconstrained minimization that produces the n-dimensional vectors as the classified output. After applying the Quad Programming-based classification process, identified normal region in apple scab and rice crop images is shown in Figures 11 and 12.

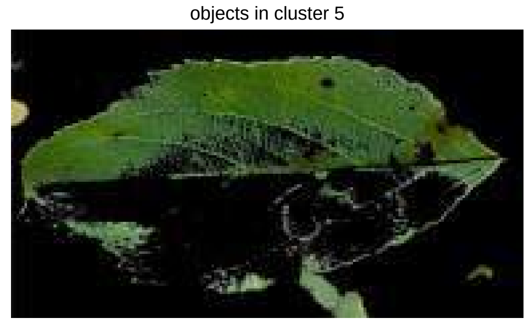

Figure 11: Normal region classified in apple scab image using SVM Quad programming algorithm

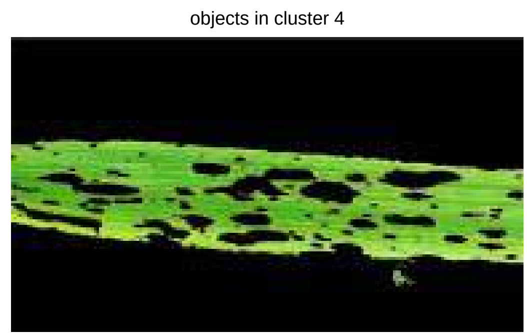

Figure 12: Normal region classified in rice crop image using SVM Quad programming algorithm

5. PERFORMANCE EVALUATION

Performance Evaluation is conducted to validate the quality of the suggested plan. Matlab software is used to evaluate this experiment by holding the apple leaf and rice images as input to the scheme. The validating parameters such as Mean Squared Error and Peak Signal to-Noise Ratio both are applied to appraise the tone of the organization. The Mean Squared Error (MSE) is the idea of variance between the real value and predicted value. This value describes the deviation error of the output created by the system. Peak Signal to-Noise Ratio (PSNR) provides the proportion between the image signal and interference present in the picture. PSNR is almost effortlessly conditioned by the Mean Squared Error (MSE).

The CCF achieves the least Mean Square Error (MSE) approximation value as of 4.71 and eminent Peak Signal to Noise Ratio (PSNR) value as 62.615 dB. Cognitive Fuzzy C-Means achieves precision value as 95% and specificity as 96% values. Figures 13 and 14 show the MSE and PSNR results achieved by the filters, Mean, Median, Gaussian, Wiener and Cross Central filter.

Figures 15–17 represent the performance evaluation of MSE, Mean Absolute Error (MAE) and PSNR metrics for

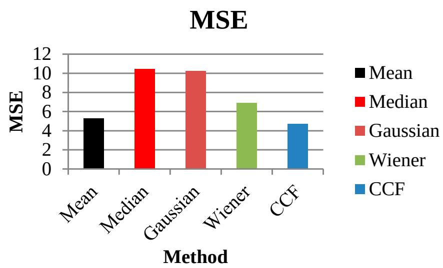

Figure 13: Performance evaluation of Mean, Median, Gaussian, Wiener and proposed CCF Filtering algorithm in terms of MSE

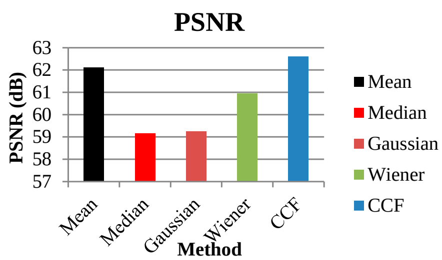

Figure 14: Performance evaluation in terms of PSNR for Mean, Median, Gaussian, Wiener and proposed CCF Filtering approaches

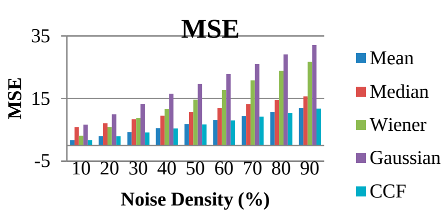

Figure 15: MSE performance evaluation for filtering approaches by varying the noise density in the input image

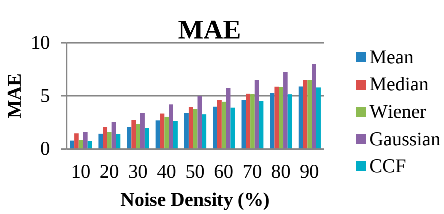

Figure 16: MAE performance evaluation of filtering approaches for various noise density

various filtering scheme by increasing the noise density from 10% to 90%.

Figure 18 provides the evaluation of Structural Similarity Index (SSIM) for various filtering approaches. This evaluation is conducted by increasing the noise density in the input image. Figures 19 and 20 illustrate the performance evaluation of sensitivity and classification accuracy in terms of precision for both existing FCM segmentation and proposed CFCM segmentation algorithm.

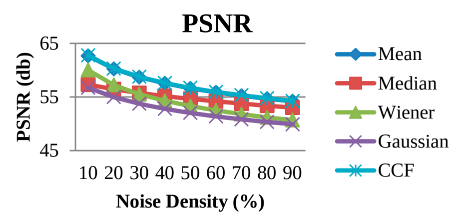

Figure 17: PSNR comparison of Wiener, Gaussian, Mean, Median, CCF filters for various noise density

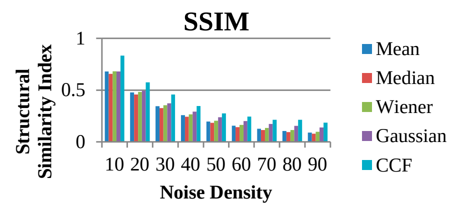

Figure 18: Structural Similarity Index evaluation of various filters by increasing noise density

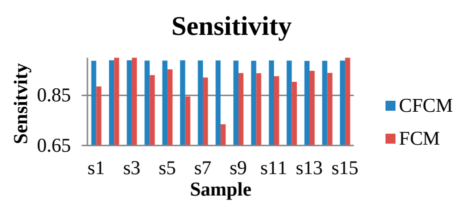

Figure 19: Sensitivity evaluation of FCM and CFCM segmentation approaches for various input images

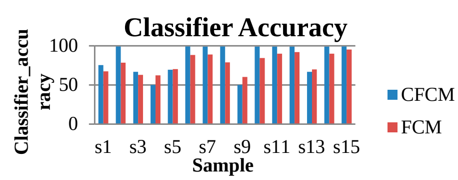

Figure 20: Classification accuracy evaluation of FCM and CFCM segmentation approaches for various input images in terms of precision

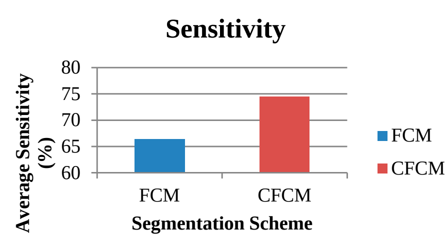

Figure 21: Average sensitivity evaluation of FCM and CFCM segmentation approaches

Figures 21 and 22 show average results of sensitivity and accuracy of the segmentation approaches.

Table 1 exhibits the performance evaluation of FCM and CFCM for sensitivity, precision, and accuracy. It clearly

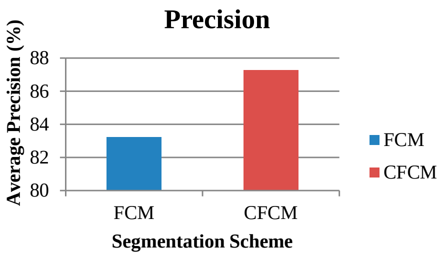

Figure 22: Average precision evaluation of FCM and CFCM segmentation approaches

Table 1: Comparative evaluation

Evaluation metric	FCM	CFCM
Sensitivity	66.45	74.54
Precision	83.22	87.27
Accuracy	78.59	83.47

outcomes the proposed model achieves the best results compared to the existing design.

6. CONCLUSION

In this work, CAD system-based image analysis procedure is used to identify the suspicious region in crops and plants such as rice and apple tree. The image processing stages such as noise removal and image segmentation are used to identify the ROI in the crop image. It will discover the major regions found in the image which leads to ensure that the harvest is not touched by whatever disease. The noise removal process is used by using the CCF which combines the features of Gaussian filter and Mean Filter operations. Cognitive Fuzzy C-Means algorithm is applied to Image segmentation process for the object segments. The process of classification is evolved by using the Quad Programming-based SVM classifier. In future, the 10-fold cross-validation technique can be applied to validate the classification process.

ORCID

S. Sampathkumar http://orcid.org/0000-0002-5368-3357

REFERENCES

1. A. B. Mankar, "Data mining – an evolutionary view of agriculture," *Int. J. Appl. Innovation Eng. Manage.*, Vol. 3, no. 3, pp. 102–105, March 2014.
2. R. C. Gonzalez, and R. E. Woods. *Digital image processing.* Boston, MA: Addison Wesley Longman Publishing Co., Inc., 1992.
3. Y. L. Boureau, F. Bach, Y. LeCun, and J. Ponce, "Learning mid-level features for recognition," *Conf. Comput. Vision Pattern Recognit.*, 2559–66, 2010.
4. S. Yun, W. Xianfeng, Z. Shanwen, and Z. Chuanlei, "PNN based crop disease recognition with leaf image features and meteorological data," *Int. J. Agric. Biol. Eng.*, Vol. 8, no. 4, pp. 60–68, Aug 2015.
5. L. Guigues, J. Cocquerez, and H. Le Men, "Scale-sets image analysis," *Int. J. Comput. Vision*, Vol. 68, pp. 289–317, 2006.
6. G. Hill, R. Wilkins, and W. Hall, "Open and reconfigurable hypermedia systems: a filter-based model," *Hypermedia*, Vol. 5, no. 2, pp. 103–18, 1993.
7. J. M. Slingo, A. J. Challinor, B. J. Hoskins, and T. R. Wheeler, "Introduction: food crops in a changing climate," *Philos. Trains. Roy. Soc. Lond. B Biol. Sci*, Vol. 360, no. 1463, pp. 1983–9, Nov. 2005.
8. K. Zhang, L. Zhang, K. M. Lam, and D. Zhang, "A level set approach to image segmentation with intensity inhomogeneity," *IEEE Trans. Cybern.*, Vol. 46, no. 2, pp. 546–57, 2016.
9. F. Faria, J. A. Dos Santos, S. Torres, and A. Rocha, "Automatic classifier fusion for produce recognition," in *2012 25th SIBGRAPI Conference on Graphics, Patterns and Images (SIBGRAPI)*, IEEE, 2012, pp. 252–9.
10. E. Lee, S. Kim, W. Kang, D. Seo, and J. Paik, "Contrast enhancement using dominant brightness level analysis and adaptive intensity transformation for remote sensing images," *IEEE Geosci. Remote Sens. Lett.*, Vol. 10, no. 1, pp. 62–6, 2013.
11. L. Shao, R. Yan, X. Li, and Y. Liu, "From heuristic optimization to dictionary learning: a review and comprehensive comparison of image denoising algorithms," *IEEE Trans. Cybern.*, Vol. 44, no. 7, pp. 1001–13, 2014.
12. G. Gupta, "Algorithm for image processing using improved median filter and comparison of mean, median and improved median filter," *Int. J. Soft Comput. Eng. (IJSCE)*, Vol. 1, no. 5, pp. 304–11, 2011.
13. P. Patidar, M. Gupta, S. Srivastava, and A. K. Nagawat, "Image de-noising by various filters for different noise," *Int. J. Comput. Appl.*, Vol. 9, no. 4, pp. 45–50, 2010.
14. S. Kumar, P. Kumar, M. Gupta, and A. K. Nagawat, "Performance comparison of median and Wiener filter in image de-noising," *Int. J. Comput. Appl.*, Vol. 12, pp. 27–31, 2010.
15. S. S. Bedi, and R. Khandelwal, "Various image enhancement techniques-a critical review," *Int. J. Adv. Res. Comput. Commun. Eng.*, Vol. 2, no. 3, pp. 267–274, 2013.
16. W. Sun, L. Han, B. Guo, W. Jia, and M. Sun, "A fast color image enhancement algorithm based on max intensity channel," *J. Mod. Opt.*, Vol. 61, no. 6, pp. 466–77, 2014.
17. Y. Zhang, K. Sohn, R. Villegas, G. Pan, and H. Lee, "Improving object detection with deep convolutional networks via Bayesian optimization and structured prediction," in *IEEE*

Conference on Computer Vision and Pattern Recognition, 2015, pp. 249–58.

18. K. Kabassi, and M. Virvou, "Combining decision-making theories with a cognitive theory for intelligent help: a comparison," *IEEE Trans. Human-Mach. Syst.*, Vol. 45, no. 2, pp. 176–86, 2015.

19. J. Yue, W. Zhao, S. Mao, and H. Liu, "Spectral–spatial classification of hyperspectral images using deep convolutional neural networks," *Remote Sens. Lett.*, Vol. 6, no. 6, pp. 468–77, 2015.

20. F. Zhu, M. Bosch, N. Khanna, C. J. Boushey, and E. J. Delp, "Multiple hypotheses image segmentation and classification with application to dietary assessment," *IEEE. J. Biomed. Health. Inform.*, Vol. 19, no. 1, pp. 377–88, Jan. 2015.

21. J. Zhang, R. Wang, C. Xie, and R. Li, "Crop pests image recognition based on multi-features fusion," *J. Comput. Inf. Syst.*, Vol. 10, no. 12, pp. 5121–9, 2014.

22. Y. Chen, W. Su, J. Li, and Z. Sun, "Hierarchical object oriented classification using very high resolution imagery and lidar data over urban areas," *Adv. Space Res.*, Vol. 43, no. 7, pp. 1101–10, 2009.

23. Z. Jiang, Z. Chen, J. Chen, J. Liu, J. Ren, Z. Li, L. Sun, and H. Li, "Application of crop model data assimilation with a particle filter for estimating regional winter wheat yields," *IEEE J. Sel. Topics Appl. Earth Obs. Remote Sens.*, Vol. 7, no. 11, pp. 4422–31, 2014.

24. S. Niu, Q. Chen, L. de Sisternes, Z. Ji, Z. Zhou, and D. L. Rubin, "Robust noise region-based active contour model via local similarity factor for image segmentation," *Pattern Recognit.*, Vol. 61, pp. 104–19, 2017.

25. F. Mesadi, M. Cetin, and T. Tasdizen, "Disjunctive normal parametric level set with application to image segmentation," *IEEE Trans. Image Process.*, Vol. 26, no. 6, pp. 2618–31, 2017.

26. E. Erdil, M. U. Ghani, L. Rada, A. O. Argunsah, D. Unay, T. Tasdizen, and M. Cetin, "Nonparametric joint shape and feature priors for image segmentation," *IEEE Trans. Image Process.*, Vol. 26, no. 11, pp. 5312–23, Nov. 2017.

27. Y. Zheng, B. Jeon, D. Xu, Q. M. Wu, and H. Zhang, "Image segmentation by generalized hierarchical fuzzy C-means algorithm," *J. Intell. Fuzzy Syst.*, Vol. 28, no. 2, pp. 961–73, Jan 2015.

28. Q. Chen, Z. Song, J. Dong, Z. Huang, Y. Hua, and S. Yan, "Contextualizing object detection and classification," *IEEE Trans. Pattern Anal. Mach. Intell.*, Vol. 37, no. 1, pp. 13–27, 2015.

29. M. Tanveer, "Robust and sparse linear programming twin support vector machines," *Cognit. Comput.*, Vol. 7, no. 1, pp. 137–49, 2015.

30. J. Pont-Tuset, P. Arbelaez, J. T. Barron, F. Marques, and J. Malik, "Multiscale combinatorial grouping for image segmentation and object proposal generation," *IEEE Trans. Pattern Anal. Mach. Intell.*, Vol. 39, no. 1, pp. 128–40, 2017.

Authors

S. Sampath Kumar received the B.Tech. degree in Information Technology from Kumaraguru College of Technology, Coimbatore in 2006 and M.Tech. degree in Information Technology from Anna University of Technology, Coimbatore, in 2010. He is currently working for Ph.D. degree in the area of Image Processing at Anna University, Chennai. His area of interest is Image Processing, Theoretical Computation, and Machine Learning. He is working as an Assistant Professor in CSE Department in the Sri Eshwar College of Engineering having an experience of 9 years and 10 months.

Corresponding author. Email: sampath.shanmugam@gmail.com

R. Rajeswari received the B.E. (EEE) Degree from TCE, MK University in the year 1995 and M.E. (Power System Engineering) from TCE, MK University in the year 1998. She has completed the Doctoral Degree from Anna University, Chennai, in the area of Power System Protection in the year 2009. Her area of interest is Power System Engineering. Presently she is working as Asst. Prof. (Senior)/EEE at Government College of Technology, Coimbatore.

Email: rreee@gct.ac.in

Wireless Personal Communications (2021) 117:3343–3358
https://doi.org/10.1007/s11277-021-08073-3

An Optimal Approach to Enhance Context Aware Description Administration Service for Cloud Robots in a Deep Learning Environment

R. Subha[1] · Anandakumar Haldorai[1] · Arulmurugan Ramu[2]

Accepted: 10 January 2021 / Published online: 1 February 2021

Abstract

As the advancements in the field of artificial intelligence technologies continue to grow, robots are being built by the researchers as an attempt to render services to the people. In this regard, the robots can communicate effectively with the people and be able to complete all the tasks adequately given to them. These service robots while being developed requires the dialogue services to be developed to interact effectively with human beings providing far better user experience. Thus, the robot been built can provide domain-specific knowledge as well as able to provide consultations in various domains. We in this paper adopted a service-oriented approach for developing context-aware communication services for the cloud robot. The proposed work aims at training the context-aware model developed. The context-aware model is responsible for answering the questions put forward by the users and possess the ability to exploit the answers corresponding to the questions presented. An integrated framework is used to combine the contextual information and communication services. The performance of the proposed model can be evaluated based on Inverse Rank Mean (IRM). Evolutionary testing methods are used for testing the data in the proposed model. The results thus obtained shows the effectiveness of the proposed approach.

Keywords Context-aware · Communication · Neural networks · Human–robot interaction · Deep learning · Training data

✉ R. Subha
kris.subha@gmail.com

Anandakumar Haldorai
anandakumar.psgtech@gmail.com

Arulmurugan Ramu
arulmr@gmail.com

[1] Department of Computer Science and Engineering, Sri Eshwar College of Engineering, Coimbatore, Tamil Nadu, India

[2] Department of Computer Science and Engineering, Presidency University, Bangalore, India

1 Introduction

Issues concerning the service robots with their development and deployment is the proper execution of tasks providing human–robot interaction in a natural way. For this, a system-level architecture is constructed with which the cloud computing platform can be collaborated with the robots and its design can be created effectively. The services mentioned are mainly labouring services where the people can get assistance from the robots. The main responsibility of the robots lies with the delivery of knowledge and the ability to communicate with the human beings in a more natural way. Hence, in this work, a framework for representing the human−robot dialog is represented.

A service-oriented architecture has been proposed that helps in deploying the services much more effectively. On the other hand, the resources such as robotic services and processors for computation are provided with the help of cloud computing architecture [1, 2]. The onboarding computation process can no longer limits the operations of the robot and as a result even more intelligent robots can be generated. The service-oriented architectures on the other hand helps in generating prototypes for the robotic services. These architectures been proposed helped in the development of robotic services [3, 4].

In order to provide knowledge-based services, human–robot interaction is very much essential. A dialog system is developed that ensures human interaction based on natural languages. Thus, the dialog system been developed acts as a vocal interface between the user and the robot. There are also non-goal oriented dialogue systems such as the chatboxes that focus on performing open domain conversations. The proposed work mainly focuses on services that are domain-specific and are goal-directed. Here, a knowledge base is present that performs the dialogue services based on a question–answer means [5].

The question-answering system mainly aims at generating the relevant responses from the communication at any given instance. There are two methods for obtaining the response in general namely the selection-based method and the deep learning method. Among these two methods, the selection-based method is the most widely used one. It is because, this method is capable of producing more responses. The mapping between the questions and answers in the human–robot language has been developed to an advanced stage with the intervention of machine learning approaches and several other advanced technologies [6–8].

Mapping between words and characters in a dialogue model of a particular sequence can be mapped to other sequences by using a model called as sequence to sequence (seq2seq) model [9, 10]. Particularly besides the dialogue data, contextual content plays a major role in ascertaining the relevance of the result obtained from the question posed by the user. This contextual factor is equipped to discover any dialogues and questions posed that can affect the corresponding response form the robot [11, 12]. As an instance, environmental conditions or the users' responses and emotions. To enhance user experiences the service system's application services are enabled by combining contextual information into the application to automatically change in response to the circumstances.

The significance of incorporating the context-aware data with the computational approaches has been emphasized with the help of deep learning approaches. With the addition of external knowledge, the process of selecting the answers has been made more precise. As far as the relevant answers are in the information center the robot was trained to find the precise answer for the question opposed to it. As for the unfamiliar questions and content not available in the information center we have developed a reasoning procedure to attend to it. In brief, this is designed to search for related questions from the information center. These questions are further sent for evaluation in order to come up with the precise answer.

Predominantly, our work introduces an alternate approach where the contextual information is embedded at the encoder level of seq2seq model to generate results and answers. A series of experiments are conducted to evaluate this approach. Firstly, we have evaluated the context-based service and imaging content by capturing image-based data. Second, comes evaluation of performance of the training data. Here, we train the human–robot dialoguing model of questioning and answering. Then we have focused on testing the mechanism of search the model employs to enhance its answer searching capacity. Finally, to verify and validate the contextual awareness of the dialoguing service, a series of experiments are conducted and the different methods are compared and studied. The final results attest to the improvement and efficiency of this method.

2 Background and Related Work

System architecture plays a significant impact on resource sharing and training the dialoguing model. These are the most important concerns on creating contextual awareness in Robot-Human communication services. The following section presents the related studies on resource sharing and training of a model in brief.

As mentioned, choosing an appropriate software architecture is crucial in the development of ROS. There are a number of work and related studies being proposed to come up with an effective way of creating different service applications. RoboEarth [1] is the most remarkable work and is also available in an open source cloud robotics platform [2]. With RoboEarth, accessing information center and distributing complex computational tasks to the cloud has become way easier. Further works on the platform have also enabled us to deploy software architecture by incorporating robotic hardware to the cloud services. To give an instance, in a software framework called DAvinCi parallelism and extensibility was achieved by integrating the hardware and cloud services and it was also found to draw on many advantages over the existing system [13]. A middleware called Rosbridge was developed to further perform advanced tasks like providing socket-based access to the robotic system and algorithms by making use of Web Technologies [4]. A standard application development framework [14] has also enabled effective communication between the middleware and the browser.

Along with Roboearth, that worked on the development of cloud ROS. One such work was Koubaa [15] that made use of web services as a middleware. They developed a new system called RoboWeb and proposed that they can be used as a service for end users by organizing all the resources. Another work by Du et al. [16] developed a hypothesis to use the architecture to manage functional modules in the Robot cloud. They proposed by doing this one can achieve more structure and flexibility in the cloud at the same time make the resources reusable and extensible to a certain extent. Furthermore, Bastos and Pereira proposed the use of robotic system in a remote environment. By doing this, it was said that one would be able to develop various applications in a remote environment. Examples of other works are illustrated in detail in [18–20]

In contrast to other works, this project has exploited many advantages over other models already developed. We have mainly focused on providing users with reusability and scalability of resources by developing a robot and considering it as a service. By regarding robot as a service and making it web-enabled we were able to allocate robot services developed by different organizations in the cloud. The expandability and shareability of the system is ensured by using the robotic system as different operational nodes.

Another concern addicting to the cloud service framework is the design of ROS. Developing communication services for cloud-based ROS is by using human language to train robots and use them as the primary interaction language. Communication systems uses the classic approaches of NLP. There approaches were primarily based on handcrafted rules and templates, e.g. [22] and [23]. But today, with the advancement in machine learning and data science, utterances can be automatically generated as machine responses with a data-driven approach [24, 25]. These issues can be alleviated by deep learning techniques available today that focuses on representing data in a distributed approach. This method is known to have achieved significant improvements. As these approaches can be adopted to develop communication service, the relevant works have described in brief the following paragraphs.

Generally, seq2seq network models are used in deep learning techniques in order to generate results with a function with the most occurring result estimation. But today, the sequence-to-sequence model is predominantly employed for conversation generation [6]. For the most part, it focuses on enhancing the contextual quality of the results obtained by improving the encoding approach and the communication infrastructure. For instance, Shang generated dialogue responses by using a RNN encoder-decoder [25]. Another work by Serban et al. focused on using a new approach called Long-Short Time Memory [LTSM] infrastructure network. Similarly, Wen presented a work-based approach to respond to the dialogues with more precision by generating relevant answers [26, 27].

Furthermore, adding to the works mentioned above to develop enhanced communication models, there are researches which hypotheses on regrading contextual information in addition to the contextual information such as dialogues of humans (e.g. [11, 12, 28]). There are many works and studies in recent years whose primary focus was to integrate context information in the textual content for enhancing the machine responses with more meaningful content. As an instance, In [17] showed that by using an entire dialogue history of a person the context-sensitive response generation concerns can be addressed more effectively [11]. Serban et al. where he used the approach of capturing more meaningful individual utterances by using a hierarchical model and then integrated them as discourses [29] is another example. This model aimed at revealing all the hidden layers in the network and in the contextual dialogue history with which it is trained. This was done by making use of high level RNN in the context Cues. This approach was further extended by [21]. where attention mechanism was added to capture attention at every stage including words, utterances, and annotations in the dialogue [30].

Today's studies and relative works have focused more on contextual data and in adding more emotion to the human–robot utterances. Yet, doing this has been crucial for many today for various reasons. The main reason is the difficulty in obtaining high-quality emotion in large scale corpus. This is because emotions are more difficult and harder to annotate. In addition to this is the difficulty of balancing the intonation and expressions of the dialogues grammatically as needed. This is argued in [12]. To avoid this in effect, many researchers have tried to intensify the human–robot emotion. Zhou adopted one such service which developed a model named as emotional chatting machine (ECM) [31]. Zhou further presented that we can train the model for large scale conversation thereby to obtain well annotated emotion.

To train the robot, human voice and expressions taken in real time were considered to be an advanced characteristic. Zhang et al. captured the textual information post sequence to enable the system to generate the response for every time of emotion by adopting a sequence-to-sequence learning framework [32]. This model comprised of two major components to produce multiple emotional responses by using a response generator. The output delivered were captured by an output selector to choose and select the relevant results by predefining sets of policies related to the model. Sun et al. added an additional category to encoder-decoder as an additional source and used LTSM neural network to achieve conversational modelling [33].

Contrary to the relevant studies, this project aims to allow robot to act as a service thereby to provide platform-specific knowledge service. To achieve that, we have created a robot with contextual awareness as a communication service. This service also comes with supplementary mechanisms for enhanced knowledge improvement. Particularly, we have aimed at integrating image-based context awareness along with the emotions of human and ecological workspace. We have focused on the use of deep learning techniques in the initial encoder level. This mechanism is briefly explained in the following sections.

3 Context–Aware Communication Services Development for the Robotic System

3.1 Developing the System Framework

The communication services for the human–robot is developed based on the service-oriented framework defined previously. The service-oriented framework defined already provides the required interactive services and network resources. It is to be noted that the network resources are sharable. The computing process is further divided into two parts—for those processes that require immediate response, the onboard processors are mounted on the robot. In the second part, the computing services are performed with the help of the computing nodes that are responsible for preparing operations such as deep learning. As the service repository is situated in the cloud, it is easy for the developers to submit their robotic services that are reusable for sharing. These varying services can be effectively delivered with the help of the framework based on the robotic system. This system framework for the robotic system is shown in Fig. 1.

Here the service request is sent by the robot to the master node. The responsibility of the master node is to organize the robotic system network. The request is then transferred from the master node to the task manager. The task manager is responsible for planning and evoking the services respectively. Based on the predefined task characteristics, the services from the service repository can be retrieved to configure the composite services until suitable services are found. The framework consists of varying computing nodes that help in identifying the required cloud-based services. Consider an example: imaging services, which involves the set of services for collecting the required images. Here the cloud node defined assists in the capturing of images which is then sent to the topic of the master node. From this master node, it is possible for other nodes that deal with the images to retrieve the required data. The context-aware model for the human–robot interaction is clearly shown in the following Fig. 1.

This makes it possible to deploy the robotic functions in the virtual machine nodes. Through the robotic system framework, the services are combined to form a new robotic function. In the following sections of the paper, we have discussed the interactive services, context-aware communication services that are integrated into the cloud robots. As a result,

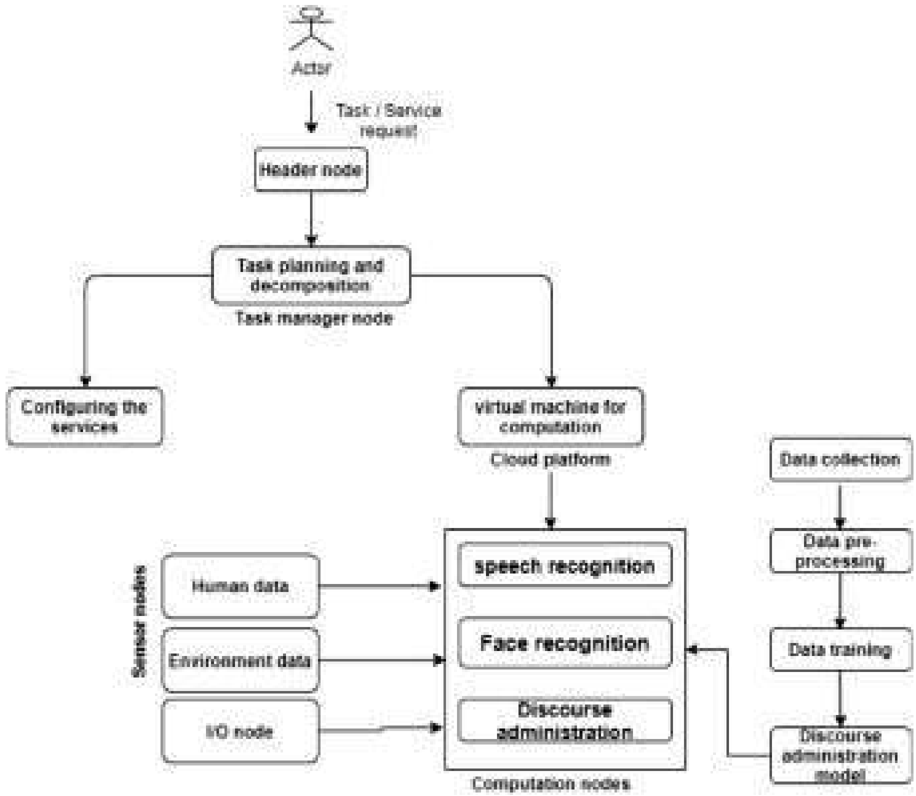

Fig. 1 Context-aware model for human–robot communication services

the robots are indulged with the role-playing of knowledgeable consultants to the target audience.

3.2 Operations Involved in Communication Service

The communication services have been developed to provide enough knowledge about the specific domains such that the user can get the answer to his/her questions with regards to the local circumstances. In other words, with communication services, a communication can be established between the questions posed by human beings and the corresponding responses from the robots. The current trend of robotics technology is the automatic speech recognition and synthesizing text to speech and the devices responsible for performing such functions are considered as the robotic equipment. With these toolkits, the required services and the functions can be performed effectively. A training module has been proposed where the communication models can be obtained from the deep learning method along with the datasets. These datasets contain domain-specific knowledge with which the model can be trained based on the question–answer pairs. These question–answer pairs are in other words termed as the indexed knowledge.

Here, we consider two models for training which then maps the question and answer pairs and to obtain the responses respectively. The first model is trained as a question answering model that maps the questions from human beings to the corresponding answers from the robots. Here the text sentences termed as the content along with the images termed as the context are combined for a 3-tupe data record. The content and the context pair is then combined together to form a pair. This pair is then used for training the model further. The second model on the other hand is considered as an additional mechanism that is used to obtain a suitable response which the first model fails to retrieve. Based on this, checkpoints were included which is represented by grey circles as shown in Fig. 2. These checkpoints were used to indicate the correctness of the answer provided. The correctness of the answers indicates the results required. These results are then used for evaluating the second model. Before adopting the second model, an external knowledge base is requested by the system to obtain the response. This external knowledge base in turn is used to train the neural model in a data-driven manner. This shows that the datasets should be of better quality as well as the quantity such that they have a critical impact over the trained models. This in turn indicates the ability of the model to respond to the questions posed by human beings.

To improve the ability of the robots in providing consultation, an external knowledge base such as DBpedia is attached to the system that helps in handling the cases where the trained model finds it difficult to provide a satisfactory response to the questions posed. But still, if the solution is not found, then the system attempts with a different strategy. Meanwhile, the system makes use of the second model to match the questions from the knowledge repository and based on which the answers are obtained for evaluation. The second model is further used to find an alternative question which in turn acts as the alternative for the previous question posted by the user. This question is then sent to the first model which is already trained to obtain its answer. This process of designing the question and identifying the answer requires a neural model to be trained with the help of the learning method. This procedure is used for a question to question mapping instead of the question to answer mapping as done by the first training model.

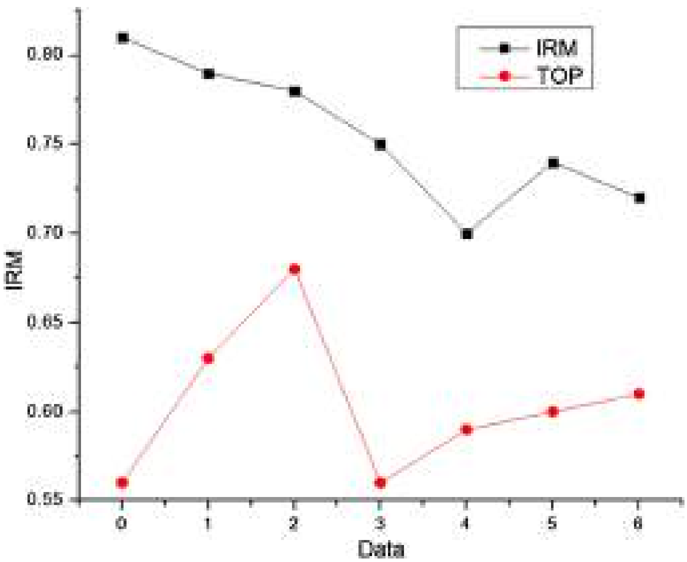

Fig. 2 Performance comparison between IRM and TOP

The following pseudocode indicates how the functions are invoked and operated. Upon activating the service, the contextual information is obtained based on the topic subscribed. This information in turn is required for performing the corresponding task. The information that is obtained is then is subjected to data pre-processing. The result thus obtained is then sent to the trained model to generate the corresponding answer. One of the unique features of the robotic system is the data flow based on the topics chosen. This feature of the robotic system enables reusing services with varying robots.

Procedure for the computing node

Loop till the computing node shuts down

Input

Test information

Identify the task type

Do

Choose the data from the human data pool or the environment data pool

If data pool not empty **then**

Fetch the required message to the robotic system

Convert the image into both text and image format

Data pre-processing is done

Generate the response based on the conversation model

Store the results obtained

Convert the results into a robotic system message

Communicate the message thus generated to the voice synthesis node

End loop

3.3 Processing and Embedding of Sentences

The communication services have been proposed can interact with human beings with the help of natural languages. Here, the main focus of the operation is to identify the response to the questions posed. The instances are used in establishing conversations where the instances are considered as the question–answer pair obtained from the knowledge base. The method of selecting the answer is done with the help of deep learning neural model. To use this model to train the communication model, a question–answer dataset is required. The text sentences can be further tokenized with the help of the Stanford tokenizer. The word embedding method selected is the Glove (Global Vectors for Word Representation). This method maps the words to their corresponding vectors. The performance is enhanced with the help of a package called "genism" that makes use of the pre-trained model. This pre-trained model consists of vocabularies from the text processed previously which is then converted into vectors. This helps in obtaining the vector representation for our data that has been trained. This vector in turn is used as the input for the training algorithm for the application model proposed. The mapping method encodes the words that are present in the system to form a vector representation based on the numerical identifiers. The embedding algorithm not only performs mapping but also identifies the semantic relationship between the words. This enables human beings and robots to communicate with each other.

3.4 Deep Learning Model for Context: Aware Communication System

The sentences corresponding to the user inquiries are generated based on the contextual information obtained and communication service. The contextual information chosen in this approach is the user information. The model thus proposed can also be applied to other contexts such as the environmental situations and the like.

3.4.1 Model

The sentences corresponding to the user inquiries are generated based on the contextual information obtained and communication service. The contextual information chosen in this approach is the user information. The model thus proposed can also be applied to other contexts such as the environmental situations and the like.

3.4.2 Training

In order to train the deep learning model mentioned above, it is required to organize a training data set. Thus, in a given dataset, there exists a positive answer Y+ corresponding to the question X and the associated context C. This positive answer is highly likely to be the correct of all the available answers. The word embedding feature defined above, encodes the question into a vector form which then flows through the hierarchical memory network (HMN) and the neural network (NN) layer. This output thus obtained is then merged with the context network features.

The HMN function is used to calculate the output vector O and the hidden vector H as follows

$$O = EMBED\left\{i_1 \ldots i_n, w\right\} \tag{1}$$

$$H = HMN(O, W) \tag{2}$$

The feature vector F corresponding to the given image is described as follows

$$F = conv(I, L) \tag{3}$$

where I is the input data, L represents the filters applied in calculating the feature vector.

4 Performance Evaluation and Results

To evaluate the performance of the proposed context-aware model, initially a cloud-based platform is constructed. This platform is then used for evaluating the robotic services. Once the framework for evaluating the robotic services are constructed, the question–answer model is then trained based on the dataset chosen. The dataset chosen consists of question–answer pairs. The ability to search the answer is increased with further experiments.

4.1 Deploying the Cloud Framework for the Robotic System

A robotic system framework based on cloud is used for evaluating the performance of the proposed model. Here, the robot used is the Turtlebot which contains a webcam and a microphone. Upon capturing the target images, it is detected and recognized based on the vision-based services. The results obtained were used for the future work of this paper. The performance of the vision service is evaluated based on the series of experiments that make use of the face dataset available online. To recognize the best of the front-face images, trained classifiers are used. The angle with which the face is viewed, if it is within 10 degrees, it shows that the face is recognized successfully. The public image dataset consisting of various emotions are used to train the context-aware communication model. The following Table 1 shows the performance evaluation of the various context emotions.

4.2 Performance Metrics

Three criteria were mainly employed in evaluating the method used for experimenting the human–robot communication services. The criteria are as follows

1. the loss previously defined
2. the predictive result should be same as that of the expected result. It is represented as top precision. It is calculated as follows

$$\text{top precision} = (\text{matches that are correct})/n$$

The model performance is evaluated based on the inverse rank mean (IRM). Performance comparison between TOP and IRM is shown in Fig. 2. It represents the inverse value of the first correct answer's rank. Inverse rank mean is given by

$$IRM = 1/n \sum_{i=1}^{n} \frac{1}{rank_i} \tag{4}$$

4.3 Evaluating the Performance of the Training Model

This part describes the first phase of the experiment. For experimental purposes, a dataset without contextual information is selected. The selected dataset roughly consists of 13,000 questions and 20,000 corresponding answers. Out of this the number of questions and the number of answers adopted for testing is roughly around 2000 and 3500 respectively. these questions and answers that were selected were pre-processed. In this

Table 1 Performance evaluation of various context emotions

Context (emotions)							
Emotion no	0	1	2	3	4	5	6
Results							
Top	0.56	0.63	0.68	0.56	0.59	0.60	0.61
IRM	0.81	0.79	0.78	0.75	0.70	0.74	0.72

procedure, the unwanted data is removed. Next comes the learning phase. The positive and negative answers formed for the given question helps in obtaining the training instance. In the dataset obtained, the positive answers corresponding to the question X is considered as the correct answer and the remaining answers are considered as the wrong answer. The wrong answers can be identified easily with the help of the training model. These incorrect answers are represented as Y.

The dataset chosen for the experiment is divided into two-parts. One part (60%) contributes to the training and the other part (40%) contributes to the testing. Both the correct and incorrect answers are combined to form the training data. These changes that occur while training the model is shown in Fig. 3.

4.4 Additional Strategy Evaluation

To perform the evaluation process, a dataset containing questions and similar answers are chosen. The dataset roughly consists of about 1,50,000 questions. It is also found from the dataset that each question has a similar question which is the contrast. Here the associate model is used to retain the model efficiently. Two sets were chosen for the experiment:

- In the first set, vocally similar and semantically different questions were included.
- In the second set, randomly sampled questions were used.

Here, the results obtained from the second set is higher than that of the first. The accuracy of the training model is shown in the following Fig. 4.

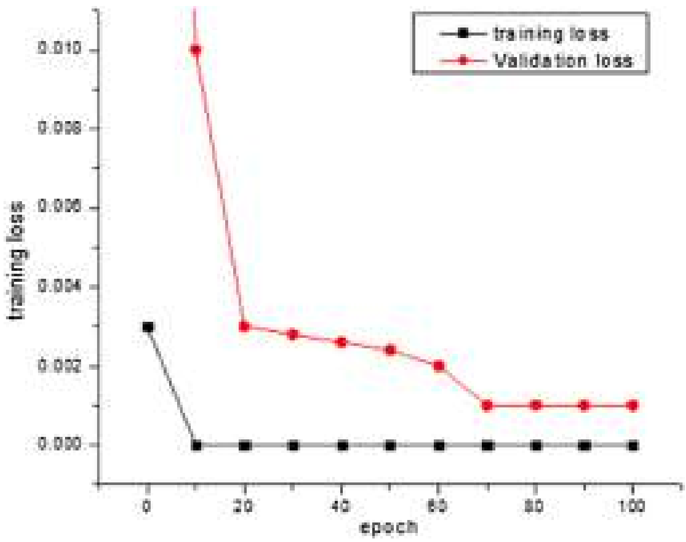

Fig. 3 Loss related changes while training the model

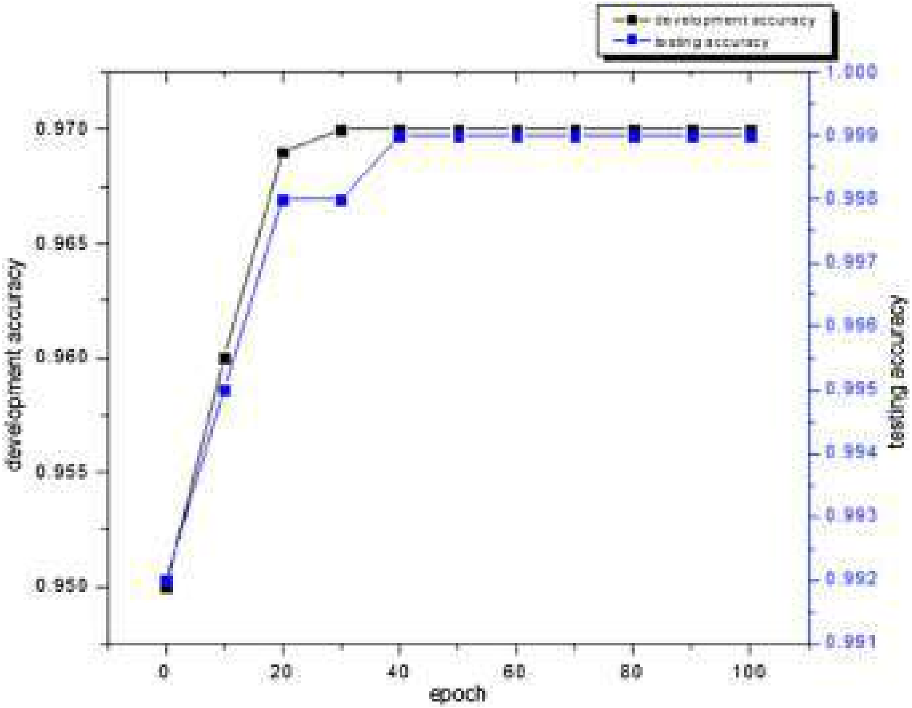

Fig. 4 Accuracy related changes while training the model

4.5 Evaluating the Training of Context-Aware Communication Services

There are not many datasets that capture the emotion of the user while speaking. Hence, as an alternative, facial dataset is chosen instead of a text dataset. To build a training instance, both positive and negative answers are required, based on which the computational time is reduced. Here, the Kaggle dataset is chosen to represent the change in emotions in the dialogues. 4100 images were chosen for sampling, out of which 3100 samples were used for training and the rest for testing. The images once sampled were attached to the question–answer pair randomly in the communication dataset. The HMN model is used for training the dataset. If the content part as well as the context part were found to be correct, it marks successful prediction. Experimental trials were performed to ensure that prediction is achieved successfully. When the testing loss (validation loss) is reduced, the training loss is also reduced gradually to the point of zero. Table 2 shows the performance of Top and IRM with the environmental contexts.

Table 2 Performance of top and IRM with the environmental contexts

Environmental context								
Environment No	0	1	2	3	4	5	6	7
Best result								
Top	0.75	0.76	0.72	0.76	0.76	0.73	0.75	0.71
IRM	0.78	0.79	0.82	0.83	0.85	0.89	0.84	0.82

Once the inferred models were tested after training, it is found from the results obtained that the top precision can be improved. It also shows that the performed can as well be improved. It is because whenever the overfitting problem arises, the performance decreases. Figure 5 shows the performance of the TOP and IRM with the environmental contexts.

The following experiments helps in evaluating the performance further. Two situations are considered where the incorrect image category is included in the training dataset to identify the dependence of the training model on the contextual information. The second situation is to show the dependence of the training model on the conversational content.

The system is then tested with the testing data using any one of the traditional testing techniques to ensure that the system works without any flaws. Here, the context-aware system is tested without imposing any constraints. For this, it is essential to differentiate the test input and the test environment to enable better testing. It is also to be noted that when the test case is being executed, the context is bound to change.

5 Conclusion

It is found from the obtained results clearly states that, the successful human–robot communication depends on the effective context-aware communication services. Here the acts as the consultant in retrieving the knowledge or the information thereby providing the user with the domain-specific information. A cloud-based framework has been adopted to deploy the services successfully. Hence the computational tasks that are considered as time-consuming are allocated to the cloud computing nodes and the services thus created are stored in the repository of the robotic system. A deep learning method has been used to obtain the responses to the questions posed using training the neural model. The model is trained in such a way that the context information and the content information are coupled together. The speech-to-text system helps in collecting the information whereas the images

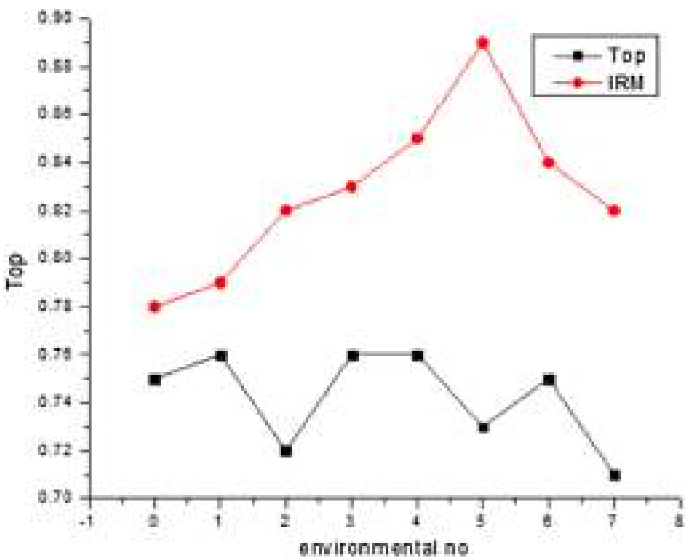

Figure 5 Performance of Top and IRM with the environmental contexts

captured via the vision system of the robot helps in deriving the contextual information. A series of experiments have been conducted to evaluate the proposed approach. Upon analysing the information, it shows that the proposed context-aware model performs far better when compared to the other existing models. The experiments were done under various restrictions due to the presence of annotated datasets that simultaneously contains both the information.

Future work involves developing methods to overcome this challenge using a knowledge transfer method. With this approach, the datasets can be enriched automatically and the knowledge can be shared among multiple domains. Our future work also involves developing an even more effective context-aware model to increase the performance of the robots.

Compliance with Ethical Standards

Conflict of interest The authors have declared to have no conflict of interest.

Human and Animal Rights This research includes no studies involving animals or humans controlled by the authors.

References

1. Waibel, M., et al. (2011). RoboEarth: A world wide web for robots. *IEEE Robotics and Automation Magazine, 18*(2), 69–82.
2. Mohanarajah, G., Hunziker, D., D'Andrea, R., & Waibel, M. (2015). Rapyuta: A cloud robotics platform. *IEEE Transactions on Automation Science and Engineering, 12*(2), 481–493.
3. Remy, S. L., & Blake, M. B. (2010). Distributed service-oriented robotics. *IEEE Internet Computing, 15*(2), 70–74.
4. Osentoski, S., Jay, G., Crick, C., Pitzer, B., DuHadway, C., & Jenkins, O. C. (2011). Robots as web services: Reproducible experimentation and application development using rosjs. In *Proceedings IEEE international conference on robotics and automation* (pp. 6078–6083).
5. Huang, J.-Y., Lee, W.-P., Yang, T.-H., & Ko, C.-S. (2017). Resource sharing for cloud robots: Service reuse and collective map building. In *Proceedings of the 18th IEEE international conference on advanced robotics* (pp. 303–309).
6. Vinyals, O., & Le, Q. A neural conversational model. arXiv preprint arXiv:1506.05869.2015.
7. Feng, M., Xiang, B., Glass, M. R., Wang, L., & Zhou, B. (2015). Applying deep learning to answer selection: A study and an open task. In *2015 IEEE workshop on automatic speech recognition and understanding (ASRU)* (pp. 813–820). IEEE.
8. Hu, B., Lu, Z., Li, H., & Chen, Q. (2014). Convolutional neural network architectures for matching natural language sentences. In *Proceedings advance neural information processing system* (pp. 2042–2050).
9. Chen, H., Liu, X., Yin, D., & Tang, J. (2017). A survey on dialogue systems: Recent advances and new frontiers. *ACM SIGKDD Explorations Newsletter, 19*(2), 25–35.
10. Gao, J., Galley, M., & Li, L. (2018). Neural approaches to conversational AI. In *Proceedings of the 41st international ACM SIGIR conference on research & development in information retrieval* (pp. 1371–1374).
11. Sordoni A., et al. (2015). A neural network approach to context-sensitive generation of conversational responses. In *Proceedings of the conference on North American chapter of the association for computational linguistics: human language technologies* (pp. 196–205).
12. Ghosh, S., Vinyals, O., Strope, B., Roy, S., Dean, T., & Heck, L. (2016). Contextual LSTM (CLSTM) models for large scale NLP tasks. arXiv preprint arXiv:1602.06291.
13. Arumugam, R., Enti, V. R., Bingbing, L., Xiaojun, W., Baskaran, K., Kong, F. F., et al. (2010). DAvinCi: A cloud computing framework for service robots. In *2010 IEEE international conference on robotics and automation* (pp. 3084–3089). IEEE.

14. Crick, C., Jay, G., Osentoski, S., & Jenkins, O. C. (2012). ROS and rosbridge: Roboticists out of the loop. In *Proceedings of the 7th ACM/IEEE International Conference on Human-Robot Interaction* (pp. 493–494).
15. Koubaa, A. (2014). A service-oriented architecture for virtualizing robots in robot-as-a-service clouds. In *Proceedings international conference on architecture of computer system* (pp. 196–208).
16. Du, Z., He, L., Chen, Y., Xiao, Y., Gao, P., & Wang, T. (2017). Robot cloud: Bridging the power of robotics and cloud computing. *Future Generation Computer Systems, 74,* 337–348.
17. Pereira, A. B. M., & Bastos, G. S. (2017). ROSRemote, using ROS on cloud to access robots remotely. In *Proceedings of the 18th IEEE international conference advance robotics* (pp. 284–289).
18. Kehoe, B., Patil, S., Abbeel, P., & Goldberg, K. (2015). A survey of research on cloud robotics and automation. *IEEE Transactions on Automation Science and Engineering, 12*(2), 398–409.
19. Saha, O., & Dasgupta, P. (2018). A comprehensive survey of recent trends in cloud robotics architectures and applications. *Robotics, 7*(3), 47.
20. Wan, J., Tang, S., Yan, H., Li, D., Wang, S., & Vasilakos, A. (2016). Cloud robotics: Current status and open issues. *IEEE Access, 4,* 2797–2807.
21. Yang, T.-H., & Lee, W.-P. (2016). Intelligent service reconfiguration for home robots. In *Proceedings of the advance reconfigurable mechanics robots II* (pp. 735–745). Cham: Springer.
22. Perera, V., et al. (2015). Learning task knowledge from dialog and web access. *Robotics, 4*(2), 223–252.
23. Thomason, J., Zhang, S., Mooney, R., & Stone, P. (2015). Learning to interpret natural language commands through human-robot dialog. In *Proceedings of the 24th international conference on artificial intelligence* (pp. 1923–1929).
24. Kowsigan, M., & Balasubramanie, P. (2019). An efficient performance evaluation model for the resource clusters in cloud environment using continuous time Markov chain and Poisson process. *Cluster Computing, 22*(5), 12411–12419.
25. Shang, L., Lu, Z., & Li, H. (2015). Neural responding machine for short-text conversation. In *Proceedings of the 53rd annual meeting of the association for computational linguistic* (Vol. 1, pp. 1577–1586).
26. Serban, I. V., Sordoni, A., Bengio, Y., Courville, A., & Pineau, J. (2015). Hierarchical neural network generative models for movie dialogues. arXiv preprint arXiv:1507.04808, *7*(8), 434–441.
27. Wen, T.-H., Gašić, M., Mrkšić, N., Su, P.-H., Vandyke, D., & Young, S. (2015). Semantically conditioned LSTM-based natural language generation for Spoken dialogue systems. In *Proceedings conference on empirical methods in natural language processing* (pp. 1711–1721).
28. Zhou, H., Huang, M., & Zhu, X. (2016). Context-aware natural language generation for spoken dialogue systems. In *Proceedings of the 26th international conference on computations linguistics, technical papers* (pp. 2032–2041).
29. Serban, I. V., Sordoni, A., Bengio, Y., Courville, A., & Pineau, J. (2016). Building end-to-end dialogue systems using generative hierarchical neural network models. In *Proceedings of the AAAI* (pp. 3776–3784).
30. Xing, C., Wu, Y., Wu, W., Huang, Y., & Zhou, M. (2018). Hierarchical recurrent attention network for response generation. In Proceedings of the AAAI Conference on Artificial Intelligence (pp. 5610–5617).
31. Zhou, H., Huang, M., Zhang, T., Zhu, X., & Liu, B. (2018). Emotional chatting machine: Emotional conversation generation with internal and external memory. In *Proceedings of the 32th AAAI conference on artificial intelligence* (pp. 730–738).
32. Sarkar, T., Salauddin, M., KumarHazra, S., & Chakraborty, R. (2020). A novel data science application approach for classification of nutritional composition, instrumental colour, texture and sensory analysis of bael fruit (*Aegle marmelos* (L) correa). *International Journal of Intelligent Networks, 1,* 59–66.
33. Zhang, R., Wang, Z., & Mai, D. (2018). Building emotional conversation systems using multi-task Seq2Seq learning. In *Proceedings of the natural CCF conference on natural languages processing and Chinese computing* (pp. 612–621).
34. Kalpana Devi, M., & Umamaheswari, K. (2020). Modified Artificial Bee Colony with firefly algorithm based spectrum handoff in cognitive radio network. *International Journal of Intelligent Networks, 1,* 67–75.
35. Mohan, K., & Palanisamy, B. (2019). A novel resource clustering model to develop an efficient wireless personal cloud environment. *Turkish Journal of Electrical Engineering and Computer Sciences, 27*(3), 2156–2169.

Publisher's Note Springer Nature remains neutral with regard to jurisdictional claims in published maps and institutional affiliations.

Dr. R. Subha had obtained B.E in Computer Science and Engineering from Periyar university in 2002 and M.E. in Software Engineering from Anna University, Chennai in 2006. Also, she had received her Ph.D. from Anna University, Chennai in 2014. She has more than 15 years of experience in teaching and currently she is working as Professor and Head in the Department of Computer Science and Engineering at Sri Eshwar College of Engineering, Coimbatore. Her research interests include Software Engineering, Theory of Computation and Data Mining.

Dr. Anandakumar Haldorai Professor (Associate) and Research Head in Department of Computer Science and Engineering, Sri Eshwar College of Engineering, Coimbatore, Tamil Nadu, India. He has received his Master's in Software Engineering from PSG College of Technology, Coimbatore and PhD in Information and Communication Engineering from PSG College of Technology under, Anna University, Chennai. His research areas include Big Data, Cognitive Radio Networks, Mobile Communications and Networking Protocols. He has authored more than 114 research papers in reputed International Journals and IEEE conferences. He has authored 11 books and many book chapters with reputed publishers such as Springer and IGI. He is an Editor in Chief of Keai- Elsevier IJIN. He served as a reviewer for IEEE, IET, Springer, Inderscience and Elsevier journals. He is also the guest editor of many journals with Elsevier, Springer, Inderscience, etc. He has been the General Chair, Session Chair, and Panellist in several conferences. He is senior member of IEEE, IET, ACM and Fellow member of EAI research group.

Dr. Arulmurugan Ramu is a Professor, Presidency University, Bangalore, India. His research focuses on the automatic interpretation of images and related problems in machine learning and optimization. His main research interest is in vision, particularly high-level visual recognition. He has authored more than 35 papers in major computer vision and machine learning conferences and journals. He is the recipient of Ph.D. degrees in Information and Communication Engineering from the Anna University at Chennai, M.Tech in Information Technology Anna University of Technology and B.Tech degree in Information Technology. He is guided many Ph.D. research scholar under the area of Image Processing using Machine Learning. He is an Associate Editor of Inderscience IJISC journal. He is awarded as Best Young Faculty Award 2018 and nominated for Best Young Researcher Award (Male) by International Academic and Research Excellence Awards (IARE-2019).

Wireless Personal Communications (2021) 117:2641–2643
https://doi.org/10.1007/s11277-021-08250-4

EDITORIAL

Big Cloud Innovation for Sustainable Wireless Management

Chan-Yun Yang[1] · Muhammad Sharif[2] · Sri Devi Ravana[3] · Anandakumar Haldorai[4]

Published online: 19 February 2021

Big data and Cloud Computing paradigm poses new challenges to the communication technology as numerous heterogeneous objects will need to be connected and supports a wide variety of applications. With the recent growth of Big Cloud computing based applications the usage of big data services is increasing exponentially. Big Cloud is a promising technology that enables intelligent data collection and processing on various sustainable cloud applications. The next generations of big cloud emerging application domains are approaching existing principles and technologies to their limits. Opportunely, Cloud development community is responding to these challenges with new theories and technologies capable of handling increasing dynamism, context-awareness and large-scale adaptation and evolution of software, development and environments.

The wireless network communication for the big data and cloud system would enable maximum utilization of resources, causing an enhancement in the wireless communication system efficiency, by sharing the infrastructure among multiple applications or service provisioning. Cloud and bigdata access can leverage on the sustainable wireless network offerings and gain complete solution over the network to strengthen wireless communication services. Big cloud techniques help in establishing flexible framework over the infrastructure, thereby assisting in optimizing the operations in a more fruitful manner.

The digital revolution led by the big cloud wireless management is already reshaping several traditional business sectors. In this issue, we discuss how data science for sustainable cloud applications, cloud platform for privacy preserving data science, social data relationship ranking on data grid, data grid applications for cognitive communication, machine

✉ Chan-Yun Yang
cyyang@mail.ntpu.edu.tw

Muhammad Sharif
muhammadsharifmalik@yahoo.com

Sri Devi Ravana
sdevi@um.edu.my

Anandakumar Haldorai
anandakumar.h@sece.ac.in

1 College of Electrical Engineering and Computer Science, National Taipei University, Taipei, Taiwan

2 COMSATS University Islamabad, Wah Campus, Wah Cantt, Pakistan

3 University of Malaya, Kuala Lumpur, Malaysia

4 Sri Eshwar College of Engineering, Coimbatore, Tamil Nadu, India

learning and big data in cloud development, next generation wireless communication and smart city initiative and cloud services/infrastructures can alleviate some real environmental problems. This issue focuses high quality research papers that address significant and new big cloud and related system development issues in the emerging sustainable application domains.

We would like to thank the Editor-in-Chief Professor Ramjee Prasad, Ms. Angelina Wagner Journal Development Manager, Mr. Meertinus Faber Project Coordinator of Production at Springer Nature, and Mr. Joseph Ian Reyes Springer's Journal's Editorial Office Assistant for their support in this special issue. We thank all the authors for their excellent contributions and reviewers for their treasurable comments. We anticipate that this issue will open new entrance for further research and technology improvements in this important area.

Dr. Chan-Yun Yang is the Director of the Intelligent Modeling and Control Lab and Professor with the Department of Electrical Engineering, College of Electrical Engineering and Computer Science, National Taipei University, Taiwan. His career in robotics and artificial intelligence research has spanned many countries. He was awarded a Ph.D. degree from the Department of Bio-Industrial Mechatronics Engineering, National Taiwan University. After obtaining his Ph.D. degree he became a Research Fellow at the Keio-NUS CUTE Centre, which is a collaborative research center with locations in both the National University of Singapore (NUS) and Keio University in Japan. He is also actively serving several robotics and AI related journals and conferences as Editorial Board member, Organizing Committee member, workshop organizer and reviewer.

Dr. Muhammad Sharif (IEEE Senior Member) is an Associate Professor at COMSATS University Islamabad, Wah Cantt Pakistan. He has completed his Ph.D. in Image Processing from COMSATS Institute of IT, Islamabad in 2013. He got his M.S. (CS) degree from the same institute in 2007 and MCS degree from Quaid-e-Azam University, Islamabad Pakistan in 1995. He has more than 150 research publications in IF, SCI and ISI journals as well as in national and international conferences and obtained 100 + Impact Factor. His research interests include Medical Imaging, Biometrics, Computer Vision, Machine Learning and Agriculture/Plants imaging.

Dr. Sri Devi Ravana received the bachelor's degree in information technology from the National University of Malaysia, in 2000, the master's degree in software engineering from the University of Malaya, Malaysia, in 2001, and the Ph.D. degree from the Department of Computer Science and Software Engineering, The University of Melbourne, Australia, in 2012. She is currently an Associate Professor at the Department of Information Systems, University of Malaya. Her research interests include information retrieval heuristics, text indexing, data analytics, and data mining. She received a couple of best paper awards in international conferences within the area of information retrieval.

Dr. Anandakumar Haldorai Professor (Associate) and Research Head in Department of Computer Science and Engineering, Sri Eshwar College of Engineering, Coimbatore, Tamil Nadu, India. He has received his Master's in Software Engineering from PSG College of Technology, Coimbatore, Ph.D. in Information and Communication Engineering from PSG College of Technology under, Anna University, Chennai. His research areas include Cognitive Radio Networks, Mobile Communications and Networking Protocols. He has authored more than 118 research papers in reputed International Journals and IEEE, Springer Conferences. He has authored 11 books and many book chapters with reputed publishers such as Springer and IGI. He has served as Editor in Chief in Keai—Elsevier IJIN and reviewer for IEEE, IET, Springer, Inderscience and Elsevier journals. He is also the guest editor of many journals with Wiley, Springer, Elsevier, Inderscience, etc. He has been the General chair, Session Chair, and Panelist in several conferences. He is a senior member of IEEE, MIET, MACM and Fellow member of EAI research group.

ARTICLE IN PRESS

Materials Today: Proceedings xxx (xxxx) xxx

Contents lists available at ScienceDirect

Materials Today: Proceedings

journal homepage: www.elsevier.com/locate/matpr

Rigorous investigation of stator current envelope of an induction motor using hilbert spectrum analysis

W. Rajan Babu [a,*], R. Senthil Kumar [b], R. Satheesh Kumar [b]

[a] Department of EEE, Sri Eshwar College of Engineering, Coimbatore 641 202, India
[b] Department of EEE, SNS College of Technology, Coimbatore 641 035, India

ARTICLE INFO

Article history:
Received 24 August 2020
Received in revised form 31 October 2020
Accepted 4 November 2020
Available online xxxx

Keywords:
Induction motor
Hilbert spectrum analysis
Stator faults, hex bridge inverter
Rigorous investigation
Stator current envelope

ABSTRACT

This proposed Rigorous Investigation of Stator Current (RISC) Envelope, provides a better way in predetermining the healthy condition of an induction motor under the effect of stator faults. The stator faults analysed here are open circuit and short circuit faults. Stator current is captured and investigated to understand the condition of the motor. Rigorous analysis of the stator current is done using Hilbert Spectrum Analysis (HSA) method to understand the responses of induction motor under the influence of the stator faults. The performance of induction motor under faults are analysed, to predict the satisfactory operation of motor. Simulation is carried out in MATLAB platform. The investigated performance analysis of the induction motor exhibits the effective process of monitoring the healthiness of the induction motor.

Selection and peer-review under responsibility of the scientific committee of the International Conference on Advances in Materials Research.

1. Introduction

Induction motors have recognized its prime locations in almost all of the industry sectors. Induction motors are singly excited AC machine and can even operate using inverter fed DC supply. These motor are interconnected with many mechanical and rotating members in an industry which is to be operated continuously during the entire day or process. Though induction motors have many benefits over other families of the motor, they are also vulnerable to possible electrical and mechanical faults [1,2]. Faults in an Induction motor will setback the production in any industry. Hence it is obligatory and vital to monitor and to identify the healthiness of the motor. Consistent monitoring of induction motors will help to detect possible failures at the initial stage itself [3]. Induction motors may fail in its stationary part-stator, rotating part-rotor and in its mechanical orientation-bearings. Stator faults constitute of 38%, rotor fault 10% and mechanical alignment fault approaching almost 40% [4].

Many researchers have conceded out various techniques to classify the nature of fault based on stator current. Multiple reference frames theory are used for the diagnosis of stator faults in three-phase induction motors [5]. Online detection of stator winding short-circuit and inter turn faults are analyzed and discussed on stator fault analysis of three-phase induction motors using information measures and artificial neural networks[6,7]. Hilbert–Huang Transformation (HHT) derived from the neural networks and its application in vibration signal study of a deployable structure [8].

The symptoms for the induction motor faults are as follows: increased torque pulsations, unbalanced air–gap voltages and line currents, increased losses and reduction in efficiency, reduced average torque, increased losses and decrease in efficiency and excessive heating [9]. Most of the failures occurring in an induction motors are indicated in the stator current envelope. Hence possible stator failures are considered and analyzed here, by monitoring the stator current envelope. Rigorous Investigation of Stator Current Envelope technique fulfils the monitoring process of the motor.

2. Stator current fault analysis

(a) For Stator Fault Detection:

Overall, uneven distribution of the air–gap flux waveform around the stator cross section is caused by stator faults, which formulates the stator currents to be modulated by rotor slot fre-

* Corresponding author.
E-mail address: rajanbabu.w@sece.ac.in (W. Rajan Babu).

https://doi.org/10.1016/j.matpr.2020.11.054
2214-7853/
Selection and peer-review under responsibility of the scientific committee of the International Conference on Advances in Materials Research.

quency and the feature frequencies in current signals can be found at characteristic frequencies [10].

fsf = fs [1 ± mN_b [(1-s)/p]] (1)

The equation can be expressed in terms of rotor frequency for convenience of field engineers by Barendse & Pillay (2007).

fsf = fs 1 ± mN_b fr (2)Where fr rotor speed, fs supply frequency, Nb number of rotor bars, s the motor slip, m = 1, 2, 3… is the harmonics orders and p is number of pole-pairs.

(b) Analysis of Turn-To-Turn failure in stator:

The turn-to-turn stator failure is identified by symmetrical three phase windings with the failure phase subjective to the corresponding impedance variation $\Delta z(\Delta z = \Delta R + j\Delta x)$. Deviation in impedance depends on the faults such as a number of turns and open or short circuit. The diagnosis of the turn-to-turn stator failure is similar to the broken bar fault. The computation of Δzas follows [11]:

The pre-fault condition the stator resistance is:

$$R_1 = r_w \frac{2N_1 l_c}{N_{t1} A_{c1} a_1} \tag{3}$$

The linkage inductance of stator is:

$$\mathrm{X}^*{}_{\mathrm{d1}} = \mathrm{X}^*{}_{\mathrm{s1}} + \mathrm{X}^*{}_{\mathrm{d1}} + \mathrm{X}^*{}_{\mathrm{E1}} \tag{4}$$

Assuming N turns are shorted, substituting $N_1 \hat{A} \doteq N_1 - N$ for N_1 in the above two formula, it obtains the stator parameter after fault, and thenΔz. In the case of open turn fault assuming N turns are opened, then$N_1 \hat{A} \doteq N_1 + N$. European standard is specified for the level of voltage balance present in the system, an unbalanced system can be mathematically broken down into three balanced systems from the theory of Symmetrical components as positive sequence, negative and zero sequence systems [12].

(c) Analysis of stator current using Hilbert Spectral Analysis (HSA)

The stator current of the symmetrical Induction Motor results in an ideal sine wave if the power supply to the motor is an ideal three phase ac supply. The phase and line current of one phase of such a motor is given by;

$v_A(t) = V_m \, Cos\,(\omega_1 t)$ (5)

$i_A\,(t) = I_m \, Cos\,(\omega_1 t\text{-}\varphi)$ (6)

in which V_m and I_m are the maximum value or amplitude of the voltage and current respectively, and φ is the power factor angle of the induction motor. The associated flux linkages due to the interaction between the two windings present in the stator and rotor are expressed as:

In Stator;

The final representation of the signal as the sum and a residue is given as;

$$x(\mathrm{t}) = \sum\nolimits_{j=1}^{n} (C_j(t) + r_n(\mathrm{t})) \tag{7}$$

After application of the Hilbert transform $C_j(t)$ to equation, then,

$$\mathrm{H[Cj(t)]} = \frac{1}{\pi} \int_{-\alpha}^{+\alpha} \frac{Cj(t)}{t-\tau} d(\tau) \tag{8}$$

The complex signal which is formed after the transform by applying Hilbert transform is:

$$\mathrm{Zj(t)} = Cj(t) + iH[Cj(t)] \tag{9}$$

Zj(t) Expressed in complex exponential form as:

$$\mathrm{Zj(t)} = aj(t)e^{i\theta j(t)} \tag{10}$$

Where the envelope of the amplitude is:

$$\mathrm{Zj(t)} = \sqrt{Cj(t) + H[Cj(t)]^2} \tag{11}$$

The phase angle is given as:

$$\theta \mathrm{j(t)} = arctan\left\{\frac{H[Cj(t)]}{Cj(t)}\right\} \tag{12}$$

the instantaneous frequency is represented as:

$$\omega \mathrm{j(t)} = \left\{\frac{\mathrm{d}\theta \mathrm{j(t)}}{d(t)}\right\} \tag{13}$$

and, thus the original signal is expressed as:

$$x(\mathrm{t}) = \sum\nolimits_{j=1}^{n} \mathrm{aj(t)e}^{i\int \omega j(t)dt} \tag{14}$$

In which the residue is not considered, and this expression is considered as the representation of generalized Fourier expression.

3. Fault analysis and discussion in Simulation platform

Voltage Source Inverter (VSI) fed induction motor model is considered here for analysis, since variable frequency based induction motor drive (VFD) are utilized in many of the industries. IGBT based Hex bridge VSI drive feeds the induction motor and three phase PWM pulses are generated for triggering the inverter switches. Mathematical modelling is developed to create faults and to analyse it. The whole system is simulated using MATLAB Simulink.

(a) Fault analysis by RISC without HHT

Stator faults of an induction motor are analyzed with different percentage of short circuit and open circuit. From Fig. 1 it is obvious that short circuit in stator increases the current and lags the actual current.

From Fig. 2 it is clear that open circuit in stator decreases the current and lags the actual current. It is clear that depends on

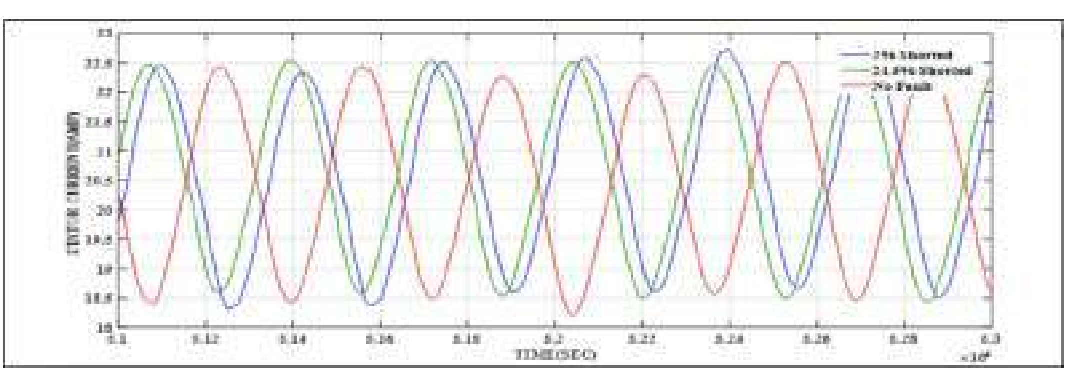

Fig. 1. . Simulation result of motor under SC stator.

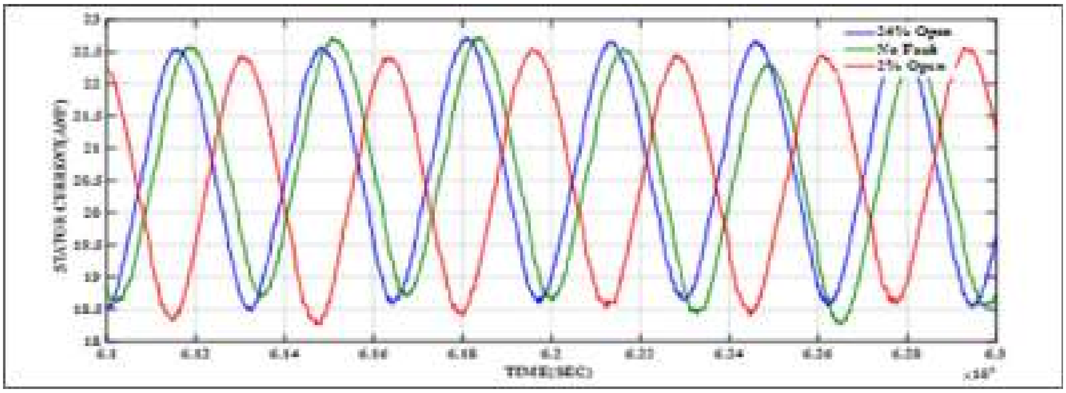

Fig. 2. . Simulation result of motor under OC stator.

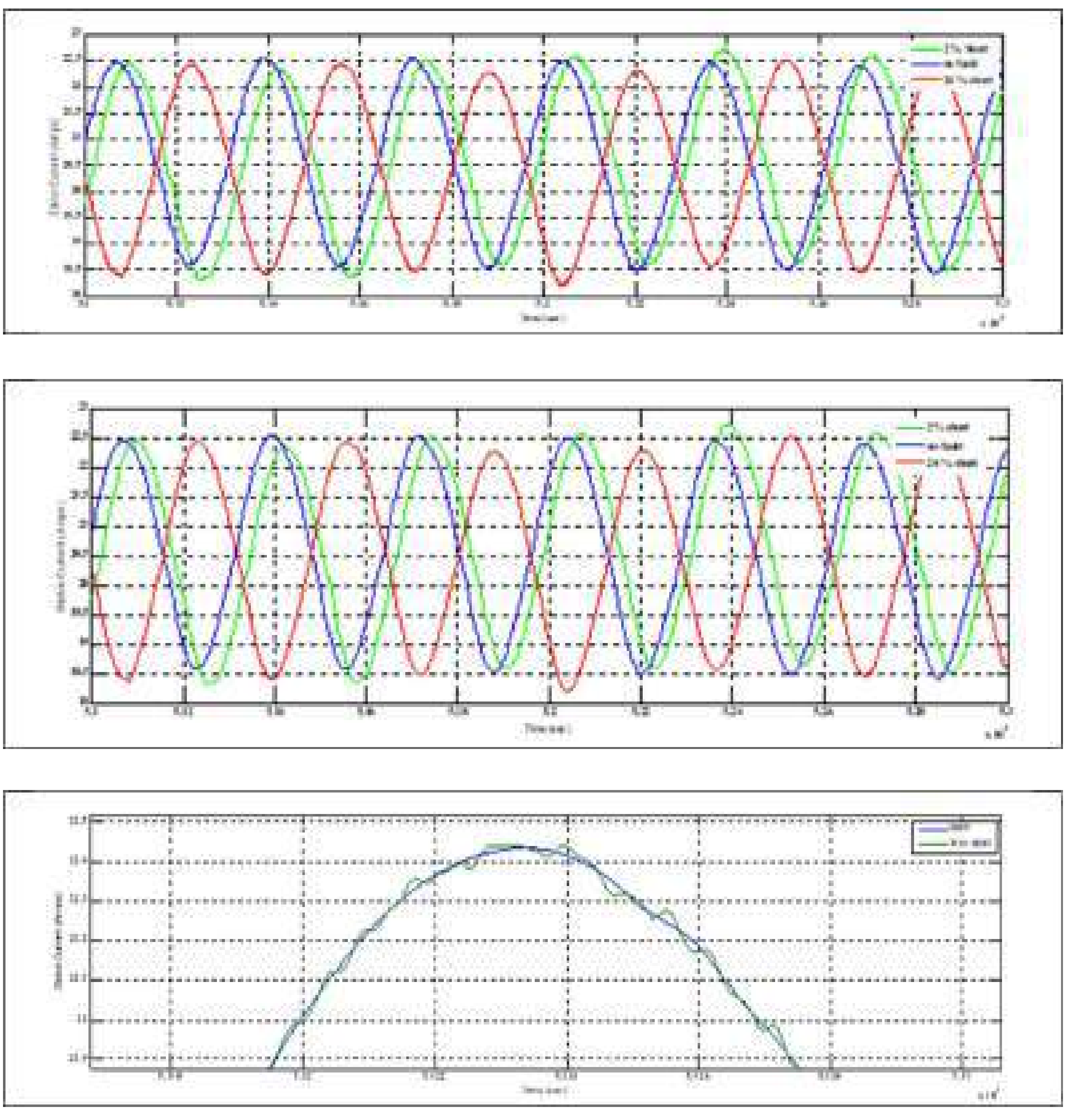

Fig. 3. (a) Stator Current wave form without HHT. (b) Stator Current wave form with HHT. (c) Stator Current wave form for one phase without HHT and with HHT.

the fault in an induction motor magnetic flux density varies continuously.

(b) Fault Analysis by RISC with HHT

The three phase distributed winding in the stator produces the required Rotating Magnetic Field (RMF) when energized with three phase balanced voltage. Even though the windings are insulated with enamel to avoid inter-turn faults, due to reasons like heat in the winding wires, accidental mechanical damages caused during the winding process, etc., causes severe damage during its operation which ends in the failure of the motor. The inter-turn

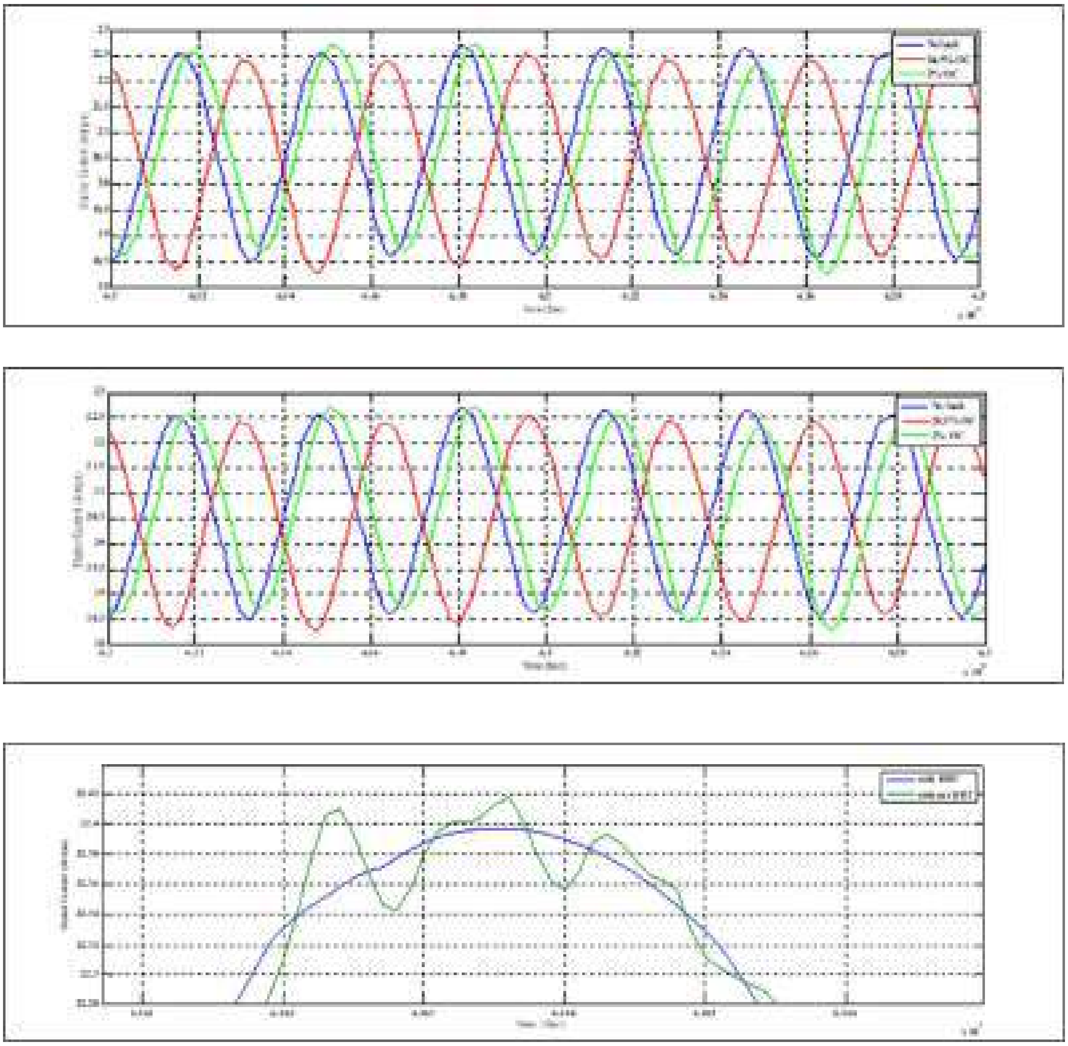

Fig. 4. (a) Stator Current wave forms for OC fault without HHT. (b) Stator Current wave forms for OC fault with HHT. (c) Stator Current wave forms for open circuit fault without HHT and with HHT.

fault may occur in the slot of same phase winding, short between coils, short between two coil phases or between the coil turn and the body. Fig. 3(a) to Fig. 3(c) shows the stator current profile during the no fault condition and fault condition.

When the stator winding is under short circuited condition, it is found that the current demanded by the stator varies according to the percentage of the short. 24% short lags more than the 2% short from the fundamental wave track. When Hilbert-Huang Transform is done to the captured current signal, the filtering occurs as shown in Fig. 4(c) and thus the nature of the fault can easily be predicted without any misunderstanding. Similarly, the current profiles for an induction motor when exposed to open circuit in the windings of the stator are as shown in the Fig. 4(a) to Fig. 4(c)

The motor fault diagnosis such as short circuit and open circuits conditions have been analyzed in induction motor by adapting non-stationary signal processing Hilbert-Huang Transform technique. Thus responses from the table 1 predicts the condition of the induction machine as an error free result and less harmonic histograms.

Table 1
The results and inferences for different fault conditions.

Sl. No	Type of Fault		Fault Description and its Stator Current in Amperes		
			No Fault	2%	24%
1	Open Circuit Fault	Without HHT	20.36	20.63	20.583
		with HHT	20.3483	20.635	20.51
	Inference: The difference in Stator current between 2% and 24% fault is only 0.047 A in case of without HHT which leads to misinterpretation of faults				
2	Short Circuit Fault	Without HHT	20.407	20.525	20.41
		with HHT	20.4275	20.5427	20.402
	Inference: The difference in Stator current between no fault and 24% fault is almost same in case of without HHT which may lead to misinterpretation of faults				

4. Conclusion

The proposed Rigorous Investigation of Stator Current (RISC) envelope was carried out in medium voltage induction motor (MVIM) to understand the performance of the motor under the influence of various possible faults. Different fault conditions were simulated using MATLAB and the stator current was captured and analysed after applying Hilbert-Huang Transformation. The result obtained after filtering the unnecessary noise signals yielded a clear understanding in the current pattern which reflected the real condition of the motor under the influence of various faults. The main advantage of applying HHT for a non-stationary signal like stator current is that the feature extraction is possible when compared to Fourier Transform (FT) and Wavelet Transform (WT) methods. The stator current lags or leads based on the nature of fault. Thus, various anticipated faults subjected to induction motor and its performance evaluation yields healthiness of the motor.

CRediT authorship contribution statement

W. Rajan Babu: Conceptualization, Methodology, Software, Data curation, Writing - original draft, Supervision, Validation. **R. Senthil Kumar:** Visualization, Investigation. **R. Satheesh Kumar:** Writing - review & editing.

Declaration of Competing Interest

The authors declare that they have no known competing financial interests or personal relationships that could have appeared to influence the work reported in this paper.

References

[1] P. Zhang, Y. Du, T.G. Habetler, B. Lu, A survey of condition monitoring and protection methods for medium-voltage induction motors, IEEE Trans. Ind. Appl. 47 (1) (2011) 34–46.
[2] E.H. El Bouchikhi, V. Choqueuse, M. Benbouzid, J.F. Charpentier, Induction machine fault detection enhancement using a stator current high resolution spectrum, IECON Proceedings (Industrial Electronics Conference) (2012).
[3] E.H. El Bouchikhi, V. Choqueuse, M. Benbouzid, Induction machine faults detection using stator current parametric spectral estimation, Mech. Syst. Sig. Process. 52–53 (1) (2015) 447–464.
[4] Delgado-Arredondo, PA, Garcia-Perez, A, Morinigo-Sotelo, D, Osornio-Rios, RA, Avina-Cervantes, JG, Rostro-Gonzalez, H & Romero-Troncoso, RDJ 2015, Comparative Study of Time-Frequency Decomposition Techniques for Fault Detection in Induction Motors Using Vibration Analysis during Startup Transient, Shock and Vibration, vol. 2015, no. 2015, pp. 1-9.
[5] S.M.A. Cruz, A.J. Marques Cardoso, Multiple reference frames theory: A new method for the diagnosis of stator faults in three-phase induction motors, IEEE Trans. Energy Convers. 20 (2005) no. 3.
[6] M. Eftekhari, M. Moallem, S. Sadri, M.-F. Hsieh, Online detection of induction motor's stator winding short-circuit faults, IEEE Syst. J. 8 (4) (2014) 1272–1282.
[7] G. Henrique, P. Rogério, W. Endo, A. Goedtel, W. Fontes, R. Henrique, C. Palácios, Stator fault analysis of three-phase induction motors using information measures and artificial neural networks, Electr. Power Syst. Res. 143 (2017) 347–356.
[8] Shi, Xz, Qiu, Xy, Zhou, J, Chen, X, Fan, Yq & Lu, Ew 2016, Application of Hilbert-Huang transform based delay time identification in optimization of short millisecond blasting' Transactions of Nonferrous Metals Society of China.
[9] Iorgulescu, M & Beloiu, R 2014, Faults diagnosis for electrical machines based on analysis of motor current, 2014 International Conference on Optimization of Electrical and Electronic Equipment, OPTIM 2014, pp. 291-297.
[10] J. Cusidó, L. Romeral, J.A. Ortega, A. Garcia, J. Riba, Signal injection as a fault detection technique, Sensors (Basel, Switzerland) 11 (3) (2011) 3356–3380.
[11] P.S. Barendse, P. Pillay, The detection of unbalanced faults in inverter-fed induction machines 2007, in: IEEE International Symposium on Diagnostics for Electric Machines, Power Electronics and Drives, SDEMPED, 2007, pp. 46–51.
[12] W. Rajanbabu, C.S. Ravichandran, Fault phase identification for MVIM under unbalanced stator voltage and stator winding faults using RACE, Transylvanian Rev. 24 (9) (2016) 1356–1364.

Biosc.Biotech.Res.Comm. Special Issue Vol 13 No (4) 2020 Pp-299-306

Employment of Matrix Converters in Multi-Mode Electric Vehicle Charging Station Using Venturini and PWM Algorithm

Dr. Senthil Kumar Rasappan[1], Bharath Suriyakumar[2] and Dr. Rajan Babu Williams[3]

[1]*Associate Professor, Department of EEE, SNS College of Technology, Coimbatore, Affiliated to Anna University Chennai*

[2]*Assistant Professor, Department of EEE, SNS College of Technology, Coimbatore, Affiliated to Anna University Chennai*

[3]*Associate Professor, Department of EEE, Sri Eshwar College of Engineering, Coimbatore, Affiliated to Anna University Chennai*

ABSTRACT

The major concern of today's situation is the increase in global warming due to high pollution level. The basic human necessities such as transport sector, commercial sector and the industrial sector are the reasons for these environmental pollutions. In particular, the transport sector, emits nearly about 87% of green house gases (GHG) in India. Electric Vehicles (EVs) could be the remedial solutions for the transport sector issue. EVs, which are energized by a battery storage system, are becoming very attractive because they keep the environment clean. Furthermore, in due course the cost of EVs is also becoming cheap, when the production increases. The proposed EV charging station supplies four modes of regulated power. A synchronized three phase power is extracted using three phase matrix converter (TPMC), a single phase matrix converter (SPMC) is also utilized to act as a power electronic converter for extracting regulated DC power and single phase AC power. Venturini algorithm integrated with vector control is proposed here for TPMC, PWM technique is proposed for SPMC. A simulated EV charging station is assessed in MATLAB/ Simulink platform. The results obtained here show a better power transfer to charge for a variety of EVs. Concluding that, the proposed charging station is able to provide a constant and convenient charging voltage, with prescribed total harmonic distortion (THD).

KEY WORDS: BATTERY CHARGING STATION, ELECTRIC VEHICLE, PWM TECHNIQUE, SINGLE AND THREE PHASE MATRIX CONVERTER, THD, VENTURINI ALGORITHM.

INTRODUCTION

Most of the vehicles running in the transport sector are still depends on liquid fossil fuels, which are slowly being depleted. Fifty percent of crude oil produced in the world are utilized by the vehicles in the transport sector. The continuous consumption of liquid fossil fuels will lead to increase the atmospheric absorptions of green house gases, such as carbon dioxide, carbon monoxide and nitrogen oxide. To sustain the green earth, electric vehicles (EVs) are started evolving, where emission of green house gases and the consumption of liquid fuels will be in decreasing order. In this perspective, full electric vehicle (EV) or hybrid electric vehicles (HEV) have attracted attention as good solutions for the problems cited above. [Ali Saadon et.al,. 2019].

ARTICLE INFORMATION

**Corresponding Author: senkumarme@gmail.com*

Received 4th May 2020 Accepted after revision 15th June 2020
Print ISSN: 0974-6455 Online ISSN: 2321-4007 CODEN: BBRCBA

Thomson Reuters ISI Web of Science Clarivate Analytics USA and Crossref Indexed Journal

NAAS Journal Score 2020 (4.31) SJIF: 2020 (7.728)
A Society of Science and Nature Publication,

Online Contents Available at: http//www.bbrc.in/

An electric motor produces traction power in vehicle, where batteries supplies electrical power to the motor. The battery charger receives power from the external electrical sources that charges the battery of the electric vehicle. The motor acts as a generator and provides power back to the batteries during regenerative braking. When compared to the battery discharging the vehicle slows down accordingly. As per the size and the recharge time of the battery, the speed and the driving range are limited. This depends on the charging method and the type of the battery [Clemente and Ottorino et al., 2015]. There are two charging techniques available for EVs, namely AC and DC charging. For AC charging, single-phase or three-phase regulated AC power is required to an on-board AC–DC power converter in the EV. For DC charging, the DC power is directly fed to the battery of the EV through an off-board AC–DC power converter [Kawamura et.al,. 2012], [Arancibia et.al,. 2012].

The utilization of on-board chargers will certainly increase the effortless charging methods of the vehicle; meanwhile, off board chargers permit all usage of battery charging techniques with even higher rating circuits. As the name indicates, on-board charger is the comparatively faster than off board since it is a part of EVs, whereas an off board is an external unit belongs to a charging station. A typical off board charger may consist of multiple charging units, and is capable of supplying a preferred level AC / DC charging voltages.

The design of a consistent, proficient, high power capacity and variable level off board charging unit has become a great challenge, due to the cutting edge technologies in the production of EVs. The charging units of EVs consist of power electronic converter, which normally induces harmonics. The harmonics creates power quality (PQ) issues of the low-voltage (LV) distribution networks surrounded by the charging station. Hence for a reputed charging station, the quality of power delivered should be good, and more over it should not affect the quality of the distribution network.

Figure 1: Schematic representation of Electric Vehicle Charger

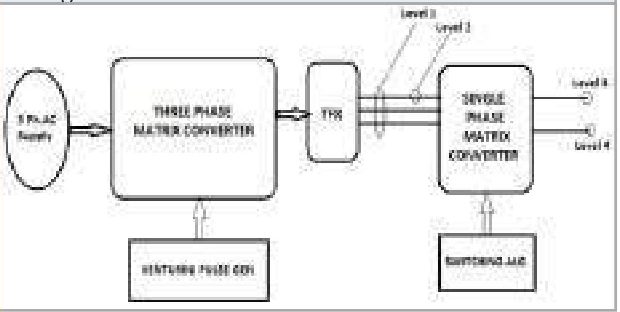

The existing EV chargers are capable to charge only in one level, and hence there is need of providing multi-modes of EV charging station. Level 3 charging can draw 1.4–1.9 kW of power and the time required for charging is 6–8 hours. This may be a DC power. The DC power here may be controlled voltage or uncontrolled voltage. Level 2 charging power is 7.7–25.6 kW, and it requires 4–8 hours to fully charge the batteries of middle level EVs. The EV may be an electric car, where a single phase AC supply may be required. The Level 1 charging can draw a three phase power of 50–100 kW, and it requires 1–3 h to fully charge the battery of a heavy duty EVs. [NREL Book 2013], [Mehta Book 2010].

Matrix Converter: Matrix converter is employed for EV charging station [Harish et.al,. 2012]. Matrix converter is a single stage power transferring device capable of converting AC to AC. One of the prime advantage of matrix converter is it fulfills the necessities to provide a sinusoidal voltage at the load side and, it is also possible to vary to maintain unity power factor on the supply side. There is no DC link in matrix converter, as in the case of converter – inverter combination circuit and the matrix converter can be built in a full- one silicon structure [Venturini et.al,. 1989].

Three phase matrix converter (TPMC) consists of nine bi-directional switches which are arranged in terms of three sets of three. This arrangement makes that any of the three input lines can be connected to any of the three output lines. The inputs phase are V_{i1}, V_{i2}, V_{i3} and the outputs phase are V_{o1}, V_{o2}, V_{o3}. The matrix switching components s_{11}, s_{12}, ..., s_{33} represent nine bi-directional switches which are accomplish blocking of voltage in both directions and connects the switching without any delays. The matrix converter converts the three given inputs of constant amplitude, V_i and constant frequency, fi into controllable amplitudes, V_o and controllable frequency, f_o as output. This is possible in accordance with pre-calculated switching angles.

Several switching algorithm are available for TPMC, where Venturini's modulation algorithm is most prominent algorithm with more flexibility. This algorithm also provides unity fundamental displacement factor at the input regardless of any load displacement factor. In Venturini algorithm, a set of three-phase input voltages with fixed amplitude and fixed frequency is considered, for manipulating the duty cycle of each of the nine bidirectional switches. The result thus obtained and when implemented allows the generation of a set of three-phase output voltages by sequential piecewise sampling of the input waveforms [Sunter et.al,. 2003].

Single phase matrix converter (SPMC) was derived by Zuckerberger earlier [Zuckerberger et.al,. 1997]. It has been shown that the SPMC could be realized as a direct AC-AC single-phase converter [Idris 2006], DC chopper, rectifier and inverter [Senthil Kumar et.al,. 2017]. For AC-DC and DC-AC conversion different converters are used, but in certain applications like uninterruptable power supply, two converters are required, one acting as rectifier, used to convert AC into DC for charging the batteries and another acting as inverter, used to supply regulated AC power from battery. [Ajay kumar Gola et.al,. 2009]

MATERIAL AND METHOD

The proposed EV charging station consist of Three Phase Matrix Converter (TPMC), Single Phase Matrix Converter (SPMC), Isolation Transformer, Venturini Pulse Generator for TPMC, PWM Pulse Generator with modified switching algorithm and other supplementary components. The schematic representation is shown in figure 1. Here four modes of output voltages are considered as charging points. The four charging points are mentioned as level 1, 2, 3 and 4. The output of level 1 is regulated three phase AC supply, level 2 is single phase AC variable frequency supply, level 3 is unregulated DC supply and level 4 is regulated DC voltage. Therefore this charging unit is called as Universal EV charging station, which is suited for a multi mode off board charger. Two stage converters are proposed here, where TPMC transfer three phase AC input into variable three phase AC output as one stage. SPMC transfer single phase AC into variable AC/DC voltages as second stage. A unique PWM algorithm is generated and it is given to SPMC in order to perform as a rectifier unit and controlled converter unit.

Venturini Control Algorithm: A modified version of the Venturini algorithm is used here. This algorithm is distinct in terms of the three-phase input and output voltages at each sampling instant and is also convenient for closed loop operations [Sunter 1995]. For the real-time implementation, any two of the three input voltages are to be measured. Then, V_{im} and ω_{it} are calculated as shown in equation (1) and (2).

$$V_{im} = \frac{4}{9}\left(v_{AB} + v_{BC} + v_{AB}v_{BC}\right) \quad (1)$$

$$\omega_{it} = \arctan\left[\frac{v_{BC}}{\sqrt{3}\left(\frac{2}{3}v_{AB} - \frac{1}{3}v_{BC}\right)}\right] \quad (2)$$

$$V_{om} = \frac{4}{9}\left(v_a + v_b + v_c\right) \quad (3)$$

$$\omega_{ot} = \arctan\left[\frac{v_b - v_c}{\sqrt{3}(v_a)}\right] \quad (4)$$

Similarly the target output peak voltage and the output position can be calculated as in equation (3) and (4), where V_{AB}, V_{BC} are the instantaneous input line voltages and va, v_b, v_c are the output voltages per phase. Alternatively, in a closed loop system, voltage magnitude and angle may be direct outputs of the control loop. Then, the voltage ratio is calculated as in equation (5).

$$q = \sqrt{\frac{V_{om}}{V_{im}}} \quad (5)$$

where q is the desired voltage ratio, and V_{im} is the peak input voltage. Triple harmonic terms are found

$$k_{31} = \frac{2}{9} \times \frac{q}{q_m} \sin(\omega_{it}) \sin(3\omega_{it}) \quad (6)$$

$$k_{32} = \frac{2}{9} \times \frac{q}{q_m} \sin\left(\omega_{it} - \frac{2\pi}{3}\right) \sin(3\omega_{it}) \quad (7)$$

$$k_{33} = \sqrt{V_{im}}\left[\frac{1}{6}\cos(3\omega_{ot}) - \frac{1}{4} \times \frac{q}{q_m}\cos(3\omega_{it})\right] \quad (8)$$

where q_m is the maximum voltage ratio (0.866). Then, the three modulation functions for output of phase 'a' are given as

$$M_{Aa} = \frac{1}{3} + k_{31} + \frac{2}{3V_{im}^2}\left(v_a + k_{33}\right)\left(\frac{2}{3}v_{AB} + \frac{1}{3}v_{BC}\right) \quad (9)$$

$$M_{Ba} = \frac{1}{3} + k_{32} + \frac{2}{3V_{im}^2}\left(v_a + k_{33}\right)\left(\frac{2}{3}v_{BC} - \frac{1}{3}v_{AB}\right) \quad (10)$$

$$M_{Ca} = 1 - \left(M_{Aa} + M_{Ba}\right) \quad (11)$$

The modulation functions for the other two output phases, 'b' and 'c' are obtained by replacing v_b and v_c with v_a, respectively in equation (9) and (10). Note that the modulation functions have third harmonic components at the input and output frequencies added to them to produce output voltage, v_o. This is a prerequisite to get the maximum possible voltage ratio. It should be noted that in equation (3) there is no prerequisite for the target outputs to be sinusoidal. In general, three phase output voltages and input currents can be defined in terms of the modulation functions in matrix form as

Output voltage per phase = M function*Input voltage per phase

$$\begin{bmatrix} v_a \\ v_b \\ v_c \end{bmatrix} = \begin{bmatrix} M_{Aa} & M_{Ba} & M_{Ca} \\ M_{Ab} & M_{Bb} & M_{Cb} \\ M_{Ac} & M_{Bc} & M_{Cc} \end{bmatrix} \begin{bmatrix} v_A \\ v_B \\ v_C \end{bmatrix} \quad (12)$$

Input current per phase = Transpose of M function*Output current per phase

$$\begin{bmatrix} v_a \\ v_b \\ v_c \end{bmatrix} = \begin{bmatrix} M_{Aa} & M_{Ba} & M_{Ca} \\ M_{Ab} & M_{Bb} & M_{Cb} \\ M_{Ac} & M_{Bc} & M_{Cc} \end{bmatrix} \begin{bmatrix} v_A \\ v_B \\ v_C \end{bmatrix} \quad (13)$$

where the superscript T mention a transpose vector, and M is the instantaneous input per phase to output per phase transfer matrix of TPMC. v_{iph} and v_{oph} represent the input and output phase voltage vectors, and i_{iph} and

i_{oph} represent the input and output phase current vectors. From Eqs. (12) and (13), the output-line voltages and input-line currents can be expressed as

Output line voltage = m-function*Input line voltage

$$\begin{bmatrix} V_{ab} \\ V_{bc} \\ V_{ca} \end{bmatrix} = \begin{bmatrix} m_{Ab} & m_{Bb} & m_{Cb} \\ m_{Ac} & m_{Bc} & m_{Cc} \\ m_{Aa} & m_{Ba} & m_{Ca} \end{bmatrix} \begin{bmatrix} V_{AB} \\ V_{BC} \\ V_{CA} \end{bmatrix} \quad (14)$$

Input line current = Transpose of m-function*Output line current

$$\begin{bmatrix} i_{AB} \\ i_{BC} \\ i_{CA} \end{bmatrix} = \begin{bmatrix} m_{Ab} & m_{Ac} & m_{Aa} \\ m_{Bb} & m_{Bc} & m_{Ba} \\ m_{Cb} & m_{Cc} & m_{Ca} \end{bmatrix} \begin{bmatrix} i_{ab} \\ i_{bc} \\ i_{ca} \end{bmatrix}. \quad (15)$$

$$\begin{aligned} m_{\text{[illegible]}} &= \tfrac{1}{3}(M_{\text{[illegible]}} - M_{\text{[illegible]}}) - \tfrac{1}{3}(M_{\text{[illegible]}} - M_{\text{[illegible]}}) \\ m_{\text{[illegible]}} &= \tfrac{1}{3}(M_{\text{[illegible]}} - M_{\text{[illegible]}}) - \tfrac{1}{3}(M_{\text{[illegible]}} - M_{\text{[illegible]}}) \\ m_{\text{[illegible]}} &= \tfrac{1}{3}(M_{\text{[illegible]}} - M_{\text{[illegible]}}) - \tfrac{1}{3}(M_{\text{[illegible]}} - M_{\text{[illegible]}}) \\ m_{\text{[illegible]}} &= \tfrac{1}{3}(M_{\text{[illegible]}} - M_{\text{[illegible]}}) - \tfrac{1}{3}(M_{\text{[illegible]}} - M_{\text{[illegible]}}) \\ m_{\text{[illegible]}} &= \tfrac{1}{3}(M_{\text{[illegible]}} - M_{\text{[illegible]}}) - \tfrac{1}{3}(M_{\text{[illegible]}} - M_{\text{[illegible]}}) \\ m_{\text{[illegible]}} &= \tfrac{1}{3}(M_{\text{[illegible]}} - M_{\text{[illegible]}}) - \tfrac{1}{3}(M_{\text{[illegible]}} - M_{\text{[illegible]}}) \\ m_{\text{[illegible]}} &= \tfrac{1}{3}(M_{\text{[illegible]}} - M_{\text{[illegible]}}) - \tfrac{1}{3}(M_{\text{[illegible]}} - M_{\text{[illegible]}}) \\ m_{\text{[illegible]}} &= \tfrac{1}{3}(M_{\text{[illegible]}} - M_{\text{[illegible]}}) - \tfrac{1}{3}(M_{\text{[illegible]}} - M_{\text{[illegible]}}) \\ m_{\text{[illegible]}} &= \tfrac{1}{3}(M_{\text{[illegible]}} - M_{\text{[illegible]}}) - \tfrac{1}{3}(M_{\text{[illegible]}} - M_{\text{[illegible]}}) \end{aligned} \quad (16)$$

where $M_{A\alpha}$, M_{Ab}, are calculated as the displaced vectors of M_{Aa}, M_{Ab}, M_{Ac} respectively. Similarly modulation index values of other two phases are calculated as given in equation (16).

Figure 2: Block diagram model of TPMC

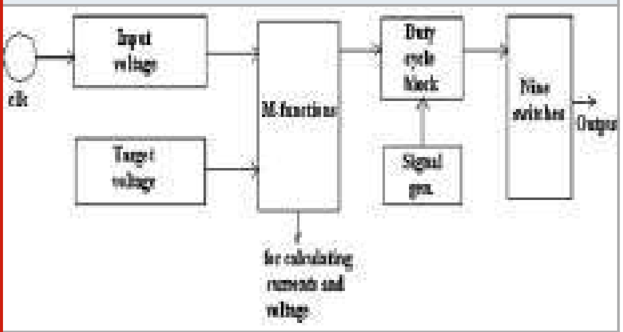

Three Phase Matrix Converter Model: Figure 2 shows the model block diagram of the three phase matrix converter. The input variables of the matrix converter are the clock, input voltages (Vi) and target output voltages obtained from any controller, here the target voltages is given as second input (Vo). The input voltage block represent Eqn.(1) and (2). The target output block represents Eqn (3) and (4). The M function blocks, represent Eqs. (9), (10), and (11) for one phase, and similar three phase calculation are performed. ''M functions'' consists of the modulation functions and is taken out for calculating the output voltages and input currents using Eqs. (14) and (15) respectively. The switching frequency of the matrix converter is determined by the signal generator block (in this case fs = 2 kHz).

The block duty cycle generator, consist of logic gates and simple mathematical algorithms. Here the modulation functions are compared with the signal generator waveform, probably square or saw tooth at the input and arranged to have logic levels. Logic gates are used at the output to get three gate signals proportional to the duty cycle of the power switches for one output phase. It has three inputs [in (1), in(2) and in(3)] and one output. It operates in accordance with the following logic:

--- if in(2)>0 then the output signal is in(1)
--- else output signal is in in(3).
Similarly nine switches are used in the "switch block" such a manner that the three phase output voltages is obtained. The simulated model of TPMC using MATLAB / Simulink is shown in Fig.3. All the switches utilized are ideal switches. Three phase uncontrolled AC power is transferred into controlled AC power.

Figure 3: Simulation of three phase matrix converter (TPMC)

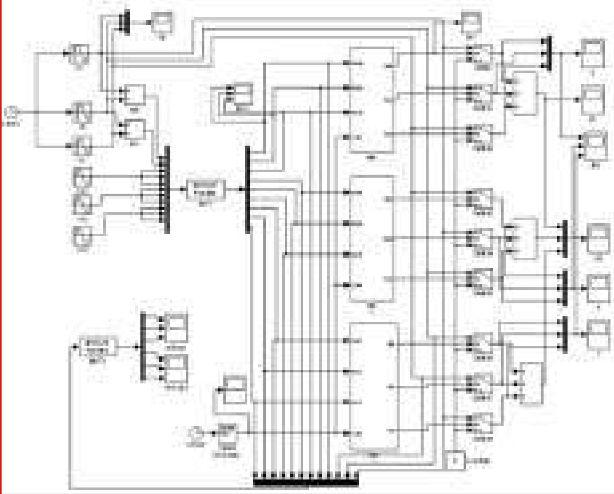

Figure 4: Basic circuit of a SPMC

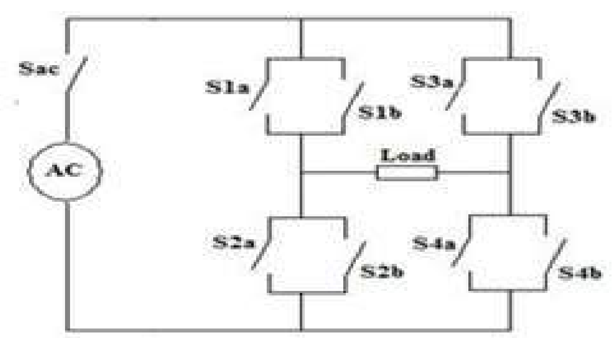

Single Phase Matrix Converter Model: Single phase matrix converter (SPMC) consists of four bi-directional switches and a simple switching logic. A unique PWM algorithm is being developed to realize this converter as a single stage total power electronic converter. The basic circuit of single-phase matrix converter is shown in figure 4. It consist of four bi-directional switch connected in between a single phase AC input and to single phase AC output (load).

The four ideal switches are S_1, S_2, S_3 and S_4 capable of allowing current in both the directions, blocking forward and reverse voltages and also switching between its states. Each bi-directional switch consisting of two diodes and two IGBTs connected back to back [4]. The bi-directional switches have two basic rules: (i) do not connect two different input lines to the same output lines to avoid short circuit and (ii) do not disconnect the output lines to avoid open circuit. Normal sinusoidal PWM with a unique algorithm is used to amalgamate this converter. The converter is then executed in computer simulation model to explicate its basic behavior. The instantaneous input voltage is V_i (t) and its output voltage is V_o (t). The AC input voltage is converted into variable amplitude or variable frequency AC voltage by varying the modulating frequency.

If the input signal is

$$Vi\ (t) = Vim\ \cos\omega i\ t \qquad (17)$$

Then, the fundamental output voltage will be

$$Vo(t) = Vom\ \cos\omega ot \qquad (18)$$

With a fundamental frequency

$$fo = fm - fi \qquad (19)$$

where, fo=Output Frequency, fm=Modulation Frequency, fi=Input Frequency.

Figure 5: (a) and (b)Switching states as Rectifier and Converter

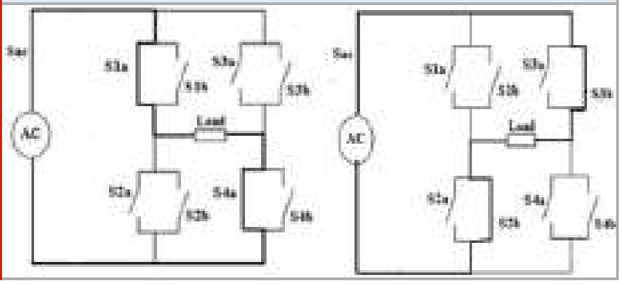

The switching combinations for a matrix converter are explained as, the state of the 4 bi-directional switches Sij(i = 1,2,3,4 and j = a,b) where ‘a’ and ‘b’ represent driver one and two respectively following the rules [4] below; At any time ‘t’, any two switches S_{ij} below will be ON.

Table 1. Switching strategy for SPMC

CONVERTER	INPUT SUPPLY	SWITCHING PULSE	OUTPUT NATURE
Rectifier	AC	S1a, S4a (positive half cycle)	DC (un-controlled)
		S2b, S3b (negative half cycle)	
Converter	AC	S1a, S4a (positive half cycle)	DC (controlled)
		S2b, S3b (negative half cycle)	

Realization as rectifier and controlled rectifier (converter) is shown in figure 5, where input is AC and the output is either un-controlled DC or variable DC. Variable output is obtained by giving switching pulse at a delay. Figure 5(a) represents for positive half cycle and 5 (b) for negative half cycle. The bold line signifies the current conduction.

The Switching strategy for matrix converter acting as uncontrolled and controlled rectifier is represented in the table 1 above. The simulation of SPMC is presented in figure 6. It has four bi-directional switches, a pulse generation block and a clamp circuit.. A clamp circuit does not restrict the peak-to-peak expedition of the signal, but moves it up or down by a fixed value. Diodes are used for clamping and a capacitor is used to maintain an altered dc level at the clamper output. Hence the clamp circuit acts a protective device for converter. For simplicity, a resistive load is connected. Two way realizations are performed to extract uncontrolled rectifier and controlled rectifier.

Figure 6: Simulation of single phase matrix converter (SPMC)

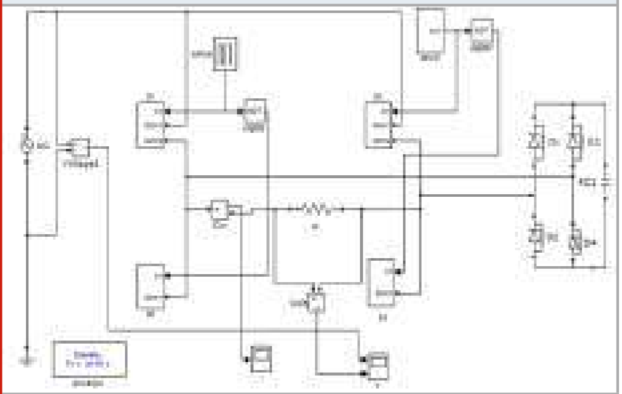

RESULTS AND DISCUSSION

Simulation result of TPMC (Level 1 & 2): The total EV charging station is realized in simulink platform and the results obtained are discussed here. The input three phase AC supply is given to TPMC, whose specifications are listed below.

Input specifications of TPMC: Input waveform is represented in figure 7.
Input Voltage, Vi = 311 V
Input Frequency, fi = 50 Hz
Vo/Vi = 50 %

Output target specifications of TPMC:
Switching Frequency, fs=2000 Hz
Output Voltage, Vo=155 V
Output Frequency, fo=50 Hz

Level 1 output current = 5 A, 50 Hz with THD content of 8.62%

Figure 7: Three phase AC input supply

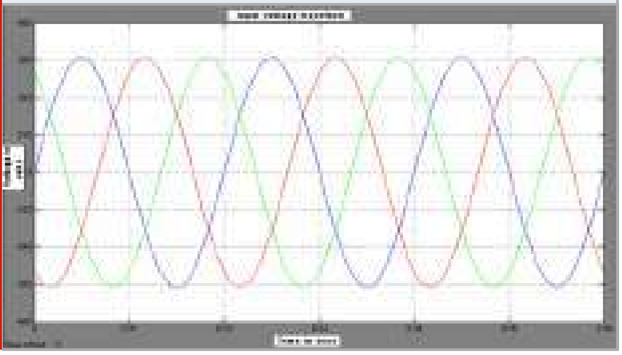

Figure 8: Nine M – function waveforms of TPMC

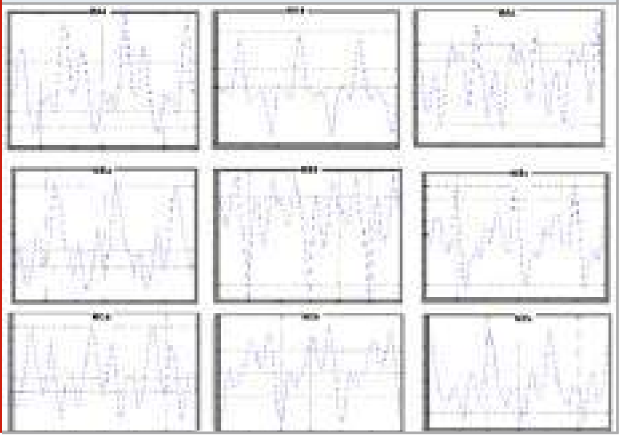

Figure 9: Level 1 output current for phase A,B and C

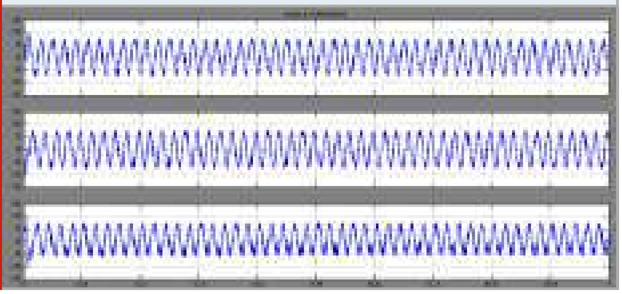

Figure 10: Level 1-THD of one phase (A)

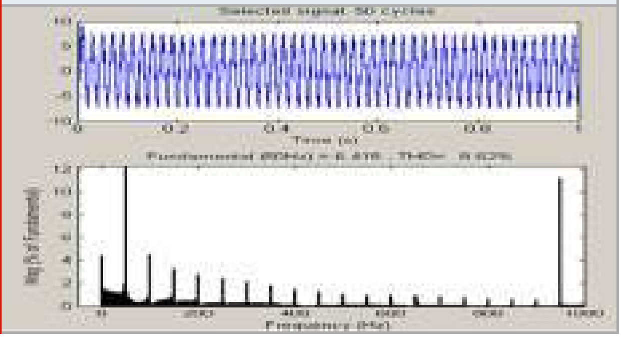

The modulation function created by venturini algorithm is shown in figure 8. These functions are used to create triggering pulses which, then are fed to the nine bidirectional switches of TPMC. The level 1 three phase currents are exposed in figure 9 and its THD component of one phase is depicted in figure 10. A single phase AC output of TPMC is taken outside as level 2. With suitable algorithm, the derived frequency is 10 Hz, which is represented in figure 11. This is level 2 type of charging.

Figure 11: Level 2 – variable frequency single phase AC voltage

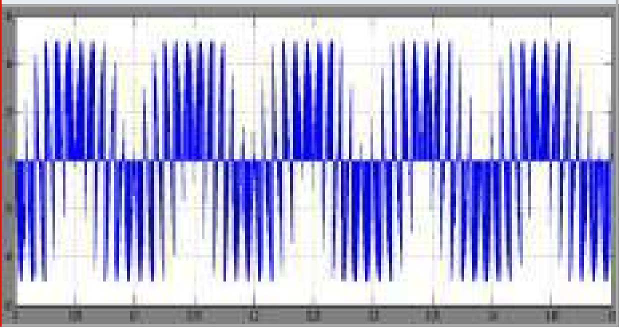

Figure 12: Level 2 THD of variable frequency single phase AC

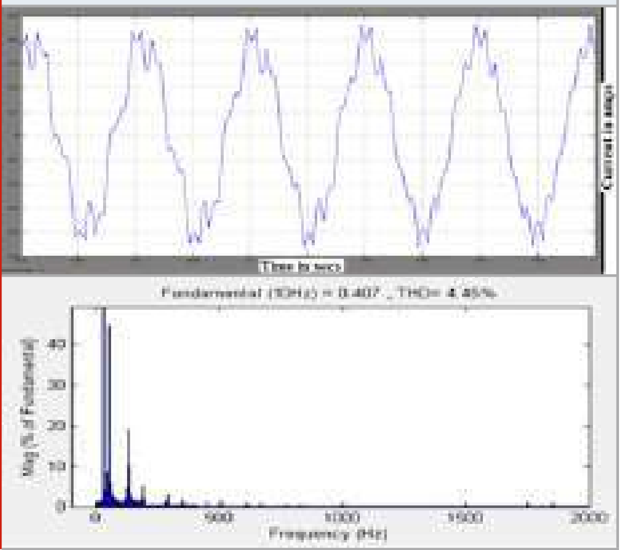

The current waveform with its THD component of level 2 is extracted as 4.45% which is in the prescribed limit of IEEE standards and is also depicted in figure 12.

Simulation result of SPMC (Level 3 & 4)

The specifications of SPMC: Input power is 100 V, 50 Hz for SPMC, which is obtained from TPMC. The PWM signal is generated with an amplitude of triangular wave, Vc =1v and the amplitude of sine wave, Vref = 0.75v is compared. The modulation index is,

Mi=Vc/Vref=1/0.75=0.75. The switching frequency, fs =1.8 KHz. Resistive load, R = 10 Ohms.

SPMC acted as rectifier is depicted in figure 13, whose values are given below, which represents level 3 charging unit. It is noted that the voltage magnitude is fixed.

Output Voltage, Vo = 100 V, DC
Output Current, Io=Vo/R=100/10 =10 A, DC in nature.

Figure 13: Level 3 voltage and current waveforms of rectifier

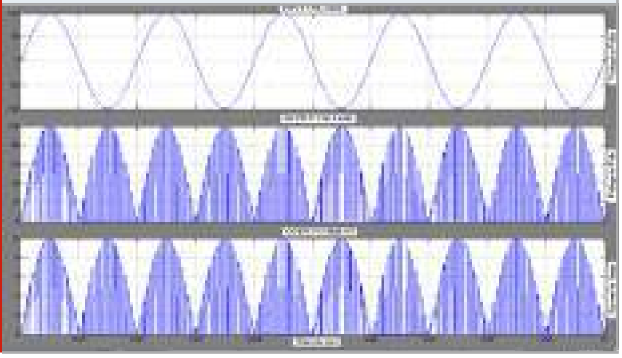

Figure 14: Level 4 voltage and current waveforms of controlled rectifier (converter)

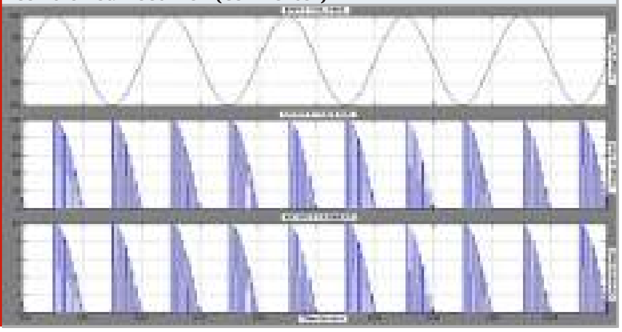

SPMC acted as converter is depicted in figure 14, whose values are given below, which represents level 4 charging unit. Here the voltage magnitude can be varied by applying suitable triggering pulse.

Output Voltage, Vo = 100 V, DC, at 900pulse triggering (π/2 rad)

Output Current, Io=Vo/R=100/10 =10 A, DC at 900pulse triggering (π/2 rad)

CONCLUSION

The proposed multi mode EV charger was successfully simulated in simulink platform. The EV charger is able to provide a controllable and constant charging voltage for various EVs and is composed of four levels of charging: (i) Three phase variable magnitude AC supply, (ii) Single phase variable frequency AC supply, (iii) Fixed voltage DC supply and (iv) Variable voltage DC supply. A modulated Venturini algorithm satisfies accurate operation of TPMC for first two levels of charging. A new modulated switching strategy of SPMC gives the second two levels of charging states. It is clear that the control algorithm perfectly regulates the output voltage of both TPMC and SPMC. At the same time, it also ensures a sinusoidal output current with minimum switching ripples and a prescribed low THD content. The results obtained demonstrate high performance total (multi mode) EV charging station. Thus all of the intension of an ideal EV charging was derived.

REFERENCES

Ajay Kumar Gola et al (2009) Implementation of an Efficient Algorithm for a single phase Matrix converter Journal of Power Electronics Vol 9 No 2.

Ali Saadon etal (2019) Three-Level Universal Electric Vehicle Charger Based on Voltage-Oriented Control and Pulse-Width Modulation Energies 12 Pages 2375.

Arancibia A Strunz K (2012) Modeling of an electric vehicle charging station for fast DC charging In Proceedings of the IEEE International Electric Vehicle Conference (IEVC) Greenville SC USA Pages 4–8.

Clemente C Ottorino V (2015) Experimental study of a DC charging station for full electric and plug in hybrid vehicles Appl Energy 153 Pages 131–142.

Harish S Krishnamoorthy (2012) A Matrix converter-based topology for high power Electric vehicle battery charging and V2G application IECON 2012 - 38th Annual Conference on IEEE Industrial Electronics Society

Idris Zet al (2006) Implementation of single-phase Matrix converter as a direct AC-AC converter with commutation strategies Proc of 37th IEEE Power Electronics Specialists Conference PESC 06 Pages 1 – 7.

Kawamura N Muta M (2012) Development of solar charging system for plug-in hybrid electric vehicles and electric vehicles In Proceedings of the International Conference Renewable Energy Research and Applications (ICRERA) Nagasaki Japan Pages 11–14.

Metha S (2015) Electric plug-in vehicle/electric vehicle status report Electrical Eng Pages 1–15.

National Renewable Energy Laboratory (NREL) (2013) Plug-In Electric Vehicle Hand Book for Public Charging

Station Hosts US Department of Energy Washington DC USA Pages 1–20.

Senthil Kumar R and Vivekanandan C (2017) A Novel Switching Strategy for Realization of Single Phase Matrix Converter as a Universal Power Electronic Converter International Journal of Control Theory and Applications Vol 10 issue 2 Pages 305-320.

Sunter S and Altun H (2003) Matrix converter induction motor drive modeling simulation and control Springer-Verlag Electrical Engineering (86) Pages 25–33.

Sunter S (1995) A vector controlled matrix converter induction motor drive PhD Thesis Department of Electrical and Electronic Engineering University of Nottingham.

VenturiniM and Alesina A (1989) Analysis and Design of Optimum-Amplitude Nine-Switch Direct AC-AC Converters IEEE Transactions on Power Electronics.

ZuckerbergerZ (1997) Single phase Matrix converter IEEE proceeding of Electrical Power Application Pages 144235–240.

Chaos, Solitons and Fractals 138 (2020) 109912

Contents lists available at ScienceDirect

Chaos, Solitons and Fractals

Nonlinear Science, and Nonequilibrium and Complex Phenomena

journal homepage: www.elsevier.com/locate/chaos

Solutions to fractional neutral delay differential nonlocal systems

N. Valliammal[a], C. Ravichandran[b], Kottakkaran Sooppy Nisar[c,*]

[a] Department of Mathematics, Sri Eshwar College of Engineering (Autonomous), Coimbatore 641 202, Tamil Nadu, India
[b] Post Graduate and Research Department of Mathematics, Kongunadu Arts and Science College (Autonomous), Coimbatore 641 029, Tamil Nadu, India
[c] Department of Mathematics, College of Arts and Sciences, Prince Sattam bin Abdulaziz University, Wadi Aldawasir, Saudi Arabia

ARTICLE INFO

Article history:
Received 5 May 2020
Revised 9 May 2020
Accepted 17 May 2020

MSC:
47H08
47H10
34K37

Keywords:
Mönch fixed point theorem
Neutral equations
Noncompact measure
Delay

ABSTRACT

The study of neutral fractional delay system governed by nonlocal conditions is presented and proved. With the aid of fractional theory, noncompact measure and Mönch's technique, we established some sufficient conditions to confirm the existence of neutral delay differential system. An illustration of derived results is also offered.

1. Introduction

It is renowned fact that the study involving fractional calculus is an emerging area with wider applications in signal processing, mechanics, economics, biology, electro magnetics etc. In the field of science and engineering, fractional calculus act as a essential tool in describing several complex phenomena. To get a few developments about the field, one can refer [1,10,12,15,17–20,22–24,26,27,29–31,35,36,39,40].

As is well-known, the nonlocal problems are more desirable when compared with Cauchy problems [9,11,21,37,38]. In considerations with real life phenomena, generally, the physical changes of a system depends on both of its present and past state. In order to face certain situations, it is important to know the previous history of the function.

Such systems are connected to delay differential systems. Neutral delay differential equations are considered as a branch of delay differential equations. It contains the derivative of the unknown function both with and without delays. In functional differential equations, the neutral type serves a major part and several delay systems are framed as neutral differential models.

Fractional differential equation with delay features including nonlocal nature arises in certain domains like physical and medical with non-constant delay or state-dependent delay and has drawn the attention [2,5–8,13,14,16,28,30,33,34] instance. Ravichandran et al. [33] investigated the existence of mild solutions of neutral differential system along state-dependent delay in Banach space. Further Aissani et al. [2] established sufficient conditions for the existence of mild solutions for fractional integro-differential inclusions with state-dependent delay. Besides Benchohra et al. [8] explored the existence of neutral systems with α-resolvent family. In particular Belmekki et al. [4] studied the existence of mild solutions for fractional semilinear functional differential system with state-dependent delay via of measure of noncompactness. Inspired by such instances, we consider the fractional neutral delay differential system in Banach space

$$ {}^{C}D^{p}_{\mathfrak{z}}[\omega(\mathfrak{z}) + \mathcal{H}(\mathfrak{z}, \omega(\mathfrak{z} - \rho(\omega(\mathfrak{z}))))] = \mathcal{A}[\omega(\mathfrak{z}) + \mathcal{H}(\mathfrak{z}, \omega(\mathfrak{z} - \rho(\omega(\mathfrak{z}))))] + \mathcal{E}(\mathfrak{z}, \omega(\mathfrak{z} - \rho(\omega(\mathfrak{z})))) + \int_0^{\mathfrak{z}} \mathcal{F}(\mathfrak{z} - s)\omega(s)ds, \quad \mathfrak{z} \in \hbar := [0, d], \tag{1.1} $$

$$ \omega(\mathfrak{z}) = \phi_0(\mathfrak{z}) + f(\omega)(\mathfrak{z}), \ \ \mathfrak{z} \in [-r, 0], \tag{1.2} $$

where ${}^{C}D^{p}_{\mathfrak{z}}$, derivative of fractional order with Caputo sense and $0 < p < 1$. In Banach space $\mathcal{X}$, the linear operators $\mathcal{A}$ and $(\mathcal{F}(\mathfrak{z}))_{\mathfrak{z} \geq 0}$ are closed and dense. Here $\mathcal{E}$, $\mathcal{H}$ are continuous functions as $\hbar \times C_{\mathcal{X}}([-r, 0], \mathcal{X})$ to $\mathcal{X}$, $f : C_{\mathcal{X}}([-r, 0], \mathcal{X}) \to C_{\mathcal{X}}([-r, 0], \mathcal{X})$. Also ρ and $\phi_0 \in C_{\mathcal{X}}([-r, 0]$ are continuous functions.

The rest of this article arranged as: Section 2, deals few fundamental facts. In Section 3, the existence of our nonlocal delay system derived using Mönch's technique. In Section 4, an illustration is given to explain our abstract conclusions.

* Corresponding author.
E-mail address: n.sooppy@psau.edu.sa (K.S. Nisar).

https://doi.org/10.1016/j.chaos.2020.109912

2. Basic results

Here, we discuss some basic definitions, lemmas and assumptions.

Definition 2.1. For $p > 0$ and for a function f,

$$I^p f(\mathfrak{z}) = \frac{1}{\Gamma(p)} \int_0^{\mathfrak{z}} f(s)(\mathfrak{z}-s)^{-1+p} ds, \quad \mathfrak{z} > 0,$$

defines the integral of fractional order $p > 0$ for the given function.

Definition 2.2. Podlubny [27] For $p > 0$ and $m-1 < p < m$, $m \in N$ and for a function f,

$${}^{(R-L)}D^p_{0+} f(\mathfrak{z}) = \frac{1}{\Gamma(m-p)} \left(\frac{d}{d\mathfrak{z}}\right)^m \int_0^{\mathfrak{z}} (\mathfrak{z}-s)^{m-p-1} f(s) ds,$$

represents R-L fractional derivative for the given function.

Definition 2.3. Podlubny [27] For $p > 0$ and $f : [0, \infty) \to \mathbb{R}$, $m - 1 < p < m$,

$$D^p f(\mathfrak{z}) = D^p \left(f(\mathfrak{z}) - \sum_{k=0}^{m-1} \frac{\mathfrak{z}^k}{k!} f^{(k)}(0) \right)$$

defines the Caputo derivative of the given function.

Remark 2.1. If $f(\mathfrak{z}) \in C^m_{\mathcal{X}}[0, \infty)$ and $m-1 < p < m$, we have

$${}^C D^p f(\mathfrak{z}) = \frac{1}{\Gamma(m-p)} \int_0^{\mathfrak{z}} f^{(m)}(s)(\mathfrak{z}-s)^{m-(p+1)} ds = I^{m-p} f^{(m)}(\mathfrak{z}).$$

For any $\omega \in \mathcal{X}$, $\mathfrak{z} \geq 0$, $\aleph \in (0, \infty)$, $S_p(\mathfrak{z})$ and $T_p(\mathfrak{z})$ are as follows:

$$S_p(\mathfrak{z})\omega = \int_0^\infty \xi_p(\aleph) S(\mathfrak{z}^p \aleph)\omega \, d\aleph,$$

$$T_p(\mathfrak{z})\omega = p \int_0^\infty \aleph \xi_p(\aleph) S(\mathfrak{z}^p \aleph)\omega \, d\aleph,$$

where the probability density function defined by

$$\xi_p(\aleph) = \frac{1}{p} \aleph^{-1-\frac{1}{p}} \overline{\omega}_p(\aleph^{-\frac{1}{p}}) \geq 0,$$

$$\overline{\omega}_p(\aleph) = \frac{1}{\pi} \sum_{m=1}^{\infty} (-1)^{m-1} \aleph^{-mp-1} \frac{\Gamma(mp+1)}{m!} sin(m\pi p).$$

Lemma 2.1. *Zhou and Jiao [41] $S_p(\mathfrak{z})$ and $T_p(\mathfrak{z})$ acquire the subsequent properties.*

(i) Some fixed $\mathfrak{z} \geq 0$, for some $\omega \in \mathcal{X}$, $\|S_p(\mathfrak{z})\omega\| \leq \mathcal{M}_1 \|\omega\|$ and $\|T_p(\mathfrak{z})\omega\| \leq \frac{\mathcal{M}_1 p}{\Gamma(1+p)} \|\omega\|$.
(ii) $\{S_p(\mathfrak{z}), \mathfrak{z} \geq 0\}$, $\{T_p(\mathfrak{z}), \mathfrak{z} \geq 0\}$ are strongly continuous.
(iii) S and T are equicontinuous provided $S_p(\mathfrak{z})_{\mathfrak{z} \geq 0}$ is equicontinuous in $\mathcal{X}$.

Throughout the paper, we considered: $B(\mathcal{X})$, the space of bounded linear operators $\mathcal{X}$ in to $\mathcal{X}$ and $\|N\|_{B(\mathcal{X})} = \sup\{\|N(\omega)\| : \|\omega\| = 1\}$. $C_{\mathcal{X}}(\hbar, \mathcal{X})$ defines functions from $\hbar$ in to Banach space which are all continuous. Moreover $L^\infty([0, d], \mathcal{X})$, bounded measurable functions with $\|\omega\|_{L^\infty} = \inf\{\epsilon > 0 : \|\omega(\mathfrak{z})\| < \epsilon$, a.e. $\mathfrak{z} \in [0, d]\}$.

Definition 2.4. Bana's and Goebel [3] In $\mathcal{X}$, the bounded subset $\Omega_{\mathcal{X}}$, the Kuratowski measure $\Lambda : \Omega_{\mathcal{X}} \to [0, \infty)$ exemplified by

$$\Lambda(\mathcal{B}) = inf \left\{ \varepsilon > 0 : \mathcal{B} \subseteq \bigcup_{i=1}^{m} \mathcal{B}_i, \; diam\,(\mathcal{B}_i) \leq \varepsilon \right\};$$

where $\mathcal{B} \in \Omega_{\mathcal{X}}$ and

(i) $\Lambda(m_1) = 0 \Leftrightarrow \bar{m}_1$ is compact
(ii) $\Lambda(m_1) = \Lambda(\overline{m_1})$
(iii) $m_1 \subset m_2 \Rightarrow \Lambda(m_1) \leq \Lambda(m_2)$
(iv) $\Lambda(m_1 + m_2) \leq \Lambda(m_1) + \Lambda(m_2)$
(v) $\Lambda(K m_1) = |K| \Lambda(m_1); K \in \mathbb{R}$
(vi) $\Lambda(conv\, m_1) = \Lambda(m_1)$

Theorem 2.1. *Monch and spaces [25] The closed convex subset $\mathcal{V}$ of $\mathcal{X}$ satisfies $0 \in \mathcal{V}$, the continuous function $\Omega : \mathcal{V} \to \mathcal{V}$ and for every $\mathcal{V}_1 \subseteq \mathcal{V}$ and Ω has a fixed point if*
$\mathcal{V}_1 = \overline{conv}\, \Omega(\mathcal{V}_1) \Rightarrow \Lambda(\mathcal{V}_1) =$ zero.

Lemma 2.2. *Szufla [32] The closed convex subset $\mathcal{V}$ of $C_{\mathcal{X}}(\hbar, \mathcal{X})$. The continuous function $\mathcal{F}$ on $\hbar \times \hbar$ and the Caratheodory function $g : \hbar \times C_{\mathcal{X}}([-r, 0), \mathcal{X})$ to $\mathcal{X}$ for any $p \in L^1(\hbar, \mathbb{R}_+)$, for all $\mathfrak{z} \in \hbar$, $\mathcal{D} \subset C_{\mathcal{X}}([-r, 0], \mathcal{X})$ is bounded, we have*
$\lim_{k \to 0^+} \Lambda(g(\hbar_{\mathfrak{z},k} \times \mathcal{D})) \leq p(\mathfrak{z}) \Lambda(\mathcal{D})$, *where* $\hbar_{\mathfrak{z},k} = [\mathfrak{z} - k, \mathfrak{z}] \cap \hbar$.
If $\mathcal{V}_1 \subseteq \mathcal{V}$ is equicontinuous,
$$\Lambda\left(\left\{ \int_\hbar \mathcal{F}(s, \mathfrak{z}) g(s, w_s) ds; \omega \in \mathcal{V}_1 \right\}\right) \leq \int_\hbar \|\mathcal{F}(\mathfrak{z}, s)\| p(s) \Lambda(\mathcal{V}_1(s)) ds.$$

3. Main sequels

Definition 3.1. $\omega : [-r, d] \to \mathcal{X}$ is called the solution of (1.1) and (1.2) if $\int_0^{\mathfrak{z}} (\mathfrak{z}-s)^{p-1} \omega(s) ds \in \mathcal{D}(\mathcal{A})$, for $\mathfrak{z} \in \hbar$ and $\int_0^s (\mathfrak{z}-s)^{p-1} \mathcal{F}(s-\nu) T_p(\mathfrak{z}-s) \mathcal{H}(\nu, \omega(\nu - \rho(\omega(\nu)))) d\nu$ is integrable provided for $\mathfrak{z} \in \hbar$,

$$\begin{aligned}
\omega(\mathfrak{z}) =& S_p(\mathfrak{z})[\phi_0(0) + f(\omega)(0) - \mathcal{H}(0, \phi_0(-\rho(\omega(0))) + f(\omega)(-\rho(\omega(0)))] \\
&+ \mathcal{H}(\mathfrak{z}, \omega(\mathfrak{z} - \rho(\omega(\mathfrak{z})))) + \int_0^{\mathfrak{z}} (\mathfrak{z}-s)^{p-1} T_p(\mathfrak{z}-s) \mathcal{E}(s, \omega(s - \rho(\omega(s)))) ds \\
&+ \int_0^{\mathfrak{z}} (\mathfrak{z}-s)^{p-1} T_p(\mathfrak{z}-s) \left(\int_0^s \mathcal{F}(s-\nu) \mathcal{H}(\nu, \omega(\nu - \rho(\omega(\nu)))) d\nu \right) ds, \; \mathfrak{z} \in \hbar, \\
\omega(\mathfrak{z}) =& \phi_0(\mathfrak{z}) + f(\omega)(\mathfrak{z}), \quad \mathfrak{z} \in [-r, 0]
\end{aligned}$$

is satisfied.

In order to achieve our outcomes, we introduce the subsequent hypotheses:

H1 The functions $\mathcal{E}$ and $\mathcal{H}$ are Caratheodory.
H2 Functions $p, q \in L^\infty([0, d], \mathbb{R}_+)$ yields $\|\mathcal{E}(\mathfrak{z}, \omega)\| \leq p(\mathfrak{z}) \times (\|\omega\|_\infty + 1)$, $\|\mathcal{H}(\mathfrak{z}, \omega)\| \leq q(\mathfrak{z})(\|\omega\|_\infty + 1)$, for a.e $\mathfrak{z} \in \hbar$, $\omega \in C_{\mathcal{X}}([-r, 0], \mathcal{X})$.
H3 For all $\mathfrak{z} \in [0, d]$ and some $\mathfrak{z}_1, \mathfrak{z}_2 \in C_{\mathcal{X}}([-r, 0]$, a constant $\mathcal{L}_g > 0$, such that

$$\|\mathcal{H}(\mathfrak{z}, \mathfrak{z}_1) - \mathcal{H}(\mathfrak{z}, \mathfrak{z}_2)\| \leq \mathcal{L}_g \|\mathfrak{z}_1 - \mathfrak{z}_2\|_{\mathcal{X}}.$$

H4 There is a function $\mathcal{G}(\cdot)\omega \in C_{\mathcal{X}}([0, d], \mathcal{X})$, $\mu(\cdot) \in L^1(\hbar, \mathbb{R}^+)$ provided that

$$\|\mathcal{G}(s)\| \leq \mu(s), \; 0 \leq s < \mathfrak{z} \leq d.$$

H5 For $\mathcal{L}_f : [-r, 0] \to \mathbb{R}^+$, a continuous function and a constant $\mathcal{N} > 0$ yields

$$\|f(\omega)(\mathfrak{z}) - f(\mathcal{Y})(\mathfrak{z})\| \le L_f(\mathfrak{z})\|\omega(\mathfrak{z}) - \mathcal{Y}(\mathfrak{z})\|, \mathfrak{z} \in [-r, 0]$$

and $\|f(\omega)\|_{[-r,0]} \le \mathcal{N}$, for every $\omega \in \mathcal{C}_{\mathcal{X}}([-r, 0], \mathcal{X})$.

H6 For all $\mathfrak{z} \in \hbar$, $\mathcal{D} \subset \mathcal{C}_{\mathcal{X}}([-r, 0], \mathcal{X})$ is bounded, we have

$$\lim_{k\to 0^+} \Lambda\Big(\mathcal{E}(\hbar_{\mathfrak{z},k} \times \mathcal{D})\Big) \le p(\mathfrak{z})\Lambda(\mathcal{D}), \quad \lim_{k\to 0^+} \Lambda\Big(\mathcal{H}(\hbar_{\mathfrak{z},k} \times \mathcal{D})\Big) \le q(\mathfrak{z})\Lambda(\mathcal{D}).$$

Theorem 3.1. *Let* ***H1–H6*** *holds, the system (1.1) and (1.2) has atleast one solution on $[-r, d]$ provided*

$$\mathcal{M}_1[\|\phi_0(0) + \mathcal{N}\|] + \|q\|_{L^\infty}(1 + c)\Big(2 + \frac{\mathcal{M}_1 d^p}{\Gamma(p+1)}\int_0^d \mu(\nu)d\nu\Big) < 1.$$

Proof. Revert (1.1) and (1.2) with $\Psi : \mathcal{C}_{\mathcal{X}}([-r, d], \mathcal{X}) \to \mathcal{C}_{\mathcal{X}}([-r, d], \mathcal{X})$ as

$$\Psi(\omega)(\mathfrak{z}) = \begin{cases} \phi_0(\mathfrak{z}) + f(\omega)(\mathfrak{z}), & \mathfrak{z} \in [-r, 0], \\ S_p(\mathfrak{z})\Big[\phi_0(0) + f(\omega)(0) - \mathcal{H}(0, \phi_0(-\rho(\omega(0))) + f(\omega)(-\rho(\omega(0)))\Big] \\ +\mathcal{H}(\mathfrak{z}, \omega(\mathfrak{z} - \rho(\omega(\mathfrak{z})))) \\ + \int_0^{\mathfrak{z}}(\mathfrak{z} - s)^{p-1}T_p(\mathfrak{z} - s)\mathcal{E}(s, \omega(s - \rho(\omega(s))))ds \\ + \int_0^{\mathfrak{z}}(\mathfrak{z} - s)^{p-1}T_p(\mathfrak{z} - s)\Big(\int_0^s \mathcal{F}(s - \nu)\mathcal{H}(\nu, \omega(\nu - \rho(\omega(\nu))))d\nu\Big)ds, \\ \mathfrak{z} \in \hbar. \end{cases}$$

Let $\delta > 0$ be such that

$$\delta \ge \mathcal{M}_1[\|\phi_0(0) + \mathcal{N}\|] + \|q\|_{L^\infty}(1 + c)\Big(2 + \frac{\mathcal{M}_1 d^p}{\Gamma(p+1)}\int_0^d \mu(\nu)d\nu\Big).$$

Construct the set:

$\mathcal{E}_\delta = \{\omega \in \mathcal{C}_{\mathcal{X}}([-r, d], \mathcal{X}); \|\omega\|_\infty \le \delta\}$.

It shows that $\mathcal{E}_\delta$ is closed, convex and bounded. Now consider the decomposition $\Psi = \Psi_1 + \Psi_2$ of the operator Ψ, as

$$\begin{aligned}\Psi_1(\mathfrak{z}) = {} & S_p(\mathfrak{z})[\phi_0(0) + f(\omega)(0) - \mathcal{H}(0, \phi_0(-\rho(\omega(0))) + f(\omega)(-\rho(\omega(0)))] \\ & + \mathcal{H}(\mathfrak{z}, \omega(\mathfrak{z} - \rho(\omega(\mathfrak{z})))) \\ & + \int_0^{\mathfrak{z}}(\mathfrak{z} - s)^{p-1}T_p(\mathfrak{z} - s)\Big(\int_0^s \mathcal{F}(s - \nu)\mathcal{H}(\nu, \omega(\nu - \rho(\omega(\nu))))d\nu\Big)ds, \\ \Psi_2(\mathfrak{z}) = {} & \int_0^{\mathfrak{z}}(\mathfrak{z} - s)^{p-1}T_p(\mathfrak{z} - s)\mathcal{E}(s, \omega(s - \rho(\omega(s))))ds,\end{aligned}$$

Step 1: Ψ_1 is continuous completely.

Consider the sequence $\{\omega_n\}$ such that $\omega_n \to \omega$ as n approaches to ∞ in $\mathcal{C}_{\mathcal{X}}([-r, d], \mathcal{X})$, for some $\mathfrak{z} \in \hbar$, $-r \le s - \rho(\omega(s)) \le s$, for all $s \in \hbar$, we obtain

$$\begin{aligned}&\|\Psi_1(\omega_n)(\mathfrak{z}) - \Psi_1(\omega)(\mathfrak{z})\| \le \mathcal{M}_1\Big[\|f(\omega_n)(0) - f(\omega)(0)\| \\ &\quad + \|\mathcal{H}(0, \phi_0(-\rho(\omega_n(0))) + f(\omega_n)(-\rho(\omega_n(0))) - \mathcal{H}(0, \phi_0(-\rho(\omega(0))) + f(\omega)(-\rho(\omega(0)))\|\Big] \\ &\quad + \|\mathcal{H}(\mathfrak{z}, \omega_n(\mathfrak{z} - \rho(\omega_n(\mathfrak{z})))) - \mathcal{H}(\mathfrak{z}, \omega(\mathfrak{z} - \rho(\omega(\mathfrak{z}))))\| \\ &\quad + \int_0^{\mathfrak{z}}(\mathfrak{z} - s)^{p-1}\|T_p(\mathfrak{z} - s)\|(\times)\Big\|\int_0^s \mathcal{F}(s - \nu)\Big[\mathcal{H}(\nu, \omega_n(\nu - \rho(\omega_n(\nu)))) - \mathcal{H}(\nu, \omega(\nu - \rho(\omega(\nu))))\Big]\Big\|d\nu ds,\end{aligned}$$

$\|\Psi_1(\omega_n)(\mathfrak{z}) - \Psi_1(\omega)(\mathfrak{z})\| \to 0$ as $n \to \infty$. Hence $\|\Psi_1(\omega_n) - \Psi_1(\omega)\|_\infty \to 0$ as $n \to \infty$. This confirms Ψ_1 is continuous.

Now, we show Ψ_1 is bounded. For every $\omega \in \mathcal{E}_\delta$ and $\mathfrak{z} \in \hbar$, we observe

$$\begin{aligned}&\|\Psi_1(\omega)(\mathfrak{z})\| \\ &\le \mathcal{M}_1[\|\phi_0(0) + f(\omega)(0)\|] + \|q\|_{L^\infty}(c+1) + \|q\|_{L^\infty}(c+1) \\ &\quad + \frac{\mathcal{M}_1 d^p}{\Gamma(1+p)}\|q\|_{L^\infty}(c+1)\int_0^d \mu(\nu)d\nu \\ &\le \mathcal{M}_1[\|\phi_0(0)\| + \mathcal{N}] + 2\|q\|_{L^\infty}(c+1) + \frac{\mathcal{M}_1 d^p}{\Gamma(1+p)}\|q\|_{L^\infty}(c+1)\int_0^d \mu(\nu)d\nu \\ &= \mathcal{M}_1[\|\phi_0(0)\| + \mathcal{N}] + \|q\|_{L^\infty}(c+1)\Big(2 + \frac{\mathcal{M}_1 d^p}{\Gamma(p+1)}\int_0^d \mu(\nu)d\nu\Big) \le \delta.\end{aligned}$$

Hence $\Psi_1(\mathcal{E}_\delta) \subset \mathcal{E}_\delta$. In other side, we prove that $\Psi_1(\mathcal{E}_\delta)$ is equicontinuous. For this need, let us consider $\lambda_1, \lambda_2 \in \hbar$ such that $\lambda_2 > \lambda_1$. Also for some $\omega \in \mathcal{E}_\delta$ and $\epsilon > 0$ small enough, we get

$$\begin{aligned}&\|\Psi_1(\omega)(\lambda_2) - \Psi_1(\omega)(\lambda_1)\| \\ &\le \|\mathcal{H}(\lambda_2, \omega(\lambda_2 - \rho(\omega(\lambda_2)))) - \mathcal{H}(\lambda_1, \omega(\lambda_1 - \rho(\omega(\lambda_1))))\|\end{aligned}$$

$$
\begin{aligned}
&+\left\| \int_0^{\lambda_2} (\lambda_2 - s)^{p-1} T_p(\lambda_2 - s) \int_0^s \mathcal{F}(s-\nu)\mathcal{H}(\nu, \omega(\nu - \rho(\omega(\nu))))d\nu ds \right\| \\
&-\left\| \int_0^{\lambda_1} (\lambda_1 - s)^{p-1} T_p(\lambda_1 - s) \int_0^s \mathcal{F}(s-\nu)\mathcal{H}(\nu, \omega(\nu - \rho(\omega(\nu))))d\nu ds \right\| \\
&\leq \mathcal{L}_g \|\lambda_2 - \lambda_1\| \\
&+\left\| \int_0^{\lambda_1-\epsilon} \Big((\lambda_2 - s)^{p-1} T_p(\lambda_2 - s) - (\lambda_1 - s)^{p-1} T_p(\lambda_1 - s) \Big) \right. \\
&\quad \left. (\times) \int_0^s \mathcal{F}(s-\nu)\mathcal{H}(\nu, \omega(\nu - \rho(\omega(\nu))))d\nu ds \right\| \\
&+\left\| \int_{\lambda_1-\epsilon}^{\lambda_1} \Big((\lambda_2 - s)^{p-1} T_p(\lambda_2 - s) - (\lambda_1 - s)^{p-1} T_p(\lambda_1 - s) \Big) \right. \\
&\quad \left. (\times) \int_0^s \mathcal{F}(s-\nu)\mathcal{H}(\nu, \omega(\nu - \rho(\omega(\nu))))d\nu ds \right\| \\
&+\left\| \int_{\lambda_1}^{\lambda_2} (\lambda_2 - s)^{p-1} T_p(\lambda_2 - s) \int_0^s \mathcal{F}(s-\nu)\mathcal{H}(\nu, \omega(\nu - \rho(\omega(\nu))))d\nu ds \right\|.
\end{aligned}
$$

As ϵ, sufficiently small, $\|\Psi_1(\omega)(\lambda_2) - \Psi_1(\omega)(\lambda_1)\| \to 0$ as $\lambda_1 \to \lambda_2$. This completes the need.

Step 2: Ψ_2 is continuous completely.

For some $\omega \in \mathcal{E}_\delta$, we have

$$
\begin{aligned}
\|\Psi_2(\omega)(\mathfrak{z})\| &\leq \int_0^{\mathfrak{z}} (\mathfrak{z} - s)^{p-1} \|T_p(\mathfrak{z} - s)\mathcal{E}(s, \omega(s - \rho(\omega(s))))\| ds \\
&\leq \frac{\mathcal{M}_1 p}{\Gamma(1+p)} \int_0^{\mathfrak{z}} (\mathfrak{z} - s)^{p-1} p(s)(\|\omega(s)\|_C + 1) ds \\
&\leq \frac{\mathcal{M}_1 d^p}{\Gamma(1+p)} (c+1)\|p\|_{L^\infty} \leq \delta.
\end{aligned}
$$

Moreover Ψ_2 is continuous and $\Psi_2(\mathcal{E}_\delta) \subset \mathcal{E}_\delta$.

Now, we show that $\Psi_2(\mathcal{E}_\delta)$ is equicontinuous. For this need, consider $\lambda_1, \lambda_2 \in \hbar$, $\lambda_2 > \lambda_1$. Then for any $\omega \in \mathcal{E}_\delta$, $\epsilon > 0$ and $\epsilon \leq \lambda_1 \leq \lambda_2$, we perceive that

$$
\begin{aligned}
&\|\Psi_2(\omega)(\lambda_2) - \Psi_2(\omega)(\lambda_1)\| \\
&\leq \left\| \int_0^{\lambda_1-\epsilon} \Big((\lambda_2 - s)^{p-1} T_p(\lambda_2 - s) - (\lambda_1 - s)^{p-1} T_p(\lambda_1 - s) \Big) \mathcal{E}(s, \omega(s - \rho(\omega(s)))) ds \right\| \\
&\quad+\left\| \int_{\lambda_1-\epsilon}^{\lambda_1} \Big((\lambda_2 - s)^{p-1} T_p(\lambda_2 - s) - (\lambda_1 - s)^{p-1} T_p(\lambda_1 - s) \Big) \mathcal{E}(s, \omega(s - \rho(\omega(s)))) ds \right\| \\
&\quad+\left\| \int_{\lambda_1}^{\lambda_2} (\lambda_2 - s)^{p-1} T_p(\lambda_2 - s) \mathcal{E}(s, \omega(s - \rho(\omega(s)))) ds \right\| \\
&\leq (c+1)\|p\|_{L^\infty} \frac{\mathcal{M}_1 p}{\Gamma(1+p)} \left(\int_0^{\lambda_1-\epsilon} \Big((\lambda_2 - s)^{p-1} - (\lambda_1 - s)^{p-1} \Big) ds \right. \\
&\quad \left. + \int_{\lambda_1-\epsilon}^{\lambda_1} \Big((\lambda_2 - s)^{p-1} - (\lambda_1 - s)^{p-1} \Big) ds + \int_{\lambda_1}^{\lambda_2} (\lambda_2 - s)^{p-1} ds \right).
\end{aligned}
$$

As sufficiently small ϵ and $\lambda_1 \to \lambda_2$, $\|\Psi_2(\omega)(\lambda_2) - \Psi_2(\omega)(\lambda_1)\| \to 0$. So $\Psi_2(\mathcal{E}_\delta)$ is completely continuous.

Let $\upsilon_1 \subseteq \mathcal{E}_\delta$, $\upsilon_1 \subset \overline{conv}(\Psi(\upsilon_1) \cup \{0\})$. Moreover υ_1 is bounded, equicontinuous and $\kappa \to \kappa(\mathfrak{z}) = \Lambda(\upsilon_1(\mathfrak{z}))$ is continuous on $[-r, d]$. By **H6**, for every $\mathfrak{z} \in [-r, d]$,

$$
\begin{aligned}
\kappa(\mathfrak{z}) &\leq \Lambda(\Psi(\upsilon_1)(\mathfrak{z}) \cup \{0\}) \leq \Lambda(\Psi(\upsilon_1(\mathfrak{z}))) \\
&\leq q(\mathfrak{z})\Lambda(\kappa(\mathfrak{z})) + \int_0^{\mathfrak{z}} (\mathfrak{z} - s)^{p-1} \|T_p(\mathfrak{z} - s)\| p(s)\Lambda(\kappa(s)) ds \\
&\quad + \int_0^{\mathfrak{z}} (\mathfrak{z} - s)^{p-1} \|T_p(\mathfrak{z} - s)\| \int_0^s \|\mathcal{F}(s-\nu)\| q(\nu)\Lambda(\kappa(\nu)) d\nu ds \\
&\leq q(\mathfrak{z})\Lambda(\kappa(\mathfrak{z})) + \frac{\mathcal{M}_1 p}{\Gamma(1+p)} \int_0^{\mathfrak{z}} (\mathfrak{z} - s)^{p-1} p(s)\Lambda(\kappa(s)) ds \\
&\quad + \frac{\mathcal{M}_1 p}{\Gamma(1+p)} \int_0^{\mathfrak{z}} (\mathfrak{z} - s)^{p-1} \int_0^s \mu(s-\nu) q(\nu)\Lambda(\kappa(\nu)) d\nu ds \\
&\leq q(\mathfrak{z})\Lambda(\kappa(\mathfrak{z})) + \frac{\mathcal{M}_1 d^p}{\Gamma(1+p)} \|\kappa\|_\infty \left(\|q\|_{L^\infty} \int_0^d \mu(\nu) d\nu + \|p\|_{L^\infty} \right).
\end{aligned}
$$

From the above discussions, we can have

$$\|\kappa\|_{\infty}\left(1-\frac{\mathcal{M}_1 d^p}{\Gamma(1+p)}\left(\|q\|_{L^\infty}\int_0^d \mu(\nu)d\nu+\|p\|_{L^\infty}\right)\right)\leq 0.$$

Finally, for each $\mathfrak{z}\in[-r,d]$, $\|\kappa\|_{\infty}=\kappa(\mathfrak{z})=0$. By applying Arzela theorem, ν_1 is relatively compact in E_δ. $\therefore$ Ψ has a fixed point. □

4. Example

Recognize the system

$$\frac{\partial^p}{\partial \mathfrak{z}^p}\left[\omega(\mathfrak{z},\mu)-\phi_1(\mathfrak{z})|\omega(\mathfrak{z}-\nu(\omega(\mathfrak{z},\mu)),\mu)|^2\right]$$
$$=\frac{\partial^2}{\partial x^2}\left(\omega(\mathfrak{z},\mu)-\phi_1(\mathfrak{z})|\omega(\mathfrak{z}-\nu(\omega(\mathfrak{z},\mu)),\mu)|^2\right)$$
$$+\phi_2(\mathfrak{z})\left||\omega(\mathfrak{z}-\nu(\omega(\mathfrak{z},\mu)),\mu)|^2\right|$$
$$+\int_{-r}^{\mathfrak{z}}\upsilon(\mathfrak{z}-s)\omega(s,\mu)ds,\quad \text{for } \mathfrak{z}\geq 0,\ \mathfrak{z}\in[0,d];\quad \mu\in[0,\pi], \tag{4.1}$$

$$\omega(\mathfrak{z},0)=\omega(\mathfrak{z},\pi)=0;\quad \mathfrak{z}\in[0,d], \tag{4.2}$$

$$\omega(\aleph,\mu)=s_0(\aleph,\mu);\ -r\leq\aleph\leq 0;\ -\nu_{\max}\leq\mathfrak{z}\leq 0, \tag{4.3}$$

where ϕ_1 and ϕ_2 are continuous from $[0,\mathfrak{z}]$ to $\mathbb{R}$. Reverting (4.1)–(4.3) of (1.1) and (1.2), consider $\mathcal{X}=L^2([0,\phi],\mathbb{R}]$, $\mathcal{A}:\mathcal{D}(\mathcal{A})\subset\mathcal{X}$ to $\mathcal{X}$ satisfies $\mathcal{A}\vartheta=\vartheta''$.

$$\mathcal{D}(\mathcal{A})=\Big\{\vartheta\in\mathcal{X};\vartheta,\vartheta' \text{are absolutely continuous; } \vartheta''\in\mathcal{X},$$
$$\vartheta(0)=\vartheta(\pi)=0\}.$$

Also, the normalized eigen functions of $\mathcal{A}$ are $T_m(\mu)=\sqrt{\frac{2}{\pi}}\sin(m\mu)$ and

(i) For $0<p<1$, $(-\mathcal{A})^p:\mathcal{D}(-\mathcal{A})^p\subset\mathcal{X}\to\mathcal{X}$ provided $(-\mathcal{A})^p\omega=\sum_{m=1}^{\infty}m^{2p}\langle\omega,\Lambda_m\rangle\Lambda_m$, for every $\omega\in\mathcal{D}((-\mathcal{A})^p)$, $\mathcal{D}((-\mathcal{A})^p)=\left\{\omega\in\mathcal{X}:\sum_{m=1}^{\infty}m^{2p}\langle\omega,\Lambda_m\rangle\Lambda_m\in\mathcal{X}\right\}$.

(ii) For $\omega\in\mathcal{X}$, $T(\mathfrak{z})\omega=\sum_{m=1}^{\infty}e^{-m^2}(\omega,\Lambda_m)\Lambda_m$.

(iii) $\{\Lambda_m;\ m\in N\}$ is an orthonormal basis in $\mathcal{X}$.

Therefore $T(\mathfrak{z})$, $\mathfrak{z}\geq 0$ is uniformly bounded. Let the well defined continuous functions $\mathcal{E}(\mathfrak{z},\zeta)\mu=\phi_1(\mathfrak{z})|\zeta(\mu)|^2$, $\mathcal{H}(\mathfrak{z},\zeta)\mu=\phi_2(\mathfrak{z})|\zeta(\mu)|^2$, which allows to convert (4.1)–(4.3) in to (1.1) and (1.2). Hence there is a mild solution $\omega\in\mathcal{C}_{\mathcal{X}}([-r,d],L^2)$.

5. Conclusion

A neutral delay fractional differential system has been cultivated with the existence results by the state of the art demonstrations. In depth involvement of noncompact measure and fixed point techniques, the interesting discussions arrived. Highly fitted illustration for the analytical result is offered at the end. Further, one can extend this study for controllability results with different domain.

Funding

None

Availability of data and Material

None

Declaration of Competing Interest

The authors declare that they have no known competing financial interests or personal relationships that could have appeared to influence the work reported in this paper.

CRediT authorship contribution statement

N. Valliammal: Conceptualization, Writing - original draft. **C. Ravichandran:** Conceptualization, Writing - original draft, Formal analysis. **Kottakkaran Sooppy Nisar:** Writing - original draft, Software, Methodology.

References

[1] Agarwal RP, Meehan M, O'Regan D. Fixed point theory and applications. Cambridge tracts in mathematics, 141. Cambridge: Cambridge University Press; 2001.
[2] Aissani K, Benchohra M. Fractional integro-differential equations with state-dependent delay. Adv Dyn Syst Appl 2014;9(1):17–30.
[3] Bana's J, Goebel K. Measures of noncompactness in Banach spaces. New York: Marcel Dekker; 1980.
[4] Belmekki M, Mekhalfi K. On fractional differential equations with state-dependent delay via Kuratowski measure of noncompactness. Filomat Univ Niš Fac Sci Math Niš 2017;31(2):451–60.
[5] Belmekki M, Mekhalfi K, Ntouyas SK. Existence and uniqueness for semilinear fractional differential equations with infinite delay via resolvent operators. J Fract Calc Appl 2013;4(2):267–82.
[6] Belmekki M, Mekhalfi K, Ntouyas SK. Semilinear functional differential equations with fractional order and finite delay. Malaya J Mat 2012;1(1):73–81.
[7] Belmekki M, Benchohra M. Existence results for fractional order semilinear functional differential equations with nondense domain. Nonlinear Anal 2010;72(2):925–32.
[8] Benchohra M, Bennihi O, Ezzinbi K. Existence results for some neutral partial functional differential equations of fractional order with state-dependent delay. Cubo 2014;16(3):37–53.
[9] Benchohra M, Bouteffal Z, Henderson J, Litimein S. Measure of noncompactness and fractional integro-differential equations with state-dependent nonlocal conditions in Frechet spaces. AIMS Math 2019;5(1):15–25.
[10] Dananea J, Allali K, Hammouch Z. Mathematical analysis of a fractional differential model of HBV infection with antibody immune response. Chaos Solitons Fractals 2020;136:109787.
[11] JPC DS, Vijayakumar V, Murugesu R. Existence of mild solutions for nonlocal cauchy problem for fractional neutral integro-differential equation with unbounded delay. Commun Math Anal 2013;14(1):59–71.
[12] Gao W, Veeresha P. Doddabhadrappla Gowda Prakasha, Haci Mehmet Baskonus, Gulnur Yel. New numerical results for the time-fractional phi-four equation using a novel analytical approach. Symmetry 2020;12(3):478.
[13] Jothimani K, Valliammal N, Ravichandran C. Existence result for neutral fractional integro-differential equation with state-dependent delay. J Appl Nonlinear Dyn 2018;7(4):371–81.
[14] Kexue L, Junxiong J. Existence and uniqueness of mild solutions for abstract delay fractional differential equations. Comput Math Appl 2011;62(3):1398–404.
[15] Kilbas AA, Srivastava HM, Trujillo JJ. Theory and applications of fractional differential equations. North-Holland mathematics studies. Amsterdam: Elsevier Science; 2006.
[16] Kucche KD, Sutar ST. On existence and stability results for nonlinear fractional delay differential equations. Bol Soc Parana Mat 2018;36(4):55–75.
[17] Kumar S, Nisar KS, Kumar R, Cattani C, Samet B. A new Rabotnov fractional exponential function based fractional derivative for diffusion equation under external force. Math Methods Appl Sci 2020:1–12. doi:10.1002/mma.6208.
[18] Kumar S, Kumar R, Singh J, Nisar KS, Kumar D. An efficient numerical scheme for fractional model of HIV-1 infection of CD4+T-cells with the effect of antiviral drug therapy. Alexandria Eng J 2020. doi:10.1016/j.aej.2019.12.046.
[19] Kumar S, Kumar A, Momani S. Numerical solutions of nonlinear fractional model arising in the appearance of the strip patterns in two-dimensional systems. Adv Differ Equ 2019;2019:413. doi:10.1186/s13662-019-2334-7.
[20] Kumar S, Kumar A, Odibat Z, Aldhaifallah M, Nisar KS. A comparison study of two modified analytical approach for the solution of nonlinear fractional shallow water equations in fluid flow. AIMS Math 2020;5(4):3035–55.
[21] Li F, ŃGuèrèrkata GM. An existence result for neutral delay integro-differential equations with fractional order and nonlocal conditions. Abstr Appl Anal 2011;2011:1–20.
[22] Alqudah MA, Ravichandran C, Abdeljawad T, Valliammal N. New results on Caputo fractional-order neutral differential inclusions without compactness. Adv Differ Equ 2019;2019:1–14.
[23] Miller KS, Ross B. An introduction to the fractional calculus and differential equations. New York: John Wiley; 1993.
[24] Horani MAL, Khalil R. Total fractional differentials with applications to exact fractional differential equations. Int J Comput Math 2018;95(6–7):1444–52.

[25] Monch H. Boundary value problems for nonlinear ordinary differential equations of second order in Banach spaces. Nonlinear Anal 1980;4(5):985–99.
[26] Nisar KS, Shaikh A, Rahman G, Kumar D. Solution of fractional kinetic equations involving class of functions and Sumudu transform. Adv Differ Equ 2020;2020(1):1–11.
[27] Podlubny I. Fractional differential equations. San Diego: Academic Press; 1999.
[28] Ravichandran C, Baleanu D. Existence results for fractional neutral functional integro-differential evolution equations with infinite delay in Banach spaces. Adv Differ Equ 2013;2013:215–27.
[29] Ravichandran C, Jothimani K, Baskonus HM, Valliammal N. New results on nondensely characterized integro-differential equations with fractional order. Eur Phys J Plus 2018;133(109):1–9.
[30] Ravichandran C, Valliammal N, Nieto JJ. New results on exact controllability of a class of fractional neutral integro-differential systems with state-dependent delay in Banach space. J Frankl Inst 2019;356(3):1535–65.
[31] Belmor S, Ravichandran C, Jarad F. Nonlinear generalized fractional differential equations with generalized fractional integral conditions. J Taibah Univ Sci 2020;14(1):114–23.
[32] Szufla S. On the application of measure of noncompactness to existence theorems. Rend Semin Mat Univ Padova 1986;75:1–14.
[33] Valliammal N, Ravichandran C, Hammouch Z, Baskonus HM. A new investigation on fractional-ordered neutral differential systems with state-dependent delay. Int J Nonlinear Sci Numer Simul 2019;20(7–8):803–9.
[34] Valliammal N, Ravichandran C. Results on fractional neutral integro-differential systems with state-dependent delay in Banach spaces. Nonlinear Stud 2018;25(1):159–71.
[35] Vanterler da C Sousa J, de Oliveira E C, Kucche KD. On the fractional functional differential equation with abstract Volterra operator. Bull Braz Math Soc New Ser 2019;50(4):803–22.
[36] Veeresha P, Baskonus HM, Prakasha DG, Gao W, Yel G. Regarding new numerical solution of fractional schistosomiasis disease arising in biological phenomena. Chaos Solitons Fractals 2020;133:109661. doi:10.1016/j.chaos.2020.109661.
[37] Wang JR, Fan Z, Zhou Y. Nonlocal controllability of semilinear dynamic systems with fractional derivative in Banach spaces. J Optim Theory Appl 2012;154(1):292–302.
[38] Zhang X, Li Y. Existence of solutions for delay evolution equations with nonlocal conditions. Open Math 2017;15:616–27.
[39] Zhou Y. Basic theory of fractional differential equations. World Scientific Press; 2014.
[40] Zhou Y, Jiao F, Li J. Existence and uniqueness for fractional neutral differential equations with infinite delay. Nonlinear Anal 2009;71:3249–56.
[41] Zhou Y, Jiao F. Existence of mild solutions for fractional neutral evolution equations. Comput Math Appl 2010;59(3):1063–77.

Received: 18 August 2020 | Revised: 4 October 2020 | Accepted: 15 October 2020
DOI: 10.1002/num.22628

RESEARCH ARTICLE

WILEY

Existence and uniqueness of solutions for fractional nonlinear hybrid impulsive system

Vidushi Gupta[1] | Fahd Jarad[2,3] | Natarajan Valliammal[4] | Chokkalingam Ravichandran[5] | Kottakkaran Sooppy Nisar[6]

[1]Department of Mathematics, Chandigarh University, Chandigarh, India
[2]Department of Mathematics, Çankaya University, Ankara, Turkey
[3]Department of Medical Research, China Medical University Hospital, China Medical University, Taichung, Taiwan
[4]Department of Mathematics, Sri Eshwar College of Engineering (Autonomous), Coimbatore, India
[5]Post Graduate and Research Department of Mathematics, Kongunadu Arts and Science College(Autonomous), Coimbatore, India
[6]Department of Mathematics, College of Arts and Sciences, Prince Sattam Bin Abdulaziz University, Wadi Aldawaser, Saudi Arabia

Correspondence
Kottakkaran Sooppy Nisar, Department of Mathematics, College of Arts and Sciences, Prince Sattam Bin Abdulaziz University, Wadi Aldawaser, Saudi Arabia.
Email: n.sooppy@psau.edu.sa

Abstract

The investigation of existence and uniqueness of impulsive dynamical fractional systems with quadratic perturbation of second type subject to nonlocal boundary conditions is presented and proved. By employing the fractional theory, Banach contraction technique, and Krasnoselskii's fixed point theorem, we derived some sufficient conditions to ensure the existence of our system. An example is offered to enhance the applicability of the results obtained.

KEYWORDS

fixed point theorems, fractional derivatives and integrals, hybrid differential equations, impulsive conditions, nonlocal boundary conditions

1 | INTRODUCTION

The fractional calculus has a deep-rooted history just like the traditionalistic calculus. It is the type of calculus which dabbles with both differentiation and integration of arbitrary order. It has become a significant field of investigation due to its numerous applications in applied sciences and engineering [1–8, 32, 33]. Recently, this field of mathematics has been receiving a great attraction of young researchers and scientists. For knowing about the depth of this theory, one can refer to some famous monographs on fractional calculus of Podlubny [9], Kilbas [10], and Miller [11], in which authors specifically focused on the application part and discussed importance of the subject.

Studying the qualitative properties of differential equations in the framework of fractional derivatives such as the existence and uniqueness, stability and controllability have pulled the attention of many researchers. Since the fixed point theories play an important role in the existence uniqueness issue, scientists have started to their contemporary result to fractional differential or integral equations see [12–31, 34–39].

Dynamical systems with quadratic perturbation constitute a general class of hybrid differential equations. Nowadays such type of hybrid dynamical systems have receiving a huge fame among the researchers due to wide range of application of hybrid differential equations in several areas of real life problems. The study of hybrid differential equations with nonlocal boundary constraints is a common kind of literature but it becomes special in case of added impulsive conditions of noninteger order. Because of the geometrical complexity of the impulsive conditions, it is typical to diagnose the dynamical systems when such conditions are included. In various scientific and engineering disciplines such as physics, chemistry, digital control system, automotive control, transportation systems, mobile robotics, and so on can be seen easily. For more details once can read the articles related to the applications of hybrid differential equations [40–44]. Sometimes it has found that the ordinary differential equation cannot be solved directly and difficult to find out the analytical solution, thus, to come out from this situation these perturbation techniques play an important role and can be helpful. The growth of hybrid fractional differential equations can found in the following works where authors proved the existence and uniqueness results by adopting Banach contraction principle.

Ahmad in [45] explained the existence and uniqueness results for following hybrid system involving the Hadamard fractional derivative. Furthermore, Mahmudov extended the above result [45] in [46] for hybrid differential system of arbitrary order involving Caputo fractional derivative. El Allaoui investigated the results for coupled system of hybrid differential equation in [47]. In continuation of this study Houas [48] extensively studied the main results for the following coupled hybrid differential system subject with integral boundary conditions

$$\begin{cases} D^{\alpha_1}\left(\frac{u_1(t)}{g_1(t,u_1(t),u_2(t))}\right) = f_1(t,u_1(t),u_2(t)), & t \in [0,1], \quad \alpha_1 \in (0,1) \\ D^{\alpha_2}\left(\frac{u_2(t)}{g_2(t,u_1(t),u_2(t))}\right) = f_2(t,u_1(t),u_2(t)), & t \in [0,1], \quad \alpha_2 \in (0,1) \\ u_1(0) = \int_0^{\theta_1} A_1(s)u_1(s)ds, \quad \theta_1 \in (0,1), \\ u_2(0) = \int_0^{\theta_2} A_2(s)u_2(s)ds, \quad \theta_2 \in (0,1), \end{cases}$$

here D^{α_i}, $i = 1, 2$ represents the Caputo's derivative for noninteger order. A_i, $i = 1, 2$ are continuous on [0, 1].

This article is distinguished among the five parts as follows: Section 2 represents the framework and formulation of the hybrid model in which we defined the importance of this article and why we needed to study hybrid kind models. Section 3 is devoted for recalling some fundamentals and needs of basic definitions and lemmas. Section 4 is main part of this paper which presents the outcomes with some appropriate assumptions and applying fixed point techniques. In Section 5, an illustration is given to explain our abstract conclusions.

2 | PROBLEM FORMULATION AND DESCRIPTION

Motivated and provided by the aforementioned articles, we have considered the Caputo fractional derivative ${}^cD^{\alpha}_{0^+}$ with single starting point $t = 0$ of order $\alpha \in (1, 2)$,

$$ {}^cD^{\alpha}_{0^+}\left[\frac{\omega(t)}{f(t,\omega(t))}\right] = H(t,\omega(t)), \quad t \in [0,P], \ \ t \neq t_k, \tag{1}$$

$$\Delta\omega(t_k) = I_k(\omega(t_k^-)), \quad k = 1,2, \ldots , m, \tag{2}$$

$$\Delta^c D^q\left[\frac{\omega(t_k)}{f(t_k,\omega(t_k))}\right] = J_k(\omega(t_k^-)), \quad q \in (0,1), \ \ k = 1,2, \ldots , m, \tag{3}$$

$$\omega(0) = a_1 - y(\omega), \quad a_1 \in \mathbb{R}, \tag{4}$$

$$\omega(P) = a_2 - \int_0^P g(s)\left[\frac{\omega(s)}{f(s,\omega(s))}\right] ds, \quad a_2 \in \mathbb{R}, \tag{5}$$

where the continuous functions are defined from $f : [0,P]\times\mathbb{X} \to \mathbb{X}\backslash\{0\}$ and $H : [0,P]\times\mathbb{X} \to \mathbb{X}$. For $0 = t_0 < t_1 < \cdots < t_m < t_{m+1} = P$, the impulsive functions $I_k,\ J_k : \mathbb{X} \to \mathbb{X}$ are continuous and bounded which characterize the jump of solutions at the impulsive point $t = t_k$. Additionally $\Delta\omega(t_k) = \omega(t_k^+) - \omega(t_k^-)$ and $\Delta^c D^q\left[\frac{\omega(t_k)}{f(t_k,\omega(t_k))}\right] = {}^cD^q\left[\frac{\omega(t_k^+)}{f(t_k^+,\omega(t_k^+))}\right] - {}^cD^q\left[\frac{\omega(t_k^-)}{f(t_k^-,\omega(t_k^-))}\right]$, $\omega(t_k^+)$ and $\omega(t_k^-)$ define the right and left-hand limits of $\omega(t)$ at $t = t_k$, respectively, with $\omega(t_i^-) = \omega(t_i)$. Here, $\omega : \mathbb{X} \to \mathbb{X}$, representing a nonlinear function and $g : [0,P] \to \mathbb{X}$ are also continuous functions.

Inspiration by the applications of hybrid dynamical systems, the present work initiates the study of hybrid differential equations with quadratic perturbation of second type in abstract Banach space involving two nonlinearities and derive the basic results by adopting Banach contraction technique and Krasnoselskii's fixed point theorem using some classical tools of functional analysis and fractional calculus.

Definition 2.1 If a continuously differentiable function $\omega \in PC^1_t([0,P],\mathbb{X})$ fulfills:

$$\omega(t) = \begin{cases} f(t,\omega(t))\left[\int_0^t \frac{(t-s)^{\alpha-1}}{\Gamma(\alpha)}H\big(s,\omega(s)\big)ds + a_1 - y(\omega)\right. \\ -\frac{t}{P}\left\{\int_0^P \frac{(P-s)^{\alpha-1}}{\Gamma(\alpha)}H\big(s,\omega(s)\big)ds\right. \\ +\sum_{i=1}^m \frac{I_i(\omega(t_i^-))}{f(t_i,\omega(t_i))} + a_1 - y(\omega) \\ \left.\left. +\sum_{i=1}^m (P-t_i)\left(\frac{\Gamma(2-q)}{t_i^{1-q}}J_i(\omega(t_i^-))\right) + \frac{a_2 - A(\omega)}{f(P,\omega(P))}\right\}\right], \quad t \in [0,t_1), \\ \ldots, \\ f(t,\omega(t))\left[\int_0^t \frac{(t-s)^{\alpha-1}}{\Gamma(\alpha)}H\big(s,\omega(s)\big)ds\right. \\ +\sum_{i=1}^k \frac{I_i(\omega(t_i^-))}{f(t_i,\omega(t_i))} + \left(\frac{P-t}{P}\right)(a_1 - y(\omega)) \\ -\frac{t}{P}\left\{\int_0^P \frac{(P-s)^{\alpha-1}}{\Gamma(\alpha)}H\big(s,\omega(s)\big)ds + \sum_{i=1}^m \frac{I_i(\omega(t_i^-))}{f(t_i,\omega(t_i))}\right. \\ +\sum_{i=1}^m (P-t_i)\left(\frac{\Gamma(2-q)}{t_i^{1-q}}J_i(\omega(t_i^-))\right) \\ \left. +\frac{a_2 - A(\omega)}{f(P,\omega(P))}\right\} + \left.\sum_{i=1}^k (t-t_i)\left(\frac{\Gamma(2-q)}{t_i^{1-q}}J_i(\omega(t_i^-))\right)\right], \quad t \in (t_k,t_{k+1}], \end{cases} \tag{6}$$

where

$$A(\omega)=\frac{1}{1-\frac{1}{f(P,\omega(P))}\int_0^P tg(t)dt}\left[\int_0^P g(t)\left(\int_0^t \frac{(t-s)^{\alpha-1}}{\Gamma(\alpha)}H\big(s,\omega(s)\big)ds\right)dt\right.$$
$$+\sum_{i=1}^{k}\frac{I_i(\omega(t_i^-))}{f(t_i,\omega(t_i))}\int_0^P g(t)dt+(a_1-y(\omega))\int_0^P\left(\frac{P-t}{P}\right)g(t)dt$$
$$-\frac{1}{P}\left\{\int_0^P\frac{(P-s)^{\alpha-1}}{\Gamma(\alpha)}H\big(s,\omega(s)\big)ds+\sum_{i=1}^{m}\frac{I_i(\omega(t_i^-))}{f(t_i,\omega(t_i))}\right.$$
$$\left.+\sum_{i=1}^{m}(P-t_i)\left(\frac{\Gamma(2-q)}{t_i{}^{1-q}}J_i(\omega(t_i^-))\right)+\frac{a_2}{f(P,\omega(P))}\right\}\int_0^P tg(t)dt$$
$$\left.+\sum_{i=1}^{k}\left(\frac{\Gamma(2-q)}{t_i{}^{1-q}}J_i(\omega(t_i^-))\right)\int_0^P(t-t_i)g(t)dt\right],$$

then it is said to be the solution of problem (1)–(5).

3 | PRELIMINARIES

To treat the impulsive conditions, define the space $PC_t=PC([0,P],\mathbb{X})$, $t\in[0,P]$, the functions $\omega:[0,P]\to\mathbb{X}$ are continuous everywhere except finite number of points t_i, $i=1,2,\ldots,m$, where $\omega(t_i^+)$ and $\omega(t_i^-)$ exist provided $\omega(t_i^-)=\omega(t_i)$ and

$$\|\omega\|_{PC_t}=\sup_{t\in[0,P]}\{\|\omega(t)\|_{\mathbb{X}},\ \ \omega\in PC\},$$

and $PC_t^1=PC^1([0,P],\mathbb{X})$, $t\in[0,P]$, the functions $\omega:[0,P]\to\mathbb{X}$ are continuously differentiable everywhere except finite number of points t_i, $i=1,\ldots,m$, where $\omega'(t_i^+)$ and $\omega'(t_i^-)$ exist provided $\omega'(t_i^-)=\omega'(t_i)$ and

$$\|\omega\|_{PC_t^1}=\sup_{t\in[0,P]}\{\|\omega(t)\|_{PC},\|\omega'(t)\|_{PC}\}.$$

Definition 3.1 [9] The fractional integral of order α for $g:[0,\infty)\to\mathbb{R}$ is

$$I_t^\alpha g(t)=\int_0^t\frac{(t-s)^{\alpha-1}}{\Gamma(\alpha)}g(s)ds,\quad t>0,\ \ \alpha>0,$$

provided the right side is point-wise defined on $[0,\infty)$.

Definition 3.2 [9] The Riemann–Liouville derivative of $g:[0,\infty)\to\mathbb{R}$ is

$${}^{L}D_t^\alpha g(t)=\frac{1}{\Gamma(n-\alpha)}\left(\frac{d}{dt}\right)^n\int_0^t(t-s)^{n-\alpha-1}g(s)ds,\quad t>0,\ \ n-1<\alpha<n.$$

Definition 3.3 [9] The Caputo derivative of $g:[0,\infty)\to\mathbb{R}$ is:

$${}^{c}D_t^\alpha g(t)={}^{L}D_t^\alpha\left[g(t)-\sum_{k=0}^{n-1}\frac{t^k}{k!}g^{(k)}(0)\right],\quad t>0,\ \ n-1<\alpha<n.$$

Remark 3.1 [9] If $g(t) \in C^n[0, \infty)$ for order $n-1 < \alpha < n$, then

$$^cD_t^\alpha g(t) = \frac{1}{\Gamma(n-\alpha)} \int_0^t \frac{g^{(n)}(s)}{(t-s)^{\alpha+1-n}} ds = I_t^{n-\alpha} g^{(n)}(t), \quad t > 0.$$

Theorem 3.1 [49] *Assume that S is a nonempty, closed convex, and bounded subset of $\mathbb{X}$ and $A : \mathbb{X} \to \mathbb{X}$, $B : S \to \mathbb{X}$ be two operators provided*

a. *A is Lipschitzian with a function ψ,*
b. *B is continuous completely,*
c. *$u = AuBv \Rightarrow u \in S$ for all $v \in S$, and*
d. *$\psi M < 1$, with $M = \|B(S)\| = \sup\{\|Bu\| : u \in S\}$.*

Then $AuBu = u$ has a solution in S.

Lemma 3.2 [9] *Let $\alpha > 0$, then the differential equation*

$$^cD^\alpha h(t) = 0,$$

has solutions $h(t) = c_0 + c_1 t + c_2 t^2 + \cdots + c_{n-1} t^{n-1}$ and $I^{\alpha c} D^\alpha h(t) = h(t) + c_0 + c_1 t + c_2 t^2 + \cdots + c_{n-1} t^{n-1}$ where $c_i \in \mathbb{R}$, $i = 0, 1, \ldots, n-1$, $n = [\alpha] + 1$.

4 | DISCUSSION ON MAIN RESULTS

For the purpose of deriving the existence of mild solution of the hybrid boundary value problem, consider the following suppositions:

(A_0) $\omega \to \frac{\omega}{f(t,\omega)}$ is increasing function in $\mathbb{X}$ almost everywhere, $t \in [0, P]$.
(A_1) f and H satisfy the Lipschitz conditions with $L_1, L_2 > 0$, that is

$$\|f(t, \omega_1) - f(t, v_1)\|_{\mathbb{X}} \le L_1 \|\omega_1 - v_1\|_{\mathbb{X}},$$
$$\|H(t, \omega_2) - H(t, v_2)\|_{\mathbb{X}} \le L_2 \|\omega_2 - v_2\|_{\mathbb{X}},$$

where $\omega_i, \; v_i \in \mathbb{X}, \; i = 1, 2$, and $t \in [0, P]$.

(A_2) For $M_1 > 0$ provided

$$\|y(\omega_1) - y(\omega_2)\|_{\mathbb{X}} \le M_1 \|\omega_1 - \omega_2\|_{\mathbb{X}}, \quad \forall \omega_1, \; \omega_2 \in \mathbb{X}.$$

(A_3) For some functions $h_1, \; h_2 : [0, P] \to \mathbb{X}$, $\Omega : \mathbb{X} \to \mathbb{X}$ is continuous and nondecreasing function provided

$$\| H(t, \omega,)\|_{\mathbb{X}} \le h_1(t)\Omega(\| \omega\|_{\mathbb{X}}),$$
$$\| f(t, \omega,)\|_{\mathbb{X}} \le h_2(t)\Omega(\| \omega\|_{\mathbb{X}}),$$

where $t \in [0, P], \; \forall \omega \in \mathbb{X}$.

(A_4) For a constant $M_2 > 0$ yields

$$\|y(\omega)\|_{\mathbb{X}} \le M_2, \; \forall \omega \in \mathbb{X}.$$

(A_5) $0 \le g(t) \le \eta$, and $1 - \frac{\eta P^2}{2f(P,\omega(P))} \ge 0$, $\forall t, \; \eta \in [0, P], \; \omega \in \mathbb{X}$.

Theorem 4.1 *Assume that* (A_0)–(A_5) *hold and*

$$\begin{aligned}\omega = {} & \frac{2P^{\alpha}}{\Gamma(\alpha+1)}\big(L_1 \parallel h_1 \parallel \Omega(r) + L_2 \parallel h_2 \parallel \Omega(r)\big) + 2mL_1\left\|\frac{I_i(\omega(t_i^-))}{f(t_i,\omega(t_i))}\right\| \\ & + 2m \parallel h_2 \parallel \Omega(r)\left\|\frac{I_i(\omega(t_i^-))}{f(t_i,\omega(t_i))} - \frac{I_i(\upsilon(t_i^-))}{f(t_i,\upsilon(t_i))}\right\| + 2\{L_1M_2 + \parallel h_2 \parallel \Omega(r)M_1\} \\ & + 2mL_1P^q\Gamma(2-q)\|J_i(\omega(t_i^-))\| + 2m \parallel h_2 \parallel \Omega(r)P^q\Gamma(2-q) \parallel J_i(\omega(t_i^-)) - J_i(\upsilon(t_i^-)) \parallel \\ & + \frac{\eta P}{2f(P,\omega(P)) + \eta P^2}\left\{\frac{3L_2P^{\alpha}}{\Gamma(\alpha+1)} + 3m\left\|\frac{I_i(\omega(t_i^-))}{f(t_i,\omega(t_i))} - \frac{I_i(\upsilon(t_i^-))}{f(t_i,\upsilon(t_i))}\right\|\right. \\ & \left. + M_1 + 2mP^q\Gamma(2-q)\|J_i(\omega(t_i^-)) - J_i(\upsilon(t_i^-))\|\right\} \\ \leq {} & 1,\end{aligned}$$

is fulfilled, Then the system (1)–(5) *will possess a unique solution.*

Proof. Define an operator $\mathcal{F} : PC_t \to PC_t$ defined as

$$\begin{aligned}\mathcal{F}\omega(t) = f(t,\omega(t)) & \left[\int_0^t \frac{(t-s)^{\alpha-1}}{\Gamma(\alpha)}H\big(s,\omega(s)\big)ds + \sum_{i=1}^{k}\frac{I_i(\omega(t_i^-))}{f(t_i,\omega(t_i))} + \left(\frac{P-t}{P}\right)(a_1 - y(\omega))\right. \\ & - \frac{t}{P}\left\{\int_0^P \frac{(P-s)^{\alpha-1}}{\Gamma(\alpha)}H\big(s,\omega(s)\big)ds\right. \\ & \left. + \sum_{i=1}^{m}\frac{I_i(\omega(t_i^-))}{f(t_i,\omega(t_i))} + \sum_{i=1}^{m}(P-t_i)\left(\frac{\Gamma(2-q)}{t_i^{1-q}}J_i(\omega(t_i^-))\right) + \frac{a_2 - A(\omega)}{f(P,\omega(P))}\right\} \\ & \left. + \sum_{i=1}^{k}(t-t_i)\left(\frac{\Gamma(2-q)}{t_i^{1-q}}J_i(\omega(t_i^-))\right)\right].\end{aligned}$$

Using the dominated convergence theorem, the continuity of H and f implies the continuity of $\mathcal{F}$ at any $\omega \in PC_t$. Hence $\mathcal{F}(PC([0,P]),\mathbb{X}) \subset PC([0,P],\mathbb{X})$. Let us consider a closed ball $B_r = \{\omega \in PC_t([0,P],\mathbb{X}) : \|\omega\|_{PC} \leq r\}$ for some $r \geq 0$. Accordingly,

$$\begin{aligned}\parallel \mathcal{F}\omega(t)\|_{\mathbb{X}} \leq {} & [\| f(t,\omega(t)) - f(t,0) \parallel + \parallel f(t,0) \|]\int_0^t \frac{(t-s)^{\alpha-1}}{\Gamma(\alpha)} \parallel H(s,\omega(s)) \parallel ds \\ & + \sum_{i=1}^{k}\left\|\frac{I_i(\omega(t_i^-))}{f(t_i,\omega(t_i))}\right\| + \frac{|P-t|}{P}(a_1 + \parallel y(\omega) \|) \\ & + \frac{|t|}{P}\left\{\int_0^P \frac{(P-s)^{\alpha-1}}{\Gamma(\alpha)} \parallel H\big(s,\omega(s)\big) \parallel ds + \sum_{i=1}^{m}\left\|\frac{I_i(\omega(t_i^-))}{f(t_i,\omega(t_i))}\right\|\right. \\ & \left. + \sum_{i=1}^{m}|P-t_i|\left(\frac{\Gamma(2-q)}{|t_i^{1-q}|} \parallel J_i(\omega(t_i^-)) \parallel\right) + \frac{a_2 + \parallel A(\omega) \parallel}{f(P,\omega(P))}\right\} \\ & + \sum_{i=1}^{k}|t-t_i|\left(\frac{\Gamma(2-q)}{|t_i^{1-q}|} \parallel J_i(\omega(t_i^-)) \parallel\right).\end{aligned}$$

Using the given assumptions, we get

$$\begin{aligned}\|\mathcal{F}\omega(t)\|_{PC_t} \leq {} & \frac{(L_1r + F_0 + 1)P^{\alpha}}{\Gamma(\alpha+1)} \parallel h_1 \parallel \Omega(r) \\ & + 2m\left\|\frac{I_i(\omega(t_i^-))}{f(t_i,\omega(t_i))}\right\| + a_1 + M_2 + 2mP^q\Gamma(2-q) \parallel J_i(\omega(t_i^-)) \parallel + \frac{a_2 + \gamma}{f(P,\omega(P))}\end{aligned}$$

$$\leq r.$$

Clearly, $\mathcal{F}$ maps B_r into itself. For the contraction principle $\omega, \upsilon \in PC([0,P],\mathbb{X})$, and $t \in [0,P]$, we have

$$
\begin{aligned}
&\| \mathcal{F}\omega(t) - \mathcal{F}\upsilon(t)\|_{\mathbb{X}} \\
&\leq \left\| f\big(t,\omega(t)\big) \int_0^t \frac{(t-s)^{\alpha-1}}{\Gamma(\alpha)} H\big(s,\omega(s)\big)ds - f\big(t,\upsilon(t)\big) \int_0^t \frac{(t-s)^{\alpha-1}}{\Gamma(\alpha)} H\big(s,\upsilon(s)\big)ds \right\| \\
&+ \left\| f\big(t,\omega(t)\big) \sum_{i=1}^{k} \frac{I_i(\omega(t_i^-))}{f(t_i,\omega(t_i))} - f\big(t,\upsilon(t)\big) \sum_{i=1}^{k} \frac{I_i(\upsilon(t_i^-))}{f(t_i,\upsilon(t_i))} \right\| \\
&+ \left| \frac{P-t}{P} \right| \|f\big(t,\omega(t)\big)y(\omega) - f\big(t,\upsilon(t)\big)y(\upsilon)\| + \| f(t,\omega(t)) \frac{t}{P} \left\{ \int_0^P \frac{(P-s)^{\alpha-1}}{\Gamma(\alpha)} H\big(s,\omega(s)\big)ds \right. \\
&+ \sum_{i=1}^{m} \frac{I_i(\omega(t_i^-))}{f(t_i,\omega(t_i))} + \sum_{i=1}^{m} (P-t_i) \left(\frac{\Gamma(2-q)}{t_i{}^{1-q}} J_i(\omega(t_i^-)) \right) \\
&+ \left. \frac{A(\omega)}{f(P,\omega(P))} \right\} - f(t,\upsilon(t)) \frac{t}{P} \left\{ \int_0^P \frac{(P-s)^{\alpha-1}}{\Gamma(\alpha)} H\big(s,\upsilon(s)\big)ds \right. \\
&+ \left. \sum_{i=1}^{m} \frac{I_i(\upsilon(t_i^-))}{f(t_i,\upsilon(t_i))} + \sum_{i=1}^{m} (P-t_i) \left(\frac{\Gamma(2-q)}{t_i{}^{1-q}} J_i(\upsilon(t_i^-)) \right) + \frac{A(\upsilon)}{f(P,\upsilon(P))} \right\} \| \\
&+ \left\| f\big(t,\omega(t)\big) \sum_{i=1}^{k} (t-t_i) \left(\frac{\Gamma(2-q)}{t_i{}^{1-q}} J_i(\omega(t_i^-)) \right) - f\big(t,\upsilon(t)\big) \sum_{i=1}^{k} (t-t_i) \left(\frac{\Gamma(2-q)}{t_i{}^{1-q}} J_i(\upsilon(t_i^-)) \right) \right\| \\
&\leq \| f(t,\omega(t)) - f(t,\upsilon(t)) \| \int_0^t \frac{(t-s)^{\alpha-1}}{\Gamma(\alpha)} \| H(s,\omega(s)) \| ds \\
&+ \| f(t,\upsilon(t)) \| \int_0^t \frac{(t-s)^{\alpha-1}}{\Gamma(\alpha)} \| H(s,\omega(s)) - H(s,\upsilon(s)) \| ds \\
&+ \| f(t,\omega(t)) - f(t,\upsilon(t)) \| \sum_{i=1}^{k} \left\| \frac{I_i(\omega(t_i^-))}{f(t_i,\omega(t_i))} \right\| + \| f(t,\upsilon(t)) \| \sum_{i=1}^{k} \| \left\| \frac{I_i(\omega(t_i^-))}{f(t_i,\omega(t_i))} - \frac{I_i(\upsilon(t_i^-))}{f(t_i,\upsilon(t_i))} \right\| \\
&+ \left| \frac{P-t}{P} \right| [\| f\big(t,\omega(t)\big) - f\big(t,\upsilon(t)\big) \| \| y(\omega) \| + \| f\big(t,\upsilon(t)\big) \| \| y(\omega) - y(\upsilon) \|] \\
&+ \left| \frac{t}{P} \right| \left[\| f\big(t,\omega(t)\big) - f\big(t,\upsilon(t)\big) \| \left\{ \int_0^P \frac{(P-s)^{\alpha-1}}{\Gamma(\alpha)} \| H\big(s,\omega(s)\big) \| ds \right. \right. \\
&+ \sum_{i=1}^{m} \left\| \frac{I_i(\omega(t_i^-))}{f(t_i,\omega(t_i))} \right\| + \sum_{i=1}^{m} | P-t_i | \left(\frac{\Gamma(2-q)}{t_i{}^{1-q}} \| J_i(\omega(t_i^-)) \| \right) \\
&+ \left. \frac{\| A(\omega) \|}{f(P,\omega(P))} \right\} + \| f(t,\upsilon(t)) \| \left\{ \int_0^P \frac{(P-s)^{\alpha-1}}{\Gamma(\alpha)} \| H\big(s,\omega(s)\big) \right. \\
&- H(s,\upsilon(s)) \| ds + \sum_{i=1}^{m} \left\| \frac{I_i(\omega(t_i^-))}{f(t_i,\omega(t_i))} - \frac{I_i(\upsilon(t_i^-))}{f(t_i,\upsilon(t_i))} \right\| \\
&+ \sum_{i=1}^{m} | P-t_i | \left(\frac{\Gamma(2-q)}{t_i{}^{1-q}} \|J_i(\omega(t_i^-)) - J_i(\upsilon(t_i^-))\| \right) \\
&+ \left. \left. \frac{\| A(\omega) - A(\upsilon) \|}{f(P,\omega(P))} \right\} \right] + \| f(t,\omega(t)) - f(t,\upsilon(t)) \| \sum_{i=1}^{k} | t-t_i | \left(\frac{\Gamma(2-q)}{t_i{}^{1-q}} \|J_i(\omega(t_i^-))\| \right)
\end{aligned}
$$

$$+ \parallel f(t,\upsilon(t)) \parallel \sum_{i=1}^{k} \mid t - t_i \mid \left(\frac{\Gamma(2-q)}{t_i{}^{1-q}} \parallel J_i(\omega(t_i^-)) - J_i(\upsilon(t_i^-)) \parallel \right).$$

By the axioms (A_0)–(A_5), we obtain

$$\begin{aligned}\parallel \mathcal{F}\omega(t) - \mathcal{F}\upsilon(t)\|_{PC_t} \leq & \left[\frac{2P^\alpha}{\Gamma(\alpha+1)}(L_1 \parallel h_1 \parallel \Omega(r) + L_2 \parallel h_2 \parallel \Omega(r)) + 2mL_1 \left\| \frac{I_i(\omega(t_i^-))}{f(t_i,\omega(t_i))} \right\| \right.\\ & + 2m \parallel h_2 \parallel \Omega(r) \left\| \frac{I_i(\omega(t_i^-))}{f(t_i,\omega(t_i))} - \frac{I_i(\upsilon(t_i^-))}{f(t_i,\upsilon(t_i))} \right\| \\ & + 2\{L_1M_2 + \parallel h_2 \parallel \Omega(r)M_1\} + 2mL_1P^q\Gamma(2-q)\|J_i(\omega(t_i^-))\| \\ & + 2m \parallel h_2 \parallel \Omega(r)P^q\Gamma(2-q) \parallel J_i(\omega(t_i^-)) - J_i(\upsilon(t_i^-)) \parallel \\ & + \frac{\eta P}{2f(P,\omega(P)) + \eta P^2} \left\{ \frac{3L_2P^\alpha}{\Gamma(\alpha+1)} + 3m \left\| \frac{I_i(\omega(t_i^-))}{f(t_i,\omega(t_i))} - \frac{I_i(\upsilon(t_i^-))}{f(t_i,\upsilon(t_i))} \right\| \right. \\ & \left.\left. + \; M_1 + 2mP^q\Gamma(2-q)\|J_i(\omega(t_i^-)) - J_i(\upsilon(t_i^-))\| \right\} \right] \parallel \omega - \upsilon\|_{PC_t} \\ \leq & \; \omega \parallel \omega - \upsilon\|_{PC_t}.\end{aligned}$$

As $\omega < 1$, we emphasize that $\mathcal{F}$ satisfies the contraction principle, hence by Banach fixed point theorem, (1)–(5) will have a unique solution. ■

Theorem 4.2 *If* (A_0)–(A_5) *are valid and the following hypothesis* (A_6) *hold*:

$$\frac{L_1P^\alpha}{\Gamma(\alpha+1)}\|h\| \lim_{r\to+\infty} \frac{\Omega(r)}{r} < 1.$$

Then the initial-boundary value problem (1)–(5) *has at least one solution.*

Proof. Let us consider the closed ball $\mathcal{B}_r = \{\omega \in PC_t([0,P],\mathbb{X}) : \|\omega\| \leq r\}$ for some $r \geq 0$. Define P and T on $\mathcal{B}_r$ as

$$\begin{aligned}(P\omega)(t) = f(t,\omega(t)) & \left[\sum_{i=1}^{k} \frac{I_i(\omega(t_i^-))}{f(t_i,\omega(t_i))} + \sum_{i=1}^{k}(t-t_i)\left(\frac{\Gamma(2-q)}{t_i{}^{1-q}} J_i(\omega(t_i^-)) \right) \right. \\ & \left. - \frac{t}{P} \left\{ \sum_{i=1}^{m} \frac{I_i(\omega(t_i^-))}{f(t_i,\omega(t_i))} + \sum_{i=1}^{m}(P-t_i)\left(\frac{\Gamma(2-q)}{t_i{}^{1-q}} J_i(\omega(t_i^-)) \right) \right\} \right], \\ (T\omega)(t) = f(t,\omega(t)) & \left[\int_0^t \frac{(t-s)^{\alpha-1}}{\Gamma(\alpha)} H\big(s,\omega(s)\big)ds + \left(\frac{P-t}{P} \right)(a_1 - y(\omega)) \right. \\ & \left. - \frac{t}{P} \left\{ \int_0^P \frac{(P-s)^{\alpha-1}}{\Gamma(\alpha)} H\big(s,\omega(s)\big)ds + \frac{a_2 - A(\omega)}{f(P,\omega(P))} \right\} \right].\end{aligned}$$

Step 1: To prove, there exists $r_0 > 0$ with $P\omega + Q\upsilon \in \mathcal{B}_{r_0}$, for $\omega, \upsilon \in \mathcal{B}_{r_0}$. If this were not true, then for each $r > 0$, for some ω_r, $\upsilon_r \in \mathcal{B}_r$ and $t_r \in [0, P]$ provided $\|(P\omega_r)(t_r) + (T\upsilon_r)(t_r)\| > r$. Hence

$$\begin{aligned} r & < \|(P\omega_r)(t_r) + (Q\upsilon_r)(t_r)\| \\ & \leq \frac{(L_1r + F_0 + 1)P^\alpha}{\Gamma(\alpha+1)} \parallel h_1 \parallel \Omega(r) + 2m \left\| \frac{I_i(\omega(t_i^-))}{f(t_i,\omega(t_i))} \right\| + a_1 + M_2 \\ & \quad + 2mP^q\Gamma(2-q) \parallel J_i(\omega(t_i^-)) \parallel + \frac{a_2 + \gamma}{f\big(P,\omega(P)}.\end{aligned}$$

Dividing by r and applying the lower limit as $r \to \infty$,

$$1 \leq \frac{L_1 P^\alpha}{\Gamma(\alpha+1)} \|h\| \lim_{r\to+\infty} \frac{\Omega(r)}{r},$$

which shows contradiction to (A_6). Thus, there exists $r_0 > 0$ with $P\omega + Q\upsilon \in \mathcal{B}_{r_0}$, for all $\omega, \upsilon \in \mathcal{B}_{r_0}$.

Step 2: For all $t \in [0, P]$ and $\omega, \upsilon \in \mathcal{B}_r$, we obtain

$$\begin{aligned}
&\|(P\omega)(t) - (P\upsilon)(t)\| \\
&\leq \left\| f\big(t,\omega(t)\big)\sum_{i=1}^{k}\frac{I_i(\omega(t_i^-))}{f(t_i,\omega(t_i))} - f\big(t,\upsilon(t)\big)\sum_{i=1}^{k}\frac{I_i(\upsilon(t_i^-))}{f(t_i,\upsilon(t_i))}\right\| \\
&\quad + \left\| f\big(t,\omega(t)\big)\sum_{i=1}^{k}(t-t_i)\left(\frac{\Gamma(2-q)}{t_i^{1-q}}J_i(\omega(t_i^-))\right)\right. \\
&\left. - f\big(t,\upsilon(t)\big)\sum_{i=1}^{k}(t-t_i)\left(\frac{\Gamma(2-q)}{t_i^{1-q}}J_i(\upsilon(t_i^-))\right)\right\| \\
&\quad + \left\| f\big(t,\omega(t)\big)\frac{t}{P}\left\{\sum_{i=1}^{m}\frac{I_i(\omega(t_i^-))}{f(t_i,\omega(t_i))} + \sum_{i=1}^{m}(P-t_i)\left(\frac{\Gamma(2-q)}{t_i^{1-q}}J_i(\omega(t_i^-))\right)\right\}\right. \\
&\quad \left. - f\big(t,\upsilon(t)\big)\frac{t}{P}\left\{\sum_{i=1}^{m}\frac{I_i(\upsilon(t_i^-))}{f(t_i,\upsilon(t_i))} + \sum_{i=1}^{m}(P-t_i)\left(\frac{\Gamma(2-q)}{t_i^{1-q}}J_i(\upsilon(t_i^-))\right)\right\}\right\| \\
&\leq \|f\big(t,\omega(t)\big) - f\big(t,\upsilon(t)\big)\| \sum_{i=1}^{k}\left\|\frac{I_i(\omega(t_i^-))}{f(t_i,\omega(t_i))}\right\| + \|f\big(t,\upsilon(t)\big)\|\sum_{i=1}^{k}\left\|\frac{I_i(\omega(t_i^-))}{f(t_i,\omega(t_i))} - \frac{I_i(\upsilon(t_i^-))}{f(t_i,\upsilon(t_i))}\right\| \\
&\quad + \|f\big(t,\omega(t)\big) - f\big(t,\upsilon(t)\big)\| \sum_{i=1}^{k}|(t-t_i)|\left(\frac{\Gamma(2-q)}{t_i^{1-q}}\|J_i(\omega(t_i^-))\|\right) \\
&\quad + \|f\big(t,\upsilon(t)\big)\|\sum_{i=1}^{k}|(t-t_i)|\left(\frac{\Gamma(2-q)}{t_i^{1-q}}\|J_i(\omega(t_i^-)) - J_i(\upsilon(t_i^-))\|\right) \\
&\quad + \left|\frac{t}{P}\right|\left[\ \| f(t,\omega(t)) - f(t,\upsilon(t))\ \| \left(\sum_{i=1}^{m}\left\|\frac{I_i(\omega(t_i^-))}{f(t_i,\omega(t_i))}\right\|\right.\right. \\
&\quad \left.\left. + \sum_{i=1}^{m}|(P-t_i)|\left(\frac{\Gamma(2-q)}{t_i^{1-q}}\|J_i(\omega(t_i^-))\|\right)\right)\right] \\
&\quad + \left|\frac{t}{P}\right|\left[\|f\big(t,\upsilon(t)\big)\|\left(\sum_{i=1}^{m}\left\|\frac{I_i(\omega(t_i^-))}{f(t_i,\omega(t_i))} - \frac{I_i(\upsilon(t_i^-))}{f(t_i,\upsilon(t_i))}\right\|\right.\right. \\
&\quad \left.\left. + \sum_{i=1}^{m}|(P-t_i)|\left(\frac{\Gamma(2-q)}{t_i^{1-q}}\|J_i(\omega(t_i^-)) - J_i(\upsilon(t_i^-))\|\right)\right)\right].
\end{aligned}$$

By the axioms (A_0)–(A_5), we have

$$\begin{aligned}
\|(P\omega)(t) - (P\upsilon)(t)\| \leq &\left[2mL_1\left\|\frac{I_i(\omega(t_i^-))}{f(t_i,\omega(t_i))}\right\| + 2m\|h_2\|\Omega(r)\left\|\frac{I_i(\omega(t_i^-))}{f(t_i,\omega(t_i))} - \frac{I_i(\upsilon(t_i^-))}{f(t_i,\upsilon(t_i))}\right\|\right. \\
&+ 2mL_1P^q\Gamma(2-q)\|J_i(\omega(t_i^-))\| \\
&\left. + 2m\|h_2\|\Omega(r)P^q\Gamma(2-q)\|J_i(\omega(t_i^-)) - J_i(\upsilon(t_i^-))\|\right]\ \|\omega - \upsilon\|_{PC_t}
\end{aligned}$$

$$\leq \omega\|\omega - v\|_{PC_t}.$$

As $\omega < 1$, we emphasize that P is contraction mapping.

Step 3: Since the continuity of H implies T is continuous. It is enough to ensure, T is a compact operator. By Theorem 4.1, it follows that $T(\mathcal{B}_{r_0})$ is uniformly bounded on $PC_t([0,P],\mathbb{X})$. Hence, we first move on to $T(\mathcal{B}_{r_0})$ is equicontinuous. In this need, choose for any $t_k < \varsigma_1 < \varsigma_2 < t_{k+1}$, we have

$$\begin{aligned}
&\|(T\omega)(\varsigma_2) - (T\omega)(\varsigma_1)\| \\
&\leq \Bigg\| f\big(\varsigma_2, \omega(\varsigma_2)\big) \left[\int_0^{\varsigma_2} \frac{(\varsigma_2 - s)^{\alpha-1}}{\Gamma(\alpha)} H\big(s,\omega(s)\big)ds + \left(\frac{P-\varsigma_2}{P}\right)(a_1 - y(\omega))\right. \\
&\quad \left. - \frac{\varsigma_2}{P}\left\{\int_0^P \frac{(P-s)^{\alpha-1}}{\Gamma(\alpha)} H\big(s,\omega(s)\big)ds + \frac{a_2 - A(\omega)}{f(P,\omega(P))}\right\}\right] \\
&\quad - f(\varsigma_1, u(\varsigma_1)) \left[\int_0^{\varsigma_1} \frac{(\varsigma_1 - s)^{\alpha-1}}{\Gamma(\alpha)} H\big(s,\omega(s)\big)ds + \left(\frac{P-\varsigma_1}{P}\right)(a_1 - y(\omega))\right. \\
&\quad \left. - \frac{\varsigma_1}{P}\left\{\int_0^P \frac{(P-s)^{\alpha-1}}{\Gamma(\alpha)} H\big(s,\omega(s)\big)ds + \frac{a_2 - A(\omega)}{f(P,\omega(P))}\right\}\right]\Bigg\| \\
&\leq \|h_2\|\Omega(r) \Bigg\| \left[\left(\int_0^{\varsigma_2} \frac{(\varsigma_2 - s)^{\alpha-1}}{\Gamma(\alpha)} H\big(s,\omega(s)\big)ds - \int_0^{\varsigma_1} \frac{(\varsigma_1 - s)^{\alpha-1}}{\Gamma(\alpha)} H\big(s,\omega(s)\big)ds\right)\right. \\
&\qquad \left. + (a_1 - y(\omega))\left(\frac{P-\varsigma_2}{P} - \frac{P-\varsigma_1}{P}\right) + \left(\frac{\varsigma_2}{P} - \frac{\varsigma_1}{P}\right)\int_0^P \frac{(P-s)^{\alpha-1}}{\Gamma(\alpha)} H\big(s,\omega(s)\big)ds\right]\Bigg\| \\
&\leq \|h_2\|\Omega(r) \Bigg\| \int_0^{\varsigma_2} \frac{1}{\Gamma(\alpha)}((\varsigma_2 - s)^{\alpha-1} - (\varsigma_1 - s)^{\alpha-1}) H\big(s,\omega(s)\big)ds \\
&\qquad - \int_{\varsigma_2}^{\varsigma_1} \frac{(\varsigma_1 - s)^{\alpha-1}}{\Gamma(\alpha)} H(s,\omega(s))ds + (a_1 - y(\omega))\left(\frac{P-\varsigma_2}{P} - \frac{P-\varsigma_1}{P}\right) \\
&\qquad + \left(\frac{\varsigma_2}{P} - \frac{\varsigma_1}{P}\right)\int_0^P \frac{(P-s)^{\alpha-1}}{\Gamma(\alpha)} H\big(s,\omega(s)\big)ds\Bigg]\Bigg\|.
\end{aligned}$$

Therefore, $\|(T\omega)(\varsigma_2) - (T\omega)(\varsigma_1)\| \to 0$ as $\varsigma_1 - \varsigma_2 \to 0$. By employing Ascoli theorem, T is a compact operator. Hence, there exists a fixed point for $\mathbb{F}$ on $\mathcal{B}_r$ by Krasnoselskii fixed point theorem, which is the solution of (1)–(5). ■

5 | EXAMPLE

Consider the system as:

$$^cD_{0^+}^{\frac{3}{2}}\left[\frac{\omega(t)}{f(t,\omega(t))}\right] = H(t,\omega(t)), \quad t \in [0,1], \ \ t \neq \left(\frac{3}{2}\right), \tag{7}$$

$$\Delta\omega\left(\frac{3}{2}\right) = I\left(\omega\left(\frac{3}{2}\right)\right), \quad \Delta^cD^{\frac{1}{2}}\left[\frac{\omega\left(\frac{3}{2}\right)}{f\left(\frac{3}{2},\omega\left(\frac{3}{2}\right)\right)}\right] = J\left(\omega\left(\frac{3}{2}\right)\right), \tag{8}$$

$$\omega(0) = a_1 - y(\omega), \quad \omega(1) = a_2 - \int_0^1 s\left[\frac{\omega(s)}{f(s,\omega(s))}\right]ds. \tag{9}$$

Here, consider the hybrid boundary value problem with $f(t,\omega(t)) = \frac{|\omega(t)|}{18+e^t+t^2}$, $H(t,\omega(t)) = \frac{e^{-at}|\omega(t)|}{(1+e^t)(1+|\omega(t)|)}$, $a > 0$. It is also mention that $y(\omega) = \sum_{i=1}^{m} d_i\omega(\zeta_i)$, where $0<\zeta_1<\zeta_2<\cdots<\zeta_m<1$ and d_i, $i = 1, 2, \ldots, m$ are positive constants with $\sum_{i=1}^{m} d_i = \frac{1}{9}$. We also choose that the positive real constants $a_1 = a_2 = 0$. Now let us consider $\omega, \upsilon \in PC$ and $t \in [0, 1]$. Clearly

$$|f(t,\omega)-f(t,\upsilon)| \leq \frac{1}{19}|\omega-\upsilon|, \quad |H(t,\omega)-H(t,\upsilon)| \leq \frac{e^{-at}}{1+e^t}|\omega-\upsilon|.$$

Also we have

$$|y(\omega)-y(\upsilon)| \leq \frac{1}{9}|\omega-\upsilon|.$$

It can also noted that

$$|H(t,\omega)| \leq \frac{e^{-at}}{2}, \quad |f(t,\omega)| \leq \frac{1}{18},$$

with $\Omega(r) = 1$. Here, consider $\omega \in PC$, then we get

$$|y(\omega)| \leq \frac{1}{9}.$$

Since we can observe that all the given assumptions (A_0)–(A_5) are satisfied with $L_1 = \frac{1}{19}$, $L_2 = \frac{e^{-at}}{1+e^t}$, $M_1 = \frac{1}{9}$, $M_2 = \frac{1}{9}$, $h_1 = \frac{e^{-at}}{2}$, $h_2 = \frac{1}{18}$. Thus we can determine that

$$\begin{aligned}
\omega = {} & \frac{2P^\alpha}{\Gamma(\alpha+1)}(L_1 \| h_1 \| \Omega(r) + L_2 \| h_2 \| \Omega(r)) + 2mL_1\left\|\frac{I_i(\omega(t_i^-))}{f(t_i,\omega(t_i))}\right\| \\
& + 2m \| h_2 \| \Omega(r) \left\| \frac{I_i(\omega(t_i^-))}{f(t_i,\omega(t_i))} - \frac{I_i(\upsilon(t_i^-))}{f(t_i,\upsilon(t_i))} \right\| + 2\{L_1M_2 + \| h_2 \| \Omega(r)M_1\} \\
& + 2mL_1P^q\Gamma(2-q)\|J_i(\omega(t_i^-))\| + 2m \| h_2 \| \Omega(r)P^q\Gamma(2-q)\|J_i(\omega(t_i^-)) - J_i(\upsilon(t_i^-))\| \\
& + \frac{\eta P}{2f(P,\omega(P)) + \eta P^2}\left\{\frac{3L_2P^\alpha}{\Gamma(\alpha+1)} + 3m\left\|\frac{I_i(\omega(t_i^-))}{f(t_i,\omega(t_i))} - \frac{I_i(\upsilon(t_i^-))}{f(t_i,\upsilon(t_i))}\right\| + M_1\right. \\
& \left. + 2mP^q\Gamma(2-q)\|J_i(\omega(t_i^-)) - J_i(\upsilon(t_i^-))\|\right\} \\
= {} & e^{-at}(0.03 + 0.07(1+e^t)) + 0.105\left\|\frac{I\left(\omega\left(\frac{3}{2}\right)\right)}{f\left(\frac{3}{2},\omega\left(\frac{3}{2}\right)\right)}\right\| + 0.11\left\|\frac{I\left(\omega\left(\frac{3}{2}\right)\right)}{f\left(\frac{3}{2},\omega\left(\frac{3}{2}\right)\right)} - \frac{I\left(\upsilon\left(\frac{3}{2}\right)\right)}{f\left(\frac{3}{2},\upsilon\left(\frac{3}{2}\right)\right)}\right\| \\
& + 0.02 + 0.09 \left\| J\left(\omega\left(\frac{3}{2}\right)\right) \right\| + 0.14 \left\| J\left(\omega\left(\frac{3}{2}\right)\right) - J\left(\upsilon\left(\frac{3}{2}\right)\right) \right\| \\
& + 0.5\left\{\frac{3e^{-at}}{1.33(1+e^t)} + 3\left\|\frac{I\left(\omega\left(\frac{3}{2}\right)\right)}{f\left(\frac{3}{2},\omega\left(\frac{3}{2}\right)\right)} - \frac{I\left(\upsilon\left(\frac{3}{2}\right)\right)}{f\left(\frac{3}{2},\upsilon\left(\frac{3}{2}\right)\right)}\right\| + 0.11 + 1.76\left\|J\left(\omega\left(\frac{3}{2}\right)\right) - J\left(\upsilon\left(\frac{3}{2}\right)\right)\right\|\right\} \\
< {} & 1.
\end{aligned}$$

Eventually, by using the statement of Theorem (4.1), (7)–(9) has unique solution on $t \in [0, 1]$.

CONFLICT OF INTEREST

The authors declare no conflicts of interest.

ORCID

Fahd Jarad https://orcid.org/0000-0002-3303-0623
Chokkalingam Ravichandran https://orcid.org/0000-0003-0214-1280
Kottakkaran Sooppy Nisar https://orcid.org/0000-0001-5769-4320

REFERENCES

[1] S. Kumar et al., *A new Rabotnov fractional-exponential function-based fractional derivative for diffusion equation under external force*, Math. Methods Appl. Sci. (2020), 1–12. https://doi.org/10.1002/mma.6208.
[2] S. Kumar et al., *An efficient numerical scheme for fractional model of HIV-1 infection of CD4+ T-cells with the effect of antiviral drug therapy*, Alexandria Eng. J. 59 (2020), 2053–2064.
[3] S. Kumar et al., *Analytical approach for time fractional wave equations in the sense of Yang–Abdel-Aty–Cattani via the homotopy perturbation transform method*, Alexandria Eng. J. 59 (2020), 2859–2863.
[4] S. Bhatter et al., *Fractional modified Kawahara equation with Mittag-Leffler law*, Chaos Solitons Fractals 131 (2020), 109508. https://doi.org/10.1016/j.chaos.2019.109508.
[5] S. Bhatter et al., *A new analysis of fractional Drinfeld–Sokolov–Wilson model with exponential memory*, Physica A 537 (2020), 122578.
[6] D. Kumar et al., *A new fractional SIRS-SI malaria disease model with application of vaccines, anti-malarial drugs, and spraying*, Adv. Differ. Eq. 2019 (2019), 278. https://doi.org/10.1186/s13662-019-2199-9.
[7] A. Goswami et al., *An efficient analytical approach for fractional equal width equations describing hydro-magnetic waves in cold plasma*, Physica A 524 (2019), 563–575.
[8] D. Kumar, J. Singh, and D. Baleanu, *Analysis of regularized long-wave equation associated with a new fractional operator with Mittag-Leffler type kernel*, Physica A 492 (2018), 155–167.
[9] I. Podlubny, Fractional differential equations, in *Mathematics in Science and Engineering*, Vol 198, Academic Press, San Diego, CA, 1999.
[10] A. A. Kilbas, H. M. Srivastava, and J. J. Trujillo, in *Theory and applications of fractional differential equations*, Vol 204, Jan Van Mill, Ed., North-Holland Mathematics Studies, Amsterdam, 2006.
[11] K. S. Miller, B. Ross, *An introduction to the fractional calculus and fractional differential equations*, New York: A Wiley-Interscience Publication, 1993, Wiley.
[12] V. Gupta and J. Dabas, *Existence results for a class of fractional order boundary value problems with integrable impulses*, Dyn. Contin. Discrete Impuls. Syst. A: Math. Anal. 25 (2018), 267–285.
[13] V. Gupta and J. Dabas, *Positive solutions for fractional integro boundary value problem of order (1,2) on an unbounded domain*, Differ. Eq. Appl. 11 (2019), 319–333.
[14] V. Gupta and J. Dabas, *Existence of solution for fractional impulsive integro-differential equation with integral boundary conditions*, Funct. Anal. TMA 1 (2015), 56–68.
[15] V. Gupta, J. Dabas, and M. Feckan, *Existence results of solutions for impulsive fractional differential equations*, Nonauton. Dyn. Syst. 5 (2018), 35–51.
[16] C. Ravichandran et al., *New results on nondensely characterized integro-differential equations with fractional order*, Eur. Phys. J. Plus 133 (2018), 1–9.
[17] C. Ravichandran, K. Logeswari, and F. Jarad, *New results on existence in the framework of Atangana–Baleanu derivative for fractional integro-differential equations*, Chaos Solitons Fractals 125 (2019), 194–200.
[18] R. Ameen, F. Jarad, and T. Abdeljawad, *Ulam stability for delay fractional differential equations with a generalized Caputo derivative*, Filomat 32 (2018), 5265–5274.
[19] S. Belmor, C. Ravichandran, and F. Jarad, *Nonlinear generalized fractional differential equations with generalized fractional integral conditions*, J. Taibah Univ. Sci. 14 (2020), 114–123.
[20] Sumati Kumari Panda, Thabet Abdeljawad, and C. Ravichandran, *A complex valued approach to the solutions of Riemann–Liouville integral, Atangana–Baleanu integral operator and non-linear telegraph equation via fixed point method*, Chaos Solitons Fractals 130 (2020), 109439.
[21] C. Ravichandran, N. Valliammal, and Juan J. Nieto, *New results on exact controllability of a class of fractional neutral integrodifferential systems with state-dependent delay in Banach spaces*, J. Franklin Inst. 356 (2019), 1535–1565.
[22] N. Valliammal, C. Ravichandran, and Ju H. Park, *On the controllability of fractional neutral integrodifferential delay equations with nonlocal conditions*, Math. Methods Appl. Sci. 40 (2017), 5044–5055.
[23] Manar A. Alqudah et al., *New results on Caputo fractional-order neutral differential inclusions without compactness*, Adv. Differ. Eq. 2019 (2019), 1–14.
[24] S. Kumar et al., *Numerical solutions of nonlinear fractional model arising in the appearance of the stripe patterns in two-dimensional systems*, Adv. Differ. Eq. 2019 (2019), 413.
[25] Kottakkaran Sooppy Nisar et al., *Solution of fractional kinetic equations involving class of functions and Sumudu transform*, Adv. Differ. Eq. 2020 (2020), 1–11.

[26] P. Veeresha, D. G. Prakasha, and Sunil Kumar, *A fractional model for propagation of classical optical solitons by using nonsingular derivative*, Math. Methods Appl. Sci. (2020). https://doi.org/10.1002/mma.6335.

[27] Y. Y. Gambo et al., *Existence and uniqueness of solutions to fractional differential equations in the frame of generalized Caputo fractional derivatives*, Adv. Differ. Eq. 2018 (2018), 134.

[28] F. Jarad, S. S. Harikrishnan, and K. Kanagarajan, *Existence and stability results to a class of fractional random implicit differential equations involving a generalized Hilfer fractional derivative*, Discrete Contin. Dyn. Syst. 13 (2020), 723–739. https://doi.org/10.3934/dcdss.2020040.

[29] A. A. Ali, K. Shah, and F. Jarad, *Ulam–Hyers stability analysis to a class of nonlinear implicit impulsive fractional differential equations with three point boundary conditions*, Adv. Differ. Eq. 2019 (2019), 7.

[30] A. Ali et al., *Existence and stability analysis to a coupled system of implicit type impulsive boundary value problems of fractional-order differential equations*, Adv. Differ. Eq. 2019 (2019), 101.

[31] S. Ali et al., *Computation of iterative solutions along with stability analysis to a coupled system of fractional order differential equations*, Adv. Differ. Eq. 2019 (2019), 215.

[32] B. Ghanbari, S. Kumar, and R. Kumar, *A study of behaviour for immune and tumor cells in immunogenetic tumour model with non-singular fractional derivative*, Chaos Solitons Fractals 133 (2020), 109619.

[33] Jagdev Singh, Devendra Kumar, and Sunil Kumar, *An efficient computational method for local fractional transport equation occurring in fractal porous media*, Comput. Appl. Math. 39 (2020), 137.

[34] Z. Kayar, *An existence and uniqueness result for linear fractional impulsive boundary value problems as an application of Lyapunov type inequality, Hacettepe*, J. Math. Statist. 47 (2018), 287–297.

[35] H. Khan et al., *Existence results in Banach space for a nonlinear impulsive system*, Adv. Differ. Eq. 2019 (2019), 18.

[36] Wei Gao, Haci Mehmet Baskonus, and Li Shi, *New investigation of bats-hosts-reservoir-people coronavirus model and application to 2019-nCoV system*, Adv. Differ. Eq. 1 (2020), 1–11.

[37] K. K. Ali et al., *New wave behaviors and stability analysis of the Gilson–Pickering equation in plasma physics*, Indian J. Phys. (2020). https://doi.org/10.1007/s12648-020-01773-9.

[38] M. Fečkan, Y. Zhou, and J. Wang, *Response to "Comments on the concept of existence of solution for impulsive fractional differential equations"*, Commun. Nonlinear Sci. Numer. Simul. 19 (2014), 4213–4215.

[39] J. Wang, A. G. Ibrahim, and M. Fečkan, *Nonlocal impulsive fractional differential inclusions with fractional sectorial operators on Banach spaces*, Appl. Math. Comput. 257 (2015), 103–118.

[40] B. C. Dhage, *On a fixed point theorem in Banach algebras with applications*, Appl. Math. Lett. 18 (2005), 273–280.

[41] B. Krogh and N. Lynch, Eds., Hybrid systems: Computation and control, in *Lecture Notes in Computer Science*, Vol 1790, Springer Verlag, New York, 2000.

[42] C. Altafini, A. Speranzon, and K. H. Johansson, Hybrid control of a truck and trailer vehicle, in *Hybrid Systems: Computation and Control*, Lecture Notes in Computer Science, Vol 2289, C. J. Tomlin and M. R. Greenstreet, Eds., Springer Verlag, New York, 2002.

[43] A. Balluchi, P. Soueres, and A. Bicchi, Hybrid feedback control for path tracking by a bounded-curvature vehicle, in *Hybrid Systems: Computation and Control*, Lecture Notes in Computer Science, M. Di Benedetto and A. L. Sangiovanni-Vincentelli, Eds., Springer Verlag, New York, 2001, 2034.

[44] J. Lygeros, D. N. Godbole, and S. Sastry, *A verified hybrid controller for automated vehicles*, IEEE Trans. Automat. Control 43 (1998), 522–539.

[45] V. Gupta, S. N. Bora, and J. J. Nieto, *Dhage iterative principle for quadratic perturbation of fractional boundary value problems with finite delay*, Math. Methods Appl. Sci. (2019), 1–12.

[46] B. Ahmad and S. K. Ntouyas, *Initial-value problems for hybrid Hadamard fractional differential equations*, Electron. J. Differ. Eq. 161 (2014), 1–8.

[47] N. Mahmudov and M. M. Matar, *Existence of mild solution for hybrid differential equations with arbitrary fractional order*, TWMS J. Pure Appl. Math. 8 (2017), 160–169.

[48] M. Houas, *Solvability of a system of fractional hybrid differential equations*, Commun. Optim. Theory 2018 (2018), 12.

[49] A. El Allaoui et al., *Coupled system of mixed differential equations: Linear perturbations of first and second type*, J. Univers. Math. 1 (2018), 24–31.

How to cite this article: Gupta V, Jarad F, Valliammal N, Ravichandran C, Nisar KS. Existence and uniqueness of solutions for fractional nonlinear hybrid impulsive system. *Numer Methods Partial Differential Eq.* 2020;1–13. https://doi.org/10.1002/num.22628

Chaos, Solitons and Fractals 146 (2021) 110915

Contents lists available at ScienceDirect

Chaos, Solitons and Fractals

Nonlinear Science, and Nonequilibrium and Complex Phenomena

journal homepage: www.elsevier.com/locate/chaos

An analysis of controllability results for nonlinear Hilfer neutral fractional derivatives with non-dense domain

Kottakkaran Sooppy Nisar[a,*], K. Jothimani[b], K. Kaliraj[c], C. Ravichandran[d]

[a] Department of Mathematics, College of Arts and Sciences, Prince Sattam Bin Abdulaziz University, Wadi Aldawasir, 11991, Saudi Arabia
[b] Department of Mathematics, Sri Eshwar College of Engineering(Autonomous), Coimbatore, Tamil Nadu 641202, India
[c] Ramanujan Institute for Advanced Study in Mathematics, University of Madras, Chepauk, Chennai, Tamil Nadu 600005, India
[d] Post Graduate and Research Department of Mathematics, Kongunadu Arts and Science College(Autonomous), Coimbatore, Tamil Nadu 641 029, India

ARTICLE INFO

Article history:
Received 12 December 2020
Revised 21 March 2021
Accepted 24 March 2021
Available online 8 April 2021

MSC:
34A08
46B80
93B05
37C25
34K30

Keywords:
Hilfer derivative
Controllability
Non-dense domain
Banach space
Fixed point
Fractional differential equations

ABSTRACT

In this article, the controllability results of the non-dense Hilfer neutral fractional derivative (HNFD) are presented. The results are acknowledged using semigroup theory, fractional calculus, Banach contraction principle, and Mönch technique. Moreover, a numerical analysis is given to enhance our model.

1. Introduction

The generalization of traditional calculus to arbitrary order is fractional calculus; It has attracted several researchers with great potential in the current scenario because it is reliable and growing, employing both theoretical and applied concepts. Valuable tools investigate the hereditary property and memory description of various materials and processes from fractional calculus. The fractional derivatives were developed in the past epoch by Riemann–Liouville (R-L), Grünwald–Letnikov, Riesz, Erdélyi–Kober, Caputo, Hadamard, Hilfer, and others. In recent years, fractional differential equations have been considered as a beautiful, rich domain to be studied because of its applications in life sciences and to engineering, as is witnessed by blossoming literature. Several researchers expressed the natural derivatives of arbitrary order characterized by Riemann–Liouville and Caputo's sense. One can find the results [5,8–10,15,16,19,20,29,34,37,43–47] and monographs [1,13,18,21,24,26,48].

Recently, generalizations of both Caputo and R-L derivatives are introduced and reflected on equations of probability or mathematical physics. The same was achieved with Hilfer definition proposed by Hilfer [13,14]. Shortly, it behaves as interpolator between Caputo and R-L derivative [3,11,17,30–32,35,36,38–41]. Hilfer parameter produces many types of stationary states and gives more degrees of freedom related to an initial condition. It reacts to theoretical simulation in glass-forming materials. To solve generalized fractional systems, Hilfer et al. [14] introduced applied operational calculus. Besides, Gu et al. [11], Furati et al. [7], investigated the nonexistence, existence, and stability sequels of nonlinear problems with Hilfer derivative.

Control theory generally deals with dynamic system behavior and becomes one of the essential tools in the method of mathematical control. Controllability defines the control system in terms of qualitative property and plays a significant role in the theory of control. Controllability deals with problems on optimal control, pole assignment, stability employing the corresponding system is

* Corresponding author.
E-mail addresses: n.sooppy@psau.edu.sa, ksnisar1@gmail.com (K.S. Nisar), ravichandran@kongunaducollege.ac.in (C. Ravichandran).

https://doi.org/10.1016/j.chaos.2021.110915

controllable. It is a tool used to drive the system from its arbitrary initial to the final state. The contribution of controllability by several researchers may be referred to [4,6,20,22,23,33,34,44,46], and references. The above articles refer to the investigation of controllability on C_0-semigroup with a dense operator that trivially meets Hille condition. To overcome real-life situations, one may go with non-dense operator, as suggested in Prato and Sinestrari [27]. On the other hand, optimal control of differential equations and inclusions with integer order is of interest for space technology and aviation. It also plays an important role in robotics, power plants, control of chemical processes and movement sequence of sports. Practically, optimization process can no longer be adequately modelled by integer order differential equations; instead differential equations of fractional order are employed for their description. For instance, the memory and hereditary properties of blood flow, electrical circuits, bio-mechanics, signals can be well predicted and described by some fractional differential equations. One can refer to the results in Bahaa [2], Harrat et al. [12], Pan et al. [25], Qin et al. [28].

In the year 2016, Yang and Wang [42] discussed the approximate controllability of Hilfer nonlocal differential inclusions of fractional order. Continuation of this in 2018, Du et al. [4] published an article regarding the controllability of nonlocal Hilfer fractional inclusion. In 2019, Vikram Singh [33] derived some results on the controllability of non-dense Hilfer equation of fractional order.

As per our vast search, there is no article found related to the investigation on controllability of non-dense HNFD which attracts us to make a study on the above-said title and followed by the problem as:

$$\mathcal{D}^{\alpha,\beta}_{0+}[\mathfrak{z}(\theta)-\mathcal{P}(\theta,\mathfrak{z}(\theta))]=A\mathfrak{z}(\theta)+Bu(\theta)+h(\theta,\mathfrak{z}(\theta)), \tag{1.1}$$

$$I^{(1-\alpha)(1-\beta)}_{0+}\mathfrak{z}(0)=\mathfrak{z}_0+\phi(\mathfrak{z}), \qquad \theta\in\mathcal{I}=[0,a]. \tag{1.2}$$

$\mathcal{D}^{\alpha,\beta}_{0+}$ denotes the derivative of fractional order in Hilfer sense with $\alpha\in(0,1)$, $\beta\in(0,1]$ as order and type respectively and $\vartheta=\alpha+\beta-\alpha\beta$. Here $A:\mathcal{D}_A\subset\mathcal{Z}\to\mathcal{Z}$, the non-densely closed linear operator, i.e. if we assume the conditions of Hille–Yosida with the density exception, $\mathcal{D}_A\in\mathcal{Z}$ where $\mathcal{D}_A,\mathcal{Z}$ represents the domain of A and Banach space respectively. Also the appropriate functions $\mathcal{P},h$ are defined as $\mathcal{P}:[0,a]\times\mathcal{Z}\to\mathcal{D}_A\subset\mathcal{Z}$ and $h:([0,a]\times\mathcal{Z})\to\mathcal{D}_A\subset\mathcal{Z}$. Also we consider the bounded linear operator $B:U\to\mathcal{Z}$ and the control function $u(\cdot)$ with the Banach space $L^2[\mathcal{I},U]$ of admissible control functions.

This article is outlined as: 2nd section introduces some notations and preliminary facts of semigroup theory, Mönch fixed point technique, fractional calculus and formulation of integral solution. In 3rd section, the uniqueness and controllability of integral solutions for (1.1) and (1.2) are established. 4th section refers to the existence of optimal control of our system. As a final part, in 5th section, a numerical analysis is given to compare the results with graphs.

2. Preparatory discussions

Let $\mathcal{C}(\mathcal{I},\mathcal{Z})$ be the space of continuous functions $\mathfrak{z}(\theta)$ defined on $\mathcal{I}=[0,a]$ provided with $||\mathfrak{z}||=\sup_{\theta\in\mathcal{I}}||\mathfrak{z}(\theta)||$.

$\mathcal{C}_{1-\vartheta}(\mathcal{I},\mathcal{Z})=\{\mathfrak{z}:\mathcal{Z}\to\mathcal{Z}$ such that $\theta^{1-\vartheta}\mathfrak{z}(\theta)\in\mathcal{C}(\mathcal{I},\mathcal{Z})\}$, a Banach space w.r.t. the norm $||\mathfrak{z}||_{\mathcal{C}_{1-\vartheta}}=\sup_{0\le\theta\le a}|\theta^{1-\vartheta}\mathfrak{z}(\theta)|$.

Here the basic definitions of Caputo and R-L derivatives are recalled:

$${}^{R-L}\mathcal{D}^p_{0+}z(\theta)=\frac{d^n}{d\theta^n}(z(\theta)*q_{n-p}(\theta)), \tag{2.1}$$

$${}^{C}\mathcal{D}^p_{0+}z(\theta)=\frac{d^n}{d\theta^n}z(\theta)*q_{n-p}(\theta), \qquad n-1<p<n, \tag{2.2}$$

where $z\in\mathcal{C}(\mathcal{I},\mathcal{Z})$ and $*$ denotes convolution of two functions.

Definition 2.1 (see [13]). For $\alpha\in(n-1,n)$, $n\in N$; $\beta\in(0,1]$, we define the HFD as

$$\mathcal{D}^{\alpha,\beta}_{0+}h(\theta)=\mathcal{I}^{\alpha(n-\beta)}_{0+}\frac{d}{d\theta}\mathcal{I}^{(1-\alpha)(n-\beta)}_{0+}h(\theta)=\mathcal{I}^{\alpha(n-\beta)}_{0+}\mathcal{D}^{\beta+\alpha n-\beta\alpha}_{0+}h(\theta)$$

where $\mathcal{I}^{\alpha(n-\beta)}_{0+}$ is R-L integral and $\mathcal{D}^{\beta+\alpha n-\beta\alpha}_{0+}$ is R-L derivative.

Lemma 2.2 (see [7]). *If $h\in\mathcal{C}^{\vartheta}_{1-\vartheta}[r_1,r_2]$ is such that $\mathcal{D}^{\vartheta}_{0+}h\in\mathcal{C}_{1-\vartheta}[r_1,r_2]$ then*

$$\mathcal{I}^{\vartheta}_{0+}\mathcal{D}^{\vartheta}_{0+}h=\mathcal{I}^{\alpha}_{0+}\mathcal{D}^{\alpha,\beta}_{0+} \text{ and } \mathcal{D}^{\vartheta}_{0+}\mathcal{I}^{\vartheta}_{0+}h=\mathcal{D}^{\beta(1-\alpha)}_{0+}h,$$

where $\alpha\in(0,1)$, $\beta\in(0,1]$ and $\vartheta=\alpha+\beta-\alpha\beta$.

Lemma 2.3 (see [7]). *If $h\in\mathcal{C}_{1-\vartheta}[r_1,r_2]$ and $\mathcal{I}^{1-\vartheta}_{0+}h\in\mathcal{C}^1_{\vartheta}[r_1,r_2]$ then,*

$$\mathcal{I}^{\vartheta}_{0+}\mathcal{D}^{\vartheta}_{0+}h(\theta)=h(\theta)-\frac{\mathcal{I}^{1-\vartheta}_{0+}h(r_1)}{\Gamma(\vartheta)}(\theta-r_1)^{\vartheta-1}, \quad \forall\theta\in(r_1,r_2],$$

where $\alpha\in(0,1)$, $\vartheta\in[0,1)$.

Remark 2.4 (see [11]).

(i) For $\beta=0$, $\alpha\in(0,1)$, $\mathcal{D}^{\alpha,0}_{0+}$ corresponds to classical R-L derivative: $\mathcal{D}^{\alpha,0}_{0+}h(\theta)=\frac{d}{d\theta}\mathcal{I}^{1-\alpha}_{0+}h(\theta)={}^{R-L}\mathcal{D}^{\alpha}_{0+}h(\theta)$.

(ii) If $\alpha\in(0,1)$, $\beta=1$, $\mathcal{D}^{\alpha,1}_{0+}$ corresponds to classical Caputo derivative: $\mathcal{D}^{\alpha,1}_{0+}h(\theta)=\mathcal{I}^{1-\alpha}_{0+}\frac{d}{d\theta}h(\theta)={}^{C}\mathcal{D}^{\alpha}_{0+}h(\theta)$.

Lemma 2.5 (see [10]). *We define $\kappa(\Omega)=\inf\{\epsilon>0,\ \Omega$ has finite $\epsilon-$net in $\mathcal{Z}\}$, the Hausdorff noncompact measure which satisfies:*

(1) *$\kappa(\Omega_1)\le\kappa(\Omega_2)$, for all bounded subsets Ω_1,Ω_2 of $\mathcal{Z}$ provided $\Omega_1\subseteq\Omega_2$;*
(2) *$\kappa(\Omega)=0$ if and only if Ω is relatively compact in $\mathcal{Z}$;*
(3) *for every $y\in\mathcal{Z}$, $\kappa(\{y\}\cup\Omega)=\kappa(\Omega)$, where $\Omega\subseteq\mathcal{Z}$ is nonempty;*
(4) *$\kappa(\Omega_1+\Omega_2)\le\kappa(\Omega_1)+\kappa(\Omega_2)$, where $\Omega_1+\Omega_2=\{y_1+y_2;y_1\in\Omega_1,y_2\in\Omega_2\}$;*
(5) *for any $\lambda\in R$, $\kappa(\lambda\Omega)\le|\lambda|\kappa(\Omega)$;*
(6) *$\kappa(\Omega_1\cup\Omega_2)\le\max\{\kappa(\Omega_1),\kappa(\Omega_2)\}$.*

Proposition 2.6. *Let $A_0\subset A$ generate a strongly continuous semigroup $\{\Re(\theta)\}_{\theta\ge0}$ on $\mathcal{Z}_0$ where $\mathcal{Z}_0=\overline{\mathcal{D}_A}$ satisfies $A_0y=Ay$.*

Lemma 2.7 (See [16]). *Let $\mathcal{I}$ be the set $[0,a]$, $\{z_n\}_{n=1}^{\infty}$ be a Bochner's sequence from $\mathcal{I}$ to $\mathcal{Z}$ satisfying $|z_n(\theta)|\le\widetilde{m}(\theta)$, $\theta\in\mathcal{I}$ with $n\ge1$, as $\widetilde{m}\in L(\mathcal{I},R^+)$. Moreover, the function $G(\theta)=\kappa\left(\{z_n(\theta)\}_{n=1}^{\infty}\right)$ in $L(\mathcal{I},R^+)$ fulfills*

$$\kappa\left(\left\{\int_0^{\theta}z_n(s)ds:n\ge1\right\}\right)\le2\int_0^{\theta}G(s)ds.$$

Consider $\mathcal{Z}_0=\overline{\mathcal{D}_A}$ and let A_0 be the characteristic element of A in $\mathcal{Z}_0$ defined as

$$\mathcal{D}_{A_0}=\{y\in\mathcal{D}_A:Ay\in\mathcal{Z}_0\},\ A_0y=Ay.$$

With reference [10], we introduced some assumptions for further analysis.

(H1) For couple of constants $k\in\mathbb{R},\mathcal{M}_0$ satisfying $(k,+\infty)\subseteq\rho(A)$, for each $n\ge1$ and $\lambda>k$,

$$\|(\lambda I-A)^{-n}\|_{L(\mathcal{Z})}\le\frac{\mathcal{M}_0}{\sup(\lambda-k)^n}.$$

(H2) There exists a constant $\mathcal{M}_1 > 1$ such that $\sup_{\theta\in[0,+\infty]} |\Re(\theta)| < \mathcal{M}_1$. i.e. $\{\Re(\theta)\}_{\theta>0}$ is bounded and uniformly continuous.

Now, for $\theta \geq 0$ we define,

$$T_\alpha(\theta) = \alpha\int_0^\infty \nu\psi_\chi(\nu)\Re(\theta^\alpha\nu)d\nu, \qquad P_\alpha(\theta) = \theta^{\alpha-1}T_\alpha(\theta),$$
$$S_{\alpha,\beta}(\theta) = \mathcal{I}_{0+}^{\beta(1-\alpha)}P_\alpha(\theta).$$

For $\nu \in (0,\infty)$,

$$\psi_\chi(\nu) = \frac{1}{\chi}\nu^{(-1-\frac{1}{\chi})}W_\chi(\nu^{-\frac{1}{\chi}}) \geq 0,$$
$$W_\chi(\nu) = \frac{1}{\pi}\sum_{k=1}^\infty(-1)^{k-1}\nu^{-k\chi-1}\frac{\Gamma(k\chi+1)}{k!}\sin(k\pi\chi).$$

Also, ψ_χ refers to probability density function on $(0,\infty)$.

Lemma 2.8. *(see [16]). By (H2),*

(i) $S_{\alpha,\beta}(\theta)$, $P_\alpha(\theta)$ *satisfy*

$$|S_{\alpha,\beta}(\theta)| \leq \frac{\mathcal{M}\theta^{\vartheta-1}}{\Gamma(\vartheta)} \quad\text{and}\quad |P_\alpha(\theta)| \leq \frac{\mathcal{M}\theta^{\alpha-1}}{\Gamma(\alpha)}, \quad \theta > 0.$$

(ii) *For* $\theta \geq 0$, $T_\alpha(\theta)$ *is uniformly continuous.*

(iii) *For* $\mathfrak{z} \in \mathcal{Z}_0$, $0 < \theta_1 < \theta_2 \leq a$, $\{S_{\alpha,\beta}(\theta)\}_{\theta\geq 0}$ *and* $\{P_\alpha(\theta)\}_{\theta\geq 0}$ *satisfy*

$$|S_{\alpha,\beta}(\theta_1)\mathfrak{z} - S_{\alpha,\beta}(\theta_2)\mathfrak{z}| \to 0 \text{ and } |P_\alpha(\theta_1)\mathfrak{z} - P_\alpha(\theta_2)\mathfrak{z}| \to 0$$
$$\text{as } \theta_2 \to \theta_1.$$

Lemma 2.9. *(see [7]). For* $\theta \in \mathcal{I}$, *our model (1.1) and (1.2) reduces as,*

$$\mathfrak{z}(\theta) = \frac{[\mathfrak{z}_0 + \phi(\mathfrak{z}) - \mathcal{P}(0,\mathfrak{z}(0))]}{\Gamma(\vartheta)}\theta^{\vartheta-1} + \mathcal{P}(\theta,\mathfrak{z}(\theta)) + \frac{1}{\Gamma(\alpha)}\int_0^\theta(\theta-s)^{\alpha-1}[A\mathfrak{z}(s) + h(s,\mathfrak{z}(s)) + Bu(s)]ds. \quad (2.3)$$

Lemma 2.10. *Let* $\mathfrak{z}$ *satisfy (1.1) and (1.2).* $\therefore$ *for* $\theta \in \mathcal{I}$, *we have* $\mathfrak{z}(\theta) \in \overline{\mathcal{D}_A}$. *In particular,* $\mathfrak{z}_0 + \phi(\mathfrak{z}) \in \overline{\mathcal{D}_A}$.

Definition 2.11. For each $\theta \in \mathcal{Z}$ and $h \in \mathcal{Z}_0$, we define the integral solution of (1.1) and (1.2) as

$$\mathfrak{z}(\theta) = S_{\alpha,\beta}(\theta)[\mathfrak{z}_0 + \phi(\mathfrak{z}) - \mathcal{P}(0,\mathfrak{z}(0))] + \mathcal{P}(\theta,\mathfrak{z}(\theta)) + \lim_{\lambda\to\infty}\int_0^\theta P_\alpha(\theta-s)\mathcal{B}_\lambda[A\mathcal{P}(s,\mathfrak{z}(s)) + Bu(s) + h(s,\mathfrak{z}(s))]ds, \quad (2.4)$$

where $\mathcal{B}_\lambda = \lambda(\lambda I - A)^{-1}$ such that $\mathcal{B}_\lambda\mathfrak{z} = \mathfrak{z}$ as $\lambda \to \infty$.

Lemma 2.12. *(see [16]). Let D be a closed and convex subset of* $\mathcal{Z}$, $0 \in D$. *If* $F : \overline{D} \to \mathcal{Z}$ *is continuous and of Mönch type, i.e. F satisfies the condition* $\theta \subseteq \overline{D}$, θ *is countable and* $\theta \subseteq \overline{co}(\{0\} \cup F(\theta)) \Rightarrow \overline{\theta}$ *is compact. Then F has at least one fixed point.*

3. Discussions on controllability

To ensure the outcomes, the subsequent hypotheses are introduced:

(H3) A function $h : (\mathcal{I}\times\mathcal{Z}) \to \mathcal{Z}$ satisfies:
(i). For all $\theta \in \mathcal{I}$, $h(\theta,\cdot) : \mathcal{I} \to \mathcal{Z}$ is continuous, for $\mathfrak{z} \in \mathcal{Z}$, $h(\cdot,\mathfrak{z}) : \mathcal{I} \to \mathcal{Z}$ is strongly measurable.
(ii). For functions $m_1 \in L^{\frac{1}{q}}(\mathcal{I}, R^+)$, $q \in (0,\alpha)$ and $\mathcal{L}_h : [0,\infty] \to (0,\infty)$, nondecreasing and continuous,

$$||h(\theta,\mathfrak{z}(\theta))|| \leq m_1(\theta)\mathcal{L}_h(\theta^{1-\vartheta}||\mathfrak{z}(\theta)||).$$

Also $\lim_{r\to\infty}\frac{\mathcal{L}_h(r)}{r} = \mathcal{L}_h^*$, for each $(\theta,\mathfrak{z}) \in \mathcal{I}\times\mathcal{Z}$ and $m_1^* = \max\{m_1(\theta)\}$.

(H4) There exists a constant $l_f{}^* > 0$, such that for any bounded $D_1 \subseteq \mathcal{Z}$, $\kappa(f(\theta,D_1)) \leq l_f{}^*\theta^{1-\vartheta}\kappa(D_1)$, almost everywhere $\theta \in \mathcal{I}$.

(H5) $\mathcal{P} : (\mathcal{I}\times\mathcal{Z}) \to \mathcal{Z}$ is bounded and Lipschitz continuous, which states that with some constants $m_g > 0$ and $\mathcal{L}_g \in (0,1)$ it satisfies

$$\|\mathcal{P}(\theta,\mathfrak{z}(\theta))\| \leq m_g \quad\text{and}\quad \|\mathcal{P}(\theta,\mathfrak{z}_1(\theta)) - \mathcal{P}(\theta,\mathfrak{z}_2(\theta))\| \leq \mathcal{L}_g\|\mathfrak{z}_1 - \mathfrak{z}_2\|, \quad \text{for all } \theta \in \mathcal{I}.$$

(H6) There exists a constant $l_p{}^* > 0$, such that for any bounded $D_1 \subseteq \mathcal{Z}$, $\kappa(\mathcal{P}(\theta,D_1)) \leq l_p{}^*\theta^{1-\vartheta}\kappa(D_1)$, almost everywhere $\theta \in \mathcal{I}$.

(H7) For any constant $\mathcal{M}_3 > 0$ and for all $\mathfrak{z}_1,\mathfrak{z}_2 \in \mathcal{C}$,

$$||\phi(\mathfrak{z}_1) - \phi(\mathfrak{z}_2)|| \leq \mathcal{M}_3||\mathfrak{z}_1 - \mathfrak{z}_2||_{\mathcal{C}}.$$

(H8) $W : L^2(\mathcal{I},U) \to \mathcal{Z}$ defined as:

$$Wu = \lim_{\lambda\to+\infty}\int_0^a P_\alpha(a-s)\mathcal{B}_\lambda Bu(s)ds,$$

is invertible with the inverse operator denoted by W^{-1} which takes values in $L^2(\mathcal{I},U)|\ker W$ and for $\mathcal{M}_b, \mathcal{M}_w \geq 0$, provided that $\|B\| \leq \mathcal{M}_b$, $\|W^{-1}\| \leq \mathcal{M}_w$.

(H9) For some $l_u{}^* > 0$, such that $\kappa(u(z,\mu)) \leq l_u{}^*\theta^{1-\vartheta}\nu(z,\mu)\kappa(z(\mu))$, a.e $\mu \in \mathcal{I}$ with $\sup_{\theta\in\mathcal{I}}\int_0^\theta \nu(\theta,\mu)ds = \nu^* < \infty$.

Here, we model $u(\theta,\mathfrak{z})$ as:

$$u(\theta,\mathfrak{z}) = W^{-1}\Big[\mathfrak{z}_a - S_{\alpha,\beta}(a)[\mathfrak{z}_0 + \phi(\mathfrak{z}) - \mathcal{P}(0,\mathfrak{z}(0))] - \mathcal{P}(a,\mathfrak{z}(a)) - \lim_{\lambda\to\infty}\int_0^a P_\alpha(a-s)\mathcal{B}_\lambda[A\mathcal{P}(s,\mathfrak{z}(s)) + h(s,\mathfrak{z}(s))]ds\Big](\theta)$$

with

$$\begin{aligned}
\|u(\theta,\mathfrak{z})\| &\leq ||W^{-1}\Big[\mathfrak{z}_a - S_{\alpha,\beta}(a)[\mathfrak{z}_0 + \phi(\mathfrak{z}) - \mathcal{P}(0,\mathfrak{z}(0))] - \mathcal{P}(a,\mathfrak{z}(a)) \\
&\quad - \lim_{\lambda\to\infty}\int_0^a P_\alpha(a-s)\mathcal{B}_\lambda[A\mathcal{P}(s,\mathfrak{z}(s)) + h(s,\mathfrak{z}(s))]ds\Big](\theta)|| \\
&\leq \mathcal{M}_w\Big[\|\mathfrak{z}_a\| - \frac{\mathcal{M}a^{\vartheta-1}}{\Gamma(\vartheta)}\|[\mathfrak{z}_0 + \phi(\mathfrak{z}) - \mathcal{P}(0,\mathfrak{z}(0))]\| - \|\mathcal{P}(a,\mathfrak{z}(a))\| - \frac{\mathcal{M}a^{\alpha-1}}{\Gamma(\alpha)}||\lim_{\lambda\to\infty}\int_0^a \mathcal{B}_\lambda[A\mathcal{P}(s,\mathfrak{z}(s)) + h(s,\mathfrak{z}(s))]ds||\Big] \\
&\leq \mathcal{M}_w\Big[\|\mathfrak{z}_a\| - \frac{\mathcal{M}a^{\vartheta-1}}{\Gamma(\vartheta)}\hat{\mathcal{M}} - m_g - \frac{\mathcal{M}a^{\alpha-1}\mathcal{M}_0}{\Gamma(\alpha)}\int_0^a\big[\|A\|m_g + m_1(s)L_h\big(s^{1-\vartheta}\|\mathfrak{z}(s)\|\big)\big]ds\Big] \\
&\leq \mathcal{M}_w\Big[\|\mathfrak{z}_a\| - \frac{\mathcal{M}a^{\vartheta-1}}{\Gamma(\vartheta)}\hat{\mathcal{M}} - m_g - \frac{\mathcal{M}a^\alpha\mathcal{M}_0}{\Gamma(\alpha)}\big[\|A\|m_g + m_1^*\mathcal{L}_h^*\big]\Big] \\
&\leq \mathcal{M}_w C_b^*,
\end{aligned}$$

where $C_b^* = ||\mathfrak{z}_a|| - \frac{\mathcal{M}a^{\vartheta-1}}{\Gamma(\vartheta)}\hat{\mathcal{M}} - m_g - \frac{\mathcal{M}a^\alpha\mathcal{M}_0}{\Gamma(\alpha)}[||A||m_g + m_1^*\mathcal{L}_h^*]$ and $\hat{\mathcal{M}} = ||\mathfrak{z}_0 + \phi(\mathfrak{z}) - \mathcal{P}(0,\mathfrak{z}(0))||$.

Let us consider the space $\mathcal{E} = \{\mathfrak{z} : \mathfrak{z} \in \mathcal{C}[\mathcal{I},\mathcal{Z}]\}$ equipped with the uniform convergence topology.

Theorem 3.1. *If (H1)–(H6) hold, then (1.1) and (1.2) has a unique solution provided that*

$$\frac{\mathcal{M}a^{\vartheta-1}}{\Gamma(\vartheta)}\hat{\mathcal{M}} + m_g + \frac{\mathcal{M}a^\alpha\mathcal{M}_0}{\Gamma(\alpha)}[||A||m_g + \mathcal{M}_b\mathcal{M}_wC_b^* + m_1^*\mathcal{L}_h^*] < \zeta^*, \quad (3.1)$$

and

$$\frac{\mathcal{M}a^{\vartheta-1}}{\Gamma(\vartheta)}\mathcal{M}_3+\mathcal{L}_g+\frac{\mathcal{M}a^{\alpha}\mathcal{M}_0}{\Gamma(\alpha)}\Big[\|A\|\mathcal{L}_g+m_1(a)\mathcal{L}_h a^{1-\vartheta} +\Big[\frac{\mathcal{M}a^{\vartheta-1}}{\Gamma(\vartheta)}\mathcal{M}_3+\mathcal{L}_g+\|A\|\mathcal{L}_g+m_1(a)\mathcal{L}_h a^{1-\vartheta}\Big]\Big]<1. \quad (3.2)$$

Proof. Consider $\mathcal{B}_\iota(0,\mathcal{E})=\{\mathfrak{z}\in\mathcal{Z},||\mathfrak{z}||\le\zeta\}$. Then $\mathcal{B}_\iota(0,\mathcal{E})\subset\mathcal{C}[\mathcal{I},\mathcal{Z}]$ is a closed, bounded and convex set. For $\eta>0$, define the operator $\Gamma_\eta:\mathcal{B}_\iota(0,\mathcal{E})\to\mathcal{B}_\iota(0,\mathcal{E})$ as

$$\Gamma_\eta(\mathfrak{z}(\theta))=S_{\alpha,\beta}(\theta)[\mathfrak{z}_0+\phi(\mathfrak{z})-\mathcal{P}(0,\mathfrak{z}(0))]+\mathcal{P}(\theta,\mathfrak{z}(\theta))+\lim_{\lambda\to\infty}\int_0^\theta P_\alpha(\theta-s)\mathcal{B}_\lambda\Big[A\mathcal{P}(s,\mathfrak{z}(s))+Bu(s)+h(s,\mathfrak{z}(s))\Big]ds.$$

Here, we prove the existence and uniqueness by Banach contraction principle.

Step 1: Γ_η : maps $\mathcal{B}_\iota(0,\mathcal{E})$ into itself. For $\mathfrak{z}\in\mathcal{B}_\iota(0,\mathcal{E})$,

$$\begin{aligned}\|\Gamma_\eta(\mathfrak{z}(\theta))\| &\le ||S_{\alpha,\beta}(\theta)[\mathfrak{z}_0+\phi(\mathfrak{z})-\mathcal{P}(0,\mathfrak{z}(0))]+\mathcal{P}(\theta,\mathfrak{z}(\theta))+\lim_{\lambda\to\infty}\\ &\quad\times\int_0^\theta P_\alpha(\theta-s)\mathcal{B}_\lambda[A\mathcal{P}(s,\mathfrak{z}(s))+Bu(s)+h(s,\mathfrak{z}(s))]ds||\\ &\le \frac{\mathcal{M}a^{\vartheta-1}}{\Gamma(\vartheta)}\hat{\mathcal{M}}+m_g\\ &\quad+\frac{\mathcal{M}a^{\alpha-1}\mathcal{M}_0}{\Gamma(\alpha)}\int_0^a[\|A\|m_g]+\mathcal{M}_b\|u(s)\|+\|h(s,\mathfrak{z}(s))\|]ds\\ &\le \frac{\mathcal{M}a^{\vartheta-1}}{\Gamma(\vartheta)}\hat{\mathcal{M}}+m_g\\ &\quad+\frac{\mathcal{M}a^{\alpha}\mathcal{M}_0}{\Gamma(\alpha)}\Big[\|A\|m_g+\mathcal{M}_b\mathcal{M}_wC_b^*+m_1^*\mathcal{L}_h^*\Big]\\ &\le\zeta^*.\end{aligned}$$

$\therefore$ Γ_η maps $\mathcal{B}_\iota(0,\mathcal{E})$ into itself.

Step 2: For some $\mathfrak{z},w\in\mathcal{B}_\iota(0,\mathcal{E})$,

$$\begin{aligned}||\Gamma_\eta(\mathfrak{z}(\theta))-\Gamma_\eta(w(\theta))|| &\le ||S_{\alpha,\beta}(\theta)(\phi(\mathfrak{z}))-\phi(w))||\\ &\quad+||\mathcal{P}(\theta,\mathfrak{z}(\theta))-\mathcal{P}(\theta,w(\theta))||\\ &\quad+\lim_{\lambda\to\infty}\Big|\Big|\int_0^\theta P_\alpha(\theta-s)\mathcal{B}_\lambda\\ &\quad\Big[A\mathcal{P}(s,\mathfrak{z}(s))+Bu(s,\mathfrak{z})+h(s,\mathfrak{z}(s))\Big]ds\\ &\quad-\int_0^\theta P_\alpha(\theta-s)\mathcal{B}_\lambda\Big[A\mathcal{P}(s,w(s))\\ &\quad+Bu(s,w)+h(s,w(s))\Big]ds\Big|\Big|\end{aligned}$$

$$\begin{aligned}&\le\frac{\mathcal{M}a^{\vartheta-1}}{\Gamma(\vartheta)}\mathcal{M}_3||\mathfrak{z}-w||+\mathcal{L}_g||\mathfrak{z}-w||+\frac{\mathcal{M}a^{\alpha-1}\mathcal{M}_0}{\Gamma(\alpha)}\\ &\quad\times\Big[\int_0^a||A||\Big|\Big|\mathcal{P}(s,\mathfrak{z}(s))-\mathcal{P}(s,w(s))\Big|\Big|ds+\int_0^a\mathcal{M}_b\\ &\quad\times\Big|\Big|u(s,\mathfrak{z}(s))-u(s,w(s))\Big|\Big|ds\\ &\quad+\int_0^a\Big|\Big|h(s,\mathfrak{z}(s))-h(s,w(s))\Big|\Big|ds\Big]\\ &\le\frac{\mathcal{M}a^{\vartheta-1}}{\Gamma(\vartheta)}\mathcal{M}_3||\mathfrak{z}-w||+\mathcal{L}_g||\mathfrak{z}-w||\\ &\quad+\frac{\mathcal{M}a^{\alpha}\mathcal{M}_0}{\Gamma(\alpha)}\Big[||A||\mathcal{L}_g+\mathcal{M}_b\mathcal{M}_w\\ &\quad\times\Big[\frac{\mathcal{M}a^{\vartheta-1}}{\Gamma(\vartheta)}\mathcal{M}_3+\mathcal{L}_g+||A||\mathcal{L}_g+m_1(a)\mathcal{L}_ha^{1-\vartheta}\Big]\\ &\quad+m_1(a)\mathcal{L}_ha^{1-\vartheta}\Big]||\mathfrak{z}-w||\end{aligned}$$

$$\begin{aligned}&\le\Big[\frac{\mathcal{M}a^{\vartheta-1}}{\Gamma(\vartheta)}\mathcal{M}_3+\mathcal{L}_g+\frac{\mathcal{M}a^{\alpha}\mathcal{M}_0}{\Gamma(\alpha)}\Big[||A||\mathcal{L}_g+\mathcal{M}_b\mathcal{M}_w\Big[\frac{\mathcal{M}a^{\vartheta-1}}{\Gamma(\vartheta)}\mathcal{M}_3\\ &\quad+\mathcal{L}_g+||A||\mathcal{L}_g+m_1(a)\mathcal{L}_ha^{1-\vartheta}\Big]+m_1(a)\mathcal{L}_ha^{1-\vartheta}\Big]\Big]||\mathfrak{z}-w||\\ &\le\mu^*||\mathfrak{z}-w||,\end{aligned}$$

where $\mu^*=\frac{\mathcal{M}a^{\vartheta-1}}{\Gamma(\vartheta)}\mathcal{M}_3+\mathcal{L}_g+\frac{\mathcal{M}a^{\alpha}\mathcal{M}_0}{\Gamma(\alpha)}\Big[||A||\mathcal{L}_g+\mathcal{M}_b\mathcal{M}_w\Big[\frac{\mathcal{M}a^{\vartheta-1}}{\Gamma(\vartheta)}\mathcal{M}_3+\mathcal{L}_g+||A||\mathcal{L}_g+m_1(a)\mathcal{L}_ha^{1-\vartheta}\Big]+m_1(a)\mathcal{L}_ha^{1-\vartheta}\Big]$.

Hence Γ_η is contraction. $\therefore$ Γ_η has a unique solution on $\mathcal{C}[\mathcal{I},\mathcal{Z}]$ by Banach contraction principle. □

Lemma 3.2. *If the hypotheses (H1)–(H9) hold,* $\Gamma_\eta:\mathfrak{z}\in\mathcal{B}_\iota(0,\mathcal{E})$ *is equicontinuous.*

Proof. By Lemma 2.8, $S_{\alpha,\beta}(\theta)$ is strongly continuous on $\mathcal{I}$.

For $\mathfrak{z}\in\mathcal{B}_\iota(0,\mathcal{E}),\theta_1,\theta_2\in\mathcal{I}$ and $\epsilon>0$ such that $0\le\epsilon<\theta_1<\theta_2\le a$ and there exists a $\delta>0$ such that if $0<|\theta_2-\theta_1|<\delta$, then

$$\begin{aligned}&\|(\Gamma_\eta\mathfrak{z})(\theta_2)-(\Gamma_\eta\mathfrak{z})(\theta_1)\|\\ &\le||[\mathcal{P}(\theta_2,\mathfrak{z}(\theta_2))-\mathcal{P}(\theta_1,\mathfrak{z}(\theta_1))]+\lim_{\lambda\to\infty}\theta_2^{\vartheta-1}\\ &\quad\int_0^{\theta_2}(\theta_2-s)^{\alpha-1}T_\alpha(\theta_2-s)\\ &\quad\times B_\lambda A[\mathcal{P}(s,\mathfrak{z}(s))]ds-\theta_1^{\vartheta-1}\int_0^{\theta_1}(\theta_1-s)^{\alpha-1}T_\alpha(\theta_1-s)\\ &\quad\times B_\lambda A[\mathcal{P}(s,\mathfrak{z}(s))]ds||+||\lim_{\lambda\to\infty}\theta_2^{\vartheta-1}\int_0^{\theta_2}(\theta_2-s)^{\alpha-1}T_\alpha(\theta_2-s)B_\lambda\\ &\quad\times[h(s,\mathfrak{z}(s))]ds-\theta_1^{\vartheta-1}\int_0^{\theta_1}(\theta_1-s)^{\alpha-1}T_\alpha(\theta_1-s)B_\lambda[h(s,\mathfrak{z}(s)]ds||\\ &\quad+||\lim_{\lambda\to\infty}\theta_2^{\vartheta-1}\int_0^{\theta_2}(\theta_2-s)^{\alpha-1}T_\alpha(\theta_2-s)B_\lambda[Bu(s)]ds\\ &\quad-\theta_1^{\vartheta-1}\int_0^{\theta_1}(\theta_1-s)^{\alpha-1}T_\alpha(\theta_1-s)B_\lambda[Bu(s)]ds||\end{aligned}$$

$$\begin{aligned}&\le\mathcal{L}_g||\theta_2-\theta_1||+\Big|\Big|\lim_{\lambda\to\infty}\theta_2^{\vartheta-1}\int_{\theta_1}^{\theta_2}(\theta_2-s)^{\alpha-1}T_\alpha(\theta_2-s)\\ &\quad\times B_\lambda\Big[A\mathcal{P}(s,\mathfrak{z}(s))+h(s,\mathfrak{z}(s))+Bu(s)\Big]ds\Big|\Big|\\ &\quad+\Big|\Big|\lim_{\lambda\to\infty}\int_0^{\theta_1}\Big[\theta_2^{\vartheta-1}(\theta_2-s)^{\alpha-1}-\theta_1^{\vartheta-1}(\theta_1-s)^{\alpha-1}\Big]T_\alpha(\theta_2-s)\\ &\quad\times B_\lambda\Big[A\mathcal{P}(s,\mathfrak{z}(s))+h(s,\mathfrak{z}(s))+Bu(s)\Big]ds\Big|\Big|\\ &\quad+\Big|\Big|\lim_{\lambda\to\infty}\theta_1^{\vartheta-1}\int_0^{\theta_1-\epsilon}(\theta_1-s)^{\alpha-1}\Big[T_\alpha(\theta_2-s)-T_\alpha(\theta_1-s)\Big]\\ &\quad\times B_\lambda\Big[A\mathcal{P}(s,\mathfrak{z}(s))+h(s,\mathfrak{z}(s))+Bu(s)\Big]ds\Big|\Big|\\ &\quad+\Big|\Big|\lim_{\lambda\to\infty}\theta_1^{\vartheta-1}\int_{\theta_1-\epsilon}^{\theta_1}(\theta_1-s)^{\alpha-1}\Big[T_\alpha(\theta_2-s)-T_\alpha(\theta_1-s)\Big]\\ &\quad\times B_\lambda\Big[A\mathcal{P}(s,\mathfrak{z}(s))+h(s,\mathfrak{z}(s))+Bu(s)\Big]ds\Big|\Big|.\end{aligned}$$

Using absolute continuity by virtue of the Lebesgue convergence theorem and for ϵ sufficiently small $||(\Gamma_\eta\mathfrak{z})(\theta_2)-(\Gamma_\eta\mathfrak{z})(\theta_1)||\to 0$ *as* $\theta_2\to\theta_1$. Hence Γ_η is equicontinuous. □

Lemma 3.3. *If the hypotheses (H1)–(H9) hold,* $\Gamma_\eta:y\in\mathcal{B}_\iota(0,\mathcal{E})$ *is continuous provided that*

$$k_b^*\left[\left[\frac{\mathcal{M}a^\alpha\mathcal{M}_0}{\Gamma(\alpha)}[||A||m_g+m_1^*\mathcal{L}_h^*]+m_g\right]\left[1+\frac{\mathcal{M}a^\alpha\mathcal{M}_0\mathcal{M}_b\mathcal{M}_w}{\Gamma(\alpha)}\right]\right]<1. \tag{3.3}$$

Proof. Step 1: $\Gamma_\eta(\mathcal{B}_\iota(0,\mathcal{E}))\subset\mathcal{B}_\iota(0,\mathcal{E})$.

Suppose if it fails, for all $\iota>0$, and $\mathfrak{z}^\iota\in\mathcal{B}_\iota(0,\mathcal{E})$, $\theta^\iota\in\mathcal{I}$ yields $\iota<||(\Gamma_\eta\mathfrak{z}^\iota)(\theta^\iota)||_{\mathcal{C}}$.

Consider $0<\theta<\theta^\iota$ such that $\lim_{\iota\to\infty}\frac{\iota^*}{\iota}=k_b^*$, $||\mathfrak{z}^\iota||_{\mathcal{Z}}\le\iota^*$, we get

$$\begin{aligned}
\iota &< ||(\Gamma_\eta\mathfrak{z}^\iota)(\theta^\iota)||_{\mathcal{C}}\\
&< \sup_{0\le\theta^\iota\le a}\Bigg[||S_{\alpha,\beta}(\theta^\iota)[\mathfrak{z}_0+\phi(\mathfrak{z}^\iota)-\mathcal{P}(0,\mathfrak{z}(0))]||_{\mathcal{Z}}\\
&\quad+||\mathcal{P}(\theta^\iota,\mathfrak{z}^\iota(\theta^\iota))||_{\mathcal{Z}}\\
&\quad+\left|\left|\lim_{\lambda\to\infty}\int_0^{\theta^\iota}AP_\alpha(\theta^\iota-s)\mathcal{B}_\lambda\mathcal{P}(s,\mathfrak{z}^\iota(s))ds\right|\right|_{\mathcal{Z}}\\
&\quad+\left|\left|\lim_{\lambda\to\infty}\int_0^{\theta^\iota}P_\alpha(\theta^\iota-s)\mathcal{B}_\lambda Bu(s,\theta^\iota)ds\right|\right|_{\mathcal{Z}}\\
&\quad+\left|\left|\lim_{\lambda\to\infty}\int_0^{\theta^\iota}P_\alpha(\theta^\iota-s)\mathcal{B}_\lambda h(s,\mathfrak{z}^\iota(s))ds\right|\right|_{\mathcal{Z}}\Bigg]\\
&< \frac{\mathcal{M}a^{\vartheta-1}}{\Gamma(\vartheta)}\Big[||\mathfrak{z}_0||+||\phi(\mathfrak{z}^\iota)||-m_g\Big]_{\mathcal{Z}}+m_g\iota^*\\
&\quad+\frac{||A||\mathcal{M}a^\alpha\mathcal{M}_0m_g\iota^*}{\Gamma(\alpha)}+\frac{\mathcal{M}a^\alpha\mathcal{M}_0\iota^*m_1^*\mathcal{L}_h^*}{\Gamma(\alpha)}\\
&\quad+\frac{\mathcal{M}a^\alpha\mathcal{M}_0\mathcal{M}_b\mathcal{M}_w}{\Gamma(\alpha)}\Bigg[||\mathfrak{z}_a||+\frac{\mathcal{M}a^{\vartheta-1}}{\Gamma(\vartheta)}\\
&\quad\Big[||\mathfrak{z}_0||+||\phi(\mathfrak{z}^\iota)||-m_g\Big]+m_g\iota^*\\
&\quad+\frac{\mathcal{M}a^\alpha\mathcal{M}_0\iota^*}{\Gamma(\alpha)}[||A||m_g+m_1^*\mathcal{L}_h^*]\\
&< \frac{\mathcal{M}a^{\vartheta-1}\hat{\mathcal{M}}}{\Gamma(\vartheta)}+m_g\iota^*+\frac{\mathcal{M}a^\alpha\mathcal{M}_0\iota^*}{\Gamma(\alpha)}[||A||m_g+m_1^*\mathcal{L}_h^*]\\
&\quad+\frac{\mathcal{M}a^\alpha\mathcal{M}_0\mathcal{M}_b\mathcal{M}_w}{\Gamma(\alpha)}\\
&\quad\left[||\mathfrak{z}_a||+\hat{\mathcal{M}}\iota^*+m_g\iota^*+\frac{\mathcal{M}a^{\alpha-1}\mathcal{M}_0\iota^*}{\Gamma(\alpha)}[||A||m_g+m_1^*\mathcal{L}_h^*]\right].
\end{aligned}$$

Dividing by ι and taking $\iota\to\infty$,

$$\begin{aligned}
1 &< k_b^*\Bigg[\frac{\mathcal{M}a^\alpha\mathcal{M}_0}{\Gamma(\alpha)}[||A||m_g+m_1^*\mathcal{L}_h^*]+m_g+\frac{\mathcal{M}a^\alpha\mathcal{M}_0\mathcal{M}_b\mathcal{M}_w}{\Gamma(\alpha)}\\
&\quad[m_g+\frac{\mathcal{M}a^\alpha\mathcal{M}_0}{\Gamma(\alpha)}[||A||m_g+m_1^*\mathcal{L}_h^*]\Bigg]\\
&< k_b^*\Bigg[\frac{\mathcal{M}a^\alpha\mathcal{M}_0}{\Gamma(\alpha)}[||A||m_g+m_1^*\mathcal{L}_h^*]\left[1+\frac{\mathcal{M}a^\alpha\mathcal{M}_0\mathcal{M}_b\mathcal{M}_w}{\Gamma(\alpha)}\right]\\
&\quad+m_g\left[1+\frac{\mathcal{M}a^\alpha\mathcal{M}_0\mathcal{M}_b\mathcal{M}_w}{\Gamma(\alpha)}\right]\Bigg]\\
&< k_b^*\Bigg[\left[\frac{\mathcal{M}a^\alpha\mathcal{M}_0}{\Gamma(\alpha)}[||A||m_g+m_1^*\mathcal{L}_h^*]+m_g\right]\\
&\quad\left[1+\frac{\mathcal{M}a^\alpha\mathcal{M}_0\mathcal{M}_b\mathcal{M}_w}{\Gamma(\alpha)}\right]\Bigg],
\end{aligned}$$

which contradicts the assumption (3.3). Hence for $\iota>0$, $\Gamma_\eta(\mathcal{B}_\iota(0,\mathcal{E}))\subset\mathcal{B}_\iota(0,\mathcal{E})$.

Step 2: Γ_η is continuous on $\mathcal{B}_\iota(0,\mathcal{E})$.

Let $\mathfrak{z}_k,\mathfrak{z}$ be in $\mathcal{B}_\iota(0,\mathcal{E})$, for each $k=1,2,\ldots$ provided $\lim_{k\to\infty}||\mathfrak{z}_k-\mathfrak{z}||\to0$ and $\lim_{k\to\infty}\mathfrak{z}_k(\theta)\to\mathfrak{z}(\theta)$, for all $\theta\in\mathcal{I}$. $\therefore$

$$\lim_{k\to\infty}||h(\theta,\mathfrak{z}_k(\theta))-h(\theta,\mathfrak{z}(\theta))||\to0.$$

Using $(H1)$, for $\theta\in\mathcal{I}$,

$$(\theta-s)^{\alpha-1}||h(\theta,\mathfrak{z}_k(\theta))-h(\theta,\mathfrak{z}(\theta))||\le(\theta-s)^{\alpha-1}m_1(s)\mathcal{L}_h\Big[||\mathfrak{z}_k-\mathfrak{z}||\Big]\ \text{a.e}\ s\in(0,\theta).$$

Also for $s\in(0,\theta)$ and $\theta\in[0,a]$, $(\theta-s)^{\alpha-1}m_1(s)\mathcal{L}_h\Big[||\mathfrak{z}_k-\mathfrak{z}||\Big]$ is integrable. Moreover,

$$\int_0^\theta(\theta-s)^{\alpha-1}||h(s,\mathfrak{z}_k(s))-h(s,\mathfrak{z}(s))||ds\to0\ \text{as}\ k\to\infty. \tag{3.4}$$

Hence

$$\begin{aligned}
||(\Gamma_\eta\mathfrak{z}_k)(\theta)-(\Gamma_\eta\mathfrak{z})(\theta)|| &\le a^{\vartheta-1}\Bigg|\Bigg|\lim_{\lambda\to\infty}\int_0^\theta(\theta-s)^{\alpha-1}B_\lambda T_\alpha(\theta-s)\\
&\quad\Big[A[\mathcal{P}(s,\mathfrak{z}_k(s))-\mathcal{P}(s,\mathfrak{z}(s))]\\
&\quad+[h(s,\mathfrak{z}_k(s))-h(s,\mathfrak{z}(s))]\\
&\quad+B[u_{\mathfrak{z}_k}-u_{\mathfrak{z}}]\Big]ds\Bigg|\Bigg|\\
&\le\frac{\mathcal{M}a^{\vartheta-1}\mathcal{M}_0}{\Gamma(\alpha)}\Bigg|\Bigg|\int_0^\theta(\theta-s)^{\alpha-1}\\
&\quad\Big[A[\mathcal{P}(s,\mathfrak{z}_k(s))-\mathcal{P}(s,\mathfrak{z}_k(s))]\\
&\quad+[h(s,\mathfrak{z}_k(s))-h(s,\mathfrak{z}(s))]\\
&\quad+B[u_{\mathfrak{z}_k}-u_{\mathfrak{z}}]\Big]ds\Bigg|\Bigg|.
\end{aligned} \tag{3.5}$$

By (3.4) and (3.5),

$$||(\Gamma_\eta\mathfrak{z}_k)(\theta)-(\Gamma_\eta\mathfrak{z})(\theta)||\to0\ \text{as}\ n\to\infty.$$

Hence Γ_η is continuous on $\mathcal{B}_\iota(0,\mathcal{E})$.

□

Theorem 3.4. *If the hypotheses (H1)–(H9) hold, then the system (1.1) and (1.2) is controllable on $\mathcal{I}$ provided that*

$$\begin{aligned}
&l_p{}^*\theta^{1-\vartheta}\kappa(\mathbf{S})+\frac{2\mathcal{M}\mathcal{M}_0}{\Gamma(\alpha)}(l_p{}^*+l_f{}^*)\theta^{1-\vartheta}\left[1+\frac{2\mathcal{M}\mathcal{M}_0\mathcal{M}_b\mathcal{M}_w}{\Gamma(\alpha)}l_u{}^*\nu^*\right]\\
&\qquad\int_0^a(a-s)^{\alpha-1}\kappa(\mathbf{S})ds<r.
\end{aligned} \tag{3.6}$$

Proof. In order to satisfy Mönch condition, construct the countable subset $\mathbf{S}$ of $\mathcal{B}_\iota(0,\mathcal{E})$ and $\mathbf{S}\subset\overline{\text{co}}(\{0\}\cup\Gamma_\eta(\mathbf{S}))$, then we prove $\kappa(\mathbf{S})=0$.

Let $\mathbf{S}=\{\mathfrak{z}_n\}_{n=1}^\infty$. By Lemma 3.2, we note that $\Gamma_\eta\{\mathfrak{z}_n\}_{n=1}^\infty$ is equicontinuous on $\mathcal{I}$, then

$\mathbf{S}\subset\overline{\text{co}}(\{0\}\cup\Gamma_\eta(\mathbf{S}))$ is also equicontinuous on $\mathcal{I}$.

$$\begin{aligned}
&\kappa\Big(u\big(\theta,\{\mathfrak{z}_n\}_{n=1}^\infty\big)\Big)\\
&\le\kappa\Bigg\{W^{-1}\Bigg[\mathfrak{z}_a-S_{\alpha,\beta}(a)[\mathfrak{z}_0+\phi(\mathfrak{z})-\mathcal{P}(0,\mathfrak{z}(0))]-\mathcal{P}(a,\mathfrak{z}(a))-\lim_{\lambda\to\infty}\\
&\quad\times\int_0^a(a-s)^{\alpha-1}T_\alpha(a-s)\mathcal{B}_\lambda\Big[A\mathcal{P}\big(s,\{\mathfrak{z}_n(s)\}_{n=1}^\infty\big)+h\big(s,\{\mathfrak{z}_n(s)\}_{n=1}^\infty\big)\Big]ds\Bigg]\Bigg\}\\
&\le l_u{}^*\nu(\theta)\frac{2\mathcal{M}\mathcal{M}_0\mathcal{M}_w}{\Gamma(\alpha)}\\
&\quad\times\int_0^a(a-s)^{\alpha-1}\kappa\Big(\Big[A\mathcal{P}\big(s,\{\mathfrak{z}_n(s)\}_{n=1}^\infty\big)+h\big(s,\{\mathfrak{z}_n(s)\}_{n=1}^\infty\big)\Big]\Big)ds
\end{aligned}$$

$$\leq l_u{}^*\nu(\theta)\frac{2\mathcal{M}\mathcal{M}_0\mathcal{M}_w}{\Gamma(\alpha)}\int_0^a (a-s)^{\alpha-1}\left(l_p{}^*+l_f{}^*\right)s^{1-\vartheta}\kappa\left(\{\mathfrak{z}_n(s)\}_{n=1}^{\infty}\right)ds.$$

Also by Lemma 2.7,

$$\begin{aligned}
&\kappa\left(\Gamma_\eta\left(\{\mathfrak{z}_n(\theta)\}_{n=1}^{\infty}\right)\right)\\
&=\kappa\left\{S_{\alpha,\beta}(\theta)[\mathfrak{z}_0+\phi(\mathfrak{z})-\mathcal{P}(0,\mathfrak{z}(0))]\right.\\
&+\mathcal{P}\left(\theta,\{\mathfrak{z}_n(\theta)\}_{n=1}^{\infty}\right)+\lim_{\lambda\to\infty}\int_0^\theta(\theta-s)^{\alpha-1}T_\alpha(\theta-s)\mathcal{B}_\lambda\\
&\left.\left[A\mathcal{P}\left(s,\{\mathfrak{z}_n(s)\}_{n=1}^{\infty}\right)+Bu(s)+h\left(s,\{\mathfrak{z}_n(s)\}_{n=1}^{\infty}\right)\right]ds\right\}\\
&\leq\kappa\left(\mathcal{P}\left(\theta,\{\mathfrak{z}_n(\theta)\}_{n=1}^{\infty}\right)+\lim_{\lambda\to\infty}\int_0^\theta(\theta-s)^{\alpha-1}T_\alpha(\theta-s)\right.\\
&\times\mathcal{B}_\lambda\left[A\mathcal{P}\left(s,\{\mathfrak{z}_n(s)\}_{n=1}^{\infty}\right)+h\left(s,\{\mathfrak{z}_n(s)\}_{n=1}^{\infty}\right)\right]ds\\
&\left.+\lim_{\lambda\to\infty}\int_0^\theta(\theta-s)^{\alpha-1}T_\alpha(\theta-s)\mathcal{B}_\lambda\left[Bu\left(s,\{\mathfrak{z}_n(s)\}_{n=1}^{\infty}\right)\right]ds\right)\\
&\leq l_p{}^*\theta^{1-\vartheta}\kappa\left(\{\mathfrak{z}_n(\theta)\}_{n=1}^{\infty}\right)+\frac{2\mathcal{M}\mathcal{M}_0}{\Gamma(\alpha)}\int_0^a(a-s)^{\alpha-1}\left(l_p{}^*+l_f{}^*\right)s^{1-\vartheta}\\
&\times\kappa\left(\{\mathfrak{z}_n(s)\}_{n=1}^{\infty}\right)ds+\frac{2\mathcal{M}\mathcal{M}_0\mathcal{M}_b}{\Gamma(\alpha)}\int_0^a(a-s)^{\alpha-1}\kappa\\
&\left(u\left(s,\{\mathfrak{z}_n(s)\}_{n=1}^{\infty}\right)\right)ds\\
&\times\kappa\left(\{\mathfrak{z}_n(s)\}_{n=1}^{\infty}\right)ds+\frac{2\mathcal{M}\mathcal{M}_0\mathcal{M}_b\mathcal{M}_w}{\Gamma(\alpha)}\int_0^a(a-s)^{\alpha-1}\\
&\times\left[l_u{}^*\nu(s)\frac{2\mathcal{M}\mathcal{M}_0}{\Gamma(\alpha)}\int_0^a(a-\xi)^{\alpha-1}\left(l_p{}^*+l_f{}^*\right)s^{1-\vartheta}\right.\\
&\left.\kappa\left(\{\mathfrak{z}_n(\xi)\}_{n=1}^{\infty}\right)d\xi\right]ds\\
&\times\int_0^a(a-s)^{\alpha-1}\left[l_u{}^*\nu(s)\frac{2\mathcal{M}\mathcal{M}_0}{\Gamma(\alpha)}\int_0^a\right.\\
&\left.(a-\xi)^{\alpha-1}\left(l_p{}^*+l_f{}^*\right)s^{1-\vartheta}\kappa\left(\{\mathfrak{z}_n(\xi)\}_{n=1}^{\infty}\right)d\xi\right]ds\\
&\leq l_p{}^*\theta^{1-\vartheta}\kappa(\mathbf{S})+\frac{2\mathcal{M}\mathcal{M}_0}{\Gamma(\alpha)}\left(l_p{}^*+l_f{}^*\right)\theta^{1-\vartheta}\\
&\times\left[1+\frac{2\mathcal{M}\mathcal{M}_0\mathcal{M}_b\mathcal{M}_w}{\Gamma(\alpha)}l_u{}^*\nu^*\right]\int_0^a(a-s)^{\alpha-1}\kappa(\mathbf{S})ds.
\end{aligned}$$

Using Mönch condition,

$$\begin{aligned}
\kappa(\mathbf{S})&\leq\overline{\mathrm{co}}(\{0\}\cup\Gamma_\eta(\mathbf{S}))=\kappa(\Gamma_\eta(\mathbf{S}))\\
&\leq l_p{}^*\theta^{1-\vartheta}\kappa(\mathbf{S})+\frac{2\mathcal{M}\mathcal{M}_0}{\Gamma(\alpha)}(l_p{}^*+l_f{}^*)\theta^{1-\vartheta}\\
&\quad\left[1+\frac{2\mathcal{M}\mathcal{M}_0\mathcal{M}_b\mathcal{M}_w}{\Gamma(\alpha)}l_u{}^*\nu^*\right]\int_0^a(a-s)^{\alpha-1}\kappa(\mathbf{S})ds.
\end{aligned}$$

Using Grownwall's inequality, we conclude that $\kappa(\mathbf{S})=0$. By Lemma 2.12, we observe that Γ_η has a fixed point in $\mathcal{B}_\iota(0,\mathcal{E})$. Hence the system (1.1) and (1.2) has a fixed point satisfying $\mathfrak{z}(a)=\mathfrak{z}_a$. Therefore, (1.1) and (1.2) is controllable on $[0,a]$. □

4. Results on optimal control

Consider the Lagrange problem (LP): Find a control $(\mathfrak{z}^0,u^0)\in C_{1-\vartheta}([0,b],X)\times U_{ad}$ provided that $\mathcal{J}(\mathfrak{z}^0,u^0)\leq\mathcal{J}(\mathfrak{z},u)$, for all $u\in U_{ad}$ with

$$\mathcal{J}(\mathfrak{z},u)=\int_0^b\mathcal{L}(\theta,\mathfrak{z}(\theta),u(\theta))d\theta$$

where U_{ad} denotes an admissible control set. Here $\mathfrak{z}$ is the solution of the system (1.1) and (1.2) corresponding to the control $u\in U_{ad}$. To analyze the problem (LP) we assume the subsequent hypotheses:

(H10) (i) The functional $\mathcal{L}:J\times X\times U\to\mathbb{R}\cup\{\infty\}$ is Borel measurable;
(ii) $\mathcal{L}(t,\cdot,\cdot)$ is sequentially lower semicontinuous on $X\times U$ for almost all $t\in J$;
(iii) $\mathcal{L}(t,x,\cdot)$ is convex on U for each $x,y\in X$ for almost all $t\in J$;
(iv) There exist constants $d\geq 0$, $j>0$, μ is nonnegative and $\mu\in L^P(J,\mathbb{R})$ such that

$$\mathcal{L}(\theta,\mathfrak{z},u)\geq\mu(\theta)+d||\mathfrak{z}||_C+j||u||_U^p.$$

Theorem 4.1. *If (H1)–(H10) hold, then LP has at least one optimal pair.*

Proof. If $\inf\{\mathcal{J}(\mathfrak{z},u)|(\mathfrak{z},u)\in C_{1-\vartheta}(J,X)\times U_{ad}\}=+\infty$, then the proof is trivial. Suppose

$$\inf\{\mathcal{J}(\mathfrak{z},u)|(\mathfrak{z},u)\in C_{1-\vartheta}(J,X)\times U_{ad}\}=\gamma<+\infty.$$

By (H6), we get $\gamma>-\infty$. By infimum definition, there exists a minimizing sequential pair $\{(\mathfrak{z}^n,u^n)\}\subset A_{ad}$, the set of all admissible state control pairs $(\mathfrak{z},u)$ such that $\mathcal{J}(\mathfrak{z}^n,u^n)\to\gamma$ as $n\to+\infty$. Since $\{u^n\}\subseteq U_{ad}$ for all $n\in N$, it is clear that $\{u^n\}$ is bounded on $L^P(J,U)$. Using the reflexive property, we show that there exists a sub-sequence, $\{u^0\}\in L^P(J,U)$ such that $\{u^n\}$ weakly converges to $\{u^0\}$ in $L^P(J,U)$. Since U_{ad} is closed and convex, by Mazur's lemma, $u^0\in U_{ad}$.

Let $\{z^n\}$ be the solution sequence of the integral equation

$$\mathfrak{z}^n(\theta)=S_{\alpha,\beta}(\theta)[\mathfrak{z}_0+\phi(\mathfrak{z}^n)-\mathcal{P}(0,\mathfrak{z}(0))]+\mathcal{P}(\theta,\mathfrak{z}^n(\theta))+\lim_{\lambda\to\infty}\int_0^\theta P_\alpha(\theta-s)\mathcal{B}_\lambda\left[A\mathcal{P}(s,\mathfrak{z}^n(s))+Bu^n(s)+h(s,\mathfrak{z}^n(s))\right]ds.$$

By using Lemma 2.8, the boundedness of $\{u^n\}$ and following Theorem 3.4, $\{\mathfrak{z}^n\}$ is a relatively compact subset of $C_{1-\vartheta}(J,X)$. Therefore there is a function $\mathfrak{z}^0\in C_{1-\vartheta}(J,X)$ such that

$$\mathfrak{z}^n\to\mathfrak{z}^0\in C_{1-\vartheta}(J,X).\tag{4.1}$$

Using (H3), (H5), (H7) and Eq. (4.1) with dominated convergence theorem, we get

$$\int_0^\theta P_\alpha(\theta-s)h(s,\mathfrak{z}^n(s))ds\to\int_0^\theta P_\alpha(\theta-s)h(s,\mathfrak{z}^0(s))ds,$$

$$\int_0^\theta P_\alpha(\theta-s)A\mathcal{P}(s,\mathfrak{z}^n(s))ds\to\int_0^\theta P_\alpha(\theta-s)A\mathcal{P}(s,\mathfrak{z}^0(s))ds,$$

$$\text{and}\quad\phi(\mathfrak{z}^n)\to\phi(\mathfrak{z}^0).$$

By above-said terms, we infer that

$$\begin{aligned}
\mathfrak{z}^n(\theta)\to\mathfrak{z}^0(\theta)&=S_{\alpha,\beta}(\theta)[\mathfrak{z}_0+\phi(\mathfrak{z}^0)-\mathcal{P}(0,\mathfrak{z}(0))]+\mathcal{P}(\theta,\mathfrak{z}^0(\theta))\\
&+\lim_{\lambda\to\infty}\int_0^\theta P_\alpha(\theta-s)\mathcal{B}_\lambda\\
&\left[A\mathcal{P}(s,\mathfrak{z}^0(s))+Bu^0(s)+h(s,\mathfrak{z}^0(s))\right]ds,
\end{aligned}$$

where $\mathfrak{z}^0$ represents the solution sequence of the system (1.1) and (1.2) corresponding to u^0. Using (H10) and Balder's theorem, we get

$$(\mathfrak{z},u)\to\int_0^b\mathcal{L}(\theta,\mathfrak{z}(\theta),u(\theta))d\theta$$

is sequentially lower semicontinuous in the weak topology of $L^P(J,X)$. We conclude that $\mathcal{J}$ is weakly lower semicontinuous on $L^P(J,X)$. By (H10(iv)), $\mathcal{J}$ attains its infimum at $u^0\in U_{ad}$, that is,

$$\lim_{n\to\infty}\int_0^b\mathcal{L}(\theta,\mathfrak{z}^n(\theta),u^n(\theta))d\theta\geq\int_0^b\mathcal{L}(\theta,\mathfrak{z}^0(\theta),u^0(\theta))d\theta\geq\gamma.$$

□

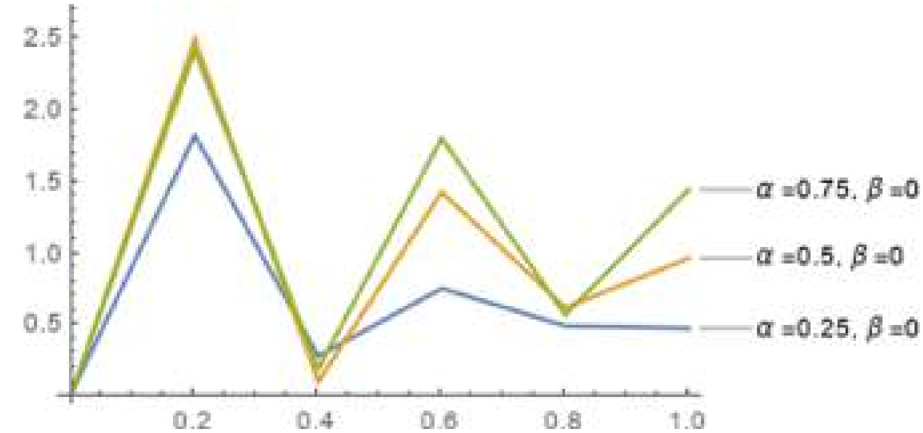

Fig. 1. Numerical approximation for R-L (Hilfer with $\beta = 0$) form.

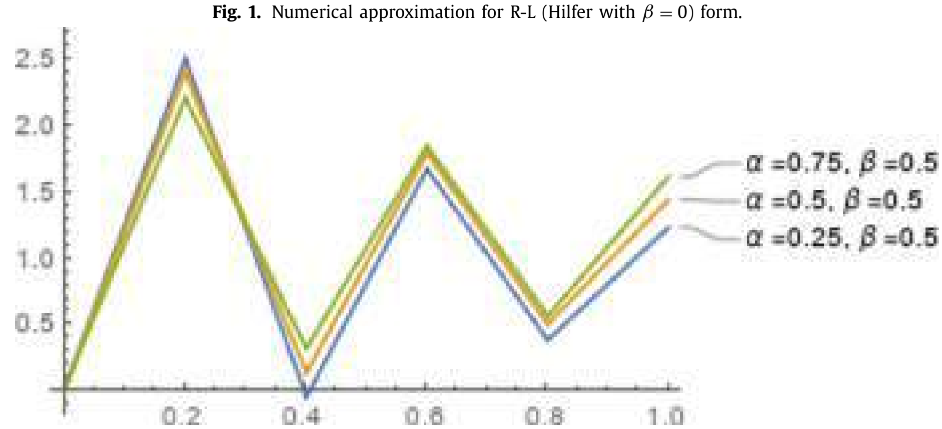

Fig. 2. Numerical approximation for Hilfer ($\beta = 0.5$) form.

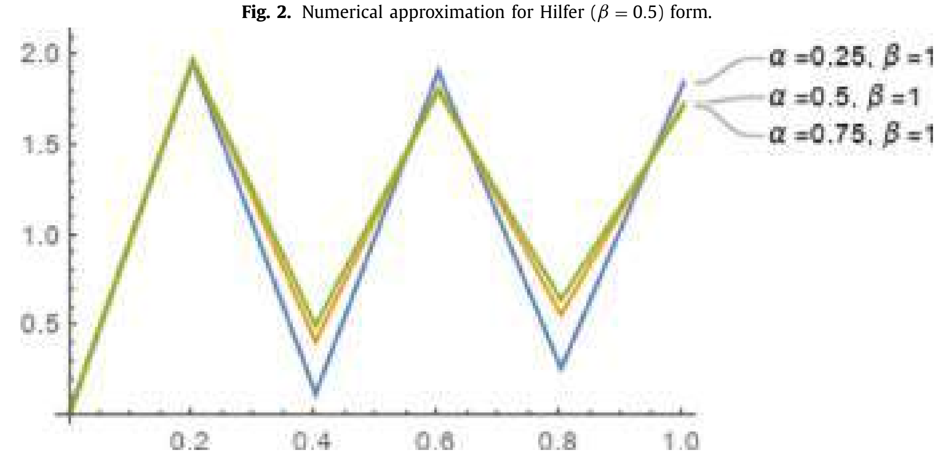

Fig. 3. Numerical approximation for Caputo (Hilfer with $\beta = 1$) form.

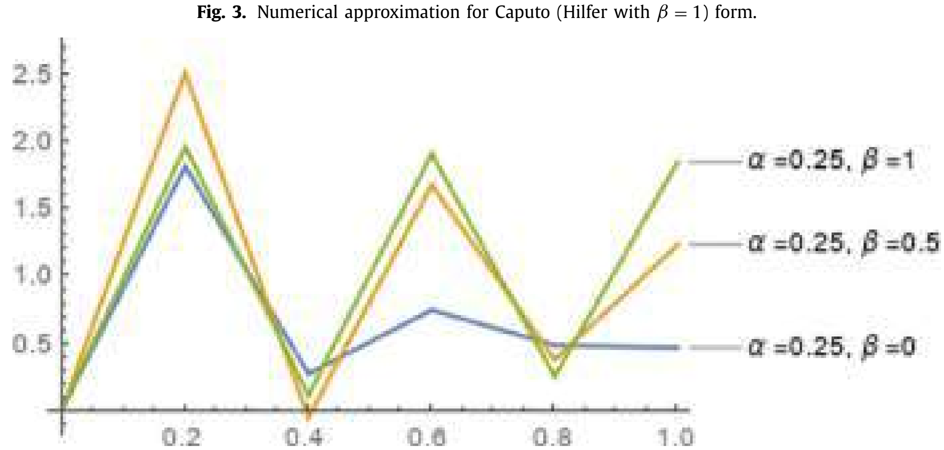

Fig. 4. Numerical approximation for $\alpha = 0.25$.

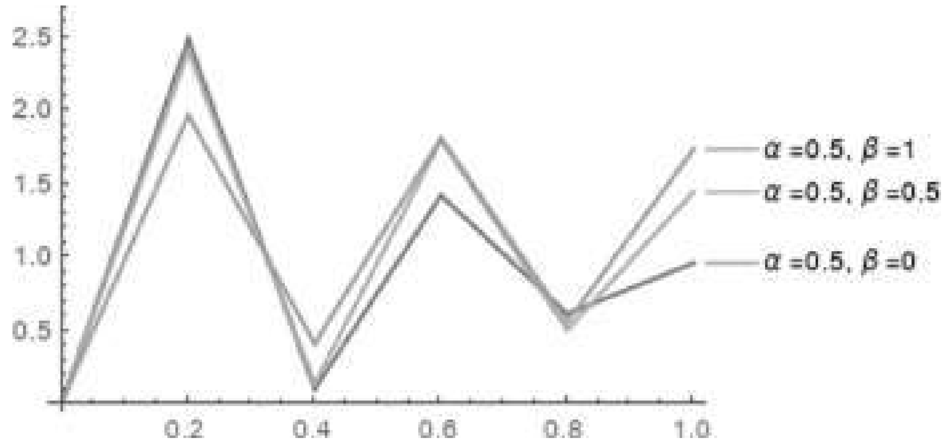

Fig. 5. Numerical approximation for $\alpha = 0.5$.

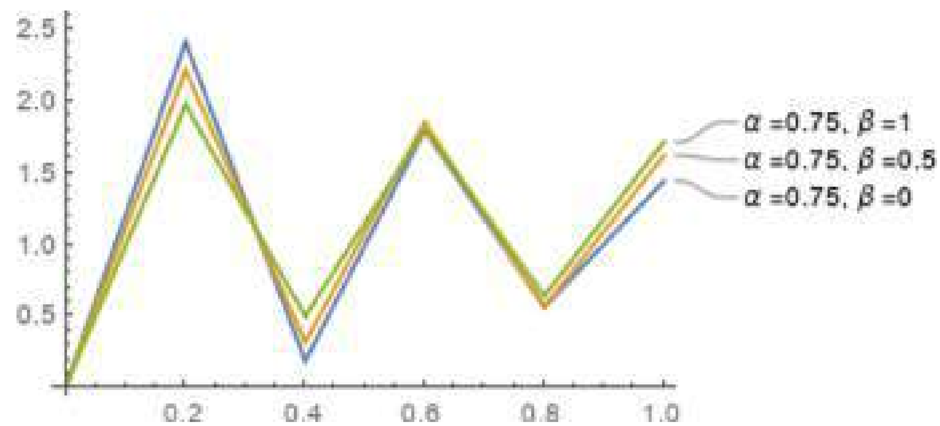

Fig. 6. Numerical approximation for $\alpha = 0.75$.

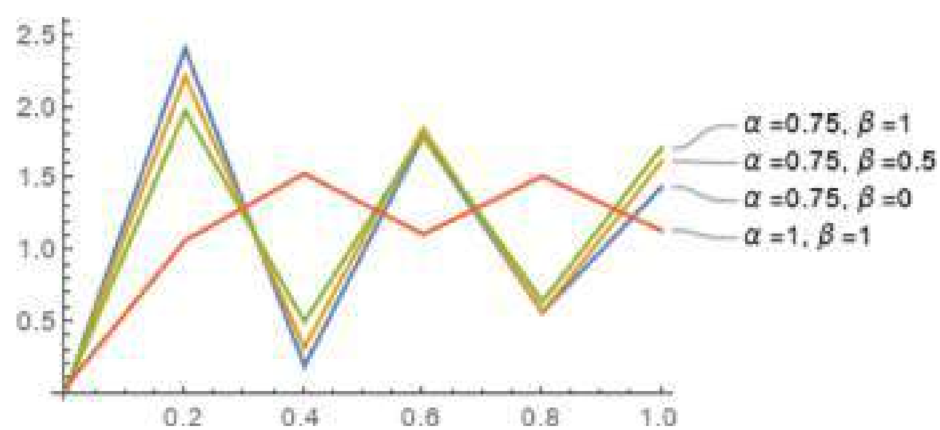

Fig. 7. Numerical approximation for $\alpha = 0.75, \alpha = 1$.

5. Numerical analysis

Consider the problem

$$\mathcal{D}_{0+}^{\alpha,\beta}[y(t) - \frac{\sin(y(t))}{40}] = Ay(t) + \frac{e^{-t}\sin(y(t))}{4}, \tag{5.1}$$

$$I_{0+}^{(1-\alpha)(1-\beta)}y(0) = 1 + \cos y, \qquad t \in \mathcal{I} = [0, 1], \tag{5.2}$$

Consider $D(A) = \{y \in \mathcal{C}^2([0, 1], R) : y(0) = y(1) = 0\}$, $Ay = y''$ where $\mathcal{H} : \mathcal{C}([0, 1], R)$ provided with the uniform topology and $A : D(A) \subset \mathcal{H} \to \mathcal{H}$.

A successive approximation of (5.1) and (5.2) is

$$y_n(t) = \frac{\left[1 + \cos y + \frac{\sin(y(0))}{40}\right]t^{\theta-1}}{\Gamma(\theta)} + \frac{\sin(y_{n-1}(t))}{40} + \frac{1}{\Gamma(\alpha)}\int_0^t (t-s)^{\alpha-1}\frac{e^{-s}\sin(y_{n-1}(s))}{4}ds,$$

where $\vartheta = \alpha + \beta - \alpha\beta$ and n varies from 1 to 6.

By Remark 2.4, we analyze the numerical approximation for existence of three types of solutions. Figs. 1–10 represent the solutions in Riemann–Liouville, Hilfer and Caputo's forms and

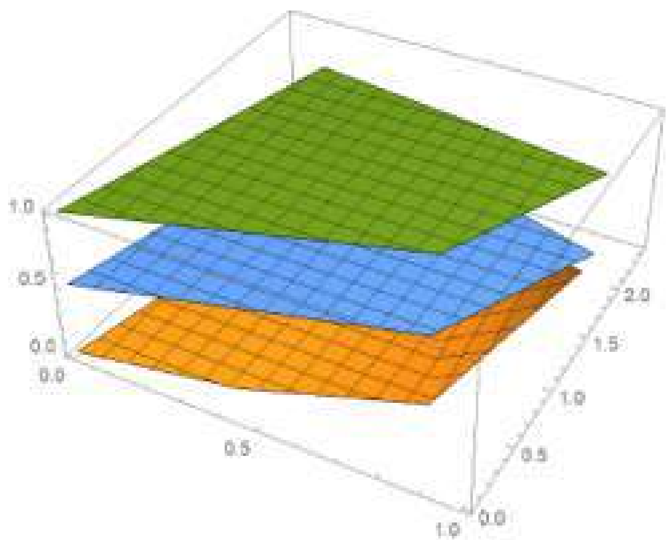

Fig. 8. Numerical approximation for $\alpha = 0.75$.

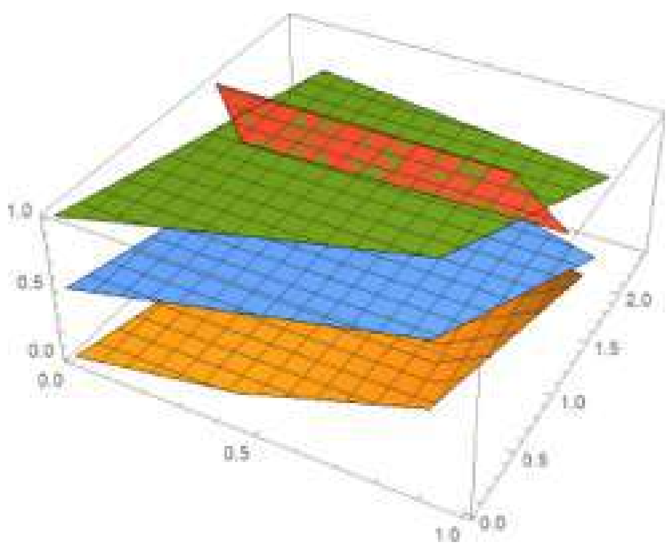

Fig. 9. Numerical approximation for $\alpha = 0.75, \alpha = 1$.

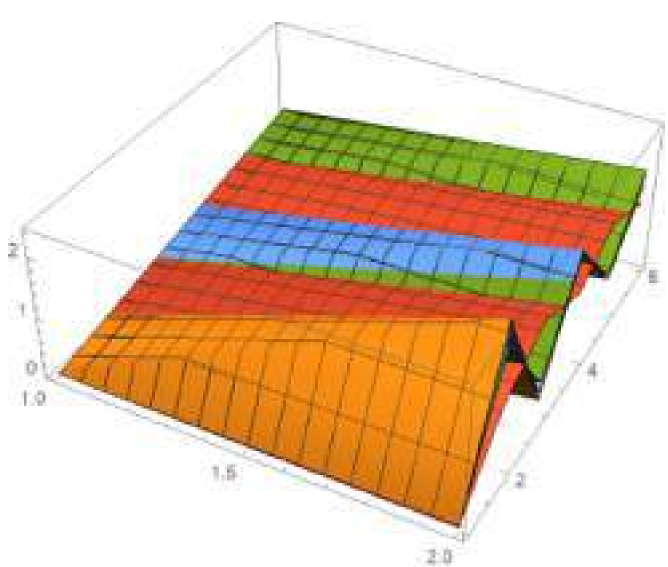

Fig. 10. Numerical approximation for $\alpha = 0.75$.

also the comparison among them for the different values of $\alpha = 0.25, 0.5, 0.75$ and $\beta = 0, 0.5, 1$.

6. Conclusion

This manuscript illustrates the controllability of neutral Hilfer fractional derivative with non-dense domain in a Banach space using semigroup theory, fixed point approach, and fundamentals of fractional calculus. Our theorem ensures the effectiveness of controllability and optimal control of the system concerned. Finally, numerical analyses have been done to compare the solution in different criteria of parameters. One can elevate this theory via some additional inclusions and different fixed point approaches.

Funding

None.

Declaration of Competing Interest

The authors declare that they have no known competing financial interests or personal relationships that could have appeared to influence the work reported in this paper.

CRediT authorship contribution statement

Kottakkaran Sooppy Nisar: Conceptualization, Writing - original draft, Software, Formal analysis, Writing - review & editing. **K. Jothimani:** Writing - original draft, Software, Validation. **K. Kaliraj:** Formal analysis, Writing - original draft, Software. **C. Ravichandran:** Conceptualization, Writing - original draft, Methodology, Software, Supervision, Writing - review & editing.

References

[1] Agarwal P, Baleanu D, Quan Y, Momani CS, Machado JA. Fractional calculus–models, algorithms, technology. Singapore: Springer; 2018.
[2] Bahaa GM. Optimal control problem and maximum principle for fractional order cooperative systems. Kybernetika 2019;55(2):337–58.
[3] Dineshkumar C, Udhayakumar R, Vijayakumar V, Nisar KS. A discussion on the approximate controllability of Hilfer fractional neutral stochastic integro-differential systems. Chaos Solitons Fractals 2020;142:110472.
[4] Du J, Jiang W, Pang D, Niazi AUK. Exact controllability for Hilfer fractional differential inclusions involving nonlocal initial conditions. Complexity 2018;2018:1–13.
[5] Fu XL. On solutions of neutral nonlocal evolution equations with non-dense domain. J Math Anal Appl 2004;299:392–410.
[6] Fu X, Liu X. Controllability of non-densely defined neutral functional differential systems in abstract space. Chin Ann Math 2007;28(2):243–52.
[7] Furati KM, Kassim MD, Tatar NE. Existence and uniqueness for a problem involving Hilfer fractional derivative. Comput Math Appl 2012;64:1616–26.
[8] Gatsori EP. Controllability results for non-densely defined evolution differential inclusions with nonlocal conditions. J Math Anal Appl 2004;297:194–211.
[9] Ghandehari MAM, Ranjbar M. A numerical method for solving a fractional partial differential equation through converting it into an NLP problem. Comput Math Appl 2013;65(7):975–82.
[10] Gu H, Zhou Y, Ahmad B, Alsaedi A. Integral solutions of fractional evolution equations with non-dense domain. Electron J Differ Equ 2017;145:1–15.
[11] Gu H, Trujillo JJ. Existence of mild solution for evolution equation with Hilfer fractional derivative. Appl Math Comput 2015;257:344–54.
[12] Harrat A, Nieto JJ, Debbouche A. Solvability and optimal controls of impulsive Hilfer fractional delay evolution inclusions with clarke subdifferential. J Comput Appl Math 2018;344:725–37.
[13] Hilfer R. Applications of fractional calculus in physics. Singapore: World Scientific; 2000.
[14] Hilfer R, Luchko Y, Tomovski Z. Operational method for the solution of fractional differential equations with generalized Riemann–Liouville fractional derivatives. Fract Calc Appl Anal 2009;12:289–318.
[15] Herrera DEB, Galeano NM. A numerical method for solving Caputo's and Riemann–Liouville's fractional differential equations which includes multi-order fractional derivatives and variable coefficients. Commun Nonlinear Sci Numer Simul 2020;84. doi:10.1016/j.cnsns.2020.105180.
[16] Jothimani K, Kaliraj K, Hammouch Z, Ravichandran C. New results on controllability in the framework of fractional integro-differential equations with non-dense domain. Eur Phys J Plus 2019;134(441):1–10.

[17] Kavitha K, Vijayakumar V, Udhayakumar R. Results on controllability of Hilfer fractional neutral differential equations with infinite delay via measures of noncompactness. Chaos Solitons Fractals 2020;139:1–9.
[18] Kilbas AA, Srivastava HM, Trujillo JJ. Theory and applications of fractional differential equations. North-Holland mathematics studies, 204. Amsterdam: Elsevier Science; 2006.
[19] Kucche KD, Chang YK, Ravichandran C. Results on non-densely defined impulsive Volterra functional integro-differential equations with infinite delay. Nonlinear Stud 2016;23(4):651–64.
[20] Kumar A, Pandey DN. Controllability results for non-densely defined impulsive fractional differential equations in abstract space. Differ Equ Dyn Syst 2021;29:227–37.
[21] Lakshmikantham V, Leela S, Devi JV. Theory of fractional dynamic systems. Cambridge Scientific Publishers; 2009.
[22] Lv J, Yang X. Approximate controllability of Hilfer fractional differential equations. Math Methods Appl Sci 2020;43(1):242–54.
[23] Liu X, Li Y, Xu G. On the finite approximate controllability for Hilfer fractional evolution systems. Adv Differ Equ 2020;22(2020). doi:10.1186/s13662-019-2478-5.
[24] Pazy A. Semigroups of linear operators and applications to partial differential equations. New York: Springer-verlag; 1983.
[25] Pan X, Li X, Zhao J. Solvability and optimal controls of semi linear Riemann–Liouville fractional differential equations. Abstr Appl Anal 2014;2014:216919.
[26] Podlubny I. Fractional differential equations. An introduction to fractional derivatives, fractional differential equations, to methods of their solution and some of their applications. San Diego: Academic Press; 1999.
[27] Prato GD, Sinestrari E. Differential operators with non-dense domain. Ann Della Scuola Norm SuperPisa 1987;14:285–344.
[28] Qin H, Zuo X, Liu J, Liu L. Approximate controllability and optimal controls of fractional dynamical systems of order $1 < q < 2$ in Banach space. Adv Differ Equ 2015;73(2015). doi:10.1186/s13662-015-0399-5.
[29] Ravichandran C, Valliammal N, Nieto JJ. New results on exact controllability of a class of fractional neutral integro-differential systems with state-dependent delay in Banach spaces. J Frankl Inst 2019;356(3):1535–65.
[30] Sousa JVC, Kucche KD, de Oliveira EC. On the Ulam–Hyers stabilities of the solutions of ψ-Hilfer fractional differential equation with abstract Volterra operator. Math Methods Appl Sci 2019;42(9):3021–32.
[31] Subashini R, Ravichandran C, Jothimani K, Baskonus HM. Existence results of Hilfer integro-differential equations with fractional order. Discrete Contin Dyn Syst Ser S 2018;13(3):911–23.
[32] Subashini R, Jothimani K, Nisar KS, Ravichandran C. New results on nonlocal functional integro-differential equations via Hilfer fractional derivative. Alexandria Eng J 2020;59(5):2891–9.
[33] Singh V. Controllability of Hilfer fractional differential systems with non-dense domain. Numer Funct Anal Optim 2019;40(13):1572–92.
[34] Vijayakumar V. Approximate controllability results for non-densely defined fractional neutral differential inclusions with Hille Yosida operators. Internat J Control 2018. doi:10.1080/00207179.2018.1433331.
[35] Vijayakumar V, Udhayakumar R. Results on approximate controllability for non-densely defined Hilfer fractional differential system with infinite delay. Chaos Solitons Fractals 2020;139:1–9.
[36] Vijayakumar V, Udhayakumar R. A new exploration on existence of Sobolev–type Hilfer fractional neutral integro-differential equations with infinite delay. Numer Methods Partial Differ Equ 2020;37(1):1–17.
[37] Wang JR, Zhang Y. Nonlocal initial value problems for differential equations with Hilfer fractional derivative. Appl Math Comput 2015;266:850–9.
[38] Wang JR, Ibrahim AG, O'Regan D. Finite approximate controllability of Hilfer fractional semilinear differential equations. Miskolc Math Notes 2020;21(1):489–507.
[39] Wang JR, Ibrahim G, O'Regan D. Controllability of Hilfer fractional noninstantaneous impulsive semilinear differential inclusions with nonlocal conditions. Nonlinear Anal Model Control 2019;24(6):743–62.
[40] Wang JR, Liu X, O'Regan D. On the approximate controllability for Hilfer fractional evolution hemivariational inequalities. Numer Funct Anal Optim 2019;40(7):958–84.
[41] Yang M, Alsaedi A, Ahmad B, Zhou Y. Attractivity for Hilfer fractional stochastic evolution equations. Adv Differ Equ 2020;130(2020). doi:10.1186/s13662-020-02582-4.
[42] Yang M, Wang QR. Approximate controllability of Hilfer fractional differential inclusions with nonlocal conditions. Math Methods Appl Sci 2017;40(4):1126–38.
[43] You Z, Feckan M, Wang JR. Relative controllability of fractional delay differential equations via delayed perturbation of Mittag–Leffler functions. J Comput Appl Math 2020;378. doi:10.1016/j.cam.2020.112939.
[44] Zhang Z, Liu B. Controllability results for fractional functional differential equations with non-dense domain. Numer Funct Anal Optim 2014;35(4):443–60.
[45] Zhang J, Wang JR, Zhou Y. Numerical analysis for time-fractional schrodinger equation on two space dimensions. Adv Differ Equ 2020;53(2020). doi:10.1186/s13662-020-2525-2.
[46] Zhou Y, Vijayakumar V, Ravichandran C, Murugesu R. Controllability results for fractional order neutral functional differential inclusions with infinite delay. Fixed Point Theory 2017;18(2):773–98.
[47] Zhou Y, Jiao F. Nonlocal cauchy problem for fractional evolution equations. Nonlinear Anal Real World Appl 2010;11:4465–75.
[48] Zhou Y. Basic theory of fractional differential equations. Singapore: World Scientific; 2014.

International Journal of Aquatic Science
ISSN: 2008-8019
Vol 12, Issue 02, 2021

Analyzing Various Graph Theory Applications Using Mathematical And Computational Intelligence Approach

[1]Dr.R.Vijaya, [2]Dr.K.Maheswari, [3]Utpal Saikia, [4]Dr.Shaik.Shakeer Basha, [5]Dr.Syed Khasim,[6]Dr. R. Sreeparimala,

[1]Assistant Professor, PG & Research Dept. Computer Science, Arignar Anna Govt. Arts College for Women , Walajapet - 632 513 , Ranipet Dist. , Tamil Nadu , India.
[2]Associate Professor, Department of Computer Science and Engineering, CMR Technical Campus, Kandlakoya (V), Medchal Road, Hyderabad 501401, Telangana,India.
[3]Assistant Professor, Department of Mathematics, Silapathar College, Dhemaji Assam-787059.
[4]Assistant Professor, Computer Science & Engineering, Avanthi Institute of Engineering and Technology, Gunthapally, Abdullahpurmet Mandal, Telangana-501512.
[5]Professor, Department of Computer Science & Engineering, Dr.Samuel George Institute of Engineering & Technology, Markapur, Prakasam Dt, Andhra Pradesh, 523316.
[6]Associate professor, Mathematics, Sri Eshwar College of Engineering, Coimbatore-641202.

Abstract
Graph theory is a part of mathematical analysis which studies the relationships between fundamental results in several fields with pure mathematics. The goal of this research is two - fold: first, to grasp the fundamental concepts of graph theory, second, to emphasise the importance of graph theory thru a practical case which was used as a framework investigation as well as character development of the structural brain system, similar to how machine learning can be used to apply models based on factors spatial information. Data pre - processing, associations, attributes, and techniques are some of the approaches used in this approach. The pictures from the Magnetic Resonance Imaging (MRI) device are used to demonstrate an automatic tool for performing a typical process. Pre-processing, graph creation for every area with various associations, mapping, essential extraction of features based on literature review, and lastly offering a collection of machine learning models which can give interpretable findings for clinicians or experts are all part of a process. This research will examine the most viable method of graph theory in numerous domains to emphasize the impact of graph theory. A summary of graph theory issues pertinent to their ideas and tactics is also included in this study.

Keywords: Graph Theory, Applications, Computational Intelligence, Set Theory, Representations

1. INTRODUCTION

When a theory is used in actual life, it will be more significant. Arithmetic modelling is the use of statistical methods or instruments to depict or simulate real-world problems. One such technique for representing real-world objects and activities called graph theory. Graphs have some of the most used patterns with both environmental & man-made structures. A graph is indeed a geometrical formal expression of vertex that connect pairings of vertex which is used to depict the connection amongst items. Graphs could be used to represent a variety of real concerns. In economic, industrial, ecological, & computer programming domains, they will be used to depict a variety of relationships underlying operation dynamics.

Along with its experience in a variety domain including such knowledge discovery and picture processing, communications & code technique, grouping & sequencing, and optimization techniques & operations, the graph idea has really become a core of engineering and innovation. Using graph theory to solve a fundamental condition is the same as estimating solutions to source of actual scenario. Graph theory is indeed a subfield of mathematics education that studies the properties and characteristics of graphs [1]. It shows the elements' interconnections. A few of the advantages of graph theory is that it provides a common framework for a range of issues. It just gives you graph techniques to solve this issue. The vertex or node indicates the objects throughout all domains wherein graph are employed for modelling, while the edge indicates the relationships among the objects. The Konignberg bridging challenge is where graph theory begins. The answer to some well conundrum gave rise to the concept of Eulerian graph.

Euler examined this Konignberg bridges challenge & discovered a workable approach in 1736, when he published Euler's resolution to the Konigsberg bridging challenge, now known as the Eulerian graph [2]. Mobius proposed the full graphs with bipartite graph in 1840, and Kuratowski used leisure puzzles to show that they have been plane. Kirchhoff invented the concept of trees (a linked graphs having no loops) in 1845, and he is using graph concepts to estimate voltages and power within electronic systems. Gutherie created the well-known four-color dilemma in 1852. Later, in 1856, Hamilton studied polyhydra loops & came up with the concept of the Hamiltonian graphs via looking at journeys which visits specific places precisely only one time.

2. GRAPH THEORETIC NOTATIONS

It is required to be knowledgeable with all elementary concepts throughout the graph to get a strong understanding about graph theory. A graph is indeed an ordered pair G = (V, E) that contains a subset V comprising node vertex and a set E of edges that connect the node in V. Graphs get their name from the fact that they're being represented graphically, and this graphical depiction helps us grasp many of their characteristics. In graphic representations of graphs, nodes are represented by spots or tiny spheres. A graph's edge is composed of 2 node (e.g., n1, n2). Edges are usually represented graphically as curving or vertical/horizontal lines connecting the spots associated with the corresponding nodes. Points which sharing edges are mostly referred to as neighboring or neighbors. Occurrence to every one of the pair of nodes refers to such an edge which connects 2 node. Adjacent edge would be those who intersect at a specific layer. The vertex in Fig.1 were Ve = a,b,c,d,e as well as the edges were (a,b),(a,c),(a,d),(b,e),(c,d),(d,e).

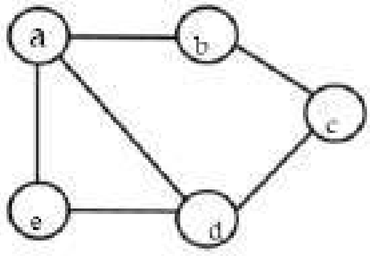

Figure 1: Graph

Definition 1: A bipartite graph is one in which the vertex set Ve(T) is made up of bipartitions X and Y, with the intersections of A and B being the empty set as well as the intersection with A or B being Ve(T). A bipartite graph's corner subset is made up entirely of lines of one endpoint in A and the other in B. The nodes of a network shown in Figure 5 could be split into 2 groups: A = D,C and B = E,F. Set A nodes only connect with set A nodes, & conversely. Entities in same subset will not link together. As a result, it was a bipartite graph.

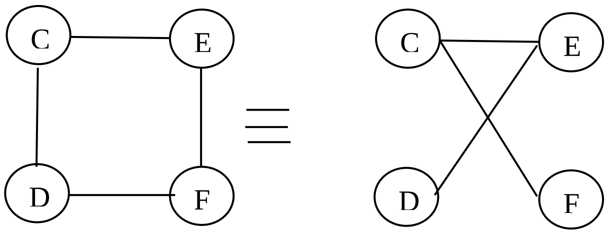

Figure 2: bipartite graph

Definition 2: A full bipartite graph was defined as a network in which each point of group A is connected to every point of group B, as shown in Figure 3

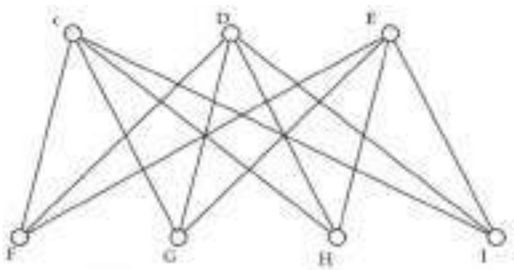

Figure 3: A complete bipartite

Definition 3: A sub-graph T0 of T, often known as T0 T, is a graph where almost every edges & vertex within T0 is indeed present in T. Figure 4 shows how this works.

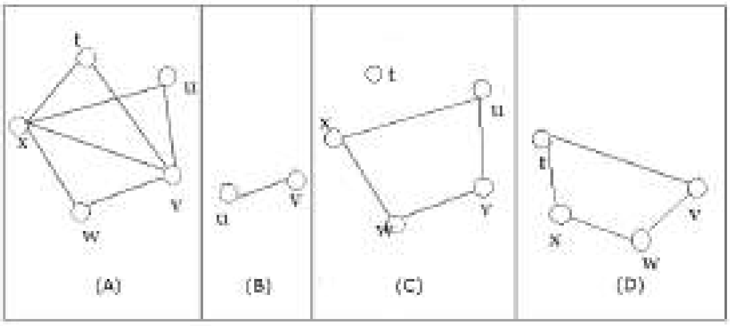

Figure 4: Graphs (B), (C) and (D) are subgraphs of the graph (A)

Definition 4: Assume that D⊆ E is a sub-set of T's nodes group. The generated sub-graph T0 = T[U] then is made up of node within D as well as solely these edges from T that have all these endpoints in D.

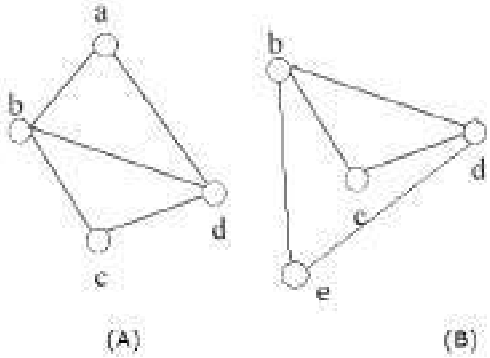

Figure 5: Graphs (B) is induced subgraphs of the graph (A)

Definition 5: A graph walk is also an alternate ordered set of nodes, with links displayed near to vertices acting as incidence edges to certain nodes. The number of edges in the array refers to the length of a path. If the path draws to a close in which it began, it is considered completed.

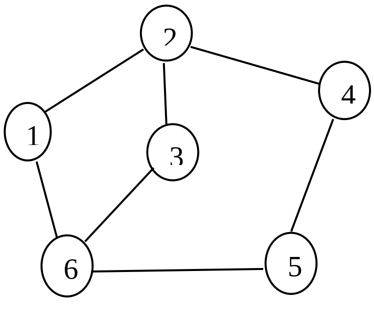

Figure 6: Example for walks in graph 1-2-3-6-5-4

Definition 6: A route inside a graph G is a sub-graph of T with V(Path) = i0,i1,i2,...,ik and E(Path) = i0i1,i1i2,...,ik1ik, wherein i0,i1,...,ik are unique graph vertices. The vertices i0 and ik are known as Path's endpoints. The number of vertices throughout the pathway determines its length, as well as a shorthand method for denoting pathways has become an ordered set with vertices (e.g. Path = i0i1...ik). Since no node were duplicated throughout the path, it is thus a route.

International Journal of Aquatic Science
ISSN: 2008-8019
Vol 12, Issue 02, 2021

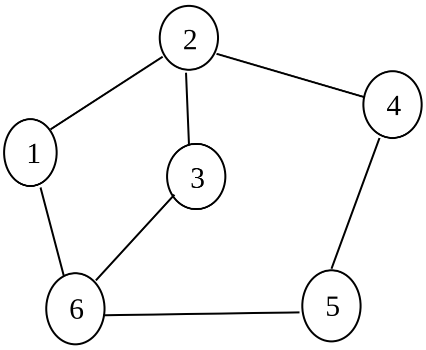

Figure 7: An example path in the graph 1-2-4-5-6

3. MATHEMATICAL REPRESENTATION OF THE GRAPH

The adjacency matrix is a arithmetical description for a graph. The adjacency matrix seems to be a a 2D array which each square represents whether or not 2 nodes are connected. Whenever there is a link among the two nodes, cell include '1', & because there's not, cells contain '0.' Whenever self-edges really aren't permitted, diagonal cells have '0.' And for graph shown in Figure 1, Figure 8 illustrate the adjacency cell matrix.

Vertex ID	a	b	c	d	e
a	0	1	1	1	0
b	1	0	0	0	1
c	1	0	0	1	0
d	1	0	1	0	1
e	0	1	0	1	0

Figure 8: Adjacency Matrix for the Graph

Controlling Sets (CS) is a word that is used frequently in graph theory . A CS for a graph T= (Ve, E) is indeed a collection Ve′ of Ve in which every vertex which isn't in Ve′ is linked with at least single component of Ve′ by an edge [4]. A controlling set of size 3 is shown in Figure 9, with the red node p, q, and r forming the controlling sets.

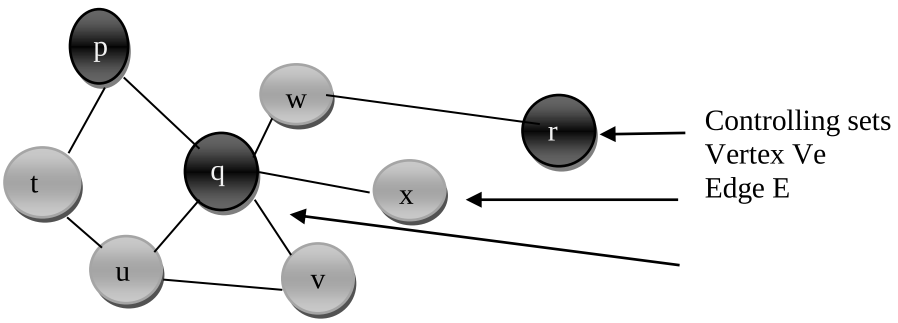

Figure 9: Dominating Set

International Journal of Aquatic Science
ISSN: 2008-8019
Vol 12, Issue 02, 2021

A Minimal Dominant Set (MDS) is a Controlling Sets that has the shortest cardinality between all the CS of T. MDS of size 2 is depicted in Figure 17, with the dark lines forming MDS.

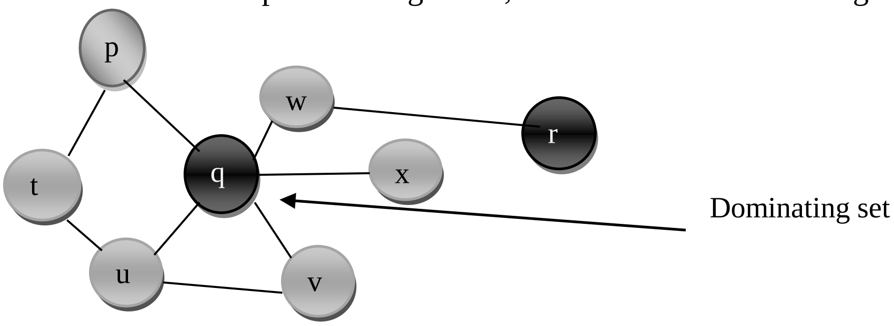

Figure 10: Minimum Dominating Set

Remember that even a node covering C is really a sub-set of the vertices in something like a simplified given Graph T that has at minimum 1 endpoint in C in each edge. As a result, in the dispute graph T, the goal is to find a min node overlap (it is an NP-complete problem). Lets take a glance at a particular instance of a Snps assembling dilemma from [8] and show how the nodes covers approach can help us solve it. A single system alteration within DNA is called a Single Nucleotide Polymerase reaction (SNPR, called "snip"). The most prevalent form of genomic variations in human chromosome is considered to be SNPs (91 percent of all human DNA polymorphisms).

This is how the SNPR Assembly Challenge is described. An SNPR assembly is indeed a trio (F, G, H), where F = f1,..., fn is a collection of n SNPRs, G = g1,..., gm is a subset of m segments, and H is a connection G: FG 0, A, B that specifies if an SNPR fi F does not appear on a fragmentation gj G (marked by 0) and if it does, the non-zero number of fi (A or B). 2 SNPs fi and fj are said to be in conflict if there are two fragments Gk and Gl with the same non-zero value in H(fi, gk), H(fi, gl), H(fj, gk), H(fj, gl) and the opposite non-zero value in H(fj, gl). The objective is to end as few SNPs as feasible in order to remove any disputes. Figure 10 depicts the simple guidelines from [7]. It's worth noting because H is only specified for such a sub-set of FG derived from experimental data. For example, since H (f1, g2) = B, H (f1,g5) = B, H (f5, g2) = B, H (f5, g5) = A, f1 and f5 are in dispute. (f4, g1) = A, H (f4, g3) = A, H (f6, g1) = B, H(f6, g3) = A, hence f4 & f6 are in dispute once more. Similarly, the table makes it simple to compute all pairings of opposing SNPRs. Figure 11 depicts the conflicts graph relating to this SNPR assembling difficulty.

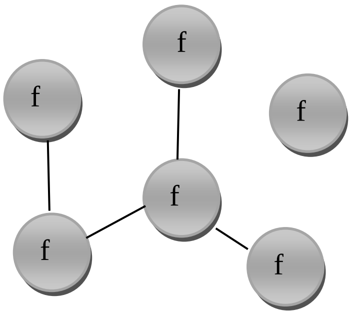

Figure 11: The conflict graph for SNP assembly problem

The minimum node coverage throughout the dispute graph are now determined using the nodes covering methodology. The no of nodes 6 is provided as an input, accompanied by adjacency matrix including its graph shown in Figure 12. If another nodes fi & fj use an edge throughout the dispute graph, the item in column j and row i of the adjacency matrix is one, otherwise it is zero.

0	0	0	0	1	0
0	0	0	1	0	0
0	0	0	0	0	0
0	1	0	0	1	1
1	0	0	1	0	0
0	0	0	1	0	0

Figure 12: The input for the vertex cover algorithm

Two unique minimum vertex coverings are discovered by the vertex software.

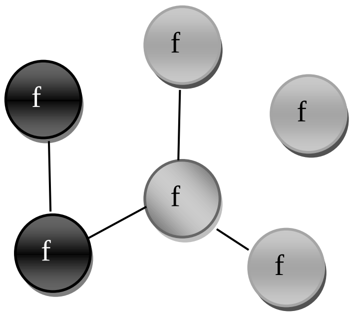

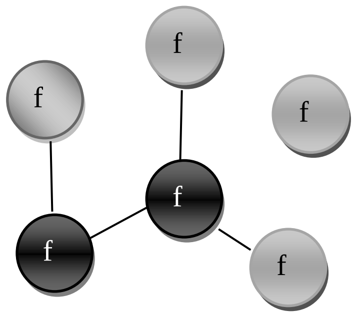

Figure 13: Minimum Vertex Cover: f1, f2

Figure 14: Minimum Vertex Cover: f2,f3

As a result, whether removing f1, f2 or removing f2, f3 addresses the SNP assembling challenge. Figure15 illustrates an image of a graph demonstrate the html page. The title, images, & phrases are used to mark the borders.

Figure 15: Web document – Graph representation

Whenever entities pass the border from one detector, i.e. the sensing area of one detector, then join the sensing zone of yet another detector, the preceding detector must correctly communicate this to the adjoining detector. The detecting strength is determined by the incidence rates among two adjacent detectors. The system is described as just an undirected weighted network T(DeT, ET, WT) wherein v corresponds to DeT and edge (u,v) belongs to ET, assuming that perhaps the device's transmit power is broad enough so the two neighbours can interact directly with one another. The detectors are represented by D, whereas the neighbours are represented by u,v. WT(u,v) is the EG's weighed edge of (u,v). The idea of wraps was employed by the scholars.

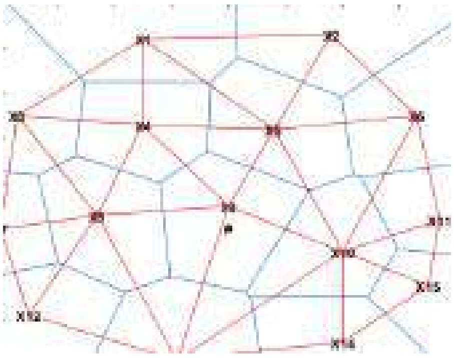

Figure 16: Voronoi diagram with regions

4. RESULTS

Whenever the methodology was put into practice, a testing based on photos from either a prior migraines project was conducted.

Table 1 Graph theory results.

Char	Area	Controls N(M/SL)	SD(M/SL)	Sporadic Migraine N(M/SL)	SD(m/SL)	Medication abuse N(M/SL)	SD(M/SL)
X	91 118	1.0678/1.0602 1.0655/1.093	0.234/0.342 0.032/0.477	1.09/1.098 1.08/1.089	0.013/0.023 0.013/0.003	1.079/1.054 1.066/1.075	0.014/0.04 0.012/0.031
M	91 118	1.004/1.045 1.003/1.05	0.003/0.008 0.003/0.006	1.095/0.323 1.098/0.008	0.008/0.002 0.004/1.02	1.006/1.045 1.005/1.031	0.001/0.007 0.002/0.005

N	91	0.993/0.895	0.005/0.283	0.997/0.987	0.001/0.9	0.994/0.05	0.003/0.015
	118	0.994/0.865	0.003/0.012	0.8976/0.98	0.993/0.84	0.9953/0.884	0.003/0.014

From the data in Table 1, a classification with different classifiers, areas, and correlations was To accomplish so, a research containing 91 & 118 segments of AAL areas, necessarily coincide, and SL with either the following criteria: X=1, M=1, N=5, and Pr=0.06 is incorporated into the technique. After 45 random iterations of a dataset, most values are standardized. The outcomes of a graph theory computations are shown in Table 1. With every one of the groups. The 3 characteristics average score & standard deviation were investigated. The findings are supplied for all of the parts (118), as well as 91 explanatory segments.

A categorization using several classifier, regions, and relationships were carried out using the data from Table 1. Table 2 indicates the results. The results of accuracy and precision are listed. The sensitivities of a classification determines its capacity to identify diseases in sick patients, whereas the specific determines its ability to recognize diseases with in lack of sickness. The new framework can handle the entire procedure, including acquiring fMRI pictures to delivering complete details that doctors or experts can understand. It is an effective algorithm in which the client merely inputs fMRI data then determine the best cartography and connections. To test this strategy, researchers looked at people who had migraines and were also drug addicts. The method does a thorough study and suggests various classifiers, some of which achieve 92.86 percent accuracy (Nn) and some others 86 percent (SVM). Different research using comparable machine learning algorithms in all the other diseases found chances of success of 76 to 88%, indicating that the suggested methodology has yielded satisfactory outcomes. The current discrepancies in classification outcomes can be attributed to a variety of factors, along with the kind of classification (supervised, uncontrolled, or partial-supervised) or the variation among classifier using same information that may achieve regional or global effectiveness.

Due to the random learning framework, some few classifier, such as NN, might produce diverse outputs. Increasing the amount of respondents inside each participating organization would allow for a more thorough investigation. These method is challenging for migraine sufferers since the noise produced by the MRI scanner causes individuals discomfort. Furthermore, one of the study results present limitations is the inability to employ automated classifier throughout conjunction with the entire map or a personal association. New atlases and relationships must be introduced in the order to improve the outcomes by allowing experts to study pathologies with a larger variety of factors.

Table 2 Classifiers.

Classifier		Success percentage	Connection percentage	AB %	Specification	Sensitivity
SVM	91	65.09/45.03	66.87/56.97	80/45	0.59/0.86	0.99/0.54

	118	67.98/68.09	78.99/56.00	60/30	0.094/0.65	0.65/0.64
K-means	91	89.00/66.98	87.99/67.95	40/70	0.87/0.77	1/1
	118	87.09/56.98	56.98/59.98	60/50	0.56/0.45	1/0.98
Knn	91	56.96/47.99	89.00/90.76	60/30	0.53/0.66	0.59/0.87
	118	57.99/52.87	48.98/65.98	0/80	0.76/0.66	0.65/0.73
AdaBoost	91	64.55/57.95	55.67/66.94	80/30	0.79/0.44	0.94/0.34
	118	64.44/46.96	63..75/66.56	60/40	0.93/0.56	0.44/0.64
Nn(3 layers)	91	86.09/45.03	84.87/56.97	100/100	0.80/0.86	0.49/0.84
	118	83.98/68.09	74.99/56.00	100/20	0.93/0.65	0.85/0.74
LDA	91	90.43/67.94	87.44/95.99	100/40	0.64/0.334	0.77/0.97
	118	51.55/21.93	45.77/86.44	60/100	0.77/0.83	0.86/0.22

Graph theory-based numerical methods are simple to develop using common graphs methods, as well as the predictions were simple to identify thanks to the graph's links and routes. Nevertheless, because graph technologies primarily analyse comparatively home network knowledge, predictive accuracy is usually poor. Graph connection estimations are frequently biassed in favour of connected dominating nodes in the cluster, resulting in poor rankings for novel medications and far less genomes. As a result, graph connectedness measurements are hardly used to estimate.

5. CONCLUSION

This study looked at several aspects of graph theory, like computer-assisted graph representations as well as graph-theoretic database systems like lists & matrices hierarchies. This study provides a better approach in representing and characterisation of a brain connection network, as well as machine learning in categorizing clusters based on factors retrieved from photographs, to emphasise the importance of graph theory. Data pre - processing, correlates, attributes, and techniques are some of the approaches used by this program. This research shows how an automated tool can be used to automate a systematic pattern utilizing MRI templates. Pre-processing, graph creation per topic using various connections, mapping, important extraction of features found in the literature, and lastly offering a set of machine learning techniques that really can give interpretable findings for doctors or experts are all component of the method. This paper also discusses a most typical advantages of graph theory in numerous domains to emphasize the highlights of graph theory. A summary of graph theory difficulties pertinent to their ideas and tactics is also included in this study.

6. REFERENCES

[1]. Bondy J A and Murty U S R., Graph theory with applications, Elsevier science publishing, 1976.
[2]. Caccetta L. and Vijayan K, Applications of graph theory, Fourteenth Australasian Conference on Combinatorial Mathematics and Computing, Ars Combinatoria, Vol. 23, 1987, 21-77.
[3]. Gary Chartrand, Ping Zhang, A First Course in Graph Theory, Dover books on mathematics, Courier Corporation, 2012.
[4]. Johan M.M. van Rooij, Hans L. Bodlaender.: Exact algorithms for dominating set. Discrete Applied Mathematics, 159 (2011), 2147–2164.
[5]. Shariefuddin Pirzada and Ashay Dharwadker, "Applications of Graph Theory", Journal of the Korean Society for Industrial and applied Mathematics, Volume 11, No.4,2007.
[6]. Narasingh; Deo; "Graph theory with applications to engineering and computer science", Prentice Hall of India, 1990.
[7]. Alexandru T. Balaban, Journal of Chemical Information and Computer Science, 1985, 25 (3), pp 334–343.
[8]. G. Lancia, V. Afna, S. Istrail, L. Lippert, and R. Schwartz,SNPsProblems, Complexity and Algorithms, ESA 2002, LNCS 2161, pp. 182-193, 2001. Springer-Verlag 2001.
[9]. Ashay Dharwadker, The Vertex Coloring Algorithm, 2006
[10]. Ashay Dharwadker, " a new proof of The four colour theorem", Institute of Mathematics, Haryana, India.
[11]. Eric Filiol, Edouard Franc, Alessandro Gubbioli, Benoit Moquet and Guillaume Roblot, Combinatorial Optimization of Worm Propagation on an Unknown Network, Proc. World Acad. Science, Engineering and Technology, Vol 23, August 2007.
[12]. Daniel Marx, "Graph Coloring problems and their applications in scheduling"
[13]. M. Abellanas, F. Hurtado, C. Icking, R. Klein, E. Langetepe, L. Ma, B. Palop, and V. Sacristan. "The farthest color Voronoi diagram and related problems". In Abstracts 17th European Workshop Comput. Geom., pages 113–116. Freie University¨at Berlin, 2001.
[14]. Manjula V (2010) Electrical networks by graph theory. Int J of Math and Eng IEEE 149: 1368 -1373.
[15]. M. A. Rajan, M. Girish Chandra, Lokanatha C. Reddy, Prakash Hiremath "Concepts of graph theory relevant to Adhoc Networks", Int. Journal of Computers, Communications & Control, ISSN 1841-9836, E-ISSN 18419844 Vol. III 2008.
[16]. C. Stam, W. De Haan, A. Daffertshofer, B. Jones, I. Manshanden, A.V.C. vanWalsum, T. Montez, J. Verbunt, J. De Munck, B. Van Dijk et al., Graph theoretical analysis of magnetoencephalographic functional connectivity in Alzheimer‟s disease, Brain 132 (2009), 213–224.
[17]. J. Wang, X. Zuo and Y. He, Graph-based network analysis of resting-state functional MRI, Frontiers in Systems Neuroscience 4 (2010), 1–14.
[18]. M.P. van den Heuvel and H.E. Hulshoff Pol, Exploring the brain network: a review on resting-state fMRI functional connectivity, European Neuropsychopharmacology 20 (2010), 519–534.

[19]. L. He, D. Hu, M. Wan and Y. Wen, Measuring temporal dynamics of resting-state fMRI data, Bio-Medical Materials and Engineering 24 (2014), 939–945.
[20]. R. Baumgartner, L. Ryner, W. Richter, R. Summers, M. Jarmasz and R. Somorjai, Comparison of two exploratory data analysis methods for fMRI: fuzzy clustering vs. principal component analysis, Magnetic Resonance Imaging 18 (2000), 89–94.
[21]. Y. Xiong, Y. Luo, W. Huang, W. Zhang, Y. Yang and J. Gao, A novel classification method based on ICA and ELM: A case study in lie detection, Bio-Medical Materials and Engineering 24 (2014), 357–363
[22]. B.C. Bernhardt, Z. Chen, Y. He, A. C. Evans and N. Bernasconi, Graph-theoretical analysis reveals disrupted smallworld organization of cortical thickness correlation networks in temporal lobe epilepsy, Cerebral Cortex 21 (2011), 2147–2157.
[23]. B.C. van Wijk, C.J. Stam and A. Daffertshofer, Comparing brain networks of different size and connectivity density using graph theory, PLoS One 5 (2010), e13701.
[24]. K. Nakajima, T. Minami, H.C. Tanabe, N. Sadato and S. Nakauchi, Facial color processing in the face-selective regions: An fmri study, Human Brain Mapping 35 (2014), 4958–4964.
[25]. A.V. Lebedev, E. Westman, A. Simmons, A. Lebedeva, F.J. Siepel, J.B. Pereira and D. Aarsland, Large-scale resting state network correlates of cognitive impairment in Parkinson‟s disease and related dopaminergic deficits, Frontiers in Systems Neuroscience 8 (2014), 1–12.
[26]. E. Bujnošková, J. Fousek, E. Hladká and M. Mikl, 22 comparison of the methods for brain parcellation, Clinical Neurophysiology 125 (2014), e31–e32.
[27]. E.J. Sanz-Arigita, M.M. Schoonheim, J.S. Damoiseaux, S.A. Rombouts, E. Maris, F. Barkhof, P. Scheltens and C.J. Stam, Loss of „small-world‟networks in Alzheimer‟s disease: graph analysis of fMRI resting-state functional connectivity, PloS One 5 (2010), e13788.
[28]. M. Jenkinson, C.F. Beckmann, T.E. Behrens, M.W. Woolrich and S.M. Smith, FSL, Neuroimage 62 (2012), 782–790
[29]. J.C. Reijneveld, S.C. Ponten, H.W. Berendse and C.J. Stam, The application of graph theoretical analysis to complex networks in the brain, Clinical Neurophysiology 118 (2007), 2317–2331
[30]. C. Stam, B. Jones, G. Nolte, M. Breakspear and P. Scheltens, Small-world networks and functional connectivity in Alzheimer‟s disease, Cerebral Cortex 17 (2007), 92–99.

International Journal of Aquatic Science
ISSN: 2008-8019
Vol 12, Issue 02, 2021

Comparison of Fuzzy Logic Systems and its Applications using Mathematical and Technological Perspective

[1]Dr.R.Vijaya, [2]Dr.K.Maheswari, [3]Dr.Chandrika V S, [4] Dr.T.Ajith Bosco Raj, [5]Dr. R. Sreeparimala, [6]Karthick S

[1]Assistant Professor, PG & Research Department of Computer Science , Arignar Anna Govt. Arts College for Women, Walajapet - 632 513 , Ranipet Dist. , Tamil Nadu , India.
[2]Associate Professor, Department of Computer Science and Engineering, CMR Technical Campus, Kandlakoya (V), Medchal Road, Hyderabad 501401, Telangana,India.
[3]Associate Professor, Department of EEE, KPR Institute of Engineering and Technology, Avinashi Road, Coimbatore – 641407.
[4]Professor, Department of Electronics and Communication Engineering, PSN College of Engineering and Technology, Tirunelveli – 627152.
[5]Associate Professor, Mathematics, Sri Eshwar College of Engineering, Coimbatore-641202
.[6]Associate Professor, Department of Electronics and Communication Engineering, Erode Sengunthar Engineering College, Perundurai, Erode, Tamilnadu, India – 638057.

Abstract

Human instincts are a difficult concept to grasp. To comprehend this drive, a comprehensive dimensional analysis of discourse knowledge is required. PC frameworks are by and by being prepared to understand how things work in a continuous climate, which will help in the improvement of clever examination. This exertion, albeit groundbreaking, has various downsides too. There is a cognitive gap between humans and machines, which puts humans one step ahead of machines. For a computer to better understand this intelligence gap, the fuzzy logic system may be utilized. Another way of putting it: fuzzy logic is a kind of computational intelligence that enables computers to understand and reason in the same manner that humans do Since it can tackle issues that have never been addressed by joining its capacities with delicate figuring methods, for example, neuro and tumult registering, hereditary calculations, likelihood thinking, and insusceptible organizations, the fluffy rationale framework is drawing in researchers and architects from everywhere the world. It's difficult the fluffy framework that has improved information-based or master framework innovation, yet it has additionally changed the granularity with which knowledge is communicated. Manufacturers of home appliances, for example, are already incorporating intelligence into particular products via the use of the fuzzy logic framework. The utilization of fuzzy logic frameworks has additionally changed mechanical cycle control and opened up new roads for item creation. Regardless of the way that hypothetical progressions in the fluffy rationale framework have for the most part been accomplished in the United States and Europe, Japanese organizations have been at the cutting edge of the innovation's commercialization since its presentation. The motivation behind this examination is twofold: first, to comprehend the fluffy rationale

framework needed for successful dynamic, and second, to exhibit the presence of an insight hole by using true guides to show the presence of a knowledge hole. Singular perusers will profit from the models, which have been chosen with care to delineate and show the fluffy rationale framework's applications.

Keywords: Fuzzy logic, Fuzzy Systems, Applications, Inverted Pendulum Technology

1. INTRODUCTION

In 1965, Lotfi A. Zadeh, a professor of computational science at the University of California at Berkeley, began Fuzzy Logic. In summary, Fuzzy Logic (FL) is a multivalued logic, which defines values such as true/false, yes/no, high/low, etc. Concepts like "tall" or "quick" may be defined mathematically and programmed into computers to emulate human thought in the programming of computers. Fuzzy systems have their roots in ancient Greek philosophy. Many misunderstandings exist regarding fuzzy logic. Fuzzy logic is not fuzzy, to begin with. Fuzzy logic is, in a significant way, exact. The second cause of misunderstanding is the duality of the meaning of fuzzy logic[1,2].

Fuzzy logic, in a limited sense, is a logical system. By and by, in a ruling significance, fluffy rationale, or FL for short, is considerably more than a coherent framework. Fluffy rationale offers a simple strategy to come to an authoritative result dependent on indistinct, questionable, uncertain, loud, or missing information data. The rationale that sees more than essential valid and bogus qualities. With regards to fluffy rationale, thoughts might be communicated utilizing levels of honesty and erroneousness. For instance, an assertion like today is radiant might be valid if there are no mists, 80% valid if there are a couple of mists, half evident if it's hazy, and 0% valid on the off chance that it rains the entire day. The fluffy rationale has become a fundamental apparatus for some, various applications spreading over from designing frameworks to counterfeit intelligence [3].

A short explanation of the fundamental concepts of fuzzy logic and fuzzy reasoning is presented in this quick introduction. The chapter on fuzzy logic control: the design of intelligent control systems that utilize fuzzy if-then rules to mimic human behavior. Math knowledge is maintained simply throughout, with many illustrations to assist with understanding. Thus, everyone interested in fuzzy ideas and their real-world applications will find this a great place to start. An important feature of natural human thinking is the use of natural language [4].

Lotfi A. Zadeh wrote the much-controversial article "Fuzzy Sets" in 1965. Zadeh's articles were referenced over 185,000 times. Later that paper's concepts were used to establish the Fuzzy Logic theory, which has proven to have a wide range of practical applications. We will be discussing Zadeh's pioneering work in Soft Computing and Artificial Intelligence and his early impact on the globe and Romania. Additionally, we shall include a few of FLb's applications. We may now posit FLn as a metatheory of fuzzy mathematics, which provides a model for the fuzziness in many facets. It can also be used as a theoretical tool for the fuzziness in various forms [5].

2. DEVELOPMENT OF FUZZY LOGIC

Fuzzy logic has developed as a useful method for evaluating hydrologic components and making decisions about water resources. Many hydrologic problems include imprecision and ambiguity, which may be easily addressed by fuzzy logic-based models. This article takes a look at several water-related applications of fuzzy logic [6]. To date, fuzzy logic-based hybrid models have been widely used in hydrologic research. A critical role in food acceptability and dietary preferences is played by sensory evaluation. This information helps food-processing companies and food scientists to better assess the sensory quality of food items. Traditional methods only provide qualitative analysis, and cannot provide a precise quantitative analysis [7].

Fuzzy set theory has recently been used for the assessment of sensory qualities of food items produced using fortification and changed processing methods. Framework regulators use fuzzy logic and tumultuous natural product fly control strategies to compute proper damping powers for the front and back bogie outline. The vehicle model has 28 levels of opportunity, and it depends on nonlinear vehicle suspension and a nonlinear heuristic wet blanket. The Modified Dahl model is developed to explain the damper's behavior. Mobile/stationary node positioning and location estimate are crucial, particularly following the amazing advances in wired and/or wireless communications, as well as the widespread use of portable devices [8].

Many end-users, application developers, and service providers all need precise location information. Wireless, multisensory, and autonomous systems have all contributed to an increase in positioning technologies. In each kind of positioning system, the accuracy, communications protocol, algorithm, and technology all vary. Since reliable Fault Detection and Identification rates may significantly reduce costs, a variety of methods have been developed for gas turbine FDI systems [9].

A gas turbine failure detection, which was previously unexplored. Despite the way that fuzzy logic has been broadly utilized in power frameworks, it has regularly been described as "a long way from full" attributable to the absence of a normalized technique for applying it. In this paper [10], we give a deliberate turn of events and execution of a nonexclusive energy stockpiling framework (GESS) coordinated with fuzzy logic for dynamic dependability support in an aggregate force framework. The responsive and genuine force directions of GESS are determined while ensuring a settling execution by lessening a quadratic security record is kept up with all through the reenactment.

3. FUZZY SYSTEMS

In classical logical systems, bivalent logic is often employed. Anything may be either true or false in the bivalent logic system. As a consequence, its ability to depict notions like "wealthy" and "tall" is impeded. Try to grasp the meaning of "tall" with this in mind. In general, the general public believes that someone taller than seven feet is tall, whereas someone who is less than five feet is certainly short. A common method for measuring tallness is to utilize a predefined number (above which everybody is tall and below which everybody is not tall). The height value of 6' would be convenient to utilize for this example. With this default value, people's heights of 7' and 5' are properly classified as tall and short. A and B are both 5'11" and 6'1".

Assumed before, 6' = A is short, B is tall. From the way it seems, it does not appear to be true. Despite having shorter legs, A's height is nearly equal to B's. Regardless matter whether we increase or decrease the preset setting, this issue remains. This issue emerges because we are utilizing a Bivalent sensible framework where esteems like 5'11" and 6'1" are naturally allocated to one of two sets: "tall" or "short." In fuzzy logic, each person's height is given a membership degree, with tall people having a higher membership degree than short people.

To illustrate, a person who is 6'1" in height will be tall to the degree that they are 6'1", while a person who is 5'8" will be tall to a different degree since they are 5'8". The way that people of various statures might be "tall" to changed degrees is clarified in this plan.

In Figure 1, the fuzzy logic system models the uncertainty of "tall" by distributing membership degrees across different heights. This figure shows how the height degree in the group of tall people is proportional to the vertical distance between the plotted points. People who are less than 5 feet tall are considered short; those who are 5 feet or more are considered tall (i.e., definitely tall). A 6'5" individual is short to the degree of 0.7. "Tall" is represented in Figure 1 as a fuzzy set representation. All domain objects must have a membership degree of 0 (not a member of the set) or 1 in a Bivalent logic system (a member of the set). Fuzzy sets include a membership degree, however, this number is between 0 and 1 rather than 0 and 100. The fuzzy logic system's usage with the Bivalent logic system produces similar results.

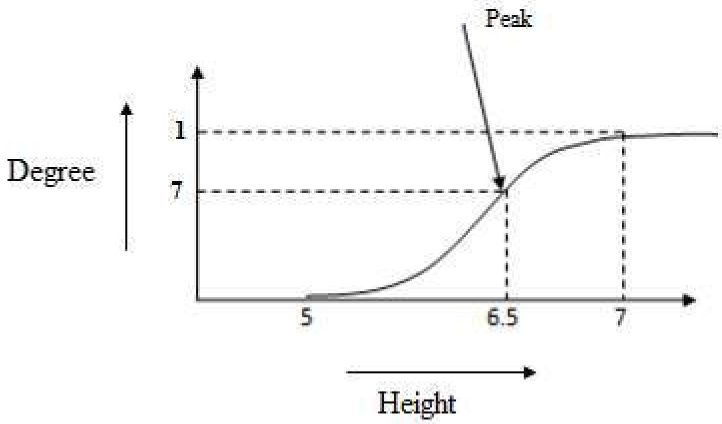

Figure 1: Fuzzy Sets Representation

The union, XUY, of two fuzzy sets X and Y is the probability distribution of the union of those sets. The intersection of two fuzzy sets is represented by the minimal membership degree of each item in the two sets. This results in the probability distribution of the intersection, XY, of the two sets. Just things that are normal to the two gatherings are held in their crossing point. 1 is subtracted from all the components of the domain to get the complementary possibility distribution of a fuzzy set.

In a seminal work on fuzzy sets, Zadeh introduced the min-max operators, which may be used to define fuzzy set-theoretic operations. Many other operators for fuzzy sets have been created by various academics over the years, including the minimum-maximum operators. There will be no discussion of these additional operator types since the scope of this essay does not allow for it. This research revolves around the widely used min-max operators because of their simplicity and appealing characteristics. The fuzzy sets Low, Medium, and High have comparative portrayals for Voltage and Current, as displayed in Figure 2.

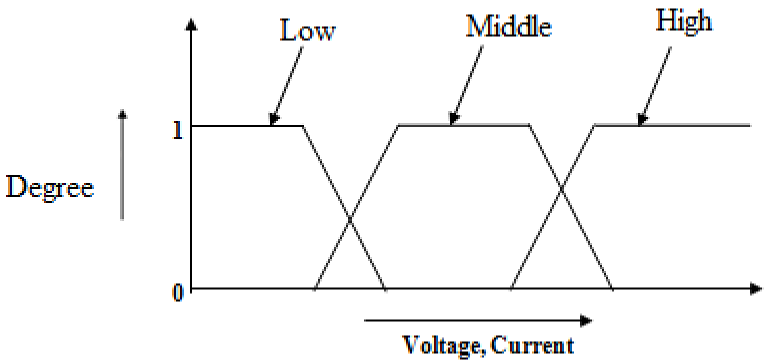

Figure 2: The fuzzy sets Low, Medium, and High

To get the appropriate current value, we shall utilize fuzzy reasoning. In Figure 4, two fuzzy standards and the fluffy info are shown graphically. To accommodate a more clear agreement, the information reality's conveyance is displayed as a marginally specked region across the premises of the two fluffy standards in Figure 3.

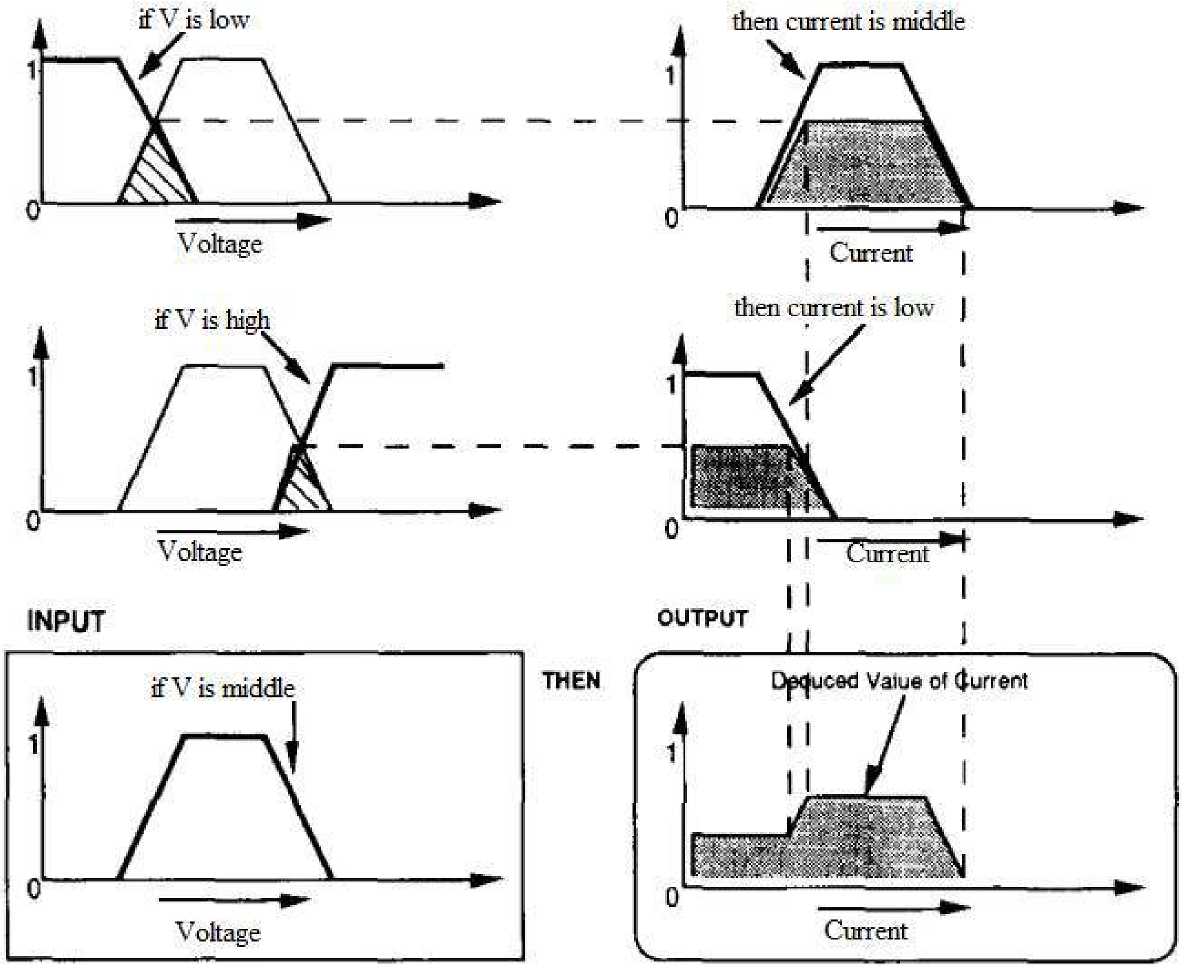

Figure 3: Approximate inference using fuzzy rules (fuzzy point)

Even if the two rules do not have a one-to-one mapping with the input fact, each rule still has a portion of a match. Since this is the case, it is expected that every one of the two guidelines will add to a definitive result. The worth to be acquired is resolved as follows:

For each of the fuzzy premises, the input fact's intersection is computed. Figure 4 illustrates the junction areas on the input premises It is dictated by registering the convergence of the yield fuzzy circulations showed concealed in the finishes of Figure 4, and the commitment of each standard to the yield answer is found by the level of the yield fuzzy conveyances (shown concealed) that is incorporated inside the crossing points. When consolidating the consequences of each standard, the current yield esteem is shaped.

4. THE INVERTED PENDULUM

The examples of fuzzy logic system applications shown in this section provide real-time examples of how these systems are used. This inverted pendulum system is simple, yet is made up of many components. An inverted pendulum system is a great option for tests and class demonstrations in a laboratory setting.

The upset pendulum is one of the exemplary techniques for investigating control methodologies. The difficult part of balancing an inverted pendulum is applying the proper force. As required, the hand may be moved in one direction or the other to balance the stick on top of it. See Figure 4 where a basic inverted pendulum is balanced by a motor.

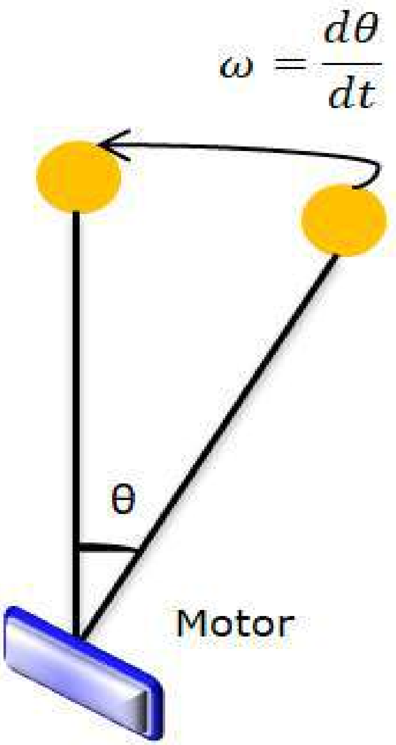

Figure 4: An inverted pendulum.

Despite its effortlessness, the transformed pendulum is a nonlinear framework. Though a system may be correctly stated, it will need to be solved for a second-order differential equation. Occasionally, such oversimplifications are used to accelerate the solving of a problem, as they should. There are exceptions to every rule, and huge displacements are no exception. for getting the best possible result, several numerical methods are needed (which are computationally intensive). Also, balancing the poles is challenging since the solution point is sensitive to the starting conditions of the system. The arrangements created are influenced by numerous elements, like the heaviness of the sway, the length of the shaft, and the engine's solidarity. The accompanying arrangement of fluffy guidelines might be utilized to oversee such a framework:

IF θ is zero AND ω is zero THEN Force-applied is zero

When clearly defined, Table 1 will demonstrate that a bunch of 12 standards might be used to administer a basic transformed pendulum, for example, the one displayed in the figure to one side. As referenced previously, the precise removal and rakish speed of the pendulum are determined and, separately. Electrical motors will also be utilized to balance the inverted pendulum, as well as to provide the required force.

Table 1: Fuzzy rules implemented to control an inverted pendulum

IF	θ	is negative-	**AN**	ω	is zero	**TH**	Curre	is positive-
IF	θ	is negative-	**AN**	ω	is zero	**TH**	Curre	is positive-small
IF	θ	is zero	**AN**	ω	is zero	**TH**	Curre	is zero
IF	θ	is positive-small	**AN**	ω	is zero	**TH**	Curre	is negative-small
IF	θ	is positive-	**AN**	ω	is zero	**TH**	Curre	is negative-
IF	θ	is zero	**AN**	ω	is negative-	**TH**	Curre	is positive-
IF	θ	is zero	**AN**	ω	is negative-	**TH**	Curre	is positive-small
IF	θ	is zero	**AN**	ω	is zero	**TH**	Curre	is zero
IF	θ	is zero	**AN**	ω	is positive-small	**TH**	Curre	is negative-small
IF	θ	is zero	**AN**	ω	is positive-	**TH**	Curre	is negative-
IF	θ	is positive-small	**AN**	ω	is zero	**TH**	Curre	is zero
IF	θ	is negative-	**AN**	ω	is positive-small	**TH**	Curre	is zero

In Figure 5, you can observe the forms of these fuzzy sets. To illustrate, you should note that the values for and are both precise. Also, the motor has to be supplied with a certain current to maintain the inverted pendulum at its designed amplitude.

Figure 5 depicts a visual representation of the inference process for crisp input values. In Figure 8, two fuzzy rules from Table 1 are shown. Two premise clauses are now included in the regulations. This statement is known as "The Inputs Have Arbitrary Values". The following numbers show the greatest degree of correspondence between the info upsides of and the premises of rule 1: r11 (which is 1) and r12 (which is 2). and in Figure 9 (about 0.5 as indicated). The value of r11 is 1 may be considered a fuzzy set with a membership degree of 0, where 0 is the single element making up the set. This section of the output, from r11 to r12, is attributable to the conclusion of the rule.

Rule 2 does not affect the outcome in Figure 5, since r21 is equal to zero. The zero minimum of r21 and r22 is always achieved. Next is the inference phase where you follow the same stages as in Figure 4. In Figure 5, the crisp numbers used as inputs are represented by the fuzzy rules that constitute the final output. However, the fuzzy output must be defuzzified, meaning it must be made crisp enough that it may be stated as the current value that is essential.

The final output crisp number in Figure 5 is almost equal to ω' (which is close to zero). Instead of measuring the location and velocity of the bob, these rules utilize the current angle and orientation of the mechanism to regulate the pendulum. The very 11 rules that might be utilized to adjust the upset pendulum paying little mind to the mass of the sway or the engine strength can be applied regardless of whether the mass of the weave or the engine strength is evolving progressively. Rather than customary control frameworks, which are delicate to changes in these boundaries, our strategy is unaffected by them.

To need more knowledge and technical talents to discover correct fuzzy rules than you'll need to solve difficult arithmetic problems. Although the particular distributions have been proven to have minimal effect on the system's performance, the fuzzy distributions, in general, have not. This greatly simplifies the procedure from an engineering perspective. Likely just as noise and breakdowns are very resistive to the system, so too are glitches in the system.

The inverted pendulum will be regulated, although not as reliably as before, even if at least one of the active fuzzy rules in Figure 5 is deactivated (for example, owing to a hardware failure). In a fuzzy logic system, mild degradation is one of the smart characteristics. These principles are specified by linguistic variables, which are established on the domains of input and output. These fuzzy rules are modeled after other fuzzy logic systems, whose rules are functionally equivalent to these fuzzy rules.

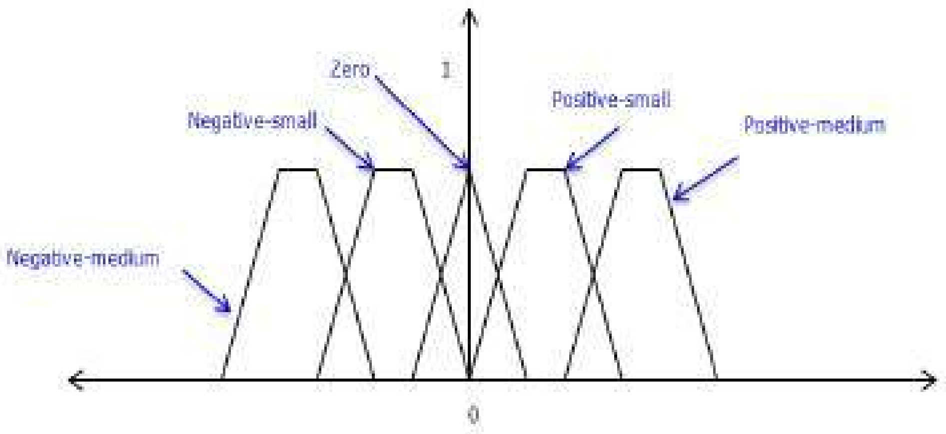

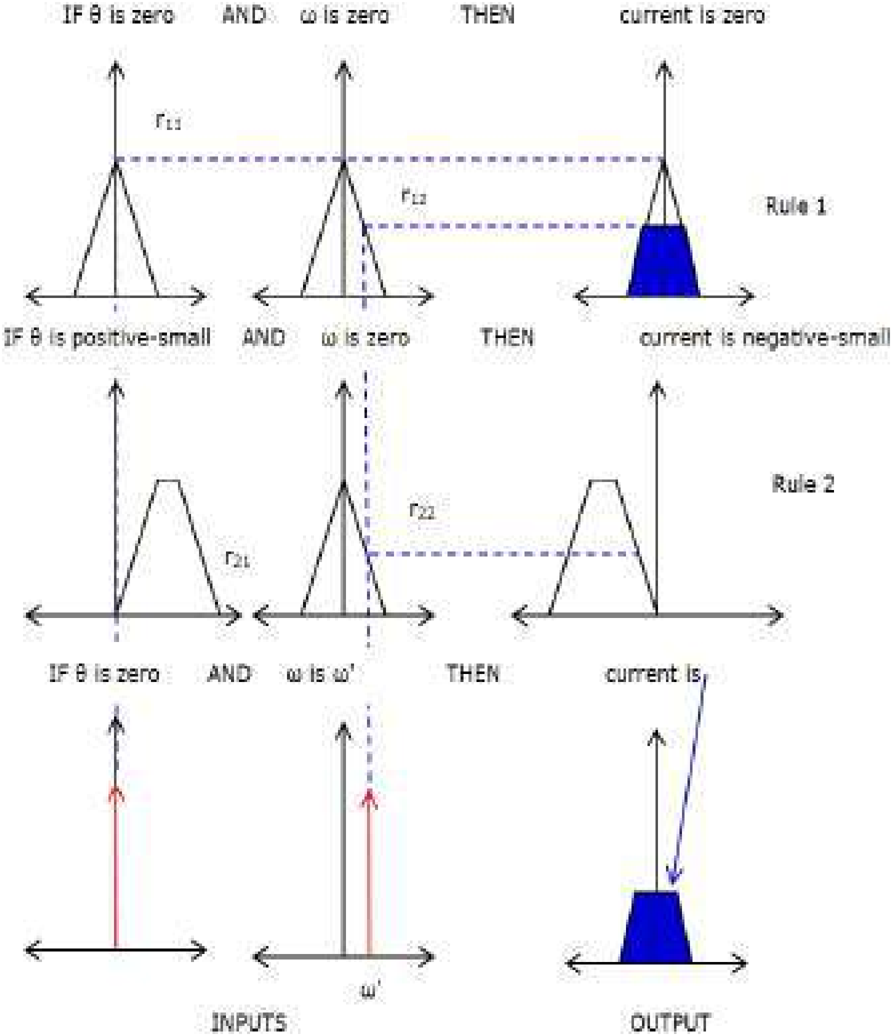

Figure 5: Fuzzy inference in the inverted pendulum

Fig. 5 shows many variations on the basic inverted pendulum. This is a sampling of them:
A flexible, pendulum-style connecting rod is assumed in Figure 7. However, even though the issue is more difficult to describe and solve if the assumption of a rigid rod is removed, we must do so if we want to get a full understanding of the problem.

Two or three joints in the (inflexible) rod supporting the pendulum bob, hence a two- or three-phased pendulum. While such a system may be described correctly, the subsequent control equations are too complicated to be solved in real-time with regular computers. Although building a real-time controller to regulate the many inverted pendulum "complex" states is challenging, According to researchers from Aptronix (China/USA), but other Japanese companies as well, certain inverted pendulum systems have been effectively managed using a fuzzy logic system. Fuzzy logic has impressed engineers who view it as a highly smart tool for directing complicated operations.

5. CONCLUSION

Air quality systems, vacuum cleaners, antiskid braking systems, washing machines, subway control, models for new product pricing, and project readiness Fuzzy logic has effectively been used in industries such as control systems engineering, image processing, power engineering, industrial automation, robotics, consumer electronics, and optimization. Mathematics has brought formerly stagnant areas of science back to life. According to most indications, the fuzzy logic system's business impact is only starting to be appreciated. In the long term, industry and business remain to acquire an incredible arrangement. While fuzzy logic can't fix everything, it does offer some benefits that have been shown. Creative products are now far more reliant on a company's ability to sell them in a cost-effective and timely way, particularly in the global market.

6. REFERENCES

[1]. Zadeh L.A. The concept of linguistic variable and its application to an approximate reasoning, Information Sciences, 8, 199-249. 1975.
[2]. Zadeh L.A. Probability measures of fuzzy events, Journal of mathematical Analyses and Applications, vol. 23, no. 2, pp. 421-427. 6, 7, 1965.
[3]. Zadeh L.A., Fuzzy sets. Information and Control, 8, 338–353, 1965.
[4]. Klir G.J., Folger T.A.: Fuzzy Sets, Uncertainty, and Information: Prentice-Hall, NJ, 1988.
[5]. Yager, R. and Zadeh, L. A., An introduction to fuzzy logic applications in intelligent systems. Springer Science & Business Media, vol. 165, 2012.
[6]. L. A. Zadeh, "Fuzzy sets as a basis for a theory of possibility," Fuzzy Sets and Systems, vol. I, pp. 3-28, 1978.
[7]. B. Knecht, "Interview with Lofti Zadeh," IEEE Computing Features, pp. 26-32, Spring 1991.
[8]. B. G. Buchanan and E. H. Shortliffe, "Rule-based expert systems." Reading, MA: Addison-Wesley, 1984.
[9]. P. C. Cheeseman, "In defense of probability," in Proc. 9th Int. Joint Conf. Artificial Intelligence., Los Angeles, pp. 1002-1009, Aug. 1985.
[10]. D. Dubois and H. Prade, Fuzzy Sets and Systems: Theory and Applications. New York: Academic, 1980.
[11]. E. H. Mamdani and S. Assilian, "A Case Study on the Application of Fuzzy Set Theory to Automatic Control," in Proc. IFAC Stochastic Control Symp., Budapest, Hungary, 1974
[12]. M. Togai and H. Watanabe, "A VLSI implementation of a fuzzy inference engine: Towards an expert system on a chip," Information Science, vol. 38, pp. 147-163, 1986.
[13]. T. Yamakawa, "Design of a fuzzy computer," IFSA, 1988.
[14]. R. C. Johnson, "New LIFE for Fuzzy Logic," Electr. Eng. Times, pp. 39-42, Sept. 18, 1989.
[15]. L. A. Zadeh, A Theory of Approximate Reasoning in Machine Intelligence, J. Hayes, D. Michie and L. I. Mikulich, Eds., vol. 9. New York: Halstead Press, 1979, pp. 149-194.
[16]. E. E. Kerre, R. B. R. C. Zenner and R. M. M. DeCaluwe, "The use of fuzzy set theory in information retrieval and databases: a survey," J. Amer. Society for Inform. Science, vol. 37, no. 5,341-345, 1986.
[17]. L. A. Zadeh, "The calculus of fuzzy if/then rules." Af Expert, pp. 23-28, Mar. 1992
[18]. L. A. Zadeh, "The concept of a linguistic variable and its applications to approximate reasoning, parts I. 11, Information Sciences, vol. 8, 1975; Part 111, vol. 9, 1976.
[19]. E. Hisdal, Guest Editor, Special Issue on Interpretation of Grades of Membership, Int. J. Fuzzy Sets and Systems, vol. 25, North Holland, 1988.
[20]. M. Sugeno, Editor, Industrial Applications of Fuzzy Control. Ams- terdam: Elsevier,

1985.
[21]. Fuzzy-C Inverted Pendulum, demonstration software distributed by Togai Infralogic Inc., Irvine, CA
[22]. "Fuzzy control ensures a smooth ride," Age of Tomorrow. Japan: Hitachi Ltd., 1987, pp. 12-19.
[23]. L. A. Zadeh, "Making computers think like people." IEEE Spectrum, pp. 26-32, Aug. 1984.
[24]. "Fuzzy logic improves high-tech gadgetry," Tokyo Business Today, Mar. 1991.

European Journal of Molecular & Clinical Medicine
ISSN 2515-8260 Volume 07, Issue 02, 2020

Data Coloring in Trusted and Ambiguous Cloud Computing using Sheltered Possessions Machine Learning Technique

[1]Ellappan Venugopal, [2]Dr Rajesh Thumma, [3] Dr. R. Sreeparimala, [4]Dr.Anusha K,[5] Dr. T. Thulasimani

[1]Assistant Professor, Department of Electronics and Communication Engineering, Image and Signal processing (SIG), School of Electrical Engineering and Computing ,Adama Science and technology University, Adama, Ethiopia.

[2]Associate Professor, Department of Electronics and Communication Engineering, Anurag Group of Institutions, Venkatapur (v), Hyderabad, Telangana-500088.

[3]Associate Professor, Department of Mathematics, Sri Eshwar College of Engineering, Coimbatore, Tamilnadu – 641202.

[4]Associate Professor, School of Computer Science and Engineering, VIT Chennai, Vellore Institute of Technology, Chennai, Tamilnadu – 600 127.

[5]Assistant Professor, Department of Mathematics, Bannari Amman Institute of Technology, Sathyamangalam-638401, Erode District, Tamilnadu, India.

Abstract - Confidence and security prevent businesses from fully embracing cloud platforms. To protect the clouds, providers must first secure virtualized data-center resources, uphold user privacy, and protect data integrity. The authors suggest that the trust overlay network be used through multiple data centers to implement a reputation system to build trust between service providers and data owners. Data coloring and software watermarking methods protect shared data objects and highly distributed software modules. These strategies protect multi-path authentication, enable a single sign-on in the cloud, and tighten access control for sensitive data in the public and private clouds. Protection against tampering is tamper proofing, so unauthorized changes to the software (for example, removing a watermark) can lead to passive code. We will briefly examine the technology available for each type of protection. P2P technology opens our work to low cost copyrighted content delivery. The advantages are mainly delivery cost, high content availability and copyright compliance in exploring P2P network resources.

Key Terms: Cloud Service, Data Coloring, Watermarking, Machine Learning, Shelter Possios

1. Introduction

Cloud computing allows a new business model that supports on-demand, spot payment and economy-of-scale IT services over the Internet. The Internet cloud acts as a service factory built into virtualized data centers. The idea is to turn desktop computing into a service-oriented platform using virtual server clusters in data centers. However, the lack of trust between cloud users and providers has hampered the universal acceptance of clouds as outsourced computing services. The main source of illegal file sharing is associates who ignore copyright laws and associate with pirates [1].

To resolve this peer-to-peer issue, we recommend a copyright-compliant system for legalized P2P content delivery. Our goal is to prevent mass piracy within the boundaries of the P2P content delivery network. In particular, our scheme appeals to protect large-scale corrupted content from deteriorating over time. The recent rise in interest in mobile agent systems has led researchers to focus on fundamentally different perspectives on security. A malicious host attack is usually a property ownership violation. The client code may contain trade secrets or copyrighted material, which, if infringed on the client's integrity, may cause financial loss to the client owner [2].

We will look at malicious-host attack situations next. Cloud users are increasingly concerned about whether data center owners could abuse the system by randomly using private datasets or releasing sensitive data to unauthorized third parties. How to increase trust between these service providers and data owners is related to cloud security. To address these issues, we propose a reputation-based trust-management scheme developed using data coloring and software watermarking. Information on relevant trust models is available elsewhere [3].

2. Problem Statement

A. Cyber-trust requirements in cloud services

Cloud Security Alliance 5 identifies some critical issues for reliable cloud computing and discusses many recent issues related to cloud security and privacy.1,6,7 Public and private clouds require different levels of security management. We can identify different service-level agreements (SLAs) using variable degrees of shared responsibility between cloud providers and customers. Serious security issues include data integrity, consumer privacy and trust between providers, individual users and user groups. The three most popular cloud service models have different security requirements [4][5].

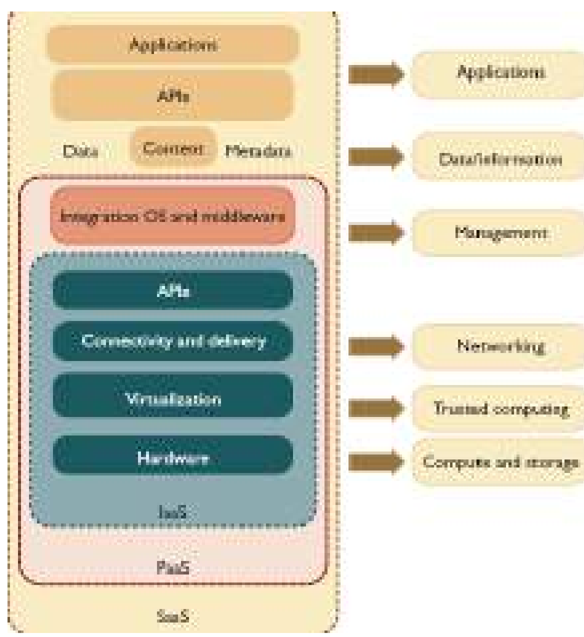

Figure 1. API Cloud Service Model

The Infrastructure-in-a-Service (IAS) model is based on an internal implementation layer that extends to create a platform-a-service (PASS) layer with OS and middleware support. PaaS extends across the Software-a-Service (SaaS) model and creates applications on data, content and metadata using specialized APIs. This indicates that SaaS requires all security measures at all levels. On the other hand, IAS protection is required primarily at the networking, trusted computing, and computer / storage levels, while PASS provides additional protection at the IAS support and resource management level [6] [7].

3. Secure infrastructure as a service

The IAS model allows users to lease computer, storage, network and other resources in a virtualized environment. The user does not control or regulate basic cloud infrastructure, but has control over the OS, storage, executed applications, and certain network components. The best example of IaaS is Amazon's Elastic Compute Cloud (EC2). At the cloud infrastructure level, CSPs can enable network security using intrusion-detection systems (IDS), firewalls, antivirus programs, and distributed denial-service (DDOS) protection.

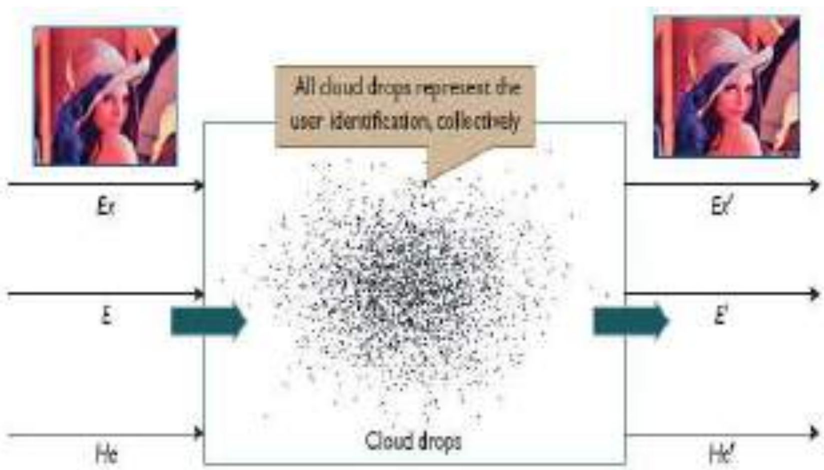

Figure 2. Forward and Backward data coloring processes by adding or removing unique cloud drops (colors) in data objects.

A. Securing the platform as a service

Cloud platforms are built on top of IaaS with system integration and virtualization middleware support. Such platforms allow users to integrate user-built software applications into cloud infrastructure using provider-supported programming languages and software tools (such as Java, Python, or .NET). Basic cloud infrastructure is not controlled by the user. Popular pass platforms include Google Play Engine (GAE) or Microsoft Windows Azure. This requires assigning VMs to enable security, security enforcement, potential risk management and confidence building across all cloud customers and providers.

B. Existing system

Internet clouds act as service factories built around web-level datacenters. Elastic cloud sources and large processed datasets are subject to security breaches, privacy breaches and copyright infringement. Provided cloud resources are vulnerable to cyber attacks. Cloud platforms built by Google, IBM and Amazon reveal these vulnerabilities. We propose a new approach to integrating trusted data accessed by virtual clusters, secure datacenters, and popular systems [7]. Specifies a range of P2P reputation systems to protect clouds and datacenters at the site level and data objects at the file-access level. Image management in cloud environments is a challenging issue. If we store these images, these images can be accessed by unauthorized persons and viruses. The current system does not have complete security for images. It only has text security [8].

C. Specific approach

The authors suggest that the trust overlay network be used through multiple data centers to implement a reputation system to build trust between service providers and data owners. Data coloring and software watermarking methods protect shared data objects and highly distributed software modules. Using water marking and data coloring techniques, we are going to create a dummy image when a guest or unauthorized person accesses the original image.

4. Watermarking and Data Coloring Techniques

Watermarking is a technology that allows you to create duplicate images of images in a cloud environment. When an unauthorized person or virus accesses that image, it can only access duplicate images. After obtaining permission only from the owner, the new person can access the image. But he cannot modify the image and settings.

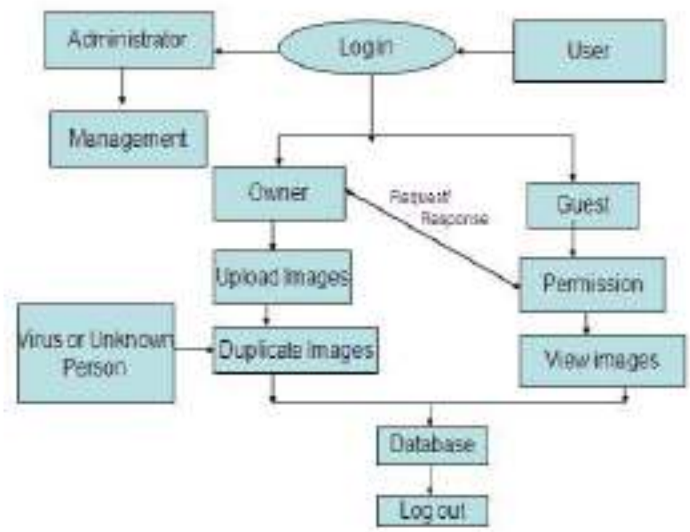

Figure 3. Data Coloring and Watermarking Representation in Cloud Space

By using shared files and datasets in cloud computing, privacy, security and copyright can be compromised in an hostile cloud computing environment. We want to work in a trusted software environment that provides useful tools for creating cloud applications on protected datasets. In the past, watermarking was primarily used for digital copyright management. Christian Kolberg and Clark Thompson suggested using watermarking to protect software modules. 12 Second Order Trust Model Die Lee & Co. to Protect Data Owners. Indicated, which provides a dim membership functionality. Colors to protect large datasets in the cloud. We consider cloud security as a community asset. To protect this, we combine the benefits of secure cloud storage and software watermarking through data coloring and trust negotiations. Figure 4 illustrates the data-coloring concept. The image of the woman is a protected data object.

A. Cyber-trust requirements in cloud services

Cloud Security Alliance 5 identifies some critical issues for trusted cloud computing and several recent works discuss common issues related to cloud security and privacy. Public and private clouds require different levels of security. We can identify different service-level agreements (SLAs) using variable degrees of shared responsibility between cloud providers and customers.

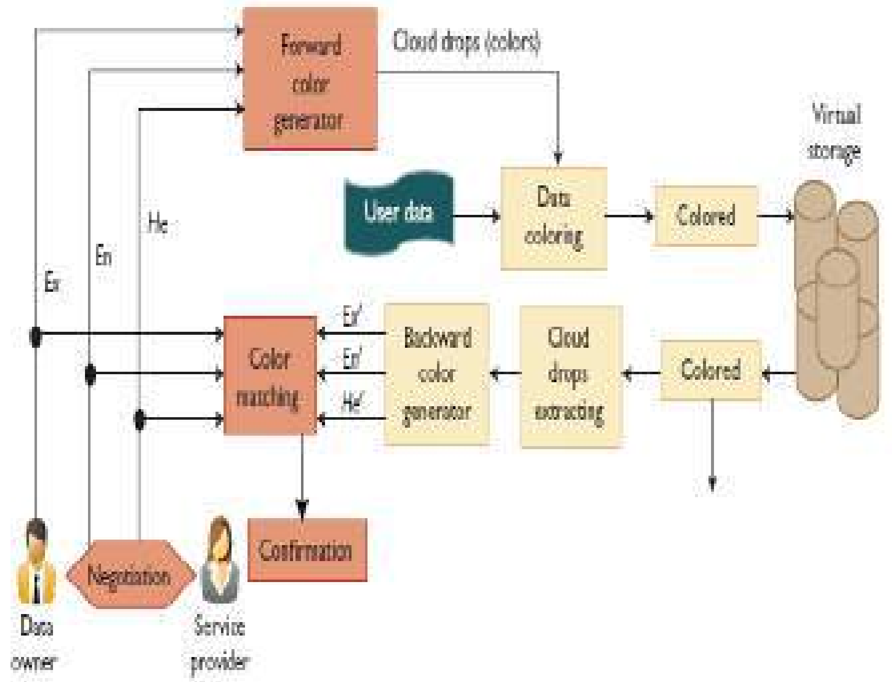

Figure 4. Data Coloring and User Identification Color Matching through Sheltered Possessions Machine Learning Technique

The Infrastructure-in-a-Service (IAS) model is based on an internal implementation layer that extends to create a platform-a-service (PASS) layer with OS and middleware support. PaaS extends across the Software-a-Service (SaaS) model and creates applications on data, content and metadata using specialized APIs.

B. Reliable cloud computing in data centers

Malware-based attacks such as worms, viruses and DoS exploit system vulnerability and allow intruders to gain access to critical information. Dangerous cloud platforms can cost businesses billions of dollars and disrupt public services. This structure helps prevent network attacks by setting up reliable work areas for various cloud applications. Security compliance requires CSPs to protect all data-center servers and storage areas. Our architecture protects VM monitors (or hypervisors) from software-based attacks and data and information from theft, corruption and natural disasters. We can build reputation systems using peer-to-peer (P2P) technology or a series of reputation systems between virtualized data centers and distributed file systems (see Figure 3). In such systems, we may protect active copyright by using active content to prevent piracy.

C. Data integrity and privacy protection

Cloud resources that they can access through security protocols such as HTTPS or Secure Sockets Layer (SSL), Security Auditing and Compliance Verification. Excellent access control to protect data integrity, repel intruders and hackers and make a single sign-on or sign-off. Shared datasets from malicious modification, deletion or copyright infringement. A way to prevent ISPs or CSPs from invading user privacy. CSPs battling spyware and web bugs; And VPN channels for personal firewalls, shared datasets, resource sites and cloud clients protected from Java, JavaScript and ActiveX applications.

D. Impression-guided data-center protection

In the past, most reputation systems were designed for P2P social networking or online shopping services. We can modify such systems to protect cloud platform resources or user applications within the cloud. A centralized assessment system is easier to implement, but requires more powerful and reliable server resources. Distribution reputation systems are more measurable and reliable to deal with failures. The reputation system we recommend for providers helps us create content-conscious trust zones using the VMware Whistle and RSA DLP package for data tracking monitoring. Reputation refers to the collective evaluation of consumers and resource owners. Researchers have previously suggested several reputation systems for P2P, multi-agent or e-commerce systems. To support trusted cloud services, we propose to build a trust overlay network to model trust relationships between data-center modules. Ranfang Shou and Kai Hwang first introduced the idea of a trust overlay for e-commerce.

5. Conclusion and future improvements

It can initiate various trust-management events, including authentication and recognition. Virtual storage supports color generation, embedding and extraction. By combining secure data storage and data coloring, data objects can be prevented from being damaged, stolen, altered or deleted. Therefore, legal users only have access to the data objects they want. The computational complexity of the three data features is much lower than that done on traditional encryption and decryption calculations on PKI services. The watermark based scheme offers very little overhead in color and fading processes. N and Hi functions work 'Ensures data owner privacy. These features can uniquely identify different data objects. Providers can implement our specific reproduction and data-coloring system to protect data-center access at the coarse-grain level and to securely secure data access at the best data level. In the future, we expect that *security as a service* (SECaaS) and *data protection as a service* (DPaaS) will grow rapidly. These are crucial to the universal acceptance of Web-scale cloud computing in personal, business, finance, and digital government applications. Internet clouds demand that we globalize operating and security standards. The interoperability and mesh-up among different clouds are wide-open problems. Cloud security infrastructure and trust management will play an indispensable role in upgrading federated cloud services.

References

1. K. Hwang, G. Fox, and J. Dongarra, *Distributed Systems and Cloud Computing: Clusters, Grids/P2P, and Internet Clouds*, Morgan Kaufmann, to appear, 2019.
2. Nandhini. R, Pavithra. P, Abinaya. P and S.Manikandan, "Information Technology Architectures for Grid Computing and Applications ", International Journal of Advanced Research Computer Engineering and Technology, ISSN:2278-1323, Vol.3, No.06, pp:2239-2242,June'2014
3. Haripriya S, Indumathi , S.Manikandan, "Virtual Network Connection Using Mobile Phones", COMPUSOFT, An International Journal of Advanced Computer Technology, ISSN:2320-0790, Vol.03, Issue: 06, pp-980-984, June-2014.
4. S. Song et al., "Trusted P2P Transactions with Fuzzy Reputation Aggregation," *IEEE Internet Computing,* vol. 9, no. 6, 2015, pp. 24–34.
5. Security Guidance for Critical Areas of Focus in Cloud Computing," Cloud Security Alliance, Apr. 2019; www.cloudsecurityalliance.org/guidance/csaguide.v2.1.pdf
6. T. Mather, S. Kumaraswamy, and S. Latif, *Cloud Security and Privacy: An Enterprise Perspective on Risks and Compliance*, O'Reilly Media, 2019.
7. J. Rittinghouse and J. Ransome, *Cloud Computing: Implementation, Management and Security,* CRC Publisher, 2018.
8. X. Lou and K. Hwang, "Collusive Piracy Prevention in P2P Content Delivery Networks," *IEEE Trans. Computers,* July 2017, pp. 970–983.
9. Bornea M.A , Vassalos V, Kotidis Y, and Deligiannakis A, (2009) "Double Index NEsted-loops Reactive join for Result Rate Optimization," Proc. IEEE Int'l Conf. Data Eng. (ICDE).

10. Negri M. and Pelagatti G. (2010) “Join During Merge: An Improved Sort Based Algorithm,” Information Processing Letters vol. 21, no. 1, pp. 11-16.
11. S. Manikandan and K. Manikanda Kumaran, "Identifying Semantic Identifying Semantic Relations Between Disease And Treatment Using Machine Learning Approach", International Journal of Engineering Research & Technology(IJERT), essn:2278-0181,Vol.2,June - 2013.

DESIGN OF INTENSIVE CARE UNIT VENTILATOR FOR TREATMENT OF COVID - 19 PATIENTS USING ASSIST CONTROL - CPAP SYSTEM

Ganeshkumar S, Sureshkumar R, Gokul S, Gowtham S

Sri Eshwar College of Engineering, Coimbatore

Abstract:

Pandemic disease COVID – 19 causes a severe impact globally which arises as a fatal disease. Literature reveals that 5% of the patients requires respirator to maintain the blood oxygen level. Due to increase of infection rate, patients starving for ventilation. Globally, government struggles to overcome the demand of ventilator system to save the lives. This research article exhibits the technique to design and deployment of the ventilator system in low cost with precision and accuracy. Moreover, this article reveals the new ventilation system's tidal volume, (RR) respiration rate, and respiratory cycles enhancement using programmable Logic controller powered byelectromagnetic valves. The solenoid valves are used to discharge the oxygen to patient at predetermined intervals and nonreturnable valves are used in expiration duct to avoid the back pressure of CO_2.The ventilator inspiration duct is equipped with Oxygen cylinder and atmospheric air. The ratio of Fraction of inspired oxygen (FIO_2) is controlled using respective valves depends up on the criticalness of patient.The digitalized valves and flow sensors is used to control the flow, measure and display of tidal volume of oxygen. The valve timings are automated by synchronizing the respiratory pattern of patient.The positive end expiratory pressure is measured using pressure sensor and FIO_2, pressure, tidal volume, respiratory rates in the respiratory cycles are maintained using valves and actuators. The research exhibits the design of intensive care unit ventilator for treatment of COVID – 19 patients and other respiratory disorders (lung failure),patients under trauma care etc., The ventilator design also can be utilized in treatment of sleep apnea.

Keyword:Electro pneumatic system, PLC Ladder programming, Respiration rate, Saturation level of O2, FIO2

1.Introduction:

In intensive care units of hospitals utilizing the ventilators to the hypoxy patients to balance the blood oxygen levels. The diseases like ARDS (Acute respiratory distress syndrome), Asthma, pandemic diseases like COVID – 19 causes failure of respiratory system. Which results in malfunction of lungs to blend the oxygen into blood. These malfunction leads to hypoxy of humans. The hypoxy results in loss of oxygen level leads to coma often leads to death. Due to the infection in alveoli of lungs, medical practioners requires an external respiratory system to balance the oxygen level[2]. The oxygen level in the blood is monitored, based on the saturation level (SP_{o2}), invasive or non-invasive ventilation is provided. More over the non-invasive techniques like external mask does not yields better results in saturating the oxygen when a patient needs more oxygen.i.e., starving rate of oxygen is high. These non-invasive techniques often cause secondary infection to the patients due to the infected air present in the surrounding atmosphere which leads to enter in to the respiratory system. Hence, invasive techniques are often used to treat the lung infection [3]& [11]. If the respiratory support requires for more than seven days of time then the patient requires supplementary surgery called as tracheostomy, which helps in arresting the secondary infection of ET (endotracheal)tubes. The tracheostomy accompanies to carry out the ventilation phenomena without secondary infection.The infected alveoli increase in respiration rate, to tends to compensate the quantity of oxygen to inhale, which leads to sub/supra sternal retraction ofchest due to less compliant of lungs which indicated the demand in respiration. This leads to low blood gas values in arteries [4]. Normally range of partial pressure PO2 50mm of Hg.Corynebacterium spp is the common contaminant found in respiratory specimen. which results in lowering of saturation level of oxygen in blood. These types of disorders requires ventilation until the recovery of patient from infection [1]&[17]. The normal range of (FIO_2) fraction of inspired oxygen is less than 0.4 to 0.6, from these range, oxygen ratio is increased up to 0.8 (80%)

2. Different modes Ventilating machines:

The most common way of treatment of respiratory disorders by continuous positive airway pressure (CPAP), The Pressurized room air is given continuously based on the requirement of patients. The ACPAP is associated technique which detects the pressure required in the upper air way (throat) by sensors and the pressure required is self-adjusted based on the requirement.Bi-level positive airway pressure (BIPAP) ventilator is often used when CPAP is not tolerated by the user. In recent technologies, equipmentare developed to increase the comfort of the user. Moreover, the common modes of ventilation used are Assist control (AC mode) [13] , pressure support ventilation and Synchronized Intermittent Mandatory Ventilation (SIMV) which provides mechanical breathing to the patients [5]

2.1 Continuous Positive Air Way Pressure(CPAP):

This CPAP is commonly used to treat obstructive sleep apnea. The air way collapses during the expiration, to overcome this disorder, airway is continuously given with the positive pressure. Due to the collapsed air way, Blood oxygen level is reduced and it sends the signal to brain to stop the sleep [15]. In CPAP ventilation, continuous positive pressure is maintained in the CPAP mask and prevents the collapsing of airway during sleep. The CPAP is divided in PEEP and PAPV.In CPAP, there is more space for oxygen intake and redistribution of fluids around the alveoli in the congested area.Moreover, CPAP increases the compliance of the lungs which increases the surface area tends to increases in gas exchange and increase in FRC [6].

2.2 Positive End ExpiratoryPressure (PEEP)

The inspiration process is due to the negative pressure created in the lung diaphragm from -5 to -8 cm of H_2 O pressure. The alveoli pressure decreases from 0 to -1 cm of H_2 O. In some diseases like ARDS, lungs cannot create the negative pressure for inflation for gas exchange. In this phenomena, small alveoli have the strong tendency to collapse. To inflat those type of alveoli, positive end pressure respiratory pressure (PEEP) is used.The patient is intubated with mechanical ventilation. The mechanical ventilator pumps the tidal volume of air in to the lungs in the positive pressure. Pumping the air into the alveoli by mechanical ventilation makes more and more positive at the end of the inspiration (In general, 10 cm of H_2O) is reached.After the inhalation, trachea is connected to the room air for expiration. The alveoli start pushing the inhaled tidal volume of air out and alveoli pressure starts falling. Commonly, in PEEP types ventilation, alveoli pressure is not allowed to 0 because sick alveoli collapse easily. The expiration is not assisted but it is accomplished due to the positive pressure inside the alveoli,the air is pushed out.The graph between FRC (Functional residual capacity) with time shows positive end expiratory pressure. The maintaining of more positive expiratory pressure decreases the cardiac output.[7] In general, 5 cm of water pressure is selected for inspiration or expiration, $FIO_2$is 0.4 to 0.6.Gradually the pressure of the lungs is increased with 1 to 2 cm of H_2O. The upper limit of pressure is 8-12 cm of water depending up on the patient and maximum level of FIO_2 is 80%. However, increasing the positive airway pressure to alveoli patients leads to barotrauma due to the injury of lungs because of the higher pressure.Theintrathoracic cavity is induced with negative pressure,the cardiac output is reduced which leads to hyper tension [8].The schematic representation of new ventilator system is shown in figure 2.1

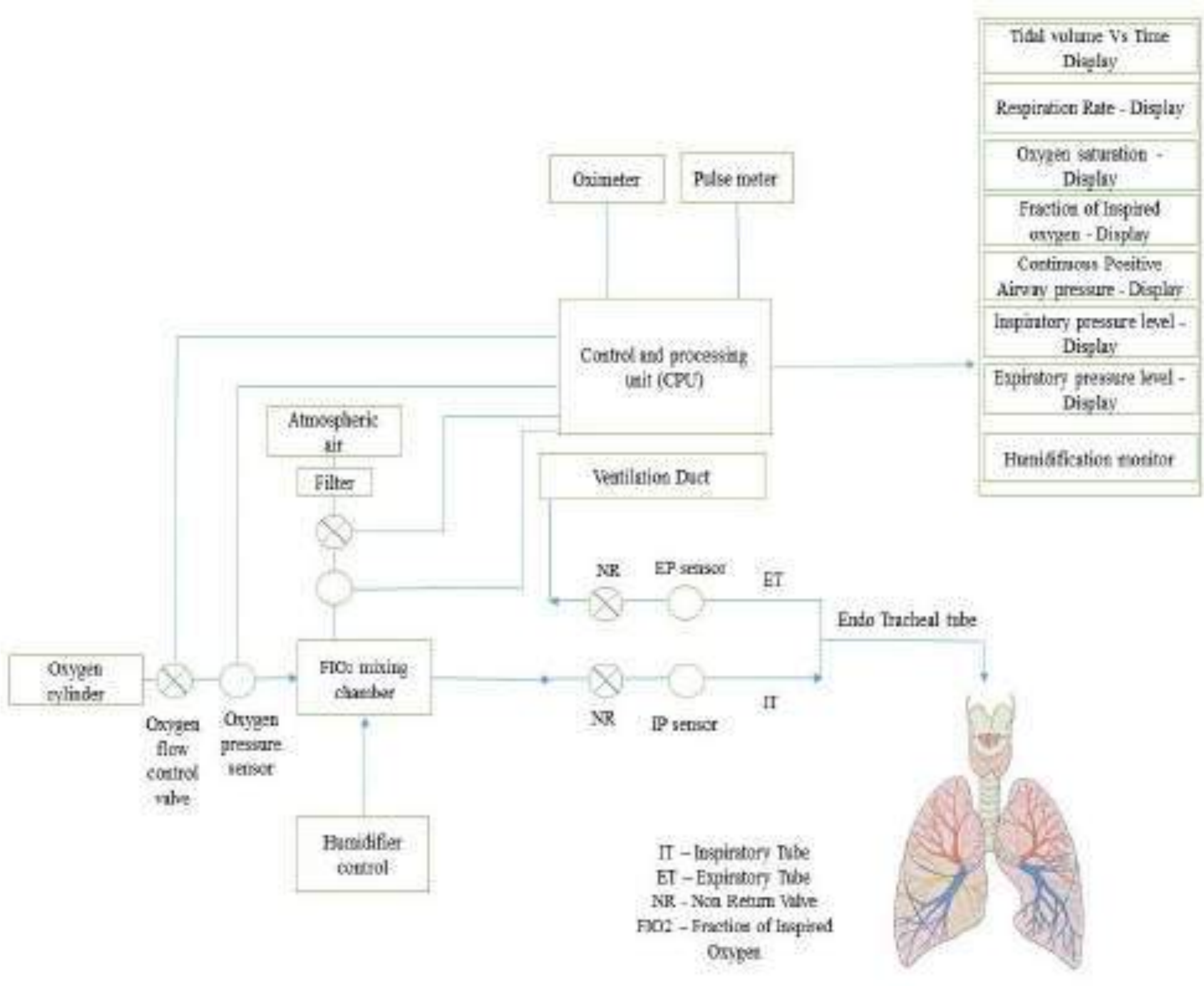

Figure:2.1 Schematic representation of Ventilator system

In this ventilator system, to equip automatic (Assist) control ventilation, sensors and controllers are given in closed loop. The Fraction of inspired oxygen (FIO_2) is given to the oxygen pressure control valve and flow sensor. In which, pressure and flow rate of oxygen is measured. The signal from the sensor is fed to the Mitshibishi Programmable logic Controller (FX 3U series) as feedback signal. The actuating signal is obtained from the controller and given to the solenoid valve. In which the flow rate is controlled based on the signal obtained from the controller. The similar technique is used in another tube which contains atmospheric air (atmospheric pressure at

1 bar) which passes through a filter, control valve and sensor. In FIO_2 mixing chamber, the oxygen valve and atmospheric air valves are synchronously operated to mix the atmospheric air and oxygen in desired amount. (Starts from 40% to 80% of oxygen). The humidifier which controls the percentage of water vapour present in the air and maintains 50% as comfort zone. The pulse meter and oximeter sensors are given to the central processing unit for monitoring the pulse and Saturation of oxygen in blood. Due to the presence of feedback system in ventilation system, user can able to utilize the ventilator in automatic (assisted mode ventilation system), in this assist mode ventilation system, ventilator senses the patient inspiratory pressure, expiratory pressure, respiration rate and tidal volume. The parameters which includes to make the patient stable are tidal volume of air, respiration rate, inspiratory and expiratory pressure [10]. These parameters are maintained in preset range using the controller. The respiratory rate can be adjusted by lowering from the range 30-15 cycles per minute depending up on the patient. This controller also enables manual mode of adjustments to increase or decrease the fraction of inspired oxygen, pressure and tidal volume of air using potentiometers. Since this machine is designed for continuous air way pressure (CPAP), inspiratory pressure is maintained from 8 to15 cm of H_2O. Moreover, higher pressure range reduces the cardiac output (Blood flow) since the reduction of space in the chest area and higher ranges of alveoli pressure leads to lung injury.The tidal volume of 500 ml per inspiration is maintained to prevent the patient from hypoxy levels [9].

3.Air flow circuit from controller to endotracheal tube (ET Tube):

At the expiration the CO_2 from the alveoli passes through the expiration duct as shown in figure 3.1. To maintain minimum pressure towards the lungs, the inlet valve opening is preset and expiratory pressure is sensed using pressure sensor. The signal from the pressure sensor assists to check the patient's respiration cycle. The exhalation of patient is sensed and based up on the expiration rate, oxygen is delivered in to ET tube (Endo tracheal tube) through inspiration duct, as shown in figure 3.1. The cycles of inspiration and expiration is sensed and based on the values, machine sets the frequency of oxygenation in assist control (AC) mode of ventilation. If user switches to manual mode, machine enables to adjust the desired quantity of tidal volume, respiratory pressure levels and respiratory rate by the user. Since the pressure is maintained in positive range above 5 cm of H_2O, (Positive pressure) the machine prevents collapsing of lungs, moreover, the functional residual capacity level of lungs is maintained in positive direction hence the plot offsets from the zero range in functional residual capacity level with time.

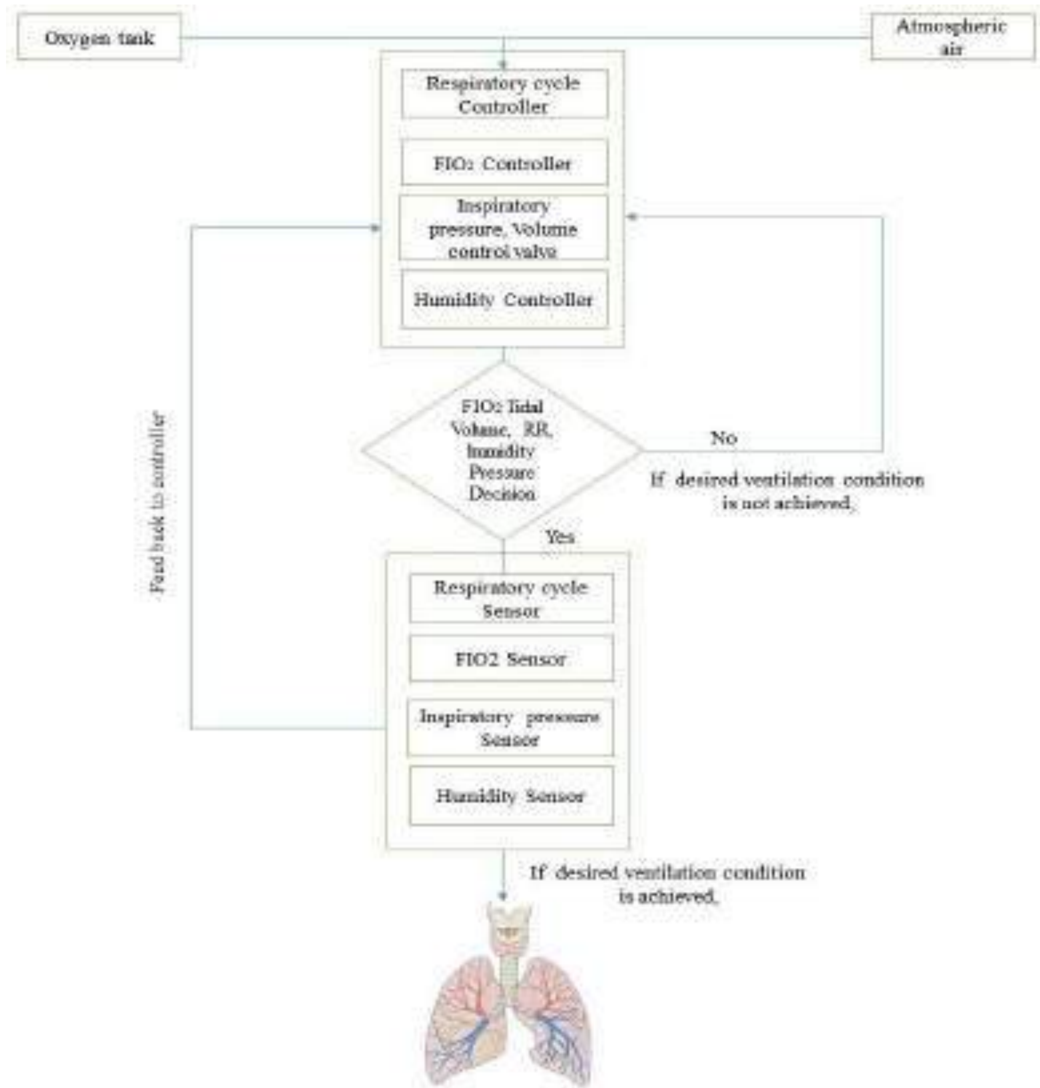

Figure:3.1 Processflow chart of Ventilation system

4.Data logging and output monitoring systems

The Mitsubishi PLC software is used in PLC Ladder logic programming sense. (Mitsubishi FX 3U series is used to control the actuators, the synchronous control of oxygen and atmospheric air is attained using this controller as shown in figure 4.1. The expiratory pressure, inspiratory pressure, respiratory rate, flow rate, oxygen pressure, atmospheric air and oxygen mixture are maintained using the programmable logic controller [16]. The graphical user interface (GUI) for monitoring the ventilation parameters are displayed and data logging is available and the tidal volume, respiratory pressure with respect to time is logged in documented. The Graphical user interface is shown in figure 4.3. The plots of FRC with time, ECG and saturation point are displayed [12]& [14].The Mitsubishi FX 3U series PLC is programmed using LADDER LOGIC diagrams and process flow is executed for the attainment of air flow diagram as shown in figure. 4.2

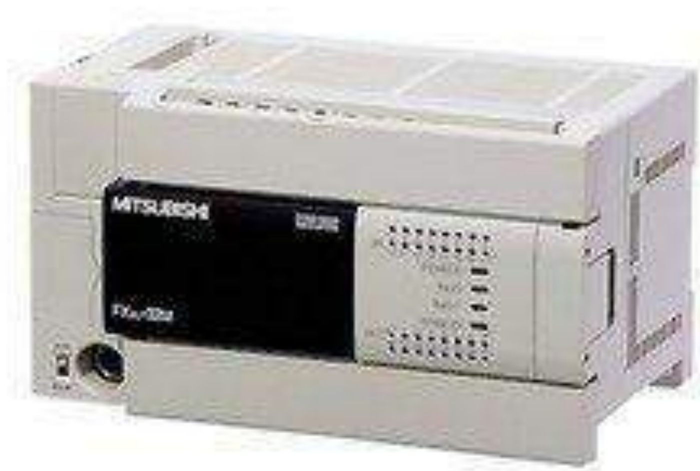

Figure 4.1 – Mitsubishi FX 3U series PLC

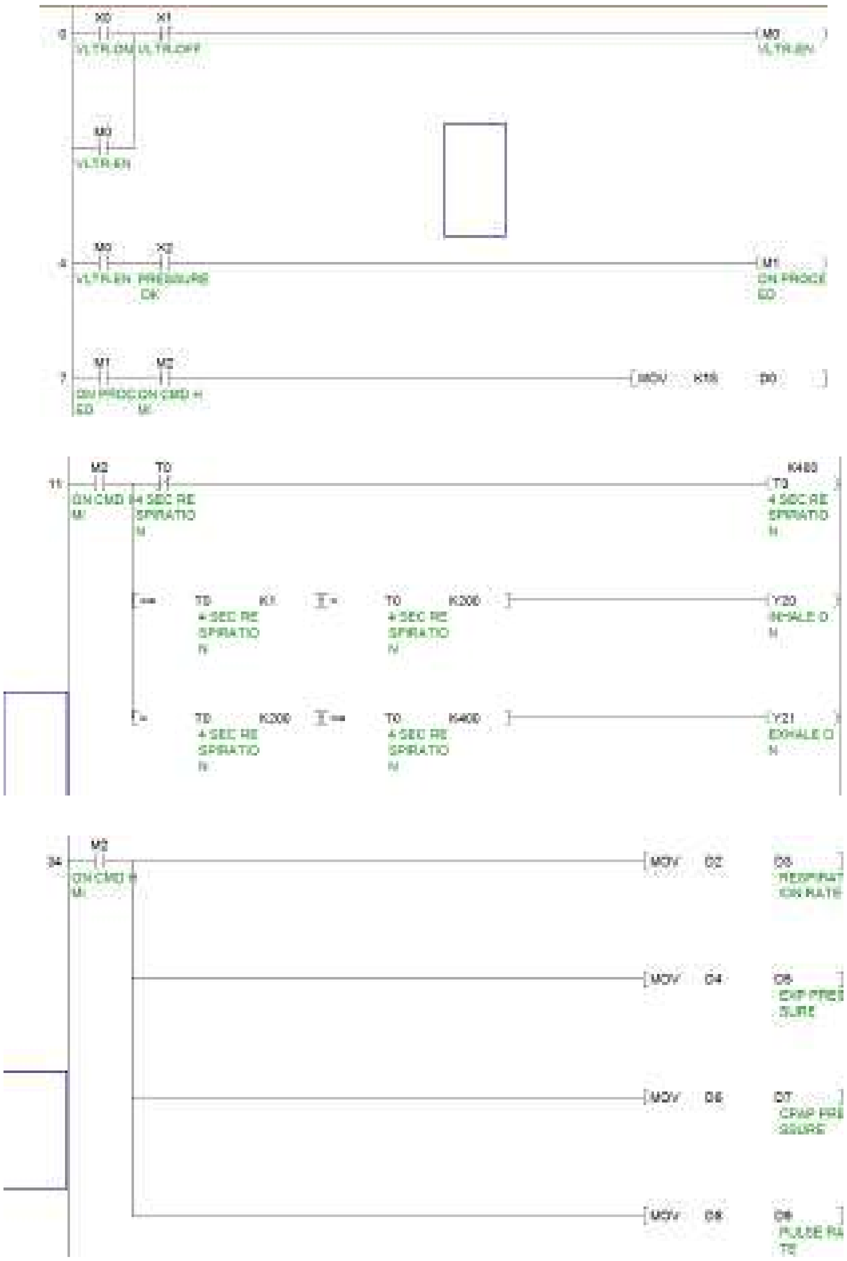

Figure 4.2 – Ladder Logic Diagram for CPAP ventilation

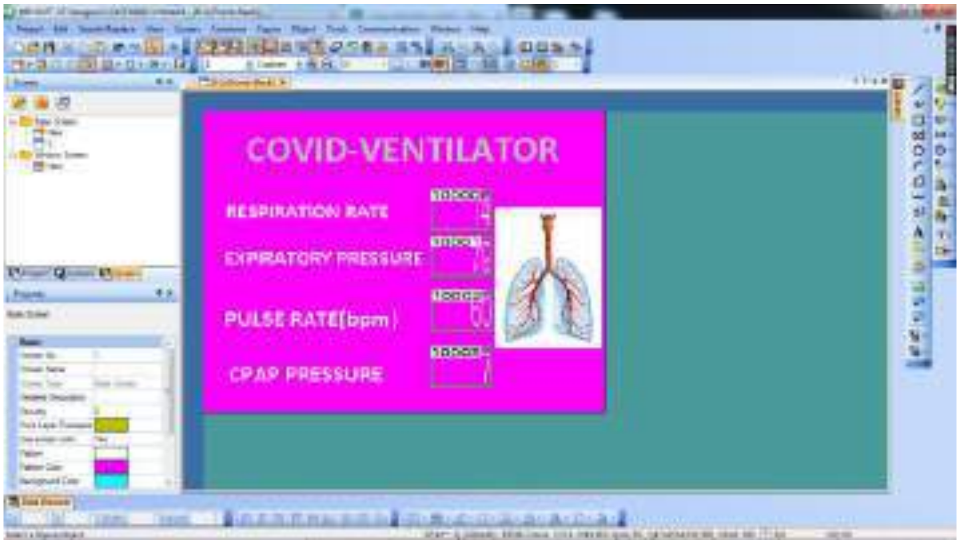

Figure 4.3 - Graphical User interface forMitsubishi electric PLC software

5.Conclusion:

The design and simulations obtained from the Mitshibishi PLC software validates the automation of inspiratory and expiratory valves is executed. The respiration phenomena also can be in assist mode (AC) mode which enables the automated mode and senses the respiratory pattern of the patient. The Tidal volume of inspired air, Fraction of inspired oxygen, expiratory pressure is also can be data logged for the future study and plotting of FRC and time is feasible in this new ventilator system design. Moreover, the cost of the equipment is reduced compared to the existing ventilator setup available in the market. Hence, this system can be utilized for treating the patients with respiratory disorders such as , pneumonia, sleep Apnea and COVID –19.

6.References:

1.Clariot, S., Constant, O., Lepeule, R. et al. Clinical relevance and impact of Corynebacterium isolation in lower respiratory tract of critically ill patients requiring mechanical ventilation. Infection (2020). https://doi.org/10.1007/s15010-020-01411-w

2.Tuder, R.M., Yun, J.H., Bhunia, A. et al. Hypoxia and chronic lung disease. J Mol Med 85, 1317–1324 (2007). https://doi.org/10.1007/s00109-007-0280-4

3. Yoshida, Y., Takeda, S., Akada, S. et al. Factors predicting successful noninvasive ventilation in acute lung injury. J Anesth 22, 201–206 (2008). https://doi.org/10.1007/s00540-008-0637-z

4.Romero, J., Vari, A., Gambarrutta, C. et al. Tracheostomy timing in traumatic spinal cord injury. Eur Spine J 18, 1452–1457 (2009). https://doi.org/10.1007/s00586-009-1097-3

5.Montes, F.R., Pardo, D.F., Charrís, H. et al. Comparison of two protective lung ventilatory regimes on oxygenation during one-lung ventilation: a randomized controlled trial. J CardiothoracSurg 5, 99 (2010). https://doi.org/10.1186/1749-8090-5-99

6.Spapen, H., Suys, E., De Regt, J. et al. An endotracheal tube providing "pressurized sealing" prevents fluid leakage in mechanically ventilated critically ill patients: a pilot study. J Anesth 34, 144–148 (2020). https://doi.org/10.1007/s00540-019-02707-4

7.Alvey, N.J., Hlaing, M., Piccoli, J. et al. Positive end-expiratory pressure titration via esophageal balloon monitoring in a morbidly obese patient undergoing laparoscopic nephrectomy. Can J Anesth/J Can Anesth (2020). https://doi.org/10.1007/s12630-020-01606-7

8. Ferreira-Coimbra, J., Ardanuy, C., Diaz, E. et al. Ventilator-associated pneumonia diagnosis: a prioritization exercise based on multi-criteria decision analysis. Eur J ClinMicrobiol Infect Dis 39, 281–286 (2020). https://doi.org/10.1007/s10096-019-03720-x

9. Lo, Y., Wu, H., Lin, Y. et al. Hypoventilation patterns during bronchoscopic sedation and their clinical relevance based on capnographic and respiratory impedance analysis. J ClinMonitComput 34, 171–179 (2020). https://doi.org/10.1007/s10877-019-00269-0

10.Kim, M.C., Lee, Y.J., Park, J.S. et al. Simultaneous reduction of flow and fraction of inspired oxygen (FiO2) versus reduction of flow first or FiO2 first in patients ready to be weaned from high-flow nasal cannula oxygen therapy: study protocol for a randomized controlled trial (SLOWH trial). Trials 21, 81 (2020). https://doi.org/10.1186/s13063-019-4019-7

11.Ti, L.K., Ang, L.S., Foong, T.W. et al. What we do when a COVID-19 patient needs an operation: operating room preparation and guidance. Can J Anesth/J Can Anesth (2020). https://doi.org/10.1007/s12630-020-01617-4

12. Patel D.M., Shah A.K., Shukla Y.B. (2020) An IEC 61131-3-Based PLC Timers Module Implemented on FPGA Platform. In: Bindhu V., Chen J., Tavares J. (eds) International Conference on Communication, Computing and Electronics Systems. Lecture Notes in Electrical Engineering, vol 637. Springer, Singapore

13.Makker, K., Cortez, J., Jha, K. et al. Comparison of extubation success using noninvasive positive pressure ventilation (NIPPV) versus noninvasive neurally adjusted ventilatory assist (NI-NAVA). J Perinatol (2020). https://doi.org/10.1038/s41372-019-0578-4

14.Zhang H., Yin H., Fu P. (2020) Design of Data Acquisition Software for Steam Turbine Based on Qt/Embedded. In: Pan JS., Li J., Tsai PW., Jain L. (eds) Advances in Intelligent Information Hiding and Multimedia Signal Processing. Smart Innovation, Systems and Technologies, vol 156. Springer, Singapore

15. De Rose, C., Valentini, P., Curatola, A. et al. Lung Ultrasound in Congenital Cardiac Abnormality: ALCAPA. Indian J Pediatr (2020). https://doi.org/10.1007/s12098-020-03208-z

16.Yang Q., Wang J., Mao Q., Fang L. (2020) A Closed - Loop Automation System for Floating Welding Scar Grinding. In: Duan B., Umeda K., Hwang W. (eds) Proceedings of the Seventh Asia

International Symposium on Mechatronics. Lecture Notes in Electrical Engineering, vol 588. Springer, Singapore

17.Bosco, G., Paganini, M., Rizzato, A. et al. Arterial blood gases in divers at surface after prolonged breath-hold. Eur J Appl Physiol 120, 505–512 (2020). https://doi.org/10.1007/s00421-019-04296-2

18. Ganeshkumar S, Sureshkumar R, Sureshbabu Y, Balasubramani S, A Review On Cutting Tool measurement In Turning Tools By Cloud Computing Systems In Industry 4.0 And IOT, Page No: 1-7, GIS science journal DOI:20.18001.GSJ.2020.V7I8.20.35604,

19.Ganesh Kumar, S & Thirunavukkarasu, V 2016, Investigation of Tool Wear and Optimization of Process Parameters in Turning of EN8 and EN 36 Steels 'Asian Journal of Research In Social Sciences And Humanities'. vol. 6, no.11, pp. 237 - 243,

20.Ganesh Kumar, S, Thirunavukkarasu, V, Sureshkumar, R, Venkatesh, S & Ramakrishnan, T 2019, 'Investigation of Wear behaviour of Silicon Carbide Tool inserts and Titanium Nitride coated tool inserts in machining of EN8 steel, 'International Journal of Mechanical Engineering and Technology', vol.10, no. 01, pp. 1862-1873 ,

21.Ganeshkumar, S., Sureshkumar, R., Sureshbabu, M. Y., & Balasubramani, M. S. A Review of Performance Investigations in Hydrogen–Oxygen Generator for Internal Combustion Engines.

22.Ganeshkumar, S., Sureshkumar, R., Sureshbabu, M. Y., & Gokul, M. S. A Critique on digital transformation of music production using virtual sound technology (VST).

A REVIEW ON CUTTING TOOLMEASUREMENT IN TURNING TOOLS BY CLOUD COMPUTING SYSTEMS IN INDUSTRY 4.0 AND IOT

Ganeshkumar S,Sureshkumar R, Sureshbabu Y, Balasubramani S
Sri Eshwar College of Engineering, Coimbatore

ABSTRACT:

Machining is an important operation in production industry, in which the sharpness of the cutting tools plays predominant factor in performance of machining. These article reviews the wear measurement, vibration measurement, surface roughness measurement, cutting force measurement techniques. The advancements in wear measurement is exhibited in this article, it assists the manufacturer to monitor the wear of the cutting tools, vibration and cutting forces online. (In the real time process). This digitalized data assists the manufacturer to transfer to another system in cloud-based data management system. The review of types of cutting force measurement techniques such as piezo electric crystal-based sensors, wheat stone bridge circuit strain gauge sensors, stereo vision system and pin on disc apparatus are explained in this article. From the review of these cutting tool parameter measurement techniques, it is concluded that the digitalization of measuring data of cutting tools such as wear, cutting forces and vibrations are transferred in cloud for data management system increases the quality of finished product and production rate. The cloud-based data management plays a key role in industry 4.0.

Keywords: Industry 4.0, Piezoelectric sensor, Cloud, Vibration sensor, cutting force, stereo vision system.

1.Cutting force measurement techniques:

In general, the cutting forces are measured using digital force sensors. The commonly used force sensors are Wheatstone bridge strain gauge, strain rings, piezo electric force sensors, quartz sensors, poly silicon resonant transducers, and capacitive sensors. The force sensors are attached to the cutting tool to sense the cutting force given to the work piece. These force sensors are designed to measure the cutting force in the three axes (X, Y and Z). In wheatstone bridge strain gauge, the resistance value of the resistor changes with respect to the cutting force applied. From the deviation in resistance of the resistor, cutting force is determined. The schematic representation of the wheatstone bridge circuit is illustrated in figure 1.1. The strain gauges are attached in lathe tool holder to measure the cutting forces as shown in figure 1.2. The cutting force measurement using strain rings is similar to the Wheatstone bridge strain gauge. The capacitive type force sensor is another method to sense the cutting force acting on the tool insert. The schematic representation of the capacitor-based lathe tool dynamometer shown in figure 1.3. In this measuring instrument, the capacitor is placed in between the lathe tool holder and insert. The capacitance of the capacitor changes with respect to the cutting force applied on the workpiece. The piezoelectric transducer type lathe tool dynamometer is similar to the capacitance type dynamometer. In Piezo electric type dynamometer, capacitor is replaced by the piezoelectric crystal. The cutting force is sensed by the piezo electric crystal by converting the mechanical energy into electrical energy. In addition, the cutting force can be measured indirectly by spindle power. i.e., the spindle motor power is measured using an ammeter and the load of the spindle is calibrated with respect to the cutting force. The schematic diagram of cutting force measuring system by the power of the spindle is illustrated in figure 1.4. The various methods of force measurement used in lathe tool dynamometers is shown in figure.1.5.

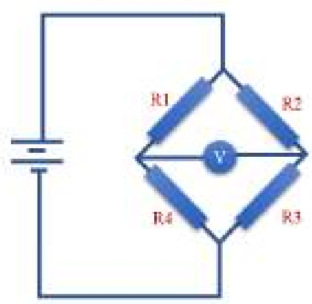

Figure:1.5 Wheatstone bridge circuit for lathe tool dynamometer

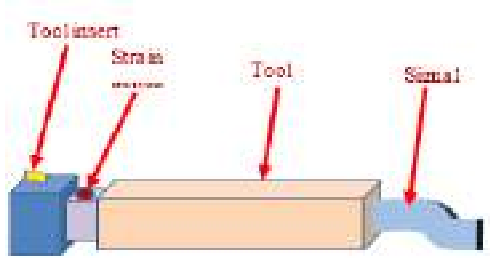

Figure:1.3 Cutting force measurement using strain gauge

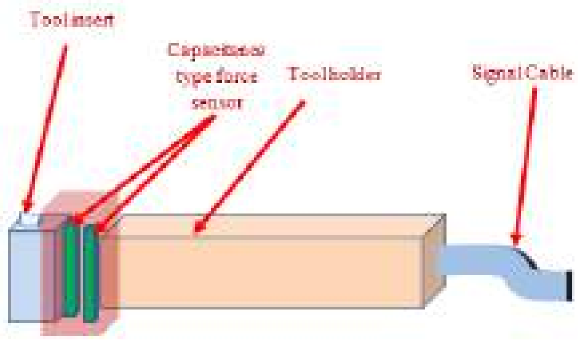

Figure:1.4 Capacitive type cutting force sensor

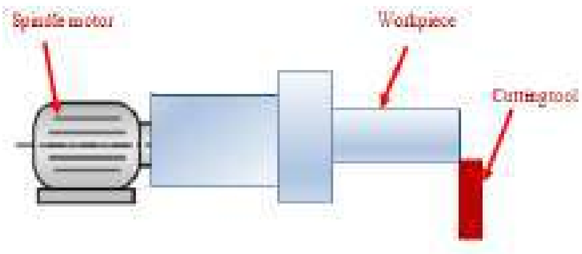

Figure:1.5 Cutting force measurement by spindle motor power

Figure:1.6 Cutting force measuring techniques

2. Wear measurement techniques

In general, the wear of cutting tools is measured by tool makers microscope, stereo vision system, pin on drum apparatus, digital image analyzer, scanning electron microscope, block on ring test, slurry abrasion tests. In stereo vision system, charge couple device (CCD) camera is mounted on the measuring table. This CCD stereo vision technique is generally used in online tool wear measurement and machine vision system. The specimen (cutting tools) are placed on the table and the image of the tool insert is captured by a CCD camera. The images are processed to find the wear of the cutting tools. The schematic representation of stereo vision system is illustrated in figure 2.1. The scanning electron microscope is used to find the wear and microscopic structure of the specimen (cutting tools).

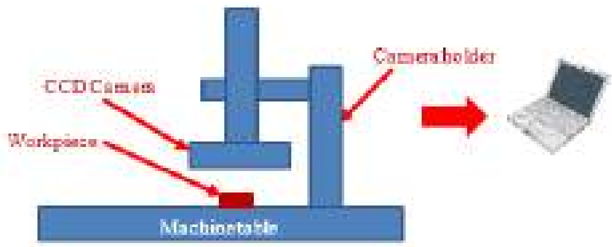

Figure:2.1 Stereo vision system (CCD Camera)

Pin on drum apparatus is another method to find the wear of the cutting tools. In this apparatus, tool inserts are placed in the rotating drum. The load is given to the specimen using a ball type tribometer. The wear is sensed using the tribometer and it is sent to the computer. The schematic representation of pin on drum apparatus is shown in figure 2.2. The block on ring wear test is another method to evaluate the wear performance of cutting tools. In block on ring test apparatus, the tool insert is placed on a ring and load is given. Block on ring test apparatus is similar to the pin on drum wear testing machine.

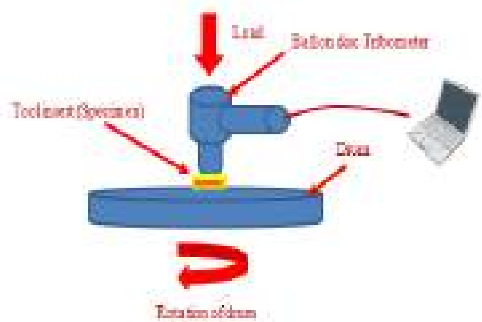

Figure:2.2 Pin on drum apparatus for wear measurement

In alumina slurry abrasion test, an alumina slurry ball is rotated on the specimen. Due to continuous rotation, specimen undergoes wear due to friction. The wear of the specimen is determined using tool makers microscope. The geometry of worn tool insert is subtracted from the unworn tool insert dimension to obtain the wear of tool insert. The techniques used to measure the wear are illustrated in figure 2.3

3. V**ibration measurement techniques:**

In general, the vibration of the system is measured by vibration sensors. accelerometers, velocity transducers, displacement transducers which converts vibrational energy into electric signals.

Figure:2.3 Tool wear measurement techniques

In accelerometer, piezoelectric crystals are used to sense the vibrations of the system. The schematic representation of piezo electric vibration sensor is shown in figure 3.1. The commonly used vibration measurement techniques are illustrated in figure 3.2.

Figure:3.1 Piezoelectric crystal vibration sensor

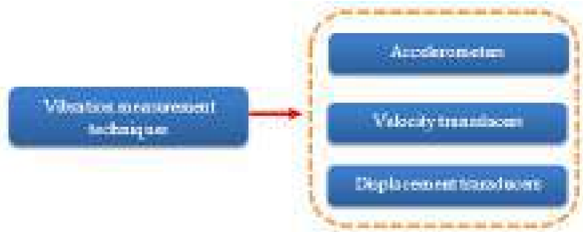

Figure:3.2 Classifications of vibration sensors

4.Surface roughness measurement techniques:

In general, the surface roughness of the specimen is be measured by interferometer, surface photographs, stylus – probe instruments. Interferometry is the technique used to measure the surface finish using interference of fringes. The specimen is illuminated by a coherent source of light and fringes obtained in the interferometer is interpreted to measure the surface finish. The stylus- probe method is commonly used to determine the surface roughness of the specimen. In this apparatus, a measuring reed (stylus) slides on the surface of the specimen. The surface roughness of the specimen is magnified and displayed in the apparatus. The commonly used surface roughness measuring techniques are depicted in figure 4.1

Figure:4.1 Types of surface roughness measurement

5.Modern wear measurement techniques:

In conventional measuring systems of wear, vibrations and cutting forces, the data are recorded offline and the decision of tool insert changing have been taken by magnitude of the wear and vibrations. It leads to time consumption. To overcome this adverse effect, online data monitoring techniques are developed to monitor the wear, cutting forces and vibrations online and the datas are digitalized and transformed to cloud to perform machining operation, tool changing decisions etc., these cloud computing systems plays a key role in industry 4.0 and automation sector. In industry 4.0. the decision making of tool changing is interpreted with deep learning and machine learning techniques. These machine learning techniques assists to syrvey the data, monitor and learn the activities of CNC machines with respect to the feed rate, speed of the spindle and depth of cut. The variations of vibrations, wear rate and cutting forces are studied, predicted for tool changing activities. The advantages of digital transformation of these wear, cutting forces and vibration data are helps in data storage and transferred from one place to other place by IOT technique.

6.Conclusion:

The conventional measurement of wear, vibration and cutting forces are demonstrated. The parameters affecting the wear, cutting forces and vibrations are exhibited. The comparison made from conventional and modern techniques of tool wear measurement, wear measurement and vibration measurement are exhibited. Smart sensors, measurement technology have been evolved in machine tool metrology to enhance industry 4.0 and internet of things to perform automation. The robotic machining centres are have been accompanied with machine learning and deep learning technologies. The modern techniques furnish the way to evolve new technologies and innovations in industry 4.0

References:

1. Ganesh Kumar, S & Thirunavukkarasu, V 2016, Investigation of Tool Wear and Optimization of Process Parameters in Turning of EN8 and EN 36 Steels ‘Asian Journal of Research In Social Sciences And Humanities’. vol. 6, no.11, pp. 237 - 243,
2. Ganesh Kumar, S, Thirunavukkarasu, V, Sureshkumar, R, Venkatesh, S & Ramakrishnan, T 2019, ‘Investigation of Wear behaviour of Silicon Carbide Tool inserts and Titanium Nitride coated tool inserts in machining of EN8 steel, ‘International Journal of Mechanical Engineering and Technology’, vol.10, no. 01, pp. 1862-1873 ,
3. Dimla D.E 2002, ‘sensor signals for tool-wear monitoring in metal cutting operations—a review of methods’, International Journal of Machine Tools & Manufacture, vol. 40, pp. 1073-1098.
4. Ghani, AK, Choudhury, IA & Husni 2002, ‘Study of tool life, surface roughness and vibration in machining nodular cast iron with ceramic tool’, Journal of Materials Processing Technology, vol. 127, pp. 17-22..
5. Lee, BY & Tarng, YS 2000, ‘Cutting-parameter selection for maximizing production rate or minimizing production cost in multistage turning operations’, Journal of Materials Processing Technology, vol. 105, pp. 61-66
6. Bilek.P, Jurci.P, Novak.M Hudakova.M& Caplovic.L 2015, ‘Tribological and mechanical properties of Cr2N–11 Ag-coatings deposited on Cr–V ledeburitic steel’, Wear, vol. 340-341,pp. 47-52.
7. Kumar, R. S., Alexis, J., & Thangarasu, V. S. (2017). Optimization of high speed CNC end milling process of BSL 168 Aluminium composite for aeronautical applications. Transactions of the Canadian Society for Mechanical Engineering, 41(4), 609-625.
8. Kumar, S. R., Alexis, J. S., & Thangarasu, V. S. (2017). Experimental Investigation of Influential Parameters in High Speed Machining of AMS 4205. Asian Journal of Research in Social Sciences and Humanities, 7(2), 508-523.
9. Balasubramani, S., & Balaji, N. (2016). Investigations of vision inspection method for surface defects in image processing techniques-a review. Advances in Natural and Applied Sciences, 10(6 SE), 115-120.
10. Balasubramani, S., Dhanabalakrishnan K.P., Balaji,N. (2015) Optimization of Machining parameters in Aluminium HMMC using Response Surface Methodology. International journal of applied engineering research, 10(20), 19736-19739.
11. Kumar, R. S., Thangarasu, V. S., & Alexis, S. J. (2016). Adaptive control systems in CNC machining processes--a review. Advances in Natural and Applied Sciences, 10(6 SE), 120-130.
12. Kumar, S., Alexis, J., & Thangarasu, V. S. (2016). Prediction of machining parameters for A91060 in end milling. Advances in Natural and Applied Sciences, 10(6 SE), 157-164.
13. Ganeshkumar, S., Sureshkumar, R., Sureshbabu, M. Y., & Balasubramani, M. S. A Review of Performance Investigations in Hydrogen–Oxygen Generator for Internal Combustion Engines.
14. Ganeshkumar, S., Sureshkumar, R., Sureshbabu, M. Y., & Gokul, M. S. A Critique on digital transformation of music production using virtual sound technology (VST).

Mechanics Based Design of Structures and Machines
An International Journal

ISSN: 1539-7734 (Print) 1539-7742 (Online) Journal homepage: https://www.tandfonline.com/loi/lmbd20

Experimental ballistic performance determination of friction stir welded magnesium (AZ31B) targets

Dharani Kumar S & Suresh Kumar Sundaram

MECHANICS BASED DESIGN OF STRUCTURES AND MACHINES
https://doi.org/10.1080/15397734.2020.1766491

Experimental ballistic performance determination of friction stir welded magnesium (AZ31B) targets

Dharani Kumar S[a] and Suresh Kumar Sundaram[b]

[a]Department of Mechanical Engineering, Sri Eshwar College of Engineering, Coimbatore, Tamil Nadu, India;
[b]Department of Mechanical Engineering, SSN College of Engineering, Kalavakkam, Chennai, Tamil Nadu, India

ABSTRACT

Nowadays there is an increasing demand to develop light weight defense vehicles, fighter aircrafts and warships in order to enhance their mobility and fuel economy. It can be achieved by using the light weight structures made up of Aluminum and Magnesium plates which will reduce the weight, increase the payload carrying capacity and efficiency of the vehicles. In the present work, experimental ballistic performance of Magnesium (AZ31B) Base Metal (BM), friction-stir-welded (FSW) and post-weld-heat treated (PWHT) target plates have been determined by using the 7.62 mm Armor Piercing Projectiles (APP). Prior to ballistic testing, Magnesium joints were prepared by the FSW process for various tool rotational and welding speeds. Defect-free welds with better tensile and impact properties, were obtained with tool rotational speed of 1200 rpm and the welding speed of 50 mm/min. PWHT was carried out with the annealing temperature at 250 °C for about 1 hour. Microhardness and microstructure of the FSW and PWHT joints were investigated. Highest hardness (67 HV) was obtained for fine grain structure and precipitated particles were observed for PWHT targets. Depth of Penetration of PWHT target plates was approximately 17.55% and 16.31% lower than the BM and FSW target plates respectively. Scanning Electron Microscopic observation of projectile penetrated channel showed the formation of Adiabatic Shear Bands (ASBs). Due to a larger number of ASB lines, ballistic impacted FSW surface showed more number of macro cracks compared to PWHT surface. The PWHT joints showed the absence of fragmentation failure, lesser cracks and ASB lines which increased the ballistic performance.

ARTICLE HISTORY
Received 2 January 2019
Accepted 5 May 2020

KEYWORDS
Magnesium plate (AZ31B); Friction stir welding; Post weld heat treatment; Armor piercing projectile; Ballistic performance

1. Introduction

In recent years, there is an increasing requirement to develop lightweight structures for the defense industry to minimize the weight of tankers, fighter aircrafts and ships in order to enhance the payload carrying capacity and fuel economy of the vehicles. Aluminum (Al) and Magnesium (Mg) alloys are being used to manufacture the ultra-lightweight armored ground vehicles tanks and aircrafts due to their properties such as, lesser bulk density, high damping characteristics and excellent dimensional stability. Jones and DeLorme (2008) have reported that, specific damping capacity of the magnesium alloy is approximately 37% and 84% higher than that of steel and aluminum alloy respectively. Mathaudhu and Nyberg (2010) reported that, Magnesium alloy (AZ31B) is generally used in tankers, cockpit, stabilizer fins and missile applications. In defense tanks, many parts need both permanent and temporary joints. Bulk volume and irregular profile

CONTACT Suresh Kumar Sundaram sureshkumars@ssn.edu.in Department of Mechanical Engineering, SSN College of Engineering, Chennai 603110, Tamil Nadu, India.
Communicated by Wei-Chau Xie

limit the traditional manufacturing process which requires welded joints, bolts and nuts which are inevitable (Holmen et al. 2015). At present, Mg plates are welded by gas tungsten arc welding (GTAW) and gas metal arc welding (GMAW) processes. Even though, reasonable welding speeds can be achieved, formation of high weld residual stress and changes in metallurgical structures are unavoidable [Lee et al. (2003)] and thus FSW was considered in the present work. This welding technique has exhibited lesser distortion and improved joint strength compared to other welding processes. Normally post weld heat treatment of welded joints can be used to reduce the residual stresses and rebuild the weld properties. Generally FSW can be used to weld all grades of aluminum alloys and lack of work has been reported to study the weld ability of Mg alloys. In this paper, weldability and ballistic performance of Mg (AZ31B) plates joined by FSW process have been investigated for gaining further additional lightweight for the existing combat structures.

Generally welding of magnesium alloys is quite difficult in contrast to steel and aluminum alloys due to its low surface tension and high surface vapor pressure. Many researchers (Fu et al. (2012); Liu and Dong (2006) and Min et al. (2009) have reported that conventional welding processes such as, GTAW, electron beam welding, and laser beam welding and resistance spot welding processes will be suitable to magnesium alloy. Padmanaban, Balasubramanian, and Reddy (2011) reported that, among these welding processes of AZ series, Mg alloy is difficult to weld due to porosity formation and defects such as solidification cracking, oxidization and hot cracks which may deteriorate the joint's strength. Several researchers (Jannet, Mathews, and Raja (2014), Munoz et al. (2008) and Zhao et al. (2010) suggested that magnesium and aluminum alloy welds manufactured by FSW process have enhanced the tensile strength, hardness and impact strength related to fusion welding process. FSW is the most successful process, enabling a possible solid-state joining technique which has enormous potential in the welding of non-ferrous alloys, because it can provide reliable joint-efficiency with lesser thermal deformation of work species.

Several researchers (Richmire, Sharifi, and Haghshenas (2018a), Lockyer and Russell (2000) have made an attempt to investigate the mechanical properties of welded Mg plates joined by FSW process. Motalleb-Nejad et al. (2014) studied the effect of FSW pin geometry on mechanical behavior and microstructural variation of AZ31B magnesium butt welded joint. Pin profiles varied from cylindrical shape, screw threaded shape and tapered profile were considered and proved that tapered and screw threaded pin profiles showed finest microstructure and higher mechanical properties. Similar observation was made by Ilangovan et al. (2015), while joining heat treatable (AA6061) and non-heat treatable aluminum alloys (AA5083). This is due to the fact of threaded taper profile causes improved flow of materials in between two alloys and formation of defect free welded joints. Padmanaban and Balasubramanian (2010) studied the effect of FSW process parameters such as, tool speed, welding feed and axial force on mechanical properties of Mg (AZ31B) alloys. They observed that, tool speed of 1600 rpm, a welding feed of 0.67 mm/s, and an axial force of 3 kN showed improved joint efficiency. It is also mentioned that, optimum level of heat developed, finer grains, and higher hardness were the main reasons for the better tensile properties of these joints. Similarly [Singarapu, Adepu, and Arumalle (2015)] observed that tool rotational speed and traverse speed are the important parameters in deciding the mechanical properties of friction-stir-processed AZ31B magnesium alloy. The observations of [Sevvel and Jaiganesh (2014)] also confirmed that tool rotational speed, traversing rate and profile (taper) plays an important role in determining the optimum mechanical properties of Mg joints. In addition, [Fu et al. (2012)] noticed that, FSW tool rotating in anti-clockwise direction shows improved mechanical properties. Shen, Wang, and Liu (2012) studied the effect of tool pin diameter on microstructure and mechanical properties of friction stir spot welded AZ31B magnesium alloy joints. It is noted that, a larger pin diameter leads to the formation of coarse grains at different zones of the welded joints. Even though, many researchers have studied the influence of several FSW process parameters on mechanical properties, lack of work has been reported to determine the influence of those properties on ballistic behavior.

Guo et al. (2009; 2011) determined the optimum post weld heat treatment parameters to obtain improved mechanical properties of the friction stir welded Magnesium (AZ31) joints. Maximum yield and tensile strength of 139.9 MPa and 238.4 MPa were obtained for the joint. The authors reported that, heat treatment after welding will be beneficial to achieve improved joint properties. Ballistic performance of the joints has not been attempted. Fukumoto et al. (2007) studied the effect of post weld heat treatment on microstructure and mechanical properties of friction welded Magnesium joints. The authors could able to achieve fine grain size at the weld region due to dynamic recrystallization and they mentioned that, effect of PWHT is significant beyond a grain size of 15 μm. Balakrishnan, Balasubramanian, and Madhusudhan Reddy (2013b) improved the ballistic performance of the welded steel joints by depositing a soft austenitic stainless-steel buttering layer in between the base metal and the hard faced layer. During this process, the welded samples were heated additionally. Wang et al. (2017) determined the optimum post weld heat parameters to achieve the improved mechanical properties and microstructures. The authors suggested that, heating the joints for about 300 °C and one hour will improve the yield strength, fatigue strength and microhardness.

Thompson et al. (2012) suggested that ballistic performance of the friction stir welded joints is superior to other welded joints prepared by arc welding process. Thompson et al. (2012) and Sullivan et al. (2011) mentioned that, among the gas welding techniques, FSW plays a key role in the manufacture of military vehicles for its structural integrity, hull structures and trailer frames of combat vehicles. The influence of post weld heat treatment has not been considered. Abdullah et al. (2015) determined the ballistic failure behavior of AZ31B magnesium alloy with addition of lead with three different proportions of lead (1%, 5%, and 10%) manufactured through the Disintegrated Melt Deposition (DMD) process. Energy absorption characteristics have been evaluated by experimental and numerical ballistic tests. It was noticed that 5% addition of lead in AZ31B increased the energy absorbing capacity and durability. Banichuk et al. (2013) mentioned that, most of the homogenous solid target plates failed by cone fracture. Jones et al. (2007) has conducted ballistic experiments on a rolled Mg plate and compared the observations with AA5083 targets. Jones et al. (2012) has proven that, Mg (AZ31B) will be a very good substitute armor material for AA5083 against armor piercing projectiles. Ben-Dor, Dubinsky, and Elperin (2006a) noticed superior ballistic resistance for monolithic target plates than composed thin target plates at equal thickness. Army research Laboratory (ARL) of US government has conducted several ballistic experiments and developed the first set of Mg alloy acceptance standards: MIL-DTL-32333 (MR). Ben-Dor, Dubinsky, and Elperin (2006b; 2010; and 2018) estimated the ballistic performance of the targets using the DOP value. The magnesium targets were thermally treated prior to ballistic experiments and the observations are limited to base metal only.

Many researchers (Padmanaban and Balasubramanian (2010), Sevvel and Jaiganesh (2014) have investigated the influencing factors affecting the mechanical properties of magnesium (AZ31B) FSW welded joints. However, the effect of PWHT on ballistic properties of magnesium -welded joints has not been investigated elaborately. Lack of work has been reported to determine the ballistic performance of friction-stir-welded magnesium joints. The primary objectives of this work are:

i. To determine the mechanical properties of AZ31B magnesium alloy (BM) and friction- stir -welded joints as per ASTM standards.
ii. To determine the optimum FSW process parameters, such as tool rotational speed (rpm) and welding speed (mm/min) for producing sound and defect-free joints with improved mechanical properties.
iii. To investigate the effect of PWHT on microhardness and microstructure of AZ31B friction -stir -welded joints.
iv. To determine the ballistic performance of BM, FSW and PWHT joints of AZ31B magnesium alloy targets using 7.62 mm Armor Piercing Projectiles (APP). In addition, the ballistic impact fracture behavior of FSW and PWHT targets will be investigated.

The objectives of the present work were achieved in three stages.

- In stage-1, the influence of FSW process parameters, namely, tool rotational speed (rpm) and welding speed (mm/min) on the mechanical properties (tensile strength, impact test and hardness) was carried out experimentally. This is to obtain the defect-free weld parameters.
- In stage-2, using the optimum parameters obtained in stage-1, sound and defect-free friction-stir-welded samples were prepared, and PWHT was carried out.
- In stage-3, ballistic performance of BM, FSW joints and PWHT joints were evaluated by impacting 7.62×39 mm APP, and fractographic examination was carried out using Scanning Electron Microscope (SEM).

2. Experimental procedure

2.1. Preparation of magnesium-welded joint by FSW process

The Base Metal (BM), as received for experiment, was magnesium alloy AZ31B which was 8 mm thick, fabricated using the Disintegrated Melt Deposition (DMD) technique. These plates were prepared by melting the magnesium alloy ingots at a temperature of 680 °C in an inert gas atmosphere in an electrical heating furnace. Further flat casted plate is configured to the required size

Table 1. Chemical composition (wt %) of AZ31B Magnesium alloy [J.W. Liu et al. (2014)].

Al	Mn	Zn	Mg
3.1	0.2	1	Bal

Table 2. Mechanical properties of AZ31B Magnesium alloy.

Yield strength (MPa)	Ultimate tensile strength (MPa)	Elongation (%)	Hardness at 0.1 kg load (Hv)	Impact energy (J)
149.5	213.679	18.285	66	6

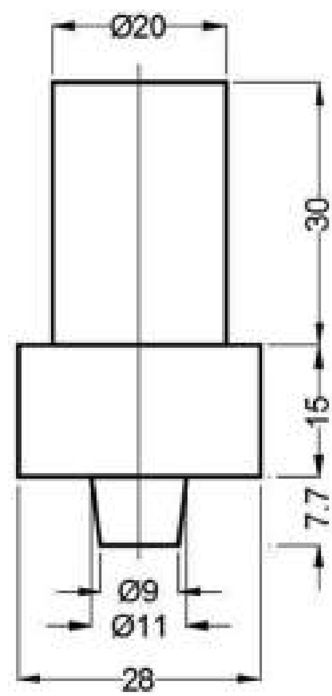

Figure 1. FSW tool dimensions.

Table 3. Details of FSW pin profile.

Sl.No	Tool parameters	Values
1	Tool material	Hot Work Tool Steel (H13) C,0.45; Cr, 5.5; Mn,0.5; Mo, 1.75
2	Tool shoulder diameter, D (mm)	28
3	Pin diameter, d (mm)	9
4	D/d ratio of tool	2.8
5	Pin length, L (mm)	7.7
6	Shoulder penetration inserted into the surface of base metal (mm)	0.2
7	Tool inclination angle (deg)	0

Table 4. Macrograph of joint cross section to fix the process parameter.

Sl. No	Welding parameter	Macrograph of joint cross section	Name of the defect / reasons
1	Tool Rotational speed less than 1000 rpm	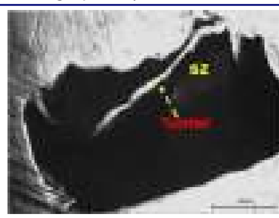	Tunnel : Insufficient heat input
2	Tool Rotational greater than 1400 rpm	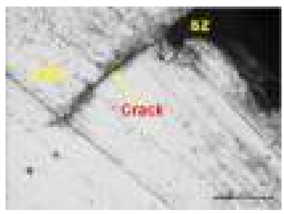	Tunnel and crack: Higher heat input
3	Welding speed less than 40 mm/min		Worm hole : Excessive heat input
4	Welding speed greater than 60 mm/min.		Tunnel : In sufficient heat input

of 100 mm × 50 mm using an abrasive cutting and vertical milling center. The chemical composition of the AZ31B Mg alloy is shown in Table 1.

Mechanical properties of the Mg alloy such as tensile strength, hardness and impact strength were determined by conducting the experiments as per ASTM standard and the values are listed in Table 2.

FSW tool was made of H13 steel with a tapered pin profile. This has a better joint efficiency and microstructure for AZ31B FSW welded joint compared to other profiles (Motalleb-Nejad

Figure 2. Macrograph image of defect free AZ31B FSW.

Table 5. Process parameters used for FSW.

Test No	Joint Designation	Tool Rotation Speed (rpm)	Welding speed (mm/min)
1	A	1000	40
2	B	1000	50
3	C	1000	60
4	D	1200	40
5	E	1200	50
6	F	1200	60
7	G	1400	40
8	H	1400	50
9	I	1400	60

Figure 3. Photographic view of nine FSW joints.

et al. (2014) and Shen, Wang, and Liu (2012). Figure 1 shows the tool dimensions and the properties of non-consumable taper pin are tabulated in Table 3.

An indigenously developed FSW machine [15 Hp; 3000 rpm; 30 KN] has been used for the fabrication of the FSW joints. The significance of the tool rotational speed and welding speed in determining the tensile strength and defect-free FSW joints are depicted in the published results (Fu et al. (2012) and Shen, Wang, and Liu (2012). To start with, FSW joints were fabricated by varying these process parameters to achieve defect-free welded joints.

Nine FSW trial runs were conducted to determine the working range of tool rotational speed, welding speed, and the specimens are extracted from each trial and it is subjected to macrostructure analysis. Table 4 shows the macroscopic joint defects noticed after different trial runs.

The following observations were made:

- A ‘worm hole’ defect was observed when the welding speed was less than 40 mm/min, and a ‘tunnel defect’ was experiential with a tool rotational speed lower than 1000 rpm.
- A crack and a few tunnel defects were observed when the tool rotational speed was more than 1400 rpm and a welding speed of more than 60 mm/min.

Reasonable process-parameter limits were selected to enable the preparation of FSW joints without any macro-level defects as shown in Figure 2.

Two parameters, each at three levels, were used for the fabrication of nine different joint designations. The process parameters considered for the FSW joints are listed in Table 5. Nine FSW joints were fabricated as shown in Figure 3.

Precisely nine macro-level defects-free FSW-welded joints of the AZ31B alloy were fabricated. Their tensile, and impact properties were examined by performing the tensile and Charpy impact tests as per the ASTM standards. Post weld heat treatment was done at a furnace with a temperature of 250 °C for about 1-hour duration. The effects of PWHT on the microstructures, hardness and ballistic properties of this FSW joint were investigated.

2.2. Ballistic test procedure of different targets

Ballistic impact experiments were performed on magnesium (AZ31B) BM, FSW joints and PWHT joints to determine the ballistic performance as per the Military standard of MIL-DTL-32333 (MR). Figure 4(a) illustrates the schematic arrangement of ballistic experimental setup and Figure 4(b) shows the photographic view of the ballistic testing machine.

Ballistic impact experiments were performed on FSW joints and PWHT joints by directing the projectile toward the stir zone (SZ) region. The target plates with a dimension of 8 mm thickness and $110 \times 110\,mm^2$ cross sections as front plates were held into the fixture. Aluminum plates (Al6062) with dimensions of 20 mm thickness and $75 \times 150\,mm^2$ cross sections were used as a backing plate. The front plate and Al6062 backing plate were clamped together rigidly with the help of holding clamps without any air gap. The ballistic impact resistance of different targets such as BM, FSW joints and PWHT joints were estimated by measuring the DOP of projectile into Al6062 backing plates. Armor piercing projectile (APP) of 7.62 mm × 39 mm with hard steel core (HSC) and a soft core of copper jacket were considered for the experiment. Photographs of the projectile before and after ballistic impact test are shown in Figure 5(a) and (b). The total mass of core was 7.85 g with the ball powder mass of 1.420 g. A projectile was fired from a gun barrel located at a distance of 10 m away from target plates at 0° degree angle of attack. An infrared light emitting diode was located between the gun barrel and the target area to measure the striking velocity of the projectile.

3. Results and discussion

3.1. Tensile properties of FSW joints

Nine macro level defects-free FSW-welded joints of the AZ31B alloy were fabricated and their tensile properties were examined by performing the tensile test as per the ASTM-E08 standard. Figure 6 shows the dimensions of tensile test specimens as per ASTM standard were machined at a right angle to FSW welding direction using a CNC milling machine.

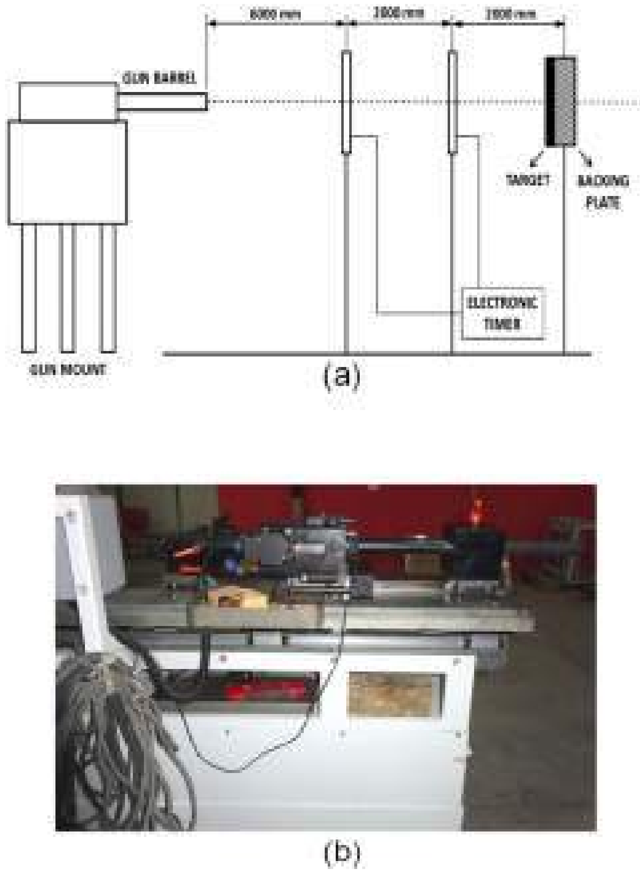

Figure 4. Ballistic Impact test set up. (a) Schematic arrangement of ballistic setup. (b) Photographic view of ballistic testing machine.

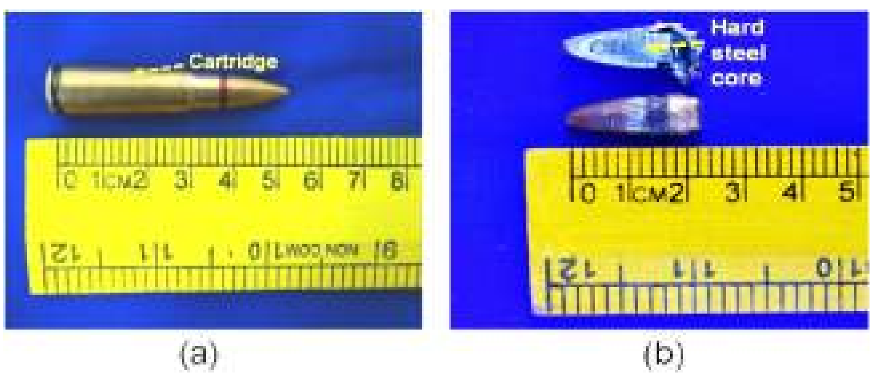

Figure 5. (a) Projectile with cartridge. (b) Projectile core.

Tensile testing was carried out by a universal testing machine of 100 KN capacity [Model: KIC-1-1000-C and Make: Kalpak, India], and its specimens are shown in Figure 7.

The specimen was loaded between the crossheads of the UTM subjected to a load of 100 KN with a strain rate of 10^{-4} s $^{-1}$ at a crosshead speed of 0.5 mm/min at room temperature. The stress-strain curves for FSW joints are shown in Figure 8(a). Yield strength, tensile strength and percentage of elongation was determined for BM and different designations of FSW joint. For

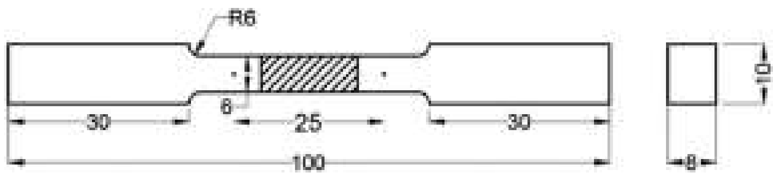

Figure 6. Dimensions of tensile test specimen.

Figure 7. Tensile specimens after tensile test.

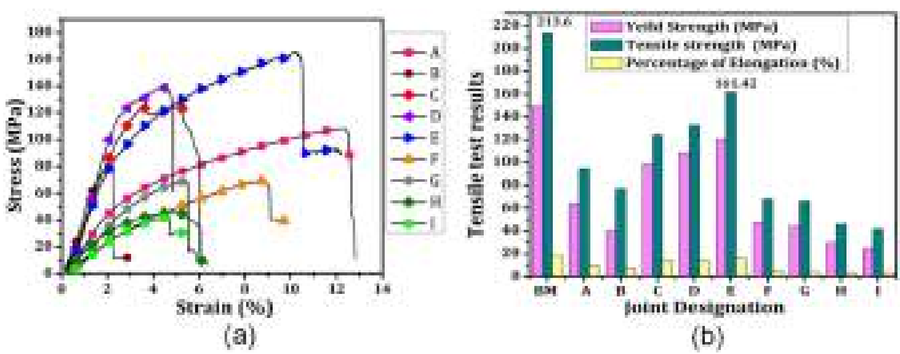

Figure 8. (a) Stress - Strain for FSW joints. (b) Tensile test results for various joint designations.

each joint designation, three specimens were tested. The average tensile results are shown in Figure 8(b).

Among the nine FSW joints, the joint which was fabricated with a tool rotational speed of 1200 rpm and the welding speed of 50 mm/min (Joint designation "E"), indicates a higher yield strength (120.5 MPa), tensile strength (161.42 MPa) and elongation (15.68%) .

The above combination of process parameters produces sufficient heat during welding, leading to a good homogeneous mixing of metal in the weld region and optimum material flow. The tensile properties of joints fabricated G (1400 rpm, 40 mm/min), H (1400 rpm, 50 mm/min) and I (1400 rpm, 60 mm/min) were 70% lower than the joint designation "E". When the tool rotational speed was increased from 1200 rpm to 1400 rpm, the heat generation within the SZ region also increases due to superior frictional heat which causes more thermal stresses at a slower cooling rate. These led to excessive grain growths, which subsequently reduces the tensile properties of the FSW joint. This result is in concurrence with that of Padmanaban and Balasubramanian (2010). Tensile fractures were observed in the SZ for the joint designations A, B, F, G, H and I and it was identified that the joint designations C, D and E fractured at the advancing side of Thermo Mechanically Affected Zone (TMAZ) and Heat Affected Zone (HAZ) regions which are shown in Figure 7. Mahmoud, Gaafer, and Khalifa (2008) and Rajakumar, Muralidharan, and Balasubramanian (2011) reported that in FSW, as the tool rotational speed increases, the heat input in the stirred zone also increased. The higher tool rotational speed resulted in higher temperature and this led to the movement of material to the top surface of the SZ region, which consequently produces microvoids in the SZ [Padmanaban and Balasubramanian (2010)] hence this, might be one of the reasons for joint designations G, H and I fractured at SZ .The joint designations A and B fractured in the SZ region due to lower tool rotational speed, which resultantly produces insufficient heat generation and inadequate metal filling in SZ which causes some internal defects in the weld joint. Similar results were observed in the work (Hassan et al. (2010) and Rajakumar, Muralidharan, and Balasubramanian (2011). The fracture occurred in the SZ region of F joint designation and this is due to higher welding speed compared to D and E. Thus, higher welding speed results faster cooling rate and insufficient heat input which might cause improper mixing of metal that produces insufficient bonding in the FSW joint. Singarapu, Adepu, and Arumalle (2015) reported an increase in welding speed decreases the tensile strength and percentage of elongation of FSW joint of AZ31B. The fracture for the joint designations C, D and E occurred at the advancing side of HAZ. The SZ which is closer to the advancing side experiences higher thermal effects. It also exhibits superior plastic deformation during the FSW process than on the retreating side. Hence, this results to the formation of coarse α-grains in the advancing side of HAZ, which eventually reduces the strength and lead to fracture. Similar observations were made by (Fu et al. (2012) and during tensile testing of Mg joints prepared by FSW process. Thus one expects joint fracture at the advancing side of HAZ. However, as mentioned earlier, the joint designation E (1200 rpm, 50 mm/min) shows the superior tensile strength compared to other joint designations. Hence the above observation indicates that an optimum combination of tool rotational speed and welding speed can influence the tensile properties of the joints.

3.2. Impact properties of AZ31B welded joints

Charpy Impact test was carried out using impact testing machine [Model: IT-30 and Make: FIE, India] at room temperature as per the ASTM-E23-04 standard. Specimens with V- notch at the middle region of weld metal were prepared as per the dimensions as shown in Figure 9.

The impact energy absorbed by each joint was compared with BM. Three experiments were conducted for each joint designation and the average values were plotted in Figure 10. The impact energy of FSW joints of AZ31B was found inferior to the BM. The highest impact energy was demonstrated by the joint fabricated, using joint designation of C, D and E which was 16% lower than the BM, but superior to all other FSW joint designations.

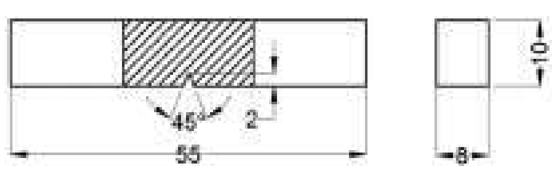

Figure 9. Dimensions of impact test specimen.

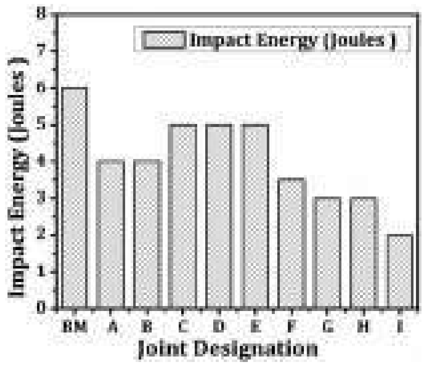

Figure 10. Effect of process parameters on impact test.

It was noted that there was a gradual decrease in the impact energy when rotational speed increases beyond 1200 rpm due to the effect of high heat input, which led to inappropriate thermal softening of material during FSW.

3.3. Microstructure studies on joints before and after PWHT

In order to understand the effect of PWHT, microstructure analysis of the BM, FSW and PWHT at different regions were examined using optical microscope [Model: SB-B1-1 and Make: Seiwa, Japan]. Before the metallographic investigation, the samples were sectioned and polished using different grit size of emery paper and finally polished with synthetic fiber cloth along with the diamond paste. The chemical etching was done using the solution containing (10 ml acetic acid (CH_3COOH), 5 ml picric acid ($C_6H_3N_3O_7$), 95 ml ethyl alcohol and 10 ml water). Figure 11(a) and (b) illustrates the micrographs taken at BM region of FSW and PWHT joints. BM region of FSW consists of non-uniform microstructure together with dendrites and the presence of intermetallic structure.

Figure 11(a) shows the microstructure consisting of primary α-Mg and the intermetallic phase of $Mg_{17}Al_{12}$ at grain boundaries. After the PWHT near the BM region, the majority of the intermetallic phase was dissolved and several halos were noticed in Figure 11(b). Energy Dispersive X-Ray Analysis (EDX) confirms the presence of Mg_{17} Al_{12} phase at particular region as shown in Figure 12.

A pattern of halos is caused by the diffusion of Al from the Mg_{17} Al_{12} intermetallic phase and supersaturated eutectic α-Mg to the surrounding primary α-Mg dendrites which are similar to the research reported in Wang, Liu, and Fan (2006; Wang et al. 2014). The SZ region of FSW joint showed in Figure 13(a) shows a more uniform microstructure as compared to the BM region. Fine-grained dynamically recrystallized structure observed in the SZ region and dendrites structure over region gets partially disappeared which due to a high-temperature effect was caused by stirring action of FSW tool. Other researchers [Richmire, Hall, and Haghshenas (2018b)] have also found related fine grains and disappeared dendrites structure in the SZ region of cast magnesium alloy FSW joint.

The SZ region of PWHT Figure 13(b) reveals much fine and equiaxed α-Mg grains compared to non-heat treated FSW joints. The average grain sizes of the SZ region –FSW were 38 µm and 12 µm at the lowest in the SZ region of the PWHT. The SEM morphology of the PWHT SZ region shown in Figure 14(a) illustrates that a few precipitations were observed at the grain boundary. The prime reason for the resemblance between the structure of the PWHT–SZ region and that of FSW–SZ region is due to heat treatment followed by cooling in the furnace. HAZ

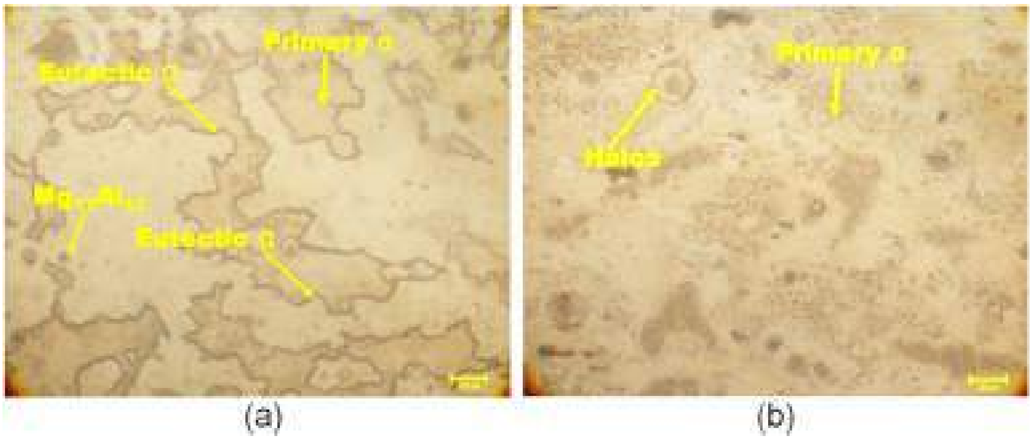

Figure 11. Optical micrographs. (a) BM-FSW. (b) BM-PWHT.

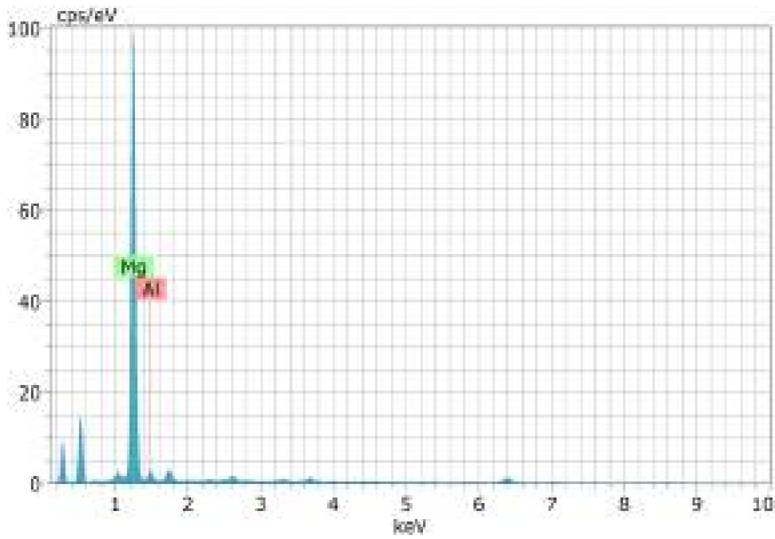

Figure 12. EDX results for Mg_{17} Al_{12} phase.

without heat-treated condition shows the coarse α-Mg and thin eutectic structure which is illustrated in Figure 13(c); however, this is because of insufficient thermal cycle and absence of plastic deformation caused by the FSW tool. This is the one of the reason of fracture observed at the FSW-HAZ region during the tensile test. Figure 13(d) shows a substantial presence of $Mg_{17}Al_{12}$ and thick eutectic structure compared to HAZ without heat-treated condition.

The average grain sizes of the HAZ region –FSW were 68 µm and 48 µm at the lowest in the HAZ region of PWHT. It was observed in the SEM image as shown in Figure 14(b), quite discontinuous precipitates near the grain boundaries. The fact that the formation of precipitates after heat-treatment slightly increases the hardness value of the SZ region compared to BM in the present study and it is in agreement with the results of [Wang et al. (2017)] whose analysis concluded that heat treatment technique improves the hardness value of AZ31B FSW joint.

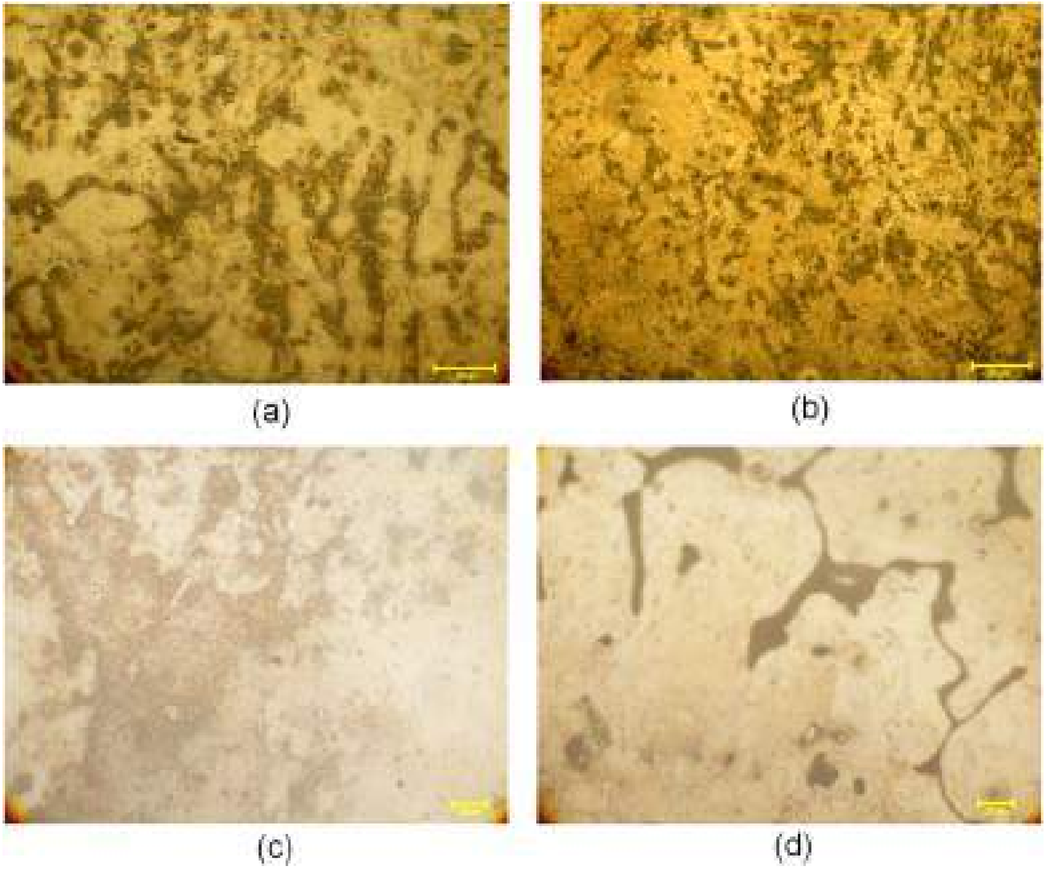

Figure 13. Optical micrographs at various regions of the welded joints. (a) SZ-FSW. (b) SZ-PWHT. (c) HAZ -FSW. (d) HAZ -PWHT.

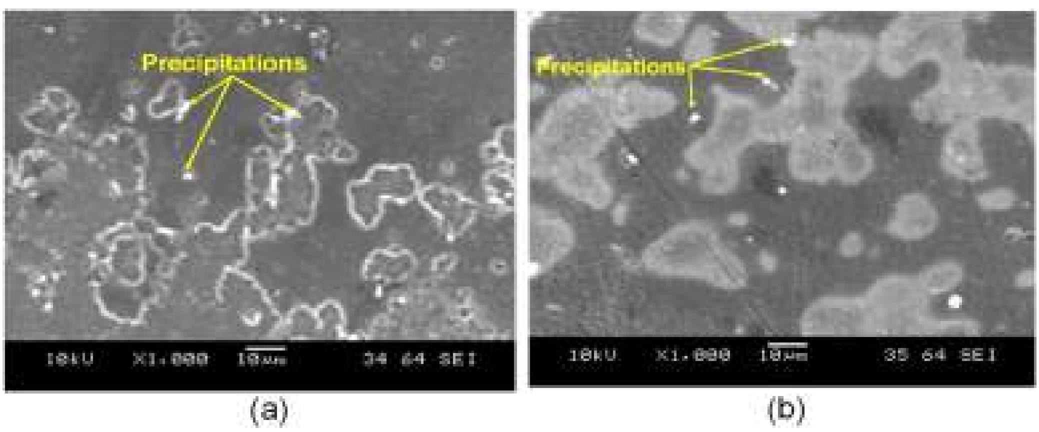

Figure 14. SEM micrographs. (a) SZ-PWHT. (b) HAZ-PWHT.

3.4. Effect of PWHT on microhardness of joints

Microhardness measurement was taken using a Vickers hardness testing machine [Model: MMT-3 and Make: Matsuzawa, Japan] as per ASTM-E-384-05 standard. Indentation load of 100 g and dwell-time of 15 s were used. The specimen had a cross-section along the transverse direction.

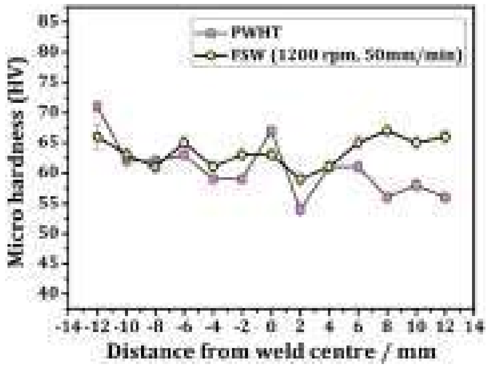

Figure 15. Microhardness variations of FSW and PWHT samples.

Hardness reading was taken at regular intervals of 2 mm on both sides of the weld. Three set of values were taken at each distance and an average results with error of the FSW and PWHT joints is shown in Figure 15. SZ of FSW joint and PWHT joint shows a considerable hardness variations, compared to the BM. Microhardness for the FSW and PWHT joints shows a decreasing trend in the TMAZ region and also a drop at the HAZ region on both sides of the joints.

The least hardness value was observed at the HAZ – non post weld heat treated FSW region, which is due to the presence of coarse α-Mg illustrated in Figure 13(c). The hardness values for PWHT condition (67 HV) is higher than non-heat treated FSW joint (63 HV). The improved hardness in the PWHT –SZ region is attributed to the formation of precipitates and fine grain structure illustrated in Figure 13(b).

The annealing effect on HAZ –PWHT had little influence on the formation of recrystallized grain size of 48 µm which is smaller compared to HAZ-FSW. The HAZ region of PWHT shows a little difference in contrast with the HAZ region of FSW hardness. The investigation confirms an improvement in hardness at SZ due to PWHT.

3.5. Ballistic results

Ballistic impact test were performed on magnesium (AZ31B) BM, FSW and PWHT joints in two stages. In stage 1, ballistic impact test of BM was conducted at three different velocities 368 ± 10 m/s (low velocity), 456 ± 10 m/s (medium velocity) and 597 ± 10 m/s (high velocity) that are referred to as S01, S02 and S03 for each target at least two test were performed as shown in Figure 16. For each projectile impact, DOP was measured on a 20 mm thick Al6062 backing plate placed behind the target.

In stage 2, the ballistic impact test of AZ31B FSW joints and PWHT joints were carried out with a striking velocity of 456 ± 10 m/s. The FSW joints were prepared from the suitable process parameter (1200 rpm, 50 mm/min) as the common designation "E". These FSW joints were defect-free and showed excellent mechanical properties. These joints were subjected to PWHT process, followed by ballistic impact test. To determine the DOP value, seven shots were made on the FSW and PWHT targets. Among these seven shots, three for FSW (S04, S05 and S06) joints and the other four shots for PWHT (S07, S08, S09 and S10) joints were performed.

3.5.1. Mechanisms in ballistic impacted AZ31B magnesium targets

Figure 17(a)–(c) illustrate the front face of BM targets namely, S01, S02 and S03, which was subjected to projectile impact. The initial impact of the projectile caused failure of S01 and S02 targets. A crack was noticed around the crater region at the front side of S01, which led to a shift in the projectile on the target.

Figure 16. Ballistic test of AZ31B base metal with three different velocities.

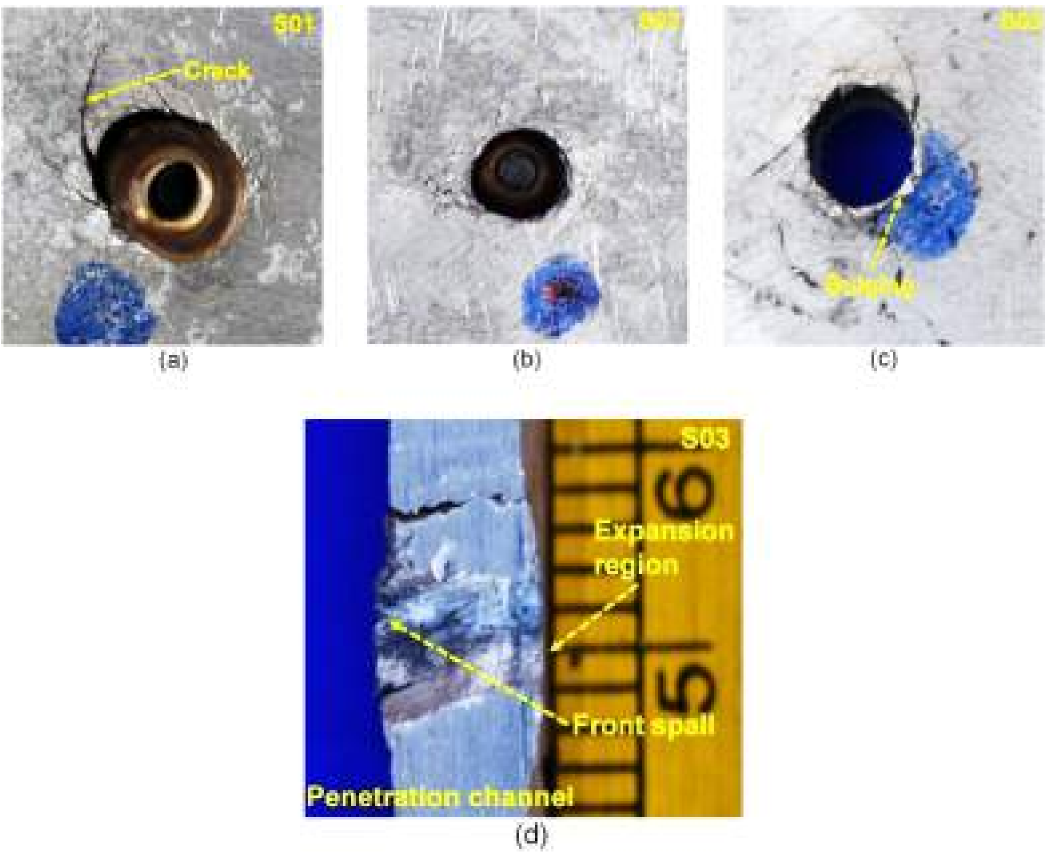

Figure 17. Front face penetration channel of AZ31B plates after ballistic test. (a) S01 plate. (b) S02 plate. (c) S03 plate. (d) S03plate penetration channel.

The above phenomenon occurred due to the higher value of initial stress rather than the ultimate strength of the material. A bulge occurred on the front face of the S03 target after the formation of the hole during the penetration of projectile. There was a failure due to ductile hole enlargement. The cross-section of the S03 penetration channel is shown in Figure 17(d). When the striking velocity was increased from 368 m/s to 597 m/s, changes in the mode of failure were observed.

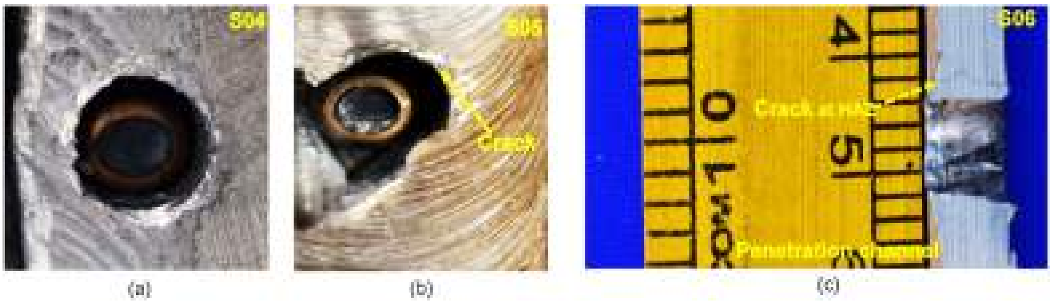

Figure 18. Front face penetration channel of FSW joints after ballistic test. (a) S04 plate. (b) S05 plate. (c) S06 plate penetration channel.

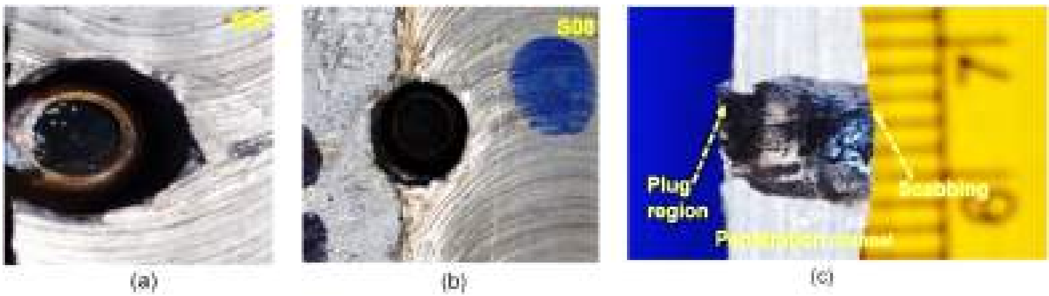

Figure 19. Front face penetration channel of PWHT joints after ballistic test. (a) S07 plate. (b) S08 plate. (c) S08 plate penetration channel.

Figure 18(a)–(c) shows the front face and penetration channel of FSW-welded targets S04, S05 and S06 which were subjected to the projectile impact velocity of 456 ± 10 m/s. The mechanism of failure in the front face was observed as a ductile hole enlargement in the S04 target.

The mechanism of failure changed from ductile hole enlargement with a little amount of spalling in the front face of the S05 target. A crack formed near the TMAZ zone and the projectile penetration shifted away from the SZ region due to the non-uniform hardness of the welded joint. Figure 18(c) shows the penetration of the projectile into the S06 target along the direction of thickness. Ballistic failure mechanism observed was plugging in addition to a limited ductile failure. The occurrence of plugging failure could be due to higher shear stress developed around the hole region. Similarly, the occurrence of a ductile failure at the exit region was due to a minor decrease in hardness along the thickness direction.

Figure 19(a) and (b) shows the front portion of the projectile penetrated region of PWHT targets of S07 and S08. Penetration channel of the S08 PWHT target is shown in Figure 19c. Combined modes, such as plugging and scabbing, were observed in these targets.

Plugging was observed at the entry stage of the projectile due to the variations in shear stress produced around the SZ region. "Scabbing" appeared at the exit region of a target. The formation of fracture produced by deformation was the result of a decrease in hardness as the ballistic resistance depends upon the hardness of the target (Balakrishnan, Balasubramanian, and Madhusudhan Reddy (2013a); Erdem et al. (2016); and Iqbal et al. (2017).

DOP of the projectile into the target and back plate was measured using a digital probe type height gauge [Model: Digimar 814 SR and Make: Mahr, Germany]. Projectile penetrated backing plates were sectioned using a band hacksaw machine and images were taken along the penetration channels for various conditions which are shown in Figure 20.

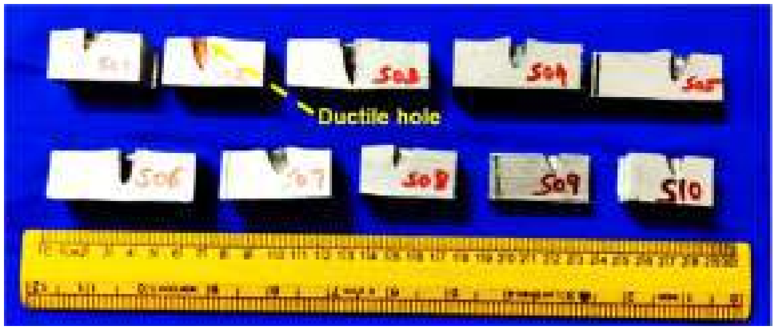

Figure 20. Penetration channel in Al6062 backing plate.

Table 6. Ballistic impact results of different targets.

Sl.No	Type of Target	Shot No	Velocity (m/s)	Depth of penetration (DOP) in mm
1	BM	S01	368	8.39
2		S02	456	13.56
3		S03	597	18.30
4	FSW	S04	448	11.19
5		S05	454	12.87
6		S06	456	13.36
7	PWHT	S07	452	10.15
8		S08	456	11.18
9		S09	454	10.10
10		S10	456	11.12

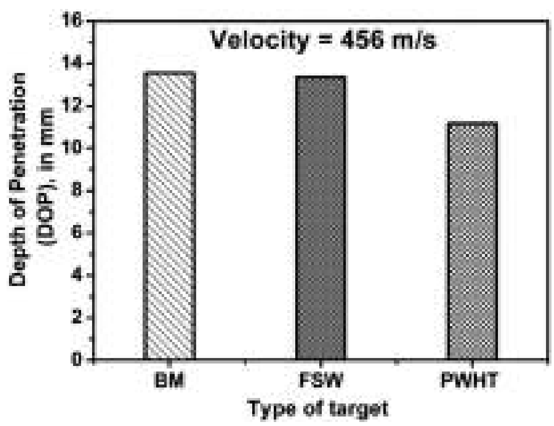

Figure 21. Comparison of DOP of various Targets.

Table 6 provides a summary of the experimental ballistics results for different types of targets, and the striking velocity. Different trials were attempted for a particular projectile velocity in order to ensure the repeatability of experimental results.

DOP measurement indicates better ballistic resistance of PWHT targets compared to FSW and BM targets. DOP values of the PWHT target were 17.55% and 16.31% lower than BM and FSW targets as shown in Figure 21. The superior performance could be due to the formation of thermal gradients during the annealing process. During the FSW process, the stirring action of the tool causes flow stress which reduces the thermal softening of the material.

Microstructure of PWHT-SZ depicts the formation of fine grains with a hardness of 67HV, when compared to non-post heat treated FSW stir zone of 63HV hardness. Improved hardness near the PWHT-SZ absorbs ballistic impact caused by the projectile and hence there was less DOP value when compared to FSW and BM targets. The annealing process of the weld region

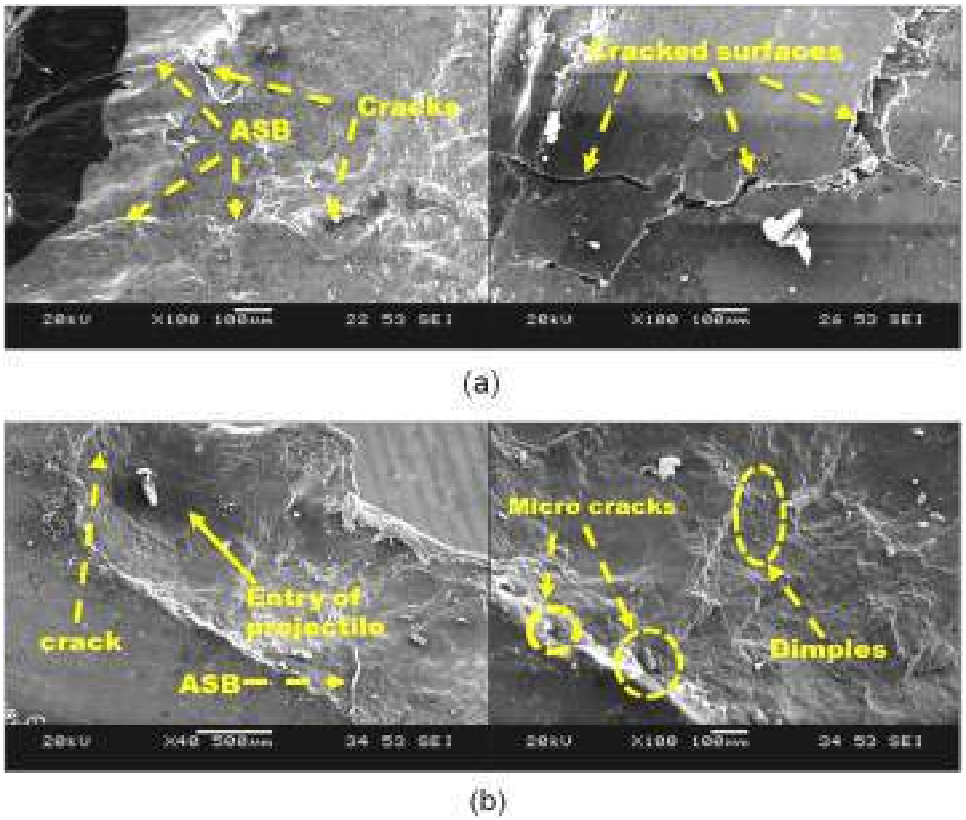

Figure 22. Fractographs of fracture surface after ballistic test of striking velocity 456 m/s. (a) FSW crater surface. (b) PWHT crater surface.

increases the hardness and formation of small precipitates when compared to non-heat treated welded plates. The improved hardness value and precipitates offer resistance against projectile penetration of the PWHT targets and thus reduces the DOP value.

The ballistic testing of PWHT targets indicates that ductile hole growth dominates in most of the targets. Hardness and ductility of the material have been the causes of this type of failure on targets (Erdem et al. 2016). Fragmentation type of failure was not observed in all three conditions of AZ31B magnesium alloy, leading to the conclusion that a solid-state welding process does not affect the ballistic performance of the FSW joints. In the case of FSW joints, the DOP value of the welded joints was slightly lower than BM. Improved ballistic resistance was observed for PWHT targets, when compared to BM and FSW targets. A fractographic analysis was carried out to understand the fracture behavior of each target.

3.6. Fractographic analysis of ballistic fractured surface

The fractographic analysis of the projectile-penetrated regions was carried out using a Scanning Electron Microscope (SEM) [Model: Sigma 300 and Make: Zeiss, Germany]. Figure 22(a) and (b) depicts the SEM fractographs captured at the middle region of the penetration channel of FSW weld region and PWHT target plates. FSW and PWHT target plates indicates the combined failure modes of ductile and shear fracture. A large number of adiabatic shear bands (ASBs) was observed at the FSW crater region, compared to PWHT surface which results in a decrease in ballistic performance.

Plugging mode failure of FSW target was due to the effect of considerable shear stress developed around the penetration region. The presence of ASBs was observed near the tensile opening region.

The presence of small dimples along the penetration channel of the PWHT target indicates that penetration process assisted by ductile hole enlargement could be the reason for the decrease in the DOP value. At a magnification of 100 μm, non-propagating microcracks were observed at two locations of the PWHT target penetration channel. In FSW target, both crack nucleation and propagation region were noticed in Figure 22(a). The results confirmed the capability of the PWHT stir zone to absorb the projectile impact energy with the formation of minimum ASBs which, in turn, resulted in a less number of microcracks. The present fracture results showed a good correlation with the observations of published results (Erdem et al. (2016); Sullivan et al. (2011); and Sukumar et al. (2013).

4. Conclusions

Experimental investigations on the consequence of FSW process parameters and PWHT on ballistic resistance of magnesium -welded joints was carried out. The present attempt is aimed to understand the suitability of magnesium plates, and welded joints for possible lightweight defense vehicle construction, and the following observations were made from the results.

1. Macro-level defect-free magnesium FSW joint was obtained using a taper pin profile tool. The tool rotational speed of 1000, 1200, 1400 rpm and the welding speed of 40, 50, 60 mm/min were considered primarily. Tool rotational speed of 1200 rpm and a welding speed of 50 mm/min showed a highest joint tensile strength (161.42 MPa) with impact energy (5J).
2. The microhardness of PWHT was improved when compare to FSW joints, which is due to annealing effect.
3. Among the BM, FSW and PWHT joints tested, PWHT joints offers maximum ballistic resistance with less depth of penetration and without any fragmentation mode of failure. The DOP of PWHT plate was observed to be 17.55% and 16.31%, which was lower than that of BM and FSW plates.
4. During the projectile impact, crack formation was observed at the HAZ of a friction-stir welded plate as the result of variations in hardness distribution. It was also prominent that the friction between the projectile and target and hardness played a vital role in ballistic resistance of the targets.
5. Post-ballistic fractographic investigation of the fracture surface showed the formation of ASBs, micro cracks and macro cracks in the PWHT and FSW target plates respectively. The PWHT target exhibited less number of ASBs lines and micro cracks when compared to the FSW target. The experimental observations indicate that magnesium AZ31B can be a suitable alternative material for developing lightweight defense vehicles.

ORCID

Suresh Kumar Sundaram http://orcid.org/0000-0001-6557-2016

References

Abdullah, M. F., S. Abdullah, M. Z. Omar, Z. Sajuri, and R. M. Sohaimi. 2015. Failure observation of the AZ31B magnesium alloy and the effect of lead addition content under ballistic impact. *Advances in Mechanical Engineering* 7 (5):168781401558542. doi:10.1177/1687814015585428.

Balakrishnan, M., V. Balasubramanian, and G. Madhusudhan Reddy. 2013a. Microstructural analysis of ballistic tests on welded armor steel joints. *Metallography, Microstructure, and Analysis* 2 (3):125–39. doi:10.1007/s13632-013-0069-5.

Balakrishnan, M., V. Balasubramanian, and G. Madhusudhan Reddy. 2013b. Effect of hardfacing consumables on ballistic performance of Q&T steel joints. *Defence Technology* 9 (4):249–58. doi:10.1016/j.dt.2013.12.007.

Banichuk, N. V., S. Y. Ivanova, F. Ragnedda, and M. Serra. 2013. An Multiobjective approach for optimal design of layered plates against penetration of strikers. *Mechanics Based Design of Structures and Machines* 41 (2): 189–201. doi:10.1080/15397734.2012.717868.

Ben-Dor, G., A. Dubinsky, and T. Elperin. 2006a. Effect of the order of plates on the ballistic resistance of ductile layered shields perforated by nonconical impactors. *Journal of Mechanics of Materials and Structures* 1 (7): 1161–77. : doi:10.2140/jomms.2006.1.1161.

Ben-Dor, G., A. Dubinsky, and T. Elperin. 2006b. Modeling of high-speed penetration into concrete shields and shape optimization of impactors. *Mechanics Based Design of Structures and Machines* 34 (2):139–56. doi:10.1080/15397730600663398.

Ben-Dor, G., A. Dubinsky, and T. Elperin. 2010. Some inverse problems in penetration mechanics. *Mechanics Based Design of Structures and Machines* 38 (4):468–80. doi:10.1080/15397734.2010.501274.

Ben-Dor, G., A. Dubinsky, and T. Elperin. 2018. Optimization of ballistic properties of layered ceramic armor with a ductile back plate. *Mechanics Based Design of Structures and Machines* 46 (1):18–22. doi:10.1080/15397734.2016.1261035.

Munoz, A., G. Rücker, B. Huneau, X. Sauvage, and S. Marya. 2008. Comparison of TIG Welded and Friction Stir Welded Al-4.5Mg-0.26Sc alloy. *Journal of Materials Processing Technology* 197 (1-3):337–43. doi:10.1016/j.jmatprotec.2007.06.035.

Erdem, M., H. Cinici, U. Gokmen, H. Karakoc, and M. Turker. 2016. Mechanical and ballistic properties of powder metal 7039 aluminium alloy joined by friction stir welding. *Transactions of Nonferrous Metals Society of China* 26 (1):74–84. doi:10.1016/S1003-6326(16)64090-6.

Fu, R. D., H. S. Ji, Y. J. Li, and L. Liu. 2012. Effect of weld conditions on microstructures and mechanical properties of friction stir welded joints on AZ31B magnesium alloys. *Science and Technology of Welding and Joining* 17 (3):174–9. doi:10.1179/1362171811Y.0000000056.

Fukumoto, S., D. Yamamoto, T. Tomita, K. Okita, H. Tsubakino, and A. Yamamoto. 2007. Effect of post weld heat treatment on microstructures and mechanical properties of AZ31B Friction Welded Joint. *Materials Transactions* 48 (1):44–52. doi:10.2320/matertrans.48.44.

Guo, W., K. Wang, W. Wang, W. Feng, and W. Wenli. 2009. Effect of heat treatment on microstructure and microhardness of friction stir-welded joints for AZ31B magnesium alloy. *Materials for Mechanical Engineering* 10:33–36.

Guo, W., K. Wang, W. Wang, W. Feng, and W. Wenli. 2011. Influences of Post-weld Heat Treatments on friction stir-welded AZ31B magnesium alloy joints. *Rare Metal Materials and Engineering* 40 (6):1075–8.

Hassan, A. S., T. S. Mahmoud, F. H. Mahmoud, and T. A. Khalifa. 2010. Friction Stir welding of dissimilar A319 and A356 aluminium cast alloys. *Science and Technology of Welding and Joining* 15 (5):414–22. doi:10.1179/136217110X12720264008358.

Holmen, J. K., T. Børvik, O. R. Myhr, H. G. Fjaer, and O. S. Hopperstad. 2015. Perforation of welded aluminum components: Microstructure-based modeling and experimental validation. *International Journal of Impact Engineering* 84:96–107. doi:10.1016/j.ijimpeng.2015.05.016.

Ilangovan, M., S. Rajendra Boopathy, and V. Balasubramanian. 2015. Effect of tool pin profile on microstructure and tensile properties of friction stir welded dissimilar AA 6061-AA 5086 aluminium alloy joints. *Defence Technology* 11 (2):174–84. doi:10.1016/j.dt.2015.01.004.

Iqbal, M. A., K. Senthil, V. Madhu, and N. K. Gupta. 2017. Oblique impact on single layered and spaced mild steel targets by 7.62 AP projectiles. *International Journal of Impact Engineering* 110:26–38. doi:10.1016/j.ijimpeng.2017.04.011.

Jannet, S., P. K. Mathews, and R. Raja. 2014. Comparative investigation of friction stir welding and fusion welding of 6061-T6 and 5083-O aluminum alloy based on mechanical properties and microstructure. *Bulletin of the Polish Academy of Sciences Technical Sciences* 62 (4):791–5. doi:10.2478/bpasts-2014-0086.

Jones, T. L., R. D. DeLorme, M. S. Burkins, and W. A. Gooch. 2007. *Ballistic evaluation of magnesium alloy AZ31B. ARL-TR-4077*. Army Research Laboratory (US).

Jones, T. L., and R. D. DeLorme. 2008. Development of a ballistic specification for magnesium alloy AZ31B. ARL-TR-4664. Army Research Lab Aberdeen Proving Ground MD Weapons and Materials Research Directorate.

Jones, T. L., J. Labukas, B. Placzankis, and K. Kondoh. 2012. Ballistic and corrosion analysis of new military-grade magnesium alloys AMX602 and ZAXE1711 for armor applications. ARL-TR-5931. Army Research Lab Aberdeen Proving Ground MD Weapons and Materials Research Directorate.

Liu, L., and C. Dong. 2006. Gas Tungsten-Arc filler welding of AZ31 magnesium Alloy. *Materials Letters* 60 (17–18):2194–7. doi:10.1016/j.matlet.2005.12.120.

Lee, W. B., J. W. Kim, Y. M. Yeon, and S. B. Jung. 2003. The joint characteristics of friction stir welded AZ91D magnesium alloy. *Materials Transactions* 44 (5):917–23. doi:10.2320/matertrans.44.917.

Liu, J. W., X. D. Peng, D. S. Chen, H. Y. Yi, and Y. Q. Yu. 2014. Microstructure and mechanical properties of centrifugal casting of AZ31B magnesium alloy ring. *Materials Research Innovations* 18 (sup4):S4-169–72. doi:10.1179/1432891714Z.000000000675.

Lockyer, S. A., and M. J. Russell. 2000. Mechanical Properties of friction stir welds in magnesium alloys. Paper presented at International Conference on Magnesium Alloys and their Applications, Germany, September.

Mahmoud, T. S., A. M. Gaafer, and T. A. Khalifa. 2008. Effect of tool rotational and welding speeds on microstructural and mechanical characteristics of friction stir welded A319 cast Al alloy. *Materials Science and Technology* 24 (5):553–9. doi:10.1179/174328408X294116.

Mathaudhu, S. N., and E. Nyberg. 2010. Magnesium alloys in U.S. military applications: Past, current and future solutions. In S. N. Mathaudhu, A. A. Luo, N. R. Neelameggham, E. A. Nyberg, W. H. Sillekens (Eds.), *Essential readings in magnesium technology* (pp. 71–6). Springer.

Min, D., J. Shen, S. Lai, and J. Chen. 2009. Effect of heat input on the microstructure and mechanical properties of tungsten inert gas arc butt-welded AZ61 magnesium alloy plates. *Materials Characterization* 60 (12):1583–90. doi:10.1016/j.matchar.2009.09.010.

Motalleb-Nejad, P., T. Saeid, A. Heidarzadeh, K. Darzi, and M. Ashjari. 2014. Effect of tool pin profile on microstructure and mechanical properties of friction stir welded AZ31B magnesium alloy. *Materials & Design* 59: 221–6. doi:10.1016/j.matdes.2014.02.068.

Padmanaban, G., and V. Balasubramanian. 2010. Prediction of tensile strength and optimization of process parameters for friction stir welded AZ31B magnesium alloy. *Proceedings of the Institution of Mechanical Engineers, Part B: Journal of Engineering Manufacture* 224 (10):1519–28. doi:10.1243/09544054JEM1667.

Padmanaban, G., V. Balasubramanian, and G. M. Reddy. 2011. Fatigue crack growth behaviour of pulsed current gas tungsten arc, friction stir and laser beam welded AZ31B magnesium alloy joints. *Journal of Materials Processing Technology* 211 (7):1224–33. doi:10.1016/j.jmatprotec.2011.02.003.

Rajakumar, S., C. Muralidharan, and V. Balasubramanian. 2011. Influence of friction stir welding process and tool parameters on strength properties of AA7075-T 6 aluminium alloy joints. *Materials & Design* 32 (2):535–49. doi:10.1016/j.matdes.2010.08.025.

Richmire, S., P. Sharifi, and M. Haghshenas. 2018a. On microstructure, hardness, and fatigue properties of friction stir-welded AM60 cast magnesium alloy. *The International Journal of Advanced Manufacturing Technology* 98 (5–8):2157–72. doi:10.1007/s00170-018-2375-1.

Richmire, S., K. Hall, and M. Haghshenas. 2018b. Design of experiment study on hardness variations in friction stir welding of AM60 Mg Alloy. *Journal of Magnesium and Alloys* 6 (3):215–28. doi:10.1016/j.jma.2018.07.002.

Sevvel, P., and V. Jaiganesh. 2014. Characterization of mechanical properties and microstructural analysis of friction stir welded AZ31B Mg alloy thorough optimized process parameters. *Procedia Engineering* 97:741–51. doi:10.1016/j.proeng.2014.12.304.

Singarapu, U., K. Adepu, and S. R. Arumalle. 2015. Influence of tool material and rotational speed on mechanical properties of friction stir welded AZ31B magnesium alloy. *Journal of Magnesium and Alloys* 3 (4):335–44. doi:10.1016/j.jma.2015.10.001.

Shen, J., D. Wang, and K. Liu. 2012. Effects of pin diameter on microstructures and mechanical properties of friction stir spot welded AZ31B magnesium alloy joints. *Science and Technology of Welding and Joining* 17 (5): 357–63. doi:10.1179/136217112X13333824902125.

Sullivan, A., C. Derry, J. D. Robson, I. Horsfall, and P. B. Prangnell. 2011. Microstructure simulation and ballistic behaviour of weld zones in friction stir welds in high strength aluminium 7xxx plate. *Materials Science and Engineering: A* 528 (9):3409–22. doi:10.1016/j.msea.2011.01.019.

Sukumar, G., B. B. Singh, A. Bhattacharjee, K. S. Kumar, and A. K. Gogia. 2013. Ballistic impact behaviour of β-CEZ Ti alloy against 7.62 mm armour piercing projectiles. *International Journal of Impact Engineering* 54: 149–60. doi:10.1016/j.ijimpeng.2012.11.002.

Thompson, B., K. Doherty, C. Niese, M. Eff, T. Stotler, Z. Pramann, J. Seaman, R. Spencer, and P. White. 2012. Friction stir welding of thick section aluminium for military vehicle. ARL-RP-417. Army Research Lab Aberdeen Proving Ground MD Weapons and Materials Research Directorate.

Wang, Y., G. Liu, and Z. Fan. 2006. Microstructural evolution of rheo-diecast AZ91D magnesium alloy during heat treatment. *Acta Materialia* 54 (3):689–99. doi:10.1016/j.actamat.2005.09.033.

Wang, X. J., S. M. Zhu, M. A. Easton, M. A. Gibson, and G. Savage. 2014. Heat treatment of vacuum high pressure die cast magnesium alloy AZ91. *International Journal of Cast Metals Research* 27 (3):161–6. doi:10.1179/1743133613Y.0000000091.

Wang, G., Z. Yan, H. Zhang, X. Zhang, F. Liu, X. Wang, and Y. Su. 2017. Improved properties of friction stir-welded AZ31 magnesium alloy by post-weld heat treatment. *Materials Science and Technology* 33 (7):854–63. doi:10.1080/02670836.2016.1243356.

Zhao, J., F. Jiang, H. Jian, K. Wen, L. Jiang, and X. Chen. 2010. Comparative investigation of tungsten inert gas and friction stir welding characteristics of Al–Mg–Sc alloy plates. *Materials and Design* 31 (1):306–11. doi:10.1016/j.matdes.2009.06.012.

Available online at www.sciencedirect.com
ScienceDirect
Trans. Nonferrous Met. Soc. China 31(2021) 156−166
Transactions of Nonferrous Metals Society of China
www.tnmsc.cn

Effect of heat treatment conditions on ballistic behaviour of various zones of friction stir welded magnesium alloy joints

S. DHARANI KUMAR[1], S. SURESH KUMAR[2]

1. Department of Mechanical Engineering, Sri Eshwar College of Engineering, Coimbatore, 641202, Tamil Nadu, India;
2. Department of Mechanical Engineering, Sri Sivasubramaniya Nadar College of Engineering, Chennai, 603110, Tamil Nadu, India

Received 19 March 2020; accepted 28 September 2020

Abstract: Ballistic behaviour of different zones of post-weld heat-treated (PWHT) magnesium alloy (AZ31B) target against 7.62 mm × 39 mm armour-piercing (AP) projectile with a striking velocity of (430±20) m/s was determined. Magnesium alloy (AZ31B) welded joints were prepared by using friction stir welding (FSW) process and subjected to different heat treatment conditions. The microhardness values of non-heat-treated and heat-treated FSW joints were investigated. The results indicated that PWHT process (250 °C, 1 h) has improved the microhardness of heat-treated FSW joints. Scanning electron microscope (SEM) microstructure showed that heat treatment has caused the formation of fine α-Mg grains and tiny precipitates and made the dissolution of β-$Mg_{17}Al_{12}$ phase into the Mg matrix. The ballistic behaviour of PWHT zones was estimated by measuring the depth of penetration (DOP) of the projectile. Lower DOP value was observed for the base metal zone (BMZ) of a heat-treated welded joint. Post ballistic SEM examinations on the cross-section of all three zones of crater region showed the formation of adiabatic shear band (ASB).

Key words: AZ31B magnesium alloy; post-weld heat treatment; ballistic behaviour; penetration depth; adiabatic shear band

1 Introduction

In recent years many researchers have tried to use magnesium alloys for defence applications due to their better damping capability and lower density when compared to the steels and aluminium alloys. Mg alloys have been used in the defence tankers and defence aircrafts to decrease the mass and increase the fuel efficiency of the vehicle used in defence applications [1]. ABDULLAH et al [2] studied the ballistic resistance of cast AZ31B Mg alloy plates produced by disintegrated melt deposition (DMD) technique and reported that the addition of lead as reinforcement enhances the ballistic resistance. In the fabrication of defence tankers and vehicles structures, inevitably, there is a need of permanent and temporary joints. However, knowledge and selection of joint are most essential in the design of defence vehicle's structures against the ballistic impact loads. The most common permanent joining technique is welding. Still, welding of magnesium is quite tricky, owing to its less surface tension and vapour pressure. However, traditional fusion welding techniques are not suitable for cast AZ31B Mg alloys due to the formation of solidification cracking, embrittlement and porosity in the weld zone [3,4]. The heat input during fusion welding process is higher compared to that during FSW [5]. THOMPSON et al [6] observed that the ballisitc limit of FSW 2xxx and 5xxx series of aluminium alloy joints is superior to that of gas metal arc welding (GMAW) aluminium alloy joints against the impact of armour-piercing (AP) projectile.

Generally, FSW is the most promising solid-

Corresponding author: S. SURESH KUMAR; E-mail: sureshkumars@ssn.edu.in
DOI: 10.1016/S1003-6326(20)65484-X

state welding technique in which no melting occurs in the base metal (BM) and width of the heat affected zone (HAZ) is less. In the FSW process, a non-consumable tool will produce frictional heat combined with plastic deformation in the nugget zone (NZ) of FSW joint. FSW is being increasingly used in tanks and military vehicle applications [7]. SULLIVAN and ROBSON [8] determined the ballistic behaviour of thick AA7010-T7651 plates joined by FSW process and noticed that the loss of hardness in the HAZ region results in 20% reduction in ballistic limit. In addition, they found a linear correlation between hardness and ballistic performance. ERDEM et al [9] determined the hardness, microstructure and ballistic performances of friction stir welded 7039 aluminium alloy plates of different zones of NZ, HAZ and BMZ. The ballistic limits of the NZ and HAZ are observed to be lower than that of BMZ. HOLMEN et al [10] studied the metal inert gas (MIG) welded AA6082-T6 alloy plates against 7.62 mm AP projectile to determine the ballistic behaviour of different weld zones. It was observed that ballistic limit of the base metal was higher than that of other weld zones and the least ballistic limit occurs in the HAZ. JHA et al [11] determined the ballistic limit of aluminium 2219 alloy plates with 6.4 and 7.8 mm in thickness joined by tungsten inert gas (TIG) welding. They observed the formation of adiabatic shear band (ASB) which caused the separation of surfaces and resulted in solidified debris on the fracture surfaces.

It is important to study the ballistic failure mechanisms and damage fracture surface of targets after the ballistic impact test. A few ballistic fracture studies have been done on various ferrous [12] and non-ferrous alloys [13]. The improved strength and microhardness of the target caused reduction of ASB formation and reduced the depth of penetration (DOP) [14]. ASBs led to cracks and micro-pores in the crater region of a high strength thick steel plate in the tempered condition [15]. SUKUMAR et al [16] observed that 920 °C WQ (Ti6Al4V) condition had a greater resistance to ASB formation when compared to 830 °C slowly cooled and then aged (STA) (Ti6Al4V) condition, but it did not reveal better ballistic performance due to its lower strength when compared to 830 °C STA condition. MANES et al [17] showed the formation of ASB along with ductile dimples through the coalescence and nucleation on the ballistic fracture surface of Al6061-T6 aluminium plates. The softening effect modifies the microstructure, accelerates the formation of dissolution and growth of coarse precipitates and results in the loss of mechanical properties. In order to restore the loss of these properties in different weld zones, one preference is to fully heat treat the welded components [8,18]. The increase in microhardness value in NZ of AA7075-T651 FSW joints after post-weld heat-treated (PWHT) process [19] was obtained. The PWHT AZ31B FSW Mg alloys considerably enhanced the tensile strength and microhardness at an annealing temperature of 250 °C [20].

Reported literatures [20,21] showed that, PWHT process can significantly improve the hardness and modify the microstructure of the FSW joints. Published research works focused on the effect of FSW parameters on ballistic behaviour of aluminium alloy [8] and compared the ballistic limit between BM and welded aluminium alloy plates [9]. However, limited works were noticed on ballistic studies of PWHT FSW joints of magnesium alloy. It was observed that that there is an improvement in ballistic behavior with hardness; in a WZ it is likely to attain the same hardness with moderate microstructures, several of which might be highly harmful to loss of ductility and toughness [5]. EREEM et al [9] and SULLIVAN et al [21] have determined the ballistic properties of different friction stir welded zones such as NZ+TMAZ (thermo-mechanical affected zone), HAZ and BMZ of aluminium alloy. Limited attempts have been noticed to determine the performance and failure behaviour of NZ+TMAZ, HAZ and BMZ of the PWHT AZ31B magnesium alloy.

In the present work, an attempt has been made to determine the ballistic behaviour of PWHT AZ31B Mg joints (8 mm in thickness) using 7.62 mm AP projectiles. The PWHT test was carried out under different annealing conditions, such as (150 °C, 1 h), (250 °C, 1 h) and (350 °C, 1 h), respectively.

2 Experimental

Magnesium plates with the dimensions of 50 mm ×50 mm × 8 mm were used and Table 1 shows the chemical composition of DMD cast

AZ31B Mg alloy.

In order to prepare square butt joints, taper pin tool made of H13 tool steel was used. Taper pin profile has shoulder diameter of 26 mm, pin diameter of 9 mm and length of 7.6 mm. The dimensions of the taper pin FSW tool are shown in Fig. 1.

Table 1 Chemical composition of DMD cast AZ31B Mg alloy (wt.%)

Al	Zn	Mn	Mg
3.29	1.10	0.32	Bal.

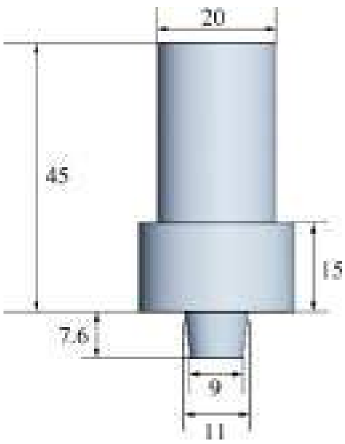

Fig. 1 Dimensions of taper pin FSW tool (Unit: mm)

The macro-level defect-free joint was prepared through a sequence of trial runs by changing the welding parameters such as tool rotation speed and welding feed which are listed in Table 2.

The trial runs indicated that rotation speed (1200 r/min) and welding feed (50 mm/min) are the optimum process parameters to produce defect-free FSW joints. Figure 2 shows the FSW joint obtained by using the above-mentioned parameters. The PWHT process was carried out in the electric furnace at three different annealing temperatures of 150, 250 and 350 °C for a period of 1 h soaking time under vacuum condition.

The microhardness values of heat-treated and non- heat-treated welded joints were measured by using Vickers hardness tester with a load of 100 g and a dwell time of 15 s. For each specimen, three measurements were taken and an average value was reported. FSW and PWHT samples were subjected to metallographic examination to obtain the microstructural changes.

Ballistic experiments were carried out in three different weld zones such as NZ + thermo mechanically affected zone (TMAZ), HAZ and BMZ. Aluminium alloy 6062 having dimensions of 200 mm × 200 mm × 22 mm was used as the backing plate. The Al-6062 backing plate and PWHT Mg alloy as a front plate were firmly clamped together using C-clamps at four edges without any air gap. The mass of the cartridge and the projectile was 18.75 and 7.85 g, respectively. The ballistic experiments were conducted as per MIL-DTL—32333 standard. The PWHT target plates were impacted against 7.62 mm × 39 mm AP projectile at 0° angle of attack with a firing range of 10 m and striking velocity of the projectile was (430±20) m/s. The mass of the gun powder was varied from 1.20 to 1.25 g to obtain the required striking velocity. The schematic diagrams of ballistic setup and the AP projectiles used in the present study are shown in Fig. 3.

In each test, infrared light-emitting diode was used to measure the impact velocity of projectile. A total of three projectiles were fired to PWHT target

Table 2 Macro graphs of different FSW joints prepared under different welding parameters

Parameter	Macro graph of FSW joint transverse section	Observation
Tool speed less than 1200 r/min		Defect: Tunnel Location: Centre of weld zone Reason: Insufficient heat input
Welding feed less than 50 mm/min		Defect: Wormhole Location: Advancing side Reason: Excessive heat input
Tool speed of 1200 r/min and welding feed of 60 mm/min		Defect: Tunnel and crack Location: Advancing side Reason: Improper heat input

Fig. 2 Defect-free AZ31B friction stir welds

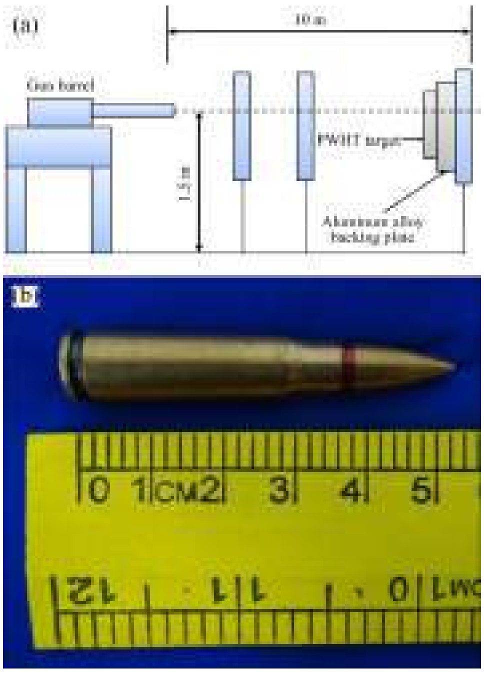

Fig. 3 Schematic diagrams of ballistic setup (a) and 7.62 mm × 39 mm AP projectile (b)

plates to obtain the ballistic performance statistically. The DOP values were considered to determine the ballistic performance of different zones of the PWHT target plates. The DOP of the penetration channel was measured using a video measuring instrument with an accuracy of ±5 μm. After the measurement of DOP value, the crater region of target plates was cut along the midpoint to investigate the nature of damage caused by the projectile impact. The damage behavior of crater sections was studied by using SEM.

3 Results and discussion

3.1 Microstructure

Figure 4 shows the SEM images of the AZ31B base metal (BM), non-heat-treated and heat-treated FSW joints. SEM image of BM shows the coarse and non-homogeneous distribution of β-phase (Fig. 4(a)). The NZ-FSW (Fig. 4(b)) shows considerable changes in microstructure when compared to the BM. NZ-FSW consists of equiaxed grains with a few precipitate particles along the grain boundaries.

It is understood that the stirring action of the FSW tool locally produces plastic deformation and frictional heat; this causes the partial dissolution of β-$Mg_{17}Al_{12}$ phase in the matrix. TUZ et al [22] reported that dissolution of the secondary phase was mainly due to the plastic deformation caused by the FSW tool. Hence, this produced the softening behaviour in the NZ compared to the BM. FSW reduced the size of the β-phase particles in the NZ of Mg alloy [23,24]. Figure 4(c) shows the NZ-PWHT microstructure under annealing condition of 250 °C and 1 h. The microstructure contains fine α-Mg phase and significant dissolution of secondary β-phase. However, the tiny precipitates were observed at the grain boundaries, due to the atomic diffusive flow of Mg and Al atoms. Hence, these strengthening precipitate particles make strong grain boundary and increase the strength of the joint. The HAZ-PWHT microstructure (Fig. 4(d)) exhibits coarse α-Mg and discontinuous precipitations compared to the NZ-PWHT microstructure. However, HAZ only experiences thermal cycle but not any plastic strain during welding, even though its heat-treated region of microstructure shows imperfect recrystallization and a few retained β-phases (β-$Mg_{17}Al_{12}$). SEM microstructure of BMZ-PWHT is shown in Fig. 4(e). It is evident that the presence of coarse α-Mg is similar to HAZ and refined spherical $Mg_{17}Al_{12}$ phases. $Mg_{17}Al_{12}$ phases were refined because of the solid solution strengthening, which is the effect of annealing process. The grain sizes of NZ, HAZ and BMZ in the PWHT samples are about 10.2, 52.7 and 26.6 μm, respectively.

3.2 Effect of PWHT temperature on microhardness

Figure 5 compares the average transverse microhardness of the three different heat-treated joints with that of non-heat treated one.

The microhardness of the HAZ of FSW joint was HV 54, while the microhardness values of the NZ and base metal were about HV 63 and HV 66, respectively. Compared to the base metal, lower

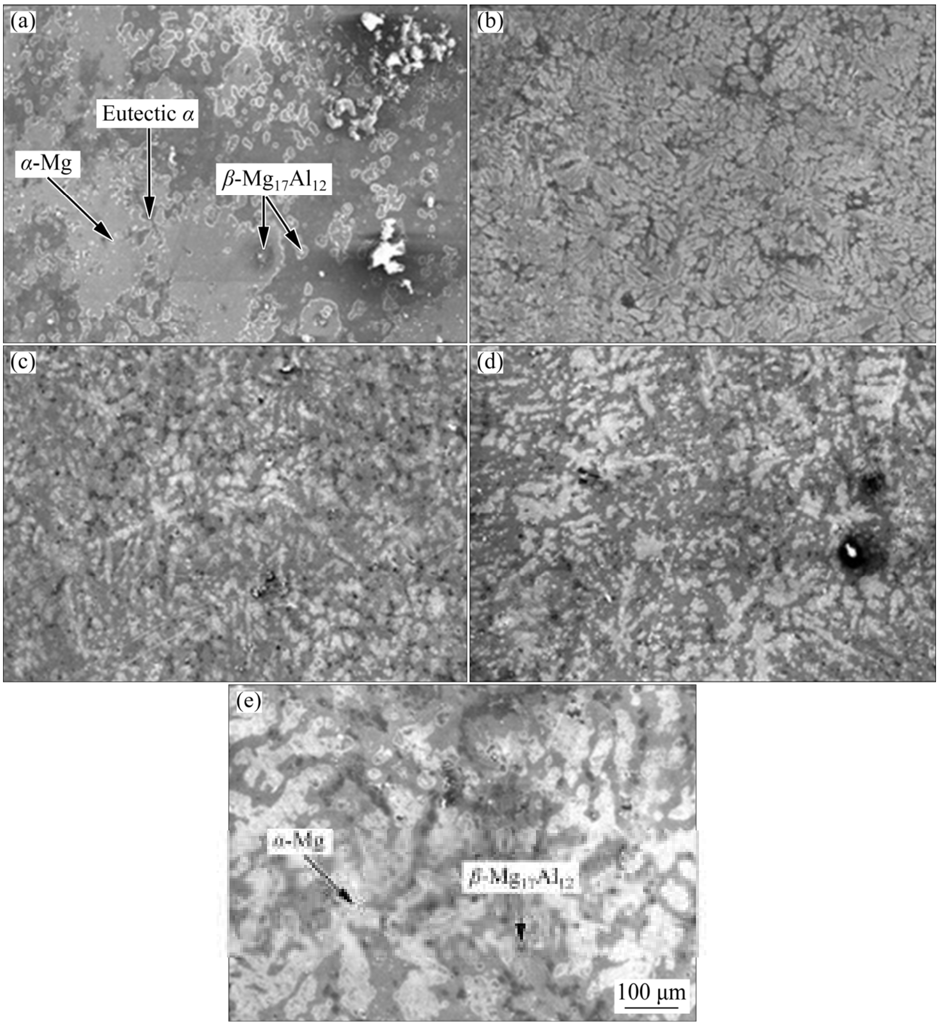

Fig. 4 SEM images of different zones of AZ31B magnesium alloys: (a) Base metal; (b) NZ-FSW; (c) NZ-PWHT; (d) HAZ-PWHT; (e) BMZ-PWHT

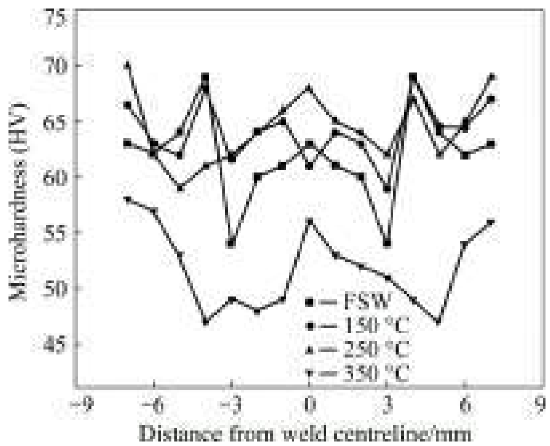

Fig. 5 Microhardness profiles of FSW and PWHT samples at different annealing temperatures

microhardness was observed in the NZ, which is attributed to the dissolution of β-phase. SINGH et al [25] also observed lower microhardness compared to the base metal. The least microhardness value was recorded in the friction stir welded zones, predominantly in the HAZ and TMAZ. However, these zones have undergone thermal softening effect caused by FSW tool. It was also observed that the variation of microhardness of the heat-treated welded joints was significantly influenced by the condition of heat treatment. The average microhardness values of NZ heat-treated welded joints obtained at annealing temperatures of 150, 250 and 350 °C for 1 h were about HV 61, HV 68 and HV 56, respectively.

3.3 Ballistic failure mechanisms of different PWHT zones

Ballistic performance of the PWHT (250 °C for 1 h) plate was determined by using 7.62 mm hard steel core projectile in the NZ+TMAZ, HAZ and BMZ. In each zone, three samples were tested and the corresponding DOP was measured using a video measuring instrument. The damage images of the front face and cross-sections of the NZ-PWHT, HAZ and BM target plates, impacted at a striking velocity of (430±20) m/s are shown in Figs. 6−8, respectively.

Figures 6(a) and (b) show the front face and cross-section images of the NZ+TMAZ crater region of PWHT targets, respectively.

The projectile impact caused the localized strain around the crater area, which led to the formation of surface crack in the weld region. It was found that the crater width at the entry was higher than that at the exit. Spalling mode failure was noted at the entry of the NZ where the hole diameter was bigger than the actual projectile diameter. It was due to the variation of hardness along the transverse direction. In addition, the ballistic failure mechanism changed from spalling

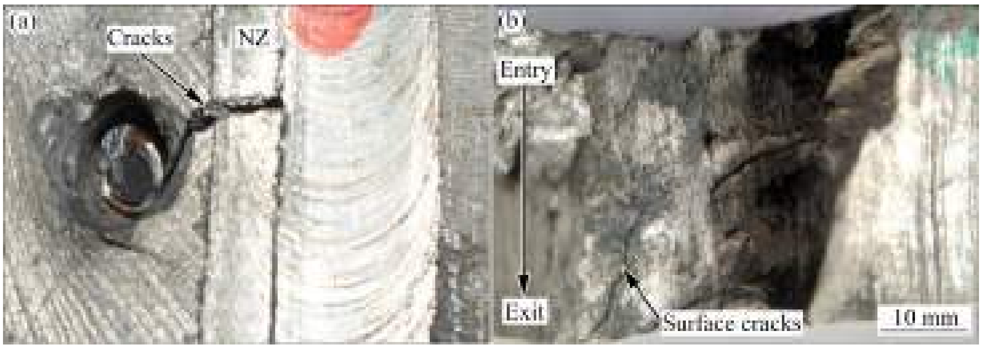

Fig. 6 Damage images of front face and cross-section of NZ-PWHT target plate after ballistic test: (a) Front view; (b) Crater path of projectile

Fig. 7 Damage images of front side and cross-section of HAZ-PWHT target plate after ballistic test: (a) Front view; (b) Crater path of projectile

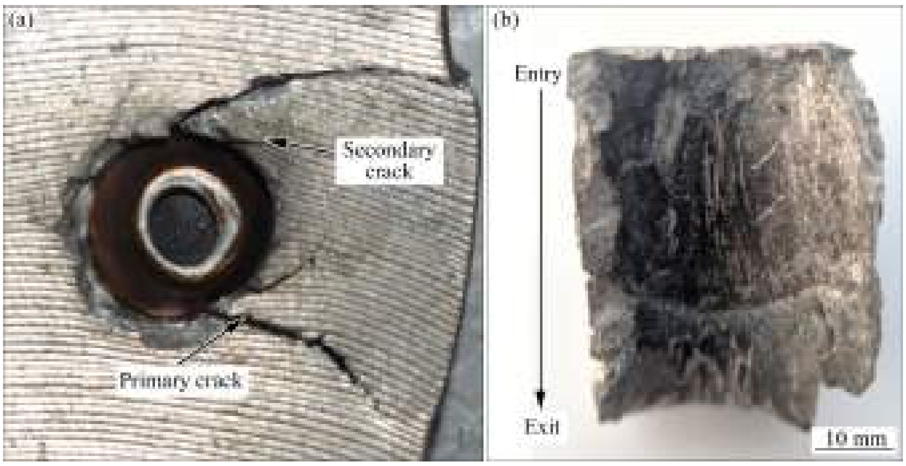

Fig. 8 Damage images of front face and cross-section of BM-PWHT target plate after ballistic test: (a) Front view; (b) Crater path of projectile

to plugging mode in the middle. This type of failure was dominated by an induced shear stress during penetration of the projectile. The presence of small surface cracks at the exit of crater clearly indicates that there is loss of ductility.

Figures 7(a) and (b) show the damage images of front face and cross-sections of HAZ target plate. Radial cracks were observed on the front face of the HAZ. The contact of the projectile on the target reduced the strength and developed high compressive stress. The compressive stress waves changed the fracture behaviour from ductile to brittle mode. Hence, it led to the formation of more cracks around the crater region compared to the NZ. Theses cracks did not propagate towards the weld regions because these regions have higher microhardness and finer grains compared to the HAZ.

The plugging failure mode was observed on the crater cross-section of the HAZ. In addition to plugging failure, the ductile deformation was observed by extending the corners of crater at the entry.

Figure 8(a) shows front face image of BM target plate, revealing the presence of primary and secondary cracks. Large continuous cracks are known as primary cracks. The cracks are formed due to the initial stress waves caused during the contact of the projectile with the target.

During the projectile impact into the target, the front steel core tip causes higher compressive stress which may exceed the ultimate compressive strength of the material. These compressive stresses produce localized stress waves that cause the formation of initial cracks. Small cracks around the crater region are considered as secondary cracks. These cracks were formed because of the reflected shock waves from the backing plate. The penetration of the projectile in the BMZ was lower than that of NZ and HAZ for the same thickness. However, the front face image clearly indicated that the projectile did not penetrate more compared to other zones. In the case of NZ and HAZ there was a shift in the projectile path which was noticed on the front face of the targets after ballistic impact. This was due to the variation of hardness along the transverse direction. The projectile path of this region was followed to the least surface hardness. Figure 8(b) shows the carter cross-section of BMZ. In this case, the failure mechanism was dominated by ductile hole expansion without any cracks on the crater wall. The crater width at the exit was less than that at the entry. However, the ballistic failure mechanism did not change from the entry to the exit of the projectile path. This was due to uniform hardness of the BMZ when compared to other zones.

In the present work, ballistic performance was determined by measuring the DOP of the projectile into the 22 mm thick Al6062 backing plate. After the projectile impact, the backing plate was detached from the target and sectioned using hack saw. The penetration channels of Al6062 backing plates for the corresponding targets are shown in Fig. 9. Ductile hole formation was observed at the penetration channels of the Al6062 backing plates corresponding to different heat-treated weld zones.

Fig. 9 Penetration channels of Al6062 backing plates after ballistic tests

The average DOP values of different heat-treated weld zones are shown in Fig. 10. It can be seen that the measured DOP values for NZ+TMAZ, HAZ and BMZ were 9.91, 21.14 and 8.46 mm, respectively. The BMZ has a slight decrease in DOP value compared to the NZ+TMAZ.

The yawed impact penetration was noticed in the backing plates due to the variation of hardness in the target plates and the maximum kinetic energy of the AP projectile absorbed by the front plate. This could be the reason for deviation of the projectile path in the backing plates. ERDEM et al [9] also noticed that the HAZ of friction-stir-welded Al7039 has the least ballistic limit when compared to the base metal and the NZ. The lower ballistic resistance in the HAZ was mainly due to thermal softening effect caused during welding. The slight reduction in ballistic performance of NZ+TMAZ was mainly due to the change of penetration mechanism from the entry to the exit crater region, whereas the penetration mechanism in the BMZ was completely ductile hole deformation.

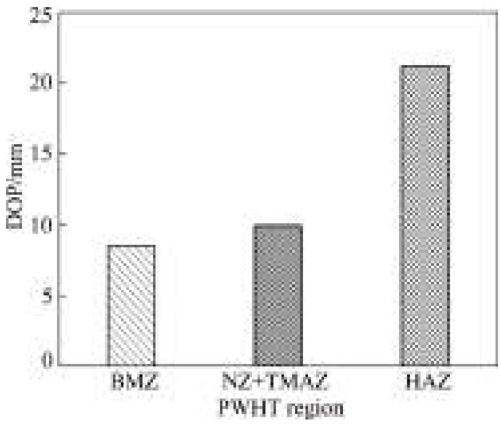

Fig. 10 DOP values of heat-treated weld zones

From the above discussion, it was observed that ballistic behaviours of the NZ+TMAZ, HAZ and BMZ were completely different. However, the crater walls of HAZ and BMZ were almost similar in appearance; whereas no such cracks were observed in the BMZ crater wall region. The deflected projectile path was noticed in the NZ+TMAZ and HAZ of the backing plate, as shown in Fig. 9. However, it was not observed in the BMZ. The variation of hardness along the transverse plane was the primary reason for the shift in the projectile path. Hence, this caused the deviation of projectile path in the backing plate. It was also noted that, in all the three regions the crater width decreased from the entry to the exit of the projectile. The least hardness value was observed in the HAZ compared to other regions which caused the increase in DOP value. It is well known that hardness is one of the important parameters that mostly influence the ballistic behaviour of a weld joint [9,21]. The DOP value of the HAZ was much higher than that of the NZ+TMAZ and BMZ.

3.4 Post-fracture SEM morphology

To investigate the fracture behaviour and failure mechanisms of targets, SEM analysis was carried out in crater region. The fracture surfaces of all three regions showed the creation of adiabatic shear bands (ASBs), especially more ASBs were observed at the entry (Fig. 11(a)). More ASBs caused the formation of cracks which in turn affected the ballistic performance. ASBs induced micro-cracks around the crater cross-section of the entry.

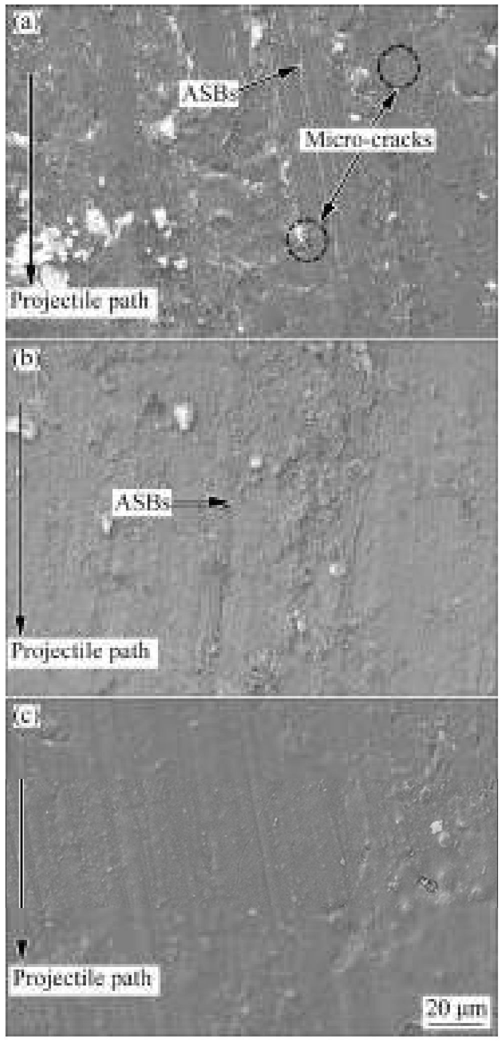

Fig. 11 SEM images of post-impact ballistic NZ-PWHT crater cross-section regions: (a) Entry; (b) Middle; (c) Exit

The presence of higher ASBs lines at the entry confirms that the majority of the kinetic energy of the projectile was absorbed in this region compared to other regions which led to the deflection of projectile and restricted the penetration (Figs. 11(b) and (c)). MISHRA et al [15] found that the deflection of projectile at the target lowered the kinetic energy of the projectile, which significantly reduced the ASBs.

Figure 12 shows the SEM images of crater cross-section in different regions of HAZ-PWHT. The fracture surface of HAZ at the entry showed the presence of dimples, which indicated the failure mechanism was dominated by ductile hole enlargement and indicative of crack growth, voids and coalescence. It was also noted that all the three regions i.e. entry, middle and exit regions showed the formation of micro-cracks. Thus, one can expect the absence of ASBs and presence of cracks in HAZ when compared to NZ. The formation of cracks was due to the inability of the material to accommodate the radial stresses. The presence of micro-cracks at the entry, middle and exit was the reason for a reduction in ballistic performance. The formation of micro-cracks on the crater surface was due to the local temperature rise; hence, it may cause thermal softening effect and produce tensile stress.

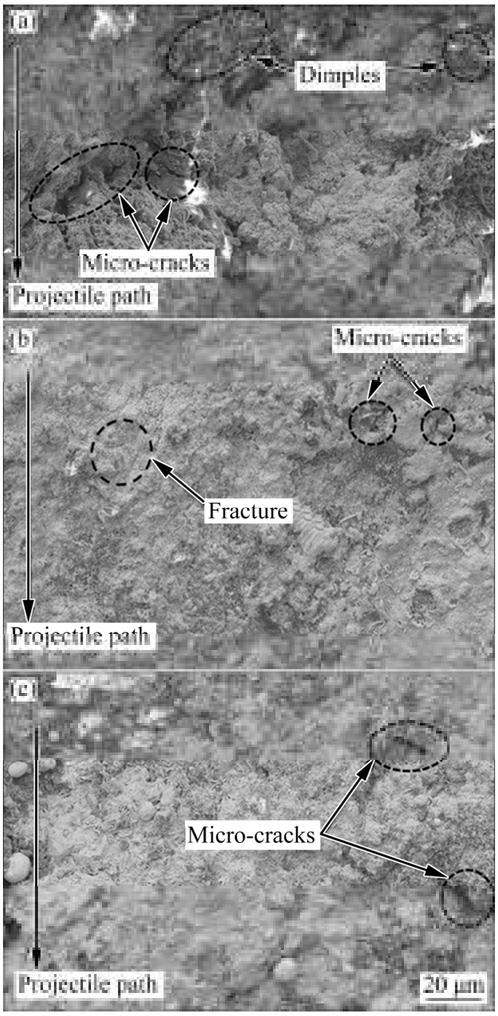

Fig. 12 SEM images of crater cross-section in different regions of HAZ-PWHT: (a) Entry; (b) Middle; (c) Exit

Figure 13 shows the SEM images of crater cross-section in different regions of BMZ-PWHT. The presence of cracks at the entry of crater cross-section indicated that the penetration process was dominated by ASBs. The crater wall surfaces showed the formation of cracks at the entry and exit, and few ASBs at the middle. The presence of the shear bands in the middle of crater surface of the BMZ confirmed that the failure caused stress waves from the circumference of the specimen. The reflected stress waves contributed to the formation of ASB [25].The contact stress waves on the front face caused crack initiation and crack propagation along the thickness direction, which was indicated in the higher magnification SEM fracture images of the entry. The formation of cracks was due to lack of ability of the target to accommodate the shear strain generated by the projectile and influences of radial and tangential stress [15]. The presence of cracks on the BMZ crater surface was mainly due to the presence of coarse α-Mg and retained spherical Mg17Al12 phase between grain boundaries that led

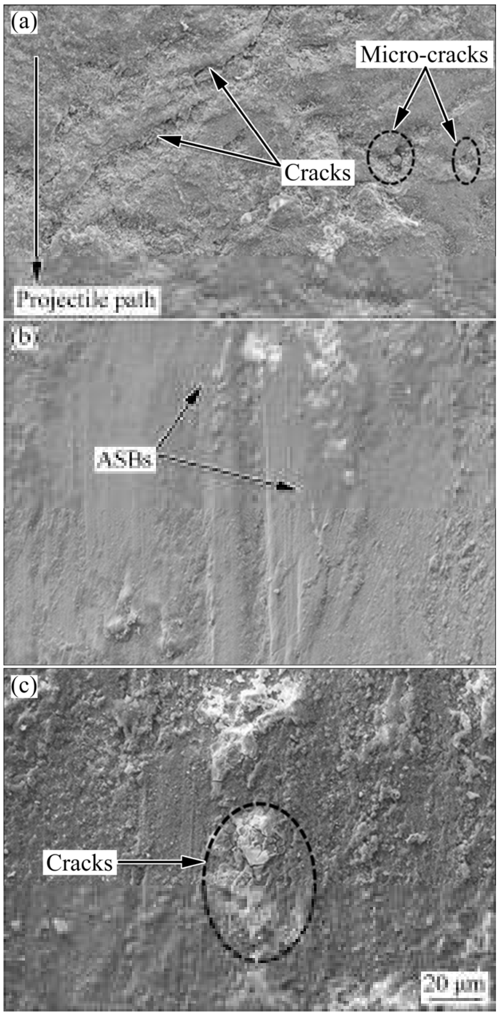

Fig. 13 SEM images of crater cross-section in different regions of BMZ-PWHT: (a) Entry; (b) Middle; (c) Exit

to the initiation of cracks during the projectile penetration. However, these cracks were not observed in the surface level as discussed earlier. The small discontinuous crack was present at the exit, which indicated that the complete projectile impact energy was not transferred to the backing plate. Hence, it slightly reduced the depth of penetration compared to NZ-PWHT. Even though a larger number of ASBs were noticed in NZ compard to BMZ, its ballistic performance was not significantly inferior to that of the BMZ. From the fracture SEM images of BMZ it was understood that there was a change in fracture mode from ductile to mixed mode. In addition, the hardness of the target significantly influenced the change in ballistic failure mechanism [9,26].

4 Conclusions

(1) The effect of different PWHT temperatures (150, 250 and 350 °C) on the microhardness was determined and compared with non-heat treated FSW joints. The maximum hardness value of HV 69 was obtained in the NZ under the PWHT condition of 250 °C, 1 h, which was 7.93% and 3.03% higher than that of the NZ-FSW and BM regions, respectively.

(2) The NZ-FSW showed homogeneous microstructure with fine α-Mg and partial dissolution of β-$Mg_{17}Al_{12}$ phase due to stirring effect. Because of heat treatment, significant dissolution of β-$Mg_{17}Al_{12}$ phase and strengthening of precipitated particles were noticed.

(3) Ballistic resistances of NZ+TMAZ and HAZ were 53.12% and 59.98% lower than that of the BMZ, respectively. The failure mechanism in the NZ+TMAZ was the combination of spalling and plugging. The least hardness of HAZ showed plugging failure along with surface cracks from the entry to the exit of penetration channel. The front face showed the formation of radial cracks.

(4) Post ballistic impact SEM images of NZ+TMAZ and BMZ showed the formation of ASBs and induced cracks. The crater in the HAZ exhibited micro-cracks in all three regions of the entry, middle and exit and along with ductile dimples at the entry. The HAZ region allows the projectile to enter easily and decreased the ballistic resistance when compared to other zones. The fragmentation failure was not observed in all three zones of PWHT target. Hence, PWHT process can be a suitable process for improving the hardness and ballistic resistance of FSW Mg alloy.

References

[1] JONES T L, KONDOH K. Magnesium Technology [M]. Heidelberg: Springer, 2011: 425−430.

[2] ABDULLAH M F, ABDULLAH S, OMAR M Z, SAJURI Z, SOHAIMI R M. Failure observation of the AZ31B magnesium alloy and the effect of lead addition content under ballistic impact [J]. Advances in Mechanical Engineering, 2015, 7: 1−13.

[3] DORBANE A, MANSOOR B, AYOUB G, SHUNMUGASAMY V C, IMAD A. Mechanical, microstructural and fracture properties of dissimilar welds produced by friction stir welding of AZ31B and Al6061 [J]. Materials Science and Engineering A, 2016, 651: 720−733.

[4] PADHEE C K, MASANTA M, MONDAL A K. Feasibility of Al−TiC coating on AZ91 magnesium alloy by TIG alloying method for tribological application [J]. Transactions of Nonferrous Metals Society of China, 2020, 30: 1550−1559.

[5] DERRY C G, ROBSON J D. Characterisation and modelling of toughness in 6013-T6 aerospace aluminium alloy friction stir welds [J]. Materials Science and Engineering A, 2008, 490: 328−334.

[6] THOMPSON B, DOHERTY K, NIESE C, EFF M, STOTLER T, PRAMANN Z, SEAMAN J, SPENCER R, WHITE P. Friction stir welding of thick section aluminum for military vehicle applications [C]//Proceedings of the 9th International Symposium on Friction Stir Welding, 2012. Huntsville, AL, 2012: 1−10.

[7] GRUJICIC M, ARAKERE G, HARIHARAN A, PANDURANGAN B. A concurrent product-development approach for friction-stir welded vehicle-underbody structures [J]. Journal of Materials Engineering and Performance, 2012, 21: 437−449.

[8] SULLIVAN A, ROBSON J D. Microstructural properties of friction stir welded and post-weld heat-treated 7449 aluminium alloy thick plate [J]. Materials Science and Engineering A, 2008, 478: 351−360.

[9] ERDEM M, CINICI H, GOKMEN U, KARAKOC H, TURKER M. Mechanical and ballistic properties of powder metal 7039 aluminium alloy joined by friction stir welding [J]. Transactions of Nonferrous Metals Society of China, 2016, 26: 74−84.

[10] HOLMEN J K, BØRVIK T, MYHR O R, FJAER H G, HOPPERSTAD O S. Perforation of welded aluminum components: Microstructure-based modeling and experimental validation [J]. International Journal of Impact Engineering, 2015, 84: 96−107.

[11] JHA A K, SHIRESHA N, MURTY S N, DIWAKAR V, SREEKUMAR K. Ballistic impact testing of AA2219 aluminium alloy welded plates and their metallurgical characterisation [J]. Indian Journal of Engineering Material Science, 2005, 12: 221−226.

[12] JENA P K, SENTHIL P P. Effect of tempering time on the ballistic performance of a high strength armour steel [J]. Journal of Applied Research and Technology, 2016, 14: 47−53.
[13] KARAMIS M B, NAIR F E, TASDEMIRCI A. Analyses of metallurgical behavior of Al−SiC_p composites after ballistic impacts [J]. Composite Structures, 2004, 64: 219−226.
[14] MONDAL C, MISHRA B, JENA P K, KUMAR K S, BHAT T B. Effect of heat treatment on the behavior of an AA7055 aluminum alloy during ballistic impact [J]. International Journal of Impact Engineering, 2011, 38: 745−754.
[15] MISHRA B, JENA P K, RAMAKRISHNA B, MADHU V, BHAT T B, GUPTA N K. Effect of tempering temperature, plate thickness and presence of holes on ballistic impact behavior and ASB formation of a high strength steel [J]. International Journal of Impact Engineering, 2012, 44: 17−28.
[16] SUKUMAR G, SINGH B B, BHATTACHARJEE A, KUMAR K S, GOGIA A K. Ballistic impact behaviour of β-CEZ Ti alloy against 7.62 mm armour piercing projectiles [J]. International Journal of Impact Engineering, 2013, 54: 149−160.
[17] MANES A, PAGANI M, SAPONARA M, MOMBELLI D, MAPELLI C A, GIGLIO M. Metallographic characterisation of Al6061-T6 aluminium plates subjected to ballistic impact [J]. Materials Science and Engineering A, 2014, 608: 207−220.
[18] YAN Z F, ZHANG H X, DUAN J W, LIU F, WANG G L. Effect of post-weld heat treatment on mechanical characteristics of AZ31 magnesium alloy welded joints [J]. Journal of Wuhan University of Technology: Mater Sci Ed, 2017, 32: 1205−1212.
[19] SIVARAJ P, KANAGARAJAN D, BALASUBRAMANIAN V. Effect of post weld heat treatment on tensile properties and microstructure characteristics of friction stir welded armour grade AA7075-T651 aluminium alloy [J]. Defence Technology, 2014, 10: 1−18.
[20] WANG G, YAN Z, ZHANG H, ZHANG X, LIU F, WANG X, SU Y. Improved properties of friction stir-welded AZ31 magnesium alloy by post-weld heat treatment [J]. Materials Science and Technology, 2017, 33: 854−863.
[21] SULLIVAN A, DERRY C, ROBSON J D, HORSFALL I, PRANGNELL P B. Microstructure simulation and ballistic behaviour of weld zones in friction stir welds in high strength aluminium 7xxx plate [J]. Materials Science and Engineering A, 2011, 528: 3409−3422.
[22] TUZ L, KOŁODZIEJCZAK P, KOLASA A. Structure of butt joint of as-cast magnesium alloys [J]. Welding International, 2016, 30: 43−47.
[23] FREENEY T A, MISHRA R S. Effect of friction stir processing on microstructure and mechanical properties of a cast-magnesium–rare earth alloy [J]. Metallurgical and Materials Transactions A, 2010, 41: 73−84.
[24] BAGHERI B, ABBASI M, ABDOLLAHZADEH A, MIRSALEHI SE. Effect of second-phase particle size and presence of vibration on AZ91/SiC surface composite layer produced by FSP [J]. Transactions of Nonferrous Metals Society of China, 2020, 30: 905−916.
[25] SINGH R K, SHARMA C, DWIVEDI D K, MEHTA N K, KUMAR P. The microstructure and mechanical properties of friction stir welded Al−Zn−Mg alloy in as welded and heat treated conditions [J]. Materials & Design, 2011, 32: 682−687.
[26] JENA P K, MISHRA B, KUMAR K S, BHAT T B. An experimental study on the ballistic impact behavior of some metallic armour materials against 7.62 mm deformable projectile [J]. Materials & Design, 2010, 31: 3308−3316.

热处理条件对搅拌摩擦镁合金接头各区域抗弹行为的影响

S. DHARANI KUMAR[1], S. SURESH KUMAR[2]

1. Department of Mechanical Engineering, Sri Eshwar College of Engineering, Coimbatore, 641202, Tamil Nadu, India;
2. Department of Mechanical Engineering, Sri Sivasubramaniya Nadar College of Engineering, Chennai, 603110, Tamil Nadu, India

摘　要：采用搅拌摩擦焊(FSW)工艺制备 AZ31B 镁合金焊接接头，并在不同条件下进行热处理。研究 AZ31B 镁合金焊后热处理(PWHT)不同区域的抗弹行为，使用 7.62 mm × 39 mm 穿甲弹，冲击速度为(430±20) m/s。分析热处理前后搅拌摩擦焊接头的显微硬度。结果表明，PWHT 工艺(250 °C, 1 h)能提高热处理后搅拌摩擦焊接头的显微硬度。扫描电镜(SEM)结果显示，热处理使 α-Mg 晶粒细化，形成细小的析出相，使 β-$Mg_{17}Al_{12}$ 相溶解到 Mg 基体中。通过穿深(DOP)试验评估 PWHT 不同区域的抗弹行为。热处理后接头母材区(BMZ)的 DOP 值较小。抗弹试验后对弹坑周边 3 个区域的横截面进行 SEM 表征，观察到绝热剪切带(ASB)的形成。

关键词：AZ31B 镁合金；焊后热处理；抗弹行为；穿深；绝热剪切带

(Edited by Wei-ping CHEN)

International Journal of Research in Engineering, Science and Management
Volume 4, Issue 6, June 2021
https://www.ijresm.com | ISSN (Online): 2581-5792

A Review On Performance Analysis of Centrifugal Pump Impeller

K. Sathish[1*], S. Abilash[2], S. Balaji[3], S. Aroon Daniel[4], V. Dhatchinamoorthi[5]
[1,2,3,4,5]*Department of Mechanical Engineering, Sri Eshwar College of Engineering, Coimbatore, India*

***Abstract*: The main objective of this review is to investigate the centrifugal pump and to increase the efficiency of the pump. The average efficiency of centrifugal pump is about 65–70 percent. The significance of efficiency in pump is selecting a proper pumping system will conserve fuel or electricity and decrease the annual pumping costs. Inefficient and poorly chosen pumping systems can increase annual costs dramatically. Obtained efficiency of centrifugal pumps with low specific speed is not high. The scope of the work is to reduce hydraulic losses. In this paper a literature review is identified by providing a modified impeller channel with design changes that are capable of improving the efficiency of the centrifugal pump.**

***Keywords*: impeller, pump, groove, CFD.**

1. Introduction

Centrifugal pump is used to convert kinetic energy to hydrodynamic energy. The type of kinetic energy is rotational kinetic energy and the rotational energy typically comes from engine to electric motor. Already obtained efficiency is not too high so the efficiency of the pump should be increased. So, the different loses should be reduced. So, the impeller should be modified with micro grooves. The characteristics of smooth impeller and the grooved impeller should be identified and compared. To evaluate this CFD calculations should be done and the application of micro geometry in centrifugal pump impeller is done and calculations are made. The main objective is to increase the efficiency of the pump.

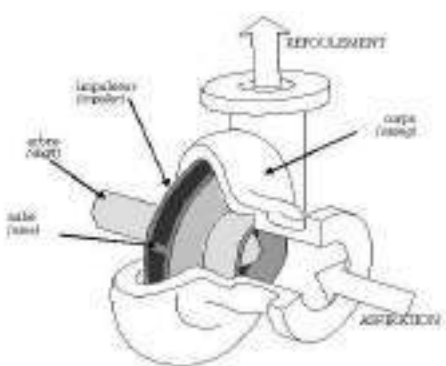

Fig. 1. Components of centrifugal pump

2. Literature Survey

Dave, S. Shukla, S, Jain, S, [1] A comprehensive overview of fluid dynamic models and experimental results that can help solve problems in centrifugal compressors and modern techniques for a more efficient aerodynamic design.

Abo Elyamin, Gamal R.H., et. al, [2] A numerical investigation is carried out on a centrifugal pump to show the effect of the impeller blades number on the pump performance. Three different impellers with 5, 7, and 9 blades are tested numerically to determine the optimum blades number at rotational speed of 2800 rpm.

Li, Jidong, et. al, [3] The three-dimensional flow field of the whole flow passage of a mixed-flow pump was numerically simulated by using CFD software on the basis of Spalart-Allmaras turbulent model according to the original design of the plant. Through analyzing the calculation results, the reason why the flow rate of this pump cannot reach to the design requirements was found out. After replacing the impeller, a new pump impeller was optimally designed.

Selamat, Farah Elida, et. al, [4] Centrifugal pump usage has increased over the past year due to its importance and efficiency. Its function is to transport liquid from one place to another using energy applied to the pump. This paper revolves around the idea of design and analysis of centrifugal pump for performance enhancement within the pump specifications.

S Muttalli, Raghavendra, et. al, [5] In order to improve the hydrodynamic performance of the centrifugal pump, an orthogonal experiment was carried out to optimize the impeller design parameters. This study employs the commercial computational fluid dynamics (CFD) code to solve the Navier-Stokes equations for three-dimensional steady flow and predict the pump performance. The prototype experimental test results of the original pump were acquired and compared with the data predicted from the numerical simulation, which presents a good agreement under all operating conditions.

Zhou, Ling, et. al, [6] In order to improve the hydrodynamic performance of the centrifugal pump, an orthogonal experiment was carried out to optimize the impeller design parameters. This study employs the commercial computational fluid dynamics (CFD) code to solve the Navier-Stokes equations for three-dimensional steady flow and predict the pump performance. The prototype experimental test results of the original pump

*Corresponding author: sathish.k@sece.ac.in

were acquired and compared with the data predicted from the numerical simulation, which presents a good agreement under all operating conditions.

Hawas, Malik N., et. al, [7] In centrifugal pumps, the flow physics and dynamic performances are generally affected by any modification in blades shape and design layout. At the present time, the dominant verification method used for investigation these characteristics are numerical simulation.

Pandya, Kapil, Patel, Chetankumar M, [8] The main objective of this work is to go through various approaches used in CFD analysis of centrifugal pump and highlight the advantages and application of CFD analysis in turbo industries. The CFD analysis is the advanced tool to overcome the limitation of conventional method to design the pump. Now a days CFD analysis is very familiar approach to improve the design of centrifugal pump and optimize it's operational parameters like Head, Power, Discharge and Speed.

Okokpujie, Imhade P., et. al, [9] The design, construction and testing of a single stage centrifugal pump is presented in this project work, electric motor drives the centrifugal pump, which draws fluid (water) from a water storage wall and delivers same through a flow control valve to a tank. The experimental results obtained shows that the tested pump can develop a head, (H) of 30m, volumetric discharge, (Q) of $9m^3$/hr and the speed of 2900 rpm for an input power of 1.5HP.

Bhosale, Anirudha S, [10] Centrifugal pumps are widely used for water supply plants, steam power plants, sewage, oil refineries, chemical plants, hydraulic power service, food processing factories and mines, because of their suitability in practically any service. Therefore, it is necessary to find out the design parameter, working conditions and maximum efficiency with lowest power consumption. Study indicates that Computational fluid dynamics (CFD) analysis is being increasingly applied in the design of centrifugal pumps.

Aung, Kyaw, et. al, [11] This paper presents the calculation and production procedure of impeller for single section centrifugal pump. The pump type is single stage centrifugal pump with close impeller type. This impeller develops a head of 20 m and delivers 0.9 m^3 /min of water. The designed impeller has 97 mm inlet diameter, 226 mm outlet diameter, 20˚ inlet vane angle and 23˚ outlet vane angle.

Kim, J. H., et. al, [12] In this study, optimization of the impeller and design of volute were carried out in order to improve the performance of a centrifugal pump. Design parameters from vane plane development for impeller design were selected and effect of the design parameters on the performance of the pump was analyzed using CFD and Response Surface Method to optimized impeller.

Gurupranesh, P, et. al, [13] Centrifugal pumps are used extensively for pumping water over short to medium distance through pipeline where the requirements of head and discharge are moderate. This project is devoted to enhance the performance of the centrifugal pump through design modification of impeller. Theories on pump characteristics are studied in detail. Vane profile of the impeller is generated using point by point method.

Kaliappan, S., et. al, [14] The impeller of an existing Mather and Platt centrifugal pump with both geometry and performance known was analyzed and redesigned using an integrated. Fluid dynamics and geometry modeling parts of the design /analysis system were systematically applied. To analyze the existing impeller say impeller A, which was designed using conventional (routine in industry) hydraulic layout procedures.

Matlakala, M. E.., et. al., [15] Centrifugal pumps contain two main parts: an impeller that imparts Centrifugal forces to the production fluid and diffuser which is the fixed part that guides the flow to the discharge. The shape of the impeller influences the performance of the pump. Thus, the area of the significance to the pump design is the impeller geometric parameters to achieve pump performance. The consumption of energy by the pump is caused by the failure to choose the right pump size for the system, improper installation, and pump operation. Poor pump performance may affect the plant operation such as maintenance cost, downtime, loss of production, increase in operating cost.

Zhang, Yu., et. al., [16], This paper presents the optimization of vibrations of centrifugal pump considering fluid-structure interaction (FSI). A set of centrifugal pumps with various blade shapes were studied using FSI method, in order to investigate the transient vibration performance. The Kriging model, based on the results of the FSI simulations, was established to approximate the relationship between the geometrical parameters of pump impeller and the root mean square (RMS) values of the displacement response at the pump bearing block.

Korakianitis, Theodosios., et. al., [17] Mechanical pumps as heart assist devices impose power and size limitations on the pumping mechanism, and therefore requires careful optimization of pump characteristics. Typically, new pumps are designed by relying on the performance of other previously designed pumps of known performance using concepts of fluid dynamic similarity. Such data are readily available for industrial pumps, which operate in Reynolds numbers region.

Kaewnai, Suthep., et. al., [18] The main objective of this work is to use the computational fluid dynamics (CFD) technique in analysing and predicting the performance of a radial flow-type impeller of centrifugal pump. The impeller analysed is at the following design condition: flow rate of 528 m^3/hr; speed of 1450 rpm; and head of 20 m or specific speed (Ns) of 3033 1/min in US-Units. The first stage involves the mesh generation and refinement on domain of the designed impeller.

Protopopov A, et. al., [19] In various industries where centrifugal pumps are used, a common problem is the starting overheating of electric motors. Such overheating can lead to motor failure, especially in the case of starting-up the centrifugal pump on the open valve. It happens due to the fact that the starting current is many times greater than the rated current, and the rated current with an open valve usually makes is much more. In this case, complex methods of centrifugal pumps analysis and manuals do not contain any methods of evaluation the magnitude of the starting overheating of centrifugal pump electric motors.

Vigovskij V, et. al., [20] The article deals with the problems associated with the analysis of high-speed low-flow centrifugal pumps. The existing methods for analysis of such pumps and their disadvantages were reviewed. A method of multi-criteria optimization of high-speed centrifugal pumps has been proposed. The method is based on the search for a compromise between the cavitation characteristics and the hydraulic head of the centrifugal pump by plotting a compromise curve. The LP-tau searching method was used for finding the points of this curve in the article.

Wang C. Y, et. al., [21] For three-dimensional inverse design of water pump, both blade-loading distribution and stacking condition of high-pressure side are important factors affecting the quality of design. For example, inclined trailing edge of blade can suppress the pressure fluctuation and reduce the sound pressure level and sound power of noise for single-suction centrifugal pump. And the lean mode of blade trailing edge can influence hydraulic performance of pump-turbine in pump mode. However, there is no clear view on the effect of lean mode of blade trailing edge on hydraulic performance for double-suction centrifugal pump.

Yan X. F, et. al., [22] The current investigation is aimed to simulate the unsteady internal flows in a centrifugal pump impeller with seven twisted blades by using a three-dimensional Navier-Stokes equation with Scale-adaptive simulation (SAS) turbulence model. A detailed analysis of the results at design flow rate Q 0 and low flow rate 0.5Q 0 and 0.3Q 0, is presented. Unsteady flow analyses in centrifugal pump are focused mainly on the volute. The calculation results of pump head and efficiency at different flow rate conditions is in good agreement with the experimental data.

Yuan J. P, et. al., [23] In order to study the characteristics of radiated noise of multistage centrifugal pump, radiated noise test system of multistage centrifugal pump was built. Radiated noise experiments were carried out for a medium specific speed multistage centrifugal pump and its modification, which was devised with a new hydraulic design method in the field of sound optimization. The experiment validation on the sound field was performed in a semi-anechoic room and the acoustic parameters of the multistage pump at the different flow rates were gathered with the LMS system (a complete set of solutions for vibration and noise test

Zhang J. F, et. al., [24] The experimental investigation in impellers was conducted at different conditions and phases by means of PIV (Particle Image Velocimetry) to study the internal flow. Meanwhile, the absolute and relative velocity distributions in impellers were obtained. Experimental results show that the head value is higher in the impeller with splitter blades and both two head curves appear hump phenomena at small flow rate. The absolute velocity value increases with radius and from pressure side to suction side at the same radius gradually. The splitter blades can scour the wake, making outlet velocity distribution more uniform and improving the internal flow. The velocity distribution becomes less even in the process of closing to tongue due to reinforced interference of tongue on internal flow.

3. Conclusion

Thus, the literature review shows a detailed study on performance improvement in centrifugal pump with by a changing the suitable design parameters, such as blade angle, number of blades, micro grooved impeller, grove thickness. This review predicts that, with the change of design parameters a considerable amount of increase in efficiency will be achieved.

References

[1] Selamat, Farah Elida Wan Izhan, Wan Hariz Iskandar, Baharudin, Bakhtiar Saffuan," Design and Analysis of Centrifugal Pump Impeller for Performance Enhancement" in Journal of Mechanical Engineering vol. 5, no. special issue 2, pp. 36-53.

[2] Aung, Kyaw, Sein, Nay Win, N. Nyi, Nyi, "Design and Fabrication of impeller for Single Suction Centrifugal Pump", in International Journal of Scientific and Research Publications (IJSRP) vol. 9, no. 8, pp. 92-110.

[3] Dave, S., Shukla, S. Jain, S., "Design and analysis of centrifugal compressor", in Technology Drivers: Engine for Growth," vol. 4, no. 2, pp. 283-288.

[4] Kaliapp.an, S., Rajkamal, M. D., Balamurali, D, "Numerical analysis of centrifugal pump impeller for performance improvement" in International Journal of Chemical Sciences vol. 14, no. 2, pp. 1148-1156.

[5] Bhosalez, Anirudha S, "A Review Paper on Improvement of Impeller Design a Centrifugal Pump using FEM and CFD" in International Journal for Innovative Research in Science & Technology vol. 4, no. 4, pp. 6-8.

[6] Kim, J. H., Oh, K. T, Pyun, K. B., "Design optimization of a centrifugal pump impeller and volute using computational fluid dynamics" in IOP Conference Series: Earth and Environmental Science vol. 15, no. part 3.

[7] Zhou, Ling, Shi, Weidong, Wu, Suqing, "Performance optimization in a centrifugal pump impeller by orthogonal experiment and numerical simulation" in Advances in Mechanical Engineering vol. 2013.

[8] Pandya, Kapil, Patel, Chetankumar M, "A Critical review on CFD Analysis of centrifugal pump impeller" in International Journal of Advance Engineering and Research Development vol. 1, no. 6, pp. 1-7.

[9] Li, Jidong, Zeng, Yongzhong, Liu, Xiaobing, Wang, Huiyan, "Optimum design on impeller blade of mixed-flow pump based on CFD" in Procedia Engineering vol. 31, pp. 187-195.

[10] S. Muttalli, Raghavendra, Agrawal, Shweta, Warudkar, Harshla, "CFD Simulation of Centrifugal Pump Impeller Using ANSYS-CFX" in International Journal of Innovative Research in Science, Engineering and Technology vol. 3, no. 8, pp. 15553-15561.

[11] Abo Elyamin, Gamal R. H., Bassily, Magdy A., Khalil, Khalil Y, Gomaa, Mohamed Sh, "Effect of impeller blades number on the performance of a centrifugal pump in Alexandria Engineering Journal vol. 58, no. 1, pp. 39-48.

[12] Selamat, Farah Elida, Wan Izhan, Wan Hariz Iskandar, Baharudin, Bakhtiar Saffuan, "Design and analysis of centrifugal pump impeller for performance enhancement" in Journal of Mechanical Engineering, vol. 5, no. 2, pp. 36-53.

[13] Aung, Kyaw, Sein, Nay Win, Nyi, Nyi, "Design and Fabrication of impeller for Single Suction Centrifugal Pump" in International Journal of Scientific and Research Publications (IJSRP) vol. 9, no. 8, pp. 92-110.

[14] Bhosalez, Anirudha S," A Review Paper on Improvement of Impeller Design a Centrifugal Pump using FEM and CFD" in International Journal for Innovative Research in Science & Technology vol. 4, no. 4, pp. 6-8.

[15] Matlakala, M. E, Kallon, D. V. V., Simelane, S. P., Mashinini, P. M., "Impact of design parameters on the performance of centrifugal pumps" in Procedia Manufacturing in 2019, vol. 35, pp. 197-206.

[16] Zhang, Yu, Hu, Sanbao, Zhang, Yunqing, Chen, Liping, "Optimization and Analysis of Centrifugal Pump considering Fluid-Structure Interaction," in Scientific World Journal in 2014, Vol. 2014.

[17] Korakianitis, Theodosios, Rezaienia, Mohammad A., Paul, Gordon M, Rahideh, Akbar, Rothman, Martin T., Mozafari, Sahand., "Optimization of Centrifugal Pump Characteristic Dimensions for Mechanical Circulatory Supp.ort Devices," in ASAIO journal in 2016, vol. 62, no. 5, pp. 545-551.

[18] Kaewnai, Suthep, Chamaoot, Manuspong, Wongwises, Somchai, "Predicting performance of radial flow type impeller of centrifugal pump using CFD," in Journal of Mechanical Science and Technology in 2009, vol. 23, no. 6, pp. 1620-1627.

[19] Protopopov, A., Bondareva, D., "On the issue of starting-up overheating of electric motors of centrifugal pumps," in IOP Conference Series: Materials Science and Engineering in 2019, Vol. 492, no. 1.

[20] Protopopov, A., Vigovskij, V., "Development of methods for high-speed centrifugal pump analysis," in IOP Conference Series: Materials Science and Engineering in 2019, Vol. 492, no. 1.

[21] Wang, C. Y., Wang, F. J., Zou, Z. C., Xiao, R. F., Yang, W., "Effect of lean mode of blade trailing edge on hydraulic performance for double-suction centrifugal pump," in IOP Conference Series: Earth and Environmental Science in 2019, Vol. 240, no. 3.

[22] Yan, X. F., Meng, G. Q.Q.G., "Pressure fluctuation characteristics of centrifugal pump at low flow rate," in IOP Conference Series: Earth and Environmental Science in 2018, Vol. 163, no. 1.

[23] Yuan, J. P., Huang, K. L., Si, Q. R., Zhou, B. L., Sheng, G. C., Tang, Y. F., "Experimental study on radiated noise characteristics of multi-stage centrifugal pump under variable speed condition," in IOP Conference Series: Earth and Environmental Science in 2019, vol. 240, no. 3.

[24] Zhang, J. F., Wang, Y. F., Yuan, S. Q., "Experimental research on internal flow in impeller of a low specific speed centrifugal pump by PIV," in IOP Conference Series: Materials Science and Engineering in 2016, vol. 129, no. 1.

[25] Venkatesh, S., Kumar, R. S., Sivapirakasam, S. P., Sakthivel, M., Venkatesh, D. and Arafath, S. Y., 2020. Multi-objective optimization, experimental and CFD approach for performance analysis in square cyclone separator. Powder Technology, 371, pp. 115-129.

[26] Kumar, R.S., Alexis, J. and Thangarasu, V.S., 2017, "Optimization of high speed CNC end milling process of BSL 168 Aluminium composite for aeronautical applications," Transactions of the Canadian society for Mechanical Engineering, 41(4), pp..609-625.

[27] Kumar, S.R., Alexis, J.S. and Thangarasu, V.S., 2017. "Experimental Investigation of Influential Parameters in High Speed Machining of AMS 4205," Asian Journal of Research in Social Sciences and Humanities, 7(2), pp. 508-523.

[28] Alexis, J. and Thangarasu, V.S., 2016. Prediction of machining parameters for A91060 in end milling. Advances in Natural and Applied Sciences, 10(6 SE), pp. 157-164.

[29] Kumar, R.S., Thangarasu, V.S. and Alexis, S.J., 2016. Adaptive control systems in CNC machining processes--a review. Advances in Natural and App.lied Sciences, 10(6 SE), pp..120-130.

[30] Suresh Kumar, R., John Alexis, S. and Thangarasu, V.S., 2015. App.lication of GA & ANN for the optimization of cutting parameters for end milling operation-A comparison. International Journal of Applied Engineering Research, 10(20).

[31] T Ramakrishnan, M Sathesh Babu, S Balasubramani, K Manickaraj, R Jeyakumar., 2021.Effect of Fiber Orientation and Mechanical Properties of Natural Fiber Reinforced Polymer Composites-A Review. paideumajournal.14 (3), pp. 17-23.

[32] Jeyakumar R, Balasubramanian K, Ramamoorthi R, Ramakrishnan T., 2021, Development of Compact Electro Gear Pump for Airborne App.lications. paideumajournal.14 (3), pp. 50-57.

[33] Ramakrishnan, T. and Sampath, P.S., 2017. Dry sliding wear characteristics of new short agave angustifolia marginata (AAM) fiber-reinforced polymer matrix composite material. Journal of Biobased Materials and Bioenergy, 11(5), pp. 391-399.

[34] Thirumalaisamy, R. and SUBRAMANI, S.P., 2018. Investigation of physico-mechanical and moisture absorption characteristics of raw and alkali treated new agave angustifolia marginata (AAM) fiber. Materials Science, 24(1), pp. 53-58.

[35] Jeyakumar, R., Sampath, P. S., Ramamoorthi, R. and Ramakrishnan, T., 2017. Structural, morphological and mechanical behaviour of glass fibre reinforced epoxy nanoclay composites. The International Journal of Advanced Manufacturing Technology, 93(1), pp. 527-535.

[36] Ramakrishnan, T. and Sampath, P. S., 2017. Experimental investigation of mechanical properties of untreated new Agave Angustifolia Marginata fiber reinforced epoxy polymer matrix composite material. Journal of Advances in Chemistry, 13(4), pp. 6120-6126.

[37] Ramakrishnan, T., Sampath, P.S. and Ramamoorthi, R., 2016. Investigation of mechanical properties and morphological study of the alkali treated agave angustifolia marginata fiber reinforced epoxy polymer composites. Asian Journal of Research in Social Sciences and Humanities, 6(9), pp. 461-472.

[38] Sathish, K., Ramakrishnan, T. and Sathishkumar, S., 2016. Optimization of turning parameters to improve surface finish of 16 Mn Cr 5 material. Advances in Natural and Applied Sciences, 10(6 SE), pp. 151-157.

[39] Ramakrishnan, T., Sathish, K., Sampath, P.S. and Anandkumar, S., 2016. Experimental investigation and optimization of surface roughness of AISI 52100 alloy steel material by using Taguchi method. Advances in Natural and App.lied Sciences, 10(6 SE), pp. 130-138.

[40] Ramakrishnan, T. and Sampath, P.S., 2016. Thermogravimetric Analysis (TGA) and the Effect of Moisture Absorption on the Mechanical Properties of New Agave Angustifolia Marginata 3 Fiber (AAMF) Reinforced Epoxy Polymer Composite Material. International Journal of Printing, Packaging & Allied Sciences, 4(5), pp. 3245-3256.

[41] Gokilakrishnan, G. and Varthanan, P.A., 2019. Development of manufacturing-distribution plan considering quality cost. International Journal of Enterprise Network Management, 10(3-4), pp. 280-304.

[42] Varthanan, P.A. and Gokilakrishnan, G., 2018. Simulation Based Swarm Intelligence to Generate Manufacturing-distribution Plan for a Bearing Industry under Uncertain Demand and Inventory Scenario. International Journal of Pure and App.lied Mathematics, 119(12), pp. 2117-2134.

[43] Gokilakrishnan, G.E., Divya, S., Rajesh, R. and Selvakumar, V., 2014. Operating torque in ball valves: a review. Int J Technol Res Eng, 2(4), pp. 311-315.

[44] Venkatesh, S., Sivapirakasam, S.P., Sakthivel, M., Ganeshkumar, S., Prabhu, M.M. and Naveenkumar, M., 2021. Experimental and numerical investigation in the series arrangement square cyclone separator. Powder Technology, 383, pp. 93-103.

[45] Venkatesh, S., Sakthivel, M., Saranav, H., Saravanan, N., Rathnakumar, M. and Santhosh, K.K., 2020. Performance investigation of the combined series and parallel arrangement cyclone separator using experimental and CFD approach. Powder Technology, 361, pp. 1070-1080.

[46] Venkatesh, S., Sakthivel, M., Avinasilingam, M., Gopalsamy, S., Arulkumar, E. and Devarajan, H.P., 2019. Optimization and experimental investigation in bottom inlet cyclone separator for performance analysis. Korean Journal of Chemical Engineering, 36(6), pp. 929-941.

[47] Venkatesh, S., Sakthivel, M., Sudhagar, S. and Daniel, S.A.A., 2018. Modification of the cyclone separator geometry for improving the performance using Taguchi and CFD approach. Particulate Science and Technology.

[48] Venkatesh, S. and Sakthivel, M., 2017. Numerical investigation and optimization for performance analysis in Venturi inlet cyclone separator. Desalination and Water treatment, 90, pp. 168-179.

[49] Venkatesh, S., Bruno Clement, I., Avinasilingam, M. and Arulkumar, E., 2017. Design of Experiment Technique for Improving the Performance of Stirling Engine. International Research Journal of Engineering and Technology, 4(5), pp. 62-65.

[50] Vennilaa, D. B., Karupp.usami, G. and Senthil, P., 2016. Analysis of different infiltration effect for selective laser sintering process through Taguchi method. Australian Journal of Mechanical Engineering, 14(3), pp. 217-223.

[51] NaveenPrabhu, V., SaravanaKumar, K., Suresh, T. and Suresh, M., 2016. Experimental investigation on tube-in-tube heat exchanger using nanofluids. Advances in Natural and Applied Sciences, 10(7 SE), pp. 272-279.

[52] Justin Dhiraviam, F., Naveen Prabhu, V., Suresh, T. and Selva Senthil Prabhu, C., 2015. Improved efficiency in engine cooling system by repositioning of turbo inter cooler. In App.lied Mechanics and Materials, vol. 787, pp. 792-796, Trans Tech Publications Ltd.

[53] Naveen Prabhu, V. and Suresh, M., 2015. Performance evaluation of tube-in-tube heat exchanger using nanofluids. In App.lied Mechanics and Materials, vol. 787, pp. 72-76). Trans Tech Publications Ltd.

[54] Prabhu, V.N. and Manigandan, N., 2014. Design and Fabrication of Solar Transport Vehicle. OSR J. Mech. Civ. Eng, 11, pp. 14-19.

[55] Manigandan, N., Naveen Prabhu, V. and Suresh, M., 2015. Experimental investigation of a brazed chevron type plate heat exchanger. International Journal of Science Technology & Engineering, 1(12), pp. 1-7.

[56] Dhiraviam, F.J., Naveen Prabhu, V. and Santhosh, M., 2017. Study the Effects of Solar Assisted Vapour Compression Air Conditioning System for Winter Applications. International Journal for Scientific Research & Development, 4(11), pp. 505-508.

[57] Manigandan, N., Naveenprabhu, V. and Devakumar, M., 2014. Design and Fabrication of Mechanical device for Effective Degreasing in Roller Bearing. Procedia Engineering, 97, pp. 134-140.

[58] Pravin, V.N.D.M.K. and Swamy, V.R.S.S.A., A Review of Evaporative Cooling of Finned and Non-Finned Heat Exchanger on Condenser.

[59] Naveenprabhu, V. and Suresh, M., 2020. Performance enhancement studies on evaporative cooling using volumetric heat and mass transfer coefficients. Numerical Heat Transfer, Part A: Applications, 78(9), pp. 504-523.

[60] Dhiraviam, F.J., Naveenprabhu, V., Satish, K. and Palanivelrajan, A.R., 2019, October. Emno.ion characteristic in CI engines using zirconium porous medium in piston head. In AIP Conference Proceedings, vol. 2161, No. 1, p. 020012. AIP Publishing LLC.
[61] Naveenprabhu, V., Dhiraviam, F.J., Gowtham, K.M., Gowtham, S., Tharick, R.A. and Arunkumar, R., 2019. Smart Hot Chamber in Refrigeration System Based on Waste Heat Recovery. Indian Journal of Science and Technology, 12, p. 20.
[62] Subramaniam, B., Natarajan, B., Kaliyaperumal, B. and Chelladurai, S.J.S., 2019. Wear behaviour of aluminium 7075—boron carbide-coconut shell fly ash reinforced hybrid metal matrix composites. Materials Research Express, 6(10), p. 1065d3.
[63] Subramaniam, B., Natarajan, B., Kaliyaperumal, B. and Chelladurai, S.J.S., 2018. Investigation on mechanical properties of aluminium 7075-boron carbide-coconut shell fly ash reinforced hybrid metal matrix composites. China Foundry, 15(6), pp. 449-456
[64] N. Balaji, S. Balasubramani, V. Pandiaraj., 2021, Fabrication and Analysis of Al6061/Al2O3/TiC Hybrid Metal Matrix Composite, Paideuma Journal of Research., Vol. 14, No 3, pp. 24-35.
[65] Balasubramani, S., Dhanabalakrishnan, K.P. and Balaji, N., 2015. Optimization of machining parameters in aluminium HMMC using response surface methodology. International journal of applied engineering research, 10(20), pp. 19736-19739.
[66] Balasubramani S, Manikandan. S Prasath. P, Suresh. D and Shanmuga Sundaram. P., 2018. "Vibration Analysis of Work Holding Devices in Composite Materials" International Journal for Scientific Research & Development, vol. 6, no. 2, pp. 2520-2523.
[67] Subramaniam, B., Purusothaman, V. R., Karupp.usamy, S. M., Ganesh, S.H. and Markandan, R.K., 2020. Review on properties of aluminium metal matrix composites. Journal of Mechanical and Energy Engineering, 4(1), pp. 57-66.
[68] Balaji, N., Balasubramani, S., Ramakrishnan, T. and Sureshbabu, Y., 2020. Experimental Investigation of Chemical and Tensile Properties of Sansevieria Cylindrica Fiber Composites. In Materials Science Forum, vol. 979, pp. 58-62, Trans Tech Publications Ltd.
[69] Balasubramani, S. and Balaji, N., 2016. Investigations of vision inspection method for surface defects in image processing techniques-a review. Advances in Natural and Applied Sciences, 10(6 SE), pp. 115-120.
[70] Ganeshkumar S, Sureshkumar R, Sureshbabu Y, Balasubramani S 2020, A Review On Cutting Tool Measurement in Turning Tools by Cloud Computing Systems in Industry 4.0 and IoI, GIS Science Journal, vol. 7, no. 8, pp. 1-7.
[71] Ganeshkumar S, Sureshkumar R, Sureshbabu Y, Balasubramani S, 2019, A Numerical App.roach to Cutting Tool Stress in CNC Turning of En8 Steel with Silicon Carbide Tool Insert, International Journal of Scientific & Technology Research, vol. 8, no. 12, pp. 3227-3231.
[72] Ganeshkumar, S., Thirunavukkarasu, V., Sureshkumar, R., Venkatesh, S. and Ramakrishnan, T., 2019. Investigation of wear behaviour of silicon carbide tool inserts and titanium nitride coated tool inserts in machining of en8 steel. International Journal of Mechanical Engineering and Technology, 10(01), pp. 1862-1873.
[73] Venkatesh, S., Sivapirakasam, S.P., Sakthivel, M., Ganeshkumar, S., Prabhu, M. M. and Naveenkumar, M., 2021. Experimental and numerical investigation in the series arrangement square cyclone separator. Powder Technology, 383, pp. 93-103.
[74] Kumar, S. G. and Thirunavukkarasu, V., 2016. Investigation of Tool Wear and Optimization of Process Parameters in Turning of EN8 and EN 36 Steels. Asian Journal of Research in Social Sciences and Humanities, 6(11), pp. 237-243.
[75] Ganesh Kumar, S., Suresh Kumar, R., Suresh Babu, M. Y. and Balasubramani, M. S., A Review of Performance Investigations in Hydrogen–Oxygen Generator for Internal Combustion Engines.
[76] Kumar, S. D. and Kumar, S.S., 2021. Effect of heat treatment conditions on ballistic behaviour of various zones of friction stir welded magnesium alloy joints. Transactions of Nonferrous Metals Society of China, 31(1), pp. 156-166.
[77] Kumar, S.D. and Kumar, S.S., 2020. Numerical and experimental ballistic performance of welded magnesium (AZ31B) plates. Emerging Materials Research, 9(4), pp. 1217-1228.
[78] Kumar, S.D., Kumar, S.S. and Kumar, K.A., 2020. Investigation of forced frequency in a commercial vehicle suspension system. Mechanics and Mechanical Engineering, 22(4), pp. 967-974.
[79] Sundaram, S. K., 2020. Experimental ballistic performance determination of friction stir welded magnesium (AZ31B) targets. Mechanics Based Design of Structures and Machines.
[80] Kumar, S. S., Kumar, S. D. and Magarajan, U., 2020. Investigation of mechanical and wear behaviour of graphene reinforced aluminium alloy 6061 metal matrix composite. Kovove Materialy-Metallic Materials, 58(5), pp. 341-349.
[81] Kumar, S. D. and Kumar, S. S., 2019. Investigation of mechanical behavior of friction stir welded joints of AA6063 with AA5083 aluminum alloys. Mechanics and Mechanical Engineering, 23(1), pp. 59-63.
[82] Magarajan, U., Arvind, D., Kannan, N. and Hemanandan, P., 2018. A comparative study on the static mechanical properties of glass fibre vs. glass-jute fibre polymer composite. Materials Today: Proceedings, 5(2), pp..6711-6716.
[83] Yessian, S. and Varthanan, P.A., 2020. Optimization of performance and emno.ion characteristics of catalytic coated ic engine with biodiesel using grey-taguchi method. Scientific reports, 10(1), pp. 1-13.
[84] Sureshbabu, Y. and AshokaVarthanan, P., 2014. Study the emno.ion characteristics of catalytic coated piston and combustion chamber of a four stroke spark ignition (SI) engine. Journal of Chemical and Pharmaceutical Sciences, JCHPS Special, (4).
[85] Sureshbabu, Y., Ashokavarthnan, P., Balasubramani, S. and Naveenprabhu, V., 2019, October. Experimental investigation on four strokes catalytic coated spark ignition (SI) engine. In AIP Conference Proceedings, vol. 2161, no. 1, p. 020041, AIP Publishing LLC.
[86] Suresh Babu, Y., Mutyalu, K. V. and Prasad, Y. S., 2012. A Relevant Document Information Clustering Algorithm for Web Search Engine. International Journal of Advanced Research in Computer Engineering & Technology (IJARCET), 1(8).

Coordination Chemistry Reviews 428 (2021) 213612

Contents lists available at ScienceDirect

Coordination Chemistry Reviews

journal homepage: www.elsevier.com/locate/ccr

Non-conventional photoactive transition metal complexes that mediated sensing and inhibition of amyloidogenic aggregates

Eththilu Babu [a], Jayaraman Bhuvaneswari [b], Kanthapazham Rajakumar [c,d], Veerasamy Sathish [c,*], Pounraj Thanasekaran [e,*]

[a] Department of Chemistry, Sri Eshwar College of Engineering, Coimbatore 641 202, India
[b] Department of Chemistry, Sri GVG Visalakshi College for Women, Udumalpet 642128, India
[c] Department of Chemistry, Bannari Amman Institute of Technology, Sathyamangalam 638 401, India
[d] Nanotechnology Research & Education Centre, South Ural State University, Chelyabinsk 454 080, Russia
[e] Department of Chemistry, Fu Jen Catholic University, New Taipei City 242, Taiwan

ARTICLE INFO

Article history:
Received 20 July 2020
Accepted 16 September 2020

This article is dedicated to the occasion of the 81st birthday anniversary of Prof. C. Srinivasan (Retired) and 70th birthday anniversary of Prof. S. Rajagopal (Retired) Madurai Kamaraj University, Madurai, India.

Keywords:
β-Amyloid aggregates
Inhibitor
Luminescent probes
Sensing
Selectivity
Transition metal complexes

ABSTRACT

Alzheimer's disease (AD), a devastating neurodegenerative disease, is associated with the abnormal accumulation and aggregation of β-amyloid proteins (Aβ) along with the deposition of high levels of Cu, Fe and Zn ions in the brain, causing neuronal cell deaths to lead the cognitive disabilities and even death. As there is a direct relationship between AD and Aβ aggregation, an intense research activity has been made to develop drug materials that serve as probes and inhibitors for controlling the pathways of Aβ peptide aggregation. However, their relatively instability in aqueous medium, tedious sample treatment, multistep syntheses, or low detection ability limit their potential applications. Therefore, the development of photoactive metal complexes for the selective detection and inhibition effects of Aβ aggregation is a thrust area in biomedical research. In this review, the use of non-conventional photoactive metal complexes including Ru(II), Re(I), Ir(III) and Pt(II) has the potential advantages of probes for monitoring and inhibiting the fibrillation as well as the toxicity of Aβ over conventional dyes such as Thioflavin T (ThT). The geometry, multiple electronic/spin states and redox nature of metal centres have made them tunable properties. Upon binding to the Aβ peptide aggregates, they exhibit promising potential as anti-AD agents due to their fascinating photophysical properties include red emissions, large Stokes shifts, and long lifetimes, which differentiate the competitive binding of other short-lived fluorescent molecules *via* photoluminescence, and time-resolved measurements. In addition, metal complexes display their remarkable selectivity and superiority over ThT. Competition study between photoactive metal complexes and ThT on fibrillation process show their effective binding of metal complex with $A\beta_{42}$ fibrils by hindering the ThT binding to give higher binding constants than that of ThT. Computational studies predicted a hydrophobic domain between amino acid binding sites and the functional group of photoactive metal complexes *via* different noncovalent interactions. Thus, attractive characteristics of photoactive metal complexes could influence remarkable evolutions in new dimensions, which in turn address current challenges in the clinical use of the detection and inhibition of Aβ fibrils.

Abbreviations: Aβ, amyloid-β; AD, alzheimers disease; AFM, atomic force microscopy; AIEE, aggregation induced emission enhancement; aminephen, 1,10-phenanthrolin-5-amine; APP, amyloid- β precursor protein; Apy, 4-aminopyridine; αS, α-synuclein; biq, 2,2′-biquinoline; bpy, 2,2′-bipyridine; BSA, bovine serum albumin; bzimpy, 2,6-bis-(benzimidazol-2′-yl)pyridine; bzq, benzoquinone; chlorophen, 5-chloro-1,10-phenanthroline; CLSM, confocal laser scanning microscopy; CR, congo red; dbbpy, 4,4′-diphenyl-2,2′-bipyridine; dmbpy, 4,4′-dimethyl-2,2′-bipyridine; dcbpy, 4,4′-dicorboxy-2,2′-bipyridine; dmdpphen, 2,9-dimethyl-4,7-diphenyl-1,10-phenanthroline; DMPO, 5,5-dimethyl-1-pyrroline N-oxide; dnbpy, 4,4′-dinonyl-2,2′-bipyridin; DNPH, 2,4-dinitrophenylhydrazine; dpphen, 4,7-diphenyl-1,10-phenanthroline; dppz, dipyrido[3,2-a:2′,3′-c]phenazine; dppzidzo, dipyrido-[3,2-a:2′,3′-c]phenazine-imidazolone; FLIM, fluorescence lifetime imaging; hAChE, human acetylcholinesterase; hBuChE, human butyrylcholinesterase; HSA, human serum albumin; IM-MS, ion mobility-mass spectrometry; MHB, Michler's hydrol blue; MLCT, metal to ligand charge transfer; MRI, magnetic resonance imaging; 1,4-NVP, 4-(1-naphthylvinyl)pyridine; PD, parkinson disease; PDGF, platelet derived growth factor; PET, positron emission tomography; phen, 1,10-phenanthroline; phq, 2-phenylquinoline; PIB, pittsburgh compound B; PL, photoluminescence; ppy, 2-phenylpyridine; RIR, restricted intramolecular rotation; Py, pyridine; SEM, scanning electron microscope; SPECT, single photon emission computed tomography; SSNMR, solid-state nuclear magnetic resonance; TAE, tetraarylethylene; TEM, transmission electron microscope; TRES, time-resolved emission spectra; ThS, thioflavin S; ThT, thioflavin T, TIRFM, total internal reflection fluorescence microscopy.

* Corresponding authors.
E-mail addresses: vsathish1985@gmail.com (V. Sathish), ptsekaran@gmail.com (P. Thanasekaran).

https://doi.org/10.1016/j.ccr.2020.213612
0010-8545/

Contents

1. Introduction

Protein misfolding (*or protein conformational*) disease, a group of pathological states, is a failure of a specific peptide's or protein's native functional conformational state, that are associated with the conversion of their soluble states into higher-order protein aggregates, known as amyloid fibrils (Fig. 1) [1-5]. These fibrils adopt diverse cross β-sheet conformations where the β-strands that are stabilized by backbone hydrogen bonds with a distance of 4.8 Å, are parallel to the fibril axis [6]. The different length of pairs of β-sheets i.e., protofilament, with a distance of 10–11 Å intertwine that make mature fibril via hydrophobic, van der Waals,π– π stacking and hydrogen bonding interactions to organize parallel or antiparallel to each other [7,8]. (Fig. 2). In general, aggregation of the proteins may precede either the formation of disordered, amorphous aggregates where no ordered intermolecular interaction can be found or ordered amyloid fibrils. For amyloid fibril formation, self-association of peptide monomers into oligomers generate critical nucleus and subsequently, elongation of nucleus takes place into sigmoidal aggregation kinetics. A number of peptides such as insulin, β-lactoglobulin, etc., self-assemble into higher-order fibrillar structures to form spherulites, spherical structures and hydrogels [9,10].

In fact, many amyloid fibrils have been shown to be associated with >20 diseases, including Alzheimer's disease (AD), Parkinson's disease (PD), Type II diabetes, cataract etc. Alzheimer's disease (AD) is a fatal neurodegenerative disease, which leads to progressive loss of memory with unable to conduct regular activities in a day-to-day life and finally results in death [11,12]. In the United States itself, 39 million peoples are suffered by AD, and expected to soar about 90 million in 2050, if not controlled [13]. The aggregates of extracellular senile amyloid plaques (AP), and intraneuronal neurofibrillary tangles (NFT), the neuropathological hallmarks of AD, alter the level of neurotransmitters in the brain which are responsible to shrinkage of the brain size, leading to trigger AD [14]. Abnormally folded protein aggregates such as amyloid-β (Aβ) aggregate, that are generated from the cleavage of amyloid precursor protein (APP) by γ-secretase [15,16], consist of 39–43 residues with a hydrophilic N-terminal domain of metal binding sites and a C-terminal hydrophobic part [8]. In addition, oxidative stress may also lead to produce free radicals which can not only influence metabolism but also promote Aβ aggregation, preceding to produce AD [17]. Besides, AD is caused by the reduced synthesis of a neurotransmitter called acetylcholine in neurons [18-21]. The histopathological studies of brain confirmed the deposition of Aβ plagues in post-mortem analysis, and so far, no drugs have been invented to prevent the β-amyloid accumulation [22,23]. Hence, the onset of AD is still under debate.

Probing the Aβ fibrillation process is an exciting area of biomedical research and the remedial measurement for the AD treatment to inhibit the formation of amyloid fibrils from the self-assembly of monomeric Aβ peptides [24,25]. In connection with tracking amyloid fibrils, the structural analysis for the formation and inhibition of amyloid fibrils can be viewed by electron microscopic techniques such as AFM and TEM [26,27]. Positron emission tomography (PET), Single Photon Emission Computed Tomography (SPECT) and magnetic resonance imaging (MRI) techniques are also used to furnish the diagnostic information on the amyloid plaques in the

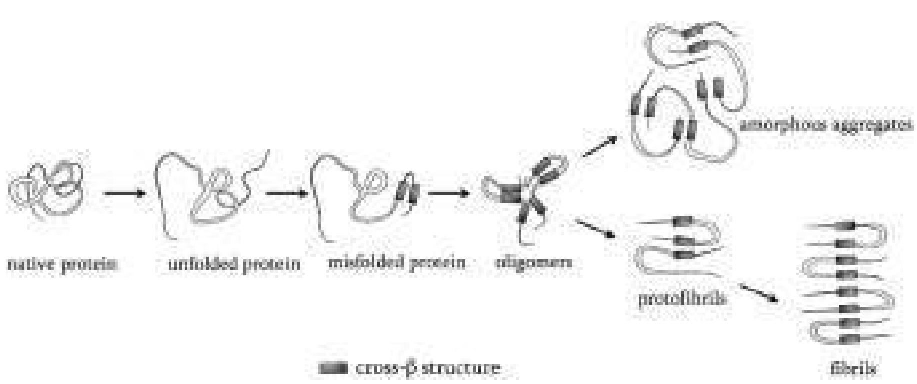

Fig. 1. Cartoon representation of protein misfolding and aggregation processes. Reproduced with permission from ref 5. Copy right (2008) John Wiley & Sons.

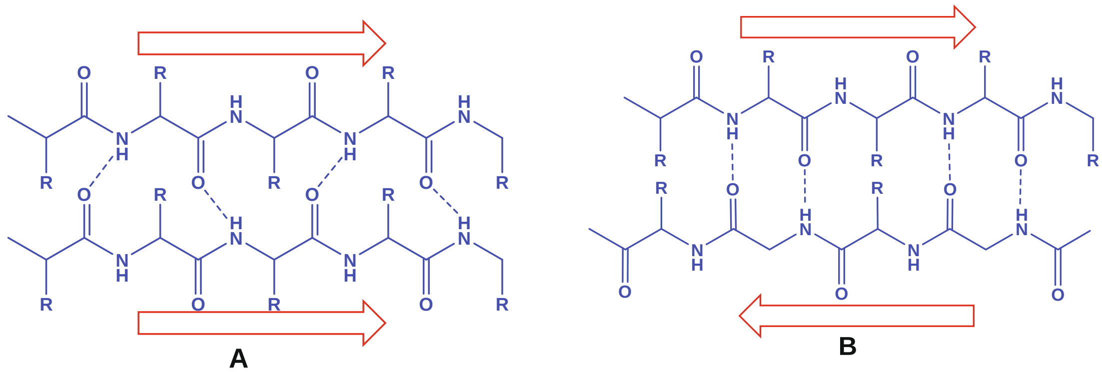

Fig. 2. (A) Parallel and (B) antiparallel β-sheets.

brain [28,29]. Moreover, the solid-state NMR (SSNMR) spectroscopy [30], 2D nuclear magnetic resonance (NMR) spectroscopy [31], and ion mobility-mass spectrometry (IM-MS) [32] are also providing the structural information on the molecular interactions between the binding of Aβ fibrils, that are amenable to single crystal X-ray diffraction analysis [33]. Out of these techniques, fluorescence spectroscopy is a powerful tool for monitoring the Aβ fibrillation owing to its high selectivity, sensitivity, simplicity, negligible background noise and wide dynamic range of bioimaging/biosensing studies [34,35].

Because of their intriguing photophysical behaviour, classical dyes such as Thioflavin T (ThT) and Congo red (CR) [36-39], radiolabeled benzothiazole compounds such as ^{11}C-PIB (Pittsburgh compound B), stilbene derivatives [40,41], Michler's hydrol blue (MHB) [42], cucurbit[7]uril [43], *p*-sulfonatocalixarenes [44], nanoparticles [45] and quantum dots [46] have been employed as probes to inhibit/sensing Aβ peptide aggregation. However, most fluorescent organic molecules have only limited potential for such applications due to their short excited-state lifetimes, small Stokes shifts, and sensitivity to photobleaching [47,48]. On the other hand, compared to organic molecules, transition metal complexes offer some noticeable features *viz.* (a) they exhibit tunable wavelengths from blue to red, high quantum yields, and long phosphorescent lifetimes [49], (b) optical properties that can be finely tuned by the selecting suitable ligands [50], (c) absorption and emission behaviours in the visible region [51], (d) three-dimensional structural features bearing a variety of coordination numbers and geometries of metal complexes results in the specific interactions between metal complexes and biomolecules [52], and (e) owing to the planar or octahedral structures, they tend to form noncovalent interactions, such as hydrogen bonding, hydrophobic, π–π stacking interactions, which play key roles on binding with biomolecules [53].

Given that many transition-metal complexes display rich photophysical and photochemical properties, which can act as an indicator of the interactions of these complexes with biological molecules, these metal complexes have been widely applied for studying their potential applications toward (i) good cellular uptake ability, (ii) inhibition of tumour growths, (iii) therapeutic activity through the simultaneous targeting and detection of a specific biomolecule using antibodies, peptides, and aptamers, resulting in increased selectivity and reduced side-effects, and (iv) promising cytotoxicity in therapeutically resistant cancer lines. Current developments in the field of photoactive transition metal complexes based- anticancer drugs, bioimaging, cancer diagnostics and theranostics and therapeutics have been efficiently reviewed by the research groups of Ma [54], Chen [55], and studied by the research groups of Tang and Liu [56], and Thomas [57]. Compared to these photoactive transition metal complexes, first-row transition metal complexes play several roles in biological processes and in medicine, but can be toxic in high concentrations. They are very sensitive to their environments and do not exist as free ions in cells [58]. Typically, the first-row transition metal ions are bound to proteins with high affinity in the cellular system so that it is difficult to separate metal ions from the proteins [59]. Especially, the dysregulation of first-row transition metals, notably copper, zinc and iron through genetic, environmental or age-related factors, promoted aggregation, and hence disease onset. The exact role and behaviour of these metals in relation to AD is reviewed in detail elsewhere [60-63]. Therefore, the choice of first-row transition metal complexes for this study is mostly negligible. However, some first-row transition metal complexes such as V(V), Co (II), and Co(III) complexes and metal ions such as Cu(I), Cu (II), Fe(II) and Zn(II) ions undergo oxidation and hydrolysis of Aβ and coordination to Aβ, respectively, for modification of Aβ aggregation pathways [64].

Inspired by these characteristics, more interest has been focused recently on the development of luminescent transition metal complexes for the diagnosis and treatment of neurogenerative diseases. The photophysical properties of these metal complexes are fine-tuned by incorporation of various auxillary ligands into the metal center and the shifts upto near-infrared region, which is more favorable for biological studies. There are several excellent reviews, perspectives, and view point, summarizing the sensing and inhibition abilities of transition metal complexes against amyloid aggregation [24,64-67]. For example, very recently, Marti and his co-workers [68] reviewed excellently the recent advances in developing luminescent organic materials, nanoparticles and some transition metal complexes for the sensing and detection of amyloid aggregates, and subsequently studied the amyloid conformations through *in vitro*, *ex vivo*, and *in vivo* applications. Mohanty et.al [69] highlighted the application of fluorescent supramolecular hosts as well as macrocyclic receptors toward the optical detection, inhibition and disintegration of amyloid fibrils. Through Raman spectroscopy, Lednev and his group [70] accounted on probing the formation and mechanism of amyloid fibrils. Despite non-emissive metal complexes are potential therapeutic agents for AD because they could sequester metal ions from the Aβ aggregates and reverse the aggregation [64-67], impact of these metal complexes was tested with fluorescent ThT staining, which is a highly sensitive probe for monitoring and visualization, on the aggregation of Aβ via photoluminescence technique. However, using this technique, there are still some drawbacks including the selectivity of the light-switching effect, interaction of exogeneous or diverse compounds with free ThT signal, leading to quench its emission or affect the binding of ThT toward fibrils, lack of high-resolution models that complicate the investigation of the binding mode to fibrils, unclear binding mode of fibrils, etc. In order to overcome these limitations, up to now, the potential scope of luminescent *d*-block transition metal complexes, which are alternative candidates to organic materials and non-luminescent metal complexes towards sensing and inhibition of amyloid aggregation is still under investigated and needs to be explored extensively. Therefore, it is worthwhile to consider collectively the potential applications of photoactive transition metal complexes mediated sensing as well as inhibition of amyloid fibrils. Distinct from previous reviews, this review provides the efforts that have been achieved on the sensing, and/or inhibition of amyloid aggregates exclusively based on *d*-block photoactive transition metal complexes. In this review article, we give a brief introduction on the advantages of luminescent transition metal complexes and explain why these complexes are promising candidates in sensing and inhibition of Aβ aggregates compared to other dyes. We also summarize the current advances in the development of Aβ-targeted luminescent d^6-based transition-metal complexes such as Ru(II), Re(I), Ir(III) and Pt(II) complexes based on their potential applications. The examples highlighted herein are only representative of the significant opportunity that metal complexes offer for exploring structural design, integration of active targeting moieties such as peptides, aptamers, etc., mode of action toward Aβ aggregation and biomedical applications. The challenges and suggestions for the future development of this field will also be highlighted. The information presented in this review is summarized in Table 1.

2. Sensing and inhibition of β-amyloid aggregation based on d-block arena

2.1. Ruthenium(II) complexes

Ruthenium(II) complexes have proven to be especially suitable for use in medical applications owing to their unique and versatile biochemical properties such as large Stokes shifts, long lifetimes, light-switching properties, favourable ligand exchange properties, and their ability to mimic iron when binding to certain biological molecules [71,72]. Therefore, the interaction of ruthenium compounds with biomolecules often leads to the development of ruthenium-based probes for sensing and inhibition of β-amyloid aggregation.

For instance, a team of Marti demonstrated first time that $[Ru(bpy)_2(dppz)]^{2+}$ (bpy = 2,2′-bipyridine; dppz = dipyrido[3,2-a:2′,3′-c]phenazine) complex (**1**) displayed unconventional “light-switching” process upon interacting with fibrillar amyloid-β aggregates in real time [73]. This Ru(II) complex, **1** showed a poor emission upon interacting with monomeric Aβ due to the weak interaction. Whereas, the interaction of **1** with Aβ fibrils led to a 50-fold enhancement in the emission intensity. This can be ascribed to the strong interaction with fibrils which makes the microenvironmental change where the rotation of dppz ligand in **1** was prevented to prefer luminescent state. Emission turn-on response of **1** after interacting with fibrils showed a sigmoidal curve, which is consistent with the ThT fluorescent response toward fibrils (Fig. 3a). The TEM image of fibril aggregates after 7 h incubation obtained from assays showed the development of fibrils and larger structures, i.e., fibril networks (Fig. 3b,c). Time-resolved measurement of Aβ assay (Ru(II) complex and Aβ fibrils in the presence of fluorophore, rhodamine B) revealed that transient spectrum of **1** showed a biexponential decay with lifetimes of 21(19%) and 221 ns (81%) along with the fluorescent background of the transient spectrum of the rhodamine B (1.6 ns). This study confirmed the detection ability of **1** toward Aβ fibrils that can be easily distinguished from a short-lived fluorescent rhodamine B background. Further studies on steady-state PL and time-resolved emission spectra (TRES) also supported the Aβ fibril detection ability of **1** over rhodamine B. Following this study, the authors [74] applied docking and molecular dynamics study for the sensing behavior of **1** toward Aβ fibrils. They found that hydrophobic domains of Val18 and Phe20 in Aβ fibrils that can efficiently hide from water by binding, were mostly responsible for the effective binding with **1** to turn-on its luminescence behavior and generate the “light switch” effect.

In another work, the same group applied $[Ru(phen)_2(dppz)]^{2+}$ (phen = 1,10-phenanthroline) (**2**) to sense α-synuclein amyloidogenic aggregates in Parkinson’s disease (PD) *in vitro* and in cells [75]. Compound **2** is also non-luminescent in solution. However, the light-switching effect of **2** displayed a minimal photoluminescence with monomer, but an 18-fold increase in intensity when mixed with αS fibrils by keeping its emission maxima remained unchanged. This emission enhancement that caused by a strong binding of **2** with αS fibrils via hydrophobic interaction was about two orders of magnitude greater than that of compound **1** under the same experimental condition. Real-time αS peptide aggregation monitoring with a photoluminescent **2** displayed a classic sigmoidal curve, showing the typical lag, elongation and equilibrium phases of amyloid formation, which are consistent with AFM and TEM images. Flow cytometry studies revealed that human neuroglioma cells (H4) treated **2** showed an increase in emission intensity because of binding with αS fibrils that overexpressing αS (H4/α-syn-GFP), a reporter for disease-associated phenotypes while untreated H4 cells did not exhibit a noticeable emission. Furthermore, addition of MG-132, an inhibitor of proteasomal degradation, to H4 or H4/α-syn-GFP cells treated **2** promoted the emission intensity dramatically (Fig. 4). This can be attributed to the binding of **2** with hydrophobic site of accumulated granular αS aggregates dispersed throughout MG-132 treated H4 cells, as evidenced by microscopy images. Fluorescence microscopy images revealed that colocalization of GFP (fluorescence) and **2** (photoluminescence) in H4 and H4/α-syn-GFP cells showed a positive correlation purely with high emission intensity of **2**. Since the fluorescence of GFP did not overlap with emission of **2**, compound **2** can be used to colocalize with any type of GFPs. This work seems to be the first report on the study of αS fibrilization or intracellular protein aggregation using a metal complex.

Another light-switching Ru(II) complex, $[Ru(phen)_2dppzidzo]^{2+}$ (phen = 1,10-phenanthroline; dppzidzo = dipyrido-[3,2-a:2′,3′-c] phenazine-imidazolone) (**3**), reported by Yao and co-workers [76] had shown promise in probing tau R3 peptide aggregation. During R3 aggregation induced by heparin, the emission intensity growth rate of **3** appeared to be small compared to Thioflavin S (ThS), indicating that aggregation process was not accelerated or hindered in the presence of **3**. Almost 95% of emission intensity of **3** was enhanced after the addition of **3** into the aggregates of tau R3 peptide. TEM supported the findings that compound **3** offered better results in terms of reliable, accurate and easier for monitoring fibrillization, which was in good agreement with the luminescence and light scattering data (Fig. 5). The presence of large Stokes shift (206 nm) and long life-time (154 ns) made compound **3** easier to differentiate background emission as well as detect fibrils via a time-gating method. Interestingly, upon R3 aggregation induced by heparin, the emission intensity growth rate of **3** was high compared to other “light switch” $[Ru(phen)_2dppz]^{2+}$ complex, showing its good sensitivity toward R3 filaments. In addition, Compound **3** can be used to distinguish tau R2 and R2-C291A mutant peptides based on the emission intensity of **3** which was obtained from different aggregation time of these peptides. Molecular docking study showed that binding of **3** with negatively charged residues produced hydrophobic protection of **3** to enhance its luminescence.

Table 1
Photophysical properties, target protein, size of fibrils, binding constant, detection limit and lifetime data for the photoactive metal complexes to the target proteins.

Compound No.	λ_{em}^{max}, λ_{ex} (nm)	Change in emission intensity	Stokes shift (nm)	Target protein & Buffer/solvent	Size of amyloid fibrils, (nm)	Detection Limit	Biological samples/Cells	Binding constant (M^{-1})	lifetime (ns)	Ref.
1	620,440	50-fold enhanced	180	amyloid-β (PBS)	NA	NA	NA	NA	21 & 221[#] 185[§]	74
2	640,440	18-fold enhanced	190	α-synuclein (PBS)	NA	NA	human neuroglioma cells (H4) and H4/α-syn-GFP cells	NA	–	76
3	610, 404	~15-fold enhanced	206	Tau (Tris HCl)	NA	NA	NA	NA	154[§]	77
4	625, 410	~10-fold enhanced	~210	Insulin (Tris HCl)	NA	NA	NA	NA	–	78
5	625, 410	~15-fold enhanced	~210	Insulin (Tris HCl)	NA	NA	NA	NA	–	78
7	650, 480	No enhanced emission	~200	amyloid-β (*PBS*)	NA	NA	Neuro2A Cells	NA	129.3 &1.23[§]	79
8	640, 460	decreased (monomers, oligomers) 15 fold enhanced (fibrils)	~180	amyloid-β (PBS)	27[a]	50 nM	NA	4.1×10^{6}	–	80
9	600, 452	Enhanced emission	148	amyloid-β (*PBS*)	137.6[c]	NA	PC12 cells	NA	–	82
10	420,330	~10-fold enhanced	90	amyloid-β (*PBS*)	NA	2.0 μM.	NA	2.2×10^{5}	–	87
11	420,330	~10-fold enhanced	90	amyloid-β (*PBS*)	40[b]	2.0 μM.	NA	2.0×10^{5}	–	87
12	484, 380	13-fold enhanced	101	Aβ42 fibrils (PBS)	NA	NA	NA	[d]276 ± 31.9 nM	–	90
13	581,469	34-fold enhanced	114	Aβ42 fibrils (PBS)	228[c]	NA	NA	[d]137 ± 18 nM	–	90
14	641,494	19-fold enhanced	148	Aβ42 fibrils (PBS)	NA	NA	NA	[d]217.4 ± 26.3 nM	–	90
16	560, 362	18-fold enhanced	~198	amyloid-β (PBS)	NA	NA	NA	NA	–	94
17	491,365	134-fold (fibrils) & 56- fold (monomers) enhanced	~130	$A\beta_{1-40}$ fibrils & monomers (PBS)	NA	NA	Neuroblastoma cells (SH-SY5Y)	NA	–	98
32	540,360	6-fold (monomer) and 12-fold (fibril) enhanced	180	$A\beta_{1-40}$ monomers & fibrils (PBS)	NA	NA	Neuroblastoma cells (SH-SY5Y)	NA	–	100
33	540,360	11-fold (monomer) and 18-fold (fibril) enhanced	180	$A\beta_{1-40}$ monomers & fibrils (PBS)	NA	NA	Neuroblastoma cells (SH-SY5Y)	NA	–	100
34	587,449	~180-fold enhanced	NA	Aβ peptide (DMSO-H_2O)	NA	NA	murine Neuro-2a (N2a) neuroblastoma cells	NA	5.8[§]	101
35	587,452	Enhanced emission	NA	Aβ peptide (DMSO – H_2O)	NA	NA	murine Neuro-2a (N2a) neuroblastoma cells	NA	11[§]	101
36	589,446	Enhanced emission	NA	Aβ peptide, α -Syn, and hIAPP (DMSO- H_2O)	NA	NA	murine Neuro-2a (N2a) neuroblastoma cells	[d]1.6×10^{-4} (monomers), [d]2.6×10^{-4} (oligomers), [d]7.1×10^{-4} (fibrils)	4.8[§]	101
37	573,441	Enhanced Emission	NA	Aβ peptide (DMSO-H_2O)	NA	NA	murine Neuro-2a (N2a) neuroblastoma cells	NA	4.4[§]	101
38	650,440	~10-fold enhanced	NA	Bovine insulin (PBS)	NA	NA	HeLa Cells	5.46×10^{4}	120[§] & 220[#]	105
39	665,440	~2-fold enhanced	NA	Bovine insulin (PBS)	NA	NA	NA	NA	–	105
40	675,440	No changes	NA	Bovine insulin (PBS)	NA	NA	NA	NA	–	105

[a] From AFM image.
[b] From TEM image.
[c] From DLS study
[d] Dissociation constant, K_d; NA = Not available.
[#] Presence of amyloid fibrils.
[§] Without amyloid; PBS- Phosphate buffer saline.

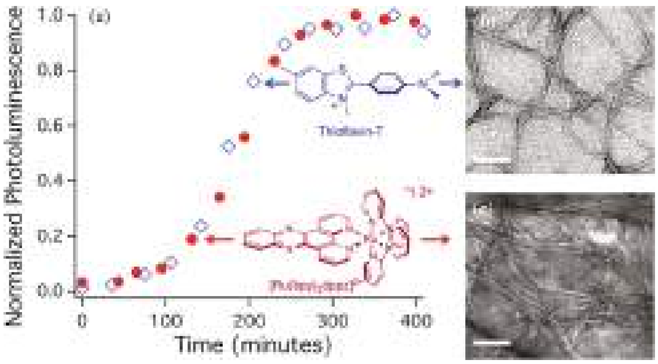

Fig. 3. (a) Real-time assay of Aβ fibrillization by ThT (blue) and compound **1** (red). TEM images of Aβ fibrils incubated in (b) ThT and (c) compound **1** after 7 h. Scale bar = 100 nm. Reproduced with permission from ref 74. Copy right (2011) American Chemical Society.

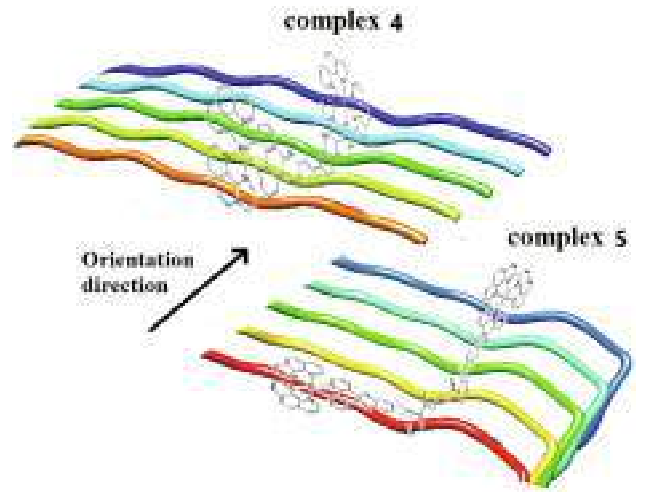

Scheme 1. Schematic representation of binding mode of compounds **4** and **5** at the surface of amyloid fibrils. Reproduced with permission from ref 78. Copyright (2014) Elsevier B.V.

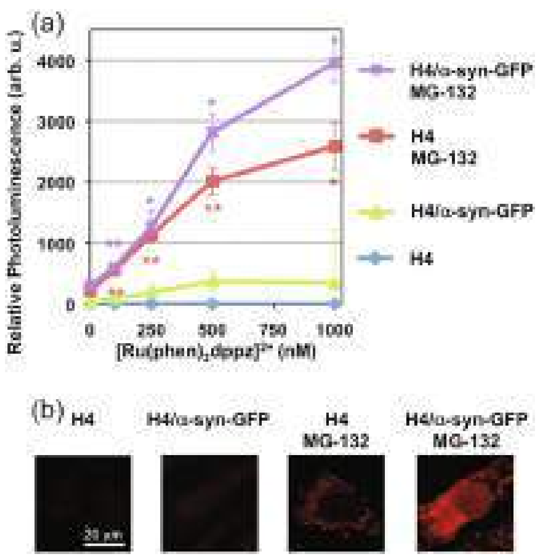

Fig. 4. (a) Relative emission intensity of H4 and H4/α-syn-GFP cells incubated with compound **2** in the absence and presence of MG-132. (b) Flow cytometry images of H4 and H4/α-syn-GFP cells incubated with compound 2 in the absence and presence of MG-132 (2 μM) for 16 h (*p < 0.05, **p < 0.005). Reproduced with permission from ref 76. Copyright (2012) American Chemical Society.

In 2014, Hanczyc reported that two binuclear ruthenium(II) complexes, [μ-(11,11′-(bidppz)(phen)$_4$Ru$_2$]$^{4+}$ (**4**) and [μ-C4-(cpdppz)(phen)$_4$Ru$_2$]$^{4+}$ (**5**) are promising candidates for sensing the amyloid fibrils using linear dichroism (LD) and fluorescence spectral techniques [77]. Complexes **4** and **5** were weakly luminescent at ~ 625 nm. Upon interacting with amyloid fibrils, rigid linker containing compound **4** showed a moderate emission while flexible linker containing compound **5** displayed luminescence enhancement. Linear dichroism studies of **4** and **5** showed that their transition dipole moments were predominantly oriented along the long axis of the molecules with λ^{ab}_{max} at 425 and 375 nm for **4** and **5**, respectively, during interaction with amyloid fibrils, which is in good agreement with previous study [74]. Based on LD and fluorescence data, it can be inferred that flexible compound **5** moved in between laminated β-sheets to force the dppz ligand inside the hydrophobic structure of fibrils, resulting in enhanced luminescence whereas rigid compound **4** preceded quenching owing to its binding geometry that differs from that of **5** (Scheme 1). The flexible linker containing compound **5** displayed a moderate photoluminescence while exciting at 800 nm using a two-photon pulse technique, which makes it attractive candidate for detecting amyloid fibrils in advanced multiphoton technique.

Carlos et al [78] designed a strategy that introduction of hydrophobic and hydrophilic moieties in luminescent Ru(II) complex might synergically recognize specific sites of fibrillar aggregates. For this study, they selected two Ru(II) complexes, cis-[Ru(phen)$_2$(Apy)$_2$]$^{2+}$ (Apy = 4-aminopyridine) (**6**) and cis-[Ru(phen)$_2$(3,4-Apy)$_2$]$^{2+}$ (3,4-Apy = 3,4-aminopyridine) (**7**) for

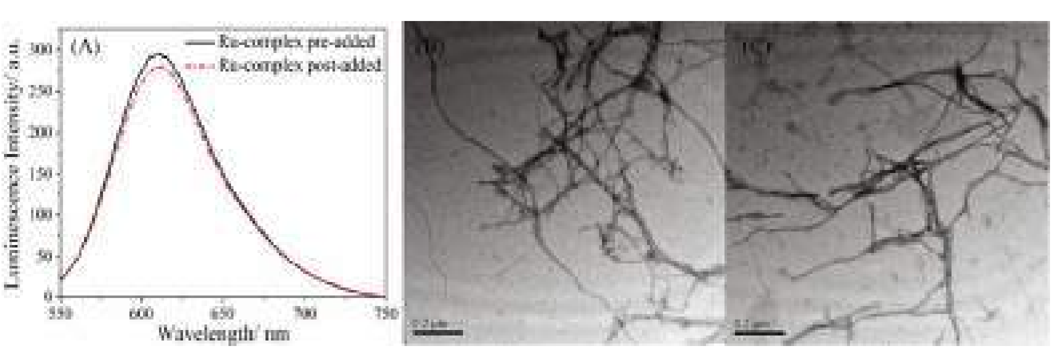

Fig. 5. (A) Emission response of compound **3** (λ_{ex} = 404 nm); the complex **3** added before the R3 aggregation process (black curve) and and the complex **3** added after the R3 aggregation (red curve). TEM images of R3 aggregation promoted by heparin in the (B) absence and (C) presence of compound **3**. Reproduced with permission from ref 77. Copyright (2015) Royal Society of Chemistry.

investigating amyloid proteins. Compound **7** featured a strong absorption in the visible region and displayed a ^{3}MLCT-based emission at 650 nm with a Stokes shift of 200 nm and a long life-time of 129.3 ns, indicating its biological applications against self-quenching and competitive fluorescent biomolecules. Confocal laser scanning microscopy revealed that these compounds were internalized into the cytoplasm of Neuro2A cells without considerable toxicity. Enzyme inhibitory assay results showed that these complexes behaved as dual inhibitors of human recombinant hAChE, and butyrylcholinesterase (hBuChE) *via* binding with more catalytic active sites. It is expected that planar aromatic 1,10-phen in **6** and **7** preferred π–π interactions with Phe295 while Apy that hindered away from hydration effects favored cation–π interactions with Trp286. Thus, these two ligands are more responsible for the interaction of compounds **6** and **7** with these enzymes. Oxidative stress study revealed that only compound **7** was able to compete with 5,5-dimethyl-1-pyrroline N-oxide (DMPO) for hydroxyl radical, showing the significance of the meta-position of amino group in pyridyl ring of **7** toward antioxidant responsibility. Compounds **6** and **7** displayed not only to differentiate the Aβ background fluorescence but also enabled in the real time self-aggregated Aβ images compared with the results of ThT, as revealed by fluorescence lifetime imaging (FLIM) technique (Fig. 6). In addition, the images of ordered structure of protofibrils and globular structures in the $A\beta_{1-40}$ and short fragment $A\beta_{15-21}$, respectively, can also be easily identified through FLIM experiment, which is first reported in this study.

Rajagopal and co-workers [79] investigated the simple and selective sensing and inhibition of amyloid-β aggregates using a light-switching aptamer–ruthenium(II) complex, [Ru(dmbpy)(dcbpy)dppz)] (**8**) ((dmbpy = 4,4′-dimethyl-2,2′-bipyridine, dcbpy = 4,4′-dicarboxy-2,2′-bipyridine) (Scheme 2). In this strategy, sterically hindered ligands that can decrease in binding with aptamers or dissociate upon the addition of targets were incorporated into Ru(II) centre to get a low energy absorption and inhibit amyloid-β fibrils. Luminescence assay showed that steric ligands containing complex **8** was a weak luminescent at ~640 nm, but upon incorporation of RNA aptamer, it showed emission enhancement with a 10 nm blue shift. Addition of amyloid β into complex **8** resulted in decrease in its luminescence owing to the binding of amyloid-β monomer and oligomers as well as the interaction of

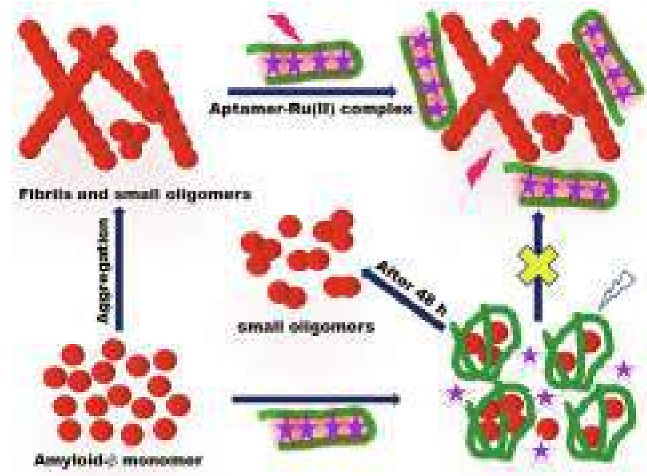

Scheme 2. Schematic illustration of compound **8** induced the formation and inhibition of fibrils. Reproduced with permission from ref 80. Copyright (2015) Elsevier B.V.

solvent molecules with a displaced complex **8**. At the same time, the interaction of **8** with amyloid monomers did not show any appreciable change in the emission intensity. On the other hand, once fibrils formed in the solution, compound **8** underwent light switching behavior, i.e., its intensity was enhanced while binding with fibrils. It exhibited a binding constant of 4.1×10^6 M^{-1} with a detection limit of 50 nM, which showed a better sensitivity than that of a previously reported compound [80]. AFM studies confirmed the morphology of amyloid fibrils with different width sizes in the range of 20, 23 and 27 nm, and different lengths in the range from 500 nm to 1 μm. However, after 48 h incubation with RNA aptamer, the growth of fibrils was inhibited and reduced to 10–20 nm sized oligomers. This work was the first report on the label free Ru(II) complex containing aptamer to sense and inhibit amyloid-β fibrils.

Using the potential photoactive tris(2,2′-bipyridine)ruthenium (II), $[Ru(bpy)_3]^{2+}$ (**9**), Park and co-workers [81] demonstrated the photodissociation of β-amyloid aggregates through oxidative damage into small, nontoxic fragments (Scheme 3). It is known that ThT

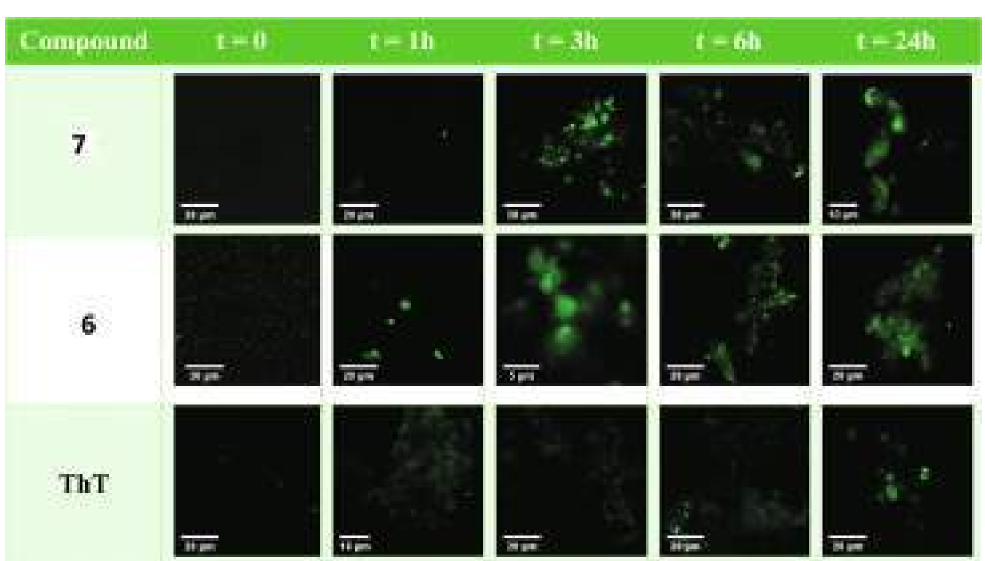

Fig. 6. Confocal images of $A\beta_{1-40}$ treated compounds **6**, **7** and ThT at different time intervals. Reproduced with permission from ref 79. Copyright (2016) American Chemical Society.

dye showed enhanced fluorescence at 485 nm upon binding with β-amyloid aggregates. In order to confirm the visible light photo-induced disassociation of Aβ aggregates, compound **9** was treated with ThT fluorescence of Aβ aggregates and the change in emission intensity of ThT and **9** was analysed. In dark condition, compound **9** did not cause any Aβ aggregates dissociation. In addition, LED light irradiation of ThT fluorescence of Aβ aggregates without **9** did not produce any noticeable changes in the fluorescence. However, addition of **9** resulted in the decrease of ThT fluorescence as well as increase of emission intensity of **9** at 600 nm under visible light irradiation. This can be ascribed to the restrained intramolecular motions of **9** in Aβ aggregates that can reduce the non-emissive energy loss as well as hydrophobic domain inside the Aβ aggregates, leading to reduce the accessibility of water molecules to the complex **9**. A significant decrease in hydrodynamic size of Aβ aggregates from 818.2 and 293.7 nm to 137.6 nm was observed upon treatment with **9**, as revealed by DLS study. AFM images after 24 h incubation of Aβ aggregates treated **9** under light irradiation dominated the formation of small amyloidic fragments in the area <0.2 × 10^6 nm^2. Furthermore, FT-IR and CD profiles showed that photo-induced complex **9** disassembled Aβ aggregates through disorder and loss of β-sheet contents. Exposure of a solution containing Aβ peptides treated **9** to a visible light irradiation in the presence of 2,4-dinitrophenylhydrazine (DNPH) that may bind with –C═O group of oxidized proteins, caused the oxidative damage of Aβ peptides by generating ROS, which was confirmed by MALDI-TOF MS study. *In vitro* studies showed that PC12 cells incubated with a solution containing Aβ aggregates treated **9** enhanced a remarkable viability of 80%, while Aβ monomers treated **9** induced a slightly detectable cytotoxicity under light illumination. The authors concluded that *in vivo* study is necessary to verify therapeutic ability of **9** for clinical uses.

2.2. Rhenium(I) complexes

Re(I) complexes exhibit immense potentials such as long emission lifetimes, photostability, phosphorescence with a large Stokes shift, environment-sensitive luminescence, high membrane permeability, stability under physiological conditions, etc. [50,82].

Aggregation induced emission (AIE)-based fluorescent probes are perfect materials for the detection of Aβ fibrils owing to the emission enhancement that are attributed to the binding of proteins [83,84]. In 2014, Rajagopal and his group found that two Re(I) complexes, $[\{Re(CO)_3(1,4\text{-NVP})\}_2(\mu_2\text{-OR})_2]$ (1,4-NVP = 4-(1-naphthylvinyl)pyridine (1,4-NVP); **10**, R = C_4H_9; **11**, $C_{10}H_{21}$) comprising of long alkyl chains and photoisomerizable 1,4-NVP ligand were able to sense amyloid fibrils [85]. These complexes had excellent photo-switching and aggregation induced emission enhancement properties [86,87]. Compounds **10** and **11** exhibited a weak emission. Upon interaction with amyloid protein, the fluorescence was enhanced drastically owing to the formation of fibrils. (Fig. 7) This enhanced emission was ascribed to π-π stacking interaction between naphthalene moiety in **10** and **11** and PHE19 and PHE4 moieties in fibrils, which is corroborated by molecular docking studies. The binding constant values obtained from Scatchard plots were found to be 2.2 × 10^5 M^{-1} and 2.0 × 10^5 M^{-1} respectively, for **10** and **11** with a detection limit of 2.0 μM. Furthermore, the formation of a 30–40 nm sized amyloid fibrils was analysed by AFM and TEM techniques. Interestingly, complexes **10** and **11** were selectively sensing the amyloid proteins compared to other biomolecules including lysozyme, PDGF, thrombin, myoglobin, haemoglobin, cytochrome C etc.

Pigge et al. [88] developed a series of AIE-based luminescent tricarbonyl Re(I) complexes, [2,2′-(2,2-di(thiophen-2-yl)ethene-1,1-diyl)bisbenzothiazole]chlorotricarbonyl rhenium(I) (**12**), [2,2′-(2,2-di([2,2′-bithiophen]-5-yl)ethene-1,1-diyl)bisbenzothiazole]chlorotricarbonyl rhenium(I) (**13**), [2,2′-(2,2-di([2,2′:5′,2′′-terthiophen]-5-yl)ethene-1,1-diyl) bisbenzothiazole]chloro tricarbonyl-rhenium(I) (**14**), and [2,2′-(2,2-di([2,2′-bithiophen]-5-yl)ethene-1,1-diyl)bisbenzothiazole]aquatricarbonyl rhenium(I) triflate (**15**) comprised of tetraarylethylene (TAE) ligands that featured the combination of bis(benzothiazole) and (oligo)thiophene units. Both ligand- and ^{3}MLCT-based emissions were observed in CH_3CN at 471, 552, 601 and 521 nm, respectively for compounds **12**–**15** upon excitation at their absorption maxima. Compound **12** underwent enhanced emission while quenching occurred for compounds **13**–**15** in 9:1 PBS (pH = 7.4):CH_3CN upon aggregation due to the formation of non-emissive H-aggregates, as previously studied related rhenium(I) complexes by this group [89]. Addition of $A\beta_{42}$ fibrils resulted in turn-on response ranging from a 13- to 34-fold enhancement in emission intensity with a bathochromic shift of 10–41 nm for **12**–**15** while no luminescence enhancement was noticed with $A\beta_{42}$ monomers. Despite compounds **12**–**15** featured an enhanced emission with $A\beta_{42}$ fibrils, a large Stokes shift and red-shifted emission at 641 nm for **14**, a 32 nm red-shifted emission with a K_d value of 137 nM for **13**, a 23 nm red-shifted emission for **15**, and a 10 nm red-shifted emission for **12**, were detected. Upon exposure to UV irradiation, a bright green colour

Scheme 3. Schematic representation of the dissociation of Aβ aggregates through oxidative damage by photoexcited compound **9**. Reproduced with permission from ref 82. Copyright (2017) Elsevier B.V.

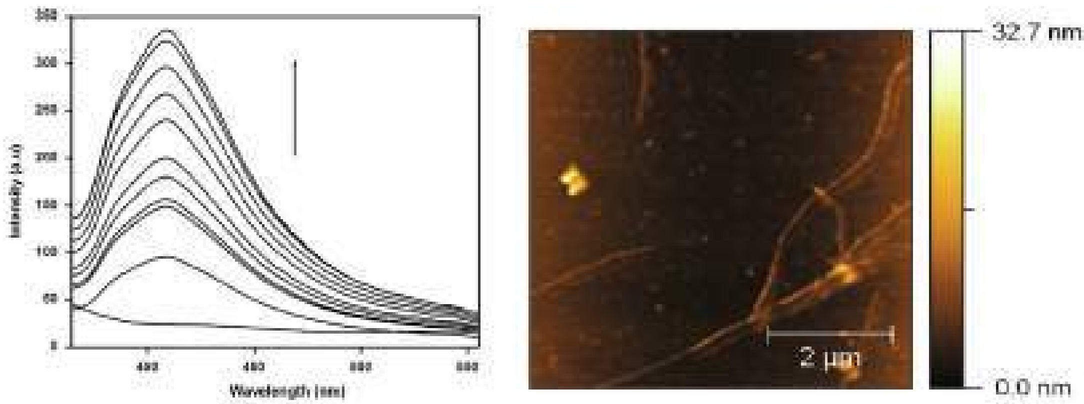

(a) (b)

Fig. 7. (a) Emission enhancement of compound **11** upon the addition of various concentrations of amyloid fibrils and (b) AFM image of amyloid fibrils upon the addition of compound **11** with amyloid samples. Reproduced with permission from ref 87. Copyright (2014) Elsevier B.V.

emission response of **13** toward $A\beta_{42}$ fibrils can simply be visualized even by the naked eyes (Fig. 8). The average nanoaggregates size were about 228 nm by dynamic light scattering (DLS) result for **13,** but in the presence of $A\beta_{42}$ fibrils, the particle size was significantly reduced with enhanced emission. Competition study between **12** and ThT on fibrillation process showed that compound **12** efficiently bound with $A\beta_{42}$ fibrils by hindering the ThT binding to give a higher binding constant (K_d = 0.28 μM) than that of ThT (K_d = 0.8 μM). On the other hand, addition of other biomolecules such as calf thymus DNA (CT DNA), bovine and human serum albumin (BSA, HSA), casein, human IgG, and pepsin did not induce emission intensity of **13** while it exhibited a remarkable emission enhancement over other fibrils such as $A\beta_{40}$, lysozyme, and α-synuclein. In contrast, ThT showed a non-selective binding with other fibrils and exhibited a fluorescence enhancement toward serum albumin, DNA and other proteins [90,91]. Thus, the emission response of compound **13** was remarkably selective and superior over ThT for the detection of fibrils. It was proposed that favorable hydrophobic interactions acted as driving force for the effective binding of **12**–**15** with amyloid fibrils.

One of the luminescent rhenium(I) complexes, $[Re(CO)_3(dppz)(Py)]^+$ (**16**, Py = pyridine) came out from the laboratory of Marti was shown to exhibit primary and secondary light-switching effects for the detection of Aβ aggregation in real time [92]. Compound **16** displayed a poor emission, however, addition of **16** into aggregated Aβ resulted in an 18-fold enhanced emission intensity, which was higher than that of emission intensity of **16** in the presence of DNA [93]. The authors observed that in the presence of Aβ fibrils, compound **16** underwent time-dependent emission enhancement at 560 nm (λ_{ex} = 362 nm), promoting secondary light-switching effect to give a 105-fold enhanced emission after 6000 s. LC-MS data confirmed the presence of a non-specific modification of the Aβ in the irradiated solution of **16** and Aβ monomers, whereas site-specific oxidation occurred only in Aβ but not in **16** upon exposure of a solution containing compound **16** treated Aβ fibrils to light irradiation. This can be ascribed to the catalytic oxidation of Aβ fibrils by **16** via the production of reactive oxygen species (ROS), which is corroborated by the irradiated solution containing **16** treated Aβ fibrils under nitrogen atmosphere where only a 2-fold emission enhancement was noticed. Therefore, it was concluded that secondary light-switching effect could be possible from either disability of oxidized aminoacids (Aβ fibrils) in deactivating excited state **16** to give enhanced emission or ligand substitution with oxidized aminoacids during irradiation. This can be in good agreement with the broadening spectrum of **16** upon irradiation. Furthermore, the authors tested the possibility of using **16** to monitor in real-time amyloid self-assembly across a wide range of aggregation conditions through sigmoidal curve (Fig. 9).

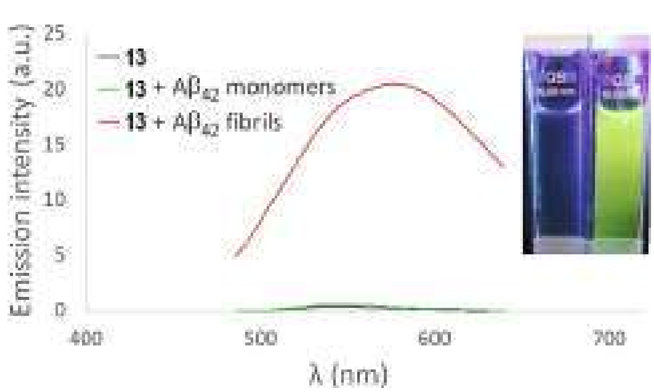

Fig. 8. Luminescence response of **13** upon untreated and treated monomers or $A\beta_{42}$ fibrils. Inset photo showing the color change during the absence and presence of fibrils with **13** under UV light. Reproduced with permission from ref 90. Copyright (2018) John Wiley & Sons.

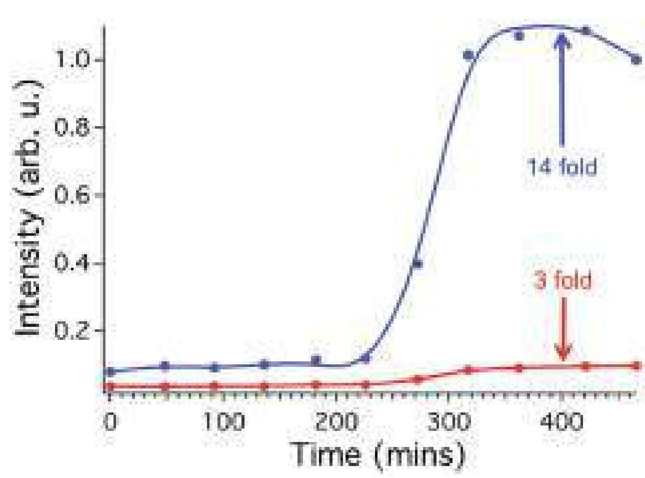

Fig. 9. Real-time assay of **16** for monitoring Aβ aggregation before (red) and after (blue) irradiation. Reproduced with permission from ref 94. Copyright (2016) American Chemical Society.

In contrast, compound $[Ru(bpy)_2(dppz)]^{2+}$, **1** did not show secondary light-switching behaviour with Aβ fibrils, indicating that dppz coordination with metal centres never involved in the secondary light-switching effect. Thus, secondary light-switching effect of **16** is unique and unusual characteristics.

2.3. Iridium(III) complexes

Another photoactive family for sensing and inhibition of fibrillar Aβ is based on Ir(III) complexes. They have attracted more attention due to their stable structures, excellent optical performances such as high emission quantum yield, high lifetime, emission colors ranging from blue to red, tunable structures, sensitivity to surrounding environment, and effective singlet oxygen photosensitization [94,95].

Ma and coworkers made the first example of spectroscopic applications of cyclometalated Ir(III) solvato complexes, $[Ir(ppy)_2(OH_2)_2]^+$ (**17**, ppy = 2-phenylpyridine), $[Ir(ppy)_2(OH_2)_2]^+$ (**18**, bzq = benzoquinoline), and $[Ir(ppy)_2(OH_2)_2]^+$ (**19**, phq = phenylquinoline) to inhibit amyloid aggregates [96]. They used total internal reflection fluorescence microscopy (TIRFM) for monitoring the inhibitory effect of **17**–**19** toward ThT labelled $Aβ_{1–40}$ fibrils. These compounds were able to inhibit the fibrillogenesis against $Aβ_{1–40}$ peptides through binding with histidine moiety of peptide and successfully blocked the misfolding of peptides to generate neurotoxic oligomers and fibrils. In the inhibitory process, compound **17** was very active compared to **18** and **19** where sterically hindered extended aromatic ligands may force to prevent histidine moiety in coordinating metal centers. These compounds were weakly luminescence in solution. However, they displayed enhanced luminescence with histidine as the complexation probe containing compounds and peptides was shielded in the hydrophobic region to minimize the non-radiative decay process. Since $Aβ_{1–40}$ fibrils produced more hydrophobic environment than that of $Aβ_{1–40}$ monomers, compound **17** inhibited $Aβ_{1–40}$ fibrils effectively to afford a 134-fold emission enhancement at 491 nm while only a 56-fold emission intensity was observed with $Aβ_{1–40}$ monomers compared to free **17**. (Fig. 10). Later, the same group also reported other Ir(III) complexes that showed the detection and inhibitory effects against $Aβ_{1–40}$ fibrils [97].

Following these studies, Ma et al [98]. again demonstrated that photoactive iridium(III) complexes **20**–**33**, $[Ir(ppy)_2(bpy)]PF_6$ (**20**, ppy = 2-phenylpyridine, bpy = 2,2′-bipyridine), $[Ir(ppy)_2(biq)]PF_6$ (**21**, biq = 2,2′-biquinoline), $[Ir(ppy)_2(dmdpphen)]PF_6$ (**22**, dmdpphen = 2,9-dimethyl-4,7-diphenyl-1,10-phenanthroline), $[Ir(ppy)_2(dbbpy)]PF_6$ (**23**, dbbpy = 4,4′-diphenyl-2,2′-bipyridine), $[Ir(phq)_2(dpbpy)]PF_6$ (**24**, phq = 2-phenylquinolin, dpbpy = 4,7-diphenyl-2,2′-bipyridine), $[Ir(phq)_2(4,7\text{-dpphen})]PF_6$ (**25**, dpphen = 4,7-diphenyl-1,10-phenanthroline), $[Ir(bzq)_2(chlorophen)]PF_6$ (**26**, bzq = benzoquinone, chlorophen = 5-chloro-1,10-phenanthroline), $[Ir(bzq)_2(phen)]PF_6$ (**27**, phen = 1,10-phenanthroline), $[Ir(bzq)_2(2,9\text{-dpphen})]PF_6$ (**28**, 2,9-dpphen = 2,9-diphenyl-1,10-phenanthroline), $[Ir(bzq)_2(aminephen)]PF_6$ (**29**, aminephen = 1,10-phenanthrolin-5-amine), $[Ir(bzq)_2(dnbpy)]PF_6$ (**30**, dnbpy = 4,4′-dinonyl-2,2′-bipyridine), $[Ir(ppy)_2(phenyl\text{-}imidazo\text{-}phen)]PF_6$ (**31**, phenyl-imidazo-phen = 2-phenyl-1H-imidazo[4,5-f][1,10]phenanthroline), $[Ir(ppy)_2(phenol\text{-}imidazo\text{-}phen)]PF_6$ (**32**, phenol-imidazo-phen = 4-(1H-imidazo[4,5-f][1,10]phenanthrolin-2-yl)phenol), $[Ir(bzq)_2(phenol\text{-}imidazo\text{-}phen)]PF_6$ (**33**) can inhibit $Aβ_{1–40}$ aggregates *in vitro* and protect neuronal cell lines upon exposed to $Aβ_{1–40}$ aggregates. Compounds **20**–**30** were unable to differentiate the effect of $Aβ_{1–40}$ monomers and fibrils based on their luminescence data. However, compound **31** displayed remarkable changes in emission intensity ($I_{fibril}/I_{monomer}$ ratio, >1.5), and thus, differentiating the detecting ability of fibrils over monomers. Therefore, they prepared its analogue compounds **32** and **33** and checked their ability against $Aβ_{1–40}$ aggregates. The aggregation kinetic curve of $Aβ_{1–40}$ aggregates toward **32** and **33** using a ThT assay displayed a typical sigmoid kinetics that featured a long lag time (nucleation lag time) followed by a rapid aggregate growth, in which compound **32** partially retarded the fibrillogenesis whereas it was completely inhibited by compound **33**. They observed that Ir(III) center was only active to inhibit $Aβ_{1–40}$ aggregates but not the ligand moiety. Total internal reflection fluorescence microscopy (TIRFM) with laser excitation and TEM images confirmed that they were capable of breaking the β-sheets and blocked partially or completely the formation of Aβ fibrils (Fig. 11). Upon binding with $Aβ_{1–40}$ monomers and fibrils, compound **32** exhibited a 6- and 12-fold increase in emission intensity at 540 nm while 11- and 18-fold emission enhancement at 540 nm was observed for **33**. These findings can be ascribed to the binding of these compounds with different hydrophobic domain of monomers and fibrils, resulting in the protection of compounds from non-radiative decay and solvent quenching to enhance their emission. A neuroprotective effect of different forms of $Aβ_{1–40}$ peptides ($Aβ_{1–40}$ monomer, $Aβ_{1–40}$ monomer with seeded fibrils and $Aβ_{1–40}$ fibril) on human SH-SY5Y neuroblastoma cells and mouse primary cortical cells against Aβ-induced toxicity showed that they were capable of inducing toxicity. Whereas, compound **33** showed effective neuroprotection to these cells toward cytotoxicity that was produced by $Aβ_{1–40}$ peptide forms with a $[Aβ_{1–40}]/[\mathbf{33}]$ ratios of 0.2, 1.0, or 5.0 while compound **31** did not show any significant effect on toxicity because it exhibited no effect on amyloid aggregation also. Thus, compound **33** could be used to protect these neuronal cells from Aβ aggregates upon low dosage administration.

Recently, Lim and co-workers [99] newly designed four Ir(III) complexes, **34**–**37** Ir-Me (**34**), Ir-H (**35**), Ir-F (**36**), and Ir-F_2 (**37**) and developed an efficient chemical strategy by modifying Aβ peptides via coordination-/photo-mediated oxidation to determine Aβ aggregation. The characteristic features of these compounds are: (i) 2-phenylquinoline containing Ir(III) complexes afford relatively high quantum yields and rates of ROS production, (ii) F atoms are capable of interacting with Aβ peptides via H-bonding to enhance photophysical behavior and biocompatibility, and (iii) H_2O molecules present in Ir(III) complexes can easily coordinate with Aβ peptides through substituting histidine (His) residue. Compounds **34**–**37** were emissive at 587, 587, 589 and 573 nm with a quantum yield of 0.0038, 0.0037, 0.0071, and 0.0027, respectively and they produced a weak singlet oxygen ($^1O_2$). In the presence of His, quantum yields were enhanced (0.19 for **34**, 0.31 for **35**, 0.26 for **36** and 0.081 for **37**) along with a shift in λ_{em} ranging from 573 to 593 nm and an increase in $^1O_2$ production, demonstrating their coordinating ability (**36** > **35** > **34** > **37**) with His, which is corroborated with

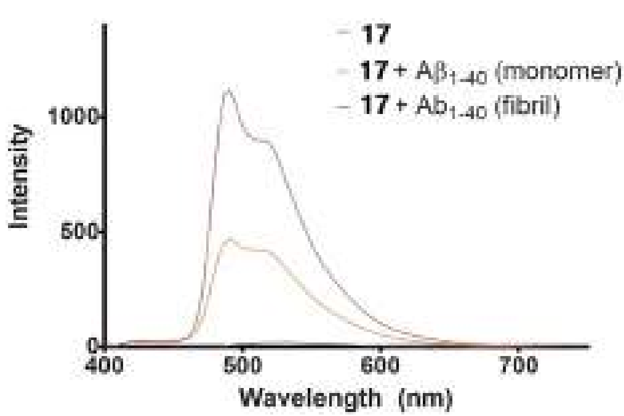

Fig. 10. Luminescence response of **17** upon untreated and treated monomers or $Aβ_{42}$ fibrils. Reproduced with permission from ref 98. Copyright (2011) Royal Society of Chemistry.

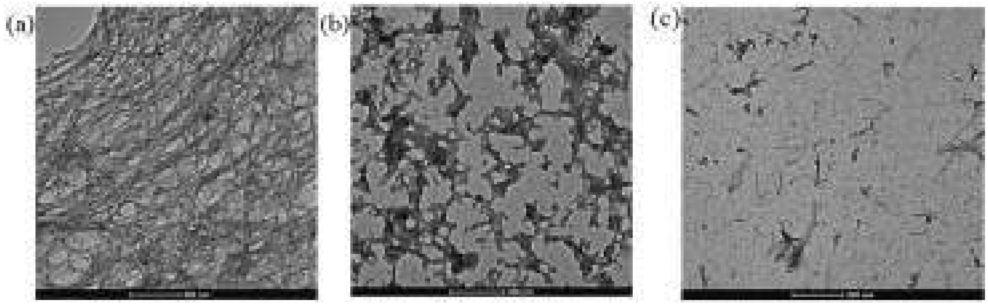

Fig. 11. TEM images of Aβ_{1-40} aggregation when (a) untreated with **32** and **33**, (b) treated with **32**, and (c) treated with **33**. Scale bar = 200 nm. Reproduced with permission from ref 100. Copyright (2015) Springer Nature.

ESI-MS data. Compound **36** showed significant binding constants with different forms of Aβ peptides such as monomers (K_d = 1.6 × 10^{-4} M), oligomers (K_d = 2.6 × 10^{-4} M) and fibrils (K_d = 7.1 × 10^{-4} M). In addition, it gave a remarkable $^1O_2$ and $O_2^{-\cdot}$ species with His binding to have the capability in modifying Aβ peptides. ESI-MS data revealed that photoactivation of **34**–**37** containing Aβ peptides resulted in the formation of oxidized Aβ_{40} residue where the oxidation sites were expected in the residues of His13, His14, and Met35. Thus, in the presence of light and O_2, Aβ_{40} or Aβ_{42} aggregation can be controlled by coordination-/photo-induced oxidation of peptides mediated by phototriggered Ir(III)-complexes, while in the absence of light and O_2, covalent interactions between Ir(III) complexes and the peptides guided Aβ_{40} or Aβ_{42} aggregation. Compounds **34**–**37** also interacted with α -synuclein (α -Syn) and human islet amyloid polypeptide (hIAPP) aggregates (Fig. 12). In addition, reduced cytotoxicity was observed upon exposure of Aβ_{40} species treated **34**–**37** to murine Neuro-2a (N2a) neuroblastoma cells in a photoirradiation-dependent manner. In their previous report [100], they observed that another Ir(III) complex induced oxidative modification of Aβ peptides and dominated their aggregation behavior.

2.4. Platinum(II) complexes

Among these photoactive transition metal complexes, square-planar geometry of d^8 Pt(II) complexes show different photophysical properties from that of pseudo-octahedral geometry of d^6 transition metal complexes. The planarity of Pt(II) complexes makes it possible to have intermolecular interaction between the -monomers in the excited and ground states that can lead to an excimer, showing a red-shifted emission [101,102]. The emission attributed from the resulting excimers are usually from MMLCT or LLCT transitions which are strongly depending on the distance of Pt-Pt. The Pt atoms in binuclear complexes connected by small ligands produce the intramolecular Pt-Pt interactions. Beyond other metal complexes, Pt(II) metal complexes have been identified to inhibit the formation of amyloid fibres through direct coordination of the Pt centre with amyloid peptides or metal-driven oxidation of crucial residues.

Recently, three water-soluble ionic supramolecular Pt(II) complexes, **38**–**40** [Pt{bzimpy($PrSO_3$)$_2$}{C≡C-C_6H_3-(CH_2OH)$_2$–3,5}]K (**38**), [Pt{bzimpy(C_4H_9)$_2$} {C≡C-C_6H_3-(CH_2OH)$_2$–3,5}]Cl (**39**) and [Pt{bzimpy($PrSO_3$)$_2$}Cl]K (**40**) (bzimpy = 2,6-bis-(benzimidazol-2′-yl)pyridine) for the sensitive and specific detection of amyloid fibrillation were reported first time by Yam and workers (Scheme 4) [103]. Compounds **38**–**40** showed ^{3}MMLCT based emission in aqueous medium at 670–690 nm that were linked to aggregate formation via Pt(II)···Pt(II) interactions. In the presence of insulin amyloid, compound **38** displayed an enhancement in its emission intensity with a hypsochromic shift that can be attributed to the binding of this complex with the hydrophobic pockets of amyloid aggregates through hydrogen bonding and hydrophobic–

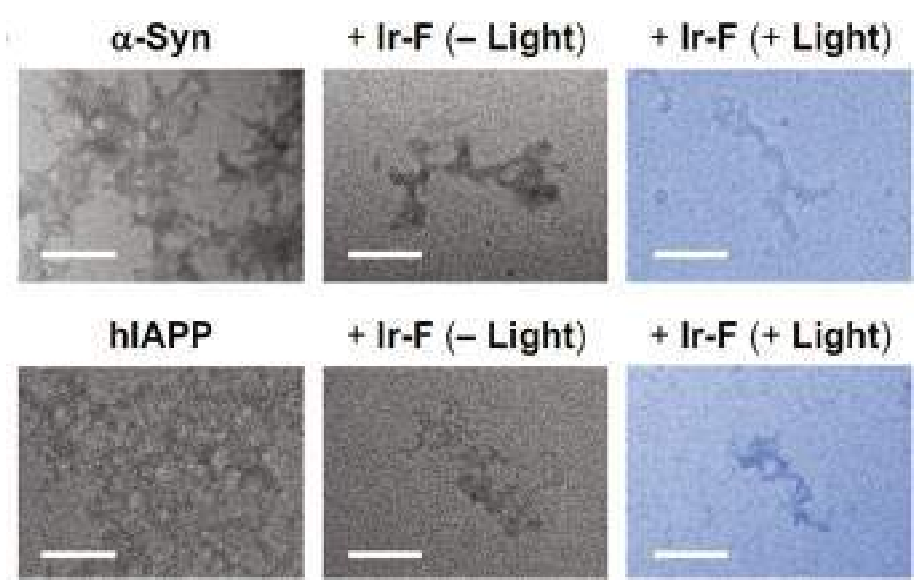

Fig. 12. TEM images of compound **36** induced peptide aggregation in the absence and presence of light. Scale bar = 200 nm. Reproduced with permission from ref 101. Copyright (2019) Royal Society of Chemistry.

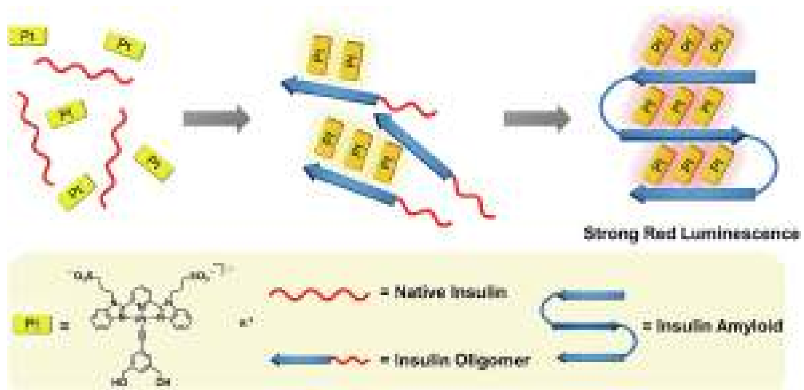

Scheme 4. Schematic illustration of compounds **38**–**40** mediated the detection of fibrils. Reproduced with permission from ref 105. Copyright (2019) American Chemical Society.

hydrophobic interactions, which was also confirmed by ^{1}H NMR studies. In **39**, insulin amyloid induced an emission enhancement with a hypsochromic shift, showing the aggregation behavior through H- bonding and hydrophobic–hydrophobic interactions. At the same time, native insulin also produced an increase in emission intensity without hypsochromic shift because of electrostatic interaction which reduced the mobility and increased the rigidity of **39**. Thus, it was not a suitable probe for the detection of fibrils selectively. In contrast, compound **40** did not display remarkable changes in its emission intensity owing to the lack of H-bonding and hydrophobic–hydrophobic interactions, which were attributed from the –OH and phenyl groups, respectively. Like the case of **39**, it cannot also be used as a probe for detecting fibrils. Interestingly, amyloid fibrillation via nucleation dependent polymerization consistently showed a sigmoidal time course monitored by relative emission intensity of **38**. The emission lifetime of **38** was also increased from 0.12 to 0.22 μs upon the addition of amyloid aggregates whereas ThT displayed a singlet lifetime of 1–2 ns even in the presence of amyloid aggregates, indicating the significance of **38** in biological uses. According to Hill equation, compound **38** showed a binding constant of 5.46×10^{4} M^{-1} with a Hill coefficient of 1.68, showing the positive cooperation of **38** with fibrils. Confocal images confirmed a bright ^{3}MMLCT-based emission intensity of **38** after binding with fibrils. Furthermore, compound **38** dominated its emission intensity on ThT-treated amyloids, indicating its photostability and selectivity over ThT. Luminescence assay showed that L-ascorbic acid can decelerate the formation of amyloid aggregates in the presence of **38**, which is in good agreement with the result obtained from ThT. One of the advantages of **38** is that metal ions such as Mg(II), Ca(II), Mn(II), Fe(II), Fe(III), Cu(II), and Zn(II) and intracellular DNA and RNA did not interfere the fibrils triggered emission intensity of **38** while they affected the emission intensity of ThT. Hence, compound **38** proved its high selectivity and sensitivity over ThT, making it a promising candidate for the detection of amyloid fibrils.

Table 1 summarizes the emission light-switching response of Ru(II), Re(I), Ir(III) and Pt(II) complexes for the detection of Aβ monomers, protofibrils and fibrils. The structure of these metal complexes is depicted in Chart 1.

3. Summary and outlook

In summary, this review summarizes the recent developments involving photoactive transition metal complexes to act as nonconventional probes for monitoring and acting as inhibitors that counter the misfolding of peptides into neurotoxic oligomers and amyloid fibrils. Given the importance of the metal binding sites, histidine residues in the Aβ fibrils, most current studies have been devoted to the design and synthesis of photoactive metal complexes containing conjugated ligands that featured dppz, imidazole, thiazole chelating groups to serve as probes for the detection and inhibition of peptide aggregation by affording high quantum yields and ROS production. Some of the probes containing fluorine atoms and hydrophobic groups imparted the ability to interact with Aβ through non-covalent interactions, such as hydrogen bonding, hydrophobic and pi-pi interactions. In addition, H_2O coordinated compounds enabled covalent coordination with Aβ through replacement with histidine residues of the peptide. These probes possessing attractive characteristics including a red-shifted emission, a large Stokes shift, and a long lifetime have the potential advantages over more conventional dyes such as ThT. In particular, the relatively long excited lifetimes of these complexes can be used not only to differentiate the binding of Aβ monomers, Aβ protofibrils and Aβ fibrils but also the competitive binding or interference associated with autofluorescence of other biomolecules or dyes using time-gated measurements. The morphology of fibrils was investigated through imaging of AFM and TEM imaging studies. Several photoactive metal complexes detected Aβ fibrils selectively with a detection limit of nM range, making them ideal candidates for the detection of Aβ fibrils *in-vivo* studies. Computational studies revealed that amino acids containing binding sites were able to interact with metal complexes through hydrophobic CH–π and π–π interactions. These compounds enabled as chemical modulators toward Aβ aggregation via coordination, oxidation, and hydrolysis routes to regulate Aβ aggregation pathways. For *in vitro* applications, as these metal complexes were easily taken up by Neuro-2a (N2a) neuroblastoma cells, PC12 cells, human SH-SY5Y neuroblastoma cells and mouse primary cortical cells with high stability and luminescence sensing, they were capable of enhancing remarkable viability to disassemble the aggregates against Aβ-induced toxicity under light illumination.

It would be more interesting to study the relationship between the structure and inhibition/emission behavior of these photoactive metal complexes. The Aβ peptide contains several aromatic (e.g. Phe4, Phe19, and Phe20) and other hydrophobic residues that are critical for aggregation. Thus, it is reasonable to predict that there are adequate opportunities for functionally important hydrophobic interactions. Compounds **1** and **13** that contained highly conjugated hydrophobic aromatic ligands dipyrido[3,2-a:2′,3′-c]phenazine and benzothiazole derivative, respectively favored the binding modes with hydrophobic sites on the Aβ surface. Upon binding to fibrillar aggregates, the rotation of hydrophobic ligands

1

2

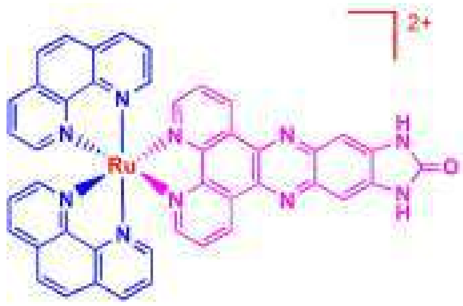

3

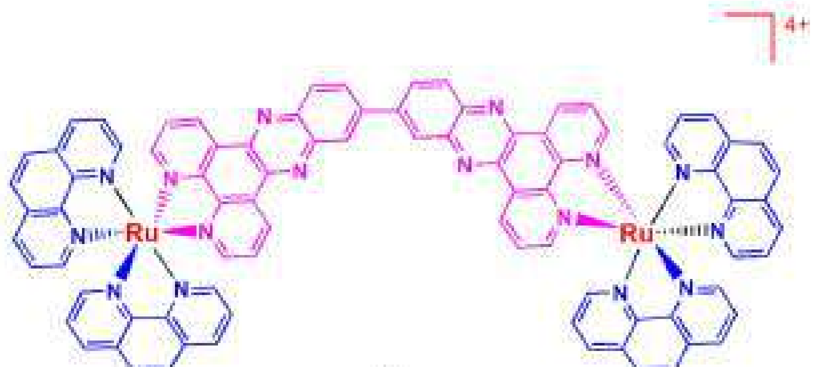

4

Chart 1. Structure of photoactive metal complexes used in this study.

became substantially restricted, thus reducing the nonradiative decay channel in its excited state. This resulted in a remarkable increase in the emission yield of compounds **1** (50-fold enhancement) and **13** (34-fold enhancement) in the presence of amyloid fibrils. Other compounds containing aromatic ligands such as bipyridyl derivatives, benzimidazole derivatives, styrylpyridines, AIE based ligands etc, contributed a significant emission enhancement upon binding with the cross-β sheet structure of amyloid fibrils. On the other hand, compounds lacking a second phenyl group (compounds **6** and **7**) were less potent inhibitors of aggregation. Among the photoactive metal complexes examined in this study, cyclometalated Ir(III) solvato complexes, **17** and **34** showed a 134- and a 180-fold emission enhancement in their emission intensity upon binding with Aβ peptides. These compounds were composed of 2-phenylquinoline, F atom, and H_2O molecules which produced high ROS production, and easily coordination with Aβ peptides through hydrogen bonding and substituting histidine (His) residue, respectively. It is worth noting that the flexible ligands might also influence activity. For example, flexible linker containing compound **5** influenced to move in between laminated β-sheets to force the dppz ligand inside the hydrophobic pockets of fibrils, resulting in enhanced its emission intensity whereas the binding geometry of rigid compound **4** preceded quenching pathway. However, the role of auxiliary ligands in their activity against target amyloid fibrils cannot excluded. Based on this observation, we hypothesized that the highly hydrophobic ligands, ROS production, coordinated H_2O molecules and substituted F atoms, flexible linkers, etc., are essential for activity.

These photoactive metal complexes displayed remarkable selectivity against the targets of interest in contrast to ThT where no selectivity was found. These metal complexes have been designed and discovered to show a high binding affinity and selectivity to the hydrophobic grooves on the β-sheet surface along the Aβ fibril axis or oxidative damage of Aβ peptides via ROS production and to exhibit a variety of responses to amyloids, such as emission intensity changes, shifts in emission maxima, variations in binding constants, detection limits, linear ranges and lifetimes over monomers, oligomers and other biomolecules. For example, compound **1** was designed to improve a 50-fold signal enhancement with a Stokes shift of 180 nm and a biexponential decay, leading to high binding affinity to amyloid-β. Compound **2** showed unusually high selectivity for αS fibrils with an 18-fold emission enhancement and a Stokes shift of 190 nm, while compound **3** displayed exceptional affinity for tau R2 fibrils over R2-C291A mutant peptides with a 15-fold emission enhancement and a Stokes shift of 260 nm. The selectivity of **2** toward αS fibrils *in vitro* was also

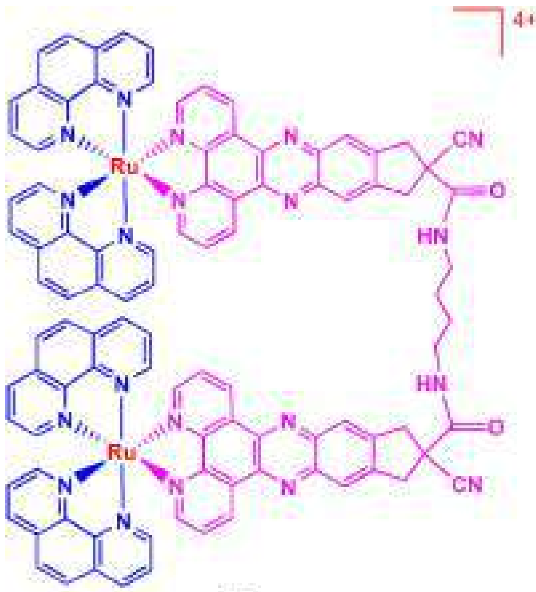

5

6

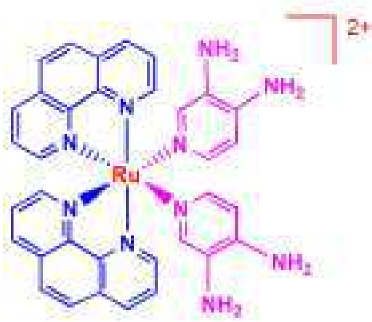

7

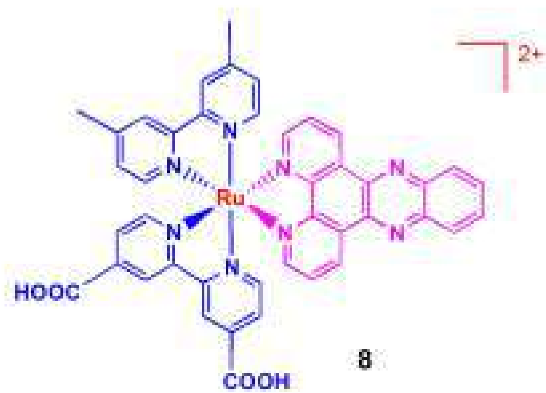

8

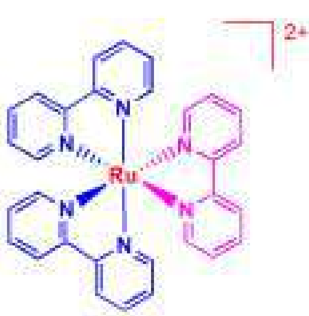

9

10, R = CH_3
11, R = $C_{10}H_{21}$

Chart 1 (*continued*)

supported with a study on human neuroglioma cells (H4) and H4/α-syn-GFP cells. The rigid linker containing compound **4** was synthesized to improve the binding affinity to insulin up to 10-fold-emission enhancement whereas flexible linker containing compound **5** exhibited a high specificity toward insulin with a 15-fold emission enhancement. The meta-position of amino group in

12

13

14

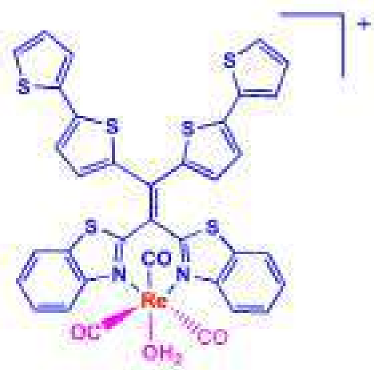

15

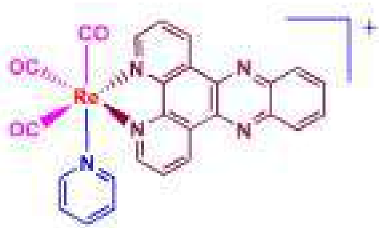

16

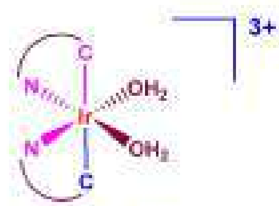

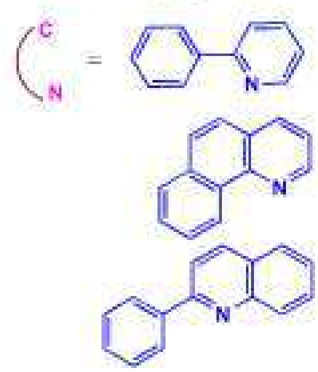

ppy, 17

bzq, 18

phq, 19

Chart 1 (*continued*)

pyridyl ring of **7** toward amyloid-β via antioxidant responsibility showed a significant selectivity with a Stoke shift of 200 nm. It also differentiated Aβ background fluorescence and enabled in the real time self-aggregated Aβ images compared with ThT. Further, *in vitro* study using Neuro2A cells encouraged its selectivity. To improve better detection sensitivity and selectivity of Aβ fibrils, compound **8** containing sterically hindered ligands which can decrease in binding with aptamers or dissociate upon the addition

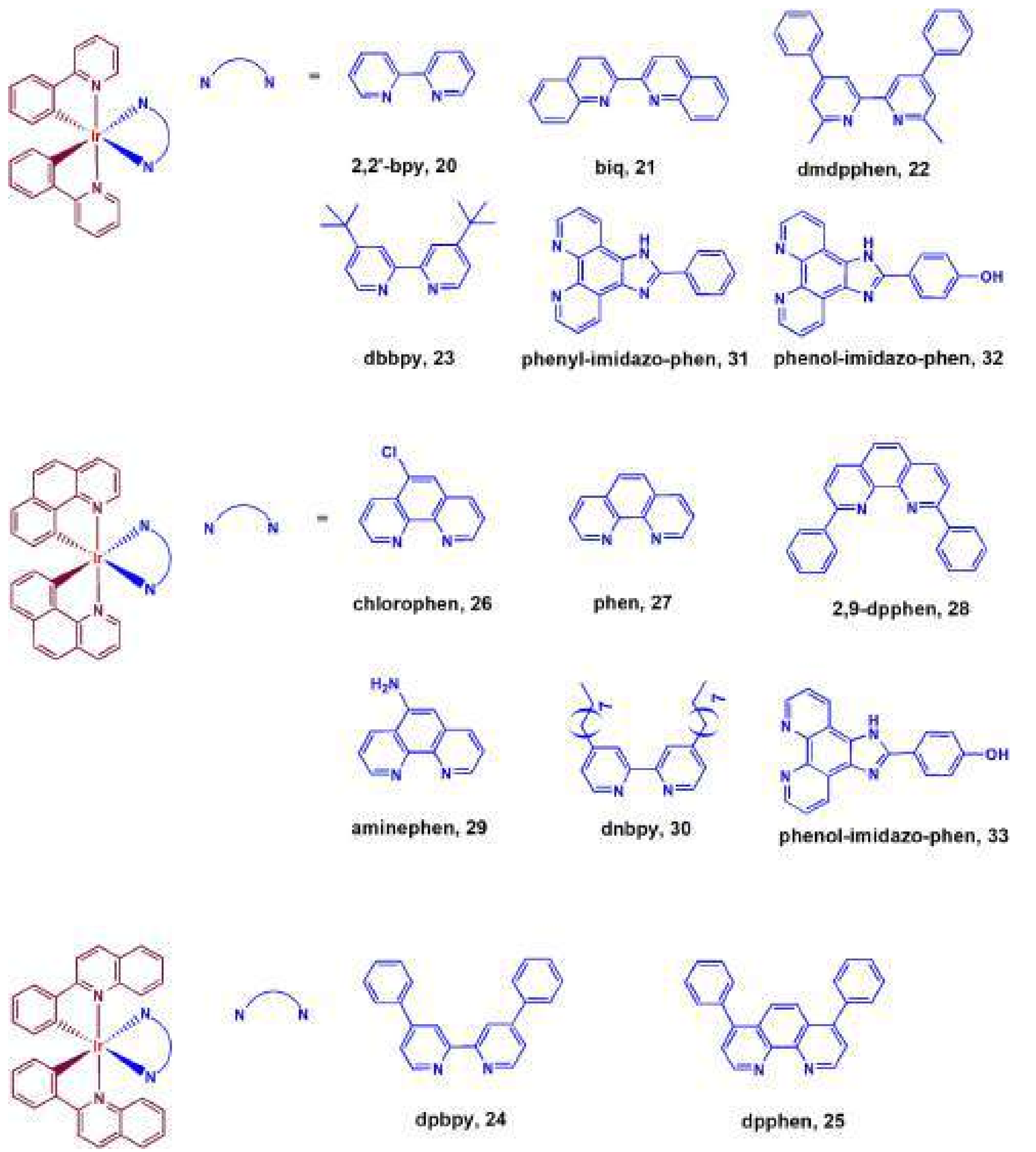

Chart 1 (*continued*)

of targets created specific probe in the presence of aptamers showed a strong binding affinity and selectivity toward Aβ fibrils with a binding constant of 4.1×10^6 M^{-1} and a detection limit of 50 nM whereas monomers and oligomers of Aβ caused the decrease in emission intensity of **8** due to binding with displaced complex **8**. Compound **9** was designed to improve the binding affinity to amyloid-β up to a 148-fold emission enhancement by oxidative damage of Aβ peptides via ROS production, which is supported by *in vitro* study using PC12 cells. The enhanced emission (10-fold) with a Stoke shift of 90 nm and binding constants of $2.0–2.2 \times 10^3$ M^{-1} was ascribed to π-π stacking interaction between naphthalene moiety in **10** and **11** and PHE19 and PHE4 moieties in fibrils, which is corroborated by molecular docking studies. Benzothiazole derivatives of **12–15** exhibited high specificities toward $A\beta_{42}$ fibrils with a high binding affinity of 137–276 nM with a 13 to 34-fold emission enhancement and Stokes shifts from 101 to 148 nm. The site-specific oxidation via the production of ROS occurred in amyloid-β upon exposure of **16** to light

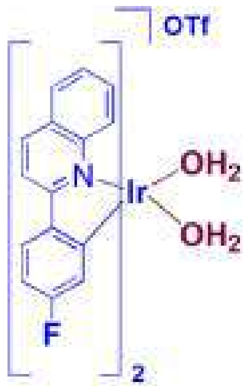

34

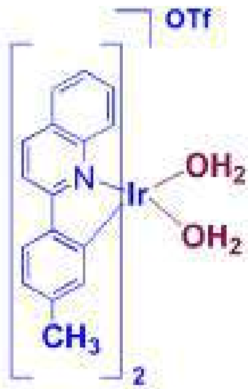

35

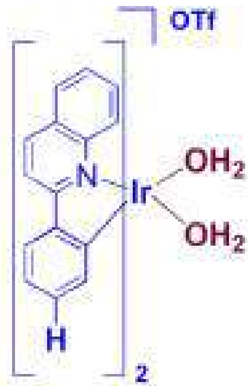

36

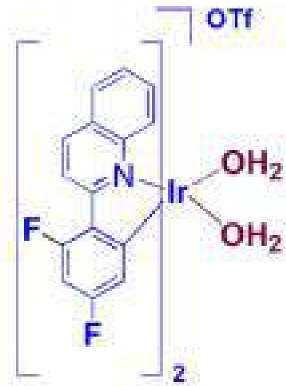

37

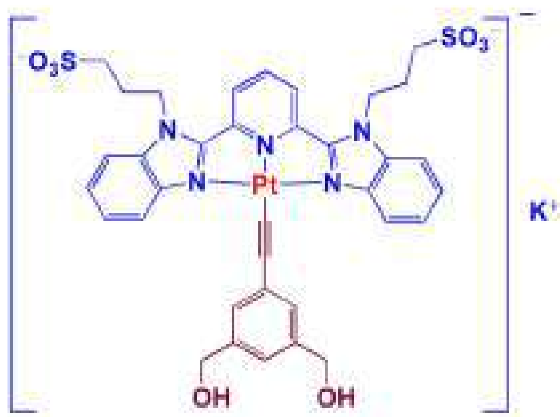

38

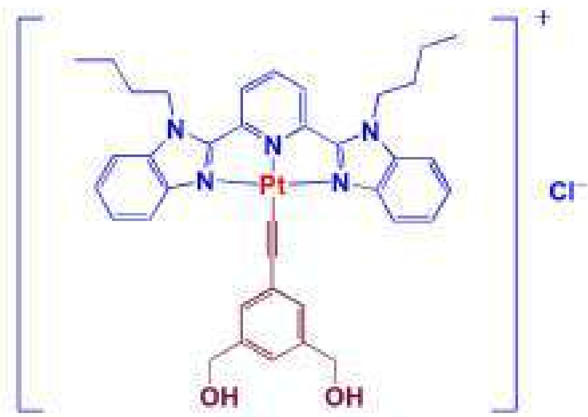

39

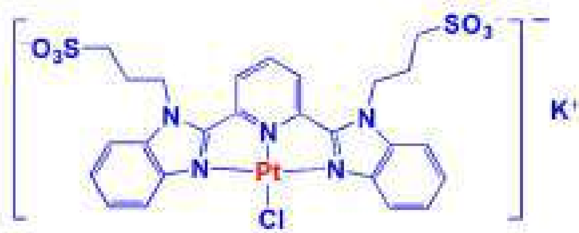

40

Chart 1 (*continued*)

irradiation, leading to afford an 18-fold emission enhancement. Comparison of compound **17** to $A\beta_{1-40}$ fibrils binding affinity data with that to monomers showed its selectivity in favor of $A\beta_{1-40}$ fibrils (134-fold emission enhancement) over monomers (56-fold emission enhancement). Compounds **32** and **33** had a strong selectivity for $A\beta_{1-40}$ fibrils (12-fold and 18-fold emission enhancement, respectively) over monomers (6-fold and 11-fold emission enhancement, respectively), which is supported by *in vitro* study using human SH-SY5Y neuroblastoma cells and mouse primary cortical cells. The $A\beta_{40}$ or $A\beta_{42}$ aggregation was selectively controlled by coordination-/photo-induced oxidation of peptides mediated by phototriggered Ir(III)-complexes, **34–37** to afford enhanced emissions with Stokes shift ranging from 223 to 253 nm. Benzimidazole derivatives of **38** and **39** exhibited the selective affinity toward bovine insulin aggregates, showing a 2 to 10-fold enhanced emission with a Stokes shift of 100 and 115 nm, respectively. These results showed that the ability to selectively detect amyloid aggregates by photoactive transition metal complexes holds not only the promise of biomedical applications but also provides new approaches for unraveling the mechanisms underlying fibrils versus monomer formation in amyloid assembly.

To gain further insights into amyloid proteins with metal complexes, computational and molecular docking studies were performed. It is useful to predict the favored orientation, binding sites and the affinity between the ligands and amyloid proteins as well as fibrils. From the obtained data, we can buttress and compare the spectroscopic investigations. While X-ray crystallography has so far been unsuccessful in determining the structure of any metal-Aβ complexes, experimental methods such as NMR, EPR, and XAS have been used in the structural determinations of metal binding sites and interactions of Aβ. These results have been supported by computational methodologies, usually *ab initio* quantum mechanical calculations. *Ab initio* MD and hybrid QM/MM-MD studies hold great promise in providing insight into the dynamical processes and the ROS chemistry resulting from the metal-peptide interactions. However, owing to rapid aggregation and disordered nature of amyloid-β along with the solvent and paramagnetic effects, the experimentally characterization of metal-peptide interactions is poorly understood. In addition, the impact of interactions, structures and dynamics, toxic species and mechanism of toxicity faces challenges that will need to be met. Thus, the interplay between computational and experimental studies is going to become even tighter in near future. For better understanding these experimental and computational aspects, please refer these excellent reviews and articles [104-108]. In addition to that, there has been tremendous interest in identifying the drug targets, finding the target molecules from the data libraries and repurposing of molecules. In view of this, Artificial Intelligence (AI) /Machine learning based drug discovery methods will be useful for the identification and the production of drugs to treat AD. It opens up new gate way for the development of drug design to treat AD, and thereby more exciting results will come up in next 5–10 years.

Despite currently available photoactive compounds have proven beneficial in AD, several current limitations need to be addressed in the design of the next generations of anti-AD agents to widen the clinical applications. Upon photoactivation, these compounds generated ROS to oxidize peptides, thereby changing properties of Aβ and modifying their pathways. Thus, it is more valuable to prepare metal complexes that would produce higher ROS. The interference of biomolecules may also result in affecting amyloidogenic aggregation pathways, and hence, the designing of photoactive metal complexes for controlling amyloidogenic aggregation would be critical. Although these compounds exhibited a superior effect in Aβ fibrils sensing compared to other conventional dyes, only a limited number of photoactive metal complexes, such as Ru(II), Re(I), Ir(III), and Pt(II), have been explored. Therefore, it is essential for the rational design of other transition metal complexes or incorporating newly designed ligands with metal centers, for the qualitative detection of these fibrils. Most of the reported compounds displayed absorption and emission wavelengths in the visible range. (Table 1) NIR-active metal complexes that can have target specificity and biocompatibility with a low photodamage, minimal fluorescence (background), and low light scattering compared to visible or UV lights are highly desirable for the detection of peptide aggregates both *in vitro* and *in vivo* studies. In addition, they can afford higher clarity and deeper tissue penetration into a living system to monitor aggregates. We thus expect more studies from the collaboration between chemistry, computational and medical communities, pushing forward exciting process toward real applications in the future.

Declaration of Competing Interest

The authors declare that they have no known competing financial interests or personal relationships that could have appeared to influence the work reported in this paper.

Acknowledgements

This article is dedicated to the occasion of the 81st birthday anniversary of Prof. C. Srinivasan (Retired) and 70th birthday anniversary of Prof. S. Rajagopal (Retired) Madurai Kamaraj University, Madurai, India. VS thanks to the Management of Bannari Amman Institute of Technology, Sathyamangalam for their supports. Research reported in this publication was supported by the Ministry of Science and Technology, Taiwan under Award Number MOST-106-2113-M-001-032 and MOST-109-2811-M-030-500.

Appendix A. Supplementary data

Supplementary data to this article can be found online at https://doi.org/10.1016/j.ccr.2020.213612.

References

[1] F. Chiti, C.M. Dobson, Annu. Rev. Biochem. 75 (2006) 333–366.
[2] P.C. Ke, R. Zhou, L.C. Serpell, R. Riek, T.P.J. Knowles, H.A. Lashuel, E. Gazit, I.W. Hamley, T.P. Davis, M. Fandrich, D. Erik Otzen, M.R. Chapman, C.M. Dobson, D. S. Eisenberg, R. Mezzenga, Chem. Soc. Rev 49 (2020) 5473–5509.
[3] T.P. Knowles, M. Vendruscolo, C.M. Dobson, Nat. Rev. Mol. Cell. Biol. 15 (2014) 384–396.
[4] C.M. Dobson, Nature 426 (2003) 884–890.
[5] E. Herczenik, M.F.B.G. Gebbink, FASEB J. 22 (2008) 2115–2133.
[6] H. Ramshini, C. Parrini, A. Relini, M. Zampagni, B. Mannini, A. Pesce, A.A. Saboury, M. Nemat-Gorgani, F. Chiti, PLoS One 6 (2011) e16075.
[7] H.A. Lashuel, S.R. LaBrenz, L. Woo, L.C. Serpell, J.W. Kelly, J. Am. Chem. Soc. 122 (2000) 5262–5277.
[8] L.C. Serpell, Biochim. Biophys. Acta. 1502 (2000) 16–30.
[9] M.R. Krebs, K.R. Domike, A.M. Donald, Biochem. Soc. Trans. 37 (2009) 682–686.
[10] C.J. Bowerman, B.L. Nilsson, Biopolymers 98 (2012) 169–184.
[11] J. Hardy, D. Allsop, Trends Pharmacol Sci. 12 (1991) 383–388.
[12] A.S. DeToma, S. Salamekh, A. Ramamoorthy, M.H. Lim, Chem. Soc. Rev. 41 (2012) 608–621.
[13] Alzheimer's Disease International, World Alzheimer Report 2015: The Global Impact of Dementia, 2015. http://www.worldalzreport2015.org/.
[14] G. Stix, Sci. Am. 302 (2010) 51–57.
[15] I.W. Hamley, Chem. Rev. 112 (2012) 5147–5192.
[16] J.A. Hardy, G.A. Higgins, Science 256 (1992) 184–185.
[17] W.R. Markesbery, Free Radical Biol. Med. 23 (1997) 134.
[18] N. Okamura, M.T. Fodero-Tavoletti, Y. Kudo, C.C. Rowe, S. Furumoto, H. Arai, C. L. Masters, K. Yanai, V.L. Villemagne, Expert Opin. Med. Diagn. 3 (2009) 705.
[19] M.L. Steven, Brain Res. 760 (1997) 298–303.
[20] L. Guilloreau, L. Damian, Y. Coppel, H. Mazarguil, M. Winterhalter, P. Faller, J. Biol. Inorg. Chem. 11 (2006) 1024–1038.
[21] R. Jakob-Roetne, H. Jacobsen, Angew. Chem., Int. Ed. 48 (2009) 3030–3059.
[22] C.M. Wischik, M. Novak, H.C. Thogersen, P.C. Edwards, M.J. Runswick, R. Jakes, J.E. Walker, C. Milstein, M. Roth, A. Klug, Proc. Natl. Acad. Sci. USA 85 (1988) 4506–4510.
[23] R.N. Rambaran, L.C. Serpell, Prion 2 (2008) 112–117.
[24] D. Valensin, C. Gabbiani, L. Messori, Coord. Chem. Rev. 256 (2012) 2357–2366.
[25] S. Laurent, M.R. Ejtehadi, M. Rezaei, P.G. Kehoe, M. Mahmoudi, RSC Adv. 2 (2012) 5008–5033.
[26] S.L. Gras, L.J. Waddington, K.N. Goldie, Methods Mol Biol. 752 (2011) 197–214.
[27] T.W. Nakayama, K. Ono, M. Itami, R. Takahashi, D.B. Teplow, M. Yamada, Proc. Nat. Acad. Sci. USA 113 (2016) 5835–5840.
[28] K. Chen, M. Cui, Med. Chem. Commun. 8 (2017) 1393–1407.
[29] A.C. Sedgwick, J.T. Brewster II, P. Harvey, D.A. Iovan, G. Smith, X.-P. He, H. Tian, J.L. Sessler, T.D. James, Chem. Soc. Rev. 49 (2020) 2886–2915.
[30] R. Tycko, Annu. Rev. Phys. Chem. 62 (2011) 279–299.
[31] J.-X. Lu, W. Qiang, W.-M. Yau, C.D. Schwieters, S.C. Meredith, R. Tycko, Cell 154 (2013) 1257–1268.
[32] C. Bleiholder, N.F. Dupuis, T. Wyttenbach, M.T. Bowers, Nat. Chem. 3 (2011) 172–177.
[33] P. Sikorski, E.D.T. Atkins, L.C. Serpell, Structure 11 (2003) 915–926.
[34] H. Xiang, J. Cheng, X. Ma, X. Zhou, J.J. Chruma, Chem. Soc. Rev. 42 (2013) 6128–6185.
[35] X. Wang, O.S. Wolfbeis, R.J. Meier, Chem. Soc. Rev. 42 (2013) 7834–7869.
[36] N. Amdursky, Y. Erez, D. Huppert, Acc. Chem. Res. 45 (2012) 1548–1557.
[37] W.E. Klunk, R.F. Jacob, R.P. Mason, Anal. Biochem. 266 (1999) 66–76.
[38] P.K. Singh, M. Kumbhakar, H. Pal, S. Nath, J. Phys. Chem. B 114 (2010) 2541–2546.
[39] A.A. Reinke, J.E. Gestwicki, Chem. Biol. Drug Des. 77 (2011) 399–411.
[40] W.E. Klunk, Y. Wang, G.-F. Huang, M.L. Debnath, D.P. Holt, C.A. Mathis, Life Sci. 69 (2001) 1471.
[41] H.F. Kung, C.-W. Lee, Z.-P. Zhuang, M.-P. Kung, C. Hou, K. Ploessl, J. Am. Chem. Soc. 123 (2001) 12740.
[42] C.C. Kitts, T.B. Somfai, B. Norden, Biochemistry 50 (2011) 3451–3461.
[43] H.H. Lee, T.S. Choi, S.J.C. Lee, J.W. Lee, J. Park, Y.H. Ko, W.J. Kim, K. Kim, H.I. Kim, Angew. Chem., Int. Ed. 53 (2014) 7461–7465.

[44] M.N. Shinde, N. Barooah, A.C. Bhasikuttan, J. Mohanty, Chem. Commun. 52 (2016) 2992–2995.
[45] C. Wang, D. Liu, Z. Wang, Chem. Commun. 48 (2012) 8392–8394.
[46] Y. Liu, L.-P. Xu, W. Dai, H. Dong, Y. Wen, X. Zhang, Nanoscale 7 (2015) 19060–19065.
[47] M.S. Viegas, T.C. Martins, F. Seco, A. do Carmo, Eur. J. Histochem. 51 (2007) 59–66.
[48] S.A. Hudson, H. Ecroyd, T.W. Kee, J.A. Carver, FEBS J. 276 (2009) 5960–5972.
[49] K. Kalyanasundram, Photochemistry of Polypyridine and Porphyrin Complexes, Academic Press, San Diego, 1992.
[50] A. Kumar, S.-S. Sun, A.J. Lees, Top. Organomet. Chem. 29 (2010) 1.
[51] V. Sathish, A. Ramdass, P. Thanasekaran, K.-L. Lu, S. Rajagopal, J. Photochem. Photobio. C. Rev. 23 (2015) 25–44.
[52] H.K. Saeed, S. Sreedharan, J.A. Thomas, Chem. Commun. 56 (2020) 1464–1480.
[53] E. Meggers, Chem. Commun. (2009) 1001–1010.
[54] C.-N. Ko, G. Li, C.-H. Leung, D.-L. Ma, Coord Chem Rev 381 (2019) 79–103.
[55] J. Li, T. Chen, Coord Chem Rev 418 (2020) 213355.
[56] Y. Yuan, R.T.K. Kwok, B.Z. Tang, B. Liu, J. Am. Chem. Soc. 136 (2014) 2546–2554.
[57] H.K. Saeed, S. Sreedharan, P.J. Jarman, S.A. Archer, S.D. Fairbanks, S.P. Foxon, A. J. Auty, D. Chekulaev, T. Keane, A.J.H.M. Meijer, J.A. Weinstein, C.G.W. Smythe, J.B. de la Serna, J.A. Thomas, J. Am. Chem. Soc. 142 (2020) 1101–1111.
[58] T.D. Rae, P.J. Schmidt, R.A. Pufahl, V.C. Culotta, T.V. O'Halloran, Science 284 (1999) 805–808.
[59] S. Mounicou, J. Szpunar, R. Lobinski, Chem. Soc. Rev. 38 (2009) 1119–1138.
[60] K.P. Kepp, Coord. Chem. Rev. 351 (2017) 127–159.
[61] J.A. Duce, A.I. Bush, Prog. Neurobiol 92 (2010) 1–18.
[62] M.A. Greenough, J. Camakaris, A.I. Bush, Neurochem. Int. 62 (2013) 540–555.
[63] H. Kozlowski, M. Luczkowski, M. Remelli, D. Valensin, Coord. Chem. Rev. 256 (2012) 2129–2141.
[64] J.-M. Suh, G. Kim, J. Kang, M.H. Lim, Inorg. Chem. 58 (2019) 8–17.
[65] D.-L. Ma, C. Wu, G. Li, T.-L. Yung, C.-H. Leung, J. Mater. Chem. B 8 (2020) 4715–4725.
[66] D.J. Hayne, S.C. Lim, P.S. Donnelly, Chem. Soc. Rev. 43 (2014) 6701–6715.
[67] G. Li, L. Sun, L. Ji, H. Chao, Dalton Trans. 45 (2016) 13261–13276.
[68] A. Aliyan, N.P. Cook, A.A. Martí, Chem. Rev. 119 (2019) (1856) 11819–11821.
[69] A.C. Bhasikuttan, J. Mohanty, Chem. Commun. 53 (2017) 2789–2809.
[70] D. Kurouski, R.P. Van Duyne, I.K. Lednev, Analyst 140 (2015) 4967–4980.
[71] G. Li, L. Sun, L. Jia, H. Chao, Dalton Trans. 45 (2016) 13261–13276.
[72] F.E. Poynton, S.A. Bright, S. Blasco, D.C. Williams, J.M. Kelly, T. Gunnlaugsson, Chem. Soc. Rev. 46 (2017) 7706–7756.
[73] N.P. Cook, V. Torres, D. Jain, A.A. Marti, J. Am. Chem. Soc. 133 (2011) 11121–11123.
[74] N.P. Cook, M. Ozbil, C. Katsampes, R. Prabhakar, A.A. Marti, J. Am. Chem. Soc. 135 (2013) 10810–10816.
[75] N.P. Cook, K. Kilpatrick, L. Segatori, A.A. Martí, J. Am. Chem. Soc. 134 (2012) 20776–20782.
[76] X. Gao, L. Wang, H.-L. Huang, L.-L. Wang, J.-L. Yao, S. Shi, T.-M. Yao, Analyst 140 (2015) 7513–7517.
[77] P. Hanczyc, Chem. Phys. 445 (2014) 1–4.
[78] D.E.S. Silva, M.P. Cali, W.M. Pazin, E. Carlos-Lima, M.T. Salles Trevisan, T. Venâncio, M. Arcisio-Miranda, A.S. Ito, R.M.J. Carlos, J. Med. Chem. 59 (2016) 9215–9227.
[79] E. Babu, P. Muthu Mareeswaran, V. Sathish, S. Singaravadivel, S. Rajagopal, Talanta 135 (2015) 348–353.
[80] A.B. Iliuk, L. Hu, W.A. Tao, Anal. Chem. 83 (2011) 4440–4452.
[81] G. Son, B.I. Lee, Y.J. Chung, C.B. Park, Acta Biomater. 67 (2018) 147–155.
[82] L.C.-C. Lee, K.-K. Leung, K.K.-W. Lo, Dalton Trans. 46 (2017) 16357–16380.
[83] Y. Hong, L. Meng, S. Chen, C.W.T. Leung, L.T. Da, M. Faisal, D.A. Silva, J. Liu, J.W. Y. Lam, X. Huang, B.Z. Tang, J. Am. Chem. Soc. 134 (2012) 1680–1689.
[84] Y.L. Wang, C. Fan, B. Xin, J.P. Zhang, T. Luo, Z.Q. Chen, Q.Y. Zhou, X.N. Li, Z.L. Huang, C. Li, M.Q. Zhu, B.Z. Tang, Mater. Chem. Front. 2 (2018) 1554–1562.
[85] V. Sathish, E. Babu, A. Ramdass, Z.-Z. Lu, M. Velayudham, P. Thanasekaran, K.-L. Lu, S. Rajagopal, Talanta 130 (2014) 274–279.
[86] V. Sathish, A. Ramdass, E. Babu, Z.-Z. Lu, T.T. Chang, M. Velayudham, P. Thanasekaran, K.-L. Lu, W.S. Li, S. Rajagopal, RSC Adv 3 (2013) 18557–18566.
[87] V. Sathish, A. Ramdass, Z.-Z. Lu, M. Velayudham, P. Thanasekaran, K.-L. Lu, S. Rajagopal, J. Phys. Chem. B 117 (2013) 14358–14366.
[88] M.T. Gabr, F.C. Pigge, Chem. - Eur. J. 24 (2018) 11729–11737.
[89] M.T. Gabr, F.C. Pigge, Dalton Trans. 46 (2017) 15040–15047.
[90] M. Groenning, J. Chem. Biol. 3 (2010) 1–18.
[91] M. Biancalana, S. Koide, Biochim. Biophys. Acta Proteins Proteom. 1804 (2010) 1405–1412.
[92] A. Aliyan, B. Kirby, C. Pennington, A.A. Martí, J. Am. Chem. Soc. 138 (2016) 8686–8689.
[93] V.W.W. Yam, K.K.-W. Lo, K.-K. Cheung, R.Y.-C. Kong, J. Chem. Soc., Dalton Trans (1997) 2067–2072.
[94] T.-S. Kang, J.-T. Zhang, K. Vellaisamy, D.-L. Ma, C.-H. Leung, Dalton Trans. 47 (2018) 13314–13317.
[95] M.L.P. Reddy, K.S. Bejoymohandas, J. Photochem. Photobiol. C 29 (2016) 29–47.
[96] B.Y.-W. Man, H.-M. Chan, C.-H. Leung, D.S.-H. Chan, L.-P. Bai, Z.-H. Jiang, H.-W. Li, D.-L. Ma, Chem. Sci. 2 (2011) 917–921.
[97] C.-Y. Wong, L.-H. Chung, L. Lu, M. Wang, B. He, L.-J. Liu, C.-H. Leung, D.-L. Ma, Curr. Alzheimer Res. 12 (2015) 439–444.
[98] L. Lu, H.-J. Zhong, M. Wang, S.-L. Ho, H.-W. Li, C.-H. Leung, D.-L. Ma, Sci. Rep. 5 (2015) 14619.
[99] J. Kang, J.S. Nam, H.J. Lee, G. Nam, H.-W. Rhee, T.-H. Kwon, M.H. Lim, Chem. Sci. 10 (2019) 6855–6862.
[100] J. Kang, S.J.C. Lee, J.S. Nam, H.J. Lee, M.G. Kang, K.J. Korshavn, H.-T. Kim, J. Cho, A. Ramamoorthy, H.-W. Rhee, T.-H. Kwon, M.H. Lim, Chem. Eur. J. 23 (2017) 1645–1653.
[101] V.H. Houlding, V.M. Miskowski, Coord. Chem. Rev. 111 (1991) 145–152.
[102] V.W.-W. Yam, V.K.-M. Au, S.Y.-L. Leung, Chem. Rev. 115 (2015) 7589–7728.
[103] A.S.-Y. Law, L.C.-C. Lee, M.C.-L. Yeung, K.K.-W. Lo, V.W.-W. Yam, J. Am. Chem. Soc. 141 (2019) 18570–18577.
[104] B. Strodel, O.C. Weber, J. Chem. Inf. Model. 59 (2019) 1782–1805.
[105] M.C. Heffern, P.T. Velasco, L.M. Matosziuk, J.L. Coomes, C. Karras, M.A. Ratner, W.L. Klein, A.L. Eckermann, T.J. Meade, ChemBioChem 15 (2014) 1584–1589.
[106] A. Iscen, C.R. Brue, K.F. Roberts, J. Kim, G.C. Schatz, T.J. Meade, J. Am. Chem. Soc. 141 (2019) 16685–16695.
[107] A.M. Andrews, J.-E. Shea, Annu. Rev. Phys. Chem. 66 (2015) 643–666.
[108] A. Aliyan, T.J. Paul, B. Jiang, C. Pennington, G. Sharma, R. Prabhakar, A.A. Martı, Chem 3 (2017) 898–912.

Research Article

Antibacterial, Antifungal and Anticorrosion Properties of Green Tea Polyphenols Extracted Using Different Solvents

ThirumalaiRaj Brindha[1,*], Ramasamy Rathinam[2], Sivakumar Dheenadhayalan[3]

[1]Department of Science and Humanities, Faculty of Engineering, Karpagam Academy of Higher Education (Deemed to be University), Coimbatore, Tamil Nadu, INDIA.
[2]Department of Science and Humanities, Sri Eshwar College of Engineering, Coimbatore, Tamil Nadu, INDIA.
[3]Department of Science and Humanities, Erode Sengunthar Engineering College, Perundurai, Erode, Tamil Nadu, INDIA.

Submission Date: 03-01-2021; Revision Date: 06-03-2021; Accepted Date: 07-04-2021

ABSTRACT

The purpose of this study was to examine the antibacterial, antifungal and anticorrosion properties of green tea polyphenols extracted using different solvents like water, 70% ethanol, 70% methanol and dimethyl form amide. The extracted polyphenols were separated using TLC analysis. The antibacterial and antifungal activities were done by well diffusion method and it was found that polyphenols extracted using methanol and ethanol showed increased inhibition activity. Anti-corrosion property was investigated using weight loss measurements and showed significant inhibition effect for DMF extract.

Key words: Antimicrobial activity, Anticorrosion property, Green Tea, Polyphenols, TLC analysis, Ethanol, Methanol.

Correspondence:
Dr. T. Brindha
Assistant Professor, Department of Science and Humanities, Faculty of Engineering, Karpagam Academy of Higher Education (Deemed to be University), Coimbatore-641021, Tamil Nadu, INDIA.

Phone no: +91 8610313821
Email: brindhuchem@gmail.com

INTRODUCTION

Green tea leaves contains a bio-active component called polyphenol with activity against wide spectrum of microorganisms. For the past two decades, several studies were conducted on the testing of antimicrobial properties of green tea polyphenols. A number of surveys have indicated that green tea consumption reduces the risk of cardiovascular disease,[1] stroke[2] and obesity.[3] In addition to the therapeutic and biological activities many studies found to show *in vitro* antimicrobial activity against many bacteria and virus, specifically *Helicobacter pylori* (responsible for gastritis and implicated as a risk factor for stomach cancer) and α-haemolytic streptococci (the main aetiological agents of dental caries),[4] rotavirus, enterovirus and influenza virus,[5] yeasts,[6] filamentous fungi,[7] chlamydia, mycoplasmas[8] and parasites.[9]

SCAN QR CODE TO VIEW ONLINE

www.ajbls.com

DOI: 10.5530/ajbls.2021.10.10

Hence the present work aims to extract high purity with good yield of polyphenols from green tea by using various solvents and the analysis of polyphenols fractions by TLC. The green tea polyphenols were tested for its antibacterial, antifungal by well diffusion method and anticorrosion properties by gravimetric analysis.

MATERIALS AND METHODS

Plant Materials and Chemicals

Green tea (Camellia Sinensis) were purchased from local market and the solvents used were AR grade. Ethanol, methanol, chloroform, ethyl acetate and DMF were used of LR grade.

Extraction of Polyphenols from Green Tea

The extraction of polyphenols was done in three steps, viz., the sample for analysis were prepared following the conditions developed for optimized extraction of tea polyphenols in the laboratory. 25 g of coarse green tea was taken in round bottomed flask and 300 ml of water was added to it. The flask was kept for refluxing for 2 hr at 80°C. After refluxing the contents were filtered and volume of the extract was measured. The extracted filtrate was partitioned with chloroform (1:1,vol %) ratio to remove caffeine and related impurities. The aqueous phase was collected and the organic layer (chloroform layer) were discarded. Then the aqueous layer is extracted with ethyl acetate (1:1 ratio) and then the ethyl acetate layer was collected. Then ethyl acetate layer was evaporated by using rotary vacuum evaporator, to remove ethyl acetate. Then the concentrated filtrate was obtained and it was freeze dried. The crude sample of polyphenol was obtained. Similar procedure was adopted for all the solvents.

Antibacterial and antifungal activities of green tea polyphenols

A fungus (Penicillium) and bacteria (*Staphylococcus aureus*) were inoculated into two different conical flasks Containing 50 ml of SDA and NA (medium) using a flamed loop. Drops of fungus/water culture was mixed with the warm, melted, autoclaved PDA and poured into separate plates under aseptic conditions. The plates were covered and allowed to cool. As soon as the agar was partly solidified, the plates were inverted and left few minutes. When cooled, 5 wells were made at the centre of the plate. The wells were made by using a 6 mm cork borer or puncher that was sterilized with alcohol and flame. Ethanol and methanol extracted samples were dissolved in a solvent at final concentration of 10mg/1mL was pipette into the different wells in a sterilized environment at different volumes (0.1-0.2-0.4-0.6 ml) in plates, using a micro plates. Control wells were inoculated by Chloromphenicol and Ketakonizol for bacteria and fungi, respectively. The plates were labelled, covered, inverted and kept for incubation for about 48h. Zone of inhibition was measured.

Anticorrosion property of green tea polyphenols

The anti-corrosion properties of green tea polyphenols extracted using different solvents were investigated using weight loss measurements at room temperature. The mild steel specimen of the dimensions 2.5 cm × 1 cm × 0.1 cm has been used and was polished using different grades of emery papers, washed with double distilled water, dried and finally degreased with the acetone. In this method previously weighed coupon was completely immersed in 100 ml 1 M hydrochloric acid with and without green tea extracts in an open beaker. After an hour, the corrosion product was removed by washing each coupon using double distilled water. The washed coupon was rinsed in acetone and dried in the air before reweighing. From the average weight loss (mean of three replicate analysis) results, the inhibition efficiency of the inhibitor, and the corrosion rate of mild steel were calculated.

RESULTS AND DISCUSSION

TLC analysis of polyphenols

TLC profile of the extracted polyphenols was carried out and it was observed that separation of catechins on silica using the mobile phase ethylacetate:n-butanol:formic acid:water(10:6:2:2 v/v/v/v) showed the presence of two major bands with ethanol and methanol. The results of TLC analysis of catechin compounds on silica with the above mobile phase are presented in Figure 1. The presented results of TLC analysis on silica gel was obtained after standardizing various mobile phases and the mobile phase comprising ethyl acetate:n-butanol:formic acid:water showed a higher sensitivity on development of the plate with vanillin:suplhuric acid reagent.

Two major spots were noted in all the samples; coloured green and orange with R_f value of 0.22 for the green spot and 0.90 for the orange spot for the water extract. The R_f values for ethanol and methanol extracts were also found to be 0.18 (green spot) and 0.91,0.85 (orange spot) respectively. More or less the R_f values for water, ethanol and methanol extracts were found to be same (Table 1), from this we can infer that the catechin fractions were separated on silica gel by the application of the mobile phase.

Antibacterial and antifungal activities of ethanol and methanol extracted green tea polyphenols

The methanol and ethanolic extract of polyphenols showed significant antibacterial activity and antifungal activity by agar gel diffusion method.[10] The methanolic

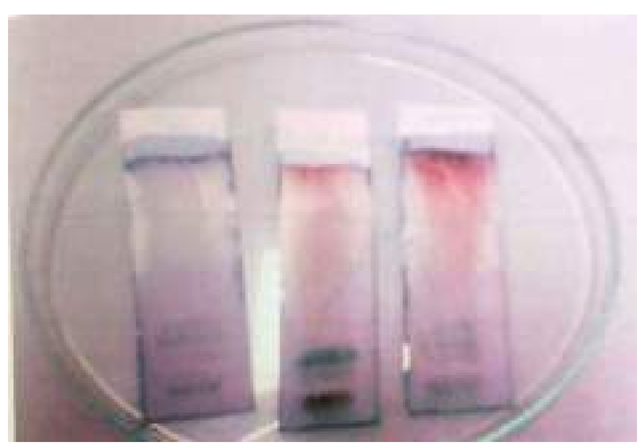

Figure 1: TLC Chromatogram of Catechin fractions of Green Tea Polyphenols water, ethanol and methanol.

extract showed marked antibacterial and antifungal activity against *Staphylococcus aureus* and Pencillium sps., respectively compared to other extracts. The antibacterial susceptibility of the methanolic and ethanolic extract of polyphenols seen in the Figure 2, 3 on *Staphylococcus aureus* indicate that even low concentrations of the extract was effective. Figure 4, 5 shows the antifungal susceptibility of the methanolic and ethanolic extract of the polyphenols on *Pencillium* sps., There was no antibacterial or antifungal activity for both the extracts when the concentration was 0.1 mg. The zones of inhibition of the extracts were distinct (Table 2) and comparable to the standard drug.

Table 1: R_f values of TLC Separated Polyphenols.

Type of extract	Colour of the spot	Rf value
Water	Green	0.22
	Orange	0.90
Ethanol	Green	0.18
	Orange	0.91
Methanol	Green	0.18
	Orange	0.85

The maximum inhibitory concentration (MIC) for antibacterial and antifungal activity of the methanol extract (0.4 ml) resulted in 26 mm and 15 mm respectively it was found to more or less similar to the inhibition levels of the standard chloromphenicol drug (43 mm). The result of the study showed that the solvent extracts of polyphenols produced prominent zones of inhibition against *Staphylococcus aureus* and *Penicillium*. This indicates the presence of potent antibacterial activity antifungal activity, and confirms reports on its use as anti- infective. Although both the methanol and ethanol extract of polyphenols produced inhibitory actions against the test organisms, methanol extracts showed more inhibitory effects than the ethanol extract. This tends to show that the active constituents in the leaves were better extracted with methanol than the other solvents.

Anticorrosion properties of green tea polyphenol extracts

The corrosion inhibition of green tea polyphenol extracted using water, 70% ethanol, 70% methanol and

Figure 2: Antibacterial activity of Green Tea Polyphenols extracted with water.

Figure 5: Antifungal activity of Green Tea Polyphenols with Ethanol.

Figure 3: Antibacterial activity of Green Tea Polyphenols extracted with Ethanol.

Figure 4: Antifungal activity of Green Tea Polyphenols extracted with Water.

Table 2: Antibacterial and antifungal activity of polyphenols.

Type of extract	Antibacterial activity		Antifungal activity	
	Concentration of the extract (ml)	Zone of inhibition (mm)	Concentration of the extract (ml)	Zone of inhibition (mm)
Ethanol	0.1	17.0	0.1	-
	0.2	18.0	0.2	17.0
	0.3	21.0	0.3	18.0
	0.4	32.0	0.4	20.0
Methanol	0.1	15.0	0.1	-
	0.2	24.0	0.2	18.0
	0.3	30.0	0.3	20.0
	0.4	26.0	0.4	15.0

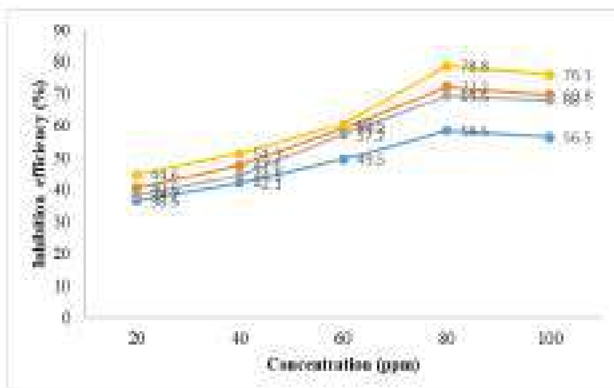

Figure 6: Plot of Inhibition efficiencies versus green tea polyphenols of different extracts on carbon steel in 1 M HCl.

dimethylformamide was investigated using weight loss measurements at room temperature on carbon steel in 1 M HCl. The inhibition efficiencies were calculated and its corresponding plot is given in the Figure 6. On analysing the graph it was found that inhibition efficiencies of green tea polyphenols extracted by all the solvents increases when its concentration increases.[11] But a significant corrosion protection of 78.8 % was found for DMF extract at 80 ppm. This may be attributed to the solvent effect which plays a greater role in the extraction of green tea polyphenols.

CONCLUSION

The antibacterial and antifungal activity carried out in this study revealed that even lower concentration (0.1 mg) of polyphenol extracted using ethanol and methanol were more effective against *Staphylococcus aureus* and *Pencillium* sps., It can be concluded that the green tea polyphenols not only possess antimicrobial property but also it have a strong efficiency towards corrosion on carbon steel in acid medium. Based on this study, it can be concluded that the extraction with ethanol and methanol are especially suitable for the antimicrobial and anticorrosion properties.

ACKNOWLEDGEMENT

I thank my organization for providing the opportunity to carry out the work.

CONFLICT OF INTEREST

The authors declare that there is no conflict of interest.

ABBREVIATIONS

TLC: Thin layer chromatography; **DMF**: Dimethyl formamide; **AR:** Analar; **LR:** Laboratory; **SDA:** Sabouraud dextrose agar; **NA:** Nutrient agar; **Rf:** Retention factor; **HCl:** Hydrochloric acid.

REFERENCES

1. Hertog MG, Feskens EJ, Hollman PC, Katan MB, Kromhout D. Dietary antioxidant flavonoids and risk of coronary heart disease: The Zutphen Elderly Study. Lancet. 1993;342(8878):1007-11.
2. Keli SO, Hertog MG, Feskens EJ, Kromhout D. Dietary flavonoids, antioxidant vitamins, and incidence of stroke: The Zutphen study. Arch Intern Med. 1996 ; 156(6) :637-42.
3. Bell SJ, Goodrick GK. A functional food product for the management of weight. Crit Rev Food Sci Nutr. 2002; 42(2):163-78.
4. Taylor PW, Hamilton-Miller JMT, Stapleton PD. Antimicrobial properties of green tea catechins. Food Sci Technol Bull. 2005; 2: 71-81.
5. Song JM, Lee KH, Seong BL. Antiviral effect of catechins in green tea on influenza virus. Antiviral Res. 2005; 68(2) :66-74.
6. Hirasawa M, Takada K. Multiple effects of green tea catechin on the antifungal activity of antimycotics against *Candida albicans.* J Antimicrob Chemother. 2004; 53 (2):225-9.

7. Okubo S, Toda M, Hara Y, Shimamura T. Antifungal and fungicidal activities of tea extract and catechin against Trichophyton, Nihon Saikingaku Zasshi. Japanese Journal of Bacteriology. 1991; 46(2) :509-14.
8. Chosa H, Toda M, Okubo S, Hara Y, Shimamura T. Antimicrobial and microbicidal activities of tea and catechins against Mycoplasma, Kansenshogaku Zasshi. The Journal of the Japanese Association for Infectious Diseases.1992; 66(5) :606-11.
9. Paveto C, Güida MC, Esteva MI, Martino V, Coussio J, Flawiá MM, *et al.* Anti-*Trypanosoma cruzi* activity of green tea (*Camellia sinensis*) catechins. Antimicrob Agents Chemother. 2004; 48(1) :69-74.
10. Arun SD, Minal MK, Karibasappa GN, Prashanth VK, Girija AD, Harish CJ. Comparative assessment of antibacterial efficacy of aqueous extract of commercially available black, green, and lemon tea: an *in vitro* study. Int J Health Sci . 2017;11(4): 42-6.
11. Zhang B, Yao R, Li L, Wang Y, Luo R, Yang L, *et al*. Green Tea Polyphenol Induced Mg2+-rich Multilayer Conversion Coating: Toward Enhanced Corrosion Resistance and Promoted *in situ* Endothelialization of AZ31 for Potential Cardiovascular Applications. ACS Appl Mater Interfaces. 2019;11(44):41165-77.

Cite this article: Brindha T, Rathinam R, Dheenadhayalan S. Antibacterial, Antifungal and Anticorrosion Properties of Green Tea Polyphenols Extracted Using Different Solvents. Asian J Biol Life Sci. 2021;10(1):62-6.

EAI Endorsed Transactions
on Energy Web
Research Article EAI.EU

Design and Analysis of Energy Efficient Domino Logic Architectures with Single Electron Transistors in Pull Down Network and Keeper Topology

B. AnishFathima[1,*], M. Mahaboob[2]

[1] Assistant professor, Sri Krishna College of Engineering and Technology, Coimbatore, India

[2] Assistant professor, Sri Eshwar College of Engineering, Coimbatore, India

Abstract

Nanotechnology and VLSI goes hand in hand. Modernization of electronics and communication systems has demanded for compactness of the devices with low power and high speed. Conventionally CMOS logic is preferred due to its low power and its high speed benefits. Researches demand a new logic style that can effectively replace conventional CMOS. Many styles including Domino logic are already gaining attention in this regard. The proposed work introduces Single Electron Transistors (SET) instead of NMOS in Pull Down Network and Keeper transistor of Domino Logic. As SETs are predominant in Nanotechnology, when employed in domino logic circuits as a fusion with normal MOS transistors will contribute effectively in terms of area, power and delay. The parameters are estimated with Cadence 45nm (SET- Spice Model) technology. The proposed domino logic architectures come up with an average of 68% energy efficiency when compared with conventional CMOS circuit and its Domino logic predecessors.

Keywords: Energy Efficient Domino Logic Design, Single Electron Transistor, Nanotechnology

Received on 11 September 2020, accepted on 19 November 2020, published on 27 November 2020

doi: 10.4108/eai.27-11-2020.167287

*Corresponding author. Email: anishfathimab@skceet.ac.in

1. Introduction

Emerging fields such as Artificial Intelligence, Machine Learning, Deep Learning, and Data Science requires compact devices with energy efficient characteristics at all levels. This compactness in area and energy efficiency has been explored over the years by researches throughout the world. Conventional CMOS logic devices have been used extensively in all VLSI circuits for its low power dissipation capabilities. Many logic styles such as Pseudo NMOS Logic, Pass Transistor Logic, Dynamic Logic and Domino Logic are already in the process of CMOS Logic for few circuits. In the proposed work, Domino logic is explored with various enhancements and optimizations. Initially Domino logic with normal NMOS & PMOS transistors were analysed [5]. Later the key element in most Nanotechnology applications called Single Electron Transistor (SET) are used instead of NMOS transistors as a hybrid combination [1, 4] especially in the predominant parts of Domino Logic Style of design. This replacement has proved to be better in case of power, delay and area efficiency. This enhanced version of Domino logic style can be very helpful in applications which demand for compact circuits with good energy efficiency as well.

The research paper is organised as follows: Section 2 about an overview of SETs and their literature; Section 3 gives an insight on exploring Domino logic style of designing circuits; Section 4 deals with the idea behind proposed method. Section 5 deals with the advantage of using SET also in keeper transistor. Section 6 deals result and further inferences from the result. Section 7 concludes the paper and discusses about the future scope and research possibilities.

2. SETs- An Overview

Single Electron Transistors are more likely nano-crystals with nano-size diameter where the source and drain are similar to normal MOSFETs except the channel which is replaced by a small dot like Tunnel Junction Diode. A vacuum or insulation layer is created by this Tunnel Junction Diode which gives the same gate capacitance (C_g) effect as that of normal MOSFET's. The gate voltage V_g is used to control the change on the Gate-Dot capacitance (C_g). The equivalent circuit of a SET and its symbolic representations are given in Figure 1. In Set, a very thin nearly 1nm thickness vacuum is the insulator which separates two piece of metals namely source and drain. The discrete electronic configuration of SET permits only one electron inside the tunnel with specific criteria. SET's are mainly explored for their faster performance than normal transmitters and can be widely explored in Single – electron memory and logic systems. But these sets can be implemented only for simple architectures. They suffer "offset charges" (i.e.,) the V_g (gate voltage) have to meet peak current which varies randomly from 1 device to other. This makes it highly impossible for complex circuits. Due to their unmatchable faster switching times, they can be implemented for denser & critical signal and image processing systems.

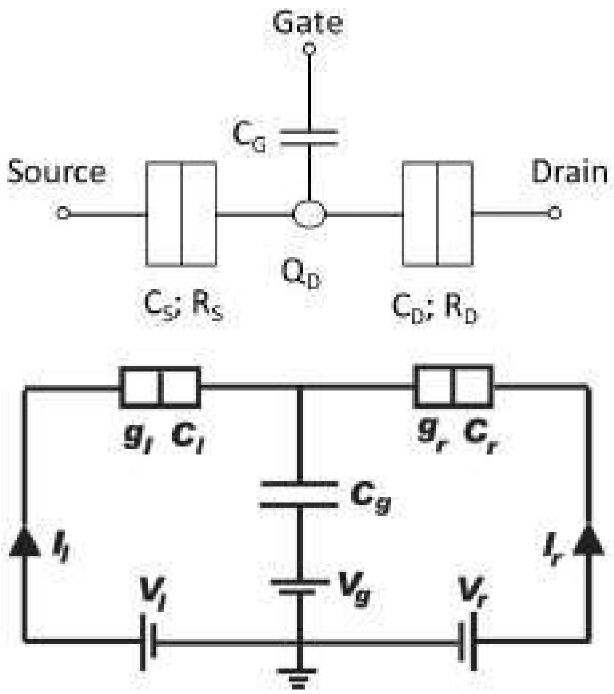

Figure 1. Symbolic representation and equivalent circuit of SET

SET research all started off with a hybrid SET-MOS architecture which was later converted to negative differential resistance architecture by shorting Gate and Drain terminals [1]. Another hybrid CMOS-SET circuit Monte Carlo Simulations were carried out to analyse its sustainability for CAD frameworks in designing IC's [2]. In order to minimize the power utilization for embedded system design [3] was proposed which quite succeeded in fulfilling the need. The gate input voltage had to be much more than the power supply for the SET for decent switching properties was proposed in [4] which eventually failed as it was practically unrealizable for building circuits.

3. Exploring Domino Logic Circuits

In order to overcome the occurrence of a hardware glitch because of dynamic logic, domino logic circuits were proposed. The general architectures of a domino logic stages is shown in Figure 2 and 3.

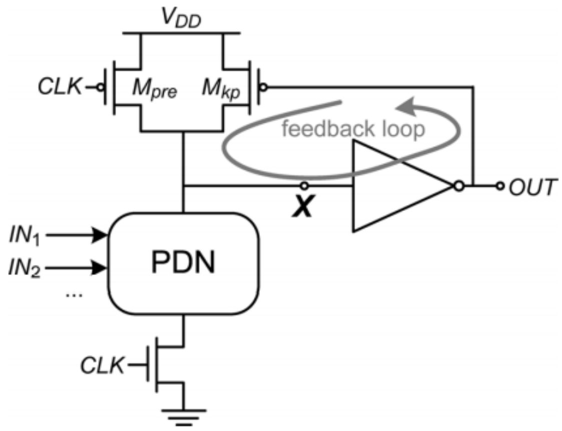

Figure 2. General architecture of Domino Logic

As seen in Figure 2, a Domino Logic contains a Pull Down Network(PDN) comprising only NMOS transistors. It contains a Precharge transistor and Evaluation transistor which works with every trigger of clock pulses. The architecture usually contains an inverter. Special enhancement to domino logic has introduced another transistor called keeper transistor. Figure 3 shows how number of Fan- in can affect the working of PDNs.

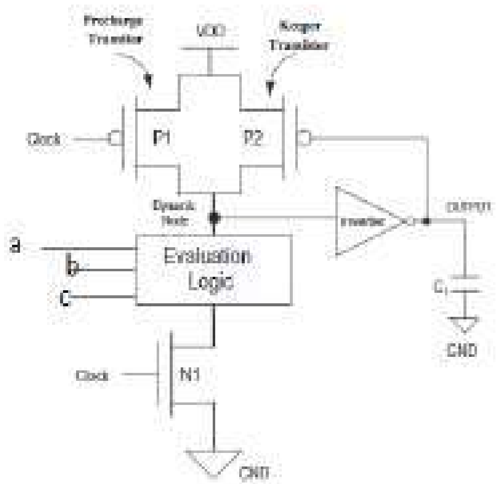

Figure 3. Architecture of Domino Logic with inputs

The inverter creates an output (with reference to Figure 2) as follows:$F\ (a, b, c) = \bar{F}$.This domino logic is basically non-inverting in nature because of a inverter at the exit part of

architecture. Domino logic works with clock values [12] in two phases.
Phase I: When clock $\phi = 0$, it initiates the pre changing phase where C_x pre changes to $V_x = V_{DD}$.
Phase II: When clock $\phi = 1$, it initiates the evaluation phase when the logic corresponding to the bank of nFETs are performed. Domino logic is always preferred in cascades. (i.e.,) output of 1st stage connected to input of next stage. But all stages are controlled by same clock signal ϕ.

Domino logic researches are going on from early 1990's. The various issues of domino logic circuits were discussed [5]. Later the variable threshold voltage keeper transistor was introduced to overcome the issues in noise margin [6].In this work, single electron transistors were used along with normal MOSFET's to overcome the issues associated with high power dissipation and more propagation delay of domino logic. Certain researches tried to incorporated single electron transistor with dynamic logic [7,13] where sets are used as pseudo transistors with great advantage that it is consistent in voltage levels and can be used for realizing hybrid circuits. A technique similar to our proposed work was elucidated in [9] but that used Fin FET Technology and analysed better noise performance and improve power delay product.

4. Proposed Domino Logic Architecture with SET in Pull-Down Network

Various CMOS logic architectures such as Inverter, NAND, NOR, OR, AND, EX-OR circuits were analysed. Their power, delay and area were found to be good enough for sustaining in the current scenario. But for future Nano-scale devices and technologies, we are in need of more precise and compact devices (deep sub-micron devices) [14,15] and therefore VLSI architectures. In this view, we have proposed using domino logic as an alternative to basic circuits as mentioned above. There is a twist to this switch over. We not only use normal MOSFET's, but also use SET's (Single Electron Transistor) in the architecture.

SET's are used only in the pull-down network of domino structures. Normal MOSFET's are used in the clock handling PMOS and NMOS part. This is because when clock is in pre-charge phase, the power dissipation will be higher than in the evaluation phase. To control power dissipation in pre-charge, MOSFET's are used. The architectures include for analysis are BUF, NAND2, NAND4, NOR2, NOR4, NOR8, and NOR16.

Even though SET's are used for bringing down the power consumption and area utilized. This proposed method also encounters the delay variation problem like normal domino logic. In order to overcome this delay variation, the loop and keeper transistors are utilized.

5. Keeper Transistor Modification Using SET

5.1 Analysis of Delay Variation

From [10], a small modification to our proposed method gave a good result even in the delay variations. Let us consider Figure 4 as a test circuitry for evaluation of delay variations. It is a well-known fact that there is always a trade-off between noise immunity and speed in domino logic circuit which basically rely on the keeper ratio (K) which is defined as the ration between saturation current of keeper transistor and overall pull down network. To overcome delay, K must be low than unity (preferably from 0.1 to 0.5). For this we need the PMOS of output in inverter four times wider than its NMOS.

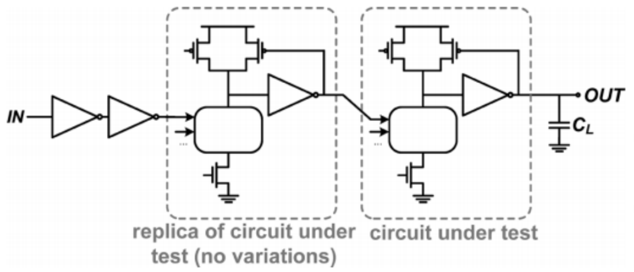

Figure 4. Circuit for evaluation of delay variations

In order to analyse delay variations, the above mentioned test circuit is treated with 200 runs of Monte Carlo simulations in 45nm CMOS spice tool. The Mean (μ), Standard Deviation (σ), Variability (σ/μ) are all noted for the delay. This test is done with load capacitance to kept at a minimum value by fixing the aspect ratio of inverter and PDN network as $(W/L)_{inv}$ is twice that of $(W/L)_{PDN}$. M_{kp} is sized to achieve keeper ratio K=0.1

5.2 Modifying Positive Feedback Loop to Reduce Delay Variations

A better architecture to split the keeper transistor and hence decrease its transconductance effect while keeping the same strength is shown in Figure 5.

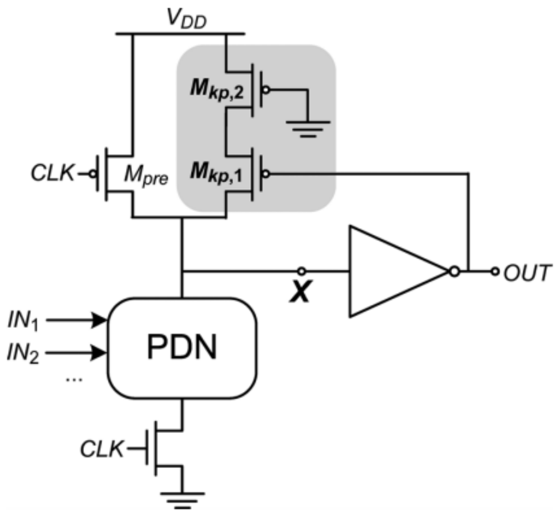

Figure 5. Split keeper transistors

(i.e) as per the methodology used in [10], the original keeper transistor is split into two M_{kp1} and M_{kp2} whose aspect ratios are accordingly

$$\left(\frac{L}{W}\right)_{kp1} + \left(\frac{L}{W}\right)_{kp2} = \left(\frac{L}{W}\right)_{kp}$$

Where kp→Keeper transistor; kp1 and kp2→ splitted values; (L/W) →inverse of Aspect Ratio to split kp equally, W→width of channel; L→Length of channel

To achieve this $W_{kp1} = W_{kp2} = W_{kp}$and $L_{kp1} + L_{kp2} = L_{kp}$ is followed. Even though the transistors are split, the resistance value will be maintained as given below:

$$R \cong [\,\mu p\ cox \left(\frac{W}{L}\right)_{kp2} (V_{DD} - |VtP|)]^{-1}$$

Where R→Dynamic Resistance; µp→mobility of PMOS; cox-→oxide capacitance; VDD→Supply voltage; Vtp-> threshold voltage of PMOS.

In our proposed system, the two split keeper transistors are also replaced with Single Electron Transistor (SET's). This modification brings down delay variations as well as improves the overall working performance of the domino logic circuits, with almost 80% decrease in power consumption and 63% decrease in speed.

6. Design Consideration, Simulation Results and Inferences

In the proposed work, the simulations for all the architectures are carried with the following specifications.

Pre-charge and Evaluation MOSFET Specification

The aspect ratios of precharge and Evaluation transistors are considered with the specification

$$(W/L)_{pre} = 1 \text{ and } (W/L)_{Eval} = 1$$

This can be achieved if

$$W_{pre} = W_{Eval} = 45\text{nm and } L_{pre} = L_{Eval} = 45\text{nm}$$

6.1 Pull Down Network SET Specification

The aspect ratios of Pull Down Network transistors are considered with the specification

$$(W/L)_{PDN} \Rightarrow \text{series of } (W/L)_{SETS}$$

Which are having same aspect ratio as that of pre-charge and evaluation transistors but the channel insulation layer is very thin approximately 5 to 10nm.

6.2 Keeper Transistor Specification

As per the approach proposed in [10], for the reduced delay in domino logic, keeper transistor is split into two with following specification,

$$\left(\frac{L}{W}\right)_{kp1,SET} \ and\ \left(\frac{L}{W}\right)_{kp2,SET}$$

$$W_{kp1} = W_{kp2} = 45\text{nm}$$
$$L_{kp1} + L_{kp2} = 45\text{nm}$$
$$L_{kp1} = L_{kp2} = 22.5\text{nm}$$

With these design consideration, the result obtained is 45nm CMOS Cadence SPICE tool with SET are discussed below. On an average of 10 buffer samples are considered for final values. In order to show the difference, CMOS logic is also included in the discussion of Table1.

Table 1 compares the Parameters considered for Area, Power, and Delay [11] constraints of a Buffer Architecture in CMOS logic, Traditional Domino with Keeper logic, and Domino with Split Keeper logic and proposed Domino with SET in PDN & Keeper logic (DSPK).

Table 1. Circuit Analysed: Buffer

Logic	Area (LUTS)	Power (mW)	Delay (ns)	Delay Variation (%)
CMOS	15	1.8	2.85	-
Traditional Domino with Keeper	13	1.632	5.19	8.86
Domino with Split Keeper	14	1.412	5.08	3.21
DSPK	**13**	**1.210**	**2.88**	**3.05**

Table 2 compares the Parameters considered for Area, Power, Delay constraints of a 2 input NAND Architecture in all four logic styles.

Table 2. Circuit Analysed: NAND2

Logic	Area (LUTS)	Power (mW)	Delay (ns)	Delay Variation (%)
CMOS	20	7.5	8.15	-
Traditional Domino with Keeper	18	6.99	10.53	10.34
Domino with Split Keeper	19	6.56	10.02	7.45
DSPK	**18**	**6.33**	**7.94**	**7.00**

Table 3 compares the Parameters considered for Area, Power, Delay constraints of a 4 input NAND Architecture in all four logic styles.

Table 3. Circuit Analysed: NAND4

Logic	Area (LUTS)	Power (mW)	Delay (ns)	Delay Variation (%)
CMOS	33	17.3	18.15	-
Traditional Domino with Keeper	28	16.69	12.73	12.76
Domino with Split Keeper	29	16.65	12.42	11.45
DSPK	**28**	**16.23**	**11.43**	**10.00**

Table 4 compares the Parameters considered for Area, Power, Delay constraints of a 2 input NOR Architecture in all four logic styles.

Table 4. Circuit Analysed: NOR2

Logic	Area (LUTS)	Power (mW)	Delay (ns)	Delay Variation (%)
CMOS	21	7.52	8.25	-
Traditional Domino with Keeper	19	6.97	10.89	10.50
Domino with Split Keeper	18	6.46	10.70	7.39
DSPK	**19**	**6.32**	**7.86**	**6.89**

Table 5 compares the Parameters considered for Area, Power, Delay constraints of a 4 input NOR Architecture in all four logic styles.

Table 5. Circuit Analysed: NOR4

Logic	Area (LUTS)	Power (mW)	Delay (ns)	Delay Variation (%)
CMOS	33	17.23	18.25	-
Traditional Domino with Keeper	28	16.95	12.37	13.86
Domino with Split Keeper	29	16.32	12.4	12.62
DSPK	**28**	**16.03**	**11.99**	**11.38**

Table 6 compares the Parameters considered for Area, Power, Delay constraints of an 8 input NOR Architecture in all four logic styles.

Table 6. Circuit Analysed: NOR8

Logic	Area (LUTS)	Power (mW)	Delay (ns)	Delay Variation (%)
CMOS	43	27.33	28.55	-
Traditional Domino with Keeper	38	26.00	22.73	23.86
Domino with Split Keeper	39	24.58	21.09	22.62
DSPK	37	24.00	21.20	11.00

Table 7 compares the Parameters considered for Area, Power, Delay constraints of a 16-input NOR Architecture in all four logic styles.

Table 7. Circuit Analysed: NOR16

Logic	Area (LUTS)	Power (mW)	Delay (ns)	Delay Variation (%)
CMOS	54	39.77	38.79	-
Traditional Domino with Keeper	47	36.25	32.45	28.55
Domino with Split Keeper	48	33.20	31.30	23.21
DSPK	**47**	**32.69**	**31.35**	**12.50**

From the above tables [1 to 7], it is inferred that when these structures are simulated and analysed in SPICE platforms like Cadence, the proposed system gives on an average an improvement of 80% improvement in power consumed and 63% improvement in speed. Thus 68% energy efficiency is obtained from the proposed architecture. This is achieved because of the effective usage of SETs in both PDN and Keeper transistors of Domino architectures. Also the delay variations are comparatively lesser than the conventional architectures of Domino logic. Moreover, the area utilized is also less making it prominent for Compact size applications especially Nano-electronics and other Nano applications.

7. Conclusion

The replacement of static CMOS logic in VLSI was never easier. Few steps have shown significant improvements in other logic styles as well but restricted to their applications. In this work also, the proposed hybrid architecture works with wonderful performance if used only for fundamental circuits. The effective replacement of MOSFET's with SET's both in pull down network and in keeper transistor have worked really well for improving power and delay variability performance in domino logic style. This will have its drawbacks for complex circuits as SET's will degrade noise immunity of domino. Hence, it is best suited for simple basic gates which can find great application in Nano Technology like Nano electronics, Nano robotics. The future work of this paper will try to bring in SET's even more effectively into domino logic style. To conclude, this proposed work has brought 80% of power enhancement and 63% of delay improvement when compared with its predecessors.

Further this work can be continued by applying optimized aspect ratio values to SETs in PDN and keeper topology as a future work.

References

[1] A.M.Lonescu, S.Mahapatra, V.Pott, "Hybrid SETMOS architecture with column blockade Oscillation and High Current Device", IEEE Electron devices Letters, Volume 25, Issue 6, 2004.

[2] Santanu Mahapaba, Vaiba Vaish, Christoper Wasshumber, Kaustar Banajee, Adrias Mihai Lonesan, "Analytical modelling of Single Electron Transistor for hybrid CMOS-SET analysis IC Design", IEEE Transaction an Electron Devices, 2004.

[3] Changyun Zhu, Zhenyu Gu, Listang, Robert P Dick, Robert G Kobel, "Towards an ultra – low – power architecture using Single Electron Tunnelling Transistors", Proceedings of 44th Annual Design Automation Conference, page 312-317, 2007.

[4] Aranggan Venkataraman, Ashok K Gocl, "Design and Simulation of Logic Circuits whith hybrid architectures of Single Electron Transistors and Conventional MOS devices at Room Temperature", Microelecronics Journal 39(12), page 1461-1468, 2008.

[5] P.Srivasta, A.Puraa, L Welch,"Issues in the design of Domino Logic Circuits", Proceedings of the 8th Great Lakes Symposium on VLSI, page 108-112, 1998.

[6] Volkan Kursun, Eby G Friedman, "Domino Logic with Variable Threshold Voltage Keeper", IEEE Transaction on Very Large Scale Integration(VLSI) systems, 11(6), page 1080-1093,2003.

[7] Ken Udhida, Kaznya Matsuzawa, Akirra Torium, "A New Design scheme for Logic circuits with Single Electron Transistor", Japanese Journal of applied Physics, Volume 38, Part 1, Number A, 1999.

[8] Ken Uchida, "Single Electron transistor and circuits for future Ubiquestors Computing Applications", ,2006, Proceeding of 32nd European solid state circuits conference, 17-20, 2006.

[9] Sandeep Hang, Taurn K Gupta, "SCDNDTDL: A Technique for Designing low-power Domino circuits in Fin FET Technology", Journal of Computational and Electronics, 2020.

[10] Gateano Palumb, Melita Pennisi, Massino Alito,"A simple circuit to approach to reduce delay variations in domino logic gates", IEEE Transications on Circuits & Systems, page 1549, 2012.

[11] A. Srivastava, D. Sylvester, and D. Blaauw, "Statistical Analysis and Optimization for VLSI: Timing and Power", New York: Springer, 2005.

[12] R. Sung and D. Elliott, "Clock-logic Domino circuits for high-speed and energy-efficient microprocessor pipelines," IEEE Trans. Circuits Syst.II,Exp.Briefs,vol.54,no.5,pp.460–464,May2007.

[13] F. Frustaci, P. Corsonello, S. Perri, and G. Cocorullo, "High-performance noise tolerant circuit techniques for CMOS dynamic logic," IET Circuits Devices Syst.,vol.2,no.6,pp.537–548,Jun.2008.

[14] J.-J.Liou, A.Krstic, Y.-M.Jiang and K.-T.Cheng, "Modeling, testing, and analysis for delay defects and noise effects in deep submicron devices," IEEE Trans.Comput.-Aided Design Integr.Circuits Syst.,vol. 22, no. 22, pp. 756–769, Jun. 2003.

[15] J.A.Croon, W.Sansen and H.E.Maes, "Matching Properties of Deep Sub-Micron MOS Transistors", NewYork: Springer, 2005.

IJE TRANSACTIONS B: Applications Vol. 33, No. 11, (November 2020) 2215-2221

International Journal of Engineering

Journal Homepage: www.ije.ir

An Ultra-low-power Static Random-Access Memory Cell Using Tunneling Field Effect Transistor

N. Arunkumar[a], N. Senathipathi[a], S. Dhanasekar*[b], P. Malin Bruntha[c], C. Priya[d]

[a] *Department of ECE, P.A College of Engineering and Technology, Pollachi, India*
[b] *Department of ECE, Sri Eshwar College of Engineering, Coimbatore, India*
[c] *Department of ECE, Karunya Institute of Technology and Sciences, Coimbatore, India*
[d] *Department of ECE, Karpagam College of Engineering Coimbatore, India*

PAPER INFO

Paper history:
Received 28 February 2020
Received in revised form 04 August 2020
Accepted 03 September 2020

Keywords:
Static Random-Access Memory
Homojunction
Heterojunction
Tunneling Field Effect Transistor
Complementary Metal Oxide Semiconductor

ABSTRACT

In this research article, an Ultra-low-power 1-bit SRAM cell is introduced using Tunneling Field Effect Transistor (TFET). This paper investigates feasible 6T SRAM configurations on improved N-type and P-type TFETs integrated on both InAs (Homojunction) and GaSb-InAs (Heterojunction) platforms. The voltage transfer characteristics and basic parameters of both Homo and Heterojunctions are examined and compared. The proposed TFET based SRAM enhances the stability in the hold, read, and write operations. This work evaluates the potential of TFET which can replace MOSFET due to the improved performance with low-power consumption, high speed, low sub-threshold slope, and supply voltage (VDD = 0.2 V). The results are correlated with CMOS 32nm technology. The proposed SRAM TFET cell is implemented using 30nm technology and simulated using an H-SPICE simulator with the help of Verilog-A models. The proposed SRAM TFET cell architecture achieves low power dissipation and attains high performance as compared to the CMOS and FINFET.

doi*: 10.5829/ije.2020.33.11b.13*

NOMENCLATURE

C_d	Depletion layer capacitance	Q	Elementary charge
C_{ox}	Gate oxide capacitance	Const	Device dimensions and materials parameter
T	Temperature	Vgs	Gate source voltage
k	Boltzmann constant		

1. INTRODUCTION

In the present scenario, several researchers are working towards reducing the size of the transistors to make miniature Integrated Chip (IC) [1]. The silicon CMOS technology has become an effective fabrication process for high performance and lucrative VLSI circuits. Most of the VLSI industries are using CMOS, which is having a high sub-threshold slope and high-off current at room temperature [5]. Due to this factor, the leakage current and heat of the system is also increased [7]. In SRAM cell, thick gate oxide present in the long channel device is used to reduce the leakage current. OFDM transceiver IC is used to provide high-speed data transmission in wideband wireless communication [8]. TFET is a forthcoming transistor that is studied extensively on the way towards power-efficient integrated circuits as a replacement of CMOS in the supply voltage regime below VDD = 0.3 V [3-5].

In this work, the TFET characteristics are briefly explained and TFET based SRAM cell is designed with two different types: Homojunction and Heterojunction [9-12]. These results are compared with the 32 nm CMOS SRAM design. The sub-threshold slope, power and supply voltages are reduced. The switching speed of the system can also be increased by using TFETs [10].

*Corresponding Author Email: *dhanasekar.sm@gmail.com* (S. Dhanasekar)

Please cite this article as: N. Arunkumar, N. Senathipathi, S. Dhanasekar, P. Malin Bruntha, C. Priya, An Ultra-low-power Static Random-Access Memory Cell Using Tunneling Field Effect Transistor, International Journal of Engineering (IJE), IJE TRANSACTIONS B: Applications Vol. 33, No. 11, (November 2020) 2215-2221

This paper methodized the Tunneling Field Effect Transistor in Section 2. Homojunction and Heterojunction TFETs are presented in Section 3. Section 4 portrays the proposed TFET based SRAM design. The results of SRAM design are discussed in Section 5. The article concluded in Section 6.

2. TUNNELING FIELD EFFECT TRANSISTOR

For achieving low energy electrons, a new type of transistor TFET is proposed, which is used in the family of Field Effect Transistor (FET) under the division of MOSFET [2]. The MOSFET is working based on the thermionic emission principle but TFET operates based on the quantum tunneling mechanism, because of this sub-threshold slope of TFET is less than 60mV/dec at room temperature [6].

2. 1. Structure and Operation of TFET

The TFET structure is analogous to the MOS transistor excluding the source and drain terminals shown in Figure 1. In TFET, the source terminal is doped with a p-type material and the drain terminal is doped with an n-type material. The TFET structure also named as P-I-N (P-type source terminal, intrinsic region, and N-type drain terminal) structure [3].

The tunneling process occurs at the sufficient gate bias where the electron moves from the lower band of the p-type source terminal to the upper band of drain terminal [5]. If the gate bias is reduced, the current cannot flow a long time because of band misalignment [13-14]. When the transistor attains off condition it is in the same mode and there are no electrons will move from p-type to n-type terminal [15-17].

The NTFET Tunneling process is shown in Figure 2. The operation of NTFET is the same as the operation of PTFET but the difference attains only the majority carriers. In NTFET, the majority carriers are electrons and holes are the majority carriers in PTFET. The gate voltage is a negative voltage for PTFET, it is same as the MOSFET but there is no body bias in TFET [11]. In the N-channel case, the Fermi level is very close to the valence band edge due to high density of states for holes. In the P-channel, the Fermi level degeneracy is quite high due to low density of states for electrons. This causes a high energy tail, which limits the sub-threshold slope and gives rise to a strong temperature dependence similar to that of a MOSFET [23].

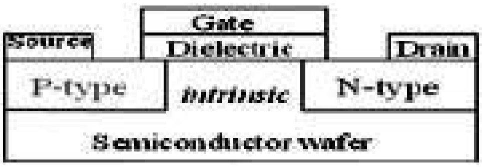

Figure 1. Basic Structure of TFET

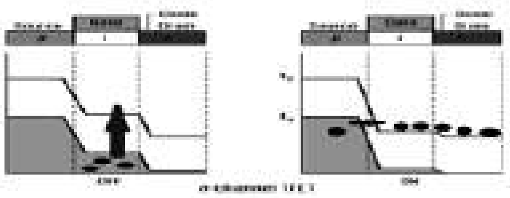

Figure 2. NTFET Tunneling Process

2. 2. Sub-threshold Swing

The sub-threshold swing is the reciprocal value of the sub-threshold slope. The sub-threshold slope is a slope of logarithmic drain current and gate voltage characteristic of MOSFET. The sub-threshold swing of MOSFET is given below:

$$SS_{MOSFET} = \ln(10)\left(\frac{kT}{q}\right)\left(1+\frac{C_d}{C_{ox}}\right) \text{ [mV/dec]} \quad (1)$$

Based on Equation (1), the leakage current of the conventional device lies in the sub-threshold region. The above equation is used only for MOSFET. For calculating the sub-threshold swing of TFET, another equation is used as the mechanism depends on the tunneling barrier width [4] which is given by:

$$SS_{TFET} = \frac{V_{gs}^2}{5.75(Vgs+Const)} \text{ [mV/dec]} \quad (2)$$

If the sub-threshold swing of a device is small, then the leakage current, power dissipation and the threshold voltage of a device will also occur quite low [18]. Field Programmable Gate Array (FPGA) provides more flexible, accurate in simulating, testing and gives end to end solutions for reprogramming the proposed designs in the hardware [19].

3. HOMOJUNCTION AND HETEROJUNCTION TUNNEL FIELD EFFECT TRANSISTORS

The sub-threshold slope, power consumption and delay of the TFET are reduced based on the band-gap of the materials which is used for TFET fabrication. TFET is divided into two categories based on semiconducting materials.

3. 1. InAs Homojunction

A Homojunction is a semiconductor material that has equal band gaps in between two layers of similar semiconductors with different doping concentrations. InAs is used for high electron mobility and it is a direct band-gap material [12]. The values of basic parameters for InAs are energy gap=0.354 eV, Intrinsic carrier concentration=1.1015 cm-3, Intrinsic resistivity=0.16 Ω.cm, Effective conduction band density of states =8.7x1016 cm-3, Effective valence band density of states=6.6x1018 cm-3.

3. 2. GaSb-InAs Heterojunction A Heterojunction is a semiconductor material which is having unequal band gaps in between two layers of dissimilar semiconductors. The energy band diagram of Heterojunction types is shown in Figure 3. It works at high frequency and also used in High Electron Mobility Transistors (HEMT). TFET operates at minimum voltage when the band gaps of crystalline semiconductors are unequal [20]. The Heterojunction semiconductor alignment is divided into three types. Those are a Straddling gap, Staggered gap and Broken gap [12].

In this paper, the two types of TFETs, Homojunction and Heterojunction are simulated. these two TFETs are compared with its basic parameters based on the results. When it is in contact, GaSb and InAs have non-overlapping band-gap, which forms more interesting phenomena in heterostructure from those materials. In an intrinsic heterostructure, the carriers are generated by the migration of charges from GaSb to InAs layers. Here the sheet densities of mobile electrons and holes are the same [11].

For a large number of experiments, it is useful to control the electron-hole ratio. In the broken band-gap arrangement of GaSb-InAs heterostructure, InAs conduction band occurs lower in energy than the GaSb valence band, it causes charge. Mobilization from the GaSb to the InAs layers [21]. Due to this arrangement, intrinsic populations of mobile electrons and holes are generated in the absence of doping. For thin InAs wells, quantization of the confinement energy becomes significant at low temperature, leading to quasi-two-dimensional behavior as the carrier wave functions are restricted in growth to the direction for a number of states corresponding to discrete sub-band energies [22].

4. PROPOSED TUNNEL FIELD EFFECT TRANSISTOR BASED STATIC RANDOM-ACCESS MEMORY DESIGN

Static Random-Access Memory (SRAM) is a volatile semiconducting memory, which is used to store on condition without periodic data as long as the power supply is refreshed. SRAM is a high-speed memory cell in the RAM family. The 6T TFET SRAM circuit is shown in Figure 4.

4. 1. SRAM Cell Operation The SRAM cell contains six TFET transistors which are X1, X2, X3, X4,

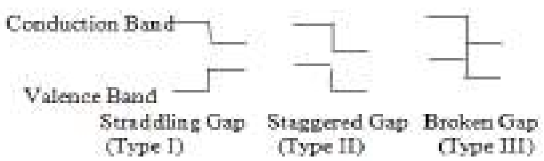

Figure 3. Heterojunction Types

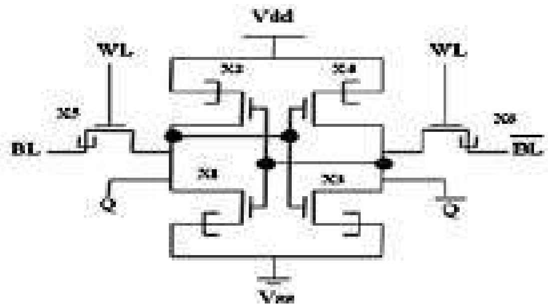

Figure 4. 6T TFET SRAM Circuit

X5, and X6. Here two TFET inverters (X1, X2, X3 and X4) are cross-coupled. During read and write operations the access is controlled by two additional TFET transistors X5 and X6. Because of this architecture, the supply voltage of a cell is less than 0.25 V, the power dissipation is also very low and it has high noise immunity. There are three stages present in SRAM named as read, write and hold mode operations. The working of these stages is given below.

4. 1. 1. Hold For the hold operation the word line should be 0 (WL = 0). So, the access transistors X5 and X6 are not able to connect with the bit lines because of this SRAM keeps the present data in the cross-coupled inverters (X1, X2, X3, and X4) as long as the supply voltage is ON.

4. 1. 2. Reading To read the data from SRAM cell Word Line (WL) is always in the ON condition and both the bit lines should be recharged. The sense amplifier is used to sense the data from the SRAM cell. The output of the SRAM cell is given as input of sense amplifier. The Q and $\overline{Q}$ are the inputs of sense amplifier, if Q < $\overline{Q}$ then the output of sense amplifier is 0, and if Q > $\overline{Q}$ then the output is 1.

4. 1. 3. Writing To write a 1 into the SRAM cell, first WL and BL (Bit Line) should be 1 and $\overline{BL}$ should be 0. If 0 is written to the SRAM cell, then the value of BL should be inverted.

5. RESULTS AND DISCUSSION

5. 1. SRAM Write Operation by using TFET In Homojunction TFET when the word line is ON (WL=1), the SRAM circuit allows the external input inside the cell to store the data. If WL=0, then SRAM circuit keeps the previous data which is shown in Figure 5. The power of the Homojunction SRAM is 17.8 nW.

In Heterojunction TFET, when the word line is ON (WL=1), the SRAM circuit allows the external input, inside to store the data. If WL=0, then the GaSb-InAs

SRAM circuit keeps the previous data which is shown in Figure 6. The power of the Heterojunction SRAM is 0.38nW.

5. 2. SRAM Read Operation by using TFET In 6T TFET SRAM Read Operation, the sense amplifier is connected to read the stored data from SRAM cell. For read operation, the word line should be 0 (WL=0). The output of the Homojunction TFET SRAM read operation result is shown in Figure 7. The power of the Homojunction SRAM cell is 208.2 nW.

For a read operation, the word line should be 0 (WL=0). The output of the Hetrojunction TFET SRAM read operation result is shown in Figure 8. The power of Heterojunction SRAM cell is 1.87 nW.

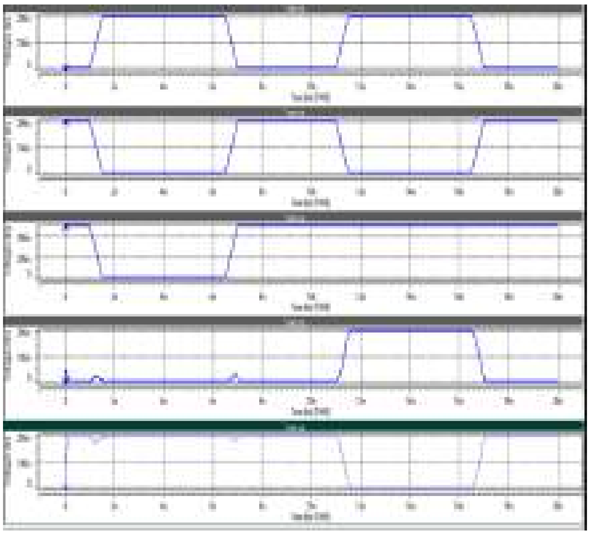

Figure 5. Homojunction 6T SRAM write operation result

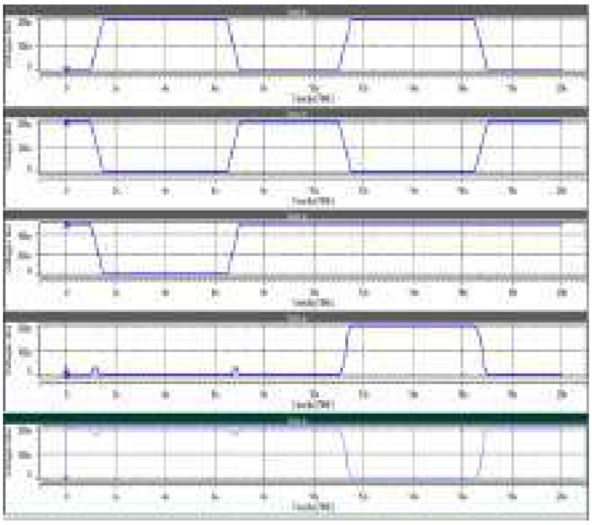

Figure 6. Heterojunction 6T SRAM write operation result

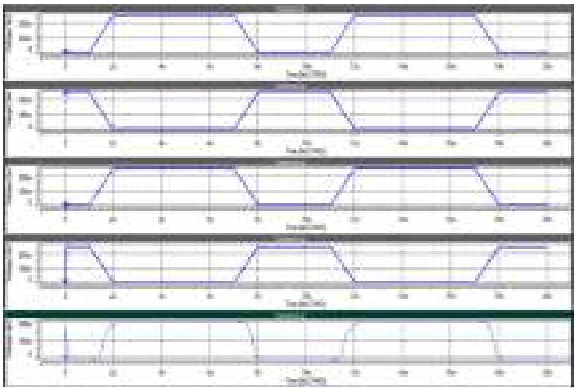

Figure 7. Homojunction TFET SRAM read operation result

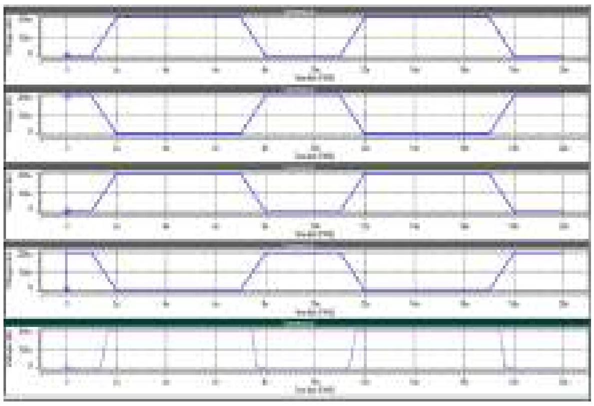

Figure 8. Heterojunction TFET SRAM read operation result

5. 3. Heterojunction vs Homojunction The sub-threshold slope of the device is very low if we use Heterojunction GaSb-InAs TFET. Heterojunction TFET has a small band-gap, when compared to the Homojunction TFET. Due to the small band-gap the charge carriers can move easily which enhances the speed of the transistor. Hence GaSb-InAs Heterojunction TFET is best for device fabrication because the power consumption and the propagation delay are very low is given in Table 1.

TABLE 1. Performance Comparison of Homojunction Vs Heterojunction

Circuit	Homo junction			Hetrojunction		
	Power (nW)	tpLH (ns)	tpHL (ns)	Power (nW)	tpLH (ns)	tpHL (ns)
SRAM Write	17.8	10.1	15.1	0.38	10.1	9.9
SRAM Read	208.2	9.9	0.18	1.87	0.0007	0.0128

5. 4. SRAM Operation Using 32nm Technology

5. 4. 1. Write Operation In the CMOS 32 nm SRAM write operation circuit, when the word line is ON (WL=1), the SRAM circuit allows the external input, to store the data. If WL=0, then the SRAM circuit keeps the previous data which is shown in Figure 9. The power of the 32nm CMOS SRAM is 0.704 nW.

5. 4. 2. Read Operation The CMOS 32nm SRAM read operation is done by using a sense amplifier which is used for reading the stored data from the memory device. For read operation the word line should be 0 (WL=0). Then, the output of the SRAM cell is connected as an input to the sense amplifier. The power of 32nm CMOS SRAM cell is 14.1 nW. Q and $\overline{Q}$are the inputs of a sense amplifier and also the output of the SRAM cell. After writing the data into SRAM memory cell, the reading operation will take place. The simulation result of CMOS SRAM read operation is shown in Figure 10.

5. 4. 3. CMOS Vs TFET The heterojunction TFET SRAM and CMOS SRAM parameters are compared because it has already proved that Heterojunction is better than Homojunction. From Table 2, it is concluded that the TFET is better than the CMOS by comparing the parameters like power and propagation delay.

After comparison of CMOS, TFET and FINFET Technologies in Table 3, it is concluded that TFET is better than CMOS and FINFET. TFET gives very low sub-threshold swing at room temperature compared with CMOS and FINFET. TFET transistor shows higher performance than FINFET-based logic due to its lower parasitic capacitance. In addition, the leakage power of TFET is also reduced compared to FINFET and CMOS. Hence, TFET operates on high speed with low power, and low supply voltage.

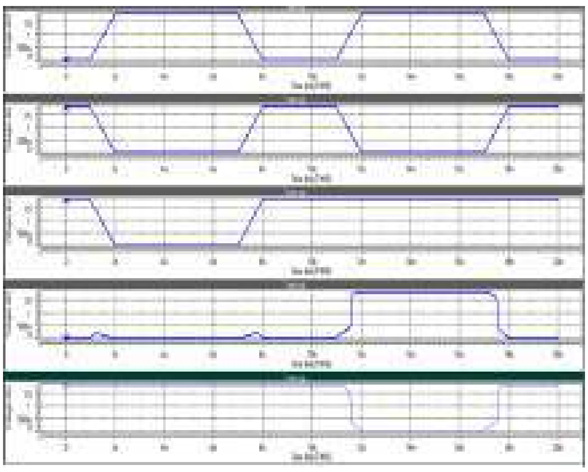

Figure 9. 6T CMOS SRAM write operation result

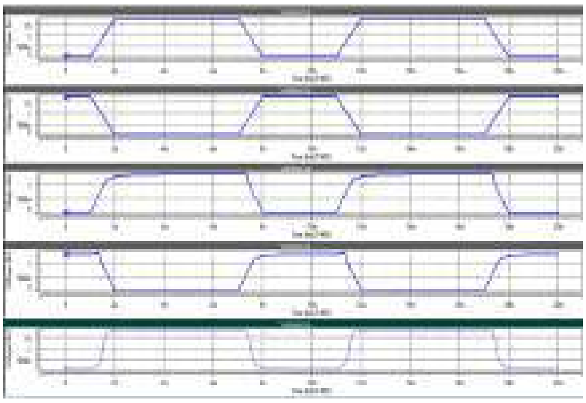

Figure 10. CMOS SRAM read operation result

TABLE 2. Performance Comparison of CMOS Vs TFET

Circuit	CMOS			TFET (Hetrojunction)		
	Power (nW)	tpLH (ns)	tpHL (ns)	Power (nW)	tpLH (ns)	tpHL (ns)
SRAM Write	0.704	10.2	10	0.38	10.1	9.9
SRAM Read	14.1	0.00095	0.0024	1.87	0.0007	0.0128

TABLE 3. Basic parameters values for CMOS, TFET and FINFET

Parameters	CMOS		TFET	FINFET
Channel Length	32 nm		30nm	22nm
Supply Voltage	1.8V		0.25V	0.9V
Threshold Voltage	0.53V		0.05V	0.36
Sub-threshold Slope	60mV/dec		17mV/dec	>70mV/dec
Leakage Power	1.74pW		0.39pW	0.98pW
I_{ON} (uA/um)	HVT	LVT	400	850
	90	380		

6. CONCLUSIONS

In this paper Heterojunction and Homojunction 6T SRAM cell is designed and simulated using TFET and it is observed that the Heterojunction SRAM cell performs better than the Homojunction in terms of speed and power consumption. Also, the performance of 30 nm TFET is compared with the 32 nm CMOS technology based on the various parameters such as channel length, supply voltage, threshold voltage, power and sub-threshold slope. Hence the proposed 6T-TFET SRAM offers better results than 6T-CMOS SRAM.

7. REFERENCES

1. Dhanasekar S, Ramesh J, "VLSI Implementation of Variable Bit Rate OFDM Transceiver System with Multi-Radix FFT/IFFT Processor for wireless applications", ***Journal of Electrical Engineering***, Vol. 3, No. 1, (2018), 1-10.
2. Emanuele Baravelli, Elena Gnani, Antonio Gnudi and Susanna Reggiani, "TFET Inverters with n-/p-devices on the same technology platform for low-voltage/low-power applications", ***IEEE Transactions on Electron Devices***, Vol. 61, No. 2, (2014), 473-478, doi: 10.1109/TED.2013.2294792
3. Anthony Villalon, Gilles Le Carval, Sebastien Martinie, Cyrille Le Royer, Marie-Anne Jaud and Sorin Cristoloveanu, "Further insights in TFET operation", ***IEEE Transactions on Electron Devices***, Vol. 61, No. 8, (2014), 2893-73-2898, doi: 10.1109/TED.2014.2325600
4. Yingxin Qiu, Runsheng Wang, Qianqian Huang and Ru Huang, "A comparative study on the impacts of interfece traps on tunneling FET and MOSFET", ***IEEE Transactions on Electron Devices***, Vol. 61, No. 5, (2014),1284-1291, doi: 10.1109/TED.2014.2312330
5. Siyuranga O. Koswatta, Mark S. Lundstrom and Dmitri E. Nikonov, "Performance comparison between p-i-n tunneling transistors and conventional MOSFETs", ***IEEE Transactions on Electron Devices***, Vol. 56, No. 3, (2009), 456-465, doi: 10.1109/TED.2008.2011934
6. Sung Hwan Kim, Sapan Agarwal, Zachery A Jacobson, Peter Matheu, Chenming Hu and Tsu-Jae King Liu, "Tunnel field effect transistor with raised germanium source", ***IEEE Electron Device Letters***, Vol. 31, No. 10, (2010), 1107-1109, doi: 10.1109/LED.2010.2061214
7. Ramanathan Gandhi, Zhixian Chen, Navab Singh, Kaustav Banerjee and Sungjoo Lee, "Vertical Si-Nanowire n-type tunneling FETs with low sub-threshold swing(<=50mV/decade) at room temperature", ***IEEE Electron Device Letters***, Vol. 32, No. 4, (2011), 437-439, doi: 10.1109/LED.2011.2106757
8. Dhanasekar S, Ramesh J, "FPGA Implementation of Variable Bit Rate OFDM Transceiver System for Wireless Applications", Proceedings of IEEE International Conference on Innovations in Electrical, Electronics, Instrumentation and Media Technology, (2017), 343-346, doi: 10.1109/ICIEEIMT.2017.8116863
9. Chun-Hsing and Nguyen Dang Chien, "Sub-10-nm tunnel field-effect transistor with graded Si/Ge heterojunction", ***IEEE Electron Device Letters***, Vol. 32, No. 11,(2011), 1498-1500, doi: 10.1109/LED.2011.2164512
10. Rui Li, Yeqing Lu, Guangle Zhou, Qingmin Liu, Soo Doo Chae, Tim Vasen, Wan Sik Hwang, Qin Zhang, Patrick Fay, Tom Kosel, Mark Wistey, Huili Xing and Alan Seabaugh, "AlGaSb/InAs tunnel field-effect transistor with on-current of 78μA/μm at 0.5V", ***IEEE Electron Device Letters***, Vol. 33, No. 3, (2012), 363-365, doi: 10.1109/LED.2011.2179915
11. Ram Asra, Mayank Shrinivastava, Kota V. R. M. Murali, Rajan K. Pandey, Harald Gossner and V. Ramgopal Rao, "A tunnel FET for Vdd Scaling Below 0.6V with a CMOS-comparable performance", ***IEEE Transactions on Electron Devices,*** Vol. 58, No. 7,(2011), 1855-1863, doi: 10.1109/TED.2011.2140322
12. Lining Zhang and Mansun Chan, "SPICE modelling of double-gate tunnel-FETs including channel transports", ***IEEE Transactions on Electron Devices,*** Vol. 61, No. 2, (2014), 300-307, doi: 10.1109/TED.2013.2295237
13. Yoonmyung Lee, Daeyeon Kim, Jin Cai and Isaac Lauer, "Low-power circuit analysis and design based on hetero- junction tunneling transistors (HETTs)", ***IEEE Transactions Very Large Scale Integration Systems***, Vol. 21, No. 9, (2013), 1632–1643, doi: 10.1109/TVLSI.2012.2213103
14. Y.-N. Chen, M.-L. Fan, V. P.-H. Hu, P. Su, and C.-T. Chuang, "Design and analysis of robust tunneling FET SRAM", ***IEEE Trans. Electron Devices***, Vol. 60, No. 3, (2013), 1092–1098, doi: 10.1109/TED.2013.2239297
15. N. Hossain, A. Iqbal, H. Shishupal, and M. H. Chowdhury, "Tunneling transistor based 6T SRAM bitcell circuit design in sub-10nm domain",Proc. Midwest Symp. Circuits Syst., (2017), doi: 10.1109/MWSCAS.2017.8053215.
16. A. Sharma, A. G. Akkala, J. P. Kulkarni, and K. Roy, "Source-underlapped GaSb-InAs TFETs with applications to gain cell embedded DRAMs", ***IEEE Transactions on Electron Devices***, Vol. 63, No. 6, (2016), 2563–2569, doi: 10.1109/TED.2016.2555627
17. Ming-Hsien Tu, Jihi-Yu Lin, Ming-Chien Tsai and Chien-Yu Lu "A single-ended disturb-free 9T sub-threshold SRAM with cross-point data-aware write word-line structure, negative bit-line, and adaptive read operation timing tracing", ***IEEE Journal of Solid-State Circuits***, Vol. 47, No. 6, (2012), 1469–1482, doi: 10.1109/JSSC.2012.2187474
18. Sebastiano Strangio, Pierpaolo Palestri, David Esseni, Luca Selmi and Felice Crupi, "Impact of TFET unidirectionality and ambipolarity on the performance of 6T SRAM cells", ***IEEE Journal of Electron Devices Society***, Vol. 3, No. 3, (2015), 223–232, doi: 10.1109/JEDS.2015.2392793
19. Dhanasekar S, Malin Bruntha P,Martin Sagayam K, "An Improved Area Efficient 16-QAM Transceiver Design using Vedic Multiplier for Wireless Applications", ***International Journal of Recent Technology and Engineering***, Vol.8, No. 3, (2019), 4419-4425, doi: 10.35940/ijrte.C5535.098319
20. Alan C. Seabaugh and Qin Zhang, "Low-voltage tunnel transistors for beyond low-voltage tunnel transistors for beyond CMOS logic", Proc. IEEE, Vol. 98, No. 12, (2015), 2095–2110, doi: 10.1109/JPROC.2010.2070470
21. Mahmood Uddin Mohammed and Masud H. Chowdhury, "Reliability and Energy Efficiency of the Tunneling Transistor-Based 6T SRAM Cell in Sub-10 nm Domain", ***IEEE Transactions on Circuits and Systems-II,*** Vol. 65, No. 12, (2018),1829-1833, doi: 10.1109/TCSII.2018.2874897
22. Jheng-Sin Liu,, Michael B. Clavel and Mantu K. Hudait, "An Energy-Efficient Tensile-Strained Ge/InGaAs TFET 7T SRAM Cell Architecture for Ultralow-Voltage Applications", ***IEEE Transactions On Electron Devices***, Vol. 64, No. 5, (2017), 2193-2200, doi: 10.1109/TED.2017.2675364
23. Sayeed Ahmad, Syed Afzal Ahmad, Mohd Muqeem, Naushad Alam and Mohd Hasan "TFET-Based Robust 7T SRAM Cell for Low Power Application", ***IEEE Transactions on Electron Devices***, Vol. 66, No. 9, (2019), 3834-3840, doi: 10.1109/TED.2019.2931567

Persian Abstract

چکیده

در این مقاله تحقیقاتی ، یک سلول ۱ بیتی SRAM بسیار کم مصرف با استفاده از ترانزیستور تاثیر Tunneling Field Effect (TFET) معرفی شده است. در این مقاله پیکربندی های T SRAM٦ امکان پذیر در TFET های نوع N و P از نوع یکپارچه شده در هر دو سیستم عامل (InAsهم سازگاری) و GaSb-InAs (Heterojunction) بررسی شده است. مشخصات انتقال ولتاژ و پارامترهای اساسی هر دو همو و توابع هتروژن بررسی و مقایسه می شوند. SRAM مبتنی بر TFET پایداری در عملیات نگه داشتن ، خواندن و نوشتن را افزایش می دهد. این کار پتانسیل TFET را ارزیابی می کند که می تواند به دلیل بهبود عملکرد با مصرف کم انرژی ، سرعت زیاد ، شیب زیر آستانه کم و ولتاژ تغذیه (VDD = 0.2 ولت) جایگزین MOSFET شود. نتایج با فناوری CMOS 32nm در ارتباط است. سلول پیشنهادی SRAM TFET با استفاده از فناوری nm۳۰ پیاده سازی شده و با استفاده از شبیه ساز H-SPICE با کمک مدلهای Verilog-A شبیه سازی شده است. معماری سلول پیشنهادی SRAM TFET باعث اتلاف انرژی کم و عملکرد بسیار بالاتر در مقایسه با CMOS و FINFET می شود.

Multimodal Biometric System Based on Dorsal and Palm Vein Images

Gurunathan V[1], Sathiyapriya T[2], Dhanasekar J[3]

[1&2]*Department of Electronics and Communication Engineering, Dr. Mahalingam College of Engineering and Technology*

[3]*Department of Electronics and Communication Engineering, Sri Eshwar College of Engineering*

***Abstract*— One of the latest biometric modality used for person identification is hand vein biometric. The security is an important issue in many sectors like forensic and military applications in recent times. In this paper, we have utilized palm vein and dorsal vein biometric modalities for person identification. Initially the palm vein and dorsal vein images are captured using NIR Cameras. To enrich the palm and dorsal vein patterns of the captured palm and dorsal vein images, it is further moved for preprocessing. The Contrast Limited Adaptive Histogram Equalization (CLAHE) technique is used for preprocessing. From the preprocessed vein images, the Region of Interest (RoI) is separated. After that, the features are extracted from the preprocessed images. With the help of preprocessed palm and dorsal vein images, the features are separated using HOG (Histograms of Oriented Gradients) feature extraction. The edge direction is achieved by Gradient and Orientation of the edges. These extracted features are fused at feature level with simple sum rule. Then these features are stored in the database for further process. Classification is done with the aid of Support Vector Machine (SVM) classifier. The experimental results show that the proposed multimodal biometric system provides better recognition rate when compared to unimodal system. Finally, the proposed system provides the Equal Error Rate as 0.285% and accuracy of 95.5%.his document gives formatting instructions for authors preparing papers for publication in the Proceedings of an IEEE conference. The authors must follow the instructions given in the document for the papers to be published. You can use this document as both an instruction set and as a template into which you can type your own text.**

***Keywords*— Biometrics, Equal Error Rate, Hand vein images, Multimodal System, Region of Interest, Support Vector Machine Classifier**

I. Introduction

In Recent days, biometrics plays an important role in Personal identification. It is applied to various applications like E-Commerce, Access control and Criminal identification etc. Basically, Biometrics is the statistical measurement of human physiological or behavioral modalities. Biometric techniques for personal authentication provides better result compared to conventional methods, because conventional methods such as passwords, keys and PIN numbers based systems have difficulties in terms of theft, loss, and reliance on the user's memory. The hand vein biometrics provides better recognition accuracy over other state-of-the-art techniques. Analyzing all the available biometric traits, our proposed hand vein trait has many benefits like: (i) universality and uniqueness, (ii) non-invasive and the type of acquisition used is contact less and (iii) although the vein is underneath the skin; so, it is very difficult to falsify. Our proposed vein based recognition technology, promotes the new emerging trends in biometrics [1-4]. Unimodal and multimodal biometric systems are the broad classification of biometric systems. The unimodal biometric system uses single biometric modality and it suffers from several problems such as lack of distinctiveness, noisy data, low recognition accuracy and spoof attacks. These problems are resolved by means of multimodal biometric system, which uses more than one biometric modality for authenticating the person. We can blend one or more biometric modalities with the help of different level of fusion in multimodal biometric system. The different fusion levels used in biometric systems are sensor level, feature level and score level and decision level. In this paper, we have used palm and dorsal vein images for person authentication. Here, the feature level fusion is adapted for combining dorsal and palm vein features.

II. Related Works

Nabil Hezil et al [5] investigated the fusion of two biometric traits such as ear and palm print at feature level. In the paper, they have derived the local discriminant features from images using the Local texture descriptors such as weber local descriptor and local binary pattern. The statistical features are extracted and fused at feature level improve the recognition rates compared with that produced by single-modal biometrics. Mohamed Cheniti et al [6] proposed a new framework for score level fusion based on S- sums for combining the biometric modalities. Sumit Shekhar et al [7] described about the representation of test data in a sparse linear combination and it is known as sparse representation method. Kernelize the algorithm to handle nonlinearity in data are illustrated. Gurjit Singh Walia et al [8] in the paper described about the optimal score level fusion multimodal biometric system. Backtracking Search Optimization Algorithm (BSA) is adopted for the performance of specific classifier. MaXin and JingXiaojun [9] presented an idea for the fusion of feature level multimodal biometric system with the help of multiset generalized canonical discriminant projection (MGCDP. They also presented MGCDP (S-MGCDP) and parallel MGCDP (P-MGCDP) strategies for fusion. D.Jagadiswary and D.Saraswady [10] figures out the usage of feature extraction (using fingerprint, retina and finger vein) and key generation (using RSA) in the development of enhanced multimodal authentication system . ChenYarui et al [11] in the paper, implemented the block based feature-image matrix for face and fingerprint images to design the multimodal fusion framework. They also created Variational Bayesian Extreme Learning Machine (VBELM) recognition algorithm was created. Libing Wu et al [12] proposed and implemented LVID, a multimodal biometrics authentication system on smartphones which takes the merits of vice and lip.

III. Proposed Work

Fig. 1 gives the overview of our proposed biometric system that helps in attest the persons.

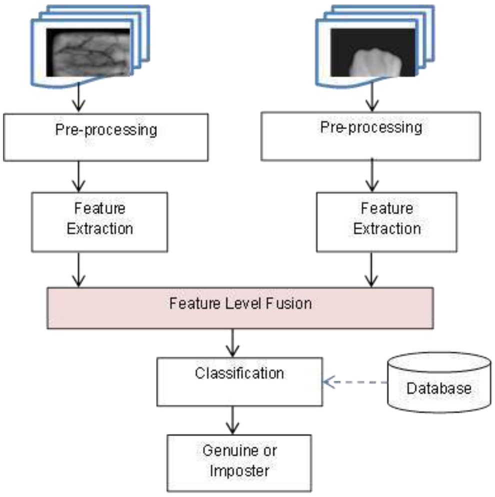

Fig. 1 Block diagram of proposed system

A. Image Acquisition and Preprocessing

Before entering into the further processing steps, we are utilizing one of the best pre-processing method known as Image enhancement for better image quality. Basically the images are obtained with the help of NIR cameras. These images are low quality in nature because of poor lighting condition. Hence, the palm and dorsal vein images are pre-processed using image enhancement technique. Moreover the proposed system focus on the vessel line features, it's essential to pre-process the image before matching. The vein line patterns are enhanced by using the contrast limited adaptive histogram equalization technique. After pre-processing, the Region of Interest (RoI) is extracted from the image by adapting the RoI extraction method [14]. In spite of applying the algorithm throughout the entire image to enrich the contrast, we can use the CLAHE (Contrast limited adaptive histogram equalization) an adaptive contrast histogram equalization method [13] on small regions of the images to improvise the contrast.

B. Feature Extraction

In our proposed system we have implemented one of the generally used descriptor Histogram of Oriented Gradients (HOG), which is commonly used for facial detection and object recognition. Under different conditions also, it provides high performance. By means of representing the target shape, we can fetch the necessary information from the target edges in the local regions with the support of HOG descriptor. Within the image, characterization of the orientation (θ) and magnitude (m) values of the pixels are calculated by the HOG method. Particularly this method is used in our system, to describe the image as a group of local histograms. The following are the steps used for calculating HOG feature descriptor. HOG descriptor gives a detailed description about the structure or the shape of an image along with edge direction. The edge direction can be detected by deriving the gradient and orientation of the edges. Although the gradients and orientations are measured in each and every part of the image in a way that the full image is segmented into smaller regions and in the 'localized' portions the orientations are also calculated. Individually the histograms are created for each and every region with the help of HOG where the histogram is evolved from the pixel values that contains the gradients and orientations.

Step1: For each pixel, calculate the Vertical and Horizontal gradient.

$$HX = [-1\ 0\ 1]$$
$$HY = [-1\ 0\ 1]^T$$

Step2: Implementing multidimensional filtering using Convolution.
Step3: To define the values of magnitude and gradient by using equation (1, 2).

$$Magnitude(m) = \sqrt{grade_x^2 + grade_y^2} \tag{1}$$

$$Orientation(\theta) = \arctan \frac{grade_x}{grade_y} \tag{2}$$

The obtained Histogram of Orientation gradients (HOG) is used to calculate the various distant metrics that is used to extract some useful information.

C. Feature Level Fusion

Feature level fusion combines the feature obtained from different biometric modality. With the derived features we can figure out a feature vector. We can develop a single feature vector from different biometric modality with the help of simple sum rule, if the features obtained from different biometric modalities are well suitable.

D. Matching and Classification

The database contains the images with the features and compares the derived features with a well-known search process referred as 'Feature matching'. A new way is adopted to find the similarities between the vectors with the help of various distance measures such as Euclidean, City Block and Hamming distance .The distance between the test and stored feature vector in database are small, and then the test and trained images are considered as same. The different distance measures expressions are given in the equation (3-5).

1. Euclidean Distance

$$ED(p,q) = \sqrt{\sum_{i=1}^{n} (p_i - q_i)^2} \tag{3}$$

2. City Block Distance

$$C(a,b) = \sum_{i=1}^{n} |a_i - b_i| \tag{4}$$

3. Hamming Distance

$$HD = \frac{1}{N}(CodeA \oplus CodeB) \tag{5}$$

A well-recognized supervised learning approach for both classification and regression is adopted and is referred as SVM(Support Vector Machine).To classify the features, we have to obtain the hyper plane in N dimensional space and this is the main objective of SVM classifier. Here, the SVM is used to classify the palm and dorsal vein features. SVM with Radial Basis Function (RBF) is used.

IV. RESULTS AND DISCUSSION

For our experimental analysis, we have used the dorsal and palm images taken from standard database. Fig. 2(a) to 2(f) gives the results of our proposed multimodal biometric system.

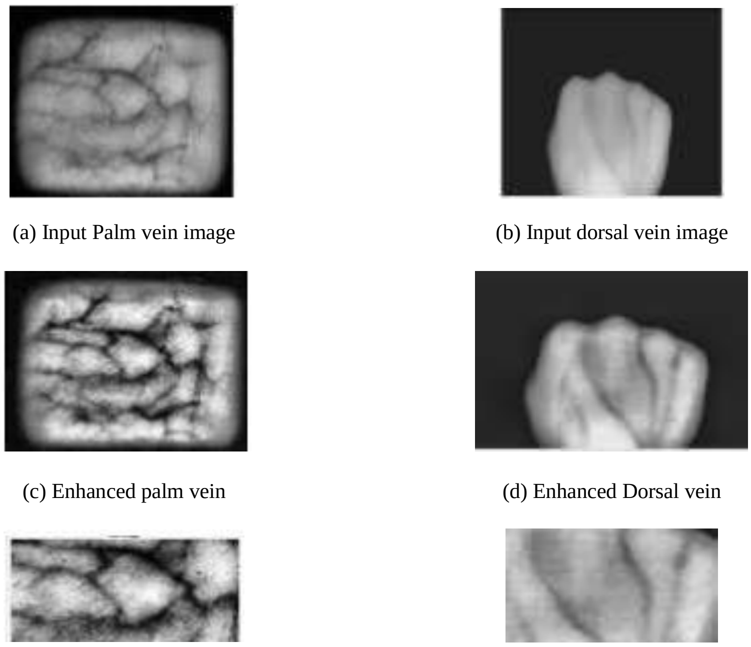

(a) Input Palm vein image

(b) Input dorsal vein image

(c) Enhanced palm vein

(d) Enhanced Dorsal vein

(e) RoI extraction of palm vein

(f) RoI extraction of dorsal vein

Fig.2 Input, Pre-Processed and RoI extracted Palm and Dorsal vein images

We have employed three metrics that shows that our proposed system works better and is very efficient. The metrics are:

False Acceptance rate (FAR): FAR is one which gives the ratio of improper matching of input pattern to the nonmatching pattern that is available in database. It also gives the percentage of irrational inputs that are falsely accepted.

False rejection rate (FRR): FRR metric gives the possibilities of finding a match between the input and matching pattern in the database. It also describes about the incorrectly rejected valid inputs.

Equal error rate (EER): EER is a performance benchmark where both the FAR and FRR are equal. Along with the support of Receiver Operating Curve(ROC), we can easily detect the value of EER. Table

1 shows the performance metrics of palm vein images. Table 2 shows the performance metrics of dorsal vein images. Table 3 gives an overview about the performance metrics of our proposed biometric system.

TABLE I. PERFORMANCE METRICS OF PALM VEIN IMAGE

S.No	Metrics	No of images	FAR	FRR
1	Euclidean Distance	100	0.1555	0.844
2	City Block Distance	100	0.066	0.933
3	Hamming Distance	100	0.111	0.888

TABLE II. PERFORMANCE METRICS OF DORSAL VEIN IMAGE

S.No	Metrics	No of images	FAR	FRR
1	Euclidean Distance	100	0.56	0.85
2	City Block Distance	100	0.58	0.88
3	Hamming Distance	100	0.45	0.65

TABLE III. PERFORMANCE METRICS OF DORSAL VEIN AND PALM VEIN FUSED IMAGE

S.No	Metrics	No of images	FAR	FRR
1	Euclidean Distance	100	0.12	0.75
2	City Block Distance	100	0.22	0.75
3	Hamming Distance	100	0.016	0.083

We have also calculated accuracy of the biometric system with palm vein, dorsal vein and fused palm and dorsal vein images. The figure 3 shows the efficiency of the proposed system.

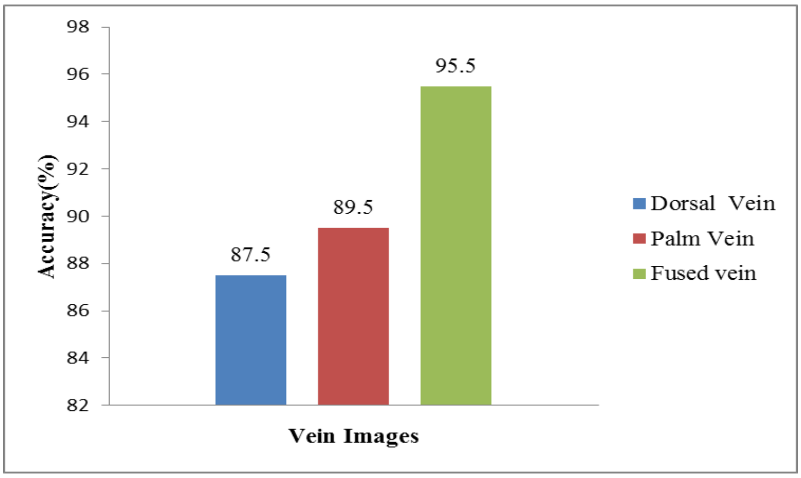

Fig.3 Accuracy of Proposed system

V. Conclusions

In this paper we have proposed a novel multimodal vein recognition system for human authentication since the vein image is unique to every individual. Here, the low quality captured palm and dorsal vein images are preprocessed using CLAHE and then Region of interest (RoI) is extracted. The line characteristics are extracted using Histograms of Oriented Gradients (HoG) from both the vein images. The feature level fusion strategy was employed to combine the vein features of both the vein images. We have adapted various distance metrics such as Euclidean distance, City Block distance and Hamming distance to find the similarity between the features. In addition to this, we have used a well-known classifier SVM for classification. Finally the proposed system provides better recognition rate in terms of EER= 0.285 % and Accuracy= 95.5%. In future we have to implement the VLSI architecture for the proposed multimodal biometric system and also the template security algorithm has to be designed to protect the database features.

Acknowledgment

We express our sincere gratitude and thanks to our college management for supporting us and contributing all facilities for us.

References

[1] Maneet Singh, Richa Singh and Arun Ross, “A comprehensive overview of biometric fusion”, Information Fusion, vol.52, pp- 187-205, 2019.

[2] Jinfeng Yang and Xu Zhang, “Feature-Level Fusion of Fingerprint and Finger-Vein for Personal Identification”, Pattern Recognition Letters, vol.33, no.5, pp. 623–628, 2012.

[3] Maleika Heenaye and Mamode Khan, “A Multimodal Hand Vein Biometric based on Score Level Fusion”, Procedia Engineering, International Symposium on Robotics and Intelligent Sensors, Kuching, Sarawak, Malaysia, (2012), September 4-6.

[4] Ajay Kumar and Yingbou Zhou, “Human Identification Using Finger Images”, IEEE transactions on Image Processing, vol. 21, no.4, pp. 2228-2244,2012.

[5] Nabil Hezil and Abdelhani Boukrouche, “Multimodal biometric recognition using human ear and palmprint”, IET Biometrics, vol. 6, no.5, pp.351- 359, 2017.

[6] Mohamed Cheniti, Naceur-Eddine Boukezzoula and Zahid Akhtar, “Symmetric sum-based biometric score fusion”, IET Biometrics, vol.7, no.5,pp. 391-395,2018.

[7] Sumit Shekhar, Vishal M. Patel, Nasser M. Nasrabadi and Rama Chellappa, “Joint Sparse Representation for Robust Multimodal Biometrics Recognition”, IEEE Transactions on Pattern Analysis and Machine Intelligence, vol.36, no.1, pp.113 – 126,2014.

[8] Gurjit SinghWalia , TarandeepSingh, KuldeepSingh and NeelamVerma, “Robust multimodal biometric system based on optimal score level fusion model”, Expert Systems with Applications, vol.116, pp.364-376,2019.

[9] MaXin and JingXiaojun, “Correlation-based identification approach for multimodal biometric fusion”, The Journal of China Universities of Posts and Telecommunications, vol.24, no.4, pp.34-39,50,2017.

[10] D.Jagadiswary and D.Saraswady, “Biometric Authentication Using Fused Multimodal Biometric, Procedia Computer Science”, vol.85, pp.109-116,2016.

[11] ChenYarui, YangJucheng, WangChao and LiuNa, “Multimodal biometrics recognition based on local fusion visual features and variational Bayesian extreme learning machine”, Expert Systems with Applications, vol.64, no.1, pp. 93-103,2016.

[12] Libing Wu, Jingxiao Yang, Man Zhou, Yanjiao Chen and Qian Wang, “LVID: A Multimodal Biometrics Authentication System on Smartphones”, IEEE Transactions on Information Forensics and Security, vol.15, pp.1572 – 1585,2019.

[13] Srinivasan.S and Balram.N, “Adaptive Contrast En-hancement Using Local Region Stretching”, Proceedings of ASID ’06, New Delhi, (2006) , October 8 -12.

[14] Mingwen Wang and Dongming Tang, “Region of interest extraction for finger vein images with less information losses”, Multimedia Tools and Applications, vol.76,pp.14937–14949,2017.

Archives of Computational Methods in Engineering
https://doi.org/10.1007/s11831-020-09466-6

ORIGINAL PAPER

A Comparative Review of Recent Advances in Decoding Algorithms for Low-Density Parity-Check (LDPC) Codes and Their Applications

Michaelraj Kingston Roberts[1] · **Anguraj Parthibaraj**[1]

Received: 30 September 2019 / Accepted: 6 July 2020

Abstract

In the domain of wireless communication systems, Error Control Coding (ECC) schemes are one of the widely relied upon or responsible methodology for securing the integrity and authenticity of the data transmission process. In the last decade, due to the advent of modern communication standards and their wide range of services, there has been a resurgence of interest and support in the research community towards the conception of efficient and versatile ECC techniques. Recent developments in the wireless communication based technologies have witnessed the pliable nature of low-density parity-check (LDPC) codes and their contributions which cannot be overstated. As of now, the decoding schemes based on LDPC codes have emerged as one of the most promising and effective coding scheme for addressing several key problems of reliable data communication. In this article, comprehensive overview on the current state-of-the art LDPC decoding algorithms and their applications are provided. In addition, a thorough investigation and comparison is carried out on various LDPC decoding algorithms based on their performance, similarities, scalability, numerical stability and feasibility for hardware realization. Finally, at the end of this review, views on the open research problems, challenges and the scope for future prospects are forecasted through discussions.

1 Introduction

1.1 Background

Error Control Coding (ECC) is one of the most widely preferred methodology adopted by various communication and memory systems to minimize the likelihood of errors [1]. In general, many wireless communication based applications strives to provide seamless high quality service to its users by employing cost effective and much less computationally intensive methods [2, 3]. In today's digital era, it is not practically possible for a particular class of coding scheme to facilitate error free transmission of data due to the challenges and vulnerabilities which are preponderantly associated with the communication channels [4]. In literature, several techniques have been investigated towards the design and development of promising coding schemes which can lower the data transmission and reading errors [5, 6].

Among various coding schemes, Low-Density Parity-Check (LDPC) codes are a special class of linear block codes which has become popular in recent years due to its versatile error correcting characteristics [7]. Originally, LDPC discovered by Gallager [8] was initially brought in as a generalized version for various applications by Mackay and his research team in [9, 10]. Since their reminiscence, LDPC codes are gaining traction as a popular choice of coding scheme in various wireless application areas [11]. Basically, according to their error correcting mechanisms, decoding algorithms for LDPC codes can be categorized into two main classes, i.e., soft-decision [12] and hard-decision [13] based approaches. Figure 1 illustrates the general taxonomy of decoding approaches available for LDPC codes.

In some of the recent noteworthy developments, the LDPC based decoding schemes are more often deployed as a viable error correcting solution for facilitating reliable and secure data transmission over a wide range of communication channels [14]. However, with the continuous improvement in the field of digital services, many communication and service providers are skeptical about error control coding mechanisms of LDPC codes due to their computational requirements [15]. Figure 2 shows that there is a substantial rise in the growth of publication trends pertaining to LDPC

✉ Michaelraj Kingston Roberts
king.pane@gmail.com

[1] Department of Electronics and Communication Engineering, Sri Eshwar College of Engineering, Coimbatore 641202, Tamil Nadu, India

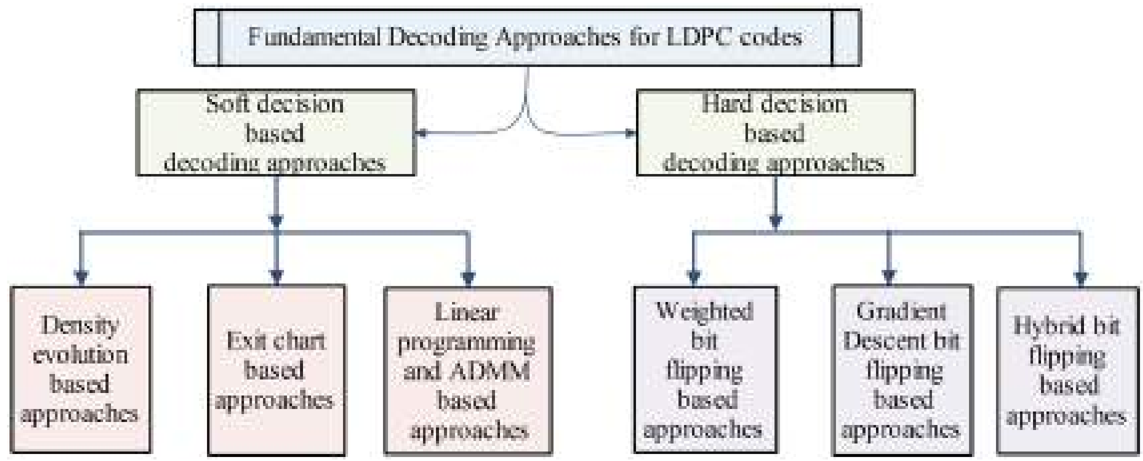

Fig. 1 General taxonomy of various decoding approaches for LDPC codes

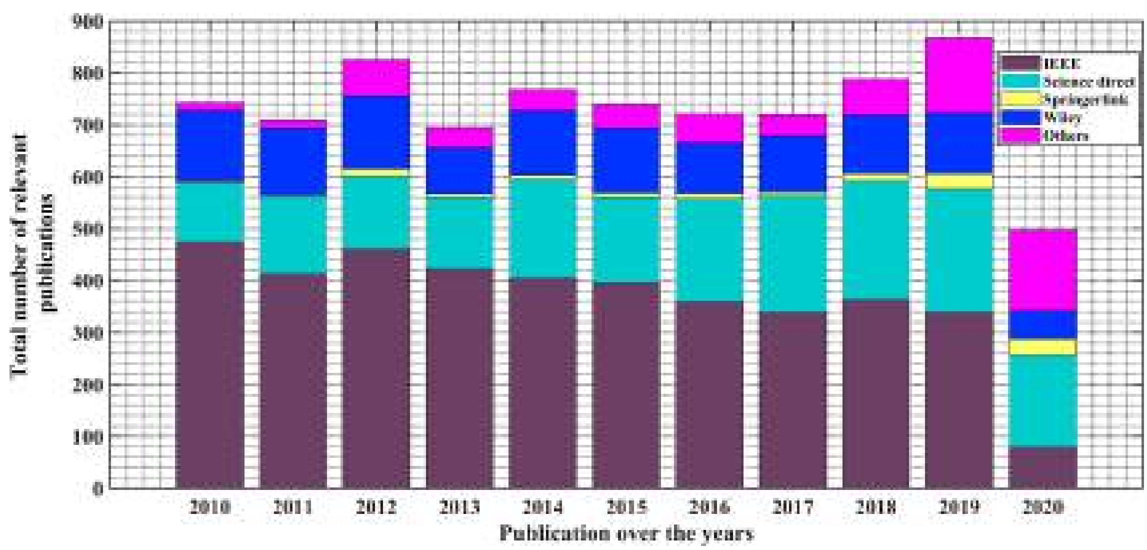

Fig. 2 Summary of publication count related to LDPC decoding algorithms from 2010 to 2020

based decoding algorithms in the research community from 2010 to 2020. Also, from the light of recent studies on LDPC decoding approaches, it is pretty evident that there still exists a need for improvement for solving a variety of issues related to hardware resource utilization, coding gain improvement, convergence speed and throughput requirements [16].

1.2 Related Surveys

With continuous improvement in the field of data storage and wireless service applications, many viable LDPC decoding schemes have been proposed by the prominent researchers from both academia and industries [17]. In recent years, several comprehensive reviews and survey's describing the enhanced computational capabilities of LDPC codes have been published. Each of these survey works were focused on addressing a particular characteristic of LDPC codes. An overview on the fundamentals of LDPC codes was first presented as a study by Bonello et al. [18]. In this work, all the important aspects of LDPC codes starting from its discovery, desirable properties of encoding and decoding along with its scientific implications was presented briefly.

In Wang et al. [19] explored the significance and functionality of some popular LDPC decoding algorithms and their VLSI architectures through a survey. However, the discussion of only a few popular decoding methods in this survey limits its scope. An interesting survey on the challenges and new directions in channel coding techniques was presented by Ankan et al. [20]. This survey was oriented towards the exploration of spatially coupled LDPC codes and non-binary LDPC codes. Since the decoding algorithms for LDPC codes were on the edge of this survey's relevance, only few studies on LDPC decoding were referred. Andrade et al. [21] proposed a systematic survey on programmable LDPC decoders. This work was aimed at exploring the design issues, challenges and methodologies related to the reconfigurable and programmable LDPC decoders.

In Fang et al. [22] have proposed an exclusive survey on the design and analysis of protograph based LDPC codes. The evaluation of protograph LDPC codes under different channel and modulation conditions, along with their applications were discussed briefly. However, in this survey only few LDPC based decoding algorithms were discussed as the survey was focused exclusively towards the encoding design of binary protograph based LDPC codes. Similarly, in the, Hailes et al. [23] evaluated the performance of several FPGA based LDPC decoders and summarized their performance characteristics as an exclusive survey. In this survey, nearly 140 FPGA based LDPC decoders were evaluated based on various technical parameters. In addition, the open challenges and directions for future work in FPGA based LDPC decoders was discussed briefly. A major shortcoming of this survey is that it failed to emphasize the importance of LDPC decoding algorithms and their role in decoder design.

Fang et al. [24] proposed a survey which focused on analyzing the design guidelines of LDPC codes for magnetic recording systems. In this survey a detailed discussion on the code construction techniques along with the design guidelines for LDPC encoders and decoders were provided. Most recently, Shao et al. [25] provided an overview and comparison of LDPC, Polar and Turbo codes. In particular, this work was focused towards the ASIC implementation of decoders using these three codes for the cellular communication systems. Some further studies related to coding theory was proposed by Georgios Tzimpragos [26] and Komal Arora [27] summarizes the significance of LDPC codes and their applications. However, these works are broad and does not uncover the ad-hoc nature of LDPC decoding algorithms and their applications to solve trivial diversified problems of modern communication systems [28, 29].

1.3 Contribution and Organization

In general, the holistic view of recent surveys on LDPC based decoding algorithms and its applications reveal that there exists a substantial gap between the amount of recent research advancements and their coverage in survey papers [18–25]. Also, from the aforementioned surveys it is pretty evident that these works are too narrow or specific in addressing a particular research issue or its variants without any significance for new research directions. Motivated by the existence of this research gap, an extensive and exhaustive review on the key facets of both the hard decision and soft decision based LDPC decoding algorithms are presented in this survey. For many researchers, this informative survey will serve as a reference for identifying and understanding the research gaps of existing decoding methodologies and their future directions.

This article is structured as follows: First, in Sect. 2 the importance of LDPC based decoding algorithms and their worldwide development status is summarized briefly. Then, in Sect. 3, an overview of some popular hard decision based decoding algorithms using weighted bit flipping concept will be presented. After that, in Sect. 4, a brief analysis of some popular Gradient descent optimization based bit flipping methodologies for LDPC codes will be provided. Later, in Sect. 5 a detailed discussion on the salient features of the various linear programming based decoding approaches for LDPC codes and its applications will be provided. Finally, in Sect. 6 by analyzing the future research opportunities, concluding remarks will be drawn for this research work. A summary of mathematical notations used in this work are provided in Table 1.

2 Importance of LDPC Based Decoding Algorithms

In recent times, many continuous efforts were carried out to improve the performance of LDPC codes to support various services of cellular communication and broadcasting applications [30]. The existing error correcting methodologies using LDPC codes were found less compatible for a particular complex service oriented problems which requires more than one solution. This type of scenarios are most common in today's 5G-technology where the error free service facilitation requires flexibility and adaptability to support wide range of code length and rates [31]. Also, from the hardware realization perspective, the decoder design should offer adequate parallelism and flexibility to support multi-mode operating standards which can achieve high peak throughput.

2.1 Development Status

Recent studies on the research challenges and issues related to LDPC codes, it is evident that there still exists a wide demand and need for the selection of computationally efficient decoding algorithm and architectures which are expected to be permanent [32]. Therefore, in this survey, efforts will be carried out to review and summarize the most appealing decoding algorithms for LDPC which can provide more than one solution for a particular complex real world problem using simple and computationally efficient techniques [33, 34]. Furthermore, the decoding algorithms chosen for this survey are classified based on their performance, high citation count, novel decoding framework, cost efficiency and robustness for hardware implementation.

Table 1 A summary of mathematical notations and their meaning

Symbols	Explanations
q_k	A Gaussian distributed random variable with zero mean
α	A normalization factor
$\Psi(x)$	A nonlinear function
λ_n	A posteriori LLR value for each bit node v
β	An offset value
a_{ki}	An adjustment factor
θ_{attn}	An attenuation factor
$B(p0)$	Bernoulli distribution with parameter
$s_i \triangleq \prod_{j\in N(i)} z_j, i \in [1, m].$	Bipolar syndrome
$x = [x_0, x_1, \dots, x_{N-1}]$	Bipolar Sequence
$z = [z_0, z_1, \dots, z_{N-1}]$	Binary hard decision Vector
y_n	Channel output information
d_c	Check node degree (Row weight)
$u = [u_0, u_1, \dots, u_{N-1}]$	Codeword length
R_C Or $R = {}^{k}/_{n}$	Code rate
λ	Constant weight of the third term or Quantization factor
P	Denote the vector of element-wise differences between the input vector of Euclidean projection of the current iteration
$v_n^{(k)}$	Denote by the value of the variable node v_n at the k-th iteration
$v_{i,j}^{(k)}$	Denote by the value of the variable node v_n at the k-th iteration
η and $\chi^{(l)}$	Denote the "bipolar" versions of y and $\hat{x}^{(l)}$
F_2	Denotes the binary Galois field
k	Denotes the dimension
$l_{\max}$	Denote the maximum number of iterations
R_{cv}	*D*enote the check-to-variable message conveyed from the check node c to the variable node v
$N(c)$	Denotes the set of bit nodes that are connected with the check node c
$M(v)$	Denotes the set of check nodes that are connected with the bit node v
$N(c)\backslash v$ and $M(v)\backslash c$	Denotes the set $N(c)$ and $M(v)$ excluding bit node v and check node c
$E_{v_n}^{(k)}$ or $E_{v_{i,j}}^{(k)}$	Energy function
$e_{m,n}^{(k)}$	Extrinsic information contributed to the received bit $Z_n^{(k)}$ including bits that participate in the checksum
E_n	Flipping Function
F_2^n	For $n \in N$, the n-dimensional vector space over F_2 .
$sign(x) \triangleq \begin{cases} +1, x \ge 0 \\ -1, x < 0 \end{cases}$	Function of *sign(x)*
q_n	Gaussian Distributed Random Variable
w_m or $w'_{m,n}$	Initialization process
h_{ij}	*ij* element of Parity check matrix *H*
$\Lambda_{v_n}^{(k)}$ or E_k	Inversion function
E_j	Inversion Function Evaluation
For a and $b\,(>\ a) \in N$	Let $[a, b]$ denote an index set from a to b
n	Length of Code
M	Length of the code word
N	Length of message sequence
$z_i \triangleq \mathrm{sign}(y_i)$	Let $z = (z_1, z_2, \dots z_n) \in \{+1, -1\}^n$ be the hard-decision sequence
(n, k)	Linear block code
γ_n	Log-Likelihood Ratio (LLR) received from AWGN channel
$G_{\max}$	Maximum generation

Table 1 (continued)

Symbols	Explanations
$H_{m.n}$	mth row and nth column of the parity check matrix
$Z_n^{(k)}$	nth received sequence (hard decision)
w	Optimal value
β_{vc}	Outgoing a priori LLR information from bit node v *to* check node c
α_{cv}	Outgoing a priori LLR information from check node c to bit node v
H	Parity Check Matrix
L	Population size
$\hat{x}^{(l)}$	Produce the estimated codeword
$R_n^{(k)}$ or $R_{i,j}^{(k)}$	Random signal
$\alpha_i^{(0)}$	Randomly generate input parameters
y	Received vector
$y \triangleq c + w$	Received sequence $y = (y_1, y_2, \ldots, y_n) \in R^n$
$\mu \in \{0, 1\}$	Referred to as the mode flag
$\theta \in R$	Referred to as the inverse threshold
θ_1	Referred to as the inverse threshold
L_{vc}	*R*epresent the variable-to-check message conveyed from the variable node v to the check node c
(M, N)	Representation of the parity check matrix
σ^2	Represents the variance of the channel noise
δ	Scale factor
N	Set of positive integers
R	Set of real numbers
$\hat{x}.H = 0$	Termination process of decoding algorithm
$c_m^{(k)}$	The binary value of the check node c_m parity check node at iteration k
$\tilde{C} \triangleq \{(1-2c_1, 1-2c_2, \ldots 1-2c_n \mid c \in C\}.$	The bipolar codes $\tilde{C} \subset \{-1, +1\}^n$,which corresponds to C
$c_{a,b}^{(k)}$	The binary value of the check node c_m parity check node at iteration k
$c_m^{(k)}$	The binary value of the CN c_m parity check node at iteration k
$\oplus$	The component-wise modulo-two sum
d_i, d_{v_i}	The degree of variable node i
γ_v	The degree of a node v is the number of its neighbors
$E_{v_n}^{(k)}$	The energy of VN v_n at the k-th iteration
$Ft_{v_n}^{(k)}$	The flipping times of VN v_n at the k-th iteration
$\frac{2r_v}{\sigma^2}$	The intrinsic information
$L_n^{(0)}$	The Log-Likelihood Ratio (LLR) value generated from channel output
$C \triangleq \{c \in F_2^n \mid Hc^t = 0\}.$	The $m \times n$ parity check matrix H
$H_{m,n}$	The mth row and nth column of the parity check matrix.
$L_{i\to j}^{(k)}$	The message $L_{i\to j}$ from variable node v_i to check node c_j is calculated
$L_{j\to i}^{(k)}$	The message $L_{j\to i}$ from check node c_j to variable node v_i is calculated
R^n	The n-dimensional real vector space
θ_2 and θ_1	Threshold value
α, β	The penalty parameter
$y = [y_0, y_1, \ldots, y_{N-1}]$	The Received Vector With Channel Information
r_v	The received soft symbols
V	The set of N variable nodes
C	The set of M check nodes
N_v	The sets of neighbors of nodes v
N_c	The sets of neighbors of nodes c
$N(m)$ and $M(n)$	The set of n bit nodes that are connected $N(m)$ and $M(n)$ to m check nodes and the set of m check nodes that are connected to n bit nodes

Table 1 (continued)

Symbols	Explanations
$N(m)/n$ and $M(n)/m$	The set of $N(m)$ and $M(n)$ excluding the bit node n and check node m
S_{cv}	The sign part of R_{cv}
S_m	The syndrome bits
s	The Syndrome or local optima
$c \in \tilde{C}$	The transmitted codeword
w_j^{new}	The vector projected onto the check poly-tope corresponding to the j-th check node in the previous iteration
$R_n^{(k)}$	The reliability measure of nth received sequence
x_v	The value of the bit associated with variable node v
$e_n^{(k)}$	Total extrinsic information contributed to the received bit $Z_n^{(K)}$ excluding bits that participate in the checksum
d_v	Variable node degree (Column weight)
α	Weighting Factor
$w \in R^n$	White Gaussian noise vector

Figure 3 shows the overall classification of some popular LDPC decoding algorithms which are analyzed in this survey. To the best of our knowledge, this is the only survey till date which has been devoted to address both the hard decision and soft decision based decoding coding schemes which are highly cited and still under intense study.

2.1.1 International Status

LDPC codes are one of the most widely preferred and recognized class of linear block codes which are proven to attain improved bit error rate (BER) performance near Shannon's limit [35]. For the past few years, research works on LDPC codes have been carried out in the scientific community by the coding researchers and theorists throughout the world. The most prominent research efforts were dedicated in bringing theoretical ideologies of LDPC codes to practice with simplified computational effort. The overall summary of recent research works related to LDPC codes worldwide are highlighted in Table 2.

From the details summarized from Table 2 it is evident that the research works based on LDPC codes is carried out in many countries with the assistance from various funding agencies.

2.1.2 National Status

At national level, many prominent researchers and academicians from reputed institutions are actively pursuing research in the LDPC domain which is the advanced area of coding theory. Recently, a research team from IISC Bangalore has published a research article which focuses on the design and development of efficient LDPC decoding architectures [46]. This research ideology is directed towards the design and development of LDPC decoders compatible for various storage applications. A dedicated research team from IIT Madras has been working in the area of coding theory, and they have introduced many new decoding schemes related to LDPC in the past few years. As of late, a new performance enhancement technique related to protograph LDPC codes was proposed [47]. This work introduced a simple and effective methodology to improve the error rate performance of the LDPC codes in various types of noisy channel conditions.

Since their resurgence in mid 1990 s, LDPC codes have proven their importance in various fields and domains. In IIEST Shipur, a group of researchers have succeeded in adopting LDPC codes for image reconstruction and have extended it to space applications for better coding gain improvement and noise reduction [48]. In a new perspective, a researcher from NIT Rourkela has proposed a new Digital Forensic approach using LDPC codes [49]. In this method, the log-likelihood ratio (LLR) computation method is adopted from the LDPC decoding algorithm to enhance the efficiency and precision for enhanced error analysis. The outcome of this research shows that there is substantial improvement in the estimation and detection of erroneous data during forensic evaluation. In addition to these research works, at national level many research ideas based on LDPC codes were published by leading scientific journals of various domains [50–52]. Hence, it is pretty evident that still research ideas based on LDPC codes are widely studied and explored in INDIA.

3 Overview of Some Popular Hard Decision Based Weighted Bit Flipping LDPC Decoding Algorithms

Hard decision based decoding algorithms for LDPDC codes have gained immense popularity and significant research interest among the researchers over the past decade [53]. In

Fig. 3 Classification of LDPC decoding algorithms and the corresponding structure of this survey

Table 2 Summary of most recent and popular research works in LDPC codes

Sr.No.	Research work title and year	Methodology	Funding agency	Research publications
1.	A Study on Iterative Decoding With LLR Modulator by Neural Network Using Adjacent Track Information in SMR System [36]	Algorithm approach utilizing Probability theory and Neural network	Advanced Storage Research Consortium (ASRC)- JAPAN	IEEE Transactions on Magnetics
2.	Performance analysis of interleaved LDPC for optical satellite communications [37]	Performance evaluation and analysis is done using MATLAB simulations	National Research Foundation of Korea under MISP	Optics Communications (ELSEVIER)
3.	Performance Analysis of Finite-Length LDPC Codes Over Asymmetric Memory-less Channels [38]	Algorithm approach, Channel variations and real time transmission through MATLAB simulations	Singapore Ministry of Education Academic Research Fund; SpOT-LITE programme	IEEE Transactions on Vehicular Technology
4.	Code-design for efficient pipelined layered LDPC decoders with bank memory organization [39]	Code construction and scheduling through software simulation, layered hardware realization and verification process through FPGA.	Joint Franco-Romanian ANR-UEFISCDI "DIAMOND" research project	Microprocessors and Microsystems (ELSEVIER)
5.	Decoder-in-the-Loop: Genetic Optimization-Based LDPC Code Design [40]	Genetic Algorithm design, Complexity and latency evaluation through MATLAB	DFG research grant GERMANY	IEEE Access
6.	Using Low-Density Parity-Check codes to improve the McEliece cryptosystem [41]	Algorithm design, security and efficiency analysis carried out in Random Oracle model	DP-FMI, FCT -Portugal, POCI, PTDC, FEDER and COMPETE- Lisbon, LASIGE Research Unit	Information Sciences (ELSEVIER)
7.	Low-Complexity High-Throughput Bit-Wise LDPC Decoder [42]	Algorithm simulation through MATLAB, Design and Implementation through ASIC process	IITP & MSIT funding through Korean Government	Journal of Signal Processing Systems (SPRINGER)
8.	Design of Binary LDPC Codes With Parallel Vector Message Passing [43]	Algorithm enhancements and design of LDPC codes through MATLAB	National Natural Science Foundation grants China	IEEE Transactions on Communications
9.	Second Minimum Approximation for Min-Sum Decoders Suitable for High-Rate LDPC Codes [44]	Algorithm approach through MATLAB Simulations, Implementation through ASIC process	Spanish Ministerio de Ciencia e Innovación and FEDER Grant and partially funded by the Institut Universitaire de France	Circuits, Systems, and Signal Processing (SPRINGER)
10.	High-throughput 2 bit low-density parity-check forward error correction for C-RAN optical front-haul based on a hard-decision algorithm [45]	Algorithm design and implementation enhancements through FPGA process	ANR LAMPION French project and with the support of Elopsys Limosin region competitiveness cluster.	IET Circuits, Devices & Systems

the recent years, many outstanding works have been accomplished in various domains using the hard decision based decoding approaches. In this section, a brief overview on the characteristics of some popular hard decision based decoding algorithms and their characteristics will be presented.

3.1 Preliminaries

Let the set of variable nodes that participate in mth check node is denoted as $N(m)$, and set of check nodes that participate in nth variable nodes is denoted as $M(n)$. For a (N, K) LDPC code with parity check matrix H, both d_v and d_c is small compared to the block length N and information length K of the code. Let $C = (C_0, C_1, \dots C_{N-1}) \in \{GF(2)\}^N$ denote the codeword C which is mapped into the bipolar sequence $x = (x_0, x_1, \dots x_{N-1})$ before transmission, where $x_n = (2C_n - 1)$ with $0 \le n \le N-1$. Let $y = (y_0, y_1, \dots, y_{N-1})$ be the soft decision received at the receiver. For $0 \le n \le N-1$, $y_n = x_n + w_n$, where w_n is the Gaussian random variable with zero mean and variance σ^2 which is independent of x_n. Assuming that AWGN has power spectral density $N_o/2$ the variance is given as $\sigma^2 = (2R_c \cdot E_b/N_0)^{-1}$. The corresponding binary hard decision of the received sequence is given by $Z^{(0)} = (Z_0^{(0)}, Z_1^{(0)}, \dots Z_{N-1}^{(0)})$. Then the syndrome of the hard decision sequence $Z^{(0)}$ is denoted by $S = (S_0, S_1, \dots S_{M-1})$. During the iterative message passing sequence the high precision information are transmitted between the check nodes and bit nodes via the edges of the Tanner graph (bipartite graph) [54]. Figure 4 depicts the graphical representation of the iterative message passing schedule using the Tanner graph.

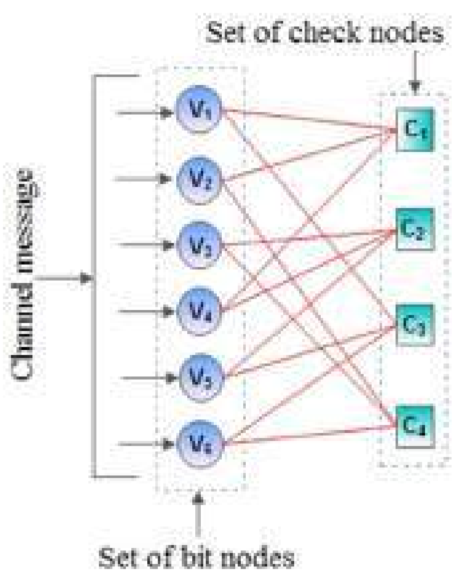

Fig. 4 An illustration of a message passing schedule using a Tanner Graph

3.2 Weighted Bit Flipping Algorithm (WBF) and its Variants

The concept of bit flipping based decoding algorithm (BFA) [55] was originally devised by Gallager in the year 1963 to overcome the computational complexity issues of belief propagation algorithm (BPA) [55, 56]. The decoding process of the conventional BFA involves broadcasting of high precision binary data bits between the two set of nodes namely bit nodes (variable nodes) and check nodes (constraint nodes) in an iterative manner. The input information for this decoding process is obtained from the channel output as the hard decision vector. During the initial stage the check node performs exclusive OR (XOR) operation for the message computation. Then, this processed data bits are flipped in the bit node updating process if the interconnected check nodes does not satisfy the predefined threshold condition. This overall message computation process is very simple and can be carried out using simple arithmetic operations. However, when compared to BPA, this algorithm has poor error correction capability. Hence, this novel decoding scheme was not preferred by academicians and researchers for several real time applications due to its mediocre error rate performance with a slower rate of convergence. After several decades, an improvement to the BFA was proposed by Kou et al. [57] which is known as weighted bit flipping algorithm (WBFA). In this decoding process, the bit reliability information is exploited to improve the error rate performance and decoding stability. The decoding steps of this algorithm can be described in the following steps:

Step 1: Syndrome vector calculation
In this step, the syndrome vector is calculated using the hard decision vector $Z_n^{(k)}$

$$S_m = \sum_{n=0}^{N-1} Z_n^{(k)} \cdot H_{mn} \tag{1}$$

If $S_m = 0$ then the valid code word is obtained, else step 2 is computed.
Step 2: Initialization process
This step computes the most unreliable bit associated with each check node using the equation

$$w_m = \min_{n \in N(m)} \{|y_n|\} \tag{2}$$

Step 3: Variable node updating process
The error calculation for the processed messages are computed in this step as

$$e_n^{(k)} = \sum_{m \in M(n)} (2\,S_m - 1) \cdot w_m \tag{3}$$

Step 4: $k \leftarrow k+1$ from tentative hard decision $Z_n^{(k)}$ based on following decision rule: for $0 \le n \le N-1$

$$Z_n^{(k)} = \left\{0 \text{ if } e_n^{(k)} \le 0 \text{ or } 1 \text{ if } e_n^{(k)} > 0\right\} \tag{4}$$

Step 5: Flip the bit Z_n^k for $n = \arg\max_{1 \le n \le N} e_n^{(k)}$ to obtain a modified received sequence $Z_n^{(k+1)}$ This process is repeated until maximum decoding iterations are reached or parity checksum is zero.
Step 6: Output $Z^{(k+1)}$ as the decoded codeword.

This WBF algorithm inspired many researchers to purse active research in the specialization of hard decision based decoding. However, the main shortcoming of this method is that it includes only the check message to measure the reliability of each bit which results in average error rate performances. To address this research challenge, many advancements of WBF algorithm was proposed over the last few years consistently. An important modification to WBF algorithm (MWBF) was proposed by Juntan Zhang et al. [58]. In this modified approach, both the check and bit data information were utilized to measure the reliability of each bit. The simulation results show that the MWBF algorithm by utilizing optimal weighting factor achieves better trade-off between decoding performance and complexity. An improvement to MWBF (IMWBF) was formulated by Jiang et al. [59]. In this method, a weighting factor is adopted to avert the issues of SNR dependency. This new weighting factor is obtained by theoretical derivation is shown to exhibit good improvement in terms decoding performance and numerical stability.

The method of reliability ratio based WBF (RRWBF) algorithm was proposed by Guo et al. [60]. In this method, a new reliability ratio factor was formulated to improve the coding performance of WBF algorithm. Even though the coding gain improvement of 1 dB achieved by this algorithm comes at the cost of increased decoding iterations which requires very high computational time for the iterative decoding process. To overcome this drawback an efficient implementation of RRWBF algorithm (IRRWBF) was introduced by Lee et al. [61]. In this scheme, the initialization process is modified using a new normalization factor to minimize the computational effort. The simulation results show that this novel scheme can significantly reduce the computational time required to correct the channel errors without degrading the error rate performances.

A novel channel independent weighted bit flipping (CIWBF) algorithm was proposed by Chen [62] to improve the decoding performances of MWBF and IMWBF algorithms [58, 59]. This work utilizes the bit flipping criterion which is theoretically derived from the soft decision based BPA scheme. The experimental analysis demonstrate that this scheme can achieve coding gain improvement of around 1.6 dB at BER of 10^{-5} while reducing up to 47% of the decoding iterations. Zhang et al. [63] in their research work proposed a modification to CIWF (MCIWBF) algorithm. In this algorithm, the modification is carried out by replacing the conventional BPA based flipping criterion with additive offset adjustment factor. This in turn improves the coding gain by 0.45 dB at BER of 10^{-5} without increasing the overall complexity when compared with the CIWBF algorithm [62].

Huang et al. [64] focused their research efforts towards the formulation of a hybrid bit flipping scheme which is obtained combining RRWBF and IMWBF algorithms (CMWBF). This algorithm is proven to exhibit good decoding performance with a faster rate of convergence for Finite Geometry (FG) based LDPC codes. Ismail et al. [65] presented a new class of bit flipping algorithm using the concept of Turbo principle and bit-local thresholding operation. This novel work achieves better decoding stability than the conventional WBF algorithm and its variants. Also, in this work the need for block-wise minimum operation is averted which further reduces the computational complexity. Chen [66] introduced a new adaptive-weighted multi bit-flipping based decoding algorithm using the concept of ordered statistics. This work effectively utilizes the multi bit-flipping criterion to dynamically adapt the flipping threshold during the iterative decoding process. This algorithm achieves very good trade-off between error rate performance and numerical stability with a faster rate of convergence.

Tiwari et al. [67] in their inspiring work proposed a novel hybrid weighted bit flipping based decoding algorithm (HWBF) for LDPC codes. A unique advantage of this method is that the error vector computation in the bit node can be carried out by sorting it in the ascending-descending order to establish the relation between the largest error term. Then, by using the new bit flipping criterion multiple bits can be flipped in a single decoding iteration. Unlike other WBF based algorithms, this hybrid approach is designed in such a manner that it can correct up to a maximum of 3 erroneous bits parallelly during the iterative decoding process. Simulation results show that the HWBF algorithm can reduce up to 45% of the decoding iterations and 40% of the computation time compared to other popular schemes. In a similar kind of work, Ma et al. [68] proposed a new improved parallel WBF algorithm (IPWBF). This work proved that by employing a reliable saturation strategy using multiple thresholds in variable node updating process, decoding failures and error floors can be minimized to a greater extent.

Nguyen et al. [69] introduced a class of two new bit flipping algorithms for the binary symmetric channel (BSC) conditions. The framework of this methodology involves incorporation of two new bits additionally at the check node and bit node computation units respectively. Furthermore, by exploiting the trapping set procedure, this scheme is shown to exhibit high convergence speed and lower error floor when validated with a certain class of BF algorithms. Roberts et al. [70] introduced a newly formulated hybrid technique for bit flipping algorithm (ILCHWBF). A noteworthy characteristic feature of this algorithm lies in its ability to facilitate precise detection and correction of multiple hard decision bits parallelly. Moreover, the bit flipping criterion used in this work was derived using soft decision based min-sum algorithm (MSA) [71]. The performance of this hybrid weighted bit flipping algorithm was reported to be superior in terms of coding gain improvement, iteration count and decoding time reduction when compared with other popular bit flipping algorithms.

A new type of multi-thresholding based bit flipping (MTBF) algorithm for decoding structured LDPC codes was proposed by Liu et al. [72]. For efficient decoding of structured LDPC codes, a multi-threshold bit flipping criterion is formulated in such a manner it requires only logical operations for the decoding process. The experimental results show that this novel scheme achieves better decoding performance than WBF algorithm with reduced complexity and decoding time. Chang et al. [73] developed a new dynamic WBF algorithm which overcomes the limitations of conventional bit flipping algorithms by utilizing a novel two-stage flipping function. In this innovative approach, two new modifications namely flipped bit selection (FBS) rule and check sum weight updating schedule are utilized to improve the reliability of CNU and VNU updating process. Moreover, this methodology can be adapted to achieve the desired performance complexity trade-off. Elsanadily et al. [74] designed a modified bit flipping based decoding algorithm for generalized LDPC codes over binary channels. In this algorithm design, the modifications are carried out in both the VNU and CNU computations by introducing an extra bit to influence the decision reliability of each node. The numerical results illustrate that the modified BF algorithm attains good coding gain improvement when compared with other popular BF algorithms.

An improvement to this method was proposed by Oh et al. [75] known as two-bit weighted bit flipping (TB-WBF) algorithm and it was extended to binary symmetric channels. In this new approach, reliability bits are generated for VNU updating process and syndrome bits for both VNU and CNU updating process. The arithmetic operations required to carryout the computation process can be accomplished by using simple bitwise operations which lowers the computational complexity. Through numerical simulation results, this algorithm is shown to achieve considerable amount of coding gain improvement for different types of LDPC codes for varying code length and code rates. A new cyclic shifting based weighted bit-flipping algorithm (CSWBF) compatible for both regular and irregular LDPC codes was introduced by Wang et al. [76]. In this approach, two selection criteria are carefully chosen to perform the bit flipping and cyclic shifting operations. By exploiting this innovative strategy, unnecessary decoding loops can be broken down to improve the decoding stability and especially it is more suitable for LDPC codes with varying degree distribution. Performance evaluation through experimental results reveal that CSWBF algorithm has a better complexity performance trade-off.

A probabilistic parallel bit flipping (PPBF) decoder design compatible for binary symmetric channel was proposed by Le et al [77]. In this decoder, a new flipping process using probabilistic approach is adopted to improve the error correcting performance. In addition, since the need for global computation is averted, all the arithmetic and numerical operations can be computed parallelly using local computing units. Furthermore, the proposed decoder design implemented using 90 nm CMOS ASIC technology shows that PPBF decoder achieves better hardware efficiency with an improved frequency of operation when compared with other BF decoders. Most recently, Liu et al. [78] introduced a hard decision bit-flipping decoder based on the concept of adaptive bit-local thresholding and demonstrated it with two novel algorithms. The originality of this work lies in its ability to adapt the threshold of each bit recursively during the iterative decoding process. Furthermore, this method is proven to be computationally efficient since it requires only logical operations and by avoiding the delay incurred during the global maximum operation.

A research led by Kalipatnapu et al. [79] from IIT Kharagpur proposed a high throughput parallel bit-flipping decoder compatible for structured LDPC codes. The proposed decoder design is based on a multi-threshold bit flipping algorithm. The decoder design is implemented using 65 nm VLSI technology for three different types of FG-LDPC codes is shown to occupy a core area of 0.1 mm^2 and 0.45 mm^2 . Compared to conventional BF decoders, this decoder design achieves decoding throughput in the range of 47.7–268.5 Gbps with an energy dissipation of 0.91 pJ/bit which most suitable high speed wireless and data storage applications. Chang et al. [80] introduced a new class of multi-stage bit flipping based decoding algorithms. In this novel approach, both the soft-decision and hard-decision bit flipping parts are adopted to improve the reliability. The main advantage of this method lies in its decoding process which uses the same BF structure which minimizes the magnitude overestimation issues and numerical instability. However, modest increase in the computational complexity occurs due to the usage of adaptive stage switching mechanism for timing adjustment. Besides this shortcoming, this work is shown to achieve excellent error

Table 3 Decoding operation summary of some popular hard decision based bit flipping algorithms

Algorithm	Check node update process	Initialization process	Variable node update process
WBF algorithm [57]	$S_m = \sum_{n=0}^{N-1} Z_n^{(k)}.H_{mn}$	$w_m = \min_{n\in N(m)}\{\lvert y_n\rvert\}$	$e_n^{(k)} = \sum_{m\in M(n)} (2S_m - 1).w_m$
MWBF algorithm [58]	$S_m = \sum_{n=0}^{N-1} Z_n^{(k)}.H_{mn}$	$w'_{m,n} = \min_{i\in N(m)\setminus n}\{\lvert y_i\rvert\}$	$e_n^{(k)} = \sum_{m\in M(n)} (2S_m - 1).w'_{m,n} - \alpha\lvert y_n\rvert$
IMWBF algorithm [59]	$S_m = \sum_{n=0}^{N-1} Z_n^{(k)}.H_{mn}$	$w'_{m,n} = \min_{i\in N(m)\setminus n}\{\lvert y_i\rvert\}$	$e_n^{(k)} = \frac{1}{\alpha}\sum_{m\in M(n)} (2S_m - 1).\frac{2w'_{m,n}}{\sigma^2} - \left\lvert\frac{2y_n}{\sigma^2}\right\rvert$
IRRWBF algorithm [61]	$S_m = \sum_{n=0}^{N-1} Z_n^{(k)}.H_{mn}$	$w_m = \sum_{n\in N(m)}\{\lvert y_n\rvert\}$	$e_n^{(k)} = \frac{1}{\lvert y_n\rvert}\sum_{m\in M(n)} (2S_m - 1).\left(\sum_{n\in N(m)}\lvert y_n\rvert\right)$
CMWBF algorithm [64]	$S_m = \sum_{n=0}^{N-1} Z_n^{(k)}.H_{mn}$	$w_m = \min_{n\in N(m)}\{\lvert y_n\rvert\}$	$e_{n1}^{(k)} = \sum_{m\in M(n)}(2S_m - 1).w'_{m,n} - \alpha\lvert y_n\rvert$ and $e_{n2}^{(k)} = \frac{1}{\lvert y_n\rvert}\sum_{m\in M(n)}(2S_m - 1).\left(\sum_{n\in N(m)}\lvert y_n\rvert\right)$
ILCHWBF algorithm [70]	$S_m = \sum_{n=0}^{N-1} Z_n^{(k)}.H_{mn}$	$w'_{m,n} = \min_{i\in N(m)\setminus n}\{\lvert y_i\rvert\}$	$e_n^{(k)} = \frac{1}{\lvert y_n\rvert}\sum_{m\in M(n)} (2S_m - 1).w'_{m,n}.\theta_{attn}$
CIWBF algorithm [62]	$S_m = \sum_{n=0}^{N-1} Z_n^{(k)}.H_{mn}$	$w_{m,n} = (1/\lvert y_n\rvert)\sum_{i\in N(m)\setminus n}\lvert y_i\rvert$	$e_n = \sum_{m\in M(n)} (2s_m - 1)\,w_{m,n}$

correcting performances when compared with some popular BF decoders.

In this section, an exhaustive analysis on several hard decision based bit flipping algorithms and their associated research challenges has been presented briefly. Table 3 summarizes the overall computation process of some popular hard decision based decoding algorithms. From the overall analysis, it is evident that the recently formulated hybrid bit flipping methods have demonstrated their dominance and superiority in terms of their convergence speed and decoding performance. Also, from the study it is evident that there exists other popular bit flipping algorithms which are suitable for various specialized applications which requires more than one solution [81, 82]. Finally, with the advent of a new wave of various bit flipping algorithms, the field of coding theory has emerged as a fresh research subject. Furthermore, it would be desirable to carry out a proportional amount of research efforts towards the hardware realization of these WBF algorithms in order to evaluate the true benefits of these methods for solving several complex-real world problems [83–85].

4 Review of Iterative Optimization Based Bit Flipping Algorithms

In recent years, iterative optimization based algorithms [86] have gained wide spread popularity and trust among the researchers working the field of coding theory [87]. From recent studies on the research challenges and issues related to hard decision based LDPC decoding algorithms, it is evident that there still exists a need for computationally efficient decoding algorithms and architectures. Among several existing iterative optimization methods in the literature, Gradient descent based optimization technique [88] has emerged as one of the fundamental algorithm for efficient bit flipping based decoding of various LDPC codes. From this view point several outstanding research proposals were formulated for hard decision based LDPC decoding algorithms using the concept of Gradient descent based bit flipping (GDBF). In this section, an in depth analysis of various Gradient descent based bit flipping algorithms and their quantified characteristic features will presented.

4.1 Gradient Descent Bit Flipping Algorithms

A novel bit flipping decoding algorithm based on the concept of simple Gradient descent formulation was introduced by Wadayama et al. [89]. In this innovative approach, to enhance the error rate performance the modification is carried out in the variable node computing process by replacing the conventional flipping criterion with an inversion or energy function. This inversion function is basically derived using a simple Gradient descent formulation which is used for flipping the corresponding bit node when it has maximum energy value compared to its neighbors. The decoding steps of the GDBF algorithm is described as follows:

Decoding steps		Computation process
Step 1	Initialization	$x : x \triangleq z$ Let, $l = 1$, $\mu = 0$, $\theta = \theta_1$ and $f_0 = -\infty$
Step 2	Parity Check	Compute the Syndrome $s_i \triangleq \prod_{j \in N(i)} z_j, i \in [1, m]$. If $s_i = +1$, for all $i \in [1, m]$, output x and then exit.
Step 3	Selection of bit-flipping mode	Compute Objective function $f(x) \triangleq \sum_{j=1}^{n} x_j y_j + \sum_{i=1}^{m} \prod_{j \in N(i)} x_j$ Let, $f_l = f(x)$. If $f_l \leq f_{l-1}$, $\mu = 1$
Step 4	Bit flipping	Inversion Function Evaluation $E_j \triangleq x_j y_j + \sum_{i \in M(j)} \prod_{j' \in N(i)} x'_j, j \in [1, n]$ If $\mu = 0$ move on Step 4.1 else 4.2.
Step 4.1	Multi-bit mode	Flip all the bits
Step 4.2	Single-bit mode	Flip the corresponding bit
Step 5	Termination	If $l \geq l_{\max}$ output= x and exit. Otherwise $l = l + 1$ and return to Step 2.

However, the check node computation process remains same as the conventional WBF algorithm [57]. One of the main drawback of this novel approach is its premature convergence which occurs due to the data dependency issue and the quality of initial value guess required to avoid decoding failure due to the trapping of search point by local optimum. Over the years, several advanced modifications were proposed by prominent researchers to overcome the drawbacks of GDBF.

4.2 Improved GDBF Algorithm Using Multiple Thresholds

An improvement to GDBF algorithm was proposed by Nakamura et al. [90] using the concept of multiple thresholds which can be effectively utilized as an escape process from the local optimum to avoid decoding failure. The main ideology behind this concept is whenever the decoding failure occurs when the search point is trapped in the local optimum, the decoder optimally adapts its operating mode from single-to-multi mode bit flipping mode. The decoding steps of this improved GDBF algorithm is given below

Decoding steps		Computation process
Step 1	Initialization	Set the hard decision sequence Z to the initial solution $x : x \triangleq z$ Let, $l = 1$, $\mu = 0$, $\theta = \theta_1$ and $f_0 = -\infty$
Step 4.2	Single-bit mode	Flip the single bit $j \triangleq \arg \min_{j' \in [1,n]} E'_j$
Step 4.3	Escape Procedure	In Step 4–2, if the flipped position is same as that of the previous iterations, a local optimum is detected. Let $\theta = \theta_2$ and $\mu = 0$.
Step 5	Termination	If $l = l_{\max}$ output= x and exit. Otherwise $l = l + 1$. If the threshold θ_2 is used in Step 4, $\theta = \theta_3$ and return to Step 2.

Even though, this improved version of GDBF has better decoding stability than GDBF, in some of the cases if the local optimum traps the search point the escape process fails and the decoding loop of the search point remains trapped. Hence, this algorithm was not widely considered for several real time applications which requires precision for smooth functioning.

4.3 Frequency Memory Based GDBF Algorithm

Asatani et al. [91] in their research work introduced a new formulation of escape method for the search method from local optimum. In this method, a new formulation in the form of list is devised to store the frequency visits to each local optimum such that the distance of each search point from local optimum is increased. This in turn accelerates the local investigation and exploration in a diversified manner. Through extensive simulation results, this method is proven to exhibit acceptable coding gain improvement with modest increase in the computational complexity. The decoding steps of this novel approach is given below

Decoding steps		Computation process
Step 1	Initialization	Set the hard decision sequence Z to the initial solution $x : x \triangleq z$ Let, $l = 1$, $\mu = 0$, $\theta = \theta_1$ and $f_0 = -\infty$ $S = 0$

Decoding steps		Computation process
Step 4.3	Escape Procedure	In Step 4–2, if the flipped position is same as that of the previous iterations, a local optimum is detected. If $s \geq 1$. Check if the same local optimum appears in the previous decoding iterations $f_1 = g_p$ for $p \in [1, s]$ If $f_1 = g_p$ is found. The frequency is updated as $\delta_p = \delta_p + 1$. Then let $\theta = \theta_2 + \delta_p \alpha$ and $\mu = 0$. Otherwise (i.e. $f_l \neq g_p$ for all $p \in [1, s]$ the number of local optima is increased as $s = s + 1$ and the value of objective function is stored in the list $g_s = f_l$ and let $\delta_s = 1$. Let $\theta = \theta_2$ and $\mu = 0$

4.4 Noisy Gradient Descent Bit Flipping Algorithm

A modification to the conventional GDBF algorithm was proposed by Sundararajan et al. [92]. This popular decoding scheme also known as Noisy GDBF (NGDBF) algorithm utilizes a newer concept of introducing random perturbations into each symbol metrics during every decoding iteration count. This innovative noisy perturbations provides a new mechanism for the local search point to escape the undesirable local optima. Also, this algorithm performs the computational process using fully parallelizable operations without the need for finding a global optima or a sort over symbol metrics. The decoding steps of the NGDBF algorithm can be derived by considering the maximum likelihood (ML) problem to find the decision vector $X_{ML} \in \hat{C}$ as

$$X_{ML} = \arg\max_{x \in \hat{C}} \sum_{k=1}^{n} x_k y_k \tag{5}$$

Then the formulated objective function can be denoted as

$$f(x) = \sum_{k=1}^{n} x_k y_k + \sum_{i=1}^{m} x_k y_k \tag{6}$$

By taking the partial derivative with respect to the symbol x_k, the inversion function can be given as

$$E_k = x_k \frac{\partial f(x)}{\partial x_k} = x_k y_k + \sum_{i \in M(k)} s_i \tag{7}$$

Then, the steps of the iterative maximization algorithm can be computed as

Step 1: Compute syndrome components

$$s_i = \prod_{j \in N(i)} x_j \tag{8}$$

For all $i \in \{1, 2, \ldots, m\}$. if $s_i = +1$ for all i, output x and stop.
Step 2: Compute inversion function. For $k \in \{1, 2, \ldots, n\}$

$$E_k = x_k y_k + \sum_{i \in M(k)} s_i \tag{9}$$

Step 3: Bit flip operation
Single bit version: Flip the bit x_k for $k = \arg\min_{k \in \{1,2,\ldots,n\}} E_k$.
Multi-bit version: Flip any bits for which $E_k < \theta$ where $\theta \in R^-$ is the inversion threshold.
Step 4: Repeat steps 1 to 3 till a valid codeword is detected or maximum number of iterations is reached.
In order to facilitate a new escape mechanism for the local search point the step 2 of the above algorithm is modified as
Step 5: Symbol node update. For $k \in \{1, 2, \ldots, n\}$ compute

$$E_k = x_k y_k + w \sum_{i \in M(k)} s_i + q_k \tag{10}$$

Now in order to enhance the convergence speed local adaptive threshold function is adopted here, then the modified steps are summarized below.

4.5 Threshold Adaptation

Step 0: Initialize $\theta_k(t = 0) = \theta$ for all k, where $\theta \in R^-$ is the global initial threshold parameter.

Step 3b: For all k, compute the inversion function E_k. If $E_k(t) \geq \theta_k(t)$, make the adjustment $\theta_k(t + 0) = \theta_k(t)\lambda$,where λ is a global adaptation parameter for which $0 < \lambda \leq 1$. If $E_k(t) < \theta_k(t)$, flip the sign of the corresponding decision x_k.

Furthermore, in order obtain a smoothened output by satisfying all the parity checks prior to the iteration count. Then the non-zero probability of erroneous bit-flipping due to noise contribution is denoted as

$$p_{f,k} = Pr\left(x_k y_k + w \sum_{i \in M(k)} s_i + q_k < \theta \right) \tag{11}$$

Then, the probability condition for at least one erroneous bit flip to occur is given by

$$P_F \geq 1 - (1 - p_f)^n \tag{12}$$

If the probability approaches infinity in the above condition for $p_f > 0$, then larger parity checks would not be satisfied in a shorter decoding cycle. This issue is resolved using a simple up/down counter at the output of every x_k. The updating condition of the counter during each decoding iteration is given as

$$X_k(t+1) = X_k(t) + x_k(t) \tag{13}$$

Through simulation results it is shown that NGDBF algorithm has error correcting performance close to the BPA [56] and it is demonstrated that it can be easily implemented in the hardware due to its simplified computational operations.

4.6 Fault-Tolerant Probabilistic GDBF Algorithm

A new class of GDBF algorithm know as Probabilistic GDBF (PGDBF) algorithm was first introduced to the research community by Rasheed et al. [93]. This modified version of GDBF algorithm is designed compatible to the binary symmetric channel (BSC) with all the decoding steps similar to that of GDBF except the modification in the bit node computation process. When compared to GDBF, the bit node computation of PGDBF varies in such a manner that all the eligible bit nodes are flipped with the probability p such that $(0 < p < 1)$. The decoding steps of GDBF algorithm for BSC channel is given by simplifying the inverse function as

$$\Delta_v^{(l)}(\hat{x}, y) = 2 - 2(\hat{x}_v^{(l)} \oplus y_v) + \gamma_v - 2 \sum_{c \in N_v} \bigoplus_{u \in N_c} \hat{x}_u^{(l)} \tag{14}$$

$$\Delta_v^{(l)}(\hat{x}, y) = \hat{x}_v^{(l)} \oplus y_v + \sum_{c \in N_v} \bigoplus_{u \in N_c} \hat{x}_u^{(l)} \tag{15}$$

Then, the decoding steps of the PGDBF algorithm can given as

input: y
$\forall v \in V: \hat{x}_v^{(0)} \leftarrow y_v$
$s^{(0)} \leftarrow \hat{x}^{(0)} H^T \; (\forall c \in C: s_c^{(0)} \leftarrow \oplus_{u \in N_c} \hat{x}_u^{(0)})$
$l = 0$
while $s^{(l)} \neq 0$ and $l \leq L$ do
$\forall v \in V$: Compute $\Delta_v^{(l)}(\hat{x}, y))$
$b^{(l)} \leftarrow \max_v(\Delta_v^{(l)}(\hat{x}, y))$
$v = 1$
while $v \leq N$ do
if $\Delta_v^{(l)}(\hat{x}, y) = b^{(l)}$ then
$\hat{x}_v^{(l+1)} \leftarrow a_v \oplus \hat{x}_v^{(l)}$
else
$\hat{x}_v^{(l+1)} \leftarrow \hat{x}_v^{(l)}$
end if
$v \leftarrow v+1$
end while
$s^{(l+1)} \leftarrow \hat{x}^{(l+1)} H^T$
$l \leftarrow l+1$
end while
Output: $\hat{x}^{(l)}$

The simulation results prove that the PGDBF algorithm out performs GDBF algorithm in terms of computational efforts and decoding performance. Furthermore, the PGDBF algorithm exhibits a unique characteristic of ensuring resilience to gate failure which in turn improves the error correcting performance. The only drawback of this method arises from due to the non adaptable nature of the flipping probability during the iterative decoding process which causes slight increase in the decoding latency.

4.7 Probabilistic Gradient Descent Bit Flipping Algorithm Based LDPC Decoders

Khoa Le et. al proposed an efficient LDPC decoder based on PGDBF algorithm with reduced computational complexity [94]. This novel hard decision based decoder architecture is designed using the short random sequences (SRS) which is used to apply the decoding rules for the optimization of maximum finder unit. The implementation results show that the decoder design when successfully implemented achieves outstanding decoding performances with modest increase in the computational overhead for different types of LDPC codes. The decoding steps of this algorithm can be given as

---

1: Initialization $k=0, v_n^{(0)} \leftarrow y_n, n=1,\ldots\ldots,N$

2: $s=Hv^{(0)^T} \bmod 2$

3: while $s \neq 0$ and $k \leq It_{\max}$ do

4: Generate $R_n^{(k)}, n=1,\ldots\ldots\ldots,N,$ from $B(p0)$

5: Compute $E_{v_n}^{(k)}, n=1,\ldots\ldots\ldots,N,$ using $E_{v_n}^{(k)} = v_n^{(k)} \oplus y_n + \sum_{c_m \in N(v_n)} c_m^{(k)}$

6: for $n=1,\ldots\ldots\ldots\ldots,N$ do

7: if $E_{v_n}^{(k)} = E_{\max}^{(k)}$ and $R_n^{(k)} = 1$ then

8: $v_n^{(k+1)} = v_n^{(k)} \oplus 1$

9: end if

10. end for

11: $s=Hv^{(k+1)^T} \bmod 2$

12: $k=k+1$

13: end while

14: Output: $v^{(k)}$

---

where $\Lambda_{v_n}^{(k)} = (1-2v_n^{(k)})\gamma_n + \sum_{c_m \in N(v_n)} (1-2c_m^{(k)})$ and $c_m^{(k)} = \bigoplus_{v_n \in N(c_m)} v_n^{(k)}$.

To overcome the shortcomings of this decoder, a new variable node shift based architecture was proposed by Khoa Le et al. in 2017. In this work, the regularity of quasi-cyclic LDPC (QC-LDPC) interconnection network is exploited for cyclic shifting the memory of the decoder to perform the VNU computations without the requirement of probabilistic signal generator. The decoding process of this scheme can be given as

1: Initialization $k=0, v_{i,j}^{(0)} \leftarrow y_{i,j}, 1 \le i \le n_c, 1 \le j \le Z$
2: $s = Hv^{(0)^T} \bmod 2$
3: while $s \ne 0$ and $k \le It_{\max}$ do
4: Compute $c_{a,b}^{(k)}, 1 \le a \le n_r, 1 \le b \le Z$, Using Eq.(16)
5: Compute $E_{i,j}^{(k)}, 1 \le i \le n_c, 1 \le j \le Z$, Using Eq.(17)
6: Search $E_{\max}^{(k)} = \max_{i,j}(E_{i,j}^{(k)})$
7: Generate $R_{i,j}^{(k)}, 1 \le i \le n_c, 1 \le j \le Z$, from $B(p0)$
8: for $1 \le i \le n_c, 1 \le j \le Z$, do
9: if $E_{v_{i,j}}^{(k)} = E_{\max}^{(k)}$ and $R_{i,j}^{(k)} = 1$ then
10: $v_{i,j}^{(k+1)} = v_{i,j}^{(k)} \oplus 1$
11: end if
12: end for
13: $s = Hv^{(k+1)^T} \bmod 2$
14: $k = k+1$
15: end while
16: Output: $v^{(k)}$

where

$$c_{a,b}^{(k)} = \bigoplus_{v_{i,j} \in N(c_{a,b})} v_{i,j}^{(k)} \tag{16}$$

$$E_{i,j}^{(k)} = v_{i,j}^{(k)} \oplus y_{i,j} + \sum_{c_{a,b} \in N(v_{i,j})} c_{a,b}^{(k)} \tag{17}$$

Through implementation results it is evident that the modified decoding architecture exhibits outstanding error rate performances than the traditional GDBF based decoding schemes with simplified computational effort.

4.8 Improved Gradient Descent Bit Flipping Decoder for LDPC Codes on BSC Channel

An improvement to GDBF algorithm known as Improved GDBF (IGDBF) algorithm compatible for BSC channel was proposed by Dao Ren and Jin Sha [95]. In this work, the important modification is carried out by reconstructing the composition of the energy function and by introducing an additional penalty factor to improve its convergence speed. The important decoding steps of this algorithm can be given as

Initialization: $k=0, v_n^{(0)} \leftarrow y_n, n=1,\ldots\ldots,N, c=Hv^{(0)^T} \bmod 2$

$\lambda=0.5$, $Ft_{v_{(n)}}^{(0)}=0$

while $c \neq 0$ and $k \leq It_{\max}$ do

Compute $E_{v_n}^{(k)}, n=1,\ldots.,N$.using $E_{v_n}^{(k)}=v_n^{(k)} \oplus y_n+\sum_{c_m \in N(v_n)} c_m^{(k)}-\lambda Ft_{v_n}^{(k)}$

$E_{\max}^{(k)}=\max_n(E_{v_n}^{(k)})$,

for $n=1,\ldots.,N$ do

if $E_{v_n}^{(k)}=E_{\max}^{(k)}$ then

$v_n^{(k+1)}=v_n^{(k)} \oplus 1$

$Ft_{v_{(n)}}^{(k+1)}=Ft_{v_{(n)}}^{(k)}+1$

end if

end for

$c=Hv^{(k+1)^T} \bmod 2$

$k=k+1$

end while

Output $v^{(k)}$

Through simulation results it is shown that the improved GDBF algorithm outperforms conventional GDBF algorithm in terms of decoding performance and convergence speed.

4.9 Modified Gradient Descent Bit-Flipping Decoding Algorithm

One of the most popular variants of GDBF algorithm based on syndromes was introduced by Hua Li et al. [96] through their research work. In this approach, the infinite decoding loop is detected and avoided using the syndrome weight. Also, the reliability of the flipped bit nodes are improved using the syndrome information. Based on the syndrome concept two new decoding algorithms for single bit and multi bit flipping was formulated in this work. The decoding steps of this modified GDBF algorithm can be given as

4.10 Single Modified GDBF Decoding

Step 1	(Initialization) Set iteration number $k=0$, maximum iteration number $k_{\max}$, syndrome-weight factor α, excluding set $B=\emptyset$, maximum excluding-set size $\Delta=2$.
Step 2	Calculate syndrome vector $s^{(k)}=z^{(k)}H^T$. If $wt(s^k)=0$ or $k=k_{\max}$, stop decoding and output $z^{(k)}$,otherwise, $k=k+1$.
Step 3	For each variable node $n \in V$, compute $E_n^*=\sum_{m\in M(n)}(1-2s_m^{(k)})$ and $E_n^*=(2z_n^{(k)}-1)y_n+E_n^*$ where $y_n=y_n+\alpha(2z_n-1)+\sum_{i\in M(n)}(1-2s_i)$
Step 4	Find the bit node n^* by $n^*=\arg\min_{n\in V\backslash B} E_n$. Find the bit n^* and update y_n by $y_{n^*}=y_{n^*}+\alpha(2z_i-1)E_n^*$.
Step 5	If $wt(s^{(k)}) \leq wt(s^{(k-1)})$, record the position of n^*. If the position of n^* is the same with the previous one, set $B=B\cup\{n^*\}$. If $\lvert B\rvert \geq \Delta$, set $B=\emptyset$ and $\Delta=\Delta+1$. Then return to step 2.

4.11 Multi Modified GDBF Decoding

Step 1	(Initialization) Set iteration number $k=0$, maximum iteration number $k_{\max}$, syndrome-weight factor α, excluding set $B=\emptyset$, maximum excluding-set size $\Delta=2$,flipping threshold $\theta=\theta_{init}$, minimum flipping threshold $\theta_{\min}$.
Step 2	Calculate syndrome vector $s^{(k)}=z^{(k)}H^T$. If $wt(s^k)=0$ or $k=k_{\max}$, stop decoding and output $z^{(k)}$,otherwise, $k=k+1$.
Step 3	For each variable node $n \in V$, compute $E_n^*=\sum_{m\in M(n)}(1-2s_m^{(k)})$ and $E_n^*=(2z_n^{(k)}-1)y_n+E_n^*$
Step 4	Find the $E_{\min}$ by $E_{\min}=\min_{n\in V\backslash B} E_n$ and the bit node n^* by $n^*=\arg\min_{n\in V\backslash B} E_n$. Find the bit set $F=\{n\mid E_n\leq\theta\}$. If $F=\emptyset$, set $\theta=\min(E_{\min},\theta_{\min})$ and $F=\{n^*\}$.

Step 5 Flip the bits in F and update their reliability y_i by $y_i = y_i + \alpha(2z_i - 1)E_i^*, i \in F$.

Step 6 If $wt(s^{(k)}) \leq wt(s^{(k-1)})$, record the position of n^*. If the position of n^* is the same with the previous one, set $B = B \cup \{n^*\}$. If $|B| \geq \Delta$, set $B = \emptyset$ and $\Delta = \Delta + 1$. Then return to step 2.

The simulation results show that the proposed single MGDBF and multi MGDBF algorithms outperforming GDBF and NGDBF algorithms in terms of decoding performance. On the other hand, there occurs a modest increase in the computational complexity due to the utilization of code-dependent variables in the decoding process. However, when compared to the other variants of GDBF algorithms, MGDBF algorithm achieves balanced trade-off between decoding performance and overall complexity.

4.12 Noisy Gradient Descent Bit Flipping Algorithm Based on Adjustment Factor for LDPC Codes

In the work of Dai et al. [97] an extensive investigation was carried out to improve the performance of NGDBF algorithm. It was proven that by proper incorporation of an adjustment factor on the syndromes can improve the reliability of the inversion function considerably. The decoding steps of this algorithm are given below

Step 1: Initialization: Set $T=0, x=u$ and $E_k^0 = x_k y_k$ for all
$k=1,2,......,n$
Step 2: Compute each bipolar syndrome $s_i = \prod_{j \in N(i)} x_j$.
if $s_i = +1$ for all $i \in \{1,2,......,m\}$, output x and stop;
Otherwise, $T = T+1$.
Step 3: Set $a_{ki} = \lambda_2$ for $k=1,2,....,n$ and $i=1,2,....,m$.
For $k' = 1,2,....n$, if $E_{k'}^{(T-1)} < \theta_1$, then $a_{ki} = \lambda_1$,
where $i \in M(k'), k \in N(i) \backslash k'$.
Step 4: Calculate inversion functions at
variable nodes using below equation
$E_k = x_k y_k + \sum_{i \in M(k)} a_{ki} s_i + q_k$
Step 5: Flip the bit x_k for $k = \arg\min_{k \in \{1,2,....,n\}} E_k : x_k = -x_k$
and $E_k^T = -E_k^T$.
Step 6: If the maximum number of iterations is not reached, then retuen to step 2;
Otherwise output x and exit.

Also, for improving the decoding efficiency for multi bit flipping mode of operation, a new adaptive inversion threshold is proposed in this work. Through simulation results it is evident that the algorithm using the adjustment factor outperforms the conventional NGDBF algorithm in terms of BER performance and achieves faster rate of convergence for various types of LDPC codes.

Table 4 Summary of the computation process of various popular soft decision based decoding schemes for LDPC codes

Algorithms	Initialization	Check node updating process	Variable node updating process
BPA	$L_n^{(0)} = \left(2/\sigma^2\right) \cdot y_n$	$\alpha_{cv} = S_{cv}.2\tanh^{-1}\left(\prod_{n\in N(c)\setminus v}\tanh\left(\frac{\lvert\beta_{nc}\rvert}{2}\right)\right)$	$\beta_{vc} = \sum_{m\in M(v)\setminus c}\alpha_{mv} + \gamma_v$
SPA	$L_n^{(0)} = \left(2/\sigma^2\right) \cdot y_n$	$R_{cv} = \prod_{n\in N(c)\setminus v}\mathrm{sgn}(L_{nc}).\Psi\left(\sum_{n\in N(c)\setminus v}\Psi(L_{nc})\right)$ where	$L_{vc} = \sum_{m\in M(v)\setminus c}R_{mv} + \frac{2r_v}{\sigma^2}$
MSA	$L_n^{(0)} = \left(2/\sigma^2\right) \cdot y_n$	$R_{cv} = \prod_{n\in N(c)\setminus v}\mathrm{sgn}(L_{nc}).\min_{n\in N(c)\setminus v}\lvert L_{nc}\rvert$	$L_{vc} = \sum_{m\in M(v)\setminus c}R_{mv} + \frac{2r_v}{\sigma^2}$
NMSA	$L_n^{(0)} = \left(2/\sigma^2\right) \cdot y_n$	$R_{cv} = \alpha.\prod_{n\in N(c)\setminus v}\mathrm{sgn}(L_{nc}).\left(\min_{n\in N(c)\setminus v}\lvert L_{nc}\rvert\right)$	$L_{vc} = \sum_{m\in M(v)\setminus c}R_{mv} + \frac{2r_v}{\sigma^2}$
OMSA	$L_n^{(0)} = \left(2/\sigma^2\right) \cdot y_n$	$R_{cv} = \prod_{n\in N(c)\setminus v}\mathrm{sgn}(L_{nc}).\max\left(\min_{n\in N(c)\setminus v}\lvert L_{nc}\rvert - \beta, 0\right)$	$L_{vc} = \sum_{m\in M(v)\setminus c}R_{mv} + \frac{2r_v}{\sigma^2}$

4.13 An Improved Gradient Descent Bit Flipping Decoder for LDPC Codes

Most recently a novel hard decision based decoding algorithm known as tabu-list random-penalty gradient descent bit-flipping (TRGDBF) algorithm was proposed by Cui et al. [98]. This novel algorithm focuses mainly on improving the error correction performance through several innovative modifications in the algorithmic process. In order avoid the premature convergence and error floor phenomenon due to trapping sets, an additional random penalty factor is employed along with the inversion function which is given as

$$\Lambda_k^{(c)} = c_{(k)} \oplus r_k + \sum_{j\in N_v^{(k)}} s_j \tag{18}$$

Then, a tabu-list process method is exploited to improve the decoding stability of the TRGDBF algorithm. The decoding process of this novel algorithm can be illustrated as follows

input: $r = (r_0, r_1, \ldots\ldots, r_{N-1})$
initialize: $c^{(0)} = r, t = 0, (l_0, l_1, \ldots\ldots, l_{N-1}) = 0$
for $t = 0$ to $T_{\max-1}$ do
for $j = 0$ to M-1 do
$s_j = \oplus_{i\in N(c)} c_i^{(t)}$
if $s = 0$ then
break
$\Lambda_{\max}^R = 0$
for $i = 0$ to N-1 do
Generate the penalty term λ_i
$\Delta_i^R(c) = c_i \oplus r_i + \sum_{j\in N_v(i)} s_j + \lambda_i$
if $\Delta_{\max}^R < \Delta_i^R$ and $l_i = 0$ then
$\Delta_{\max}^R = \Delta_i^R$
for $i = 0$ to N-1 do
if $\Lambda_i = \Lambda_{\max}$ then
if $\Delta_i^R = \Delta_{\max}^R$ and $l_i = 0$ then
$c_i^{(t+1)} = 1 - c_i^{(t)}$
$l_i = 1$
else $l_i = 0$
Output: $c^{(t)}$

Also, in addition to the algorithmic realization, a efficient decoder architecture for the proposed TRGDBF algorithm has been developed by the authors in this work. Through implementation results, the authors demonstrated that the proposed decoder architecture achieves better decoding throughput with high work frequencies with minimal hardware resources when compared to some popular LDPC decoders. Hence, the developed LDPC decoder is suited for many advanced wireless applications which requires good error rate performances with minimal hardware complexity.

In this section, a brief review highlighting the latest advancements of hard decision based decoding algorithms for LDPC codes based on Gradient descent bit flipping (GDBF) methodology is presented. From the view point of error correction, these GDBF based decoding algorithms are shown to perform better than WBF algorithms by incorporating certain novel parameters in their decoding framework. Since the decoding performance and hardware realization are primary focus of these algorithms, many rudimentary technical ways have been proposed by various researchers in the literature. Through rigorous analysis and comparison, GDBF based decoding algorithms for LDPC codes have proven to be reliable and useful to the research community [99]. Also, these GDBF algorithms, with their inherent simple, elegant and flexible decoding characteristics have demonstrated their outstanding potential towards the development of several real time prototype applications and their implementations in the practical realm [100].

5 Optimization Method Based Soft Decision Decoding Algorithms for LDPC Codes

Over the years, optimization based approaches have been widely preferred as a diversified mechanism for solving several multidisciplinary problems [101]. In recent times, the alternating direction method of multipliers (ADMM) [102] has emerged as one of the popular approach for solving several types of complex optimization problems such as non-convex constrained optimization [103], distributed convex optimization [104] and many more [105]. Notably, many recent research studies on wireless communication systems have adopted the ADMM methods successfully as solver for resolving research issues such as channel estimation [106] and PAPR reduction [107, 108]. In this section, an effort will be made to provide a cohesive analysis on the application of ADMM method for decoding LDPC codes. In particular, a brief discussion emphasizing the importance of different ADMM techniques for efficient decoding of different types of LDPC codes with varying code rates and lengths will be provided.

5.1 ADMM Penalized LDPC Decoding Algorithms and its Variants

LDPC codes are one of the very few error correcting codes that has been proven to demonstrate appealing and outstanding error correcting performance which are close to Shannon's theoretical point of accumulation (limit). In literature, several soft decision based decoding techniques have been explored for the development of LDPC decoding algorithms. Among, them the density evolution based belief propagation algorithm (BPA) [109], sum product algorithm (SPA) [110], min-sum algorithm (MSA) [111], normalized min-sum algorithm (NMSA) [112] and offset min-sum algorithm (OMSA) [113] have been widely adopted for several years in many advance communication standards. The summary of the computational process involved in the iterative decoding process of these popular algorithms are highlighted in Table 4.

Besides these popular algorithm, a new class of soft decision based decoding algorithms using ADMM framework are gradually emerging as a potential coding technique for solving a variety of transmission related problems in different research domains. Wei et al. [114] in their outstanding research work proposed a reduced complexity Linear Programming (LP) decoding algorithm for LDPC codes using the concept of ADMM method. In this ground breaking research work, the authors tried to address computational complexity issues which is associated with the Euclidean projection process onto the check polytope. To accomplish this trivial task, the observations are carried out to find whether the absolute values of the element-wise difference between the input vector of the Euclidean projection in the current and previous iteration is less than the predefined threshold value. If this criteria is satisfied then the Euclidean projections of the ongoing iterations are averted which in turn reduces the total number of Euclidean projection itself. Through simulation results it is evident that the improved ADMM based decoding algorithm can save around 20% of the decoding time while demonstrating good error rate performances.

An improved ADMM penalized decoder for irregular LDPC codes was proposed by Jiao et al. [115]. This algorithm development was focused with an objective to improve the error correcting performance of the conventional ADMM based decoding algorithm through a simplified computational approach. Formally, this was accomplished by through the modifying the penalty factor of the objective function in accordance with the varying degree distribution of the bit nodes. Also, in this work the concept of employing multiple penalty factors was introduced for the very first time in ADMM based decoding scheme for LDPC codes. Furthermore, these multiple penalty factors were optimized through the density evolution method which was introduced by Storn et al [116]. Through experimental simulations, the decoding performance of this algorithm is shown to achieve better decoding performance than the conventional ADMM based decoding algorithm for LDPC codes. However, the only shortcoming of this work lies in the appropriate selection and usage of multiple penalty factors at the high SNR region which might lead to increased the numerical instability and computational complexity if not carefully selected.

Debbabi et al. [117] introduced a fast converging ADMM penalized decoding algorithm for LDPC codes. The framework of this algorithm was formulated using an iterative horizontal layered scheduling technique by exploiting the penalized ADMM LP approach [118]. This novel modified decoding framework is shown to exhibit enhanced decoding stability with a faster rate of convergence. Through the reported simulation results, this decoding algorithm was shown to exhibit enhanced error correcting characteristics with minimal computational overhead. Also, from the view point of convergence, this scheme was shown to converge 2.3 times faster than the conventional message passing algorithms without exhibiting error floor characteristics which is quite suitable for hardware implementation.

With the advent of ADMM concept for coding theory based applications, error control coding methods have established themselves to be much more prominent in the research community. A popular variation of ADMM penalized decoder for LPDC codes was proposed by Liu et al. [119]. In general, LP based decoding algorithms have shown to exhibit outstanding error correcting characteristics at the high SNR region than the BPA. However, at the low SNR region where the noise level is dominant than the signal strength, the LP based decoding method is shown to exhibit significant degradation in the error rate performance [120]. To overcome this drawback, a new non-convex heuristics is formulated by adding a penalty term to the objective function of LP decoding. For the low and moderate SNR conditions, simulations outcomes carried out using l_1 and l_2 norm penalty factor values are shown to exhibit superior error correcting performances when validated with BPA [109] and LP decoding schemes [114, 115, 117]. On the other hand, for the high SNR region the instanton analysis proves that the error rate performance of this scheme is superior to BPA and inferior to LP based decoding with an incredibly low computational complexity than both BPA and LP schemes.

Debbabi et al. [121] proposed a novel framework for the real time LP decoding of LDPC codes. By exploring the concept of horizontal layered scheduling method, an effectual ADMM$-l_2$ based decoding algorithm is presented for digital communication systems. The software simulation results indicate that the presented ADMM$-l_2$ decoding algorithm outperforms SPA algorithm in terms of decoding performance by achieving 0.5 dB coding gain improvement. Similarly, the hardware implementation results of the decoder optimized with SIMD and SIMT processing features show that it is possible to achieve up to 500 Mbps throughput with $7\times$ times faster run time than other popular variants. Therefore, this decoding algorithm equipped with the aforementioned attractive features emerges as a strong candidate for solving several real-time information processing problems of modern communication systems [122].

An inspiring research work dedicated towards the improvement of error rate performance of ADMM penalized decoder using penalty parameters was introduced by Wang et al. [123]. The authors of this work reported that it is possible to enhance the performance of the piecewise penalty function by enlarging the steepness of the slope at the specified points of x=0 and x=1 respectively. The results obtained from the experimental trials verify that the ADMM penalized decoder equipped with improved penalty functions achieves better FER performance with a faster decoding speed when it is combined with the decoding techniques of [114, 117]. Furthermore, along with the piecewise penalty function, this function when combined with framework reported in [114, 115, 117] is proven to demonstrate outstanding error correcting performance and decoding speed.

In the work of Jiao et al. [124] a node-wise scheduling method for ADMM based LDPC decoder was proposed. In this work, the authors have adopted node-wise scheduling for ADMM instead of using the well-known edge based residual computation [125, 126]. The main idea for the node-wise scheduling of ADMM is formulated by exploiting the information dynamic scheduling (IDS) process for the computation of message residuals [127]. Then, a novel reduced complexity approximation technique is proposed to minimize the computation time required for the calculation of message residuals by avoiding the usage of Euclidean projections. Equipped with these modifications, this algorithm is shown to exhibit a faster rate of convergence than the traditional flooding and layered scheduling methods. The experimental trials carried out on different LDPC codes using simulation proves the decoding efficiency of this algorithm in terms of FER performance and better numerical stability.

The look-up table (LUT) based decoding framework for LDPC codes has been one of the traditional and vastly researched methodologies of the last decade [128]. This popular concept was recently adopted for ADMM based decoding of LDPC codes by Jiao et al [129]. In this study, an effort has been initiated towards the minimization of the computational complexity which is usually associated with the Euclidean Projections onto the check polytopes using the LUTs. In addition, to improve the memory efficiency, a quantization scheme is adopted to lower the total number of memory accessing bits per iteration. Furthermore, this technique can be extended to LDPC with varying degree distribution by utilizing check node decomposition technique. However, this concept of using LUTs did not yield the acceptable decoding performance, but lowered the hardware overhead by a huge margin. Also, the authors suggested that it would be interesting to combine this method with other popular complexity reduction techniques [130] for further enhancement of the decoding performance.

An improvement to the LUT based ADMM algorithm was proposed by Jiao et al. [131]. By exploring several existing methods in literature, the authors adopted non-uniform quantization scheme and minimum mean square error (MMSE) method in their decoding framework [132]. Through this method, they proved that it is possible to minimize the computational complexity incurred during the Euclidean projection process onto the check polytopes. To accomplish this trivial task, appropriate kernel set of quantization levels with precise quantization and MMSE guidelines are employed systematically to minimize mean square error of the Euclidean projection output. The experimental results prove that the improved LUT based ADMM decoding algorithm with these innovative modifications can achieve a good trade-off between error rate performance and the memory cost.

One of the major bottlenecks in the LP based decoding schemes for the LDPC codes lies in the Euclidean projection process of a real valued vector onto the check polytopes. From the literature, it can be observed that several research studies were proposed to address this critical issue [114, 115, 117, 119, 120]. In the work of Haoyuan et al. [133] a promising technique was introduced to overcome this computational complexity issue. The authors of this work showed that it is possible to lower the complexity of Euclidean projection process by replacing its sorting operation with simple arithmetic operations. This innovative modification substantially reduces the total number of hardware resources required for the practical implementation of the LDPC decoder. However, the inherent iterative nature of the algorithm enhances the possibilities for the occurrence of decoding latencies during the hardware implementation process. This critical research issue was assured to be addressed as a future work by the authors of this work.

An approach based on l_p Box-decoding was proposed by Wu et al. [134] for ADMM based LDPC decoders. By reviewing several existing optimization models, a parameter free continuous optimization model [135] was adopted for the decentralized processing of the high precision soft messages. The novelty of this scheme is demonstrated through the incorporation of the box constraint and l_p sphere instead of the original binary constraint of LP decoding. Also, an efficient ADMM based solver was developed to lower the computational complexity. As for the reported numerical results, the parameter free algorithm demonstrates better error correction capabilities without exhibiting error floor characteristics. Also, this algorithm proved that it is more reliable under various SNR conditions and channel constraints.

Most recently, Bai et al. [136] focused their research efforts towards the development of an efficient LP decoding framework for the LDPC codes via ADMM approach. In this research work, three important findings were presented as an extension to the existing methodologies which were focused on achieving better performances in terms of error correcting capabilities, convergence speed, decoding stability and computational complexity reduction. Based on the check node decomposition approach, the LP relaxation formulated in this work. Then, by exploiting the orthogonality structure of the LP model, the ADMM updating process can be carried out parallely and the need for Euclidean projection onto the check polytopes is avoided. The feasibility analysis of this scheme indicates that the complexity requirements of this algorithm to perform processing and computation in every single decoding iteration is much lesser when compared to the existing ADMM based decoding schemes [114, 115, 117, 119, 120]. Moreover, the simulation results illustrates the efficiency of this novel algorithm through its outstanding decoding stability at various SNR regions with a shorter computation time and guaranteed convergence.

A novel and simplified ADMM based decoding algorithm for LDPC codes was proposed by Xia et al. [137]. In this innovative approach, approximation of Euclidean projection onto the check polytopes is accomplished using a line segment projection algorithm (LSA). Compared to the other traditional ADMM based approaches, this Euclidean projection based approximation does not require any form of sorting and iterative operations. Also, when validated with the conventional cut search algorithm (CSA), this novel scheme with LSA can save about 43% of the average projection time. Moreover, with good error rate performance and simplified computational complexity, this algorithm emerges as a strong versatile decoding method for hardware implementation.

During the last few years, ADMM based decoding algorithms for LDPC codes have demonstrated their effectiveness in the field of error control coding [138]. Based on the overall analysis, it can be clearly seen that the ADMM based decoding schemes are expected to be adopted by several advanced communication systems as preferred coding scheme to facilitate error free transmission of reliable data by lowering the transmission and memory errors [139]. Considering the evolution of the technical advancements the research community has witnessed over the last few years, it would be an interesting choice to explore the application domain where these methods will be best suited to meet the needs of various challenging research endeavors [140].

6 Conclusion and Future Work

For the past few decades, the development of error control coding techniques based on LDPC decoding algorithms has emerged as an active area of research and source of inspiration for several outstanding researchers worldwide. In this paper, a comprehensive survey summarizing the current advancements in the state-of-the-art LDPC decoding algorithms is presented. Based on the context of their decoding framework, higher citation count, error correcting performance and other key features the decoding algorithms are classified and grouped. A systematic analysis has been carried out to evaluate the characteristic featured of these popular soft decision and hard decision based decoding approaches in a detailed manner to ascertain their applicability for various open research problems. Based on the meta-analysis on the current developments, it is quite interesting to observe that the hard decision based decoding algorithms have emerged as a successful technique for solving many real world problems. On the other hand, ADMM based decoding approaches for LDPC codes using LP process have demonstrated their popularity and effectiveness in tackling wide range of data transmission problems with their simple, yet powerful decoding framework. Through this informative survey, it is pretty evident that the next generation communication systems and service providers require sophisticated and powerful decoding algorithms to facilitate reliable communication. Hence, it will be absolutely necessary to develop versatile and computationally efficient decoding schemes using LDPC codes which can offer adequate parallelism and robustness for fixed and varying channel conditions. Therefore, the future development process of the research works on LDPC decoding algorithms should evaluate the use of different techniques based on optimization, linear programming and parameter estimation to motivate new and promising solutions.

Funding This research work is funded by the Department of Science and Technology, Government of INDIA through Early Career Research Award (Young Scientist) scheme of Science and Engineering Research Board (SERB) (Grant No. ECR/2016/001275).

Compliance with Ethical Standards

Conflict of interest The author's explicitly declare that there is no conflict of interest pertaining to this manuscript.

Informed Consent The consent of all the author's have been obtained before submission of this manuscript to this journal.

References

1. Huang L, Zhang H, Li R, Ge Y, Wang J (2020) AI coding: learning to construct error correction codes. IEEE Trans Commun 68(1):26–39
2. Xing Z, Liu K, Liu Y (2020) Low-complexity companding function design for PAPR reduction in OFDM systems. IET Commun 14(10):1581–1587
3. Arum SC, Grace D, Mitchell PD (2020) A review of wireless communication using high-altitude platforms for extended coverage and capacity. Comput Commun 157:232–256
4. Ye F, Dupraz E, Mheich Z, Amis K (2019) Optimized rate-adaptive protograph-based LDPC codes for source coding with side information. IEEE Trans Commun 67(6):3879–3889
5. Babar Z, Chandra D, Nguyen HV, Botsinis P, Alanis D, Ng SX, Hanzo L (2019) Duality of quantum and classical error correction codes: design principles and examples. IEEE Communications Surveys & Tutorials 21(1):970–1010
6. Egilmez ZBK, Xiang L, Maunder RG, Hanzo L (2020) The development, operation and performance of the 5G polar codes. IEEE Commun Surv Tutorials 22(1):96–122
7. Abdessalem MB, Zribi A, Matsumoto T, Dupraz E, Bouallègue A (2020) LDPC-based joint source channel coding and decoding strategies for single relay cooperative communications. Phys Commun 38:100947
8. Gallager RG (1962) Low-density parity-check codes. IRE Trans Inf Theory 8(1):21–28
9. Mackay DJC (1999) Good error correcting codes based on very sparse matrices. IEEE Trans Inf Theory 45(2):399–431
10. Davey MC, MacKay D (1998) Low-density parity check codes over GF(q). IEEE Commun Lett 2(6):165–167
11. Richardson TJ, Urbanke RL (2003) The Renaissance of Gallager's low- density parity-check codes. IEEE Commun Mag 41(8):126–131
12. Roberts MK, Mohanram SS, Shanmugasundaram N (2019) An improved low complex offset min-sum based decoding algorithm for LDPC codes. Mobile Netw Appl 24(6):1848–1852
13. Chen Y, Cui H, Lin J, Wang Z (2020) Fine-grained bit-flipping decoding for LDPC codes. IEEE Trans Circuits Syst II Express Briefs 67(5):896–900
14. Zhang Z, Zhang K, Peng Z, Zeng D, Dai M (2020) Velocity analysis of BP decoding waves for SC-LDPC ensembles on BMS channels: an interpolation-based approach. IEEE Trans Commun 68(6):3286–3301
15. Delomier Y, Le Gal B, Crenne J, Jego C (2020) Model-based design of flexible and efficient LDPC decoders on FPGA devices. J Signal Process Syst 92(7):727–745
16. Lopez H, Chan H-W, Chiu K-L, Tsai P-Y, Jou S-JJ (2020) A 75-Gb/s/mm2 and energy-efficient LDPC decoder based on a reduced complexity second minimum approximation min-sum algorithm. IEEE Trans Very Large Scale Integr Syst 28(4):926–939
17. Li Q, Shi L, Di Y, Gao C, Ji C, Liang Y, Xue CJ (2020) Process variation aware read performance improvement for LDPC-based nand flash memory. IEEE Trans Reliab 69(1):310–321
18. Bonello N, Chen S, Hanzo L (2011) Low-density parity-check codes and their rateless relatives. IEEE Commun Surv Tutorials 13(1):3–26
19. Wang Z, Cui Z, Sha J (2011) VLSI design for low-density parity-check code decoding. IEEE Circuits Syst Mag 11(1):52–69
20. Ankan E, Hassan NU, Lentmaier M, Montorsi G, Sayir J (2015) Challenges and some new directions in channel coding. J Commun Netw 17(4):328–338
21. Andrade J, Falcao G, Silva V, Sousa L (2016) A survey on programmable LDPC decoders. IEEE Access 4:6704–6718

22. Fang Y, Bi G, Guan YL, Lau FCM (2015) A survey on protograph LDPC codes and their applications. IEEE Commun Surv Tutorials 17(4):1989–2016
23. Hailes P, Xu L, Maunder RG, Al-Hashimi BM, Hanzo L (2016) A survey of FPGA-based LDPC decoders. IEEE Commun Surv Tutorials 18(2):1098–1122
24. Fang Y, Han G, Cai G, Lau FCM, Chen P, Guan YL (2018) Design guidelines of low-density parity-check codes for magnetic recording systems. IEEE Commun Surv Tutorials 20(2):1574–1606
25. Shao S, Hailes P, Wang T-Y, Wu J-Y, Maunder RG, Al-Hashimi BM, Hanzo L (2019) Survey of turbo, LDPC, and polar decoder ASIC implementations. IEEE Commun Surv Tutorials 21(3):2309–2333
26. Tzimpragos G, Kachris C, Djordjevic IB, Cvijetic M, Soudris D, Tomkos I (2016) A survey on FEC codes for 100 G and beyond optical networks. IEEE Commun Surv Tutorials 18(1):209–221
27. Arora K, Singh J, Randhawa YS (2019) A survey on channel coding techniques for 5G wireless networks. Telecommun Syst 73(4):637–663
28. Roberts MK (2019) Simulation and implementation design of multi-mode decoder for WiMAX and WLAN applications. Measurement 131:28–34
29. Nguyen TTB, Lee H (2019) Low-complexity multi-mode multi-way split-row layered LDPC decoder for gigabit wireless communications. Integration 65:189–200
30. Ahn S-K, Kim K-J, Myung S, Park S-I, Yang K (2019) Comparison of low-density parity-check codes in ATSC 3.0 and 5G standards. IEEE Trans Broadcast 65(3):489–495
31. Zhang Y, Peng K, Wang X, Song J (2018) Performance analysis and code optimization of IDMA with 5G new radio LDPC code. IEEE Commun Lett 22(8):1552–1555
32. Awais M, Razzaq A, Ahmed A, Masera G (2019) LDPC check node implementation using reversible logic. IET Circuits Dev Syst 13(4):443–455
33. Xie Q, Sun Q (2019) Computation and application of robust data-driven bandwidth selection for gradient function estimation. Appl Math Comput 361(10):274–293
34. Dai J, Zhou L, Chang C, Xu W (2020) Robust Bayesian learning approach for massive MIMO channel estimation. Sig Process 168(3):1–9
35. Xu H, Li H, Xu M, Feng D, Zhu H (2019) Two classes of QC-LDPC cycle codes approaching Gallager lower bound. Sci China Inf Sci 62:10
36. Nishikawa M, Nakamura Y, Kanai Y, Osawa H, Okamoto Y (2019) A study on iterative decoding with LLR modulator by neural network using adjacent track information in SMR system. IEEE Trans Magn 55(12):1–5
37. Nguyen DT, Park Y (2019) Performance analysis of interleaved LDPC for optical satellite communications. Opt Commun 442(7):13–18
38. Mei Z, Cai K, Song G (2019) Performance analysis of finite-length LDPC codes over asymmetric memoryless channels. IEEE Trans Veh Technol 68(11):11338–11342
39. Boncalo O, Kolumban-Antal G, Declercq D, Savin V (2018) Code-design for efficient pipelined layered LDPC decoders with bank memory organization. Microprocess Microsyst 63(11):216–225
40. Elkelesh A, Ebada M, Cammerer S, Schmalen L, Brink ST (2019) Decoder-in-the-loop: genetic optimization-based LDPC code design. IEEE Access 7:141161–141170
41. Branco P, Mateus P, Salema C, Souto A (2020) Using low-density parity-check codes to improve the McEliece cryptosystem. Inf Sci 510(2):243–255
42. Lee JH, Sunwoo MH (2019) Low-complexity high-throughput bit-wise LDPC decoder. J Signal Process Syst 91(8):855–862
43. Liu X, Xiong F, Wang Z, Liang S (2018) Design of binary LDPC codes with parallel vector message passing. IEEE Trans Commun 66(4):1363–1375
44. Català-Pérez JM, Lacruz JO, García-Herrero F, Valls J, Declercq D (2019) Second minimum approximation for min-sum decoders suitable for high-rate LDPC codes. Circuits Syst Signal Process 38(11):5068–5080
45. Li A, Meghdadi V, Cances J-P, Aupetit-Berthelemot C (2019) High-throughput 2 bit low-density parity-check forward error correction for C-RAN optical fronthaul based on a hard-decision algorithm. IET Circuits Dev Syst 13(2):111–116
46. Mondal A, Thatimattala S, Yalamaddi VK, Garani SS (2018) Efficient coding architectures for reed-solomon and low-density parity-check decoders for magnetic and other data storage systems. IEEE Trans Magn 54(2):1–15
47. Pradhan AK, Thangaraj A (2018) Protograph LDPC codes with block thresholds: extension to degree-one and generalized nodes. IEEE Trans Commun 66(12):5876–5887
48. Pramanik A, Maity SP, Sarkar S (2018) Compressed sensing image reconstruction by low density parity check codes and soft decoding of space time block codes. Comput Electr Eng 72(11):553–565
49. Mishra M (2019) LDPC codes and digital forensics—a perspective approach. IETE J Res 19:1–8
50. Gupta RS, Kamal TS, Singh PS (2019) Concatenated LDPC-TCM codes for better performance of OFDM-FSO system using gamma-gamma fading model. Wireless Pers Commun 106(4):2247–2260
51. Singh J, Gupta M, Bhullar JS (2019) Construction of girth-8 (3, L)-QC-LDPC codes of smallest CPM size using column multipliers. Des Codes Crypt 88(1):1–9
52. Aswathy GP, Nair GK, Ahamed TPI (2019) Parallel concatenated Gallager codes for reliable data transmission in cognitive radio networks. Phys Commun 37(12):1–14
53. Yatribi A, Belkasmi M, Ayoub F (2020) Gradient-descent decoding of one-step majority-logic decodable codes. Phys Commun 39:100999
54. Kabakulak B, Taşkin ZC, Pusane AE (2019) A branch-and-cut algorithm for a bipartite graph construction problem in digital communication systems. Networks 75(2):137–157
55. Gallager RG (1963) Low-density parity-check codes. MIT Press, Cambridge
56. Fossorier MPC, Mihaljevic M, Imai H (1999) Reduced complexity iterative decoding of low-density parity check codes based on belief propagation. IEEE Trans Commun 47(5):673–680
57. Kou Y, Lin S, Fossorier MPC (2001) Low-density parity-check codes based on finite geometries: a rediscovery and new results. IEEE Trans Inf Theory 47(7):2711–2736
58. Zhang J, Fossorier MPC (2004) A modified weighted bit-flipping decoding of low-density parity-check codes. IEEE Commun Lett 8(3):165–167
59. Jiang M, Zhao C, Shi Z, Chen Yu (2005) An improvement on the modified weighted bit flipping decoding algorithm for LDPC codes. IEEE Commun Lett 9(9):814–816
60. Guo F, Hanzo L (2004) Reliability ratio based weighted bit-flipping decoding for low-density parity-check codes. Electron Lett 40(21):1356–1358
61. Lee C-H, Wolf W (2005) Implementation-efficient reliability ratio based weighted bit-flipping decoding for LDPC codes. Electron Lett 41(13):755–757
62. Chen T-C (2012) Channel-independent weighted bit-flipping decoding algorithm for low-density parity-check codes. IET Commun 6(17):2968–2973
63. Zhang G, Zhou L, Wen H (2014) Modified channel-independent weighted bit flipping decoding algorithm for low-density-parity-check codes. IET Commun 8(6):833–840

64. Huang H, Wang Y, Wei G (2015) Mixed modified weighted bit-flipping decoding of low-density parity-check codes. IET Commun 9(2):283–290
65. Ismail M, Coon J, Ahmed I, Armour S, McGeehan J (2013) Turbo adaptive threshold bit flipping for LDPC decoding. IEEE Wireless Commun Lett 2(1):118–121
66. Chen T-C (2013) Adaptive-weighted multibit-flipping decoding of low-density parity-check codes based on ordered statistics. IET Commun 7(14):1517–1521
67. Tiwari HD, Tiwari HD, Lee K-Y (2014) Hybrid weighted bit flipping low density parity check decoding. Digit Signal Proc 28:82–92
68. Ma K, Li Y, Zhu C, Zhang H, Zhang Y (2014) Lowering error floor of LDPC codes using an improved parallel WBF algorithm. ETRI J 36(1):171–174
69. Nguyen DV, Vasic B (2014) Two-bit bit flipping algorithms for LDPC codes and collective error correction. IEEE Trans Commun 62(4):1153–1163
70. Roberts MK, Jayabalan R (2014) An improved low complex hybrid weighted bit-flipping algorithm for LDPC codes. Wireless Pers Commun 82(1):327–339
71. Hatami H, Mitchell DGM, Costello DJ, Fuja TE (2020) A threshold-based min-sum algorithm to lower the error floors of quantized LDPC decoders. IEEE Trans Commun 68(4):2005–2015
72. Liu Y, Niu X, Zhang M (2015) Multi-threshold bit flipping algorithm for decoding structured LDPC codes. IEEE Commun Lett 19(2):127–130
73. Chang TC-Y, Su YT (2015) Dynamic weighted bit-flipping decoding algorithms for LDPC codes. IEEE Trans Commun 63(11):3950–3963
74. Elsanadily S, Mahran A, Elghandour O (2017) Two-side state-aided bit-flipping decoding of generalized low density parity check codes. IEEE Commun Lett 21(10):2122–2125
75. Oh J, Ha J (2018) A two-bit weighted bit-flipping decoding algorithm for LDPC codes. IEEE Commun Lett 22(5):874–877
76. Wang Y, Wu G (2018) Cyclic switching weighted bit-flipping decoding for low-density parity-check codes. IET Commun 12(3):271–275
77. Le K, Ghaffari F, Kessal L, Declercq D, Boutillon E, Winstead C, Vasic B (2019) A probabilistic parallel bit-flipping decoder for low-density parity-check codes. IEEE Trans Circuits Syst I Regul Pap 66(1):403–416
78. Liu Y, Zhang M (2019) Hard-decision bit-flipping decoder based on adaptive bit-local threshold for LDPC codes. IEEE Commun Lett 23(5):789–792
79. Kalipatnapu S, Chakrabarti I (2019) High-throughput Bit Flipping decoder for structured LDPC codes. IET Commun 13(14):2168–2172
80. Chang TC-Y, Wang P-H, Su YT (2019) Multi-stage bit-flipping decoding algorithms for LDPC codes. IEEE Commun Lett 23(9):1524–1528
81. Chou H-F, Sham C-W (2018) An optimization approach for an RLL-constrained LDPC coded recording system using deliberate flipping. IEEE Commun Lett 22(10):1976–1979
82. Dai B, Liu R, Gao C, Mei Z (2019) Symbol flipping algorithm with self-adjustment strategy for LDPC codes over GF(q). IEEE Trans Veh Technol 68(7):7189–7193
83. Hu Y, Song S, Xiao S, Xu Q, Xiao N, Qin Z (2015) A dominating error region strategy for improving the bit-flipping LDPC decoder of SSDs. IEEE Trans Circuits Syst II Express Briefs 62(6):578–582
84. Liu Y-C, Chang C-F, Lee S-K, Lin M-C (2017) Deliberate bit flipping with error-correction for PAPR reduction. IEEE Trans Broadcast 63(1):123–133
85. Jung N, Park I-C (2017) Multi-bit flipping decoding of LDPC codes for NAND storage systems. IEEE Commun Lett 21(5):979–982
86. Sohrabi MK, Azgomi H (2018) A survey on the combined use of optimization methods and game theory. Arch Comput Methods Eng 27(1):59–80
87. Zhang Y, Li Q, Huang L, Dai K, Song J (2018) Optimal design of cascade LDPC-CPM system based on bionic swarm optimization algorithm. IEEE Trans Broadcast 64(3):762–770
88. Rojc M, Mlakar I (2020) A new fuzzy unit selection cost function optimized by relaxed gradient descent algorithm. Expert Syst Appl 159:113552
89. Wadayama T, Nakamura K, Yagita M, Funahashi Y, Usami S, Takumi I (2010) Gradient descent bit flipping algorithms for decoding LDPC codes. IEEE Trans Commun 58(6):1610–1614
90. Nakamura K, Wadayama T, Yagita M, Funahashi Y, Usami S, Takumi I (2008) Improved gradient descent-bit flipping decoding using multi thresholds. In: Proceedings of the IEICE general conference, pp 160 (**in Japanese**)
91. Asatani J, Kawanishi H, Tokushige H, Katayama K (2015) Frequency memory based gradient descent bit flipping algorithm. IEE J Trans Electr Electron Eng 10(5):585–591
92. Sundararajan G, Winstead C, Boutillon E (2014) Noisy gradient descent bit-flip decoding for LDPC codes. IEEE Trans Commun 62(10):3385–3400
93. Rasheed OA, Ivanis P, Vasic B (2014) Fault-tolerant probabilistic gradient-descent bit flipping decoder. IEEE Commun Lett 18(9):1487–1490
94. Le K, Ghaffari F, Declercq D, Vasic B (2017) Efficient hardware implementation of probabilistic gradient descent bit-flipping. IEEE Trans Circuits Syst I Regul Pap 64(4):906–917
95. Ren D, Sha J (2018) Improved gradient descent bit flipping decoder for LDPC codes on BSC channel. IEICE Electron Express 15(8):20180195–20180195
96. Li H, Ding H, Zheng L (2017) Modified gradient descent bit-flipping decoding for low-density parity-check codes. Wireless Pers Commun 96(4):6459–6472
97. Dai B, Liu R, Gao C, Mei Z (2018) Noisy gradient descent bit-flipping decoder based on adjustment factor for LDPC codes. IEEE Commun Lett 22(6):1152–1155
98. Cui H, Lin J, Wang Z (2019) An improved gradient descent bit-flipping decoder for LDPC codes. IEEE Trans Circuits Syst I Regul Pap 66(8):3188–3200
99. Unal B, Akoglu A, Ghaffari F, Vasic B (2018) Hardware implementation and performance analysis of resource efficient probabilistic hard decision LDPC decoders. IEEE Trans Circuits Syst I Regul Pap 65(9):3074–3084
100. Ueng Y-L, Wang C-Y, Li M-R (2017) An efficient combined bit-flipping and stochastic LDPC decoder using improved probability tracers. IEEE Trans Signal Process 65(20):5368–5380
101. Rao RV, Saroj A, Ocłoń P, Taler J (2019) Design optimization of heat exchangers with advanced optimization techniques: a review. Arch Comput Methods Eng 27(2):517–548
102. Zhang J, Peng Y, Ouyang W, Deng B (2019) Accelerating ADMM for efficient simulation and optimization. ACM Trans Graph 38(6):1–21
103. Xiu X, Liu W, Li L, Kong L (2019) Alternating direction method of multipliers for nonconvex fused regression problems. Comput Stat Data Anal 136:59–71
104. Falsone A, Notarnicola I, Notarstefano G, Prandini M (2020) Tracking-ADMM for distributed constraint-coupled optimization. Automatica 117:108962
105. Jian L, Hu J, Wang J, Shi K (2019) Distributed inexact dual consensus ADMM for network resource allocation. Optimal Control Appl Methods 40(6):1071–1087

106. Vargas H, Ramirez J, Arguello H (2020) ADMM-based $\ell 1-\ell 1$ optimization algorithm for robust sparse channel estimation in OFDM systems. Signal Process 167:107296
107. Bao H, Fang J, Wan Q, Chen Z, Jiang T (2018) An ADMM approach for PAPR reduction for large-scale MIMO-OFDM systems. IEEE Trans Veh Technol 67(8):7407–7418
108. Wang Y, Wang Y, Shi Q (2019) Optimized signal distortion for PAPR reduction of OFDM signals with IFFT/FFT complexity via ADMM approaches. IEEE Trans Signal Process 67(2):399–414
109. Chen J, Fossorier M (2002) Density evolution for two improved BP-based decoding algorithms of LDPC codes. IEEE Commun Lett 6(5):208–210
110. Kschischang FR, Frey BJ, Loeliger HJ (2001) Factor graphs and Sum-product algorithm. IEEE Trans Inf Theory 47(2):498–519
111. Oh D, Parhi KK (2010) Min-sum decoder architectures with reduced word length for LDPC codes. IEEE Trans Circuits Syst I Regular Pap 57(1):105–115
112. Mansour MM, Shanbhag NR (2003) High-throughput LDPC decoders. IEEE Trans Very Large Scale Integr Syst 11(6):976–996
113. Jiang M, Zhao C, Zhang L, Enyang X (2006) Adaptive offset min-sum algorithm for low-density parity check codes. IEEE Commun Lett 10(6):483–485
114. Wei H, Jiao X, Mu J (2015) Reduced-complexity linear programming decoding based on ADMM for LDPC codes. IEEE Commun Lett 19(6):909–912
115. Jiao X, Wei H, Mu J, Chen C (2015) Improved ADMM penalized decoder for irregular low-density parity-check codes. IEEE Commun Lett 19(6):913–916
116. Storn R, Price K (1997) Differential evolution: a simple and efficient heuristic for global optimization over continuous spaces. J Global Optim 11(4):341–359
117. Debbabi I, Gal BL, Khouja N, Tlili F, Jego C (2016) Fast converging ADMM-penalized algorithm for LDPC decoding. IEEE Commun Lett 20(4):648–651
118. Barman S, Liu X, Draper SC, Recht B (2013) Decomposition methods for large scale LP decoding. IEEE Trans Inf Theory 59(12):7870–7886
119. Liu X, Draper SC (2016) The ADMM penalized decoder for LDPC codes. IEEE Trans Inf Theory 62(6):2966–2984
120. Jiao X, Mu J (2016) Lowering the error floor of ADMM penalized decoder for LDPC codes. China Commun 13(8):127–135
121. Debbabi I, Le Gal B, Khouja N, Tlili F, Jego C (2016) Real time LP decoding of LDPC codes for high correction performance applications. IEEE Wireless Commun Lett 5(6):676–679
122. Yu L, Lin N (2017) ADMM for penalized quantile regression in big data. Int Stat Rev 85(3):494–518
123. Wang B, Mu J, Jiao X, Wang Z (2017) Improved penalty functions of ADMM penalized decoder for LDPC codes. IEEE Commun Lett 21(2):234–237
124. Jiao X, Mu J, Wei H (2017) Reduced complexity node-wise scheduling of ADMM decoding for LDPC codes. IEEE Commun Lett 21(3):472–475
125. Casado AIV, Griot M, Wesel RD (2010) LDPC decoders with informed dynamic scheduling. IEEE Trans Commun 58(12):3470–3479
126. Lee H-C, Ueng Y-L, Yeh S-M, Weng W-Y (2013) Two informed dynamic scheduling strategies for iterative LDPC decoders. IEEE Trans Commun 61(3):886–896
127. Liu X, Zhou Z, Cui R, Liu E (2016) Informed decoding algorithms of LDPC codes based on dynamic selection strategy. IEEE Trans Commun 64(4):1357–1366
128. Tehrani SS, Mannor S, Gross WJ (2008) Fully parallel stochastic LDPC decoders. IEEE Trans Signal Process 56(11):5692–5703
129. Jiao X, Mu J, He Y-C, Chen C (2017) Efficient ADMM decoding of LDPC codes using lookup tables. IEEE Trans Commun 65(4):1425–1437
130. Khittiwitchayakul S, Phakphisut W, Supnithi P (2018) Reduced complexity window decoding of spatially coupled LDPC codes for magnetic recording systems. IEEE Trans Magn 54(11):1–5
131. Jiao X, He Y-C, Mu J (2018) Memory-reduced look-up tables for efficient ADMM decoding of LDPC codes. IEEE Signal Process Lett 25(1):110–114
132. Zhang Q, Wang M, Lu Y, Zhang L, Idrees M (2019) A novel fast nonstationary noise tracking approach based on MMSE spectral power estimator. Digital Signal Proc 88:41–52
133. Wei H, Banihashemi AH (2018) An iterative check polytope projection algorithm for ADMM-based LP decoding of LDPC codes. IEEE Commun Lett 22(1):29–32
134. Wu Q, Zhang F, Wang H, Lin J, Liu Y (2018) Parameter-free l_p-box decoding of LDPC codes. IEEE Commun Lett 22(7):1318–1321
135. Wu B, Ghanem B (2019) L_p-box ADMM: a versatile framework for integer programming. IEEE Trans Pattern Anal Mach Intell 41(7):1695–1708
136. Bai J, Wang Y, Lau FCM (2019) Minimum-polytope-based linear programming decoder for LDPC codes via ADMM approach. IEEE Wireless Commun Lett 8(4):1032–1035
137. Xia Q, Lin Y, Tang S, Zhang Q (2019) A fast approximate check polytope projection algorithm for ADMM decoding of LDPC codes. IEEE Commun Lett 23(9):1520–1523
138. Bai J, Wang Y, Shi Q (2020) Efficient QP-ADMM decoder for binary LDPC codes and its performance analysis. IEEE Trans Signal Process 68:503–518
139. Wang B, Wang Z (2020) ADMM penalized decoding method based on improved penalty function for LDPC codes in the IoTs. Comput Commun 154:197–203
140. Wei Y, Zhao M-M, Zhao M-J, Lei M (2020) ADMM-based decoder for binary linear codes aided by deep learning. IEEE Commun Lett 24(5):1028–1032

Wireless Networks
https://doi.org/10.1007/s11276-020-02528-4

Channel estimation using spatial partitioning with coalitional game theory (SPCGT) in wireless communication

S. Dhanasekaran[1] · J. Ramesh[2]

Accepted: 16 December 2020

Abstract

In 5G wireless communication estimation, of downlink channel with orthogonal frequency division multiplexing (OFDM) integrated with multiple input multiple output (MIMO) is a challenging task. This arises due to the utilization of orthogonal pilots in downlink which leads to pilot overhead. To overcome this challenge spatial-temporal sparsity features with compressive sensing utilized for estimation of channels. However, this leads to the challenge of spatial common sparsity in data transmission due to the overlapping of the antenna group which is not separated. To overcome those challenges, this paper developed a spatial partitioning coalitional game theory (SPCGT) for the MIMO-OFDM downlink channel. The performance of the proposed SPCGT is based on the spectral partitioning of the MIMO antenna array. Within MIMO partitioned antenna game theory is applied for reduction of pilot overhead with improved channel estimation. The proposed SPCGT model is aimed to reduce normalized mean square error (NMSE) and bit error rate (BER) for the estimation of the available channel. The performance of the proposed SPCGT is comparatively examined with the existing techniques in terms of the slow time and fast time varying channels. The NMSE and BER stated that the proposed SPCGT offers reduced NMSE and BER for the MIMO-OFDM system.

Keywords MIMO · Spatial partitioning coalitional game theory (SPCGT) · Spatial distribution · Channel estimation · NMSE · BER

1 Introduction

Multiple Input Multiple Output (MIMO) technology has become an active research topic over the past decade due to its ability to achieve the high transmission speeds required by a growing number of data-demanding applications. MIMO technology offers many benefits to address the challenges of wireless channel degradation, particularly multipath fading [1]. It offers several important performance benefits such as antenna gain, diversity gain, and multiplexing gain. Orthogonal frequency division multiplexing (OFDM), belongs to a class of multicarrier transmission technology, which has been utilized for radio and UWB (Ultra Wide Band) communication. OFDM demand for high data rate information for data transmission with robust performance related to frequency-selective fading channel. The combination of multiple antennae with OFDM increases the capacity of a channel with diversity in the sender and receiver, this is known as MIMO–OFDM. Due to demand in wireless communication with high data rate array-based transceivers and diversity scheme based on space is adopted in emerging research domain [1].

To improve wireless system capacity both analytical and Multiple-Input Multiple-Output (MIMO) technique is developed [2]. Estimating the MIMO channel parameters is required for equalization on the receiver side and precoding on the transmitter side. Therefore, channel parameter estimation is a crucial element in MIMO communication. However, those systems aware of receiver Channel State

✉ S. Dhanasekaran
dhanselvaraj@gmail.com

J. Ramesh
jr.ece@psgtech.ac.in

1 Department of Electronics and Communication Engineering, Sri Eshwar College of Engineering, Coimbatore, Tamil Nadu 641202, India

2 Department of Electronics and Communication Engineering, PSG College of Technology, Coimbatore, Tamil Nadu 641004, India

Published online: 23 January 2021

Information (CSI) knowledge. Generally, the MIMO antenna system utilizes multiple antenna for the sender and receiver. With received signal channel parameters are estimated which is known as channel estimation. The channel parameters are computed based on the receiver pilot symbol with the computation of parameters. For every packet transmission, each channel is estimated and a pilot symbol inserted for every data packet transmission [3]. However, the adoption of the MIMO system in wireless communication provides an accurate estimation of channel state information (CSI) between the sender and receiver. Therefore, in the MIMO communication system, accurate channel estimation plays a critical role.

The channel estimation methods are divided into parametric and non-parametric categories. Nonparametric methods are unconstrained methods that exploit little or no assumptions about the channel model, so they have no associated parameters to rely on, which leads to an increase in the size of the prediction problem. Parametric methods are instead associated with parametric models defined by a finite number of parameters with clear physical meanings related to the propagation of the signal through the channel. The most popular and widely adopted approach involved in MIMO channel estimation is the insertion of pilot signals, which is also defined as training sequences. This estimates the channel based on the training symbol received data. To estimate the MIMO channel effectively training-based schemes are evolved [4]. The analysis of the existing literature stated that MIMO channel sequences are directly related to the capacity of the channel. Based on this, several flat-fading and frequency-selective fading schemes for a MIMO system are evolved. In existing, maximum likelihood (ML) with the orthogonal pilot signal, least square (LS) with OFDM is designed for estimation of the channel with reduced mean-square error (MSE). With several training schemes, multiple antenna for transmitting and a single receiver antenna is designed with the estimation of linear LS and MMSE [5, 6, 7]. The channel estimation parameters computed are relied on channel sparsity for efficient allocation of resources for data transmission.

1.1 Contribution and organization

In this paper, the massive MIMO downlink frequency selective channel estimation model is designed based on game theory-based spatial partial-common sparsity. For the proposed model, a proper pilot sequence transmission using spatial partitioning is designed, and based on game theory channel selection is performed. Thus, the proposed method is based on the spatial partial-common sparsity modeling, in which the channel vectors are estimated in multiple stages. In this scenario, game theory is used for solving the obtained sparse model, where the estimated support set of each stage. Spatial Partitioning Coalitional Game Theory (SPCGT) is adopted for effective channel assessment in the communication system. The performance of the proposed system exhibits significant performance rather than existing techniques. The rest of this paper is organized as follows. In the next section, literature related to channel estimation is presented. In Sect. 3, the proposed model and channel estimation method are introduced. The simulation results are shown in Sect. 4, followed by the conclusions and future enhancement in Sect. 5.

2 Related works

In a MIMO system, channels are defined as a path between Mobile Station (MS) and Base Station (BS). This channel path causes path delay and scattering in channel propagation with the provision of similar path delay arises due to sparsity of channel path between MS and BS antenna [8, 9]. Based on the correlation of the temporal channel it exhibits the higher path gain more than path delay. This leads to similar sparsity for channel allocation based on the coherence time. The study conducted in [10] is about channel coherence time measurement with the utilization of experimental data. The analysis of results stated that the sparse path arrival time is stable with relative delay. To improve the performance of channel estimation sparse structure and temporal correlation matrix were utilized [11]. In [12] to overcome sparsity of channel in OFDM blocks SOMP based approach was utilized. The analysis was based on the consideration of the channel model with the utilization of common sparse for a slow time-varying channel. The proposed approach was examined based on the channel superiority with consideration of experimental data. However, those techniques focused on multi-blocks path delay using temporal correlation for increased channel gain in UWB channels [13].

Among those techniques, few techniques utilized pilot sequences to reduce pilot overhead with the exploitation of MIMO channel spatial and temporal correlation [14–16]. Also, several researchers focused on channel estimation for Frequency Division Duplexing (FDD) downlink with the utilization of massive MIMO. In [17], through temporal correlation pilot overhead was minimized with delay-domain sparsity channel. Also, [18, 19] utilized spatial correlation and delay-domain sparsity for channel estimation. This research assumed that the sparsity level for the communication channel was known. Further, to resolve the channel pilot overhead problem compressed-sensing technique for the MIMO downlink system was adopted in [20].

To achieve effective channel estimation for long-term channel open-loop and closed-loop methods were utilized for statistical analysis of channel with temporal and spatial correlation. Also, in [21] pilot overhead was minimized using channel estimation based on the beam space block. With channel estimation based on consideration of the angular domain off-grid model integrated with Bayesian learning, methods were adopted for downlink channel with sparse representation. In [22], estimation of the channel in massive MIMO was developed using an adaptive pilot reuse strategy with the introduction of beam domain with compressive sensing. The design of the pilot and massive MIMO channel estimation was based on the assumption of the beam with the application of the Kalman filter. In [23] sparsity in the channel was balanced by estimation of the channel using the angle-frequency domain and angle-delay with the utilization of compressed sensing.

In [24], the adopted block expectation propagation algorithm for downlink channel estimation with clustering of all channels with the same delay. In [25], channel estimation is performed using a time-domain sequence. This time-domain model utilized prior information related to the Adaptive Structured Subspace Pursuit (ASSP) algorithm for channel estimation using the measurement of sparsity in time and spatial domain. The message passing approach was utilized for dynamic turbo orthogonal approximation for FDD tracking in massive MIMO with consideration of spatial and temporal domain. In recent years, the UWB channel was exploited with channel estimation with] Least Square (LS) methods [26]. In the channel estimation method, a greedy algorithm like Matching Pursuit (MP) was applied for UWB channels. In [27], SOMP was utilized for exploiting sparsity in OFDM blocks with consideration of the slow time-varying channel. However, these involved in multi-blocks sparse path delay and temporal correlation for UWB channel gain measurement. In [28], the TMSBL algorithm was developed for estimation of channel based on the virtual and actual signal, that can be improved with an estimation of temporal correlation for channel prediction and reconstruction. The developed TMSBL considered performance metrics such as Bit Error Rate (BER) and Mean Square Error (MSE).

Through analysis of existing literature related to channel estimation, it is observed that the complexity of MIMO–OFDM channel is improved. This challenge is due to the inclusion of spatial and time-domain features. The UWB channel highly relies on real-time data which demands effective channel estimation for real-time data transmission. Hence, this paper focused on the estimation of the channel using the Spatial Partitioning Coalitional Game Theory (SPCGT). The performance of the proposed SPCGT model is measured in terms of BER and NMSE.

3 System model

Figure 1 describes the overview of proposed game spatial partitioning with game theory (SPCGT) for minimizes the error of channel estimation in distributed MIMO systems. Space partitioning is the process of dividing a space into two or more disjoint subsets. In other words, space partitioning divides a space into non-overlapping regions. Any point in the space can then be identified to lie in exactly one of the regions. The problem of minimizing the NMSE is formulated and an algorithm based on game theory is proposed to solve it.

A spatial partitioning algorithm based on game theory is proposed to mitigate the pilot contamination in distributed MIMO systems. Firstly, the problem is transformed into an optimization problem that minimizes the NMSE of the channel estimation.

The input signal obtained from MIMO antenna based on capacity and reliability. The pilot symbols are transmitted over orthogonal transmission medium. This is single frequency transmitted over communication system. The serial to parallel converter is used to convert the serial input data into parallel data. In ICEA-DA, the converted signals are partitioned spatially for estimation of polynomial functions. Through identification cost (i.e. frequency) of channel is estimated using Improved Channel Estimation Algorithm using differential evolution. Based on the estimation used and unused channel are computed. Then, the parallel to serial converter is used to convert these signals from parallel to serial for transmission. Up converter is efficiently used to converts the low frequency components to higher frequency components. This transmitter blocks transmit the signal to the receiver

In receiver, a digital down-converter converts a digitized, band-limited signal to a lower frequency signal at a lower sampling rate in order to simplify the subsequent radio stages. Once the cyclic prefix of appropriate length has been removed, the received signal is decomposed into separate subcarriers using the DFT. Then, to equalize the gain of the desired signal, the subcarriers are multiplied with the inverse of the channel frequency response across each of the subcarriers. The Space Time Decoder is used to decode the data for improve the reliability of data transmission in wireless communication systems using multiple transmit antenna

Through the inclusion of coding scheme every signal in the system varies in 1-bit. In below Eq. (1) signal transmitted in sine and cosine form is presented as follows:

$$g_n(t) = \sqrt{\frac{2S_e}{D_s}} \cos\left(2\pi f_c t + (2n-1)\frac{\pi}{4}\right), n = 1, 2, 3, 4 \quad (1)$$

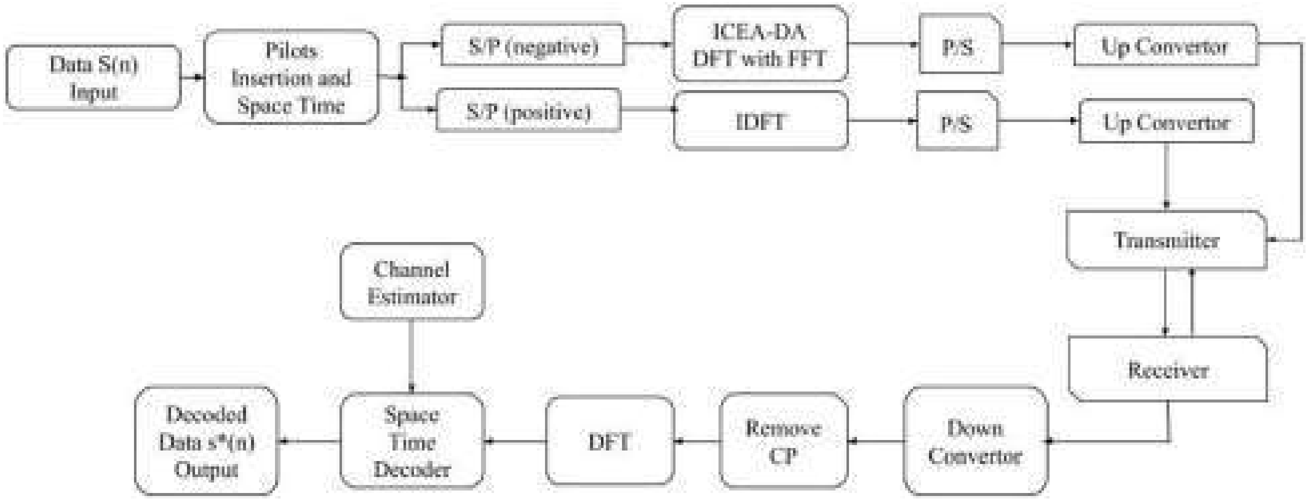

Fig. 1 Overview of proposed game theory based spatial approach

here $g_n(t)$ signifies the signal based on the time, represents the symbol energy; symbol duration is denoted as, whereas, f_c is represented as baseband of signal.

In modulator of MIMO scheme 4 phases of the signal are generated which consists of 2D signal space with unit function $\phi_1(t)$ and $\phi_2(t)$ denoted as in Eqs. (2) and (3)

$$\phi_1(t) = \sqrt{\frac{2}{D_s}} \cos 2\pi f_c t, \quad 0 \le t \le T \tag{2}$$

$$\phi_2(t) = \sqrt{\frac{2}{D_s}} \sin 2\pi f_c t, \quad 0 \le t \le T \tag{3}$$

From the above Eqs. (2) and (3) and are utilized for measurement of in-phase and quadrature component. In terms, OFDM signal consists of 4 signal constellation based on signal-space four points such as defined in Eq. (4):

$$\left(\pm\sqrt{\frac{S_e}{2}}, \pm\sqrt{\frac{S_e}{2}} \right) \tag{4}$$

In this, the signal factor 1/2 signifies the total power of the system which has been partitioned equally between the inclusion of 2 carriers. In the receiver side, the symbol is demodulated with the elimination of carrier-phase factor, the phase 2 successive received bits are ascertaining with respect to input data.

The every transmitted symbol with PSF (Point Spread Function) is represented as $p_r(t)$ and receiver side antenna filtering components is represented as $p_r(t)$. The symbols of channel composite is represented as H(t) and the time domain signal received at an array of i_Rth antenna is stated as follows

$$H_{iR,iT}(n) = \sum_{i_T=1}^{N_T} h_{iR,iT}(n) \otimes x_{iT} + J \tag{5}$$

Here in Eq. (5) the J denotes noise placed in uncorrelated spatio temporal region, represents the presence of noise in transmit time-domain signal at the ith antenna. h_{iRiT} stated as time-domain signal at a different instance of time. To eliminate Inter Symbol Interference (ISI) at the receiver end, MIMO–OFDM includes Inverse Fast Fourier Transform (IFFT). At receiver side, IFFT is applied for complex operation in the receiver side with time-domain factor consideration. The operation of IFFT is applied in the receiver side for improving flexibility, precision and execution speed of the system. For N—point receiver operation, IFFT is computed mathematically using Eq. (6):

$$u(n) = \frac{1}{N} \sum_{n=1}^{N-1} U(k) e^{\frac{-j\pi kn}{N}}, n = 0, 1, \ldots, N-1 \tag{6}$$

where N represented data frame transform size or several points in the signal. $U(k)$ denotes the FFT frequency output at kth point where k = 0,1,…, N-1. Subsequently, FFT analysis is utilized for transmute of signal in the time domain at the receiver block. In Eq. (7) mathematical formulation for FFT is presented as follows:

$$U(k) = \sum_{n=1}^{N-1} u(n) e^{\frac{-j2\pi kn}{N}}, k = 0, 1, \ldots, N-1 \tag{7}$$

Additionally, in multipath channel environment signal are transmitted with the addition of AWGN (Additive White Gaussian Noise) characteristics. In this paper, AWGN is utilized for its higher bandwidth rather than message signal. The system noise n represents complex Gaussian distribute random stationary point with mean 0 and formulate vector with identical components with message defined in Eq. (8) as below:

$$n = n_p * (N(0,1) + i * N(0,1)) \quad (8)$$

where n_p signifies the noise power and $N(0,1)$ represented message signal of the same length which comprises of normal/Gaussian random variables.

3.1 Spatial partitioning for channel estimation

Here, proposed SPCGT is based on the consideration of cost function for obtaining a solution for parallel search continuous process. The advantage of proposed SPCGT has improved convergence through the utilization of control parameters such as antenna spacing, a gain of the channel and spectral bandwidth.

The proposed game theory with Spatial Partitioning is represented in canonical form with effective handling of continuous variables with the optimization of integer variables. The proposed SPCGT involved in partitioning of the available channel with the aim of reducing BER and NMSE. Initially, populace NP (Non-deterministic Polynomial) is considered as channel size estimation parameters. Apart from those parameters, for constructed function random individuals are provided with lower–upper bounds as represented in Eq. (9)

$$v^j_{i.go} = v^j_{\min} + rand(0,1).(v^j_{\max} - v^j_{\min});\ j = 1,2,3,\ldots,D \quad (9)$$

In the above Eq. (9) denotes individual channel index, represents channel upper bounds with comprises of D parameters those are generated uniformly with the inclusion of Eq. (10) as follows:

$$V_{\min} = \left(v^1_{\min},\ldots,v^D_{\min}\right) \text{ and } V_{\max} = \left(v^1_{\max},\ldots,v^D_{\max}\right) \quad (10)$$

Next, *rand*(0,1) indicates the random generator between the range of 0–1.

For evaluating channel sparsity proposed SPCGT is utilized for estimation of NMSE of OFDM system. It is represented in Eq. (11) as below:

$$H_f^{NMSE} = R_{HHf}\left(R_{HfHf} + (\beta/SNR)I_f\right)^{-1} h_f^{LS} \quad (11)$$

Subsequently, based on the above Eq. (11) resource estimation is performed in the MIMO OFDM system. Based on constructed game theory with Spatial Partitioning new parameters are summed between two parameters with the estimation of weighted difference factor based on temporary, trial or third channels. For the generated vector scheme trail population G is represented in Eq. (12):

$$W_{i,G+1} = V_{r1.G} + \eta(V_{r2}.G - V_{r3}.G) \quad (12)$$

where V indicates a target vector $i, r_1, r_2, r_3 \in [1,2,3,\ldots NP].r_1, r_2, r_3$ of the signal with the MIMO OFDM system. Moreover, in the proposed model, arbitrarily points are represented using a scaling factor. The scaling factor is denoted as η, with a differential variation of [0,1]. After that, termination-state of NMSE is utilized for the identification of effective solution with maximal signal point generation.

In proposed SPCGT channel resources are considered with the total amount of Cx with n number of resources assigned for an individual. The allocated network resources are denoted a X = (x_1, x_2,…,x_n) for resource management in which amount of resources allocated is denoted as x_i with i = 1, 2,…, n.

The sum of allocated resources for the individual need to be less than or equal to the total measured amount, this is stated as $\sum_{i=1}^{n} x_i \le C_x$, where is the number of total resources. With Bossaer's fairness index, single resource allocation in kth-order is represented using transformation function f(x) = $x^{1/k}$for achieving fairness index with consideration of Bossaer'sindes and identification of ideal part of channel. Here, the channel assignment problem is defined in Eq. (13):

$$A_x(X) = \prod_{i=1}^{n}\left[\frac{x_i}{\max(x)}\right]^{\left(\frac{1}{k}\right)} \quad (13)$$

The fairness indices of linear product for special cases with Bossaer's fairness index is represented with consideration of stability constant G with K = 1 as shown in Eq. (14):

$$\mathrm{A_x(X) = G\ [x_i/\max(x)]} \quad (14)$$

where G = $\prod_{i=1}^{n} 1$

3.2 Spatial partition model for SPCGT

As stated, the sparsity of resources in the MIMO channel for OFDM is a complex issue that leads to pilot overhead often. The OFDM network pilot overhead and sparsity in MIMO is occurred due to the location of the antenna array in BS side by side. Usually, in the MIMO communication system vast range of array antenna is located in BS with a common antenna pattern. To resolve this issue proposed SPCGT technique divides the planar antenna array into 'M' antennas. In this, a Non-Cooperative game (NG) for the individual group for an individual antenna in one group is applied and the adjacent multicast group (MG) is represented as MG = M/NG. In Fig. 2, the MIMO antenna partitioning model for data transmission is presented. In the proposed SPCGT approach, each antenna group is assumed that all array antenna group has similar sparsity pattern. In this, every channel in the individual group is estimated

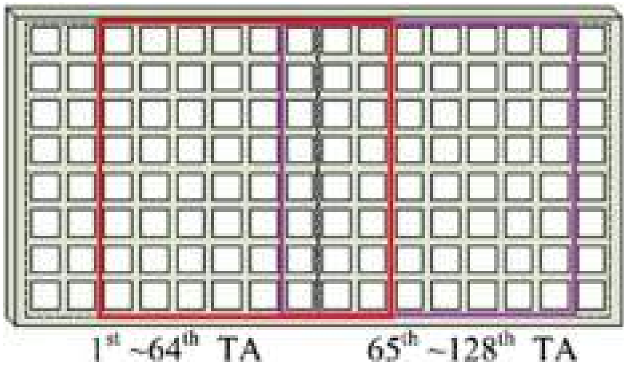

Fig. 2 2D planar array

using the Spatio-temporal sparsity method. The developed spectral partitioning for the OFDM system is presented in Fig. 2.

This paper focused on channel sparsity with minimal pilot sequence overhead through SPCGT. However, an in-depth analysis of the proposed SPCGT antenna is based on the consideration of similar MG adjacent antenna groups with similar sparsity patterns with planar antenna array, as shown in Fig. 2. The developed model consists of eight individual antennas at every column of the array element. In the proposed SPCGT model first antenna element contains a spatial sparsity antenna pattern of 1–8 array and the second group of elements contains an antenna array element of 9–16 as another sparsity network pattern. The antenna array pattern is not adequate, which leads to pilot overhead due to minimal antenna spacing of every group. In a practical scenario, this sparsity in antenna adjacent groups is not separated. This leads to wastage of network resources and causes sparsity of channel with pilot overhead.

The few antennas in 1st group select few antennae in 2nd group of antenna patterns as shown in Fig. 2, where the 8th column antenna selects few antennae in the 9th column array antenna. In a practical model, antenna array sparsity consists of both common and uncommon part. The spatial partial-common sparsity model for antenna elements is based on channel impulse response. In Fig. 3, about SPCGT sparsity model for non-zero element channel impulse response is presented. As stated in Fig. 3, nonzero elements between two adjacent antenna channel impulse responses are presented in colour cells. It is observed that interaction provided with elements is non-zero, though it is implied that support sets of the antenna impulse response of antenna array have a common and uncommon part.

In Fig. 3, the proposed SPCGT MIMO antenna array pattern in a row is presented with spatial partitioning of the array antenna. It is presented that antenna pattern frequency arrangement is between 1 and 15 columns with an available range of 10. The constructed antenna pattern operating frequency range is between 160 MHz and 52.6 GHz. However, this paper focused on the UWB application; hence the evaluation of frequency is performed between 3.1 and 10.6 GHz. The analysis of SPCGT is based on the consideration of slow-varying and fast—varying channels. The operation of the proposed SPCGT is measured in a planar rectangular antenna array pattern. The proposed SPCGT antenna array consists of M antenna with a dimension of $M1 \times M2$ with a condition of $M1 < M2$. In the antenna pattern, M1 is stated as an adjacent antenna arranged in line with similar spatial sparse. The proposed SPCGT evaluation is based on the consideration of the square antenna design of $M2 - M1 + 1$ with an array antenna dimension of $M1 \times M1$ with a rectangular array pattern in each group arranged based on partial-sparsity characteristics. The analysis is based on consideration of planar array with spacing of antenna at $\lambda 2$, carrier frequency fc = 2 GHz and sampling frequency fs = 10 MHz. For the designed spatial partitioned antenna array distance between antenna located in the square group is defined as $4\sqrt{\ }2\ \lambda$ of common sparse and maximal path delay difference is denoted as $4\sqrt{\ }2\ \lambda\ c = 4\sqrt{\ }2$ with carrier frequency value of fc = 0.0028 µs. The proposed SPCGT sampling time is denoted as Ts = 1 with a sampling frequency value of fs = 0.1 µs in this game theory is applied.

In the proposed SPCGT game theory is applied for two adjacent antenna group dimensions of $M1 \times (M1 - 1)$ antenna. As stated, each antenna group consists of more than one antenna correlated with the adjacent group for data transmission with the estimation of the channel in the individual group to increase the antenna estimation accuracy. Through SPCGT, channel in every group of the antenna is estimated with consideration of another antenna group. The proposed SPCGT is based on the consideration of a similar estimation pattern for every group of the antenna in each stage. In the first stage of the proposed

Fig. 3 Spatial antenna

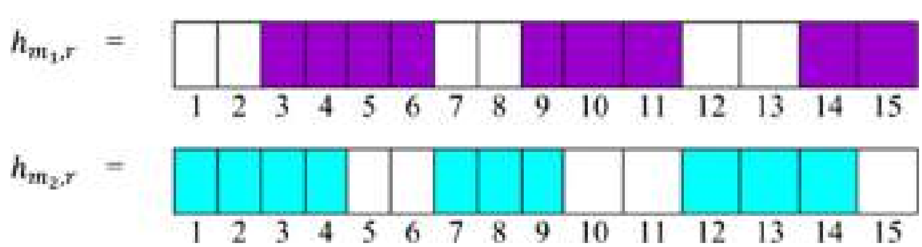

SPCGT approach channel estimation is based on the support set, sparsity level, and channel matrix. At this stage, sparsity is the level of the individual channel is measured using game theory. Using the application of game theory sparsity level of the network is estimated for the time-varying channel. The measured sparsity level provides the support set for the gamer to measure the support set for channel estimation. The channel sparsity with higher in-game is considered a member of the game and support set is utilized for sparsity adjustment between the channels in the network. After estimation of the sparsity level channel level set of the network is considered as the winner of the game, through this for sparse network channel with higher network value is considered as the winner. The steps adopted in the proposed SPCGT for pilot insertion is presented as follows:

Steps for SPCGT in the pilot insertion

Step 1: For the first group of the antenna, pilot sequence transition is estimated.

Step 2: Using, SPCGT model, channel estimation is measured for the first group of the antenna.

Step 3: Evaluation of support set for each group of the element.

Step 4: Transmission of pilot transition for kth antenna group.

Step 5: Estimate the channel in kth antenna group with consideration of channel support set.

Step 6: Estimation of channel matrix for continuous data transmission between slow and fast time-varying channels.

3.3 Spatial partitioning coalitional game theory (SPCGT)

This paper developed an SPCGT model for channel estimation with consideration of slow and fast time-varying channels for effective resource allocation with a combination of time. In this spatial partitioning of the antenna is applied for reduction of pilot overhead and channel resource estimation. The steps followed in the proposed SPCGT are presented below:

Step 1: Initially, unassigned channels are assigned for users in the network and denoted as $G_1 = \{1,2,3\ldots.8\}$, number of assigned channels are stated as CR = 0 which means $K_i = \{1,2,\ldots.6\}$

Step 2: Consider three channels with three sensing channel CR with K = 3 as stated in step 1

Step 3: After the execution of step 2, CR selects the same channel with the inclusion of coalitional game by process of merge and split rule. At this instance, CR utilizes coalitional game, and those coalitions are represented as (CR1, CR6) and (CR2, CR4, CR5) with consideration of coalition values

- Step 3.1: **Merge Rule:**Combination of coalitions$\{G1, G2, \ldots, Gl\}$ where $\{\beta_{(J=1)} = Gj\}$, therefore $\{G1G2, \ldots, Gl\} -> \beta_{(J=1)} = Gj$
- Step 3.2: **Split rule:** Spliting of coalition $\beta_{(J=1)} = Gj$ where $\{G1, G2, \ldots, Gl\}$, therefore $\beta_{(J=1)} = Gj -> \{G1G2, \ldots, Gl\}$

Step 4: Based on step 3, each channel in the cognitive network are assigned with the highest value of coalition for sensing

Step 5: After execution, of SPCGT estimated channel is assigned for data transmission based on carrier sensing

In algorithm 1, proposed SPCGT performance is presented as follows:

Algorithm1: Spatial Partitioning Coalitional Game Theory (SPCGT)

Input: QPSK channel allocation for time-varying channel

Output: Estimation and assignment of channel

Initial phase

start with a random partition αi which is represented by [s1,s2,s3…..sm]

G = The set of unassigned channels

G(i) = the total number of channels in the network

Round-1

αiselects the required channel and range will be around G-G(i) with the highest signal to noise ratio in G

Now, the game is played by the following merge and split rule,

for all α*i* € [1,2,….G] ; **do**

1. *TO_MERGE_LIST ={}*

2. α*i* looks for coalition candidates *j* for performing merge process and add them to its TO_MERGE list, each of which with its corresponding gain $G_{\{i,j\}}$

TO_MERGE_LIST = ***Examine***(α*i*)

while *TO_MERGE_LIST* is non-empty **do**

j= ***argmax***= $G_{\{i,j\}}$

α*i* sends REQ_TO_JOIN to α*j* ;

α*1*= *merge* α*2*

end while

end for

repeat until no successive merge and split operations occur

Likewise, each channel is assigned to the coalition with the highest value

Proceed with **round 2, 3 and so on** (depending upon the number of channels allocated for secondary users)

Update G and G(i) to G_{g+1} and $G_{(i+1)}$ then G_{g+2} and $G_{(i+2)}$ respectively

In Fig. 4 flow chart for estimation of the channel using SPCGT is presented.

Figure 4 revealed the flow diagram of proposed SPCG. Initialize the channel with band and time period. After the initialization of parameters OFDM signals are transmitted. If the estimated time of the particular frequency is equal to 0.9 compute band. If not time is 0.9 alters the pattern of pilot it provides correlation with the pattern. Similarly, estimate the band if it satisfies the condition that channel is allotted. Base on this channel is estimated for the framed condition.

It can observe that the NMSE performance of the proposed method for new numbers of pilot sequences is also better than that of the reference methods. The simulation results show that the proposed method estimates channels with less NMSE and BER than conventional methods, and it has a robust and stable performance

4 Results and discussion

The performance of the proposed SPCGT model is estimated for both slow and fast time-varying channels for UWB applications. The performance of the proposed SPCGT is measured with consideration of the QPSK modulation scheme in OFDM technology. As stated earlier, the proposed SPCGT is based on the consideration of sampling and carrier frequency. In Table 1, simulation parameters assigned for proposed SPCGT channel estimation is presented.

In the proposed SPCGT model, channel estimation performance is measured through consideration of 8 randomly generated paths for data transmission. The assigned channel is grouped into clusters with consideration of inter-arrival time with an exponential distribution of 0.3 ms. Also, the performance of the proposed SPCGT is assumed

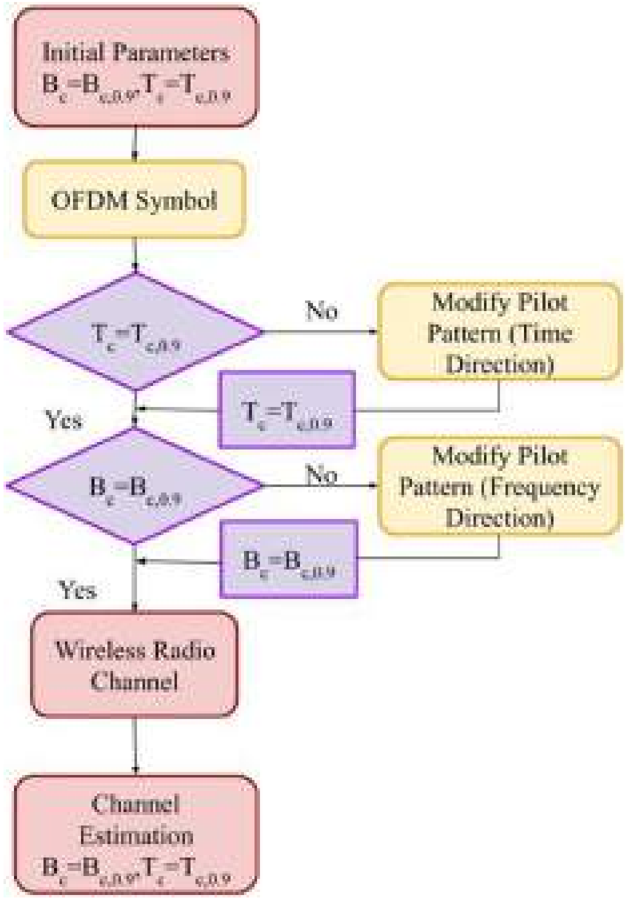

Fig. 4 Flow chart of SPCGT

to have a fixed delay sequence for the OFDM frame. The channel path is assigned as a Rayleigh distribution channel with average power that decreases exponentially due to the existence of channel delay. The data sub-carrier sequences are encoded with 1/2 non-binary with low-density parity-check (LDPC) coded with QPSK modulation. The performance of the proposed SPCGT scheme is estimated using NMSE and BER measurements.

Normalized Mean Square Error (NMSE): The channel estimation performance is measured through NMSE using Eq. (15):

$$NMSE = \frac{E\left\{|H|n - \widehat{H[n]}^2\right\}}{E\left\{|H[n]|^2\right\}} \tag{15}$$

In the above equation, the actual channel vector is denoted as H[n] and the nth vector of the estimated channel is represented as $\hat{H}$[n]. The simulation performance is comparatively examined for an existing techniques such as LS, OMP and TMSBL—2.

Bit Error Rate (BER): BER of the channel is measured estimated error rate for varying Signal to Noise ratio (SNR) level. The BER can be calculated using Eq. (16):

$$BER = \frac{N_{err}}{N_{bits}} \tag{16}$$

In the above equation, represented the total number of bits transmitted and denoted the number of error bits in the channel.

The performance of the proposed SPCGT is examined for a fast and slow time-varying channel. In the case of the slow time-varying channel, variation is delay is selected randomly between intervals [− 0.1, 0.1]ms with absolute gain interval range of [0.8,1.2] applied for consecutive blocks of OFDM scheme. In fast time-varying channel variation in delay is selected as [− 0.5, 0.5]ms with absolute gain variation is measured as [0.5,1.5] for channel cluster in consecutive blocks. Generally, SNR is defined as the variation of desire signal from the background noisy signal. In other terms, SNR is defined as the ratio of desire signal to noise. BER offer number of bits those effectively transmitted within the system. With the proposed SPCGT to calculate the channel estimation efficiency simulation is performed with SNR and BER. The analysis defines the number of bits that are error due to the presence of noise in the channel.

Table 1 Simulation parameters setting

Parameters	Values
Bandwidth	1.5 kHz
Carrier frequency	2.25 kHz
Symbol duration	171 ms
Cyclic prefix (CP) duration	10 ms
Number of the pilot sequence	200
Number of subcarriers	32
Number of null subcarriers	24
Blocks in one frame	4

Table 2 NMSE measurement for slow-varying channel

SNR/dB	LS	OMP	TMSBL-2	SPCGT
0	0.1670	0.0956	0.0345	0.0278
2	0.1570	0.089	0.0256	0.0145
4	0.1460	0.0765	0.0146	0.0096
6	0.1356	0.0677	0.00967	0.0086
8	0.1256	0.0578	0.0087	0.0075
10	0.11154	0.0457	0.0076	0.0065
12	0.0988	0.0345	0.00678	0.0056

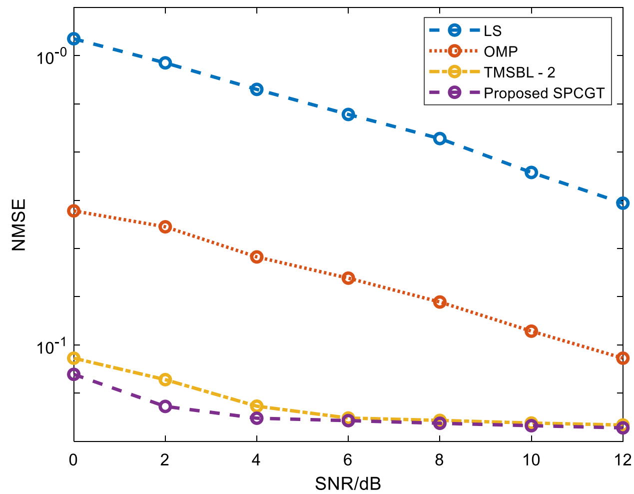

Fig. 5 Comparison of NMSE performance of slow time varying channel

Table 3 BER measurement for slow varying channel

SNR/dB	LS	OMP	TMSBL-2	SPCGT
0	0.800	0.7456	0.589	0.486
2	0.750	0.589	0.286	0.1869
4	0.65	0.375	0.168	0.0865
6	0.53	0.180	0.1276	0.0196
8	0.420	0.0685	0.0862	0.0068
10	0.240	0.0160	0.0065	0.00075
12	0.150	0.00458	0.00085	0.000246

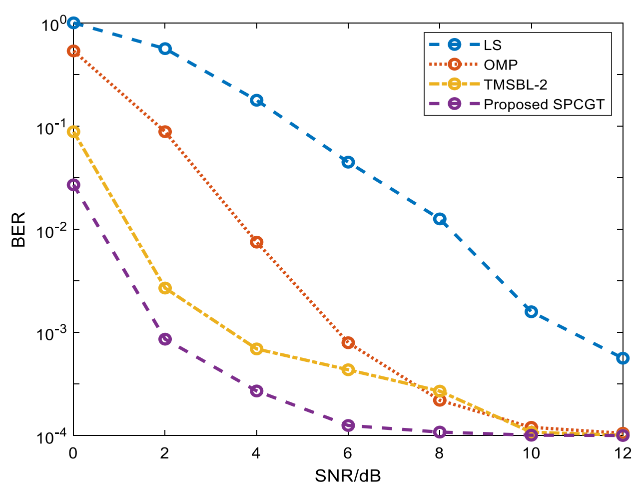

Fig. 6 Comparison of BER Performance of slow time varying channel

In performance analysis for the slow-varying channel, NMSE is comparatively examined for proposed SPCGT with existing Least Mean (LM), Orthogonal Matching pursuit (OMP), and Temporal Multiple Sparse Bayesian

Table 4 NMSE measurement for fast time varying channel

SNR/dB	LS	OMP	TMSBL-2	SPCGT
0	1.200	0.900	0.745	0.675
2	0.980	0.687	0.478	0.2455
4	0.78	0.189	0.248	0.175
6	0.57	0.0975	0.087	0.0746
8	0.246	0.0675	0.0481	0.03575
10	0.089	0.0475	0.0345	0.0248
12	0.0123	0.1276	0.012	0.0025

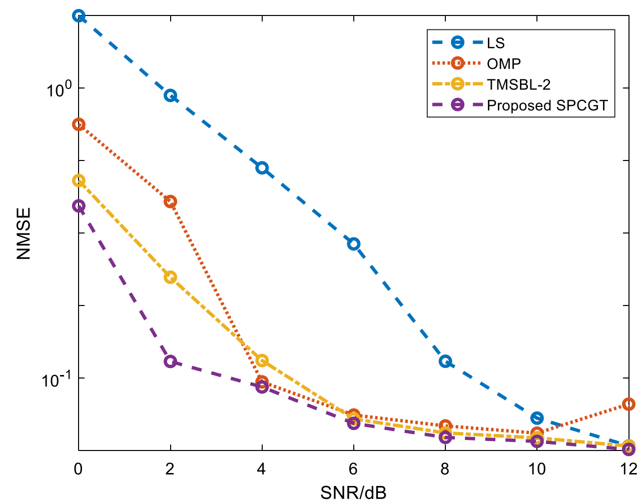

Fig. 7 Performance of NMSE for fast time varying channel

Table 5 BER measurement for fast time varying channel

SNR/dB	LS	OMP	TMSBL-2	SPCGT
0	1.50	1.400	1.186	0.9756
2	1.478	0.895	0.675	0.0756
4	1.345	0.345	0.245	0.0042
6	1.286	0.0485	0.0675	0.00242
8	1.1285	0.023	0.0175	0.00053
10	0.985	0.0068	0.0045	0.000345
12	0.894	0.0024	0.000875	0.0001

Learning (TMSBL-2) for varying SNR in dB. To measure NMSE performance for slow-varying channel SNR values are varied from 0 to 12 dB. In Table 2, NMSE measured for existing LS, OMP, and TMSBL- 2 models is presented along with proposed SPCGT.

In Fig. 5, comparative plot for slow-varying channel and measured NMSE performance was presented. For comparative analysis, existing technique LS, OMP, and TMSBL-2 for varying SNR levels are presented. In

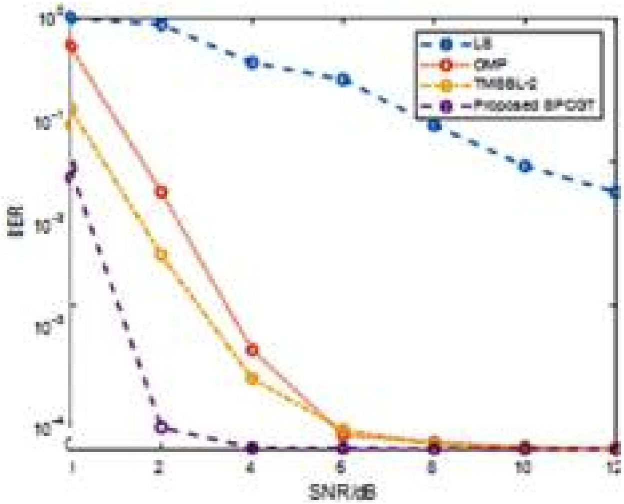

Fig. 8 Performance of BER for fast time varying channel

Table 3, the BER values measured for slow varying channel comparatively with proposed SPCGT and existing technique are tabulated.

In Fig. 6, the BER measurement of proposed SPCGT is comparatively plotted for varying SNR measurement for the slow varying channel is presented. In the next phase, the performance of the proposed SPCGT is measured for a fast time-varying channel. The 5G network relies on real-time varying application hence NMSE, and BER measure for proposed SPCGT is measured. In Table 4, the comparative measure of proposed SPCGT with an existing technique LS, OMP, and TMSBL-2 for varying SNR is presented.

In Fig. 7, NMSE measured for the fast varying channel is comparatively illustrated for LS, OMP, TMSBL-2, and proposed SPCGT.

In Table 5, BER performance for the fast time-varying system for proposed SPCGT and existing technique are presented.

In Fig. 8, The BER performance measured for the fast varying channel for varying SNR levels is comparatively examined and illustrated.

In fast time varying channel with increase in SNR level BER decreases this implies that the performance of proposed SPCGT is effective for data transmission.

5 Discussion

The proposed SPCGT is focused on improving channel estimation in MIMO-OFDM system. The proposed SPCGT performance is estimated for both slow and fast time varying channel. The performance metrics considered for analysis are BER and NMSE measurement for both slow and fast time-varying channel. NMSE analysis of proposed SPCGT with exiting techniques such as LS, OMP, and TMSBL- 2 shows that the proposed SPCGT exhibits minimal NMSE value. The performance of the proposed LS is worst rather than other techniques. In the case of OMP, its performance is significantly less than the LS. From the analysis, it is stated that for slow varying channel SPCGT provides minimal NMSE, which means channel estimation for the spatial partitioned antenna is significantly adopted. Through analysis, it can be stated that the proposed SPCGT model offers approximately 15% reduced NMSE rather than existing LS, OMP, and TMSBL -2.

The BER measurement of slow varying channels exhibited that SPCGT provides significant performance with minimal BER value. The minimal BER for proposed SPCGT causes strong temporal coherence with increased channel gain. Using spatial partitioning, based on the present channel state, game theory forecasts the future channel stat. Even with higher SNR values, channel estimation error are observed as minimal and involved in the reconstruction of received signals. This leads to satisfactory performance for the proposed SPCGT approach for channel estimation in the slow-varying channel. From the BER analysis of the slow-varying channel, it can be concluded that the proposed SPCGT provides approximately 20% reduced BER. From this, it can be concluded that the proposed SPCGT provides significant performance for slow-varying channels rather than LS, OMP, and TMSBL-2.

The analysis of NMSE for the fast time-varying channel with LM, OMP, and TMSBL-2 is presented comparatively. The analysis of LS, OMP, and TMSBL-2 stated that its performance increases drastically after the SNR of 4 dB. In proposed SPCGT the performance is significant for SNR at higher levels through effective partitioning of available antenna array element in the MIMO–OFDM system. The NMSE comparative analysis for the fast-varying channel stated that the proposed SPCGT provides approximately 30% minimal NMSE than existing LS, OMP, and TMSBL -2.

From the analysis, it is observed that NMSE and BER performance of existing LS and OMP methods are unsatisfactory for the estimation of the channel. However, TMSBL-2 performance is satisfactory rather than LS and OMP but not significant as proposed SPCGT. In the case of proposed SPCGT, NMSE and BER measurement declined drastically, with reduced channel delay. The reduced channel delay leads to increased gain in the channel. In the case of the fast-varying channel proposed SPCGT provides a reduced BER value 30% approximately than existing LS, OMP, and TMSBL-2.

6 Conclusion

MIMO-OFDM technique focused on the estimation of the time-varying channel for downlink communication. In order to achieve effective channel estimation SPCGT model is designed with integration of spatial partitioning and coalitional game theory. The performance of the proposed SPCGT is evaluated for both fast-varying and slow-varying channels. The simulation analysis of proposed SPCGT exhibited that significant for varying SNR levels in the case of both NMSE and BER. In slow-varying channel proposed SPCGT NMSE and BER rate is reduced at the rate of $\sim$ 15–20% compared with an existing techniques such as LS, OMP and TMSBL-2. Also, for fast-varying channel NMSE and BER rate is reduced $\sim$ 30% of existing technique LS, OMP and TMSBL-2. This implies that the proposed SPCGT exhibits effective channel estimation rather than other LS, OMP, and TMSBL-2. In the future, the proposed model can be applied in real-time voice call communication for improving the user experience for 5G communication.

References

1. Dai, J., Zho, L., Chang, C., & Xu, W. (2020). Robust Bayesian learning approach for massive MIMO channel estimation. *Signal Processing*. https://doi.org/10.1016/j.sigpro.2019.107345.
2. Qiao, G., Song, Q., Ma, L., Sun, Z., & Zhang, J. (2020). Channel prediction based temporal multiple sparse Bayesian learning for channel estimation in fast time-varying underwater acoustic OFDM communications. *Signal Processing*. https://doi.org/10.1016/j.sigpro.2020.107668.
3. Shalavi, N., Atashbar, M., & Feghhi, M.M. (2020). Downlink channel estimation of FDD based massive MIMO using spatial partial-common sparsity modeling. *Physical Communication*, *42*, 101138.
4. Pasangi, P., Atashbar, M., & Feghhi, M. M. (2020). Blind downlink channel estimation of multi-user multi-cell massive MIMO system in the presence of the pilot contamination. *AEU-International Journal of Electronics and Communications*. https://doi.org/10.1016/j.aeue.2020.153099.
5. Zhou, J., Yang, A., Guo, P., Zhuang, L., Guo, S., & Qiao, Y. (2020). Experimental estimation of inter-channel nonlinearity power by using differential pilot. *Optical Fiber Technology, 58,* 102256.
6. Khan, M., Das, B., & Pati, B. B. (2020). Channel estimation strategies for underwater acoustic (UWA) communication: An overview. *Journal of the Franklin Institute*, *357*, 7229–7265.
7. Ali, M. S., Li, Y., Chen, S., & Lin, F. (2020). On improved DFT-based low-complexity channel estimation algorithms for LTE-based uplink NB-IoT systems. *Computer Communications, 149,* 214–224.
8. Wu, X., Zhu, W. P., & Yan, J. (2019). Channel estimation and tracking with nested sampling for fast-moving users in millimetre-wave communication. *Digital Signal Processing, 94,* 29–37.
9. Han, J., Chepuri, S. P., & Leus, G. (2020). Joint channel and Doppler estimation for OSDM underwater acoustic communications. *Signal Processing, 170,* 107446.
10. Das, D., & Subadar, R. (2019). Performance analysis of QAM for L-MRC receiver with estimation error over independent Hoyt fading channels. *AEU-International Journal of Electronics and Communications, 107,* 15–20.
11. Fatema, N., Hua, G., Xiang, Y., Peng, D., & Natgunanathan, I. (2017). Massive MIMO linear precoding: a survey. *IEEE Systems Journal, 12*(4), 3920–3931.
12. Flordelis, J., Rusek, F., Tufvesson, F., Larsson, E. G., & Edfors, O. (2018). Massive MIMO performance—TDD versus FDD: What do measurements say? *IEEE Transactions on Wireless Communications, 17*(4), 2247–2261.
13. Shalavi, N., Atashbar, M., & Feghhi, M. M. (2020). Downlink channel estimation of FDD based massive MIMO using spatial partial-common sparsity modeling. *Physical Communication*, *42*, 101138.
14. Lu, W., Wang, Y., Wen, X., Hua, X., Peng, S., & Zhong, L. (2019). Compressive downlink channel estimation for FDD massive MIMO using weighted $ l_ p $ minimization. *IEEE Access, 7,* 86964–86978.
15. Uwaechia, A. N., Mahyuddin, N. M., Ain, M. F., Latiff, N. M. A., & Za'bah, N. F. (2019). Compressed channel estimation for massive MIMO-OFDM systems over doubly selective channels. *Physical Communication, 36,* 100771.
16. Kuai, X., Chen, L., Yuan, X., & Liu, A. (2019). Structured turbo compressed sensing for downlink massive MIMO-OFDM channel estimation. *IEEE Transactions on Wireless Communications, 18*(8), 3813–3826.
17. Chen, L., Liu, A., & Yuan, X. (2017). Structured turbo compressed sensing for massive MIMO channel estimation using a Markov prior. *IEEE Transactions on Vehicular Technology, 67*(5), 4635–4639.
18. Apelfröjd, R., Zirwas, W., & Sternad, M. (2019). Low-overhead cyclic reference signals for channel estimation in FDD massive MIMO. *IEEE Transactions on Communications, 67*(5), 3279–3291.
19. Dai, J., Liu, A., & Lau, V. K. (2018). FDD massive MIMO channel estimation with arbitrary 2D-array geometry. *IEEE Transactions on Signal Processing, 66*(10), 2584–2599.
20. Choi, J. W., Shim, B., Ding, Y., Rao, B., & Kim, D. I. (2017). Compressed sensing for wireless communications: Useful tips and tricks. *IEEE Communications Surveys & Tutorials, 19*(3), 1527–1550.
21. Zhu, F., Wu, N., & Liang, Q. (2017). Channel estimation for massive MIMO with 2-D nested array deployment. *Physical Communication, 25,* 432–437.
22. Araújo, D. C., De Almeida, A. L., Da Costa, J. P., & de Sousa, R. T. (2019). Tensor-based channel estimation for massive MIMO-OFDM systems. *IEEE Access, 7,* 42133–42147.
23. Lian, L., Liu, A., & Lau, V. K. (2019). Exploiting dynamic sparsity for downlink FDD-massive MIMO channel tracking. *IEEE Transactions on Signal Processing, 67*(8), 2007–2021.
24. Wu, S., Ni, Z., Meng, X., & Kuang, L. (2016). Block expectation propagation for downlink channel estimation in massive MIMO systems. *IEEE Communications Letters, 20*(11), 2225–2228.
25. Qiao, G., Song, Q., Ma, L., Liu, S., Sun, Z., & Gan, S. (2018). Sparse Bayesian learning for channel estimation in time-varying underwater acoustic OFDM communication. *IEEE Access, 6,* 56675–56684.
26. Yin, Y., Liu, S., Qiao, G., Yang, Y., & Yang, Y. (2015). OFDM demodulation using virtual time reversal processing in underwater acoustic communications. *Journal of Computational Acoustics, 23*(4), 1540011.

27. Zhou, Y. H., Tong, F., & Zhang, G. Q. (2017). Distributed compressed sensing estimation of underwater acoustic OFDM channel. *Applied Acoustics, 117,* 160–166.
28. Qiao, G., Song, Q., Ma, L., Sun, Z., & Zhang, J. (2020). Channel prediction based temporal multiple sparse bayesian learning for channel estimation in fast time-varying underwater acoustic OFDM communications. *Signal Processing.*, *175*, 107668. https://doi.org/10.1016/j.sigpro.2020.107668.

Publisher's Note

Mr. S. Dhanasekaran received his B.E degree in Electronics and Communication Engineering in 2008 from Sri Balaji Chockalingam Engineering College, Arani, Tamil Nadu, India. He completed his M.E in Communication Systems in 2010 from PSG College of Technology, Coimbatore, Tamil Nadu, India. He is pursuing his Ph.D in Anna University, Chennai in the area of Communication systems, MIMO, OFDM, etc., He is currently working as an Assistant Professor in the department of Electronics and Communication Engineering, Sri Eshwar College of Engineering, Coimbatore. He has around 10 years of teaching experience. He is a life time member of ISTE.

Dr. J. Ramesh received his BE degree in Electronics and Communication Engineering in 1995 from Kumaraguru College of Technology, Coimbatore Tamil Nadu, India. He completed his ME in Communication Systems in 1997 from National Institute of Technology, Trichy, Tamil Nadu, India. He completed his Ph.D in the year 2009 from Anna University, Chennai in the area of VLSI Design and Testing. His research interests include Communication system Design, Design and Testing of Mixed signal VLSI circuits and Low Power VLSI Design. He is currently working as a Professor in the department of Electronics and Communication Engineering, PSG College of Technology, Coimbatore. He has around 25 years of teaching experience. He is currently guiding 5 PhD scholars and 6 scholars have completed their Ph.D under his guidance in the area of Communication Systems, Error Control Coding, VLSI Design, Video Compression etc. He has published around 25 papers in International Journals such as Elsevier, Springer, Taylor & Francis, IET and ETRI etc, 15 International conferences and 45 National Conference proceedings. He has received 8 Best Paper awards for his various research papers. He is a life member of ISTE, SSI, and IAENG.

Received: 25 October 2019 | Revised: 17 May 2020 | Accepted: 20 January 2021

DOI: 10.1002/dac.4765

RESEARCH ARTICLE

WILEY

Certain investigations on recent advances in the design of decoding algorithms using low-density parity-check codes and its applications

Michaelraj Kingston Roberts[1] | **Saru Kumari**[2] | **Parthibaraj Anguraj**[1]

[1]Department of Electronics and Communication Engineering, Sri Eshwar College of Engineering, Coimbatore, India

[2]Department of Mathematics, Chaudhary Charan Singh University, Meerut, India

Correspondence
Michaelraj Kingston Roberts, Department of Electronics and Communication Engineering, Sri Eshwar College of Engineering, Coimbatore 641202, India.
Email: king.pane@gmail.com

Funding information
Science and Engineering Research Board, Government of India, Grant/Award Number: ECR/2016/001275

Summary

Information theory coding is an impressive and most celebrated field of research that has spawned numerous extremely important solutions to the intractable problems of secure data communications. Recent advancements in error control coding methods have seen a huge surge in using low-density parity-check (LDPC) code-based decoding algorithms to solve imperative issues related to reliable data transmission and reception. Till date, extensive research efforts have been consistently being made on LDPC codes which focus on algorithm-driven and hardware-realization-based approaches. The main intension of this research work is to provide an extensive systematic elucidation on the recent advancements in LDPC decoding algorithms. In addition, a thorough performance evaluation and analysis of several outstanding LDPC decoding techniques is presented. Finally, conclusions are drawn by summarizing the important research findings, interesting open problems, current challenges and broader perspectives for future directions of research.

KEYWORDS

computational complexity, data communication, error control coding, iterative decoding, LDPC codes

1 | INTRODUCTION

Every few years, the advancement of digital communication systems is aimed at maximizing the transmission efficiency within the limits of available bandwidth. At the same time, research efforts have been undertaken to facilitate reliable communication to the consumers by increasing the aggregate bandwidth. However, providing an error free transmission of data through a communication channel is a difficult task due to constraints such as noise, multipath effects, fading and distortions. This research issue has attracted many scientists from the diverse backgrounds whose research efforts led to the advent of several outstanding error control coding schemes. Since their redevelopment in late 1990s, low-density parity-check (LDPC) codes have inspired a large number of scientists and researchers to pursue research in the field of error control coding.[1] Over the years, owing to the continued research interest in the scientific community, LDPC codes have gained wide publicity and popularity among the researchers through their theoretical and practical significance.

1.1 | Background and motivation

The popularity of LDPC decoding algorithms arises mainly from their characteristic nature of their flexibility and linearity to satisfy low complex error correction feasibility requirements.[2] The decoding process of LDPC codes begins with the broadcasting of the soft data among the nodes (check nodes and variable nodes) which are connected through the edges of the Tanner graph.[3] Finally, this iterative process of data broadcasting is halted if the valid codeword is found or maximum iteration count is attained. The most popular algorithms for decoding LDPC codes in this category are belief propagation algorithm (BPA),[4] sum-product algorithm (SPA),[5] min-sum algorithm (MSA)[6] and its variants, namely, normalized min-sum algorithm (NMSA)[7] and offset min-sum algorithm (OMSA).[8] In literature, there exist other types of techniques for LDPC decoding such as bit flipping-based schemes which are lately gaining much attention in the research domain.[9,10]

In the last few years, soft-decision-based LDPC decoding schemes were widely preferred to minimize the probability of logic and memory errors to maintain the reliability of data communicated over noise-perturbed channel conditions. Existing research works on LDPC decoding were oriented towards reducing the overall computation complexity without affecting the decoding stability.[11] Then, gradually some improved versions of MSA were proposed using a variation of error correction factors which led to more effective outcomes in terms of computational costs and coding gain precision.[12,13] The existing studies have demonstrated the practical importance of the LDPC-based decoding algorithms and its application which is oriented towards the design and development of LDPC decoder prototype modules.[14] With recent advancements in the field of Very Large Scale Integration (VLSI) technology at its prime, many researchers have successfully demonstrated the importance of reconfigurable LDPC decoders and its applications.[15] However, the main bottleneck in decoder design arises from the need for feasibility and hardware constraints which leads to longer computation time and complications in design efforts.

Recent studies have proven that the LDPC decoding algorithms can be extended in developing several reconfigurable decoder prototype designs which can enhance the transmission reliability with minimal design efforts.[16] These decoder designs can offer flexibility both in terms of bit error rate (BER) performance and hardware cost irrespective of the nature of data transmission. More importantly, in the last decade, flurry of research progress in the context of LDPC decoding has been carried out. Notably, in recent times, many LDPC decoding schemes have been widely deployed in several applications ranging from NAND flash memory design,[17] watermarking applications[18] and satellite communication.[19] The summary of research papers (journal articles) published during the course of the last 10 years pertaining to LDPC codes is depicted in Figure 1. The database statistics shown in Figure 1 is obtained from the database of Web of Science. The overall summary of the publication count shows the growing interest among the researcher's and the evolution of LDPC codes for diverse areas of communications.

Thus, motivated by the insights and unexpected challenge faced by the researchers, an amalgamated survey of LDPC decoding algorithms is presented. This survey article strives to identify, explore and highlight the disparate work in this domain by creating a thorough overview of LDPC decoding algorithms on the basis of design principles and error correcting capabilities. Moreover, through this survey, the potential researchers will gain an insight into the basic

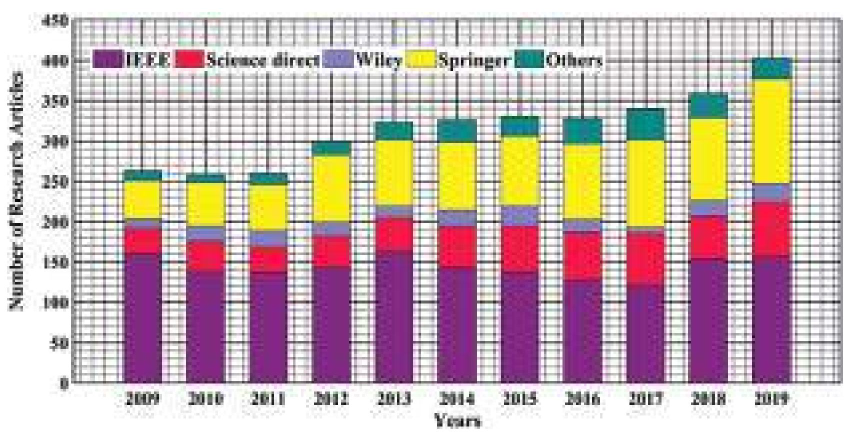

FIGURE 1 Overall journal publication count related to LDPC codes published over the years

concepts of error correcting performance and key features of various LDPC decoding algorithms which suggests possibilities for future work.

1.2 | Contributions

The overall contributions of this work are summarized as follows:

- A comprehensive review of various LDPC decoding algorithms and its key attributes which provides a useful insight about the unique technical ideas of each algorithm.
- A taxonomy and classification of LDPC decoding algorithms which emphasizes their distinctive research endeavours.
- A qualitative analysis which demonstrates the error correction capability and computational complexity of various LDPC decoding algorithms.
- A unified performance evaluation of various LDPC decoding algorithms proposing possibilities for future research.

1.3 | Organization of the paper

This survey article strives to provide a comprehensive review about the state-of-the-art LDPC decoding algorithms on the basis of working principles and error correcting capabilities. Moreover, through this survey, the potential researchers will gain an insight into the basic concepts of error correcting performance and applications of various LDPC decoding algorithms which has been widely preferred and adopted in various communication standards. Section 2 introduces the preliminaries and basic procedure of LDPC decoding. In Section 3, a basic overview of issues and challenges related to various LDPC decoding schemes is provided. Taxonomy of LDPC decoding schemes is provided in Section 4. In Section 5, a brief review of the state-of-the art BPA-based decoding schemes and features is analysed in a comprehensive manner. Section 6 presents an overview about the various features of SPA and its improvements. Important research works related to MSA-based variants and modifications are discussed briefly in Section 7. The overall performance analysis and complexity comparison of the several state-of-the-art LDPC decoding algorithms are provided in Section 8. The key findings of this survey are summarized in Section 9. Finally, Section 10 concludes the survey by discussing the research challenges and future scope of the LDPC decoding techniques. A summary of mathematical notations used in this work are provided in Table 1.

2 | PRELIMINARIES

In general, LDPC codes are represented using the Tanner graphs (bipartite graph),[3] which is the graphical representation of sparse binary parity-check matrix $\boldsymbol{H}$. A Tanner graph comprises of two fundamental nodes known as a variable node unit (VNU) or a bit node unit and check node unit (CNU) or constraint node unit. Each of these nodes are interconnected to each other through the edges of the bipartite graph $e_{(i,j)}$. The basic decoding process of LDPC code is governed by the broadcasting of the a priori message sequence among the nodes of the bipartite graph initially.[20] Then, these messages are computed based on the incoming extrinsic LLR values from the neighbouring nodes. The processed messages are broadcasted back along the edges of the corresponding nodes. This type of message passing process is carried out until the maximum iteration count is attained or until the required codeword obtained can satisfy the parity check conditions.[20] This decoding methodology is popularly known as a message passing algorithm,[21] and it is illustrated schematically in Figure 2.

2.1 | The procedure of basic LDPC decoding

The following notations describe the workflow of the iterative message passing process: For a (M,N) LDPC code, let the set of bit nodes that participate in check node c be denoted as N(c), and set of check nodes in which ν bit nodes participate be denoted as M(ν). Also N(c)\ ν and M(ν)\ c denote the set N(c) and M(ν) excluding bit node ν and check node c.

TABLE 1 A summary of mathematical notations and their meaning

Notations	Meaning
$\boldsymbol{H}$	Sparse binary parity-check matrix.
$e(i,j)$	Edges of the bipartite graph (Tanner graph).
p_n^0	Represents the probability function.
(M,N)	Representation of the parity check matrix.
M	Length of the code word.
N	Length of message sequence.
$\mathrm{N}(c)$	Denotes the set of bit nodes that are connected with the check node c.
$\mathrm{M}(v)$	Denotes the set of check nodes that are connected with the bit node ν.
$\mathrm{N}(c)\backslash v$ and $\mathrm{M}(v)\backslash c$	Denotes the set $\mathrm{N}(c)$ and $\mathrm{M}(\nu)$ excluding bit node ν and check node c.
c , m and $C_n(n = 0,1,...,N)$	Represents the check node bit and set of check nodes.
v and $V_n(n = 0,1,...,N)$	Represents the variable bit and the set of variable nodes (bit nodes).
$\hat{X} = \{\hat{\mathrm{x}}_1, ...,\hat{\mathrm{x}}_\mathrm{N}\}$	Output hard decision of the received code word.
$\Phi_\mathrm{n}, L_n^{(0)}$	The log-likelihood ratio (LLR) value generated from channel output.
y_n	Channel output information.
σ^2	Represents the variance of the channel noise.
β_{vc} , β_{ij} and $q_{nm}^{(k)}$	Outgoing a priori LLR information from bit node ν *to* check node c.
α_{cv} , α_{ij} and $r_{mn}^{(k)}$	Outgoing a priori LLR information from check node c to bit node ν.
$\beta_v^{(i)}$ and z_j	Indicates *a posteriori* high precision data computed at the each iteration.
$\alpha_{m'n}^{(i)}$	Updated information broadcasted from check node-to-bit node.
$\beta_{mn'}^{(i-1)}$	Updated information broadcasted from bit node-to-check node.
λ_n	A posteriori LLR value for each bit node v.
$\hat{\mathrm{x}}.H = 0$	Termination process of decoding algorithm.
$N(m)$ and $M(n)$	The set of n bit nodes that are connected $N(m)$ and $M(n)$ to m check nodes and the set of m check nodes that are connected to n bit nodes.
$N(m)/n$ and $M(n)/m$	The set of $N(m)$ and $M(n)$ excluding the bit node n and check node m.
$\alpha_{cv}^{(i)}$	The message broadcasted from check node m to bit node n at the ith iteration.
$\beta_{vc}^{(i)}$ and V_i	The processed data broadcasted from bit node n to check node m at the ith iteration.
$\hat{C}.H^T = 0$	Condition for obtaining a valid codeword.
$\hat{C} = \left(\hat{C}_1, \hat{C}_2......, \hat{C}_N\right)$	The set of processed information sequence.
N_1 and N_2	Error correction factors employed for error correction.
A_i	LLR value of the ith check node.
γ	Iteration level for the iterative decoding process.
$l(\gamma)$	The overall count of the processed check nodes.
$L(v_j)^i$	Updated LLR value of jth variable node after the decoding process.
$L(v_j)^{i-1}$	Updated LLR value of jth variable node after initialization.
g	Girth size (length of the shortest cycle).
$s_i(i = 0,1,...,M - 1)$	The number of length-g cycles emanating from a check node.
μ_g	The number of length-g cycles emanating through a check node.
$\bar{d}_c$	The check node degree distribution.
$\Lambda_{m\rightarrow n}(u_n)$, $L_{j\rightarrow i}^{(l)}$ and β_{ij}^{new}	Process of check node unit computational process.
$\lambda_{m\rightarrow n}(u_n)$	The process of LLR initialization.
$L(U \bigoplus V)$	The check node computation process using Maclaurin series.

TABLE 1 (Continued)

Notations	Meaning
V	The generated test error pattern.
$(-1)^{D(u)}$	The updated LLR value representation.
$m \rightarrow c$	The outgoing LLR message from c to v.
S_m	Denotes the hard decision sequence of the codeword.
S_p	The sign bit representation of the incoming message sequence.
M_p , M_1 and M_2	The magnitude bit representation of the incoming message sequence.
T_m and z	The threshold value for hard decision.
$\pm W$ and $\pm w$	The optimized integer values employed in the variable node computation process.
a_i and b_i	The representation of the estimated parameters derived in the ith iteration.
α_{ij}^{new}	The updated bit node unit computational process.
e_{ij}	The erasure bit of the iterative decoding process.
s_{ij}	The corresponding sign bit.
θ	Scaling factor for error correction.
α_1 and α_2	The magnitude of the SPA and the MSA.
α_3	The magnitude of the NMSA which is represented using the probability mass function (PMF).
ϑ	Shifting (offset) error correction factor.
ζ	The suppression factor for check node updating process..
ϑ_t	The adaptive offset error correction factor.
η	The ratio factor for error correction.
Δ	Section step size function for updating process.
t	Index value for iterative decoding process.
$\vartheta_{adaptive}$	Adaptive error correction factor.
$\xi_{d_c(m)}^{(i)}$	Optimal offset error correction factor for CNU.
$\xi_{d_v(n)}^{(i)}$	The optimal bit node offset error correction factor for VNU.
Z_V	The down scaling factor for the bit node updating process.
$S_v^{(i)}$	The received high precision soft symbol information.
O_1 and O_2	The optimized down scaling values for the bit node process.
P_T	Predetermined threshold value for iterative decoding process.

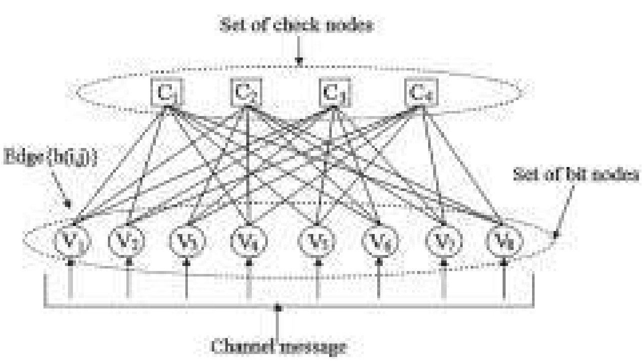

FIGURE 2 An iterative message passing process on a Tanner graph

$H_{(i,j)}$ corresponds to the entry of $\boldsymbol{H}$ at the position (i, j). The conventional iterative decoding process is based on the following steps:

Input: The *a priori* probabilities $p_n^0 = P(x_n = 0)$ and $p_n^1 = P(x_n = 1) = 1 - p_n^0$; where $n = 1, 2, ..., N$.

Output: Hard decision $\hat{X} = \{\hat{x}_1, ..., \hat{x}_N\}$.

Step 1: Initialization

During the initialization phase of the iterative message process, the check nodes receive the a priori probability from the neighbouring bit nodes.

For each bit node ν, the log-likelihood ratio (LLR) Φ_n is computed as

$$\Phi_n = \log \frac{P(p_n^0 = 0 | y_i)}{P(p_n^1 = 1 | y_i)} = \frac{2}{\sigma^2} y_i, \tag{1}$$

where, y_i denotes the channel output and σ^2 represents the variance of the channel noise.

For each $(c, \nu) \in \{(i,j) \mid H_{(i,j)} = 1\}$, the computation is carried out as

$$\beta_{\nu c} = sign(\Phi_n) \log\left(\frac{1 + e^{-|\Phi_n|}}{1 - e^{-|\Phi_n|}}\right), \tag{2}$$

where $sign(\Phi_n) = \{+1 \text{ if } \Phi_n \geq 0 \text{ and } -1 \text{ if } \Phi_n < 0\}$.

Based on the outgoing processed channel information, the bit nodes are initialized in the iterative decoding process.

Step 2: Iterative decoding process

Check node message computation process: In this step, the check nodes broadcast the a posteriori probability (extrinsic messages) to each of the neighbouring bit nodes. For each check node c and bit node ν, compute

$$\alpha_{c\nu} = \log\left|\frac{1 + e^{\beta}}{1 - e^{-\beta}}\right| \prod_{n' \in N(c) \setminus \nu} sign(\beta_{\nu c'}), \tag{3}$$

where $\beta = \sum_{n' \in N(c) \setminus \nu} |\beta_{\nu c'}|$ and $\alpha_{c\nu}^{(i)}$ is the outgoing a priori LLR information from check node c to bit node ν.

Variable node message computation process: During the course of the iterative message passing process, every bit node receives new extrinsic messages from more adjacent neighbouring nodes and fine-tunes its initial decision. For each check node c and bit node ν, compute

$$\beta_{\nu c} = sign(\Phi_{m,n}) \cdot \log\left|\frac{1 + e^{-|\Phi_{m,n}|}}{1 - e^{-|\Phi_{m,n}|}}\right|, \tag{4}$$

where $\Phi_{m,n} = \Phi_n + \sum_{m \in M(\nu) \setminus c} \alpha_{c\nu'}$ and $\beta_{\nu c}$ is the outgoing information from variable node ν to check node c.

For each bit node ν, the a posteriori LLR λ_n is updated as

$$\lambda_n = \Phi_n + \sum_{m \in M(\nu)} \alpha_{c\nu}. \tag{5}$$

Step 3: Finalization

- A hard decision updating process is performed on $\{\hat{\lambda}_1, ..., \hat{\lambda}_N\}$ to obtain $\hat{X} = \{\hat{x}_1, ..., \hat{x}_N\}$ such that $\hat{x} = 0$ if $\lambda_n > 0$ and $\hat{x} = 1$ if $\lambda_n \leq 0$ where $\hat{x}$ is the received codeword.

- The decoding process is terminated if the following condition is met $\hat{x} \cdot H = 0$; otherwise, the decoding process is again initiated from the check node computation process until the parity-check constraints are satisfied or until the maximum iteration count is reached.

The above described workflow briefly illustrates the basic decoding steps involved in the iterative message passing process.

3 | ISSUES AND CHALLENGES OF LDPC DECODING

In recent times, the error correction/detection capability of LDPC codes has been catapulted to the pinnacle of fame due to their remarkable characteristic features which led to many groundbreaking discoveries.[22] Compared to other coding schemes,[23] LDPC codes have proven the ability to facilitate reliable communication even under unreliable channel conditions.[24] However, the formulation of an LDPC decoding algorithm for the current and next generation communication standards is a challenging task. The main hurdle faced by the research community is to impart a potential in the decoding process to analyse and evaluate the large number of error patterns without increasing the computational overhead.[25] On the other hand, designing of soft-decision-based decoding algorithms which can provide both flexibility and parallelism is a trivial process.[26] Also, the most related works pertaining to LDPC decoding have emphasized the importance of convergence rate, which directly determines the outcome of the computational resource requirement. Therefore, it is absolutely necessary for minimizing the unnecessary decoding delay and time complexity issues caused by the rate of decoding convergence, which is crucial for the design and development of low-power and energy-efficient LDPC decoders.[27]

From the implementation point of view, there is a need for the development of less complex decoding algorithms which can be completely mapped on to the Instruction Set Architecture (ISA) of the programmable processors.[28] Furthermore, these hardware efficient decoding algorithms should offer sufficient parallelism such that their computational capabilities can be fully exploited. In particular, many recent studies have shown that low complex LDPC decoding schemes can minimize the critical path delay and routing congestion, which in turn can facilitate high throughput per silicon area.[29] The overall summary of the recent research issues related to the efficient design approach of LDPC decoding algorithms is shown in Figure 3.

4 | TAXONOMY OF LDPC DECODING ALGORITHMS

By analysing the recent research efforts of eminent researchers, it is conclusive that there still exists a performance gap for achieving a balance between decoding performance and implementation overhead.[30] To overcome this bottleneck situation, several research proposals were put forward by the research community.[22–24] Figure 4 depicts the taxonomy of soft-decision-based LDPC decoding algorithms. From the taxonomy illustration, LDPC codes are classified into three main categories, namely, BPA,[4] SPA[5] and MSA.[6] Many dedicated research works were proposed in the last few years to improve the quality of these standard algorithms which are employed in several applications ranging from flash memory system design, optical communications and wireless communication systems.

5 | BELIEF PROPAGATION-BASED LDPC DECODING ALGORITHMS AND ITS IMPROVEMENTS

The BPA[4] is one of the most powerful and popular form of message passing scheme. In the BPA-based scheme, the message broadcasted along the edges of the Tanner graph is construed as LLR. This decoding scheme is widely considered to be an outstanding method due to its excellent decoding stability and error rate performances. The decoding steps associated with BPA are given as $N(m)$ and $M(n)$: the set of n bit nodes that are connected to m check nodes and the set of m check nodes that are connected to n variable nodes.

$N(m)/n$ and $M(n)/m$: Denoted as the set of $N(m)$ and $M(n)$ excluding the variable node n and check node m.

$\alpha_{cv}^{(i)}$: The message broadcasted from check node m to variable node n at the ith iteration.

$\beta_{vc}^{(i)}$: The processed data broadcasted from variable node n to check node m at the ith iteration.

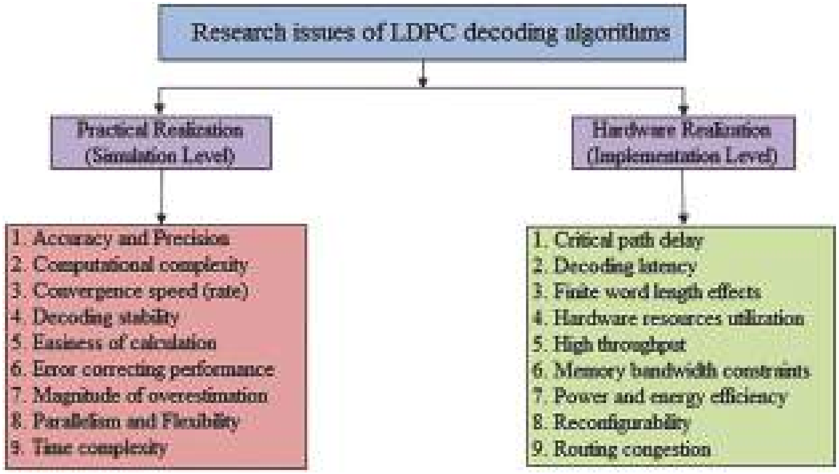

FIGURE 3 Overview and classification of important issues related to LDPC decoding

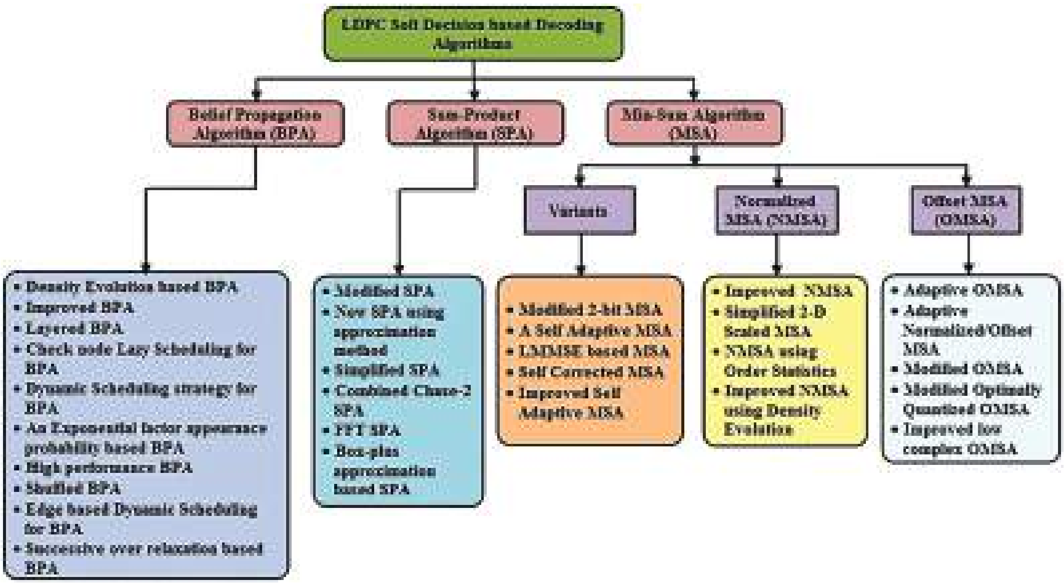

FIGURE 4 Taxonomy of LDPC decoding algorithms

$L_n^{(0)}$: The LLR value generated from channel output.

Then, the iterative message passing process of the BPA is illustrated as

Step 1: Initialization

For each iteration i,

$$L_n^{(0)} = \left(2/\sigma^2\right) \cdot y_n, \tag{6}$$

where σ^2 and y_n denote the variance and received information from the AWGN channel.

Step 2: Check (constraint) node updating process

$$\alpha_{cv}^{(i)} = \log \left[\frac{1 + \prod\limits_{n' \in N(m) \setminus n} \tanh\left(\frac{\beta_{mn'}^{i-1}}{2}\right)}{1 - \prod\limits_{n' \in N(m) \setminus n} \tanh\left(\frac{\beta_{mn'}^{i-1}}{2}\right)} \right]. \tag{7}$$

Step 3: Variable (bit) node updating process

$$\beta_{vc}^{(i)} = L_n^{(0)} + \sum_{m' \in M(n) \setminus m} \alpha_{m'n}^{(i)}, \tag{8}$$

$$\beta_{v}^{(i)} = L_n^{(0)} + \sum_{m' \in M(n)} \alpha_{m'n}^{(i)}. \tag{9}$$

Step 4: Termination process
During the decoding process is going to be terminated, whenever the valid codeword is received, that is, $\hat{C}.H^T = 0$.
Let $\hat{C} = \left(\hat{C}_1, \hat{C}_2 .... \hat{C}_N\right)$ denote the coded sequence

$$\text{where } \hat{C}_i = \begin{cases} 0, & L_i \geq 0 \\ 1, & L_i < 0 \end{cases}. \tag{10}$$

This scheme is shown to exhibit outstanding error correcting characteristics which are relatively close to Shannon's theoretical boundaries.[31] But one of the practical difficulties of this algorithm is the complexity associated with the hardware implementation which requires more computational processing units. This research problem laid the foundation to the formulation of many BPA-based decoding algorithms which can support message passing of multiple nodes concurrently without degrading the error rate performance.

5.1 | DE-based BPAs and improvements

In the early 2000s, the reference works of Chen and Fossorier reported a new stepwise approach for decoding LDPC codes.[32] This new approach induced a widespread travail, among the researchers. Inspired by these research ideologies, many novel schemes were proposed by various eminent researchers which revolutionized the design, development and practical realization of LDPC-based decoding algorithms.[33,34] The most significant contribution of this work is the concept of employing scaling and shifting correction factors to correct the channel errors. These error correction factors significantly minimized the computational overhead of the conventional BPA.[4] A research team led by Yazdani and coworkers further investigated and proposed few modifications to the BPA, and they named it as improved BPA (IBPA).[35] They reported that it is possible to minimize the error propagation in the density evolution (DE)-based BPA schemes by employing multiplicative and additive error correction factors. These new error correction factors improve the decoding performance by minimizing the overestimation issues which are often associated with the reliability of outgoing LLR information at the VNU. The improved VNU updating process of this scheme is given as

$$\beta'^{(i)}_{vc} = \beta_{vc}^{(i)} \times N_1, \tag{11}$$

$$\left(|\beta'^{(i)}_{vc}\right) = \begin{cases} \beta_{vc}^{(i)} \mid -N_2 & \beta_{vc}^{(i)} > N_2 \\ \beta_{vc}^{(i)} \mid & \beta_{vc}^{(i)} \leq N_2 \end{cases}, \tag{12}$$

where N_1 and N_2 are correction factors whose values (0.94 and 0.2) are fixed at a constant value throughout the course of the iteration process. Compared with DE-based BPA schemes,[32,33] this IBPA demonstrates improved the error correcting performance with less computational complexity.

5.2 | Reduced complexity BPA using layered decoding approach and its enhancement

The recent advancements in the field of communication systems require efficient channel coding techniques to facilitate stable transmission under extreme noisy channel conditions. An improvement to BPA algorithm using layered decoding approach was proposed by Hocevar of Texas Instruments.[36] This novel approach for BPA is proposed with an objective to achieve faster decoding convergence, which in turn facilitates a high degree of parallelism for effectual hardware realization. One of the key features of this algorithm is its flexibility and simplicity during the message passing phase which is associated with multiple nodes of the bi-partite graph. A further benefit of this layered approach is its potential to minimize the total number of hardware resources for layered message passing scheme by 50% when compared to BPA.

Zhang et al, proposed an improvement to the layered decoding approach of BPA using check-node lazy scheduling approach.[37] In this novel method, the decoding process of CNU computation involves skipping of check nodes if the reliability precision exceeds a certain threshold level. This algorithm is shown to achieve up to 30% reduction in overall iteration count required to correct the errors introduced by the noisy channel conditions. Furthermore, the decoding stability of this scheme is better than the layered BPA[36] since the unwanted check nodes are not included in the iterative decoding process. The decoding steps of this scheme are described as

$$\tanh\left(\frac{\left|\beta_{mn'}^{i-1}\right|}{2}\right) = \tanh(|A_i|), \tag{13}$$

where

$$A_i = \ln\left(\frac{P(y_i = 0)}{P(y_i = 1)}\right), \tag{14}$$

where A_i represents the LLR value of the ith check node. Using the Gaussian approximation methodology, this approach effectively minimizes the iteration levels γ. Also, $\gamma = \text{argmin}\{l(\gamma)\}$, where $l(\gamma)$ corresponds to the number of processed check nodes, which can attain same BER as that of BPA.[4] When the $(A_i > \gamma)$ condition is satisfied, the check node updating process is skipped. This in turn minimizes the time requirement for check node computation process considerably.

5.3 | Dynamic scheduling strategy-based BPA

Besides the superior error correcting performance, the conventional BPA has a slow convergence rate, which usually affects the computation time required to correct the channel errors with minimal decoding cycles. Liu et al in 2015 proposed a new dynamic scheduling strategy for belief propagation decoding.[38] This new decoding technique strives at enhancing the convergence speed by suppressing the oscillating variable nodes without introducing additional numerical instability. In this formulated approach, the variable node reliability measure is computed by re-calculating the LLR value. The LLR value of the jth variable node is re-computed as

$$L(v_j)^i \leftarrow L(v_j)^{i-1} + L(v_j)^i, \tag{15}$$

where $L(v_j)^{i-1}$ represents the LLR value of j^{th} variable node before updating and $L(v_j)^i$ represents the LLR value of j^{th} variable node after computation is updated. Through simulation results, the authors concluded that this scheme not only exhibits better convergence speed but also is shown to have excellent error correcting features.

5.4 | An exponential factor appearance probability-based BPA

Kadi et al, in 2015 investigated and reported an advanced version of BPA, which can mitigate the effects of latency based irregularities to further enhance the decoding convergence rate.[39] This version of BPA incorporates two modifications for both the CNU and VNU updating process. The first modification is carried out by re-weighting the check nodes of the Tanner graph during the message passing process. Later, the updated message broadcasted to the VNU is exploited using the exponential factor for each short cycle. The decoding steps of this scheme are initiated by calculating the short cycle or girth '**g**' in the given code $s_i(i = 0,1,. ...,M - 1)$ and followed by an iterative message passing process

$$\rho_i = \exp\left(-\frac{s_i}{k \times \mu_g}\right), \tag{16}$$

$$\alpha_{ij} = \prod_{j' \in V(i) \setminus j} sign\left(\beta'_{ij}\right) \times \phi\left(\sum_{j' \in V(i) \setminus j} \phi\left(\left|\beta'_{ij}\right|\right)\right), \tag{17}$$

$$\alpha_{ij} = \prod_{j' \in V(i) \setminus j} sign\left(\beta'_{ij}\right) \times \phi\left(\sum_{j' \in V(i) \setminus j} \phi\left(\left|\beta'_{ij}\right|\right)\right), \tag{18}$$

$$\beta_{ij} = \lambda_j + \sum_{i' \in C(j) \setminus i} \rho_{i'} \alpha_{i'j}, \tag{19}$$

$$z_j = \lambda_j + \sum_{i' \in C(j) \setminus i} \alpha_{i'j}. \tag{20}$$

This decoding scheme is experimentally proven to be compatible for both regular and irregular LDPC codes. Through simulation results, this decoding methodology is shown to outperform the dynamic scheduling-based BPA[38] in terms of convergence rate and decoding stability.

5.5 | High-performance BPA algorithm

Recently, Karimi-Lenji et al proposed an improvement to the DE-based BPA scheme using optimized error correction factors.[40] This novel decoding approach adopts both the multiplicative and additive error correction factors in the VNU computing process of the BPA algorithm. The decoding process of this methodology is given as

$$\left(\beta'^{(i)}_{vc}\right)_{k>1} = \beta^{(i)}_{vc} \times \left(\frac{\log(\mathrm{SNR})}{2\log(k)}\right)_{\bar{N}_1}, \tag{21}$$

where k is the maximum iteration count of the decoding process

$$\left(\beta'^{(i)}_{vc}\right)_{k>1} = \begin{cases} \beta^{(i)}_{vc} + \dfrac{2}{\log(\mathrm{SNR})} & \beta^{(i)}_{vc} < -2N_2 \\ \beta^{(i)}_{vc} & -2N_2 \leq \beta^{(i)}_{vc} \leq -2N_2 \\ \beta^{(i)}_{vc} - \dfrac{2}{\log(\mathrm{SNR})} & \beta^{(i)}_{vc} > -2N_2 \end{cases}, \tag{22}$$

where N_1 and N_2 indicate the error correction factor employed in the CNU computation process whose values are fixed at 0.94 and 0.2, respectively.

Also, in this algorithm formulation, the error correction factors are assumed as a constant value throughout the iterative message passing process. The experimental results show that this scheme can achieve maximum coding gain improvement of 0.6 dB when compared with the other variants of BPA.[32–35] However, the introduction of error correction factor increases the computation complexity by a modest level, which requires simple arithmetic and logical operation in the VNU updating process.

5.6 | Shuffled BPA using an information fixed scheduling method

Aslam et al[41] introduced a novel information fixed scheme for BPA-based decoding scheduling of LDPC codes. This scheme focuses on improving the convergence rate of the conventional BPA by careful selection of reliable variable nodes. These variable nodes are chosen by observing the total number of updated neighbouring nodes in the Tanner graph. Then, the processed, high-precision data are then updated in a single-decoding iteration. Thus, the error correction, speed as well as decoding convergence rate are enhanced. The CNU updating process of the BPA[4] is denoted as

$$\alpha_{cv}^{(i)} = 2\tanh^{-1}\left(\prod_{n' \in N(m)\setminus n} \tanh\left(\frac{\beta_{mn'}^{(i-1)}}{2}\right)\right). \tag{23}$$

The above equation can be modified using the difference between the message propagation achieved in the current and the previous iteration to formulate the CNU computation of the shuffled BPA

$$\alpha_{cv}^{(i)} = 2\tanh^{-1}\left(\prod_{\substack{n' \in N(m)\\ m<n}} \tanh\left(\frac{\beta_{mn'}^{(i)}}{2}\right)\right)\cdot\left(\prod_{\substack{n' \in N(m)\\ m>n}} \tanh\left(\frac{\beta_{mn'}^{(i-1)}}{2}\right)\right). \tag{24}$$

The modification incorporated in the above equation improves the convergence speed significantly. Also, this scheme when compared with BPA is shown to achieve a convergence speed improvement of 20% and 45% for both the regular and irregular LDPC codes, respectively.

5.7 | Edge-based dynamic scheduling for BPA and its improvement

In 2016, Aslam et al proposed a new BPA using e-flooding and e-shuffling schedules for decoding LDPC codes.[42] The main objective of this novel BPA is to lower the computational complexity without mitigating the convergence rate. This is accomplished by monitoring and updating only the nonconverged nodes using reliability threshold instead of updating all the nodes in the single iteration. Thus, the error correcting performance is improved to a greater extent without exhibiting the error floor behaviour.

Xie in 2018 proposed an improvement to the edge-based dynamic scheduling for BPA in his research work.[43] In this work, the author minimizes the CNU complexity overhead of the former method by introducing a new computation process to calculate the reliability threshold. The new modified threshold calculation is given as

$$p(Type-2) = \left[1-\left(\frac{e^{\Lambda}}{1+e^{\Lambda}}\right)^{\bar{d}_c}\right]\left[\frac{1}{2}-\frac{1}{2}\prod_{i=1}^{\bar{d}_c}\left(1-\frac{2e^{\Lambda}}{1+e^{\Lambda}}\right)\right], \tag{25}$$

$$p(Type-3) = \left(\frac{e^{\Lambda}}{1+e^{\Lambda}}\right)^{\bar{d}_c}\left[\frac{1}{2}-\frac{1}{2}\prod_{i=1}^{\bar{d}_c}\left(1-\frac{2e^{\Lambda}}{1+e^{\Lambda}}\right)\right], \tag{26}$$

$$p(Type-2)_{|\Lambda=\tau} = p(Type-3)_{|\Lambda=\tau}, \tag{27}$$

$$\frac{p(Type-2)}{p(Type-3)} = \gamma, \tag{28}$$

$$\tau = \ln\left(\frac{\left(\frac{1}{(1+\gamma)}\right)^{1/\bar{d}_c}}{1-\left(\frac{1}{(1+\gamma)}\right)^{1/\bar{d}_c}}\right). \tag{29}$$

From the simulation results, it is evident that the improved version not only achieves a faster rate of convergence but also exhibits outstanding decoding stability which is suited for many high speed wireless communication systems.

6 | SUM-PRODUCT-BASED DECODING ALGORITHMS FOR LDPC CODES

6.1 | Sum-product algorithm

The main drawback of BPA-based decoding schemes is the requirement of logarithmic and multiplicative computations while updating the check node computation. To overcome this drawback, Kschischang and his research team proposed a new variant of BPA, which is popularly known as the SPA.[5,44] In this novel approach, computational overhead is minimized by replacing complicated multiplications with less complex addition operations. One of the major significant improvements of SPA when compared to BPA[4] is the representation of input and output probabilities using log-domain representation. In the recent times, many advanced schemes using SPA were proposed with an objective to implementation complexity without degrading the error rate performance. The CNU updating process of the conventional SPA can be denoted as

$$\alpha_{cv}^{(i)} = 2\left(\prod_{n' \in N(m)\setminus n} sign\,(y_i)\right).\tanh^{-1}\left(\prod_{n' \in N(m)\setminus n}\left(\tanh\frac{2|y_i|}{\sigma^2}\right)\right). \tag{30}$$

However, the bit node updating process of the SPA remains the same as the BPA, the error correcting performance and computational overhead remain as a challenging task from the hardware implementation point of view.

6.2 | Modified SPA

The conventional SPA is also well known as the log-domain version of BPA. This variation of BPA has reduced computational complexity due to utilization of less complex arithmetic operations during the CNU updating process. A modified version SPA was introduced by Papaharalabos and his research team.[45] This algorithm proposes two new modifications to the hyperbolic tangent (tanh) function and its inverse function ($\tanh^{-1}$). The modified computation process is shown below

$$\tanh_{\mathrm{mod}}(x) = \begin{cases} \tanh(x), & \text{if } |x| < x_0 \\ sign(x)\tanh(x_0), & \text{if } |x| \geq x_0 \end{cases}, \tag{31}$$

$$\tanh^{-1}{}_{\mathrm{mod}}(x) = \begin{cases} \tanh^{-1}(x), & \text{if } |x| < x_0 \\ sign(x)\tanh^{-1}(x_0), & \text{if } |x| \geq x_0 \end{cases}. \tag{32}$$

Through this modified computation, a maximum coding gain improvement of 1 dB can be achieved when compared with SPA.[44] Furthermore, this algorithm is shown to minimize the decoding complexity by lowering computational overflow which occurs during the iterative message passing process.

6.3 | New SPA using an approximation method

In an attempt to achieve a good trade-off between implementation complexity and error rate performance a new SPA algorithm using an approximation method was proposed by Han and Sunwoo.[46] This decoding scheme lowers the implementation complexity by replacing multiplication and division operations with addition and subtraction operations, respectively. Furthermore, refraining from the computational use of conventional hyperbolic tangent based operations, two different quantization tables are proposed. The modifications carried out in this scheme is shown below

Step 1: LLR initialization

$$\lambda_{n\to m}(u_n)=\frac{L(u_n)}{2}. \tag{33}$$

Step 2: CNU computation process

$$\Lambda_{m\to n}(u_n)=\prod_{n'\in N(m)\setminus n} sign[\lambda_{n'\to m}(u_{n'})].\tanh^{-1}\left(\exp\left\{\sum_{n'\in N(m)\setminus n}\ln(\tanh[|\lambda_{n'\to m}(u_n)|])\right.\right), \tag{34}$$

$$\ln[\tanh(x)]=\ln\left[\frac{e^x-e^{-x}}{e^x+e^{-x}}\right], \tag{35}$$

$$\tanh^{-1}[\exp(x)]=\frac{1}{2}\ln\left[\frac{1+e^x}{1-e^x}\right]. \tag{36}$$

Through experimental results, this scheme is shown to achieve a maximum of 0.8 dB coding gain improvement with minimized complexity when compared with SPA.

6.4 | Simplified SPA for LDPC decoding

A new methodology which simplifies the check node updating complexity of the conventional SPA algorithm was introduced by Papaharalabos and Mathiopoulos in 2009.[47] The main ideology behind this decoding scheme is to introduce a new scaling factor to process the decoder's extrinsic information. The novel CNU computation process of this scheme using Maclaurin series can be expressed as

$$\begin{aligned}L\left(U\bigoplus V\right)\simeq&\operatorname{sgn}\{L(U)\}\operatorname{sgn}\{L(V)\}\min\{|L(U)|,|L(V)|\}+\\ &\max\left(0,\log 2-\frac{1}{2}|L(U)+L(V)|\right)-\max\left(0,\log 2-\frac{1}{2}|L(U)-L(V)|\right),\end{aligned} \tag{37}$$

where U and V are two statistically independent binary random variables.

The above mentioned CNU updating process can be further modified to enhance the decoding performance by employing normalized or offset correction factor. Furthermore, the authors stated that this scheme can lower implementation complexity to a greater extent since it requires only simple adder and comparator circuits instead of LUTs. The experimental results prove that the simplified SPA can achieve coding gain efficiency up to 0.2 dB when compared to computation other variants of SPA.[45,46]

6.5 | On combining chase-2 algorithm and SPA for LDPC codes

The computation of check node updating process using hyperbolic tangent function is a trivial task. Many research works oriented towards lowering the complex numerical computation were proven to perform exceptionally well for different types of LDPC codes.[45–47] One such novel SPA-based scheme was introduced by Tong and Zheng.[48] These researchers introduced a new concept of employing Test error patterns (TEPs) in the check node updating process of the conventional SPA.[44] These TEPs were adopted from the well-known chase-2 algorithm. The modified hyperbolic tangent process of this decoding scheme is given as

$$\tanh\left(\frac{m_{c\to v}}{2}\right)=\prod_{u\in N(c)\cap V}(-1)^{D(u)}\prod_{w\in N(c)\setminus V,w\neq v}\tanh\left(\frac{m_{w\to c}}{2}\right), \tag{38}$$

where V is the generated TEP and $(-1)^{D(u)}$ is the LLR value representation.

In the novel decoding process, if the SPA algorithm employed fails to output the valid codeword then instead of increasing the iteration count using SPA, the chase-2 algorithm is employed. Then, in the error correction process, the chase-2 algorithm corrects the erroneous bits using the given threshold by calculating the low-weight syndromes. Moreover, the TEPs generated by syndrome calculation perform bit-flipping to correct the erroneous bits without affecting computational complexity. Through experimental simulations, the authors demonstrated that this modified SPA has better decoding stability without exhibiting error floor characteristics. Also, through the comparison of iteration count, this novel SPA is shown to utilize minimal decoding iterations to achieve BER performance close to the conventional SPA.

6.6 | FFT-based SPA

In 2015, Roberts and Jayabalan proposed a new SPA-based decoding scheme using fast Fourier Transform (FFT).[49] In this scheme, the check node computation using the hyperbolic tangent scheme is replaced with FFT using time-shifting property. Also, the modification is carried out in the variable node updating process using optimized integer constant. The modified check node and variable node computation process are expressed as

$$r_{mn}^{(k)} = \prod_{i \in N(m) \setminus n} sign(y_i) \cdot {FFT_h}^{-1}\left(\prod_{i \in N(m) \setminus n} FFT_h\left(\frac{2|y_i|}{\sigma^2}\right)\right), \tag{39}$$

$$q_{nm}^{(k)} = q'_{nm} + \sum_{m \in M(n)} \left(1-2\left(S_m \bigoplus \widehat{C_n}\right)\right) \cdot {FFT_h}^{-1}\left(\sum_{i \in N(m) \setminus n} FFT_h\left(\frac{2|y_i|}{\sigma^2}\right)\right), \tag{40}$$

where $S_m = \sum_{n=0}^{N-1} h_{m,n} \cdot \widehat{C_n} (\text{mod}2)$, for $m = 1,2,.....,M$ and $\widehat{C_n}$ denote the hard decision of the received sequence.

$$q_n^{(k)} = q'_{nm} + \sum_{m \in M(n)} \left(1-2\left(S_m \bigoplus Z_n^{(k)}\right)\right) \cdot {FFT_h}^{-1}\left(\sum_{i \in N(m)} FFT_h\left(\frac{2|y_i|}{\sigma^2}\right)\right) \tag{41}$$

where $Z_n^{(k)} = 0$ if $q_n^{(k)} \geq 0$ and $Z_n = 1$ if $q_n^{(k)} < 0$.

The advantage of utilizing the FFT_h function is to lower the computation time required to process large number of information bits. Furthermore, by employing optimized integer constants found through heuristic simulations in the variable node updating process improves BER performance convincingly when compared with other studies.[45–47] The simulation results indicate that the overall coding gain performance achieved by this scheme is ranging from 0.04 to 0.046 dB. Furthermore, the total arithmetic operations required to correct the channel error are reduced up to 67%.

Basically, the hardware realization of SPA algorithm is a challenging task. Many researchers have tried to overcome the difficulties of the SPA algorithm by trying several modifications to the check and bit node message computation process. But still, for the advanced communication systems, the complexity associated with the computational requirement needs to be explored further to minimize the error propagation and numerical instability. Therefore, achieving a balanced trade-off between error rate performance and cost of implementation still remains as an open challenge for BPA- and SPA-based algorithms.

7 | MIN-SUM APPROXIMATION-BASED DECODING ALGORITHMS

7.1 | MSA for LDPC decoding

With the growing demand for Gbps wireless systems, increasing day-by-day, the need for hardware efficient decoding algorithms has become one of the most researched areas in the field of error control coding. From the VLSI implementation perspective, the design of low complex decoding algorithms for LDPC codes should have minimized computation complexity with acceptable decoding performance. One of the most popular decoding algorithms satisfying the constraints for the design of area and power efficient decoding architectures is known as the MSA.[6] This algorithm is formulated using the max-log approximation technique in the check node message computing process of the conventional BPA.[4] The check node computation methodology of the MSA is shown as

$$\alpha_{cv}^{(i)} = \prod_{n \in N(m) \setminus n} \operatorname{sgn}\left(\beta_{mn'}^{(i-1)}\right) \times \min_{n \in N(m) \setminus n}\left(\left|\beta_{mn'}^{(i-1)}\right|\right). \tag{42}$$

However, the variable node and hard decision message updating process is similar to that of BPA. From the hardware realization perspective, the MSA has less sensitivity for finite word length implementation, and also, the computations for iterative message passing can be carried out using only additions and multiplications. On the other hand, the only shortcoming of MSA is the decoding stability and BER performance, which is found to be very inferior compared to BPA and SPA.

7.2 | Modified 2-bit MSA

Besides the less hardware complexity, error detecting/correcting performance of MSA[6] is not suitable to meet the requirements of high data rate transmissions.[50] Therefore, to enhance the decoding stability with a faster rate of convergence, many research personnel and scientists all over the world introduced many improved versions of MSA.[50,51] In 2012, Chandrasetty and Aziz proposed a modified MSA which uses the intrinsic message quantization technique.[52] The novelty of this decoding algorithm is that it modifies both the variable node and check node computing operations to reduce the extrinsic message length in LDPC decoders. To accomplish this task, this scheme incorporates simple logical 'AND' computation logic by replacing the conventional comparator approximation operation in the CNU updating process.

$$\alpha_{cv}^{(i)} = \left(S_p \times M_p\right), \tag{43}$$

where S_p and M_p represent the sign and magnitude bit of the incoming message sequence and which is formulated by the following expressions:

$$\begin{aligned} S_p &= V_1^{(s)} \bigoplus V_2^{(s)} \bigoplus \ldots\ldots \bigoplus V_l^{(s)} \quad \forall l \neq k \\ M_p &= V_1^{(m)} \& V_2^{(m)} \& \ldots\ldots \& V_l^{(m)} \quad \forall l \neq k \end{aligned} \tag{44}$$

Also, in the VNU updating process, high-precision addition operation is utilized by eliminating scaling process. The VNU computation process is described as

$$V_i = g\left(LLR_n + \sum_{j \neq i} f(C_j)\right), \tag{45}$$

$$g(y) = \begin{cases} 01 \text{ if, } \mathrm{y} > Tm \\ 00 \text{ if, } 0 \leq y \leq Tm \\ 10 \text{ if, } 0 > x \geq -Tm \\ 01 \text{ if, } x < -Tm \end{cases}, \tag{46}$$

where T_m is the threshold

$$f(x) = \begin{cases} +W \text{ if, } x = 01 \\ +w \text{ if, } x = 00 \\ -w \text{ if, } x = 10 \\ -W \text{ if, } x = 11 \end{cases}, \tag{47}$$

where $\pm W$ and $\pm w$ indicated optimized integer values employed in the variable node computation.

Through hardware implementation and experimental simulation carried out in Xilinx Virtex 4 (XC4VLX200) FPGA, this algorithm is shown to achieve improved BER performance with minimized hardware complexity than the original MSA.[6]

7.3 | A self-adaptive termination check scheme based on MSA

A new strategy for min-sum decoding using self adaptive termination check was proposed by Cho and Chung in the year 2017.[53] The decoding technique adopted by this scheme is to minimize the interconnect complexity by compressing the intrinsic message using the difference obtained between first two minimum values. The modified check node computation process is given as

$$L_{j\to i}^{(l)} = \prod_{i' \in V_j \setminus i} \operatorname{sign}\left(L_{i'\to j}^{(l)}\right) . \min_{i' \in V_j \setminus i} \left| L_{i'\to j}^{(l)} \right|, \tag{48}$$

where $\mathrm{C2V_{message}} = \{\text{sign bits}, 1^{st}\text{minvalue}, 2^{st}\text{minvalue}, \Delta\text{min} = 1^{st}\text{minvalue} - 2^{st}\text{minvalue}\}$ Compute delta - minima using,Δmin values of $\mathrm{C2V_{message}}$if(delta - min < $\Delta\text{min}_{\text{bound}}$and l < max_iteration).

Furthermore, the VLSI implementation results show that the self-adaptive termination scheme has negligible hardware overhead with 7% increased decoding speed. Hence, this type of scheme is most suitable for advanced communication standards which require minimal power dissipation and enhanced decoding speed.

7.4 | LMMSE-based MSA

A new decoding algorithm which can improve the decoding performance of the conventional MSA significantly without increasing the hardware complexity was proposed by Wu et al in 2014.[54] This algorithm uses linear minimum mean square error (LMMSE) estimation criterion[55] to combine C2V message magnitude of both SPA and MSA, respectively. Then, this estimated parameters are determined using a popular search technique known as Golden-Section Search (GSS).[56] The decoding steps of this scheme are illustrated as

$$M_1 = \psi\left(\sum_{n \in N(m) \setminus n} \psi \left| \beta_{mn'}^{(i-1)} \right| \right), \tag{49}$$

$$M_2 = \min_{n \in N(m) \setminus n} \left(\left| \beta_{mn'}^{(i-1)} \right| \right). \tag{50}$$

Let M_1 and M_2 indicate the check to variable node message broadcasting magnitude of the BPA and MSA. Based on the parameter estimation theory, the M_1 function is derived from M_2. Let $\psi(x) = \log(e^x{+}1/e^x - 1)$, $\hat{M}_1$ denotes the estimated value of M_1, as shown below.

$$\hat{M}_1 = \max(aM_2 - b, 0), \tag{51}$$

$$\hat{M}_1 = \max(1.087a_1M_2 - 0.936b_1, 0), \tag{52}$$

where a_i and b_i represents the estimated parameters derived in the ith iteration.

Compared to other conventional decoding approach,[6,50,53] this scheme is shown to achieve coding gain improvement in the range of 0.3 to 0.5 dB with minimized computational complexity. This algorithm is implemented in Altera cyclone FPGA (EPICZ0F40017) using its intellectual property core. The implementation results show that it can save more logical and hardware resources with a moderate increase in the decoding delay.

7.5 | Self-corrected min-sum decoding algorithm

For efficient hardware implementation of LDPC decoders, memory plays a crucial role as it contributes to the overall size, power dissipation, throughput and computation times. Therefore, there is a need to minimize the overall memory accessing bits per iteration count. This in turn will enhance the convergence rate and decoding stability. In 2015, Boncalo et al introduced a new self-corrected MSA for memory trade-offs in LDPC decoders.[57] This method proposes two modified algorithms to overcome the drawbacks of memory consumption and routing complexity. The overall decoding steps of this scheme are given as follows.

Variable-node message computation process:

$$\alpha_{ij}^{new} = \left(\prod_{k \in H(i) \setminus j} s_{ik}^{new} \right) \times \min\left(\beta_{ik}^{SC}\right), \forall i \in M_L, \forall j \in H(i). \tag{53}$$

Check node message computation process:

$$\beta_{ij}^{new} = \tilde{\gamma}_i^{old} - \alpha_{ij}^{old}, \forall i \in M_L, \forall j \in H(i), \tag{54}$$

$$e_{ij}^{new} = \left(\tilde{e_{ij}^{old}}\right) . \left(s_{ij}^{new} \bigoplus s_{ij}^{old}\right), \forall i \in M_L, \forall j \in H(i), \tag{55}$$

where e_{ij} is the erasure bit and s_{ij} is the corresponding sign bit

$$\beta_{ij}^{SC} = \left(e_{ij}^{new} = 1\right) ?0 : \beta_{ij}^{new}, \forall i \in M_L, \forall j \in H(i) \tag{56}$$

where '?' is the conditional operator.

LLR message updating process:

$$\tilde{\gamma}_i^{new} = \beta_{ij}^{new} + \alpha_{ij}^{new}, \forall i \in M_L, \forall j \in H(i) \tag{57}$$

These conventional steps of this algorithm are modified in such a manner it results in two new variants. In the first variant of the algorithm, the sign bits are discharged from the check-to-variable computation process. Therefore, the requirement for storing sign bit of is eliminated. This results in the overall reduction of memory bits during the finite word length implementations.

$$sign\left(\alpha_{ij}^{old}\right) = \bigoplus s_{ik}^{old} \tag{58}$$

$$\beta_{ij}^{new} = \tilde{\gamma}_i^{old} - \alpha_{ij}^{old} \tag{59}$$

$$e_{ij}^{new} = \left(\tilde{e_{ij}^{old}}\right) . \left(s_{ij}^{new} \bigoplus s_{ij}^{old}\right) \tag{60}$$

$$\beta_{ij}^{SC} = \left(e_{ij}^{new} = 1\right) ?0 : \beta_{ij}^{new} \tag{61}$$

In the second variation of the algorithm, a novel self-correcting rule is introduced to discard the erasure bit. Hence, the hardware implementation results of this scheme indicate that up to 20% of the hardware resources are saved using this novel self-corrected min-sum.

$$sign\left(\alpha_{ij}^{old}\right) = \bigoplus s_{ik}^{old} \tag{62}$$

$$\beta_{ij}^{new} = \tilde{\gamma}_i^{old} - \alpha_{ij}^{old} \tag{63}$$

$$e_{ij}^{est} = (|\alpha_{\min 1}| = 0)?1:0 \tag{64}$$

$$e_{ij}^{new} = \left(\tilde{e_{ij}^{est}}\right) \cdot \left(s_{ij}^{new} \bigoplus s_{ij}^{old}\right) \tag{65}$$

$$\beta_{ij}^{SC} = \left(e_{ij}^{new} = 1\right)?0:\beta_{ij}^{new} \tag{66}$$

Finally, through hardware implementation, this novel self-corrected MSA is shown to consume less number of hardware resources, at the same time achieves better decoding performance due to minimized error propagation. Hence, this algorithm is very much suitable for multi-Gbps-based communication systems which require simple arithmetic optimization to minimize the critical path.

7.6 | NMSA for LDPC decoding

One of the widely adopted near-optimum min-sum-based decoding algorithm is known as scaled or NMSA.[58] This version of the MSA introduces a scaling factor θ to approximate check-to-variable (C2V) message magnitude. The general value of normalization factor is generally fixed at 0.75. The check node updating process of NMSA can be denoted as

$$\alpha_{cv}^{(i)} = \theta \times \prod_{n \in N(m) \setminus n} \operatorname{sgn}\left(\beta_{mn'}^{(i-1)}\right) \times \underbrace{\min_{n \in N(m) \setminus n}\left(\left|\beta_{mn'}^{(i-1)}\right|\right)}_{L_{v,\min}}. \tag{67}$$

This version of MSA using error correction factor not only improves the decoding stability but also minimizes the error propagation. Furthermore, this version of MSA is most widely preferred for the design of LDPC decoders suitable for various wireless standards.[59]

An improvement to conventional NMSA was proposed by Oh and Parhi.[60] In this improved version, the authors employed two normalization factors instead of a single normalization factor. The novelty of this scheme is that it employs different normalization factors separately for first minimum and second minimum messages. The decoding process for CNU update using modified scaling factor is given as

$$\theta = \begin{cases} \theta_1 \ ; \ if\ L_{v,\min} = \text{first min.message} \\ \theta_2 \ ; \ if\ L_{v,\min} = \text{second min.message} \end{cases}. \tag{68}$$

This algorithm is proven efficient when validated with both regular and irregular types of LDPC codes. For the ease of hardware implementation, the proposed scheme is implemented with finite word length using a novel non-uniform quantization scheme. The implementation results demonstrate that this methodology can reduce the memory consumption and area efficiency by 20% and 8% respectively, compared with the conventional decoder architectures.

7.6.1 | Simplified 2D-scaled MSA

Cho et al[61] proposed an improvement to the Oh and Parhi scheme.[60] This improved version involves upgrading of the scaling factor which is approximated by estimating the difference between the first minimum message and second minimum message magnitudes. The main advantage of this scheme compared to former version is that it can lower the computational complexity further by replacing multiplication operations with simple addition and shift operations. The decoding steps of this scheme are given as

$$\min_{n \in N(m) \setminus n} \left|\beta_{mn'}^{(i-1)}\right| = \left\{ \begin{array}{l} \theta_1 \times \text{min2}, \text{if index of min1} = i \\ \theta_2 \times \text{min1}, \quad \text{otherwise} \end{array} \right\}, \tag{69}$$

where $\theta_1 = 0.75$ and $\theta_2 = 0.875$.

These error correction factor values can be implemented in hardware using a combination of simple addition and shift operations as shown below

$$0.75 \times y = (y/2) + (y/4), \tag{70}$$

$$0.875 \times y = (y/2) + (y/4) + (y/8), \tag{71}$$

where $\boldsymbol{y}$ is the channel output.

The simulation results show that the proposed algorithm with two-dimensional scaling factor can outperform other MSA-based schemes,[52,5358,60] in terms of decoding performance and complexity. Most importantly, this scheme is shown to perform well for both regular and irregular LDPC codes irrespective of their code rates.

7.6.2 | NMSA using order statistics

Xue et al proposed a modified NMSA using order statistics to improve the BER performance without introducing any additional hardware overhead.[62] The novelty of this algorithm is utilization of two normalization factors concurrently without introducing any numerical instabilities for the approximation of the check node computation output. Out of the two normalization factors, the first normalization factor is employed for the first minimum position, and the second normalization factor is employed for the rest of the positions. The modified check node computation step is elaborated as

$$\alpha_{cv}^{(i)} = \begin{cases} \prod\limits_{n' \in N(m) \setminus n} \operatorname{sgn}\left(\beta_{mn'}^{(i-1)}\right) . \min\limits_{n'' \in N(m)} 1 \left|\beta_{mn''}^{(i-1)}\right| n \neq index_m \\ \prod\limits_{n' \in N(m) \setminus n} \operatorname{sgn}\left(\beta_{mn'}^{(i-1)}\right) . \min\limits_{n'' \in N(m)} 2 \left|\beta_{mn''}^{(i-1)}\right| n = index_m \end{cases} . \tag{72}$$

Then, the upgraded normalization factor is represented as

$$\alpha_1 = \frac{E(|\alpha_{21}|)}{E(|\alpha_{11}|)}, \alpha_2 = \frac{E(|\alpha_{22}|)}{E(|\alpha_{12}|)}. \tag{73}$$

If the condition $n = index_m$ is satisfied, the variables α_{21} and α_{11} are obtained from the equation Equations 72 and 30, respectively. Else $n \neq index_m$ is satisfied, the notations α_{22} and α_{12} are obtained from Equations 72 and 30, respectively.

The normalization factors employed in the check node computation process are obtained using the theory of order statistics.[63] Moreover, the implementation results of this scheme illustrate that modified normalized algorithm consumes fewer number of hardware resources while exhibiting superior error correcting performance.

7.6.3 | Improved normalized min-sum decoding algorithm using DE scheme

DE is an efficient probabilistic analysis technique[64] which is used to comprehend and realise the demarcations of LDPC decoders. In 2017, Wang et al proposed a new proposition for LDPC decoding using DE.[65] The researchers envisioned a new approach using DE theory to compute the probability density function of the C2V message updating process. In addition, a new normalization factor 'θ_i' is formulated using the weighted average of the conventional SPA and normalized MSA schemes. The following are the decoding steps associated with this scheme:

$$E|\alpha_1| = 2\sum_{n=1}^{\infty} \frac{E\left(\left(\tanh\left(L\left(q_{ij}\right)/2\right)\right)^{2n-1}\right)^{dc-1}}{2n-1}, \tag{74}$$

$$E|\alpha_2| \simeq \int_0^u \left[1 - Q\left(\frac{\mu - y}{\sigma}\right) + Q\left(\frac{\mu + y}{\sigma}\right)\right]^{dc-1} dy, \tag{75}$$

where α_1 and α_2 denote the magnitude of the SPA and the MSA, respectively. Also, d_c denotes the check node degree.

Then, by using the DE technique, the expression of NMSA can be expressed as

$$\begin{aligned} E(|\alpha_3|) &= \theta \times E\left[\min_{n \in N(m) \setminus n} \left|\beta_{mn'}^{(i-1)}\right|\right] \\ E(|\alpha_3|) &= \theta_n \times E(X) = \theta_n \times \sum_i i \times P(x = i), \end{aligned} \tag{76}$$

where α_3 denotes the magnitude of the NMSA which is represented using the probability mass function (PMF).

Finally, the new upscaled normalization factor is obtained as

$$\theta_i = \begin{cases} \frac{E(|\alpha_1|)}{E(|\alpha_2|)}, & i = 1 \\ \frac{E(|\alpha_1|)}{E(|\alpha_3|)}, & i \geq 2 \end{cases}. \tag{77}$$

This newly formulated normalized (scaling) factor utilized under different SNR conditions is shown to achieve a maximum coding gain improvement of 0.2 dB compared with NMSA. Furthermore, the hardware implementation of this scheme can save up to 24.57% of logic elements and 34.33% of memory resources when compared with LMMSE-based MSA.[54]

7.7 | OMSA for LDPC decoding and its improvement

One of the challenging tasks faced by the research community with the decoding of LDPC codes is the process of improving the inferior error-correcting performance of MSA. The research work conducted by Zhao and co-workers introduced a new concept of employing a fixed shifting (offset) correction factor ϑ for the check node updating rule of the MSA.[66] This modified approach is shown to lower error propagation and magnitude overestimation issues which in turn improve the decoding performance. The check node computation operation of OMSA can be described as

$$\alpha_{cv}^{(i)} = \prod_{n \in N(m) \setminus n} \operatorname{sgn}\left(\beta_{mn'}^{(i-1)}\right) . \max_{n \in N(m) \setminus n} \left(\min \beta \left|_{mn'}^{(i-1)}\right| - \vartheta, 0\right). \tag{78}$$

The value of offset correction factor is generally fixed at 0.15. A unique advantage of OMSA is not only the flexibility for hardware implementation but also provides a reliable error rate performance at both error floor region and cliff region. However, the conventional OMSA has its correction factor fixed throughout the decoding process. Hence, the memory consumption requirement to store the processed data during each iteration increases.

To address this issue, Xiaofu Wu et al proposed a new adaptive OMSA which uses an improved offset error correction factor.[58] In this modified version, the offset error correction factor can be adjusted according to the check node degree distribution. The CNU message updating process is given as follows:

$$\alpha_{cv}^{(i)} = \prod_{n' \in N(m) \setminus n} \operatorname{sgn}\left(\beta_{mn'}^{(i-1)}\right) . \max\left\{\min_{n' \in N(m) \setminus n} \left|\beta_{mn'}^{(i-1)}\right| - \xi, 0\right\}, \tag{79}$$

where $\xi = (1+\zeta)$. ϑ denotes the modified offset correction factor and ζ denotes the suppression factor.

This algorithm is shown to achieve excellent decoding performance without enhancing computational complexity. Furthermore, a suppression factor is employed in the check node updating process along with the offset correction factor to minimize the error propagation without introduction additional complex computational operations.

7.7.1 | Adaptive OMSA

The more efficient adjustment to the adaptive offset error correction factor was introduced by Ming Jiang et al.[67] This research work introduces a new offset error correction factor which is obtained through sectionalized normalized method. The decoding process of this algorithm is given as

$$\vartheta_t = \eta.\Delta\left[\min_{n\in N(m)\setminus n} \beta\left|_{mn'}^{(i-1)}\right|/\Delta\right], \tag{80}$$

where ϑ_t is the adaptive offset correction factor. Also, η represents the ratio factor and is formulated as ($\eta = 1 - \theta$) and Δ denotes section step size whose value is fixed at 0.8.

Compared with conventional OMSA, this decoding scheme requires an additional one left shift operation and a LUT of length 8. Then, the adaptive error correction factor is formulated as shown below

$$\vartheta_t = \frac{(1-\theta)}{2} \times t = \begin{cases} 0.1t, & t\in[1,7] \\ 0.8, & t\in[8,\infty] \end{cases}, \tag{81}$$

where index t is obtained using the expression

$$t = \left[2 \min_{n\in N(m)\setminus n} \beta\left|_{mn'}^{(i-1)}\right|\right]. \tag{82}$$

These adaptive offset correction factor values are computed and stored in a table initially before the decoding process is initiated. The simulation results indicate that this AOMSA algorithm outperforms OMSA and NMSA convincingly. However, in the bleak side, the AOMSA has a small increase in the computational complexity due to the requirement for utilizing LUTs and additional shift operations.

7.7.2 | A modified OMSA for LDPC decoding

Another modification to OMSA was proposed by Xu et al in 2010.[68] This work introduces a new modified offset correction factor which is obtained by exploiting the features of NOMSA. Through this methodology, an adaptive offset correction factor is obtained which can be iteratively adapted according to the progression of the iteration count. The decoding steps of this algorithm are described as

$$\alpha_{cv}^{(i)} = \prod_{n\in N(m)\setminus n} \operatorname{sgn}\left(\beta_{mn',MSA}^{(i-1)}\right).\max_{n\in N(m)\setminus n}\left(\min\left|\beta_{mn',MSA}^{(i-1)}\right| - \vartheta_{adaptive}, 0\right), \tag{83}$$

where $\vartheta_{adaptive}$ is the efficient error correction factor which can be computed as

$$\vartheta_{adaptive} = \alpha_{cv,MSA}^{(i)} - \alpha_{cv,MNMSA}^{(i)}. \tag{84}$$

Here, the adaptive offset error correction factor is obtained through the difference obtained between conventional MSA and MNMSA which is obtained using minimum mean square error rule. The experimental results demonstrate that this scheme can achieve superior decoding performance, which outperforming both NMSA and OMSA by 0.1 and 0.2 dB, respectively. However, the slight computational overhead is introduced in the form of additional multiplication and addition operations. Compared to AOMSA, the computational complexity introduced by this algorithm is negligible as it depends on a certain specific computation parameter which is utilized only for certain computations.

7.7.3 | The modified optimally quantized OMSA

The main research challenge associated with the performance enhancement of OMSA is the selection of error correction factor. In 2014, Roberts and Jayabalan proposed a modified optimally quantized OMSA to achieve a balanced trade-off between decoding stability and implementation complexity.[69] This algorithm has adopted a methodology of employing error correction factors to both the variable node and check node updating process which is similar to 2D-OMSA. However, unlike the former methods,[66,67,70] this error correction factor employed for both the variable node and check node computation process can adapt according to the degree distribution of both the nodes. The updated variable node and check node computation process is given as

$$\alpha_{cv}^{(i)} = \prod_{n\in N(m)\setminus n} \operatorname{sgn}\left(\beta_{mn'}^{(i-1)}\right).\max\left(\min_{n\in N(m)\setminus n}\left|\beta_{mn'}^{(i-1)}\right| - \xi_{d_c(m)}^{(i)}, 0\right), \tag{85}$$

$$\beta_{vc}^{(i)} = Z_v \cdot S_v^{(i)} + \operatorname{sgn}\left\{\sum_{m\in M(n)\setminus m} \alpha_{mn}^{(i)} - \alpha'^{(i-1)}_{mn}\right\} \cdot \max\left\{\left|\sum_{m\in M(n)\setminus m} \alpha_{mn}^{(i)} - \alpha'^{(i-1)}_{mn}\right| - \xi_{d_v(n)}^{(i)}, 0\right\}, \tag{86}$$

where $\xi_{dc(m)}^{(i)} = 0.28$ and $\gamma_{d_v(n)}^{(i)} = 0.31$ denote the check and variable node offset optimal correction factor, respectively, and Z_V represents the down scaling factor for the variable node update.

Furthermore, for efficient hardware implementations, this algorithm utilizes 6-bit non-uniform quantization scheme which can reduce up to 21.6% of the memory resources. Also, this scheme is shown to minimize the decoding iteration count in the range of 8%–14%, thus achieving a faster convergence rate.

7.8 | Other popular decoding algorithms

7.8.1 | An improved self-adaptive MSA

With the growing demand for bandwidth utilization increasing exponentially in the past few years, the need for secure data storage and processing poses a new conceptual research challenge for the scientists. During the past decade, many variations of NMSA and OMSA were put into existence by many researchers from diverse backgrounds.[61,62,64,67,68,70] These algorithms have proven their significance through their decoding stability, convergence speed and decoder design complexity. Recently, a new hybrid variation of MSA was proposed by Roberts et al, which utilizes both NMSA and OMSA recursively in accordance with the min-sum approximation rule.[71] The CNU and VNU computation process are described as follows.

Check node computation process:

$$\min_{n\in N(c)\setminus v}\left|\beta_{nc}^{(i-1)}\right| = z, \tag{87}$$

where z is the threshold utilized for the selection of appropriate approximation (normalized or offset)

$$\begin{aligned}
&(\text{If } z > P_T)\\
&\alpha_{cv}^{(i)} = \theta. \prod_{n\in N(c)\setminus v} \operatorname{sgn}\left(\beta_{nc}^{(i-1)}\right) \times \min_{n\in N(c)\setminus v}\left|\beta_{nc}^{(i-1)}\right|\\
&(\text{or})\\
&(\text{If } z < P_T)\\
&\alpha_{cv}^{(i)} = \prod_{n\in N(c)\setminus v} \operatorname{sgn}\left(\beta_{nc}^{(i-1)}\right) \times \max\left(\min_{n\in N(c)\setminus v}\left|\beta_{nc}^{(i-1)}\right| - \vartheta, 0\right).
\end{aligned} \tag{88}$$

Variable node computation process:

$$\beta_{vc}^{(i)} = L_n^{(0)} - \alpha_{m'n}^{(i-1)}, \tag{89}$$

$$\beta_{vc}^{(i,t)} = L_n^{(i)} - \alpha_{m'n}^{(i)}, \tag{90}$$

$$\operatorname{sgn}\left(\beta_{vc}^{(i,t)}\right) = = \operatorname{sgn}\left(\beta_{vc}^{(i-1)}\right), \tag{91}$$

$$\operatorname{sgn}\left(\beta_{vc}^{(i,t)}\right) \neq \operatorname{sgn}\left(\beta_{vc}^{(i-1)}\right), \tag{92}$$

$$\beta_{vc}^{(i)} = O_1\left(\beta_{vc}^{(i,t)}\right), \tag{93}$$

$$\beta_{vc}^{(i)} = O_2\left(\beta_{vc}^{(i,t)} + \beta_{vc}^{(i-1)}\right). \tag{94}$$

Moreover, in the variable node computation process, the magnitude overestimation issue and approximation errors are minimized by utilizing down scaling factors. The experimental results indicate that the self-adaptive scheme exhibits better error correcting performance with simple computation process. Furthermore, the hardware implementation results show that this algorithm requires minimal hardware resources for efficient VLSI-based LDPC decoder design.

7.8.2 | Successive overrelaxation-based BPA

Belief propagation-based decoding approaches for LDPC codes have been widely exploited in the research community for several applications related to wireless communications. Most recently, a research activity on BPA decoding was carried out independently by Saouter.[72] In this work, a new approach for BPA using successive overrelaxation has been proposed to enhance the convergence speed of the conventional BPA. In this new BPA approach, a new relaxation scheme which can interpolate between two global iterations is proposed. This in turn achieves better convergence stability with an increased convergence speed of 11.3% without enhancing hardware overhead requirements. Therefore, with acceptable coding gain and minimized computational complexity, this method was found compatible for several wireless communication standards that utilize group decoding.

7.8.3 | Box-plus approximation-based SPA

A new approach to SPA-based decoding algorithm using Box-plus operation was proposed by Papaharalabos and Lazarakis.[73] In this methodology, it was hypothesized that by using Box-plus approximation, the non-negative complexity function can be divided into simple sign and reliability operations.[74] The simplified Box-plus approximation is given as

$$g_1(x_1, x_2) = c \cdot x_1 \cdot x_2 \text{ and } |x_1|, |x_2| < \text{TH}, \tag{95}$$

where x_1 and x_2 are the incoming messages and c, respectively, and TH denotes the predefined constant values.

Moreover, this decoding method does not require any look-up tables (LUTs), instead it requires only two multiplication operations. Therefore, this methodology not only minimizes the computational complexity but also facilitates optimal performance near conventional SPA which makes it more suitable for hardware implementations.

7.8.4 | An improved low-complex OMSA

The OMSA-based decoding scheme is a popular method that has been widely preferred for efficient hardware realization of LDPC codes. One of the most challenging tasks faced by researchers in the optimal design process of OMSA is the appropriate formulation of offset error correction factor. In the literature, there exist several variants of OMSA that effectively exploits the maximization operation using DE for the formulation of optimal offset error correction factor.[67,69] Most recently, Roberts et al introduced a new offset decoding algorithm based on the concept of probability theory.[75] In this approach, a low complex offset error correction factor was obtained through simple theoretical derivation. Then, by effectively utilizing the error correction factors at various stages of decoding process adaptively, good trade-off between decoding stability and convergence rate is achieved. The low complex optimal offset error correction factor is shown below

$$\beta_k = \begin{cases} E(|L_2|) - E(|L_1|),\ k = 1 \\ E(|L_3|) - E(|L_1|),\ k \geq 2 \end{cases}, \tag{96}$$

where $L_1 = 2\tanh^{-1}\left(\prod_{i' \in R_{j \setminus i}} \tanh \frac{L(q_{i'j})}{2}\right)$; $L_2 = \prod_{i' \in R_{j \setminus i}} \mathrm{sgn}\left(L\left(q_{i'j}\right)\right) \times \min_{i' \in R_{j \setminus i}} \left(\left|L\left(q_{i'j}\right)\right|\right)$; $L_3 = \alpha \cdot |L_2|$ (or) $\frac{|L_2|}{\alpha}$.

Furthermore, this decoding process requires only few less complex arithmetic operations which in turn lower the implementation complexity issues without degrading the error rate performance.

8 | PERFORMANCE ANALYSIS OF VARIOUS LDPC DECODING ALGORITHMS

8.1 | Simulation results

In this section, experimental results are provided to illustrate the BER performance of the most popular soft-decision-based algorithms for LDPC decoding. The quantitative result summary of several state-of-the-art LDPC decoding algorithms is illustrated in Figures 5–7. The simulations are carried out in a MATLAB software with 8 GB RAM and Intel i5 core processor. For the experimental validation, the simulation scenarios adopted for this study are summarized in Table 2.

Figures 5, 6 and 7 clearly show that as the SNR increases, the error correcting performance of the various algorithms using LDPC also increases. However, the algorithms employing error correction factors are shown to exhibit better decoding stability in both error floor region and cliff region. Furthermore, the decoding algorithms utilizing multiple error correction factors in case of MSA-based schemes are shown to have better convergence speed by consuming minimal decoding iterations without introducing numerical instability.

8.2 | Analysis of computational complexity

In general, the total number of computational operations required by the check node processing step determines the overall complexity of the decoding algorithm. To compute higher precision data iteratively between the corresponding

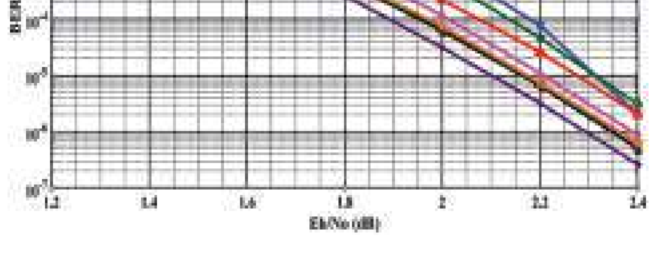

FIGURE 5 BER performance comparison and analysis of various BPA-based decoding algorithms

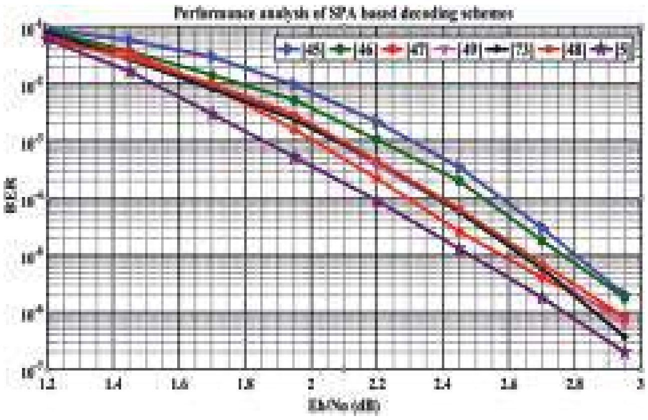

FIGURE 6 BER performance comparison and analysis of various SPA-based decoding algorithms

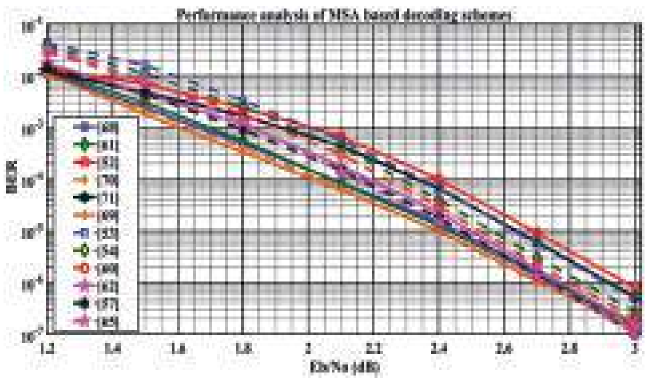

FIGURE 7 BER performance comparison and analysis of various MSA-based decoding algorithms

TABLE 2 Summary of simulation scenarios adopted for the experimental validation

S. no.	LDPC decoding algorithm	LDPC block length	Maximum decoding iteration	Channel model for transmission	Digital modulation technique
1.	BPA and its variants	(1,008, 504)	50	Additive White Gaussian Noise (AWGN)	Binary Phase Shift Keying (BPSK)
2.	SPA and its variants	(2,304, 1,152)	20		
3.	MSA and its variants		10		

Abbreviations: BPA, belief propagation algorithm; LDPC, low-density parity-check; MSA, min-sum algorithm; SPA, sum-product algorithm.

group of check nodes and bit nodes, it is highly desirable to utilize an LDPC decoding algorithm which reduces excessive complexity. To our best knowledge, there a few LDPC decoding schemes which are shown to exhibit effectual decoding performance with minimized decoder hardware complexity. The summary of the LDPC decoding algorithms which demonstrates good error correcting performances with minimal computational overhead is presented in Table 3.

9 | KEY FINDINGS

The advancements in LDPC decoding have received increased attention in the research community due to its appealing characteristics. In this paper, the important research works related to LDPC decoding approaches are carefully identified and studied. The key findings of this study are summarized as follows:

- The BPA-based decoding algorithms are widely preferred in many wireless communication standards due to its outstanding error rate performance.
- The reduction of computational complexity is a difficult and time-consuming process which requires more research efforts.

TABLE 3 The comparison of computational complexity of various LDPC decoding algorithms

Decoding algorithms	Addition	Subtraction	Multiplication	Division	Exponent	XOR	Comparison	Logarithm
Mackay[4]	$6d_c - N$	NA	0	$2d_c$	$2d_c$	$2d_c - N$	0	$2d_c$
Yazdani et al[35]	0	NA	d_c	0	0	$2d_c - N$	$2d_c$	0
Chen and Fossorier[7]	d_c	NA	0	0	0	$2d_c - N$	$3d_c$	0
Kschischang et al[5]	0	NA	$d_c - 1$	d_c	NA	NA	0	NA
Papaharalabos et al[45]	0	NA	$d_c - 1$	d_c	NA	NA	NA	NA
Han and Sunwoo[46]	$d_c - 1$	d_c	0	0	NA	NA	NA	NA
Fossorier et al[6]	0	NA	0	0	0	$2d_c - N$	$2d_c$	0
Cho et al[61]	1	1	0	0	NA	NA	$d_c+\log_2 d_c+2$	NA
Wu et al[54]	d_c	NA	d_c	0	0	$2d_c - N$	$3d_c$	0

Note. For an (M, N) LDPC code, M rows of $\boldsymbol{H}$ corresponds to the check nodes, N columns of $\boldsymbol{H}$ corresponds to bit nodes and d_c *denotes* check node degree distribution.
Abbreviation: LDPC, low-density parity-check.

- The future research direction for BPA-based schemes will be strongly oriented towards practical realization and numerical stability.
- The SPA is the log-domain version of BPA, which offers feasibility for hardware implementation.
- Exhibits faster rate of convergence and minimized error propagation for different channel conditions.
- Currently, the research efforts are oriented towards the development of low complex SPA-based variants which can offer parallelism for effectual hardware realization.
- The MSA-based decoding schemes can achieve a balanced trade-off between error rate performance and implementation complexity.
- NMSA- and OMSA-based schemes have better decoding stability and reduced control logic.
- Future research directions of MSA-based variants are focused towards the design and development of reconfigurable LDPC decoders to satisfy the transmission reach of advanced communication standards.

9.1 | Summary

In summary, the BPA-based decoding algorithms are widely preferred in many wireless communication standards due to its outstanding error rate performance. Simultaneously, a lot of research efforts have been carried out to minimize the computational complexity issues of these schemes. This research issue has inspired many scientists and academicians to contribute more by introducing different modifications to optimize BPA.[76,77]

The efficient hardware realization of SPA-based decoding algorithms is one of the most researched issues. The establishment of feasible decoder architecture and capacity approaching performance are conventionally classified into two independent issues. Indeed, it is a very complex and difficult task to develop SPA decoder architecture due to its large hardware resource requirements. The recent studies indicate a few outstanding research works regarding SPA which can achieve better decoding stability without exhibiting the inherent data dependency issues.[78] However, regarding SPA issues, there exist several gaps or limitations which still remains unexplored.[79]

In addition, this study also highlighted the evolution of MSA-based schemes over the years. In recent times, many modifications were proposed to the well-established MSA schemes and variants.[80,81] The simulation and implementation results indicate that these improved variants of MSA can achieve a balance trade-off between hardware complexity and decoding efficiency.[82,83] Furthermore, it will be an interesting task to explore the diverse extensions and abilities of these algorithms for various modulation schemes[84] and channel conditions.[85] The overall comparison of LDPC decoders for various wireless applications implemented in FPGA and ASIC technology over the years is summarized in Tables 4 and 5.

TABLE 4 Summary of FPGA-based LDPC decoders for various communication standards

	Parameters										
Reference	**Code length**	**Slices**	**Slice LUT**	**Slice register**	**Block RAM**	**Clock frequency (MHz)**	**Avg. throughput (mbps)**	**Power (mW)**	**Architecture model**	**FPGA device**	**Run time flexibility**
Zarubica et al[86]	1,200	40,613	69,038	18,945	—	100	9,100	—	Fully parallel	Virtex-4	IEEE 802.11n/16
Gunnam et al[87]	1,056, 528	46,097	68,112	44,458	—	222	470	—	Fully parallel	Virtex-4	IEEE 802.16e
Tehrani et al[88]	1,024	32,875	47,104	20,582	—	212	353	—	Fully parallel	Virtex-4	IEEE 802.3an/16
Charot et al[89]	—	20,746	33,226	32,619	75	192.4	—	—	Partially parallel	Virtex-4	IEEE 802.16
Tehrani et al[90]	2,304	6,568	11,028	6,330	100	110	61	—	Partially parallel	Virtex-2	IEEE 802.16
Ding et al[91]	—	—	19,000	10,000	92	160	10.4	—	Partially parallel	Virtex-5	IEEE 802.16
[91]	2,304	—	17,259	6,598	—	155	232.5	—	Partially parallel	Stratix-2	IEEE 802.16
Chen et al[92]	3,969	14,636	25,836	21,509	330	226.4	460	4,336	Partially parallel	Virtex-4	IEEE 802.16
Kim et al[93]	672	27,003	45,409	—	32	335	822	—	Partially parallel	Virtex-4	IEEE 802.11n
Chandrasetty and Aziz[52]	1,200, 600	33,345	58,053	15,691	—	123	10,500	—	Fully parallel	Virtex-4	DVB-S2/16
Peyic et al[94]	1,944	—	24,683	—	78	40	73.46	2,486	—	Virtex-2	IEEE 802.11n
Tao et al[95]	960	23,839	64,423	49,847	100	100	9.76	—	—	Virtex-5	IEEE 802.16
Boutillon et al[96]	192	18,758	34,846	11,712	6	61.33	2.95	—	Fully serial	Virtex-4	IEEE 802.16
Roberts and Jayabalan[97]	1,944	27,243	51,817	11,352	166	574	1,270–2,170	140.42	Partially parallel	Virtex6	IEEE 802.11n
Chandrasetty and Aziz[98]	2,304	16,803	31,305	4,066	160	82	300	16.38	Partially parallel	Virtex-4	IEEE 802.16
Chandrasetty and Aziz[98]	2,304	8,430	27,558	5,961	232	114	548	1,055	Partially parallel	Virtex-5	IEEE 802.16
Kumawat et al[99]	648, 1,944	35,105	67,204	—	—	116	308.6–1,507	451.28	Partially parallel	Virtex-4	IEEE 802.11n
Chen et al[100]	2,304	20,746	33,226	32,619	75	192.4	—	—	Partially parallel	Virtex-4	IEEE 802.16

TABLE 5 Summary of ASIC-based LDPC decoders for various communication standards

Reference no.	Parameters: Block length	Code rate	Submatrix size	# of iteration	Clock frequency (MHz)	Throughput (Gb/s)	Core area (mm^2)	Power (mW)	Technology (nm)	Decoding algorithm	Architecture model	Communication standard
Blanksby and Howland[101]	1,024	1/2	—	64	64	1.0	52.5	690	160	BPA	Fully parallel	CMMB
Urard et al[102]	2,304	8/16–14/16	64	10	125	0.640	14.3	787	180	—	Partially parallel	IEEE 802.16
Mansour and Shanbhag[103]	1,944	1/2	54	15	412	0.736	3.69	502	130	OMSA	Partially parallel	IEEE 802.11n
Karkooti et al[104]	576–2,304	1/2	96	10, 15	333	0.928	3.83	—	130	MSA	Partially parallel	IEEE 802.16
Brack et al[105]	64,800	1/4–9/10	90	50–15	400	0.060–0.708	3.861	—	65	3-MSA	Partially parallel	DVB-S2
Brack et al[105]	576–2,304	1/2–5/6	24–96	25–20	400	0.048–0.333	1.337	—	65	3-MSA	Partially parallel	IEEE 802.16
Brack et al[105]	648–1,944	1/2–5/6	27–81	25–20	400	0.054-0.281	1.023	—	65	3-MSA	Partially parallel	IEEE 802.11n
Brack et al[106]	(1,728,864)	5/6	32	20	150	0.312	—	—	130	MSPA	Partially parallel	LAN/MAN
Masera et al[107]	2,304	1/2, 2/3A, 3/4A, 2/3B, 3/4B, 5/6	24	10	100	0.068	3.4	165	180	OMSA	Partially parallel	IEEE 802.16
Gunnam et al[87]	576–2,304	2/3A	96	15	400	0.746	0.59	—	65	—	Partially parallel	IEEE 802.16e
Gentile et al[108]	2,048	1/2	—	15	300	3.3	7.3	1,416	130	MMSA	Fully parallel	IEEE 10G BASE-T
Darabiha et al[109]	648	1/2–5/6	27	11–13	240	0.410	0.74	234.6	65	LDA	Partially parallel	IEEE 802.11n
Rovini et al[110]	672	5/6	27	10	400	0.257	0.62	—	65	NMSA	Partially parallel	IEEE 802.16
Alles et al[111]	576–2,304	1/2	24, 28, 96	2–8	83.3	0.22	4.45	52	130	MSA	Partially parallel	IEEE 802.16e
Shih et al[112]	576–2,304	1/2, 2/3A, 3/4A, 2/3B, 3/4B, 5/6	24–96	20	150	0.105	6.25	264	90	MSA	Partially parallel	IEEE 802.16e
Liu et al[113]	16,200/64,800	All 15 rates	—	10	300	0.135	15.8	700	90	MSA	—	DVB-S2
Ueng et al[114]	2,304	1/2	42	4.6	200	0.106	—	—	180	MSA	Partially parallel	IEEE 802.16e
Darabiha et al[115]	660–480	0.74	—	15	300	2.44	7.3	1,383	65	MMSA	Fully parallel	IEEE 802.16
Sun and Cavallaro[116]	2,304	—	27–81/24–96	10	450	1.00	3.5	410	90	LBPA	Partially parallel	IEEE 802.11n/16e
Kuo and Willson[117]	2,304	1/2	24	10	100	0.068	3.39	—	180	OMSA	Partially parallel	IEEE 802.11n
Studer et al[118]	—	5/6	81	5	208	0.780	3.39	—	180	LOMSA	—	IEEE 802.11
Shih et al[119]	1,944	1/2	81	8	111.1	0.250	3.88	76	130	NMSA	Partially parallel	IEEE 802.11n
Liu and Shi[120]	2,048, 1,723	1/2, 2/3, 3/4, 5/6	—	16	207	5.3	14.5	—	90	SMPD	Fully parallel	IEEE 10GBASE-T
Zhang et al[121]	2,048	1/2	—	8	700	47.7	5.35	144	65	MSA	Partially parallel	IEEE 802.3an
Liu et al[122]	576–2,304	1/2, 2/3A, 3/4A, 2/3B, 3/4B, 5/6	27, 54, 81	20	300	0.212	6.22	528	90	MSA	—	IEEE 802.11n/16e
Zhang et al[123]	2,304	1/2	96	10	950	2.2	2.9	870	90	MSA	Partially parallel	IEEE 802.16
Shih et al[124]	1,536	1/2–11/12	64	2—8	125	0.086	2.46	58	130	NMSA	—	IEEE 802.11/16
Lee et al[125]	9,216	3/4	—	20	185	0.028	—	—	180	MUMP-BPA	Partially parallel	CMMB
Bao et al[126]	2,304	1/2	24–96	10	100	0.168	10.12	411	180	LDA	Partially parallel	LAN/MAN

(Continues)

TABLE 5 (Continued)

Reference no.	Parameters: Block length	Code rate	Submatrix size	# of iteration	Clock frequency (MHz)	Throughput (Gb/s)	Core area (mm^2)	Power (mW)	Technology (nm)	Decoding algorithm	Architecture model	Communication standard
Bao et al[126]	2,304	1/2–23/24	24–96	15.7	100	0.168	10.12	856	180	—	Partially parallel	IEEE 802.16/11n
Huang et al[127]	576–2,304	1/2, 2/3, 3/4	96	15	260	0.205	6.3	270	130	NMSA	Partially parallel	IEEE 802.16
Chen et al[128]	960	1/2	28	8	256.4	1.025	10.72	682	90	—	Fully parallel	—
Zhang et al[129]	2,048	0.84	64	8	700	47.7	5.35	2,800	65	OMSA	Partial parallel	IEEE 10GBASE-T
Hei and Qiao[130]	9,216	1/2–3/4	—	10	83.3	0.135	10.82	87	130	LBPA	Partially parallel	CMMB
Mohsenin et al[131]	2,048	—	—	11	195	36.3	4.84	1,359	65	TMSA	Fully parallel	IEEE 802.3an
Zhang et al[132]	9,216	1/2	256	15	431	—	4.4	115	90	MSA	Partially parallel	CMMB
Tehrani et al[133]	2,048	0.84	64	16–32	500	61.3	6.38	—	90	SLDPCD	Fully parallel	IEEE 802.3an
Xiang et al[134]	7,493	2/5, 3/5, 4/5	127	15	125	0.104	9.76	486	180	NMSA	Partially parallel	CMMB
Xiang et al[135]	576–2,304	1/2	12, 24, 76	10	214	0.874	4.84	342	130	NMSA	Partial parallel	IEEE 802.16e
Wang et al[136]	—	5/6	24–96	8–12	400	0.066–0.200	0.679	53–63.2	90	LOMSA	—	IEEE 802.16e
Zhang et al[137]	2,304	1/2	12	10	1,100	1.28	1.96	908	65	NMSA	Partially parallel	IEEE 802.16
Chen Peng et al[138]	672	1/2, 3/4, 5/8 7/8	21	10	400	6.72	1.29	537.6	65	MSA	Partially parallel	IEEE 802. 15.3c
Weiner et al[139]	672	1/2, 5/8, 3/4, 13/16	42	—	150	3.08	1.33	84	65	OMSA	Fully parallel	IEEE 802.11ad
Li et al[140]	9,216	1/2	—	10	191	0.445	6.76	173.5	130	NMSA	Partially parallel	CMMB
Naderi et al[141]	2,048–1,723	—	—	2–4	750	172.4	3.93	—	90	DSDA	Fully parallel	IEEE 802.3an
Peng et al[142]	576–2,304	1/2–5/6	76–88	10	110	1.056	3.36	115	65	LOMSA	Fully parallel	IEEE 802.16e
Peng et al[142]	2,048	0.84	64	4	137	11.69	5.35	1,559	90	LOMSA	Partially parallel	IEEE 802.3an
Chen et al[143]	672		21	10	400	6.72	1.3	537	65 LP	LNMSA	Fully parallel	IEEE 802.15.3c
Park et al[144]	672	1/2	—	10	90	1.5	1.6	38	65	MSA	Fully parallel	IEEE 802.11ad
Chen et al[145]	984	1/2–5/6	—	5	175	2.37	4.48	284.8	90	NMSA	—	IEEE 802.16 m
Chao et al[146]	648–1,944	1/2	27, 54, 81	2–8	125	0.281	1.89	135.3	90	MSA	Partially parallel	IEEE 802.11n
Yen et al[147]	672	1/2–7/8	21	5	197	5.79	1.56	361	65	LNMSA	Fully parallel	IEEE 802.15.3c
Ueng et al[148]	336–8,640	1/2, 2/3, 3/4, 5/6	27, 54, 81	8–12	400	0.348–1.952	5.53	228–517	90	SDA	Partially parallel	IEEE 802.11n
Ueng et al[148]	336-8,640	1/2, 2/3, 5/6	14–216	8–12	400	0.761–1.956	5.53	228–517	90	SDA	Partially parallel	ITU G.hn
Heidari and Jannesari[149]	2,304	1/2	32–64	10	100	0.183	6.9	–	130	NMSA	Fully Parallel	IEEE 802.16
Balatsoukas-Stimming et al[150]	672	1/2, 5/8, 3/4, 13/16	84	3	850	5.05	0.18	—	40	LOMSA	—	IEEE 802.11ad
Li et al[151]	9,216	1/2	—	15	219	0.508	5.29	142.3	130	NMSA	Dual-rate parallel	CMMB
Ajaz and Lee[152]	672	1/2, 5/8, 3/4, 13/16	42	6	215	6	1.1	89.5	65	—	Fully parallel	IEEE 802.11ad
Sun and Cavallaro[153]	9,216	1/2, 3/4	256	15	600	1.100	3.9	—	65	SMSA	Partially parallel	DVB-S2
Li et al[154]	672	1/2, 5/8, 3/4, 13/16	42	5	500	3.45	0.42	5.63	40	MSA	Row parallel	IEEE 802.11ad

TABLE 5 (Continued)

	Parameters											
Reference no.	Block length	Code rate	Submatrix size	# of iteration	Clock frequency (MHz)	Throughput (Gb/s)	Core area (mm^2)	Power (mW)	Technology (nm)	Decoding algorithm	Architecture model	Communication standard
Schläfer et al[155]	672–546	13/16	—	9	257	160.8	12.9	5,360	65	MSA	Fully parallel, unrolled	IEEE 802.11ad
Li et al[156]	—	13/16	42	3	500	5.4	0.087	57.4	28	LSPA	Partially parallel	IEEE 802.11ad
Weiner et al[157]	672	1/2	42	3.75	260	12	0.63	180	28 FD-SOI	OMSA	Row parallel	IEEE 802. 11ad
Park et al[158]	672	1/2	42	10	360	6	1.60	373.6	65	OMSA	Row parallel	IEEE 802. 11ad
Angarita et al[159]	2,048–1,723	1/2, 3/4, 7/8	—	—	226	12.8	3.84	1,040	90	RCMSA	Fully parallel	IEEE 802.3an
Roberts and Jayabalan[97]	1,944	1/2–5/6	81	10	587	1.27–2.17	1.42	140.42	130	NMSA	Partially parallel	IEEE 802. 11n
Ajaz and Lee[160]	672	1/2	—	7	400	9.25	0.58	272.9	65	MSA	Multi-mode	IEEE 802. 11ad
Chen et al[161]	—	1/2, 2/3, 3/4, 4/5	42	—	180	0.3	3.55	138, 162, 188.4, 200.4	130	NMSA	—	IEEE 1901
Yu et al[162]	1,944	1/2, 2/3, 3/4, 5/6	—	1–7	250	0.67	3.67	171	90	MSA	Partially parallel	IEEE 802.11n
Cheng et al[163]	2,048–1,723	—	—	11	195	92.8	4.84	62	90	TMSA	Fully parallel	IEEE 10G BASE-T
Zhao et al[50]	96,000	1/2, 2/3, 3/4	—	10	100	3.048	9.73	502	90	HNMS	—	—
Lee et al[164]	672	1/2–7/8	—	10	768	7.92	2.67	437.2	90	SLDPCD	Fully parallel	IEEE 802. 15.3c
Zhang et al[165]	576–2,304	5/6	24–26	10	290	2.227	2.26	146	40	MSA	Fully parallel	IEEE 802.16
Motozuka et al[166]	672	13/16	42	7	220	6.16	0.8	203	40 LP	MSA	Column-parallel	IEEE 802.11ad
Urard et al[102]	648, 1,296, 1,944	1/2	24	10	336	5.13	5.19	451	90	OMSA	Partially parallel	IEEE 802.11n
Li et al[167]	672	1/2	42	2	470	18.4	0.78	166	28	MSA	Partially parallel	IEEE 802.11ad
Kanchetla et al[168]	576–2,304	1/2	54	5	149	0.955	11.42	—	90	MSA	Fully parallel	IEEE 802.16
Li et al[169]	672	1/2, 3/4, 5/8, 7/8	21	5	157	5.28	2.25	182	90	NMSA	—	IEEE 802.15.3c
Tsatsaragkos and Paliouras[170]	1,296, 648	1/2	27, 54, 81.	10	555	4.5	4.88	523	90	MMSA	Fully parallel	IEEE 802.11n
Ghanaatian et al[171]	2,048–1,723	—	—	5	662	271	23.3	12,248	28 FD-SOI	OMSA	Fully parallel	IEEE 802.3an
Nguyen-Ly et al[30]	2,304	1/2	96	20	192	1.835	0.8	—	65	MSA	Fully parallel	IEEE 802.16
Millicevic and Gulak[83]	672	1/2	42	10	202	6.78	1.99	279	28	MSA	Partial parallel	IEEE 802.11ad
Millicevic and Gulak[83]	672	13/16	42	10	202	6.78	1.99	104	28	MSA	Partial parallel	IEEE 802.11ad
Nguyen and Lee[172]	672	1/2, 5/8, 3/4, 13/16	42	5	720	11.80	0.168	182	40	Split-row layered	Partially parallel	IEEE 802.11ad
Lee and Sunwoo[81]	672	1/2, 5/8, 3/4, 13/16	32	5	256	7.16	0.63	—	65	Layered	Partial parallel	IEEE 802.11ad
Lopez et al[173]	—	1/2, 3/4	—	5	312.5	10.5	0.14	81	28	Approximate MSA	Partial parallel	IEEE 802.11ad

10 | CONCLUSION AND FUTURE WORK

This paper provides a comprehensive review about the basic principles of LDPC decoding and their performance analysis. The overall classification of the existing soft-decision-based decoding schemes and their computational complexity evaluation is done in a concise manner. From the overall study, it can be observed that the computational overhead, decoding stability, hardware complexity and convergence speed still requires more study and experimental evaluation. To overcome these adverse issues, many eminent researchers have proposed significant decoding schemes using LDPC codes. The majority of these available techniques have proven their effectiveness in achieving better decoding stability with minimal complexity. From this proposed extensive study, it is evident that the conventional design techniques can be integrated with different methodologies such as optimization and statistics to improve the overall performance. To the best of our knowledge, several issues in the LDPC decoding such as magnitude overestimation, numerical instability and convergence speed remain unexplored. These issues can be exploited though detailed study and experimental evaluation which would be suitable for many advanced communication systems and applications.

CONFLICT OF INTEREST

The author's explicitly declare that there is no conflict of interest pertaining to this manuscript. The consent of all authors has been obtained before submission of this manuscript to this journal.

ACKNOWLEDGMENT

This research work is funded by the Department of Science and Technology, Government of India through Early Career Research Award (Young Scientist) scheme of Science and Engineering Research Board (SERB) (Grant ECR/2016/001275).

DATA AVAILABILITY STATEMENT

Data sharing not applicable—no new data generated.

ORCID

Michaelraj Kingston Roberts https://orcid.org/0000-0002-1484-703X
Saru Kumari https://orcid.org/0000-0003-4929-5383

REFERENCES

1. Gallager RG. Low-density parity-check codes. *IEEE Trans Inf Theory*. 1962;8(1):21-28.
2. Richardson TJ, Urbanke RL. The Renaissance of Gallager's low-density parity-check codes. *IEEE Commun Mag*. 2003;41(8):126-131.
3. Hu X-Y, Eleftheriou E, Arnold D-M. Regular and irregular progressive edge growth tanner graphs. *IEEE Trans Inf Theory*. 2005;51(1): 386-398.
4. Mackay DJC. Good error correcting codes based on very sparse matrices. *IEEE Trans Inf Theory*. 1999;45(2):399-431.
5. Kschischang FR, Frey BJ, Loeliger HJ. Factor graphs and sum-product algorithm. *IEEE Trans Inf Theory*. 2001;47(2):498-519.
6. Fossorier MPC, Mihaljevic M, Imai H. Reduced complexity iterative decoding of low-density parity check codes based on belief propagation. *IEEE Transactions on Communications*. 1999;47(5):673-680.
7. Chen J, Fossorier M. Near optimum universal belief propagation based decoding of low-density parity check codes. *IEEE Transactions on Communications*. 2002;50(3):406-414.
8. Zhao J, Zarkeshvari F, Banihashemi AH. On implementation of min-sum algorithm and its modifications for decoding low-density parity-check (LDPC) codes. *IEEE Transactions on Communications*. 2005;53(4):549-554.
9. Cui H, Lin J, Wang Z. An improved gradient descent bit-flipping decoder for LDPC codes. *EEE Trans Circuits Syst I Regul Pap*. 2019;66 (8):3188-3200.
10. Chen Y, Cui H, Lin J, Wang Z. Fine-grained bit-flipping decoding for LDPC codes. *IEEE Trans Circuits Syst*. 2020;67(5):896-900.
11. Fang Y, Chen P, Cai G, Lau FC, Liew SC, Han G. Outage-limit-approaching channel coding for future wireless communications: root-protograph low-density parity-check codes. *IEEE Veh Technol Mag*. 2019;14(2):85-93.
12. Yun I-W, Lee H-R, Kim JT. An alternative approach obtaining a normalization factor in normalized min-sum algorithm for low-density parity-check code. *Wirel Commun Mob Comput*. 2018;2018(11):1-7.
13. Jung Y, Jung Y, Lee S, Kim J. New min-sum LDPC decoding algorithm using SNR-considered adaptive scaling factors. *ETRI J*. 2014;36 (4):591-598.
14. Fang Y, Bi G, Guan YL, Lau FCM. A survey on protograph LDPC codes and their applications. *IEEE Commun Surv Tutor*. 2015;17(4): 1989-2016.
15. Shih X-Y, Chou H-R. Flexible design and implementation of QC-based LDPC decoder architecture for on-line user-defined matrix downloading and efficient decoding. *Dermatol Int*. 2019;64(1):40-49.

16. Debbabi B, Le Gal N, Khouja FT, Jego C. Multicore and manycore implementations of ADMM-based decoders for LDPC decoding. *J Signal Process Syst*. 2018;90(11):1551-1567.
17. Nakamura T, Deguchi Y, Takeuchi K. Adaptive artificial neural network-coupled LDPC ECC as universal solution for 3-D and 2-D, charge-trap and floating-gate NAND flash memories. *IEEE J Solid-State Circuits*. 2019;54(3):745-754.
18. Zhang W, Li C, Zhang X, Xi L, Tang X, He W. A good performance watermarking LDPC code used in high speed optical fiber communication system. *Opt Commun*. 2015;346(13):99-105.
19. Chen S, Peng K, Song J, Zhang Y. Performance analysis of practical QC-LDPC codes: from DVB-S2 to ATSC30. *IEEE Trans Broadcast*. 2019;65(1):172-178.
20. Bao J, Jiang B, Liu C. Optimized construction of protograph G-LDPC codes by modified EXIT chart and MACE for new generation wireless communications. *IEEE Access*. 2018;6(1):58139-58153.
21. Richardson TJ, Urbanke RL. The capacity of low-density parity-check codes under message-passing decoding. *IEEE Trans Inf Theory*. 2001;47(2):599-618.
22. Hashemi Y, Banihashemi AH. Characterization of elementary trapping sets in irregular LDPC codes and the corresponding efficient exhaustive search algorithms. *IEEE Trans Inf Theory*. 2018;64(5):3411-3430.
23. Zhang X, Chen S, Liu Y. Irregular LDPC-polar concatenation scheme with designed scaling factors. *Electron Lett*. 2019;55(1):57-59.
24. Bocharova IE, Kudryashov BD, Skachek V, Yakimenka Y. BP-LED decoding algorithm for LDPC codes over AWGN channels. *IEEE Trans Inf Theory*. 2019;65(3):1677-1693.
25. Boncalo O, Kolumban-Antal G, Declercq D, Savin V. Code-design for efficient pipelined layered LDPC decoders with bank memory organization. *Microprocess Microsyst*. 2018;63(8):216-225.
26. Roberts MK. Simulation and implementation design of multi-mode decoder for WiMAX and WLAN applications. *Measurement*. 2019; 131(1):28-34.
27. Català-Pérez JM, Lacruz JO, García-Herrero F, Valls J, Declercq D. Second minimum approximation for min-sum decoders suitable for high-rate LDPC codes. *Circuits, Syst Signal Process*. 2019;38(11):5068-5080.
28. Wang Z, Cui Z, Sha J. VLSI design for low-density parity-check code decoding. *IEEE Circuits Syst Mag*. 2011;11(1):52-69.
29. Lin C-H, Wu Y-S, Song C-P. Energy-efficient LDPC codec design using cost-effective early termination scheme. *IET Comput Digit Tech*. 2019;13(2):118-125.
30. Nguyen-Ly TT, Savin V, Le K, Declercq D, Ghaffari F, Boncalo O. Analysis and design of cost-effective high-throughput LDPC decoders. *IEEE Trans Very Large Scale Integr VLSI Syst*. 2018;26(3):508-521.
31. Eroz M, Sun FW, Lee LN. An innovative low-density parity-check code design with near-Shannon-limit performance and simple implementation. *IEEE Transactions on Communications*. 2006;54(1):13-17.
32. Chen J, Fossorier M. Density evolution for two improved BP-based decoding algorithms of LDPC codes. *EEE Commun Lett*. 2002;6(5): 208-210.
33. Yang Z, Fang Y, Zhang G, Lau FC, Mumtaz S, Da Costa. Analysis and optimization of tail-biting spatially coupled protograph LDPC codes for BICM-ID systems. *IEEE Trans Veh Technol*. 2019;69(1):390-404.
34. MacKay DJC, Neal RM. Near Shannon limit performance of low density parity check codes. *Electron Lett*. 1996;32(18):1645–1646.
35. Yazdani MR, Hemati S, Banihashemi AH. Improving belief propagation on graphs with cycles. *EEE Commun Lett*. 2004;8(1):57-59.
36. Hocevar DE. "A reduced complexity decoder architecture via layered decoding of LDPC codes," in Signal Processing Systems, 2004. SIPS 2004. IEEE Workshop on, 2004, pp. 107–112.2004.
37. Zhang J, Lei Y, Jin Y. Check-node lazy scheduling approach for layered belief propagation decoding algorithm. *Electron Lett*. 2014;50 (4):278-279.
38. Liu X, Zhang Y, Cui R. Variable-node-based dynamic scheduling strategy for belief-propagation decoding of LDPC codes. *EEE Commun Lett*. 2015;19(2):147-150.
39. Kadi A, Najah S, Mrabti M. An exponential factor appearance probability belief propagation algorithm for regular and irregular LDPC codes. *AEU-Int J Electron C*. 2015;69(6):933-936.
40. Karimi-Lenji MH, Zarmehi F. A high-performance belief propagation decoding algorithm for codes with short cycles. *Int J Commun Syst*. 2017;30(13):1-8.
41. Aslam A, Guan YL, Cai K, Han G. Informed fixed scheduling for faster convergence of shuffled belief-propagation decoding. *EEE Commun Lett*. 2017;21(1):32-35.
42. Aslam A, Guan YL, Cai K. Edge-based dynamic scheduling for belief-propagation decoding of LDPC and RS codes. *IEEE Transactions on Communications*. 2017;65(2):525-535.
43. Xie Q. Comments on 'edge-based dynamic scheduling for belief-propagation decoding of LDPC codes. *IEEE Transactions on Communications*. 2018;66(8):3707-3708.
44. Vatta F, Soranzo A, Babich F. More accurate analysis of sum-product decoding of LDPC codes using a Gaussian approximation. *EEE Commun Lett*. 2019;23(2):230-233.
45. Papaharalabos S, Sweeney P, Evans BG, et al. Modified sum-product algorithms for decoding low-density parity-check codes. *IET Commun*. 2007;1(3):294-300.
46. Han JH, Sunwoo MH. "New sum-product algorithm using approximation method for low complexity LDPC decoding," in 2008 International SoC Design Conference, Busan, Korea (South), pp. II-29–II-32, 2008.

47. Papaharalabos S, Mathiopoulos PT. Simplified sum-product algorithm for decoding LDPC codes with optimal performance. *Electron Lett*. 2009;45(2):116-117.
48. Tong S, Zheng H. On Combining Chase-2 and Sum-Product Algorithms for LDPC Codes. *ETRI J*. 2012;34(4):629-632.
49. Roberts MK, Jayabalan R. An improved low-complexity sum-product decoding algorithm for low-density parity check codes. *Front Inf Technol Electron Eng*. 2015;16(6):511-518.
50. Zhao M, Zhang X, Zhao L, Lee C. Design of a high-throughput QC-LDPC decoder with TDMP scheduling. *IEEE Trans Circuits Syst*. 2015;62(1):56-60.
51. Chen H, Zhang K, Ma X, Bai B. Comparisons between reliability-based iterative min-sum and majority-logic decoding algorithms for LDPC codes. *IEEE Transactions on Communications*. 2011;59(7):1766-1771.
52. Chandrasetty VA, Aziz SM. An area efficient LDPC decoder using a reduced complexity min-sum algorithm. *Dermatol Int*. 2012;45(2): 141-148.
53. Cho K, Chung K-S. Self-adaptive termination check of min-sum algorithm for LDPC decoders using the first two minima. *KSII Trans Internet Inf Syst*. 2017;11(4):1987-2001.
54. Wu Z, Su K, Guo L. A modified min sum decoding algorithm based on LMMSE for LDPC codes. *AEU-Int J Electron C*. Oct. 2014;68 (10):994-999.
55. Yang T, Liu S, Liu H, Tang M, Tan X, Zhou X. Noise benefits parameter estimation in LMMSE sense. *Digit Signal Process*. 2018;73(2): 153-163.
56. Cuevas L, Enríquez DZ, Pérez-Cisneros M. A selection method for evolutionary algorithms based on the Golden Section. *Expert Syst Appl*. 2018;106(8):183-196.
57. Boncalo O, Amaricai A, Mihancea PF, Savin V. Memory trade-offs in layered self-corrected min-sum LDPC decoders. *Analog Integr Circuits Signal Process*. 2016;87(2):169-180.
58. Mansour MM, Shanbhag NR. High-throughput LDPC decoders. *IEEE Trans Very Large Scale Integr VLSI Syst*. 2003;11(6):976-996.
59. Roberts MK, Jayabalan R. A power-and area-efficient multi-rate quasi-cyclic LDPC decoder. *Syst Signal Process*. 2015;34(6):2015-2035.
60. Oh and K. K. Parhi. Min-sum decoder architectures with reduced word length for LDPC codes. *EEE Trans Circuits Syst I Regul Pap*. 2010;57(1):105-115.
61. Cho K, Lee W-H, Chung K-S. Simplified 2-dimensional scaled min-sum algorithm for LDPC decoder. *J Electr Eng Technol*. 2017;12(3): 1262-1270.
62. Xue W, Ban T, Wang J. A modified normalized min-sum algorithm for LDPC decoding using order statistics. *Int J Satell Commun*. 2017;35(2):163-175.
63. Kamps U. A concept of generalized order statistics. *J Stat Plan Inference*. 1995;48(1):1-23.
64. Jayasooriya S, Shirvanimoghaddam M, Ong L, Lechner G, Johnson SJ. A new density evolution approximation for ldpc and multi-edge type LDPC codes. *IEEE Transactions on Communications*. 2016;64(10):4044-4056.
65. Wang X, Cao W, Li J, et al. Improved min-sum algorithm based on density evolution for low-density parity check codes. *IET Commun*. 2017;11(10):1582-1586.
66. Pandya N, Honary B. Low-complexity decoding of LDPC codes. *Electron Lett*. 2007;43(18):990-991.
67. Jiang M, Zhao C, Zhang L, Xu E. Adaptive offset min-sum algorithm for low-density parity check codes. *EEE Commun Lett*. 2006;10(6): 483-485.
68. Xu M, Wu J, Zhang M. "A modified offset min-sum decoding algorithm for LDPC codes," 2010 3rd International Conference on Computer Science and Information Technology, vol. 3, pp. 19–22, 2010.
69. Roberts MK, Jayabalan R. A modified optimally quantized offset min-sum decoding algorithm for low- complexity LDPC decoder. *Wirel Pers Commun*. 2015;80(2):561-570.
70. Wu X, Song Y, Jiang M, Zhao C. Adaptive-normalized/offset min-sum algorithm. *EEE Commun Lett*. Jul. 2010;14(7):667-669.
71. Roberts MK, Jayabalan R. An improved self adaptive min-sum decoding algorithm for flexible low-density parity-check decoder. *Natl Acad Sci Lett*. Apr. 2017;40(2):121-125.
72. Saouter Y. Acceleration of low density parity check code (LDPC) decoding by successive overrelaxations. *Electron Lett*. 2018;54(19): 1112-1114.
73. Papaharalabos S, Lazarakis F. Approximated box-plus decoding of LDPC codes. *IEEE Wireless Commun Lett*. 2015;19(12):2074-2077.
74. Tong S, Wang P, Wang D, Wang X. Box-minus operation and application in sum–product algorithm. *Electron Lett*. 2005;41(4):197–198.
75. Roberts MK, Mohanram SS, Shanmugasundaram N. An improved low complex offset min-sum based decoding algorithm for LDPC codes. *Mob Netw Appl*. 2019;24(6):1848-1852.
76. Vatta F, Soranzo A, Babich F. Low complexity bound on irregular LDPC belief-propagation decoding thresholds using Gaussian approximation. *IET Electronic Letters*. 2018;54(17):1038-1040.
77. Liu Y-H, Poulin D. Neural belief-propagation decoders for quantum error-correcting codes. *Phys Rev Lett*. 2019;122(20):1-6.
78. Luo K, Wang S, Chan KS, et al. A study on block-based neural network equalization in TDMR system with LDPC coding. *IEEE Trans Magn*. 2019;55(11):1-5.
79. Wang Z, Wu B, Ye T. An improved implementation of sum-product algorithm for LDPC decoder. *IEICE Electron Expr*. 2019;16(4):1–8.
80. Cho S, Yang K. A two-bit precision decoding algorithm for LDPC codes over the binary symmetric channel. *IEEE Wirel Commun*. 2019;8(1):109-112.
81. Lee JH, Sunwoo MH. Low-complexity high-throughput bit-wise LDPC decoder. *J Signal Process Syst*. 2019;91(8):855-862.

82. Hailes P, Xu L, Maunder RG, Al-Hashimi BM, Hanzo L. Hardware-efficient node processing unit architectures for flexible LDPC decoder implementations. *IEEE Trans Circuits Syst*. 2018;65(12):1919-1923.
83. Milicevic M, Gulak PG. A multi-Gb/s frame-interleaved LDPC decoder with path-unrolled message passing in 28-nm CMOS. *IEEE Trans Very Large Scale Integr VLSI Syst*. 2018;26(10):1908-1921.
84. Steiner F, Yacoub EB, Matuz B, Liva G, Amat AGI. One and two bit message passing for SC-LDPC codes with higher-order modulation. *J Light Technol*. 2019;37(23):5914-5925.
85. Shakiba-Herfeh M, Tanc AK, Duman TM. LDPC code design for fading interference channels. *IEEE Trans Veh Technol*. 2019;68(3): 2374-2385.
86. Zarubica R, Wilson SG, Hall E. "Multi-Gbps FPGA-based low density parity check (LDPC) decoder design," in IEEE GLOBECOM 2007 - IEEE Global Telecommunications Conference, 2007, pp. 548–552.
87. Gunnam KK, Choi GS, Yeary MB, Atiquzzaman M. "VLSI architectures for layered decoding for irregular LDPC codes of WiMax," in *2007 IEEE International Conference on Communications*, 2007, pp. 4542–4547.
88. Tehrani SS, Mannor S, Gross WJ. "An area-efficient FPGA-based architecture for fully-parallel stochastic LDPC decoding," in 2007 IEEE Workshop on Signal Processing Systems, 2007, pp. 255–260.
89. Charot F, Wolinski C, Fau N, Hamon F. "A new powerful scalable generic multi-standard LDPC decoder architecture," in 2008 *16th International Symposium on Field-Programmable Custom Computing Machines*, 2008, pp. 314–315.
90. Tehrani SS, Mannor S, Gross WJ. Fully parallel stochastic LDPC decoders. *IEEE Trans Signal Process*. 2008;56(11):5692-5703.
91. Ding H, Yang S, Luo W, Dong M, "Design and implementation for high speed LDPC decoder with layered decoding," in *2009 WRI International Conference on Communications and Mobile Computing*, 2009, vol. 1, pp. 156–160.
92. Chen X, Kang J, Lin S, Akella V. Memory system optimization for FPGA-based implementation of quasi-cyclic LDPC codes decoders. *IEEE Trans Circuits Syst I Regul Pap*. 2011;58(1):98-111.
93. Kim S, Sobelman GE, Lee H. A reduced-complexity architecture for LDPC layered decoding schemes. *IEEE Trans Very Large Scale Integr VLSI Syst*. 2011;19(6):1099-1103.
94. Peyic M, Baba H, Guleyuboglu E, Hamzaoglu I, Keskinoz M. A low power multi-rate decoder hardware for IEEE 802.11n LDPC codes. *Microprocess Microsyst*. 2012;36(3):159-166.
95. Tao Y, Park YS, Zhang Z. "High-throughput architecture and implementation of regular (2, dc) nonbinary LDPC decoders," in 2012 IEEE International Symposium on Circuits and Systems, 2012, pp. 2625–2628.
96. Boutillon E, Conde-Canencia L, Ghouwayel AA. Design of a GF(64)-LDPC decoder based on the EMS algorithm. *IEEE Trans Circuits Syst I Regul Pap*. 2013;60(10):2644-2656.
97. Roberts MK, Jayabalan R. An area efficient and high throughput multi-rate quasi-cyclic LDPC decoder for IEEE 802.11 n applications. *Microelectron Eng*. 2014;45(11):1489-1498.
98. Chandrasetty VA, Aziz SM. Resource efficient LDPC decoders for multimedia communication. *Dermatol Int*. 2015;48:213-220.
99. Kumawat S, Shrestha R, Daga N, Paily R. High-throughput LDPC-decoder architecture using efficient comparison techniques dynamic multi-frame processing schedule. *IEEE Trans Circuits Syst I Regul Pap*. 2015;62(5):1421-1430.
100. Chen X, Lin S, Akella V. QSN—a simple circular-shift network for reconfigurable quasi-cyclic LDPC decoders. *IEEE Trans Circuits Syst*. 2010;57(10):782-786.
101. Blanksby J, Howland CJ. A 690-mW 1-Gb/s 1024-b, rate-1/2 low-density parity-check code decoder. *IEEE J Solid-State Circuits*. 2002;37 (3):404-412.
102. Urard P, Yeo E, Paumier L. "A 135M/s DVB-S2 compliant codec based on 64800b LDPC and BCH codes," *in Processing 2005 IEEE International Solid-State Circuits Conference*, vol.1, pp. 446-609, 2005.
103. Mansour MM, Shanbhag NR. A 640-Mb/s 2048-bit programmable LDPC decoder chip. *IEEE J Solid-State Circuits*. 2006;41(3):684-698.
104. Karkooti M, Radosavljevic P, Cavallaro JR. "Configurable, high throughput, irregular LDPC decoder architecture: tradeoff analysis and implementation," *in* IEEE 17th International Conference on Application-specific Systems, Architectures and Processors (ASAP'06), 2006, pp. 360–367.
105. Brack T, Alles M, Kienle F, Wehn N. "A synthesizable IP Core for WIMAX 802.16E LDPC code decoding," in *2006 IEEE 17th International Symposium on Personal, Indoor and Mobile Radio Communications*, 2006, pp. 1–5.
106. Brack T, Alles M, Lehnigk-Emden T, Kienle F, Wehn N, L'Insalata NE, Rossi F, Rovini M, Fanucci L. "Low complexity LDPC code decoders for next generation standards," in 2007 Design Automation Test in Europe Conference Exhibition, 2007, pp. 1–6.
107. Masera G, Quaglio F, Vacca F. Implementation of a flexible LDPC decoder. *IEEE Trans Circuits Syst*. 2007;54(6):542-546.
108. Gentile G, Rovini M, Fanucci L. "Low-complexity architectures of a decoder for IEEE 802.16e LDPC codes," in *10th Euromicro Conference on Digital System Design Architectures, Methods and Tools (DSD 2007)*, 2007, pp. 369–375.
109. Darabiha A, Carusone A, Kschischang F. "A 3.3-Gbps bit serial block-interlaced min-sum LDPC decoder in 0.13- CMOS," *in* Processing IEEE 2007 Custom Intergrated Circuits Conference (CICC), 2007, pp. 459–462.
110. Rovini M, Gentile G, Rossi F, Fanucci L. "A scalable decoder architecture for IEEE 802.11n LDPC codes," *in IEEE GLOBECOM 2007 - IEEE Global Telecommunications Conference*, 2007, pp. 3270–3274.
111. Alles M, Vogt T, Wehn N. "FlexiChaP: a reconfigurable ASIP for convolutional, turbo, and LDPC code decoding," in 2008 5th International Symposium on Turbo Codes and Related Topics, 2008, pp. 84–89.
112. Shih X-Y, Zhan C-Z, Lin C-H, Wu A-Y. An 8.29 mm^2 52 mW multi-mode LDPC decoder design for Mobile WiMAX system in 0.13μm CMOS process. *IEEE J Solid-State Circuits*. 2008;43(3):672-683.

113. Liu C, Yen SW, Chen CL, et al. An LDPC decoder chip based on self-routing network for IEEE 802.16e applications. *IEEE J Solid-State Circuits*. 2008;43(3):684-694.
114. Ueng Y-L, Yang C-J, Wu Z-C, Wu C-E, Wang Y-L. "VLSI decoding architecture with improved convergence speed and reduced decoding latency for irregular LDPC codes in WiMAX," in 2008 IEEE International Symposium on Circuits and Systems, 2008, pp. 520–523.
115. Darabiha A, Carusone AC, Kschischang FR. Power reduction techniques for LDPC decoders. *IEEE J Solid-State Circuits*. 2008;43(8): 1835-1845.
116. Sun Y, Cavallaro JR. "A low-power 1-Gbps reconfigurable LDPC decoder design for multiple 4G wireless standards," in SOC Conference, 2008 IEEE International, 2008, pp. 367–370.
117. Kuo T-C, Willson AN. "A flexible decoder IC for WiMAX QC-LDPC codes," in 2008 *IEEE Custom Integrated Circuits Conference*, 2008, pp. 527–530.
118. Studer C, Preyss N, Roth C, Burg A. "Configurable high-throughput decoder architecture for quasi-cyclic LDPC codes," in 2008 42nd Asilomar Conference on Signals, Systems and Computers, 2008, pp. 1137–1142.
119. Shih X-Y, Zhan C-Z, Wu A-Y. "A 7.39 mm 2 76mW (1944, 972) LDPC decoder chip for IEEE 802.11 n applications," *in 2008 IEEE Asian Solid-State Circuits Conference*, 2008, pp. 301–304.
120. Liu L, Shi C-R. Sliced message passing: high throughput overlapped decoding of high-rate low-density parity-check codes. *IEEE Trans Circuits Syst I Regul Pap*. 2008;55(11):3697-3710.
121. Zhang Z, Anantharam V, Wainwright MJ, Nikolic B. "A 47 Gb/s LDPC decoder with improved low error rate performance," in 2009 Symposium on VLSI Circuits, 2009, pp. 286–287.
122. Liu C, Lin CC, Yen SW, et al. Design of a multimode QC-LDPC decoder based on shift-routing network. *EEE Trans Circuits Syst*. 2009; 56(9):734-738.
123. Zhang K, Huang X, Wang Z. High-throughput layered decoder implementation for quasi-cyclic LDPC codes. *IEEE J Sel Areas Commun Communications*. 2009;27(6):985-994.
124. Shih X, Zhan C, Wu A. "A real-time programmable LDPC decoder chip for arbitrary QC-LDPC parity check matrices," in 2009 IEEE Asian Solid-State Circuits Conference, 2009, pp. 369–372.
125. Lee S, Park J, Chung K. Memory efficient multi-rate regular LDPC decoder for CMMB. *IEEE Trans Consum Electron*. 2009;55(4):1866-1874.
126. Bao D, Xiang B, Shen R, Pan A, Chen Y, Zeng XY. Programmable architecture for flexi-mode QC-LDPC decoder supporting wireless LAN/MAN applications and beyond. *IEEE Trans Circuits Syst I Regul Pap*. 2010;57(1):125-138.
127. Huang S, Bao D, Xiang B, Chen Y, Zeng X. "A flexible LDPC decoder architecture supporting two decoding algorithms," in Proceedings of 2010 IEEE International Symposium on Circuits and Systems, 2010, pp. 3929–3932.
128. Chen Z, Brandon TL, Elliott DG, Bates S, Krzymien WA, Cockburn BF. Jointly designed architecture-aware LDPC convolutional codes and high-throughput parallel encoders/decoders. *IEEE Trans Circuits Syst I Regul Pap*. 2010;57(4):836-849.
129. Zhang Z, Anantharam V, Wainwright MJ, Nikolic B. An efficient 10GBASE-T ethernet LDPC decoder design with low error floors. *IEEE J Solid-State Circuits*. 2010;45(4):843-855.
130. Hei KGY, Qiao S. A parallel-layered belief-propagation decoder for non-layered LDPC codes. *J Commun*. 2010;5(5):400–408.
131. Mohsenin T, Truong DN, Baas BM. A low-complexity message-passing algorithm for reduced routing congestion in LDPC decoders. *IEEE Trans Circuits Syst I Regul Pap*. 2010;57(5):1048-1061.
132. Zhang K, Huang X, Wang Z. A dual-rate LDPC decoder for China multimedia mobile broadcasting systems. *IEEE Trans Consum Electron*. 2010;56(2):399-407.
133. Tehrani SS, Naderi A, Kamendje G, Hemati S, Mannor S, Gross WJ. Majority-based tracking forecast memories for stochastic LDPC decoding. *IEEE Trans Signal Process*. 2010;58(9):4883-4896.
134. Xiang B, Shen R, Pan A, Bao D, Zeng X. An area-efficient and low-power multi rate decoder for quasi-cyclic low-density parity-check codes. *IEEE Trans Very Large Scale Integr VLSI Syst*. 2010;18(10):1447-1460.
135. Xiang B, Bao D, Huang S, Zeng X. An 847–955 Mb/s 342–397 mW dual-path fully-overlapped QC-LDPC decoder for WiMAX system in 0.13μm CMOS. *IEEE J Solid-State Circuits*. 2011;46(6):1416-1432.
136. Wang Y, Ueng Y, Peng C, Yang C. Processing-task arrangement for a low-complexity full-mode WiMAX LDPC Codec. *IEEE Trans Circuits Syst I Regul Pap*. 2011;58(2):415-428.
137. Zhang K, Huang X, Wang Z. A high-throughput LDPC decoder architecture with rate compatibility. *IEEE Trans Circuits Syst I Regul Pap*. 2011;58(4):839-847.
138. Chen Z Peng X, Zhao,X, Xie Q, Okamura L, Zhou D, Goto S. "A macro-layer level fully parallel layered LDPC decoder SOC for IEEE 802.15.3c application," Proc. 2011 Int. Symp. VLSI Des. Autom. Test, pp. 1–4, 2011.
139. Weiner M, Nikolić B, Zhang Z. "LDPC decoder architecture for high-data rate personal-area networks," in 2011 IEEE International Symposium of Circuits and Systems (ISCAS), 2011, pp. 1784–1787.
140. Li J, He G, Hou H, Zhang Z, Ma J."Memory efficient layered decoder design with early termination for LDPC codes," in 2011 IEEE International Symposium of Circuits and Systems (ISCAS), 2011, pp. 2697–2700.
141. Naderi A, Mannor S, Sawan M, Gross WJ. Delayed stochastic decoding of LDPC codes. *IEEE Trans Signal Process*. 2011;59(11):5617-5626.
142. Peng X, Chen Z, Zhao X, Zhou D, Goto S. "A 115mW 1Gbps QC-LDPC decoder ASIC for WiMAX in 65nm CMOS," in IEEE Asian Solid-State Circuits Conference 2011, Jeju, South Korea, 2011, pp. 317–320.

143. Chen Z, Peng X, Zhao X, Okamura L, Zhou D, Goto S., "A 6.72-Gb/s 8pJ/bit/iteration IEEE 802.15.3c LDPC decoder chip," *in 2011 International Symposium on Integrated Circuits*, 2011, pp. 7–12.
144. Park YS, Blaauw D, Sylvester D, Zhang Z. "A 1.6-mm2 38-mW 1.5-Gb/s LDPC decoder enabled by refresh-free embedded DRAM," 2012 Symposium on VLSI Circuits Digest of Technical Papers, pp. 114–115, 2012.
145. Chen C, Lin Y, Chang H, Lee C. A 2.37-Gb/s 284.8 mW rate-compatible (491,3,6) LDPC-CC decoder. *IEEE J Solid-State Circuits*. 2012; 47(4):817-831.
146. Chao M-A, Shih X-Y, Wu A-Y. Matrix merging scheme and efficient decoding techniques for reconfigurable QC-LDPC decoders. *J Signal Process Syst*. 2012;68(2):183-202.
147. Yen S, Hung S, Chen C, Chang H, Jou S, Lee C. A 5.79-Gb/s energy-efficient multi rate LDPC Codec chip for IEEE 802.15.3c applications. *IEEE J Solid-State Circuits*. 2012;47(9):2246-2257.
148. Ueng Y, Yang B, Yang C, Lee H, Yang J. An efficient multi-standard LDPC decoder design using hardware-friendly shuffled decoding. *IEEE Trans Circuits Syst I Regul Pap*. 2013;60(3):743-756.
149. Heidari T, Jannesari A. "Design of high-throughput QC-LDPC decoder for WiMAX standard," *in processing 2013 21st Iranian Conference on Electrical Engineering (ICEE)*, 2013, pp. 1–4.
150. Balatsoukas-Stimming A, Preyss N, Cevrero A, Burg A, Roth C. "A parallelized layered QC-LDPC decoder for IEEE 802.11ad," in *2013 IEEE 11th International New Circuits and Systems Conference (NEWCAS)*, 2013, pp. 1–4.
151. Li J, Ma J, He G. A memory efficient parallel layered QC-LDPC decoder for CMMB systems. *Dermatol Int*. 2013;46(4):359-368.
152. Ajaz S, Lee H. Reduced-complexity local switch based multi-mode QC-LDPC decoder architecture for Gbit wireless communication. *Electron Lett*. 2013;49(19):1246-1248.
153. Sun Y, Cavallaro JR. VLSI architecture for layered decoding of QC-LDPC codes with high circulant weight. *IEEE Trans Very Large Scale Integr VLSI Syst*. 2013;21(10):1960-1964.
154. Li M, Naessens F, Debacker P, Raghavan P, Desset C, Li M, Dejonghe A, Van der Perre L. "An area and energy efficient half-row-paralleled layer LDPC decoder for the 802.11AD standard," in SiPS 2013 Proceedings, 2013, pp. 112–117.
155. Schläfer P, Wehn N, Alles M, Lehnigk-Emden T. "A new dimension of parallelism in ultra high throughput LDPC decoding," *in* 2013 IEEE Workshop on Signal Processing Systems, 2013, pp. 153–158.
156. Li M, Naessens F, Li M, Debacker P, Desset C, Raghavan P, Dejonghe A, Van der Perre, L. "A processor based multi-standard low-power LDPC engine for multi-Gbps wireless communication," in 2013 *IEEE Global Conference on Signal and Information Processing*, 2013, pp. 1254–1257.
157. Weiner M, Blagojevic M, Skotnikov S, Burg A, Flatresse P, Nikolic B. "27.7 A scalable 1.5-to-6Gb/s 6.2-to-38.1mW LDPC decoder for 60GHz wireless networks in 28nm UTBB FDSOI," *in 2014 IEEE International Solid-State Circuits Conference Digest of Technical Papers (ISSCC)*, San Francisco, CA, USA, 2014, pp. 464–465.
158. Park YS, Blaauw D, Sylvester D, Zhang Z. Low-power high-throughput LDPC decoder using non-refresh embedded DRAM. *IEEE J Solid-State Circuits*. 2014;49(3):783-794.
159. Angarita F, Valls J, Almenar V, Torres V. Reduced-complexity min-sum algorithm for decoding LDPC codes with low error-floor. *IEEE Trans Circuits Syst I Regul Pap*. 2014;61(7):2150-2158.
160. Ajaz S, Lee H. "Multi-Gb/s multi-mode LDPC decoder architecture for IEEE 802.11ad standard," *in 2014 IEEE Asia Pacific Conference on Circuits and Systems (APCCAS)*, 2014, pp. 153–156.
161. Chen Y, Zhang Q, Wu D, Zhou C, Zeng X. An efficient multirate LDPC-CC decoder with a layered decoding algorithm for the IEEE 1901 Standard. *IEEE Trans Circuits Syst II Express Briefs*. 2014;61(12):992-996.
162. Yu C, Chuang H, Lin B, Cheng P, Chen S. "Improvement on a block-serial fully-overlapped QC-LDPC decoder for IEEE 802.11n," in *2014 IEEE International Conference on Consumer Electronics (*ICCE*)*, 2014, pp. 446–447.
163. Cheng C, Yang J, Lee H, Yang C, Ueng Y. A fully parallel LDPC decoder architecture using probabilistic min-sum algorithm for high-throughput applications. *IEEE Trans Circuits Syst I Regul Pap*. Sep. 2014;61(9):2738-2746.
164. Lee X, Chen C, Chang H, Lee C. A 7.92 Gb/s 437.2mW stochastic LDPC decoder chip for IEEE 802.15.3c applications. *IEEE Trans Circuits Syst I Regul Pap*. 2015;62(2):507-516.
165. Zhang W, Chen S, Bai X, Zhou D. "A full layer parallel QC-LDPC decoder for WiMAX and Wi-Fi," in 2015 IEEE 11th International Conference on ASIC (ASICON), 2015, pp. 1–4.
166. Motozuka H, Yosoku N, Sakamoto T, Tsukizawa T, Shirakata N, Takinami K. "A 6.16Gb/s 4.7pJ/bit/iteration LDPC decoder for IEEE 802.11ad standard in 40nm LP-CMOS," *in* 2015 *IEEE Global Conference on Signal and Information Processing (GlobalSIP)*, 2015, pp. 1289–1292.
167. Li M, Weijers JW, Derudder V, Vos I, Rykunov M, Dupont S, Debacker P, Dewilde A, Huang Y, Van der Perre L, Van Thillo W."An energy efficient 18Gbps LDPC decoding processor for 802.11ad in 28nm CMOS," *in* 2015 IEEE Asian Solid-State Circuits Conference (A-SSCC), 2015, pp. 1–5.
168. Kanchetla VK, Shrestha R, Paily R. Multi-standard high-throughput and low-power quasi-cyclic low density parity check decoder for worldwide interoperability for microwave access and wireless fidelity standards. *IET Circuits, Devices Syst*. 2016;10(2):111-120.
169. Li M, Yang C, Ueng Y. A 5.28-Gb/s LDPC decoder with time-domain signal processing for IEEE 802.15.3c applications. *IEEE J Solid-State Circuits*. 2017;52(2):592-604.
170. Tsatsaragkos I, Paliouras V. A reconfigurable LDPC decoder optimized for 802.11n/ac applications. *IEEE Trans Very Large Scale Integr VLSI Syst*. 2018;26(1):182-195.

171. Ghanaatian R, Balatsoukas-Stimming A, Muller TC, et al. A 588-Gb/s LDPC decoder based on finite-alphabet message passing. *IEEE Trans Very Large Scale Integr VLSI Syst*. Feb. 2018;26(2):329-340.
172. Nguyen TTB, Lee H. Low-complexity multi-mode multi-way split-row layered LDPC decoder for gigabit wireless communications. *Dermatol Int*. 2019;65:189-200.
173. Lopez H, Chan H-W, Chiu K-L, Tsai P-Y, Jou S-JJ. A 75-Gb/s/mm2 and energy-efficient LDPC decoder based on a reduced complexity second minimum approximation min-sum algorithm. *IEEE Trans Very Large Scale Integr VLSI Systems*. 2020;28(4):926-939.

How to cite this article: Kingston Roberts M, Kumari S, Anguraj P. Certain investigations on recent advances in the design of decoding algorithms using low-density parity-check codes and its applications. *Int J Commun Syst*. 2021;34:e4765. https://doi.org/10.1002/dac.4765

Proceedings of the Fourth International Conference on I-SMAC (IoT in Social, Mobile, Analytics and Cloud) (I-SMAC)
IEEE Xplore Part Number:CFP20OSV-ART; ISBN: 978-1-7281-5464-0

Raspberry Pi based Smart Library for Visually Challenged Citizens

Dr. Nandalal
Professor,
Department of ECE,
Sri Krishna College of Engineering and Technology,
Coimbatore
nandalal@skcet.ac.in

Mr.V.Anand Kumar
Assistant Professor
Department of ECE
Sri Eshwar College of Engineering, Coimbatore
anandkumar.v@sece.ac.in

Dr. T. Manikandan
Professor
Department of ECE
Rajalakshmi college of Engineering, Chennai
manikandan.t@rajalakshmi.edu.in

Ms. Sindhuprika K
Student, Department of ECE,
SKCET, Coimbatore
16euec141@skcet.ac.in

Ms. Sujitha R
Student, Department of ECE,
SKCET, Coimbatore
16euec153@skcet.ac.in

Ms. Suvathy G
Student, Department of ECE
SKCET, Coimbatore
16euec156@skcet.ac.in

Abstract— **One of the major drawbacks of humanity is visual impairment, particularly information are communicated only by lots of text messages rather than voice communication. The device which is being designed helps the visual impairment of people. In this work, a device which produces speech from the image's text is designed. The fundamental structure in the framework is to extracts the region of in the image that contains text from the captured image and this device converts the extracted text to speech. It Framework is implemented using a camera and a Raspberry Pi system. The image preprocessing steps are done in the captured image to locate the text in the captured image and the preprocessing steps eliminate the image background. Tools like Optical Character Recognition (OCR) and Text to Speech (TTS) engine are used to convert the captured image into speech. Speakers or Earphones are used to hear the audio output from Raspberry Pi.**

Key Words – Real Time Systems; Text to Speech (TTS); Optical Character Recognition (OCR); Raspberry Pi; Camera Serial Interface (CSI); Pi-CAM;

I. INTRODUCTION

One of the biggest advantages is the probability in barcode reader. Because of that, the different product is identified by visually impaired persons. The code will contain all the useful information on that particular product. If any user scans the code, the product information or details will be listed via E-Braille readers. The most common problem faced by the user in the direction of the bar code [1]. There was another methodology, which uses optical enhancement solutions like an optical zooming device. This device will enhance the Braille character. But the problem here is visually impaired user should know Braille language. These are some existing system.

There are some models which are objective towards the conversion of text into a speech signal. This model is designed with some hardware like a scanner, speaker and a computer. But the drawback in this system design is it can scan trouble-free documents, it unable to extract the information text from the scanned image with the multifarious background. Now in the current system, a person or user can visualize the generation of speech from the text information or message.

The main objective of this work is that helping the readability of blind and a talking aid for vocally handicapped persons and an aid which train for commercial applications. The person who is vocally handicapped can enter the text from keyboard and ARM microcontroller will process the text and given to voice board. This voice board processes the feed and produces the speech which can be delivered with the help of the speaker.

In this work, the first objective is to perform image recognition methodology with speech processing and synthesis. The second objective of this work is to build up a cost-efficient and easy use device which convert image to speech using Raspberry Pi [4]. A text printed in a document is scanned using an inbuilt camera and Raspberry Pi will process the text from the captured image and synthesize the speech from the text. This can save energy and time of handicapped people. There are numerous language translators available where the content has to be manually entered and the application does whatever is left of the work of translating the content into the desired language. Some translation platforms even charge for this process. For example, the most popular Google Translate API charges calculated as per the usage. There is another example, which converts any language into another language using Java on Linux platform to translate. One of the examples of Java-based translation is EBMT which can translate one language into another language.

II. LITERATURE SURVEY

Paper Title Author Name	Techniques Used
Image to Speech Conversion for	The extraction of the content in the picture is finished utilizing optical

Visually Impaired Asha G Hagargund, Sharsha Vanaria Thota, Mitadru Bera Eram Fatima Shaik [3]	character acknowledgment (OCR). OCR is a field of examination in design acknowledgment, man-made consciousness and PC vision. It is the change of the pictures of composed, transcribed or printed text into a computerized book or PC design text.
Book Reader Using Raspberry Pi for Visually Impaired S Aditi, S P Annapoorani A Kanchana [4]	Albeit various perusing associates have been structured explicitly for the outwardly disabled, to the Proposed information, no current perusing collaborator can peruse text from the sorts of testing examples and foundations found on certain books. Such content data can show up in numerous scales, textual styles, hues and directions. The proposed calculation can be viably used to deal with various foundation examples, and concentrate text data from any sort of hand-held articles or books.

The principle goal of this work is that helping the coherence of visually impaired and talking help for vocally incapacitated people and a guide which train for business applications. The problems which are identified from the existing systems are overcome by this work by using Neural Optical Character Recognition (OCR) in Open CV which is developed to help visually challenged people. This system is built to give support to blind persons in understanding text form a tricky pattern for achieving that the major task is to extract text from the document. The first step of this work is to capture the object image using a webcam or a camera which is implanted with a Raspberry Pi system. This Raspberry Pi will perform image processing work. A button is used to automate the execution of the system, which monitor the document and extract the information. The extracted content of the scanned document is converted into a voice message and delivered with the assistance of the speaker. The proposed system helps people to understand the text without much space. The ready documents will be uploaded in the dropbox for future usage.

III. SYSTEM ARCHITECTURE

A. Block Diagram and Flow Diagram

The below diagram shows the system architecture of the proposed system which consist of Webcam, Raspberry Pi and Speakers

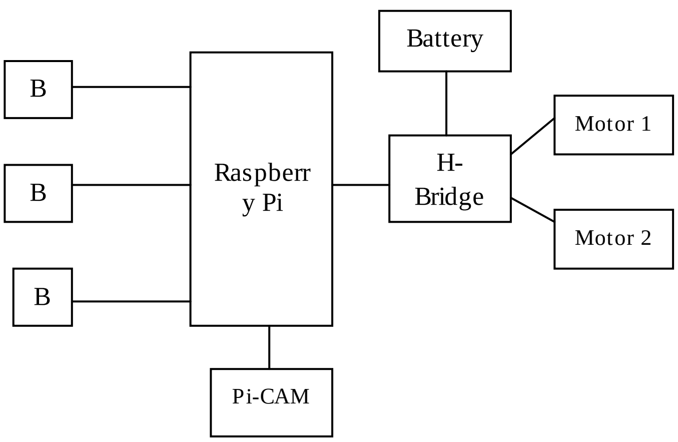

FIG 1:BLOCK DIAGRAM

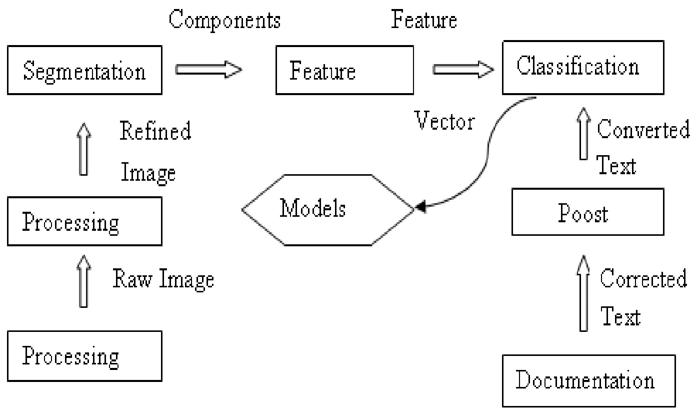

FIG 2:FLOW DIAGRAM

B. Hardware Used

The following components are used in the proposed system.

- Raspberry Pi
- Pi-CAM
- Motors
- H-Bridge
- Buttons

Raspberry Pi:

The processor consists of BCM2387 Broadcom chipset. It consists of 64 bit ARM cortex A53 Quad Core 1.2 GHz. It supports Wireless LAN standard 802.11 b/g/n and Bluetooth 4.1. it supports WEP, WPA, WPA2 at the maximum range of 100 meters. It also has Bluetooth IEEE 802.15 with symmetric encryption algorithm with 128-bit key and Graphics Processing Unit (GPU). It provides OpenGL 2.0 computer graphics, OpenVG for hardware acceleration and a high profile decoder 1080p H.264. It is capable of texture filtering with 1G Pixels per second and DMA Memory infrastructure. It has Audio output with Micro SD card running version Linux OS or Windows version 10 IoT Dimensions.

Connectors:

Connectors are supported with 10 / 100 BaseT Ethernet socket with video output. It also has HDMI port and composite Phono connector (RCA Connector). It is upgraded to the main processor in the next generation and it improves the connectivity with BLE (Bluetooth Low Energy) and onboard WiFi (BCM43143). It also upgraded to the power of 2.5 Amps which supports most of the external USB devices.

Pi-CAM:

Raspberry Pi Model is compatible with high definition camera, which provides low noise image capture, low cross talk and also provides high sensitivity. Design with lightweight with an ultra small camera for image capture. Camera Serial Interface (CSI) connector is used to connect the camera module to the Raspberry Pi board. This CSI bus provides high data rate and it carries exclusively pixel data. use a dedicated CSI interface. The dimension of the board and weight is 25mm * 23mm *9mm tiny board & 3 grams respectively. Because of tiny size and less weight, it is used in mobile and other applications.

FIG 3: RASPBERRY PI

The V2 camera Module has 8Mp Sony IMX219 sensor (match up to 5 Megapixel Omni Vision Sensor of the creative camera). Home security application and wildlife camera traps use this camera module with Pi.

Memory Card:

A flash-based Micro SD card is accommodated to meet up the capacity, performance and protection of captured image. This also uses inbuilt storage in emerging video audio electronic device. It is interfaced by an 8 pin advance communication. The interface pin is allotted for clock, command 2 pins for power line and 4 pins for data transfer. It also supports standard multimedia data transfer operations.

Motors:

Here DC motors are used which has the following features,

- Generally, the electrical machines are in the service of AC type.
- For industrial type application mostly uses a DC machine.
- The main parts of DC machines are DC motors and DC generators.
- Fine control of speed is provided by the DC machine which is not obtained by using AC motors.
- A rated torque is developed by DC motors at all speeds from idle to rated speed.
- Torque developed at ideal is several times larger than torque created by an AC motor of equal speed and power rating.

Applications of DC Machines:

- It may act as either a generator or a motor but at present because of the wide use of AC machines, generators are used for limited applications.
- Printing presses, fans, pumps, paper mills and machine tools are some of the application of large DC motors.

FIG 4: PI CAMERA

- Small DC machines with high factional horsepower rating used in speed sensing tacho generator, tracking and sensing servomotors used in robotic applications.

Some of the applications of DC machines are listed below:

- DC machine has high starting torque.
- It has speedy acceleration and deceleration.
- The speed of DC motors can be effortlessly controlled over a wide range of speed.
- DC machines are constructed in the size of various ranges.

The cost and need for regular maintenance of the machine are the major disadvantages of DC machines.

Software Description:

PYTHON 3.7

Powerful programming and easy to learn a language is Python 3.7. Python has well organized high-level data structures and an uncomplicated but an efficient approach to Object-Oriented programming language. It has a dynamic typing and well-designed syntax, collectively with its constructed nature, it is ideally used for easy scripting and rapid real-time applications developed in various platforms. It effortlessly provides absolute new data type and functions implemented in C or C++.

GEANY IDE:

A Light weighted and tiny integrated development environments are called as Geany. It provides fast developed with few dependencies for the supplementary packages. An additional goal of Geany is an independent desktop environment like GNOME or KDE; it only requires a toolkit GTK2. Because of the dependency on the GTK2 toolkit, it needs its runtime libraries to be installed to execute it.

It is quite an unproblematic way to compile Geany,

1. %./configure
2. %make
3. %make install

Above are the commands used in compiling Geany.

%./configure –help

Above command configure script provide several a detail list of help command.

DROPBOX:

It is used for business which lets a team to work at anyplace but this will synchronize important files across all teammate devices. Admin is given control to organize the information and the stay at the top of the account to control the received files. The commonly shared files and documents help everyone in the team to track the updates day by day effortlessly. With this Dropbox, all the team members can work simultaneously like they are working like sitting with each other. This provides an easy way of communicating with all team members at the same time.

An attractive feature is it will provide personal cloud storage. With a hurry of suppliers to go into the market and an escalating offer to contemptible storage space, it results in a high amount of internet traffic in cloud management. Understanding the architecture and the performance of the systems provide good knowledge in the fundamental design and effective use of cloud storage systems and also calculate their impact on the network traffic. The characterization of Dropbox is presented in this paper which leads to a solution to our datasets in personal cloud storage. The data to be analyzed are measured from 4 vantage points across Europe. The data was collected for 42 uninterrupted days.

IMAGE PROCESSING:

Image Capturing:

The inbuilt camera capture the image of the content of the printed page which is moved over the device is the primary phase. The characteristic of the captured image is high definition and can be recognized because of the camera of high definition 8 Megapixel. The initial step of the project is to place the text document under the camera and the camera captured the text image.

Pre Processing:

The pre-processing includes the process like skew correction, Noise removal and linearization which is done in the captured text image. The outcome of the captured image is getting skewed either left or right orientation of an image. The operations done in the picture are binarized and enhance the brightness. The skew identification ensures for a spot of reference sandwiched between ±15 degrees then the lines are synchronized with the horizontal axis. Before preprocessing some parameters are to be considered are noise during capture or low quality of capture the image. There are three stages in preprocessing steps: they are removal of noise, linearization and skew correction. Initial steps are to check for skewing in the captured image because the captured image may skew in orientation on either right or left. Enhancement of brightness and binarization is the basic step performed in a captured image. The angle of orientation is between ±15 degrees is checked and if there are any disturbances the image is rotated until the captured image is matched with the horizontal true axis, this is the procedure for a skew corrected captured image. Before stepping into the next step the noise introduced while capturing and noise due to worst clarity of the page should be taken care and cleared. Next pre-processing step is segmentation. Segmentation process breaks a scanned image into a sequence of segments characters and the sub-images are converted into individual symbols. Next, the segmented image is checked for inner line spacing and binarization. Here the inner line space is distinguished, and then the segmented image is converted into sets of paragraph depending upon the inner line gaps. The width of the horizontal lines is recognized by a histogram of the captured image. At the same point, the vertical space convergence is checked vertically with lines. The width of the word is recognized by Histogram.

Image to Text Converter and Text to Speech:

Raspberry Pi board process the recognized character area unit with the computer code values. Here all the characters are converted into text transcription by matching with the corresponding guide. Finally, the audio output is delivered from that corresponding text transcription. This module is initiated with preprocessed character recognition. This module converts the text into audio format. The audio jack is present onboard Raspberry Pi; this can generate audio by Pulse Width Modulation output.

LOCATION OF BOOK:

The first step in this project is to help by navigation on a book in the library. The pathway for each book is coded in Raspberry pi. The home stage and destination of the book is predefined to a wheelchair. This step-up makes it comfortable for use in the library.

IMAGE CAPTURING:

The pi cam interfaced with Raspberry pi captures an image of a printed page. OCR algorithm users the tesseract software in Raspberry pi to convert images to text. The GTTS provides a specification to convert text to audio. Words to be read per minute changed according to people.

UPLOADING DOCUMENTS:

After the completion of reading each document, the option to load that particular document is available with Raspberry Pi. Both the text and audio of the image is uploaded with date and time.

Working Flow Process:

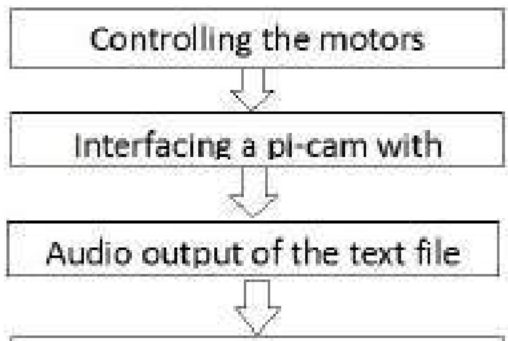

FIG 5: WORK FLOW PROCESS

IV. RESULTS

The systemshows the initialization of a portable solar panel which supplies the power secondary power to the system. The above fig. 6 and fig. 7 is the hardware output in front a mounted camera is placed to capture the image to be processed and 3B+ Raspberry Pi convert the captured image into text and then the text is processed in the speech output.

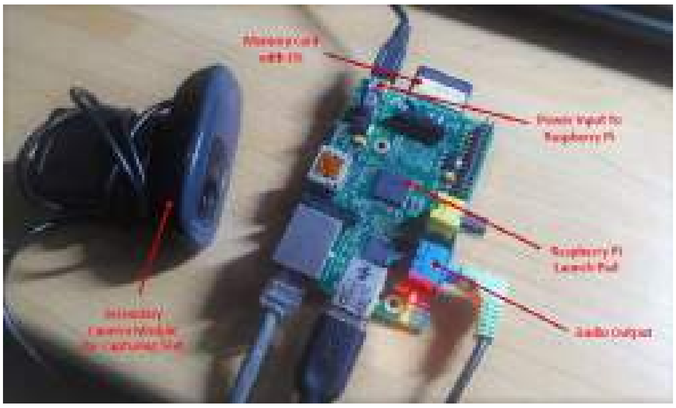

FIG 6: STAGE 1 HARDWARE OUTPUT

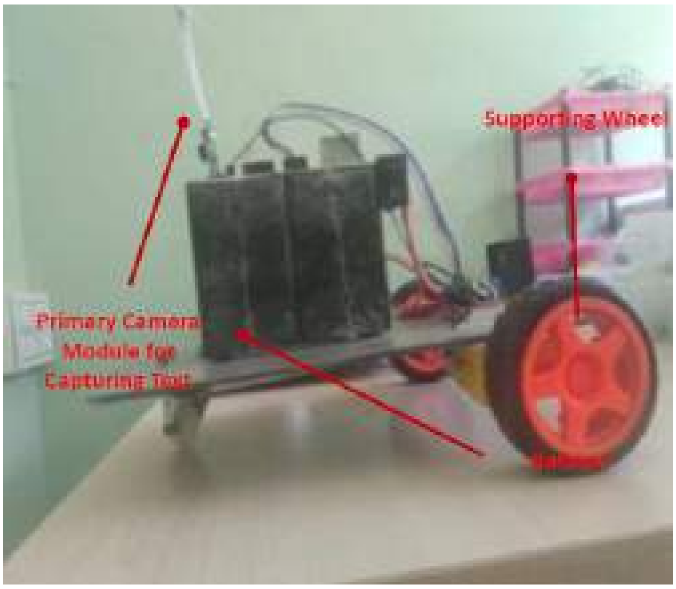

FIG 7: STAGE 2 HARDWARE OUTPUT

V. CONCLUSION

The system is a novel implementation of text to speech conversion for visually impaired people. Our algorithm processed successfully reads the text efficiently. This project demonstrates the hardware implementation with different samples. The device is compact and able to locate the books in the library and enable the retrieval of the read documents. Thus the proposed system is a multifunctional system which enhances the quality of the visually challenged people. This project is developed in various platforms like python language and runs in the 3B+ Raspberry Pi model. By this implemented system, a captured image was converted into text format and then from text to speech conversion.

REFERENCES

[1] Breen A P, "The future role of text to speech synthesis in automated service". IEEE Colloquium on Advance in Intractive voice technologies for telecommunication services, 2002

[2] Tanprasert C, Koanantakool, "Thai OCR: a Neural network application", IEEE TENCON, Aug 2002.

[3] Asha G Hagargund, Sharsha Vanria Thota, Mitadru Bera Eram Fatima Shaik "Image to speech Conversion for Visually Impaired", International Journal of Latest Research in Engineering and Technology, Volume 03 - Issue 06, June 2017, PP. 09-15.

[4] S Aditi, SP Annapoorani A Kanchana, "Book Reader Using Raspberry Pi for Visually Impaired" , International Research Journal of Engineering and Technology ,Volume: 05 Issue: 03, Mar-2018.

[5] Lucas S M, "High Performance OCR with Syntactic neural Networks", 4th international conference on ANN, 2002.

[6] https://github.com/aquatiko/Image-Text-Speech-Synthesizer-Converter

[7] Gllavata J, Ewerth R "A robust algorithm for text detection in images", IEEE ISPA,May 2004.

[8] http://code.google.com/p/tesseract-ocr.

[9] Cai M, Song J and Lyu M R, "A new approach for video text detection", International conference on Image processing, New York, 2002.

[10] Rithika H, Nithya Santhoshi B, "Image Text to speech conversion in the desired language by translating with Raspberry Pi", IEEE, 2016.

[11] Sagar G K & Shreekanth T, "Real time implementation of optical character recognition based TTS system using Raspberry Pi", IJARCSSE, 2017.

[12] Jain A K and Yu B, "Automatic text Location in Image and video frames", ICPR,Brisbane,1998.

[13] Kalaivani K, Praveena R "Real time implementation of image recognition and text to speech conversion", IJAERT, 2014.

[14] Yeong Hwa Chang, Nilima Sahoo, Hung Wei Lin " An Intelligent Walking Stick for the Visually Challenged People", IEEE Internatioal Conference on Applied System Invention, 2018.

[15] Joe Louis Paul, Sasirekha, Mohanavalli, Jayashree "Smart Eye for Visually Impaired An aid to Help the blind People", IEEE confernce on Computatational intelligence in data science,2019.

[16] Madhura Gharat, Rizwan Patanwala, Adithi Ganaparthi, "Audio Guidance System for blind", IEEE ICECA, 2017

[17] S Kowshik, VR Gautam, Suganthi, "Assistance for Visually Imared Using Finger Tip Text Reader using Machine Learing", IEEE ICoAC,2019

[18] Shubham Melvin Felix Sumer Kumar, Veeramuthu, "A Smart Personal AI Assistant for Visually Impaired People" IEEE ICEOI 2018.

Analysis And Design Of Fir Filter Using Modified Carry Look Ahead Multiplier

[1]*S. Dhanasekaran, [2] T.Thamaraimanalan, [3] V.Anandkumar , [4]A.Manikandan

Abstract: The dynamic growth in portable multimedia devices and communication system has increased the demand for area and power efficient high-speed Digital Signal Processing (DSP) system. The Finite Impulse Response (FIR) Filter is the important component for designing an efficient digital signal processing system. Usage of digital Finite Impulse Response (FIR) filter is one of the prime block in DSP. Digital multipliers and adders are the most critical arithmetic functional units in FIR filters and also decides the performance of whole system. Thus, the low power system design has become a major performance goal. This paper proposes an FIR filter which is designed using Carry-Look ahead adder and multiplier. Where the multiplier is proposed by internal circuit of Modified Carry Look ahead Adder. Carry-Look ahead Adder (CLA) is used for addition operation which uses fastest carry generation technique to increases the speed by reducing the time required to fix carry bits and multiplier performs multiplication process in a hierarchical manner. Thus, the proposed method can minimize the active power and delay of the FIR filter. The tentative results shows that the FIR filter using proposed multiplier method achieves less amount of delay and power reduction compared to conventional method. The proposed FIR filter is programmed using Verilog code and was synthesized and implemented using Xilinx ISE 14.7 tool. and the power is analyzed using Xpower analyzer.

KEYWORDS: Carry Look Ahead Adder, FIR Filter, Multiplier, Digital Signal Processing

I INTRODUCTION

Optimized design of digital logic systems is one of the most essential part of VLSI system design[1]. In modern era, a significant range of research work is carried out sprouting efficient architectures to reduce the complexity of DSP system. Digital FIR filter is the fundamental arithmetic operation used in most of the communication system and in various signal processing devices [12]. Digital FIR filter performs lot of arithmetic and logical operations that are extensively used for signal analysis and estimation, selection of band for the computation and signal preconditioning etc. Especially, it requires more rapid calculations for updating their filter coefficients [3]. In general, the longest critical path delay of the FIR filter mainly focus based on the computation time required for the multiplication and addition operation. Multipliers and Adder are the key hardware blocks of FIR filter which contributes in reduction of chip area, power and delay for each operation[2]. First considering the multipliers in FIR filter having long latency, large area and consume considerable amount of power. Therefore the main goal is to attain high speed and low power consumption multiplier.
Second, CLA is used for addition operation which improves the speed by decreasing the total time necessary to fix the carry bits. This paper deals with the implementation of FIR filter with modified multiplier based on the CLA [9]. The performance of the proposed FIR Filter are compared in terms of area, delay and power using the conventional and modified technique. The paper is structured as follows, Section II presents the concepts of FIR filter. Section III details with the basic carry look ahead adder technique. Section IV gives the proposed FIR filter using modified multiplier based CLA, Section V performs simulation results and comparative analysis, Section VI provides Conclusion.

- [1,2,3] Assistant Professor, Department of Electronics and Communication Engineering
- Sri Eshwar College of Engineering, Coimbatore-641202
- [4]Assistant Professor, Department of Electronics and Communication Engineering, Vivekanandha College of Technology, Tiruchengode, Namakkal, Tamilnadu, India
- [1]dhanselvaraj@gmail.com, [2]t.thamaraimanalan@gmail.com, [3]anand.kkr@gmail.com, [4]mani85a@gmail.com

II FIR FILTER

In this segment, the basic theoretical concepts of direct form realization of FIR filter is discussed. The FIR filter can be obtained using linear convolution which simply performs the convolution operation between the given input signal and the fixed filter coefficients. The basic representation of an FIR filter is given by equation 1

$$y(n) = \sum_{K=0}^{N-1} \square_k x(n-k) \qquad 1$$

Where y(n) is the output response, x(n) is the input signal, M is the order of the filter and represents the filter coefficients for the M tap FIR filter. The below figure1 shows the structure of a direct form M-tap FIR filter with length N. The input of the FIR filter Xn is given to the delays of the direct form structure. In this structure the b_n values are the coefficients of the operation and are designed to the multiplication of the samples. The output at time n is the summation of the delayed samples multiplied by the appropriate samples. The process in which selecting the filter coefficients and length of the filter is called Filter Design.

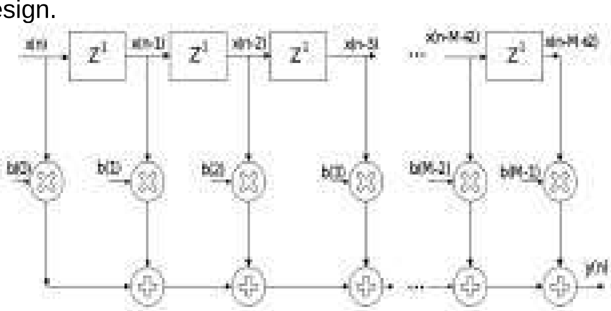

Figure 1: Direct form realization of M-tap Filter

For the instance consider the filter having input sequence (n) = [0 ,1,2,3,...,N −1] with the length of N and impulse response $b(n)$ = [0 ,1,2,3,...,M−1] with the length of M. Now performing linear convolution of $x(n)$ and $b(n)$ produces the output sequence $y(n)$ and the length of $y(n)$ is $S = N + M - 1$ (2) By adding required number of zeros to the input sequence and impulse response, the length of $x(n)$ and $b(n)$ can be made equal to S. This process is recognized as zero padding process. The total length $S = N + M - 1$ can be obtained by increasing the length of (n) by N points and length of $h(n)$ by M points. Both the sequences (n) and b(n) are finite in FIR filter, based on this sequences the linear convolution is also said to be finite. The output sequence y(n) is derived from the convolution operation of input x of length N with filter coefficient b of length M. So the output sequence y(n) is given as follows,

$$y(n) = \sum_{i=0}^{M-1} b(i)x(n-i) \qquad 2$$

By expanding the Eq. (2) the direct form structure of FIR filter is designed.

y(n) = b(0)x(n) = b(1)x(n-1)+b(2)x(n-2)+b(3)x(n-3)+ … +b(M-1)b(n-M+1) 3

This construction of direct form structure is also said as canonical structure meanwhile the number of delay blocks present in the architecture is equivalent to the order of difference equation that contains $M-1$ delay blocks, M multiplications and $M - 1$ additions.

III CARRY LOOK AHEAD ADDER (CLA)

Carry Look ahead algorithm speed up the operation to perform addition, because in this algorithm the carry for the next stages of process is calculated in advance based on the input signals given to the adder. The CLA exploits the fact that the carry generated by a bit-position depends on the three inputs to responding that position. If 'X' and 'Y' are two inputs then the function X=Y= 1, a carry is generated independently of the carry from the previous bit position and if X=Y= 0, no carry is generated. Similarly if X ≠ Y, a carry is generated if and only if the previous bit-position generates a carry. 'C' denotes the initial carry bit of adder, "S" and "Cout" are said to be output sum and carry of the adder respectively. Then the Boolean expression for calculating next carry and addition in carry look ahead adder is :

- Pi = Xi ⊕ Yi -- Carry Propagation (1)
- Gi = Xi * Yi -- Carry Generation (2)
- Ci+1 = Gi + (Pi and Ci) -- Next Carry (3)
- Si = Xi ⊕Yi ⊕ Ci -- Sum Generation (4)

  Thus, for 4-bit adder, we can extend the carry bit, as shown below:
- C1 = G0 + P0 . C0 (5)
- C2 = G1 + P1 · C1 = G1 + P1 · G0 + P1 · P0 · C0 (6)
- C3 = G2 + P2 · G1 + P2 · P1 · G0 + P2 · P1 · P0 · C0 (7)
- C4 = G3 + P3 · G2 + P3 · P2 · G1 + P3 · P2 · P1 · G0 + P3 · P2 · P1 · P0 · C0 (8)

IV FIR FILTER DESIGN

Carry Look Ahead Adder is a kind of fast adder used in digital logic circuits. The CLA computes all the carry bits before the sum, which decreases the delay time to calculate the result of the larger value bits. The CLA solves the carry delay problem by predetermination of the carry signals in advance to the basis of the input signals. This technique was contrasted with the slow adder like RCA, where the adder should wait for the pervious carry to generate the specific result and carry bits. The CLA uses additional circuitry to generate carry bits in parallel, which eliminates time required to calculate the larger value bit result. The architecture of 4-bit CLA is shown in Fig. 2. CLA can be separated as two segments: Partial Full Adder (PFA) and the Carry Look-ahead Logic. The PFA produce propagate signals pi, generate signals gi and the sum output si and the carry-out bits ci +1 was generated by the look ahead logic circuit. The structure shows that Propagate P and generate G in a partial full-adder depends on the input bits only, the carry generator also not depends on its previous carry-in. As a result, once $C0$ is computed, $C4$ can reach stable state it does not want to wait for $C3$ to propagate.

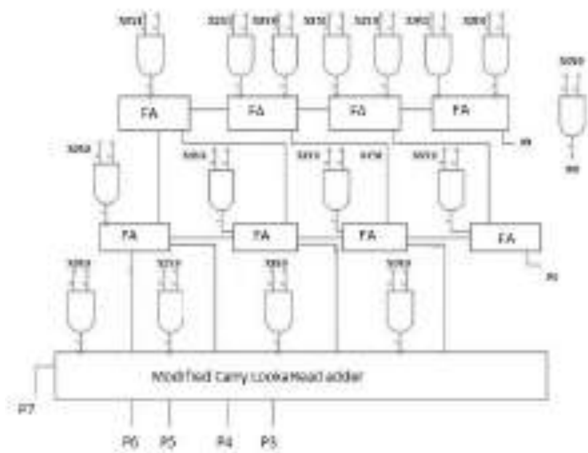

Figure 2: Proposed carry-look ahead adder in Multiplier

The multiplier is proposed by internal circuit of Modified Carry Look ahead Adder which consist of four partial full adder with XOR gates and NAND gate. In Figure 2 it shows the partial products has been taken to generate and propagate signal. These generate and propagate signal has been used in look ahead section to generate carry. Here the carry is eliminated from first section and directly utilizing the propagate operation and generate to the input block of look ahead section. The FIR filter consists of three main components:

A D-FF to implement a simple delay. A Multiplier is used to implement the filter coefficients. An Adder to sum the nodes at the end of each tap. Functional verification of all the adders and multiplier are performed and these modified architectures are applied in 4-tap FIR filter finally results are summarized.

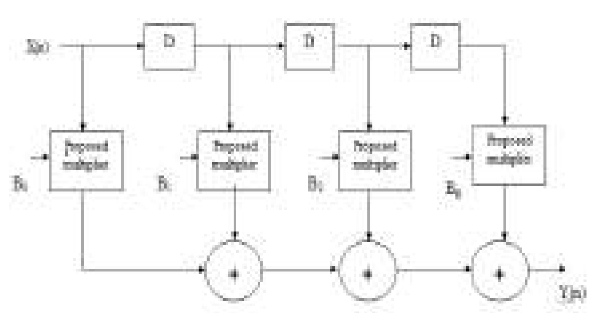

Figure 3: Direct form realization of FIR Filter based on proposed multiplier

Here X(n) is input filter coefficients and B0, B1, B2 and Bn are transfer function coefficients and Y(n) is output filter coefficient. Multipliers can be replaced with shift and add operation, that is MCM (Multiple Constant Multiplication) in which a set of constants (here h0, h1,… is multiplied with a variable (here x(n)). But the disadvantage in shift and add method is that the complexity and resource utilization is more. Another method is the use of transpose based structure.

V RESULTS AND DISCUSSION

A SIMULATION TOOL USED

Multiplier discussed above in this work is firstly designed using Xilinx 14.5 tool in Verilog HDL programming language. Different parameter like speed, power and delay of different multipliers are then analyzed.

B RTL VIEW OF CLA AND FIR

In CLA every bit in a binary sequence that to be added to the operation, the carry-look ahead logic will determine whether the bit pair will generate a carry or propagate a carry. This allows the circuit to "pre-process" the two numbers being added to establish the carry ahead of its time. Then, when the actual addition is performed, there is no delay comes out from the process when waiting for the ripple-carry effect operation.

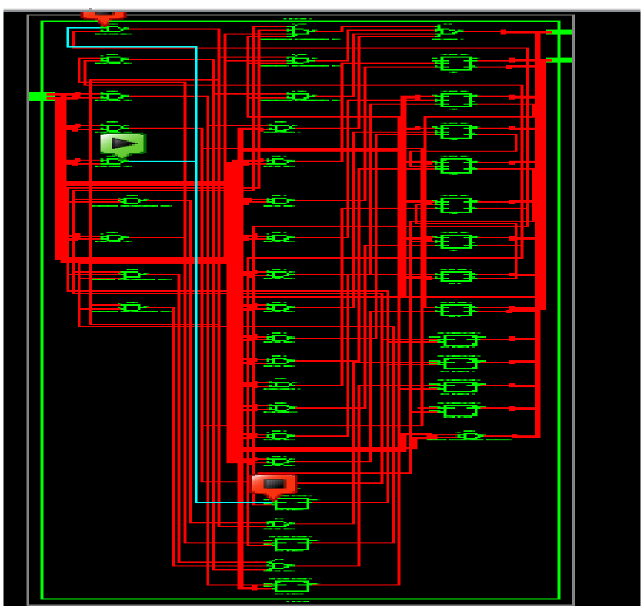

Figure 4: RTL view of carry-look ahead adder

C FIR

In FIR filter the result of the delay operates on the process of input samples. The values of hn are the coefficients in which they are used for multiplication operation. So that the output reaches at time and the summation operation is delayed for all the other samples that are multiplied by the appropriate coefficients.

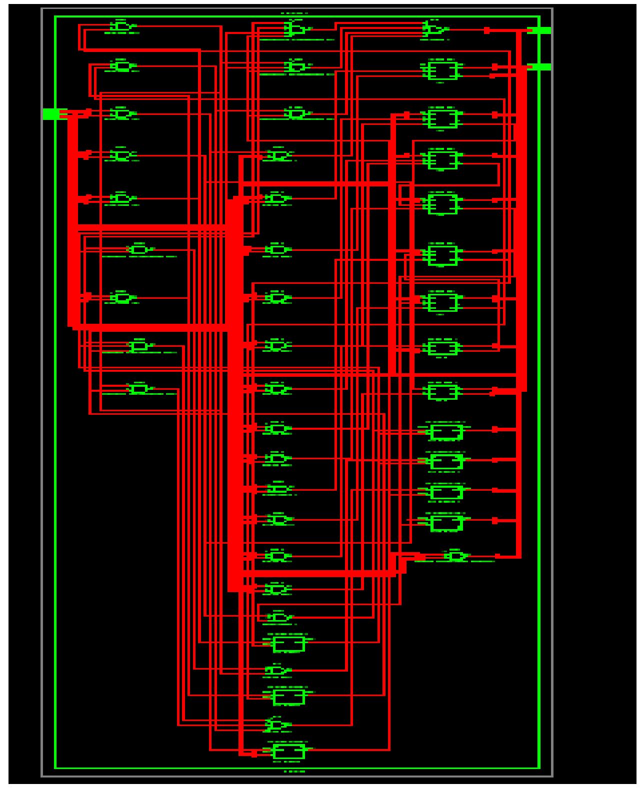

Figure 5: RTL view of FIR filter

VI SIMULATION RESULTS

In CLA every bit in a binary sequence that to be added to the operation, the carry-look ahead logic will determine whether the bit pair will generate a carry or propagate a carry. The simulations result of existing adder with the proposed CLA adder are shown in the figure 6 and figure 7.

Figure 6: Simulation result for carry look ahead adder

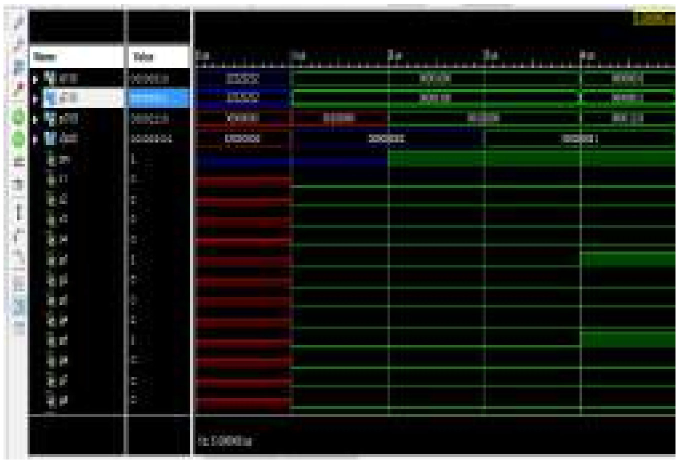

Figure 7: Simulation result for proposed CLA FIR filter

VII CONCLUSION

In this paper, the proposed design of digital FIR filter using modified multiplier based CLA is discussed. A basic analysis was performed in terms of area, power and delay. This multiplier based on CLA adder proved to be more efficient in terms of speed of operation compare to conventional multipliers. Based on the proposed multiplier, the architecture of direct form realization of digital FIR filter have been derived. The synthesis results show that the proposed FIR filter using modified multiplier based on carry look ahead adders achieves high speed and reduces the hardware cost with lesser power consumption related to conventional FIR filter with other multipliers. In future, the pipelining concept also extended to adder unit present in digital FIR filter to achieve better power and area reduction. Further the design of 16-tap FIR filter can be prolonged to n-tap that to be used in real time applications.

REFERENCES

[1] M. Agarwal, R. Barsainya, and T. K. Rawat, “Implementation of low power reconfigurable parametric equalizer with row bypassing multiplier on fpga,” in Computing, Communication and Automation (ICCCA), 2016 International Conference on. IEEE, 2016, pp. 1352–1357.

[2] S. Dhanasekaran, T. Thamaraimanalan, R. Sudha Anandhi and A. Mohanapriya, “Comparative Analysis of Low Power and High Speed Performance in 8-bit Different Multipliers,” Journal of Advanced Research in Dynamical & Control Systems, Vol. 10, 04-Special Issue, 2018 , pp. 89- 93.

[3] V. N. Kumar, K. R. Nalluri, and G. Lakshminarayanan, “Design of area and power efficient digital fir filter using modified mac unit,” in Electronics and Communication Systems (ICECS), 2015 2nd International Conference on. IEEE, 2015, pp. 884–887.

[4] E. Prabhu, H. Mangalam, and K. Saranya, “Design of low power digital fir filter based on bypassing multiplier,” International Journal of Computer Applications, vol. 70, no. 9, 2013.

[5] M. M. Mahmoud, D. A. El-Dib, and H. A. Fahmy, “Low energy pipelined dual base (decimal/binary) multiplier, dbm, design,” Microelectronics Journal, vol. 65, pp. 11–20, 2017.

[6] Z. Abid, H. El-Razouk and D.A. El-Dib, “Low power multipliers based on new hybrid full adders”, Microelectronics Journal, Volume 39, Issue 12, Pages 1509-1515, 2008

[7] Hasan Krad and Aws Yousif Al-Taie, “Performance Analysis of a 32-Bit Multiplier with a Carry-Look-Ahead Adder and a 32-bit Multiplier with a Ripple Adder using VHDL”, Journal of Computer Science 4 (4): 305-308, 2008

[8] M. Keerthi, “FPGA Implementation of Distributed Arithmetic for FIR filter”, IJERT Vol. 1, Issue 9, November- 2012.

[9] Bahram Rashidi, “Low Power FPGA Implementation of Digital FIR Filter based on Low Power Multiplexer Base Shift/Add Multiplier”, International Journal of Computer Theory and Engineering, Vol. 5, No. 2, April 2013.

[10] Mengxue Lei, “Design of High Speed FIR filter with Distributed Parallel Structure”, IEEE Information Technology, Networking, Electronic and Automation Control Conference- May 2016.

[11] Mohanty BK, Meher PK. A high-performance FIR filter architecture for fixed and reconfigurable applications. IEEE transactions on very large scale integration (vlsi) systems. 2016 Feb; 24(2): 444–-52.

[12] R. M. Deshmukh and R. Keote, “Design of polyphase fir filter using bypass feed direct multiplier,” in Communications and Signal Processing (ICCSP), 2015 International Conference on. IEEE, 2015, pp. 1640–1643

[13] Vishwanath BR, Theerthesha TS. Multiplier using canonical signed digit code. International Journal for Research in Applied Science & Engineering Technology (IJRASET). 2015; 3(5): 415–20.

[14] Kamble P, Deote N, Wanjari N, Gaikwad S. Implementation of FIR filter structure for audio application using XilinxSystem generator. International Journal of Advanced Research in Computer Science and Software Engineering. 2015; 5(1): 762–5.

[15] Yan and Chen, “Low-cost low-power bypassing-based multiplier design,” in Circuits and Systems (ISCAS), Proceedings of 2010 IEEE International Symposium on. IEEE, 2010, pp. 2338–2341.

[16] N. T. A. El-Kheir, M. S. El-Kharashi, and M. A. El-Moursy, “A low power programmable fir filter using sharing multiplication technique,” in IC Design & Technology (ICICDT), 2012 IEEE International Conference on. IEEE, 2012, pp. 1–4.

[17] Asadi, P. and K. Navi “A novel high-speed 54-54-bit multiplier”, Am. J. Applied Sci., 4 (9): 666-672, 2007

[18] Wakerly, J.F., 2006. Digital Design-Principles and Practices. 4th Edn. Pearson Prentice Hall, USA.ISBN: 0131733494.

[19] B. Ramkumar and Harish M Kittur, “Low power and area efficient carry select adder”, IEEE Transactions on Very Large Scale Integration (VLSI) Systems, vol 20, no. 2,pp. 371-375,Feb 2012

[20] S. Murugeswari and S.K. Mohideen, “Design of Area Efficient and Low Power Multipliers using Multiplexer based Full Adder”, Proceedings of 2nd International Conference on Current Trends in Engineering and Technology, pp. 388-392, 2014.

CNN algorithm for plant classification in deep learning

Article *in* Materials Today: Proceedings · March 2021

DOI: 10.1016/j.matpr.2021.01.847

1 author:

Dhanasekar Subramaniyam
Sri Eshwar College of Engineering

Materials Today: Proceedings 46 (2021) 3684–3689

Contents lists available at ScienceDirect

Materials Today: Proceedings

journal homepage: www.elsevier.com/locate/matpr

CNN algorithm for plant classification in deep learning

G. Valarmathi [a,*], S.U. Suganthi [a], V. Subashini [a], R. Janaki [a], R. Sivasankari [a], S. Dhanasekar [b]

[a] ECE, Sri Sairam Institute of Technology, Chennai 600044, India
[b] ECE, Sri Eshwar College of Engineering, Coimbatore 641202, India

ARTICLE INFO

Article history:
Received 22 November 2020
Received in revised form 22 January 2021
Accepted 26 January 2021
Available online 1 March 2021

Keywords:
Plant classification
kNN algorithm
SVM classifier
Feature extraction
CNN algorithm

ABSTRACT

The prior methodology of characterizing the plants for dependent on surface based order and another strategy depends on KNN classifier. This paper presents qualities examination of plants utilizing picture preparing methods for robotized vision framework utilized at horticultural field. In farming examination, the programmed plant attributes recognition is fundamental one in observing huge field. The proposed dynamic framework uses picture content portrayal and regulated classifier sort of neural organization. This will naturally distinguish the plant species when we import its picture as info. Picture preparing strategies for this sort of choice investigation includes pre-processing and characterization stage. At Processing, an info picture will be resized and commotion expulsion procedure is applied. At definite stage the neural organization orders the pictures as farming plant, harmful plant and therapeutic plant separately. At that point it will show the attributes of each plant.

Selection and peer-review under responsibility of the scientific committee of the International Conference on Materials, Manufacturing and Mechanical Engineering for Sustainable Developments-2020.

1. Introduction

At present, Artificial Intelligence (AI) plays a vital function in Computer Vision, Robotics, and Digital Marketing and in the field of Medical Imaging. Man-made awareness was generally created for acquiring human intelligence to machines.

The term Machine Learning (ML) is a branch of Artificial Intelligence (AI), and furthermore logical investigation of the calculation and a factual model that play out a particular test without unequivocally modified, depending on the deduction and examples[1]. The learning algorithms used in AI are supervised (learning with master) which uses set of mapped values between input and output, unsupervised (learning without a master) which uses no mapping between input output pairs and Reinforcement Learning. Machine learning handles limited number of datasets whereas deep learning handles maximum number of datasets. Convolution Neural Network (CNN) and Recurrent Neural Network (RNN) finds its applications in wide variety of diversified fields. Deep learning networks can be simulated using mathematical modelling in such a manner that data sources have been taken care by PC and machine is made to be trained accordingly to improvise its yield (Fig. 1).

* Corresponding author.
E-mail address: Valarmathi.ece@sairamit.edu.in (G. Valarmathi).

2. Existing method

The plant classification recently proposed was a technique based on KNN classifier. There are various steps in this method: A. Image acquisition B. Pre-processing C. Image Segmentation D. Feature Extraction E. Image Classification (Fig. 2).

2.1. Picture obtaining

Diseased influenced groundnut picture is photographed using high resolution imaging device [3,6]. To disclosure the specific infection influenced, the RGB shade of the gathered picture is need to be unmistakably noticeable. This resembles very good quality cell phone. These pictures are warehoused in both of cycle capable picture expansion in the information base.

2.2. Pre-preparing

Picture Prior-handling is upheld out to build the nature of base picture and dispense with the undesirable clamor in picture proceeded by clipping and smoothing of the picture. The picture enhancement is completed to build the differentiation. The info picture is changed into bifold concealed picture.

https://doi.org/10.1016/j.matpr.2021.01.847
2214-7853/
Selection and peer-review under responsibility of the scientific committee of the International Conference on Materials, Manufacturing and Mechanical Engineering for Sustainable Developments-2020.

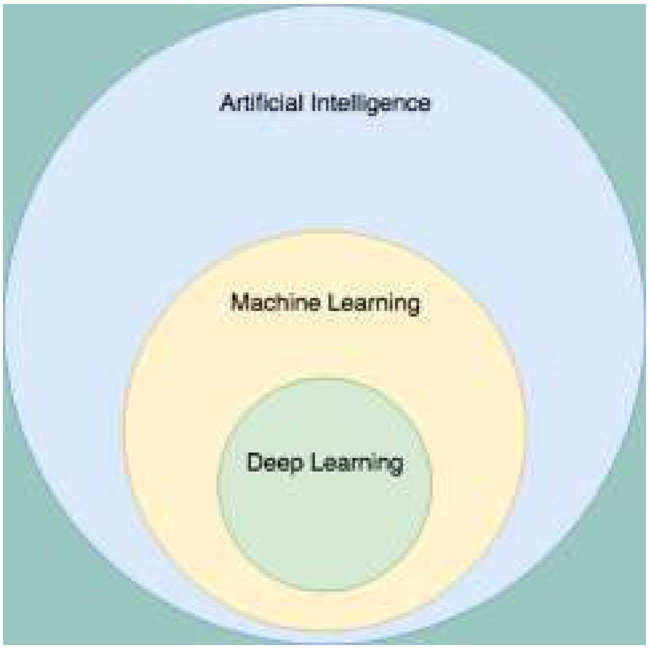

Fig. 1. Subsets of artificial intelligence.

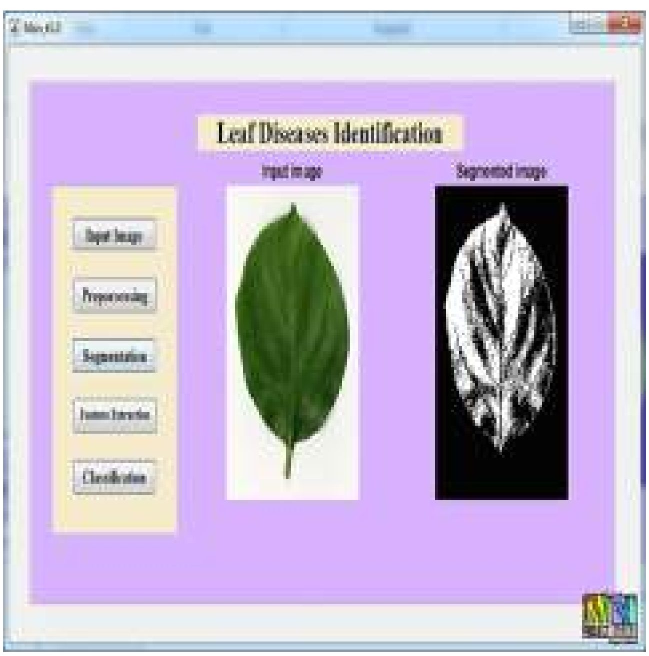

Fig. 2. Leaf disease identification.

2.3. Picture segmentation

Image division is the succession of steps associated with isolating a computerized picture into various fragments. The goal of the detachment is to make it straightforward or potentially adjust the image of a picture into more significant and easy to inspect. Picture division is basically used to put articles and limits in the pictures. In this stage Binary veiled picture is changed over into HSV picture.

2.4. Highlight extraction

In element extraction strategy highlights, for example, shading, surface, morphology and game plan are utilized in groundnut sickness recognition. The strategies utilized in shading co-event are at first the plants RGB pictures are changed over into HSV shading. For gathering of shading co-event medium every pixel plot is handled which results into three shading co-event lattice one for every one of HSV. Utilizing Fast Feature strategy to separate the highlights from the given input leaf picture [5].

2.5. Picture classifier

KNN algorithm is the strategy used for grouping and classification. The yield depends on whether k-NN is utilized for requesting or relapse In kNN portrayal, the last yield is a period collusion. A thing is portrayed by an unbelievable scope of its neighbours, with the article being relegated to the class commonly typical among its k nearest neighbours where k is a positive entire number, normally low value. If k = 1, by then the article is basically picked to the class of that only one nearest neighbour [7] (Fig. 3).

Algorithm to implement kNN (k-Nearest Neighbors Algorithm) [2]

1. Start the procedure.
2. Info Red Green Blue gray values picture to HSV picture.
3. Peruse estimation of K.
4. Sort of distance (V) & preparing information.
5. Register the difference between input test and the preparation tests.
6. Locate the K closest neighbors (v) to the preparation information.
7. Set most extreme name class of K to prepared information.
8. In the event that information isn't ordered give preparing for input picture for arrangement.
9. On the off chance that information is arranged to establish knn classifier.
10. Anticipate the infection Leaf.
11. Stop.

3. Proposed method

Critical learning is a type of AI figuring in which consist of consecutive layers. Every layer utilizes the output from the past layer as data. The learning cycle can be execution, managed or semi-controlled. LeCun et al. define the critical learning as a portrayal learning framework Portrayal figuring's involves the improvements to get the appropriate information. de Significant learning need not disengage the component and the classification considering the way that the framework subsequently isolates the features while setting up the model. It is utilized in many advanced zones, for example, picture handling, picture reclamation, discourse acknowledgment, normal language preparing and bioinformatics. CNN is favoured as a profound learning strategy in this investigation. CNN, which can undoubtedly recognize and order objects with insignificant prior-handling, is effective in dissecting really seen pictures and can without much of a stretch separate the necessary highlights with its multi-layered structure [4] (Fig. 4).

3.1. Convolutional layer

Convolution layer gives the name CNN. In this layer, a progression of numerical activities are performed to remove the element guide of the info picture. The information picture is diminished to a more modest range utilizing a filter (Fig. 5).

The filter is moved bit by bit beginning from the top of the picture. For every progression, the qualities in the picture are duplicated by the estimations of the filter and the outcome is added. Another lattice with a more modest size is made from the information picture.

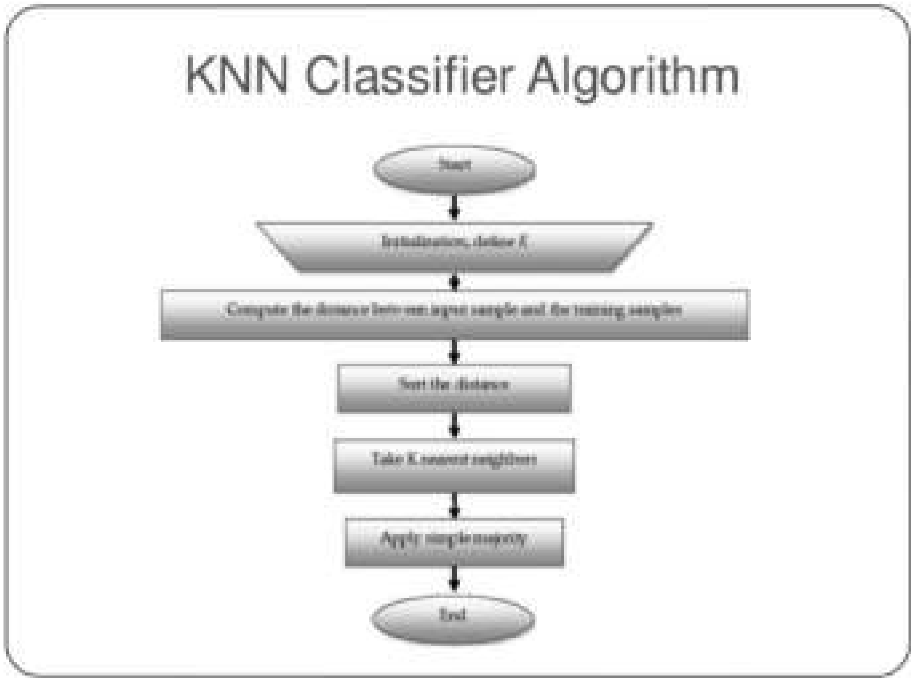

Fig. 3. Flowchart for KNN.

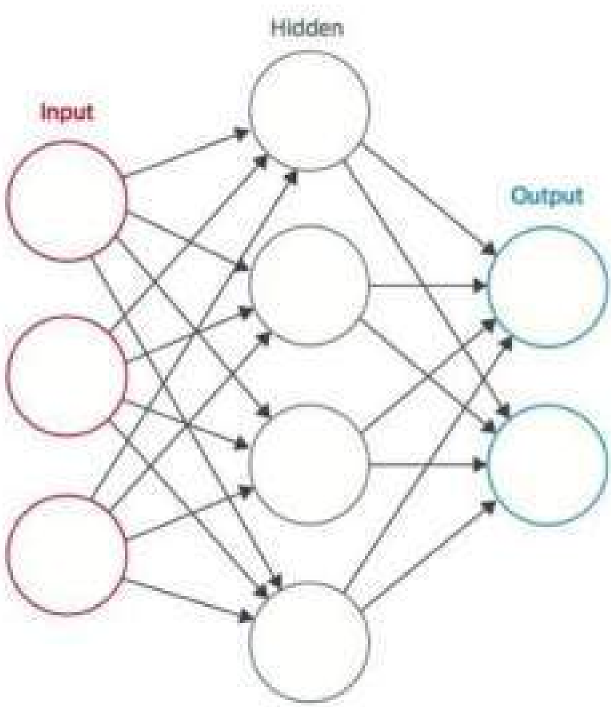

Fig. 4. Convolutional neural network layers.

3.2. Pooling layer

The pooling layer is typically set next to the convolution layer. The range of the yield network acquired from the convolution layer is decreased in this layer. In spite of the fact that filter of various sizes can be utilized in the pooling layer, by and large 2×2 size filter is utilized. Here, pooling filter with step size of 2 has been applied. The highest value in sub windows forms anew matrix, which is referred to as max pooling.

3.3. Activation layer

In artificial neural organizations, the actuation work gives a curvilinear connection among the info and yield layers. It influences the organization execution. The activation function gives the non linear learning of the model. A few enactment capacities, for example, direct, sigmoid, exaggerated digression, exist, however the nonlinear ReLU (Rectified Linear Unit) actuation work is normally utilized in CNN. In ReLU, values under zero are changed to zero, while values more noteworthy than zero are unaltered [1] (Fig. 6).

f(x) = 0, if x < 0. ×, in any case

3.4. Fully connected layer

The last acquired grid, next to the convolution, pooling and enactment activities, is taken care of into the completely associated layer as info. This layer performs Acknowledgment and segregation. Here, LVQ calculation is utilized in preparing the information classification. Algorithm for CNN based Classification:

1. Apply convolution channel in first layer.
2. The affectability of channel is decreased by smoothing the convolution channel (i.e) subsampling.
3. The sign exchanges starting with one layer then onto the next layer is constrained by enactment layer.
4. Attach the preparation time frame by utilizing redressed straight unit (RELU).
5. The neurons in continuing layer is associated with each neuron in resulting layer.
6. During preparing Loss layer is added toward the finish to give an input to neural organization.

4. Result

Thus, plant classification using cnn algorithm was performed and when the input image is given it classifies whether it is a agricultural leaf, herbal leaf or a poisonous leaf. The sample output is shown below.

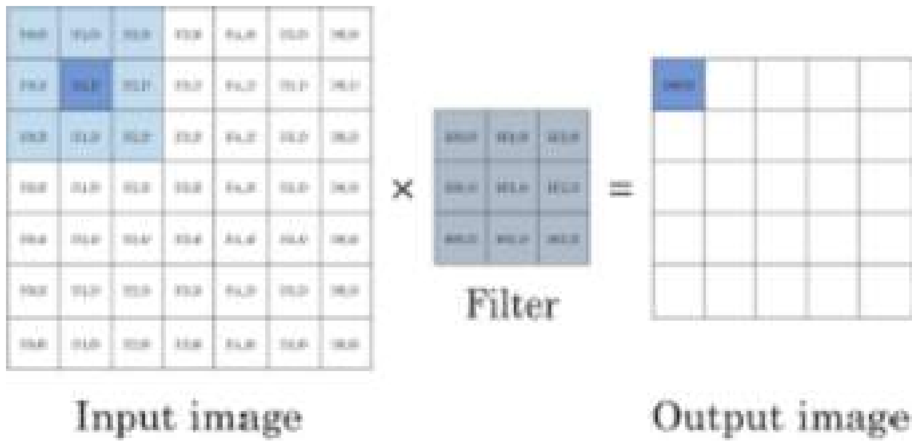

Fig. 5. Convolutional neural network architecture.

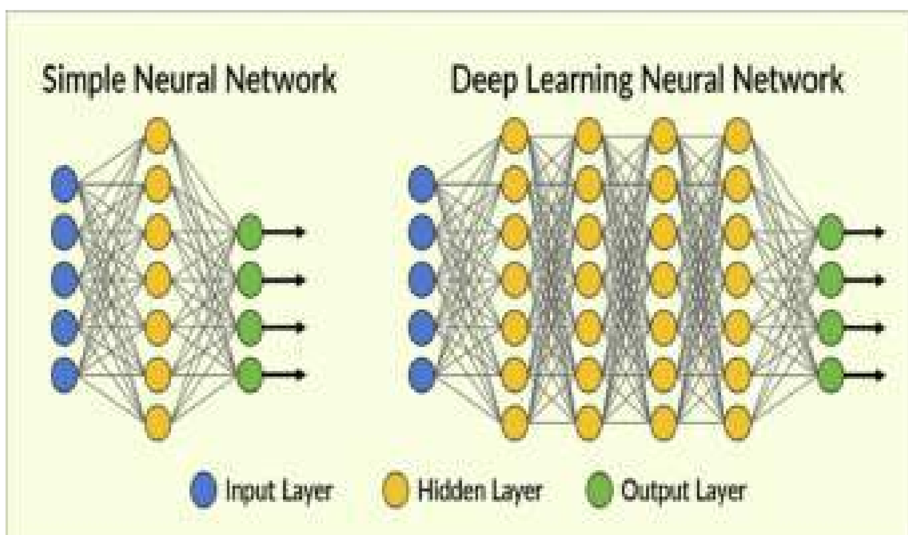

Fig. 6. Difference between basic neural network and deep learning network.

4.1. Input

Fig. 7.

4.2. Output

Fig. 8.

5. Future work

The 3D laser sensor has additionally demonstrated that it is hearty against enlightenment and environmental conditions, which empowers the robot to work dependably at any climate condition. The FX6 sensor by Nippon Signal is a lightweight 3D laser sensor. MEMS based 3D LIDAR sensor FX6 significantly helps in agricultural domain to categorize the plants as poisonous, herbal or edible. This approach finds pretty much efficient than traditional approaches like vision or stereo vision technology. The quality of the depth values depends on the color of the material reflecting the emitted light and some sensors have problems with moving objects by showing motion blur effects. The shell of the FX6 is made of aluminium alloy material and infrared band pass filter improve the overall strength. The 3D sensor is comprised of lightweight material which find its application in robotics under any weather conditions in agricultural field.

Fig. 7. Screen shot of input.

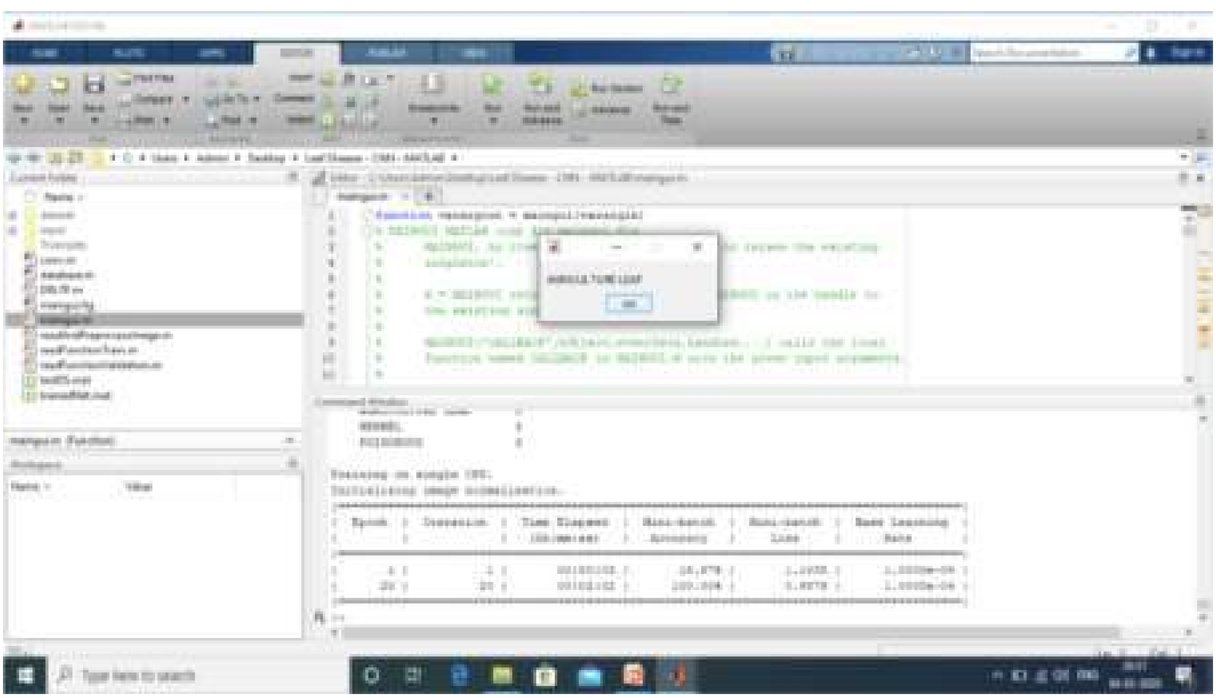

Fig. 8. Screenshot of output.

CRediT authorship contribution statement

G. Valarmathi: Conceptualization, Methodology. **S.U. Suganthi:** Data curation, Writing - original draf. **V. Subashini:** Visualization, Investigation. **R. Janaki:** Supervision. **R. Sivasankari:** Software, Validation. **S. Dhanasekar:** Writing - review & editing.

Declaration of Competing Interest

The authors declare that they have no known competing financial interests or personal relationships that could have appeared to influence the work reported in this paper.

References

[1] W. Huang, Q. Guan, J.H. Luo, J. Zhang, J. Zhao, D. Liang, L. Huang, D. Zhang, New optimized spectral indices for identifying and monitoring winter wheat diseases, IEEE J. Selected Top. Appl. Earth Observation Remote Sensing 7 (6) (2014).

[2] K. Thangadurai, K. Padmavathi, "Computer Visionimage Enhancement For Plant Leaves Disease Detection", 2014 World Congress on Computing and Communication Technologies.

[3] Monica Jhuria, Ashwani Kumar, Rushikesh Borse, "Image Processing For Smart Farming: Detection Of Disease And Fruit Grading", Proceedings of the 2013 IEEE Second International Conference on Image Information Processing (ICIIP-2013

[4] Zulkifli Bin Husin, Abdul Hallis Bin Abdul Aziz, Ali Yeon Bin Md Shakaff Rohani Binti S. Mohamed Farook, "Feasibility Study on Plant Chili Disease Detection

Using Image Processing Techniques", 2012 Third International Conference on Intelligent Systems Modelling and Simulation.
[5] K.P. Ferentinos, Deep learning models for plant disease detection and diagnosis, Comput. Electron. Agric. 145 (2018) 311–318, https://doi.org/10.1016/j.compag.2018.01.009.
[6] M. Ramakrishnan, Sahaya Anselin Nisha. A, "Groundnut Leaf Disease Detection and Classification by using Back Probagation Algorithm", IEEE ICCSP 2015 conference.
[7] L. Saxena, L. Armstrong, "A survey of image processing techniques for agriculture," 2014.

PAPER • OPEN ACCESS

Adaptive Beam forming algorithms for wireless Communication using LABVIEW

To cite this article: M. Ramya *et al* 2021 *IOP Conf. Ser.: Mater. Sci. Eng.* **1084** 012046

Adaptive Beam forming algorithms for wireless Communication using LABVIEW

M.Ramya[1], V.Thamizharasan[2] and V.Parthipan[3]
[1,2] Assistant Professor, ECE, Erode Sengunthar Engineering College, Erode.
[3] Assistant Professor, ECE, Sri Eshwar College of Engineering, Coimbatore.
eceramya25@gmail.com, ecetamil@gmail.com, parthivelusamy@gmail.com,

Abstract: Adaptive antenna arrays are being developed to cope with the high capacity requirement of the 5G wireless communications systems. As adaptive antenna arrays focus narrow high gain beams towards the desired users and nulls towards the unwanted interferers, both coverage and capacity of the network can be improved. The capacity of a Wireless network depends on the size of the antenna array, the beam pattern used and the speed with which the beam-former and Direction of Arrival estimator. To achieve the capacity demand required by a growing number of subscribers, smart antenna systems are used in the present cellular systems. In these systems cell-splitting and sectoring techniques are adopted to improve the capacity. The main disadvantage of these techniques is that decrease in trunking efficiency. It has been established that the smart antenna systems will provide a better solution for the capacity problem. Development of smart antenna includes design of antenna array and adjusting the incoming signal by changing the weights of the amplitude as well as phase using efficient Digital Signal processing algorithms using LabVIEW.

Keywords: Antenna Array, Directivity, Microstrip, Radiation Pattern, and LABVIEW

1. INTRODUCTION

As of late there has been a touchy development in the quantity of wireless clients, especially in the region of portable communication. In future remote portable frameworks will be more refined and more inescapable. This development has set off a huge interest for limit as well as better inclusion and higher caliber of administration.
A few new advances have been investigated and sent in such manner to utilize the restricted assets. One approach to improve limit is by utilizing the idea of cell innovation, which includes separating an enormous inclusion zone into little hexagonal cells. Accordingly, a solitary high force transmitter is supplanted with many low force transmitters. Every phone is assigned a bunch of recurrence channels that are not quite the same as those designated to the neighboring cells[4]. In any case, similar arrangement of frequencies can be reused by another cell as long as they are isolated alright not to cause obstruction. Since every one of these cells reuses the recurrence range, a huge expansion in limit can be accomplished.
Anyway close to home remote interchanges are getting increasingly famous and are proceeding to develop at an outstanding rate. Consequently, new innovations like cell are needed in the zone of portable interchanges to oblige future limit needs. Keen radio wires or versatile exhibits those are progressively ready to adjust to the changing traffic necessities. Insightful recieving wires, generally executed at the base

IOP Conf. Series: Materials Science and Engineering 1084 (2021) 012046 doi:10.1088/1757-899X/1084/1/012046

station, emanate thin bars to serve various clients. However long the clients are all around isolated spatially a similar recurrence can be reused, regardless of whether the clients are in a similar cell.
LABVIEW is a stage and improvement climate for a visual programming language from National instruments. LabVIEW is ordinarily utilized for information obtaining, instrument control modern computerization, Bio signal observing, Home mechanization framework, Mobile correspondences.

2. SMART ANTENNAS

Limit and execution in versatile correspondence frameworks are ordinarily confined by multipath also co-channel impedance. In multipath, when a sent sign in the engendering climate is reflected from various hindrances. This offers Elevation of various signs coming from different bearings. Meanwhile the multipath signals track various ways, they have various stages when they are showing up at the collector [5-13]. The outcome is corruption in sign quality when they are joined at the recipient because of the stage bungle. Co-channel impedance happens between two signals that work at a similar recurrence. In cell correspondence the impedance is typically brought about by a sign from an alternate cell involving a similar Frequency band.
Smart antenna is solitary of the most encouraging innovations that will empower capacity by lessening multipath and co-channel obstruction viably. This is finished coordinating the radiation the ideal way just and adjusting to changing traffic situations or sign situations. A assortment of transmitting components organized as an exhibit is utilized by Smart antenna. The signals as of these components are joined to frame a mobile or switchable pillar design that follows the ideal client. The clusters themselves are not brilliant in a Smart antenna scheme, it's the computerized signal handling that brands it smart. The way toward consolidating the signs and afterward centering the radiation a specific way is frequently alluded to as advanced beamforming. This stint will be broadly utilized in the accompanying segments.

The early Smart antenna scheme were intended for use in military applications towards smother meddling or sticking signs from the foe. Meanwhile impedance concealment was an element in this framework, this expertise was obtained toward relate to individual remote correspondences where obstruction was restricting the quantity of clients that an organization could deal with. It is a significant test to apply savvy reception apparatus innovation to individual remote interchanges since the traffic is denser. Additionally, the period accessible for complex calculations is restricted. Smart antenna scheme has be that as it may; become a utilitarian reality for cell interchanges frameworks by dispatching productive ease, digital preparing segments and arising programming based procedures.

2.1 Classification Of Smart Antennas

Fundamentally there are two ways to deal with actualizing radio wires that change their recieving wire design progressively to alleviate obstruction and multipath impacts while expanding inclusion and reach. They are the,
Switched beam •
Adaptive Arrays •
Conversely with the completely versatile approach[1], the Switched Beam method is more straightforward. Contrasted with ordinary omni-directional radio wire frameworks or area based frameworks, it bids a generous improvement in organization transmission capacity. In this method, as appeared in figure 2.1, a reception apparatus exhibit produces covering radiates that cover the encompassing zone. ase station chooses the ideal heading of the bar when an approaching sign is recognized and afterward moves to that bar to communicate through the user.

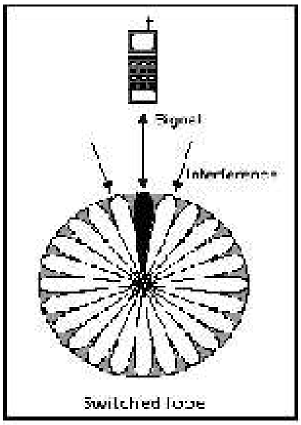

Figure 2.1 Beam formation of switched beam antenna systems

The Adaptive cluster framework is the "more intelligent" of the two methodologies. This framework tracks the portable client persistently by moving the ideal pillar towards the client and simultaneously shaping nulls undesired headings as appeared in figure 2.2. Like exchanged bar frameworks, they likewise consolidate exhibits.

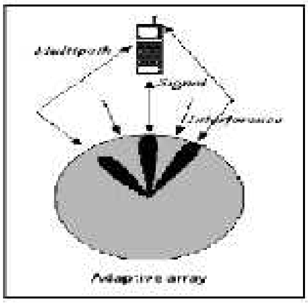

Figure 2.2 Beam formations for adaptive array antenna system

Typically, a weight remains duplicated by the acquired sign from every one of the spatially disseminated radio wire components. The loads are intricate in nature, and the plentifulness and stage are modified. These signals remain joined to yield the cluster yield. These mind boggling loads are figured by a confounded versatile calculation, which stands pre-customized into the advanced sign handling unit that deals with the signal transmitted by the base station.

3. SIGNAL PROCESSING ALGORITHMS

3.1. Least Mean Square Algorithm

LMS stands a calculation for direct versatile sifting that normally comprises of two central cycles called separating and variation. The LMS calculation is a versatile calculation that utilizes the most fair angle based cycle.

The slope vector gauges from the accessible information are utilized by the LMS calculation. LMS utilizes an iterative technique that amends the weight vector progressively toward the inclination vector's negative, which eventually adds to the base mean square mistake. The LMS calculation is moderately straightforward contrasted with different calculations; it doesn't need ascertaining the connection function.Consider a Uniform Linear Array (ULA) with N isotropic components, which frames the indispensable piece of the versatile pillar shaping framework as appeared in the figure underneath [3].The output of the antenna array is given by equation,

$$x(t) = s(t)a(\theta_0) + \sum_{i=1}^{N_u} u_i(t)a(\theta_i) + n(t)$$

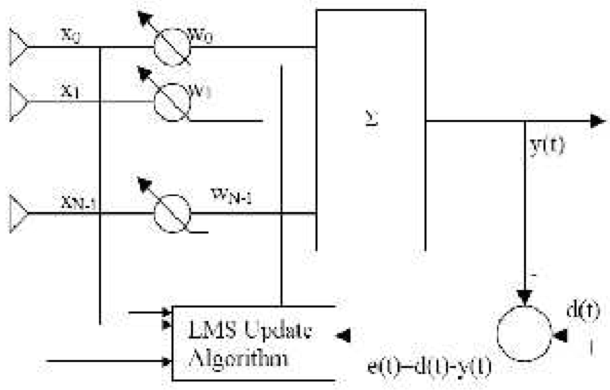

Figure 3.1 LMS adaptive beam forming network

d(t) ,e(t) and y(t) is a desired signal error . The LMS algorithm initiated with some arbitrary value for the weight vector is seen to converge and stay stable for $0 < \mu < \lambda max$

3.2 RECURSIVE LEAST SQUARE ALGORITHM

RLS calculation is an upgraded form of LMS. The most inalienable limit of RLS is its high intermingling rate when contrasted and its partner LMS. The purpose for its fast union rate is on the grounds that the blunder anytime of time is free of the factual stuffs of the signal. As opposed to LMS, RLS offers significance to the past info flags in anticipating the following input[1]. The calculation refreshes the autocorrelation grid for the following moment with the guide of the autocorrelation network determined for the current moment. Henceforth they stay called by way of Recursive. Just least square mistakes are determined thus their name. It experiences the disadvantage of having high computational unpredictability
Error calculation: $\alpha(n) = d(n)\text{-}wt(n\text{-}1)*x(n)$
Adaptive weights: $w(n) = w(n\text{-}1)+\alpha(n)*g(n)$
$\alpha(n)$ is the forgetting factor.

4. ARRAY CONFIGURATIONS

4.1 Linear Array

This cluster incorporates N-components organized in z-bearing. Expecting that all components have indistinguishable amplitudes yet each succeeding component has a β reformist stage lead current excitation comparative with the first one. A variety of indistinguishable components all of indistinguishable extent and each with a reformist stage are alluded to as a uniform cluster [2].

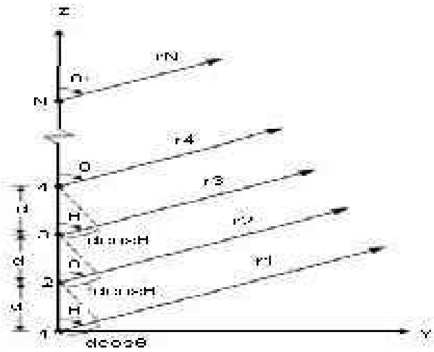

Figure 4.1 Linear array

The array factor is given by (4.1) to (4.3),

$$AF = 1 + e^{+j(kd\cos\theta+\beta)} + e^{+j2(kd\cos\theta+\beta)} + e^{+j3(kd\cos\theta+\beta)} + \cdots + e^{+j(N-1)(kd\cos\theta+\beta)} \quad (1)$$

$$AF = \sum_{n=1}^{N} e^{+j(n-1)(kd\cos\theta+\beta)}$$

----- (2)

This can be written as

$$AF = \sum_{n=1}^{N} e^{+j(n-1)\psi} \quad (2)$$

Where, $\Psi = k\, d \cos\theta + \beta$

The maximum radiation occurs at $\psi = 0$ hence $\beta = - k\, d \cos\theta$.

4.2 The Rectangular Microstrip Patch

The rectangular fix is normally planned with the goal that it can work close to a reverberation recurrence. This infers that the fanciful piece of the perplexing impedance is zero.

The bordering fields go about as an extra length to the fix. Half-wave fix length should be not exactly a half frequency to make up for the length presented by the bordering fields[2]. The measure of length, condition (4), presented relies upon the substrate media, stature and width of the fix. λ is the free-space frequency, λ_d is the frequency in the dielectric, and ε_r is the substrate dielectric consistent.

$$L \approx 0.49\,\lambda_d = 0.49\,\frac{\lambda}{\sqrt{\varepsilon_r}} \quad (3)$$

The example of a rectangular fix recieving wire is fairly expansive with a most extreme bearing typical to the plane of the radio wire. Example calculation for the rectangular fix is effortlessly performed by first speaking to periphery electric fields utilizing

$$M_s = 2E_a \times \hat{n},$$

wherever Ea is the periphery electric field. The element of 2 arises from the picture of the attractive flow in the electric ground plane if t is thought to be little.

$$E_\theta = E_o \cos\phi . f(\theta,\phi)$$
$$E_\phi = -E_o \cos\theta \sin\phi . f(\theta,\phi) \quad (4)$$

In equation (4), β stays the free-space stage consistent, the principal factor in condition is the example factor for a uniform line wellspring of width W in the y-heading. The subsequent factor is the exhibit factor for a two-component cluster along the x-pivot relating to the edge openings.

IOP Conf. Series: Materials Science and Engineering 1084 (2021) 012046 doi:10.1088/1757-899X/1084/1/012046

Distinctive impedance of a rectangular square antenna differs starting 100 to 400 Ω. Through widening the spot, the input impedance be able to be condensed. Aimed at a square spot with L = W, the L/W factor now equation (5) develops 1, then the input impedance develops a drive of the dielectric constant. For half wave patch,

$$Z_A = 90 \frac{\varepsilon_r}{\varepsilon_r - 1}\left(\frac{L}{W}\right)^2 \Omega \tag{5}$$

Nearby are dissimilar kinds of methods for nourishing the patches, viz., enquiry fed, Microstrip edge feed through quarter wave alterations, microstrip edge feedstuff with gap, two layer feed, etc. Equation (6) is the input resistance of a spot if the feeding net is edge feedstuff.

5. RESULTS AND DISCUSSIONS

5.1 SIMULATION RESULTS OF MICROSTRIP ARRAY

5.1.1 Lms Algorithm

The LMS algorithm has been simulated for adaptive arrays. Specifications for the arrays, input signal, interference are as follows[4]. The desired signal is arbitrarily chosen as sinusoidal wave of unit amplitude at an angle θ_o (say 30^o). The interference signal is also arbitrarily chosen as sinusoidal wave of amplitude less than unity, considering the signal to interference ratio SIR, at an angle θ_i (say 0^0). The value of μ is considered as 0.0208. The weights are initialized to zeros.

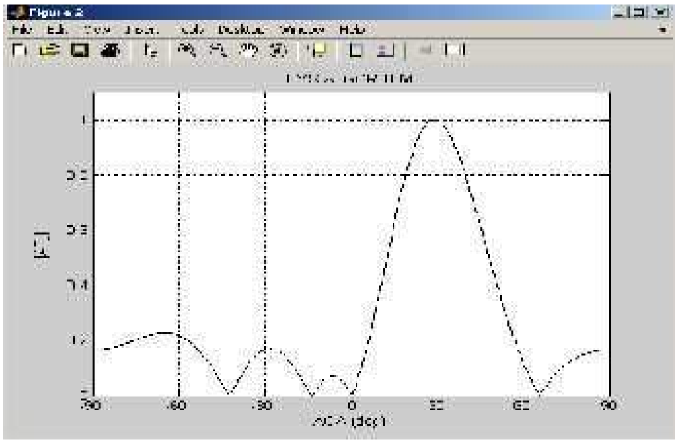

Figure 5.1 Radiation Pattern

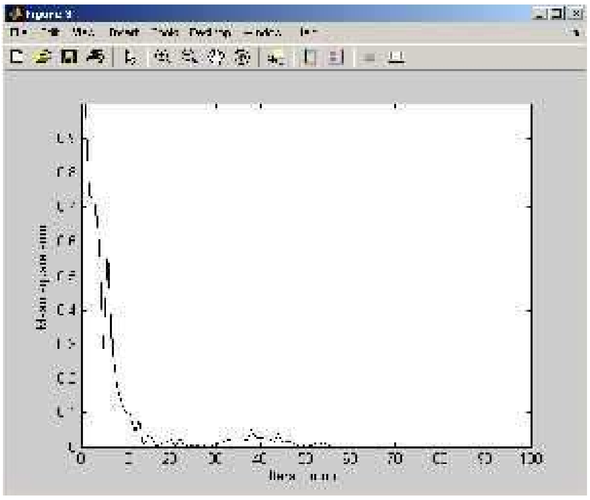

Figure 5.2 Error plot

5.1.2. Matlab Output

LINEAR ARRAY ANTENNA WITH ONE INTERFERE ANGLE

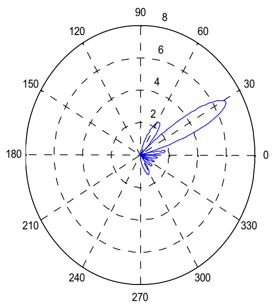

Figure 5.3 polar plot

How many element do you want in uniform linear array? **8**
What is the desired users AOA (in degrees)? **30**
What is the interferers AOA(in degrees)? **45**
Hpbw=**9.1673**
Mu=**0.0180**
The rectangular plot shows that the maximum gain produced at the desired angle and produce nulls in the interference angle at slow convergence but the gain is very small value when compare to isotropic element array.

5.1.3. Rls Algorithm
We can construct the array steering vector for the angle of arrival of 30^o and the interference angle is 0^o. After multiplying the steering vector by the signal $S(k)$ we can then find the correlation matrix.

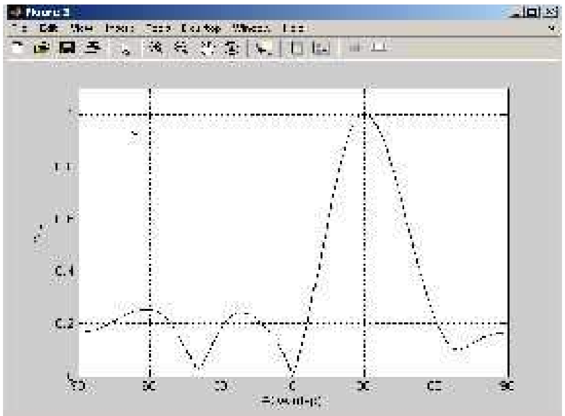

Figure 5.4 Radiation pattern

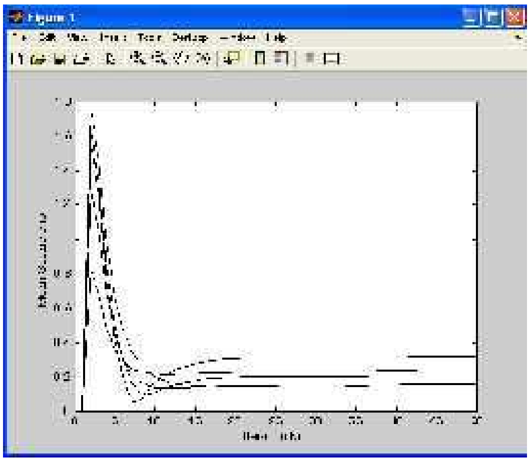

Figure 5.5 Error plot weighted RLS

5.1.4 Linear Array Antenna With Two Interfere Angle

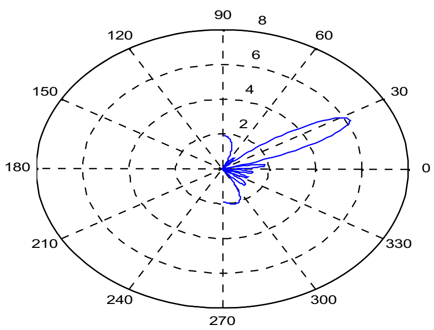

Figure 5.6 Polar plot

How many element do you want in uniform linear array? **8**
What is the desired users AOA (in degrees)? **30**
What is the interferers AOA 1(in degrees)? **45**
What is the interferers AOA 2(in degrees)? **6**

The benefit of the RLS algorithm over LMS is that a broad correlation matrix no longer needs to be inverte d. The recursive equations allow the inverse of the correlation matrix to be easily modified. Also the RLS a lgorithm converges much faster than the LMS algorithm.

5.1.5 Comparison Table

By using MATLAB, the various adaptive algorithms are simulated with the microstrip uniform linear array and the above tabulation is obtained. From the table we conclude that the RLS outperforms than LMS algorithms

Angle of arrival Degrees		No. of Elements	LMS		RLS	
Desired Angle	Interference angle		HPBW degrees	No.of iterations	HPBW degrees	No.of iterations
30	0	8	16.64	21	10.31	6
60	45		16.23	51	7.62	7
30	0	16	10.17	52	6.72	9
60	45		14.21	52	12.52	9

5.*1.6 BLOCK DIAGRAM FOR LMS AND RLS ALGORITHM USING LABVIEW*

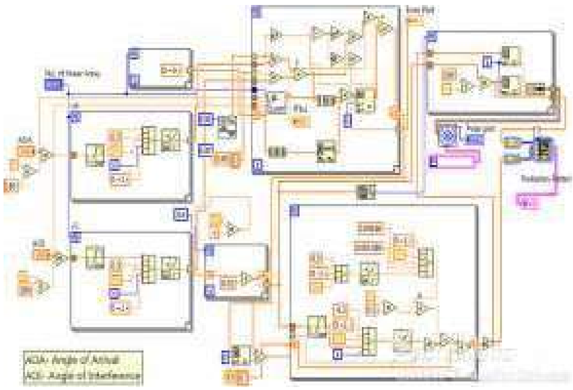

Figure 5.7 Block Diagram for LMS and RLS Algorithm Using LabVIEW

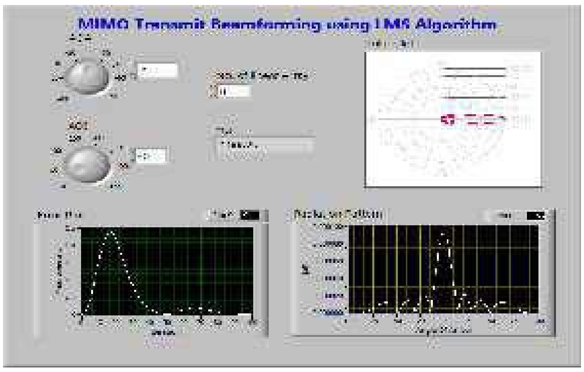

Figure 5.8 Output for LMS using LabVIEW

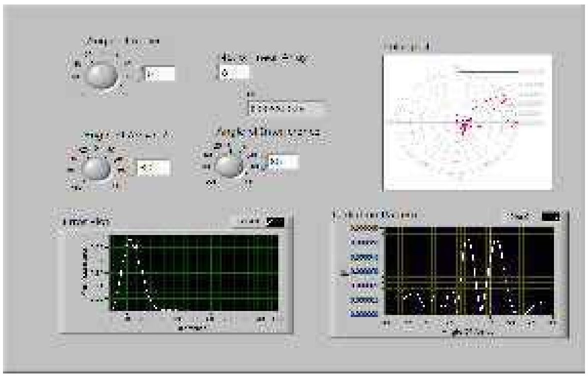

Figure 5.9 Output for RLS using LabVIEW

6. CONCLUSION

The standard LMS algorithm takes a large number of iterations, and hence the convergence takes much more time. The RLS algorithm takes a less number of iterations, and hence it has fast convergence rate. From this analysis we conclude that the RLS output forms than the LMS algorithms for micro strip uniform linear array. We started the work by analyzing different algorithms and further proceeded with the objective of improving the beam characteristics by modifying the algorithms. The various Adaptive algorithms like LMS and RLS to be implemented using VLSI and comparative analysis have to be made. From the comparative analysis, the best algorithm with improved performance may fulfill the needs of the future cellular communication networks

7. REFERENCES

[1] Anamika Rathore, Debendra Kumar Panda:DRLMS,DFELMS,LMS Adaptive Beamforming Algorithms for Smart Antenna System.In: IEEE, International Conference on Information, Communication, Instrumentation and Control (2017).

[2] M. Chryssomallis:Smart antennas.In: IEEE Antennas and Propagation Magazine, Vol. 42, No. 3, pp. 129-136, June.(2000).

[3] R. Martínez, A. Cacho, L. Haro, and M. Calvo: Comparative study of LMS and RLS adaptive algorithms in the optimum combining of uplink W-CDMA.In:IEEE, pp. 2258-2262(2002).

[4] E. Ramprasath, P. Manojkumar, P. Veena “Analysis of Direct Current Motor in LabVIEW”, World Academy of Science, Engineering and Technology, 2015

[5] S. Lim, C. H. Yoo, and S. Kim: Performance evaluation of beamforming using pilot channel in CDMA2000 reverse link.In: IEEE VTC, pp. 2740-2744, 2001.

[6] Y. Yasui, S. Kobayakawa, and T. Nakamura: Adaptive array antenna for W-CDMA systems.In: FUJITSU Sci. Tech. Journal, Vol. 38, No. 2, pp. 192-200(2002).

[7] Sivaraman, P “A New Method of Maximum Power Point Tracking for Maximizing the Power Generation from a SPV Plant” Journal of scientific and Industrial Research Vol.74, No.3 pp.411 - 415 AUG 2015.

[8] Manojkumar P Veena P and Jeyabharath R 2019 Sustainable development of universal electronic control unit for fuel saving in automobiles to protect the environment pollution Journal of Electrical Engineering Vol 19.

[9] Monson H. Hayes : Statistical Digital Signal Processing and Modeling.In:John Wiley & Sons Inc.(2004)

[10] Constantine A Balanis: ANTENNA THEORY, Analysis and Design - Second Edition, John Wiley & Sons Inc.(2005)

[11] Shubair R.M :Robust adaptive beamforming using LMS algorithm with SMI Initialization.In: IEEE Transactions on Antennas And Wireless Propagation, vol.2, pp 34-35.(2005)

[12] E. Ramprasath, P. Manojkumar and P. Veena, "Induction motor analysis using labview", Proceeding on International Conference on Electrical Engineering and Technology, vol. 2, no. 5, pp. 498, 2015.

[13] Shahera, Mohammad and Seiichi “Adaptive Beamforming Algorithms for Smart Antenna Systems” International Conference on Control, Automation and Systems 2008 Oct. 14-17, 2008 in COEX, Seoul, Korea.(2008)

[14] R. S. Kawitkar and D. G. Wakde, “Smart antenna array analysis using LMS algorithm”, IEEE Int. Symposium on Microwave, Antenna, Propagation and EMC Technologies for Wireless Communications, pp. 370-374, 2005.